

Volume 12 • No 2 • Dec. 2024 • p-ISSN: 2410-9355 • e-ISSN: 2307-549X

# ARO

The Scientific Journal of Koya University



ARO - DOI: 10.14500/2307-549X

Indexed by WoS-ESCI

## **ARO-The Scientific Journal of Koya University**

ARO, meaning "Today" in Hewramí Kurdish, is an esteemed international scientific journal proudly published by Koya University with the following identifiers: p-ISSN: 2410-9355, e-ISSN: 2307-549X, and DOI: 10.14500/2307-549X. As a reputable open-access peer-reviewed journal, ARO is dedicated to publishing original scientific research, global news, and insightful commentary. Recognized for its impact in the academic community, ARO Journal has been awarded an Impact Factor by WoS-ESCI and covers diverse areas of Multidisciplinary Sciences, welcoming both original research articles and review articles. Notably, ARO Journal is committed to providing free access to its content and proudly boasts the absence of both APC (Article Processing Charges) and ASC (Article Submission Charges) fees.



### **ARO Executive Publisher**

Dr. Mohammed H. Zangana; President of Koya University and the Executive Publisher of ARO.

### **ARO Editor-in-Chief**

Dr. Dilan M. Rostam; Editor-in-Chief and member of the Senior Executive Editorial Board.

### **ARO Co-Editor-in-Chief**

Prof. Salah I. Yahya; Co-Editor-in-Chief and member of the Senior Executive Editorial Board.

### **ARO Editorial Board**

ARO takes pride in its robust and dedicated Editorial Board, comprising a distinguished twelve-member Senior Executive Editorial Board and a dynamic six-member Associate Editorial Board, both instrumental in shaping journal policies and ensuring editorial excellence. Additionally, ARO benefits from a highly esteemed Board of Reviewing Editors, consisting of over 250 prominent scientists from diverse fields. Their invaluable expertise and rigorous peer-review process contribute to the high standards and credibility of ARO, making it a leading platform for disseminating original scientific research, global news, and insightful commentary. The ARO editorial group consists of: Senior Executive Editors and Editorial Advisory Board.

### **Senior Executive Editors**

Dilan M. Rostam, Salah I. Yahya, Fahmi F. Muhammad, Wali M. Hamad, Jorge Correia, Fouad Mohammed, Jacek Binda, Nadhir Al-Ansari, Howri Mansurbeg, Tara F. Tahir, Yazan A. Khaleel, Mohammad Gh. Faraj, and Sahar B. Mahmood.

### **Editorial Advisory Board**

Halgurd S. Maghdid, Farid Zubir, Abdulbasit K. F. AL-Talabani, Hamed M. Jassim, Saeed Roshani, Ikbal M.G. Tahir, Leila Nouri, Saddon T. Ahmad, Layth I. Abd Ali, Basim M. Fadhil and Ali Al-Wakeel.

### **This Issue Reviewers**

Abdolhamid Zahedi, Abdulbasit K. Al-Talabani, Adil M. Hussein, Ahmed A. Nafea, Akeel M. Kadim, Ali Al-Wakeel, Alia K. Abdulhassan, Ameen Hadi, Anmar Altaie, Askander K. Kaka, Bushra K. Oleiwi, Bushra Shnawa, D. Rajaraman, Dalal Sinjare, Emad K. Zangana, Eman D. Arif, Fadhil Saeed, Fahmi F. Muhammadsharif, Farhang Awlqadr, Gholam H. Roshani, Haithem T. Mohammed Ali, Halgurd S. Maghdid, Hardi Mohammed, Hassan Bayram, Hassan H. Abdallah, Hijran S. Jabbar, Iman Abduljaleel, Ismail R. Mohammed, Jabbar Qaradaghi, Jehan Sheikhsuleimany, K. Raja, Katan S. Ali, M. Bindhu, Mudhafar Jassim, Mustafa Sibahee, Pshtiwan T. Jaf, Rebaz A. Omer, Saad Sultan, Saba Inam, Saddon T. Ahmad, Saeedeh Lotfi, Saif Manji, Salah I. Yahya, Sarah Mohammed, Sewgil Anwer, Shahab Kareem, Shaker Qaidi, Shamsa Kanwal, Shaymaa F. Al-kubaissy, Srwa A. Mohammed, Tara F. Tahir, Thamer Mohammed, V. Gokula Krishnan, Venus Akef, Viðar Guðmundsson, Yazan A. Khaleel, and Zainab Bahrani.

**ARO Editorial Web and New Media:** Dilan M. Rostam and Salah I. Yahya

**Secretarial Office of the Journal:** Kenana N. Ibrahim

ARO is a distinguished online open access scientific journal that releases hardcopies biannually. All published articles are freely accessible online under the Creative Commons Attribution License (CC-BY-NC-SA 4.0). It is important to note that the responsibility for the content lies solely with the authors and not with ARO or Koya University.

**ARO the Scientific Journal Office**  
Koya University, University Park  
Danielle Mitterrand Boulevard, Koya KOY45  
Kurdistan Region - F.R. Iraq

**E-mail:** [aro.journal@koyauniversity.org](mailto:aro.journal@koyauniversity.org)

**url:** [aro.koyauniversity.org](http://aro.koyauniversity.org)

December 2024

# ARO

The Scientific Journal of Koya University

Vol XII, No 2(2024)

## Contents

<b>Aro Editorial Words</b> .....	iv
<b>Abdulrazak A. Mohammed, Ghassan A. QasMarrogy</b> .....	1
Thermal Dynamics in Optical Networks: Analyzing Spectral Bandwidth Reduction and Signal Distortion	
<b>Rebaz A. Omer, Karzan M. Ahmed, Khdir A. Othman, Wali M. Hamad, Rahman K. Faraj, Ali J. Muhialdin, Shalaw K. Salih</b> .....	10
New Thiazole Derivatives: Potent Antifungal against <i>Candida albicans</i> , with silico Docking Unveiling Key Protein Interactions	
<b>Adeeb O. Jafir, Mohammed I. Hussein, Idrees A. Nadir, Barzan N. Sabr, Ali H. Ahmed</b> .....	23
Assessment of Radioactivity in Building Materials: Implications for Health in Kurdistan Region of Iraq	
<b>Madeh I. Hamakareem , Daban A. Muhedin , Ahmed J. Hama Rash, Sangar J. Qadir, Loghman Khodakarami</b> .....	33
Toward Optimizing Coarse Aggregate Types and Sizes in High-strength Concrete	
<b>Yara Aboasfour, Lígia Nunes</b> .....	44
The Recovery of Historical Buildings in Post-war Aleppo	
<b>Aso K. Ameen, Dler H. Kadir, Dana A. Abdullah, Ismail Y. Maolood, Hewir A. Khidir</b> .....	52
Assessing E-Government Effectiveness: A Structural Equation Modeling Approach	
<b>Moneer A. Lilo, Abidulkarim K. Yasari, Mustafa M. Hamdi, Abdulkareem D. Abbas</b> .....	61
Transmission Power Reduction Based on an Enhanced Particle Swarm Optimization Algorithm in Wireless Sensor Network for Internet of Things	
<b>Myasar Kh. Ibrahim, Shireen R. Mohammed</b> .....	70
Synthesis Development and Molecular Docking Study of New Azo Chalcone Derivatives	
<b>Zena M. Saadi, Ahmed T. Sadiq, Omar Z. Akif</b> .....	79
Graphical User Authentication Algorithms Based on Recognition: A survey	

<b>Mais A. Al-Sharqi, Ahmed T. Sadiq, Safaa O. Al-Mamory</b> .....	94
Flexible Job Shop Scheduling Problem-Solving Using Apiary Organizational-Based Optimization Algorithm	
<b>Ata O. Salih, Diary A. Al-Manmi</b> .....	107
Strategies for Sustainable Water Management: Hydrochemical Profiling and Protection Zone Design in Rania Basin, Iraq	
<b>Arsalan R. Mirza, Abdulbasit K. Al-Talabani</b> .....	119
Time Series-Based Spoof Speech Detection Using Long Short-Term Memory and Bidirectional Long Short-Term Memory	
<b>Hanaa A. Muhammad, Hikmat M. Masyab, Bakhtyar A. Othman, Yaseen N. Mahmood</b> .....	130
Micropollutant Control in Wastewater Treatment: A Review of Harnessing Nitrification and Denitrification Biotransformation of Micropollutant	
<b>Bahareh Vaisi, Hiwa Farughi, Sadigh Raissi</b> .....	139
Data Envelopment Analysis-based Scenario Selection for Sequencing Pattern in a Simulated Robotic Cell	
<b>Gulan S. Qadir, Amer T. Al-Tae, Nabeel S. Othman</b> .....	148
Dual Electrochemical Methods for Determination of Anesthetic Procaine: Square Wave Voltammetry and Differential Pulse Polarography	
<b>Rawan S. Alsheikh, Etimad A. Fadel, Nadine T. Akkari</b> .....	157
Distributed Software-Defined Networking Management: An Overview and Open Challenges	
<b>Abdulilah M. Mayet, Salman A. Mohammed, Shamimul Qamar, Hassen Loukil, Neeraj K. Shukla</b> .....	167
AI-Based Evaluation of Homogeneous Flow Volume Fractions Independent of Scale Using Capacitance and Photon Sensors	
<b>Dhurgham K. Al-Fahad, Jawad A. Alpofead, Mahmoud A. Chawsheen, Ahmed A. Al-Naqshbandi, Ali T. Abas</b> .....	179
Surveillance of Antimicrobial Resistance in Iraq: A Comprehensive Data Collection Approach	
<b>Deldar M. Abdulah, Burhan A. Zaman, Zuhair R. Mustafa, Lokman H. Hassan</b> .....	194
Artificial Intelligence Integration in Academic Writing: Insights from the University of Duhok	
<b>Sobhan Roshani, Salah I. Yahya, Shahram Khazaei, Saeed Roshani, Babak Karami</b> .....	201
Design and Fabrication of a Microstrip Low-Pass Filter with a Wide Stopband Using a Windmill-Shaped Resonator	
<b>Hikmat M. Masyab</b> .....	209
Sonication Enhancement of Capsaicin Formation in Callus of Chili Pepper, <i>Capsicum annum</i> L.	
<b>Rebaz A. Omer, Khdir A. Othman, Yousif H. Azeez, Aryan F. Qader</b> .....	216
Computational Insights into the Electronic, Optical, and Reactivity Behavior of Halogenated Phenanthrene Derivatives	

<b>Aza B. Taha</b> .....	229
Helicobacter pylori Infection Associated with Type 2 Diabetes: A Case–Control Study	
<b>Ameer K. Jawad, Gholamreza Karimi, Mazdak Radmelkshahi</b> .....	234
A Novel Digital Audio Encryption Algorithm Using Three Hyperchaotic Rabinovich System Generators	
<b>Srwa A. Mohammed, Taha J. Omar, Ayad H. Hasan</b> .....	246
Fungal Population Analysis of Hydrocarbons Contaminated Soil: Samples from Taq-taq Oil Field in Koya City, Kurdistan Region, Iraq	
<b>Yousif T. Maarroof, Idrees B. Qader, Hani K. Ismail, Hardi Q. Hamad, Sardasht R. Taher</b> .....	254
Extraction of Sulfur Compounds from Model Petroleum Products using Fe <sub>3</sub> O <sub>4</sub> Nanoparticles and Acetic Acid-1-Butyl-3-Methylimidazolium Chloride based on Deep Eutectic Solvents	

## ARO Editorial Words

Dear Esteemed Readers,

It is with great pride and enthusiasm that we present to you the 23rd issue of Aro – The Scientific Journal of Koya University. This latest edition reflects the growing recognition and impact of Aro as a trusted platform for advancing scientific knowledge. Our journal has reached notable milestones, including 1,440 citations on Google Scholar with an h-index of 15, alongside 650 citations tracked by Web of Science (Clarivate Analytics). These achievements highlight the commitment of our contributors, reviewers, and editorial board to maintaining the highest standards of academic publishing.

Aro's success is a collective testament to the dedication and collaboration of our scholarly community, both locally and internationally. As a leading journal in the Kurdistan Region of Iraq and beyond, we are honored to contribute to the dissemination of research that addresses critical challenges, fosters innovation, and inspires new directions in science and engineering.

This issue features 26 diverse publications, with significant contributions in fields such as chemistry, physics, artificial intelligence, electrical engineering, and microbiology. These articles embody the multidisciplinary essence of Aro and demonstrate the caliber of work that our platform continues to attract.

As we celebrate our achievements, we remain committed to furthering excellence. Aro is continually evolving to expand its scope, refine its peer-review process, and foster a vibrant academic community. We encourage researchers from diverse disciplines and regions to share their pioneering work with us, confident that Aro offers a platform that amplifies their impact and connects them to a global audience.

We express our deepest gratitude to our authors for entrusting us with their valuable research, and to our reviewers for their meticulous and constructive evaluations. Your contributions are the cornerstone of Aro's success and reputation as a journal of integrity and quality.

As part of our mission, Aro remains steadfast in its commitment to open access, ensuring that research is freely available to academics, professionals, and the public worldwide. By providing this accessibility, we aim to foster collaboration, inspire innovation, and contribute to the advancement of society.

Looking ahead, we are excited about the opportunities to further enhance Aro's role as a hub for scholarly excellence. Together, let us continue to shape the future of research and knowledge dissemination.

**Dilan M. Rostam**

*Editor-in-Chief*

**Mohammed H. S. Zangana**

*Executive Publisher*

**Salah I. Yahya, Fahmi F. Muhammad, Wali M. Hamad, Jorge Correia, Fouad Mohammed, Jacek Binda, Nadhir Al-Ansari, Howri Mansurbeg, Tara F. Tahir, Yazan A. Khaleel, Mohammad Gh. Faraj and Sahar B. Mahmood.**

Executive Editorial Board Members

# Thermal Dynamics in Optical Networks: Analyzing Spectral Bandwidth Reduction and Signal Distortion

Abdulrazak A. Mohammed<sup>1</sup> and Ghassan A. QasMarrogy<sup>2†</sup>

<sup>1</sup>Department of Communication and Computer Engineering, Faculty/College of Engineering/Cihan University-Erbil, Kurdistan Region, F.R. Iraq

<sup>2</sup>Department of informatics and Software Engineering, Cihan University-Erbil, Kurdistan Region, F.R. Iraq

**Abstract**—The signal distribution of any fiber-optic network system is an important factor in optical communication, which determines the quality of the optical signal transmission. One of the important effects is the temperature degrees; that effect is on the main parameters of optical communication (of which the fiber optic is the main part). The main material in fiber optics is glass. And as is well known, temperature has a strong effect on the glass, especially the core of fiber optics, because the structure of fiber optics contains several glass layers with different refractive indexes. Hence, in the present article, the effect of temperature on the optical signal and other components of the optical network system has been analyzed and studied. The analysis includes aberration, dispersion, and distortion of the optical network communication signal. The result has been discussed and analyzed for variables in the BW of the spectral when the temperature changed.

**Index Terms**—Aberration, Dispersion, Fiber-optic's networks, Optical signal transmission, Temperature effects.

## I. INTRODUCTION

The effect of temperature on the communications system is a clear and real fact due to the environmental condition of the optical system field (Ghassemlooy et al., 2019). The different temperature degrees have an important effect (The range between (heating) high temperatures and (freezing) low temperatures). It is very important to measure the effect of thermal on each part of the fiber-optic communication system: transmitter (light source), link (fiber optics), and receiver (photo detector), as shown in Fig. 1 (Winzer, 2014).

There are several sources of thermal effects; it depends on the components of the optical communication system. In other words, the effect of the thermal effect depends on many factors, such as the type of component materials, the duration of the

thermal effect on the optical signal, and the way of the effect (direct or indirect) on the optical components (Yang et al., 2011).

In the present paper, the effect of a variable temperature degree on the optical signal (during analyzing the effect of thermal on the optical components) has been simulated and analyzed. The result factors (of optical signal) that have been analyzed are aberration and dispersion. Which also the result can show the quality of the optical signal and the reduction of it due to the thermal effect analyzed on the image plane. The seriousness of this research is to show the thermal effects on the optical signal of the fiber-optic communication network and to design a fiber-optic network with a minimum loss (as possible) in the optical signal.

This paper gives a better understanding of rising data transmission needs, the impact of temperature variations on data transmission, the advancements in network design, and the prediction of the modeling of fiber-optic networks. The present paper is structured into paragraphs. Paragraph two presents the related work about the thermal effect; Paragraph three presents the optical network structure; Paragraph four explains the main fiber optic and thermal effects; and Paragraph five shows the results and analysis. In the final sixth paragraph, the conclusion and future work of the paper were presented. Most previous researchers have studied the effect of thermal energy on the optical system or the general properties of the optical communication system. However, this article works on the properties of optical signals, such as bandwidth dispersion and intensity distribution at the image plane of the optical system.

## II. RELATED WORK

In recent years, many researchers have conducted a different type of simulation on the thermal effect on the fiber-optic signal. In Ref. (Fokoua et al., 2018), the author plains the reactivity of thermal delay of propagation and phase in fiber optics with a band of hollow-core photonic, where the results showed that the propagation delay is complete delay in sensitive to variation temperature degrees. In Ref. (Fokoua et al., 2019), the propagation delays thermal response and the hollow-core photonic band gap fiber phase accumulated through adequate fiber design with explanation, and the result shows the extraordinary prospects given by this exotic

ARO-The Scientific Journal of Koya University  
Vol. XII, No. 2 (2024), Article ID: ARO.11395. 9 pages  
DOI: 10.14500/aro.11395

Received 10 September 2023; Accepted 30 June 2024

Regular research paper: Published: 25 July 2024

<sup>†</sup>Corresponding author's e-mail: ghassan.qasmarrogy@cihanuniversity.edu.iq

Copyright© 2024 Abdulrazak Abdulsalam Mohammed and Ghassan A. QasMarrogy. This is an open-access article distributed under the Creative Commons Attribution License (CC BY-NC-SA 4.0).



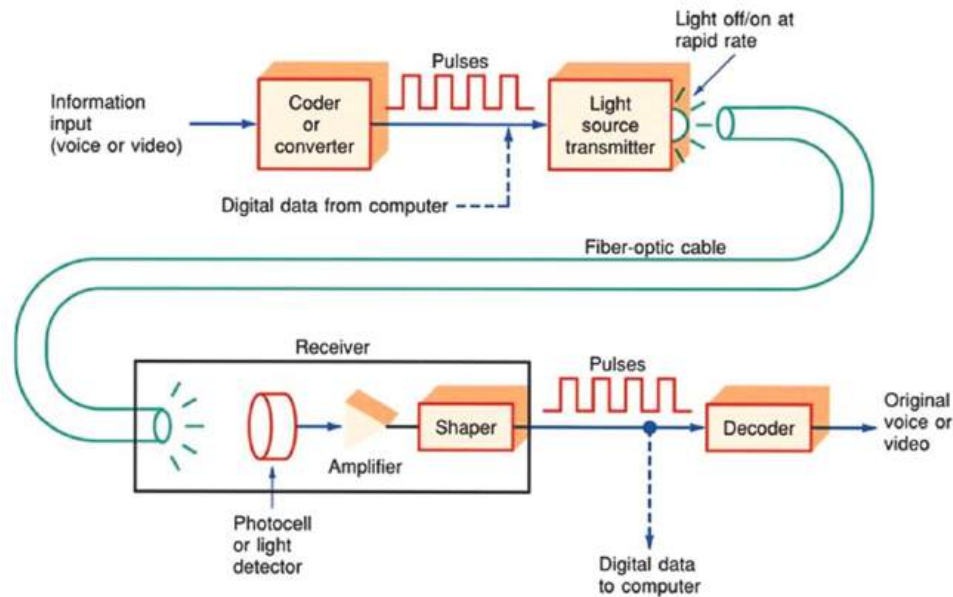


Fig. 1. Fiber optics communication system (Winzer, 2014).

property. In Ref. (Clark et al., 2019), the author shows more temperature tolerance variation using hollow-core in very fast fiber-optical communication systems, and the results show the transmission of error-free short packets with less than 625 ps clock recovery time in 25.6 gb/s real-time systems. Finally, in Ref. (Zhu et al., 2019), a comparison was held between the standard single-mode fiber (SMF-28) and the sensitivity of the thermal phase for hollow-core fiber (HCF) 180°C up to room temperature. The results show that temperature changes affect the thermal phase sensitivity of fibers without any coating, whereas HCF is fully insensitive to small temperature fluctuations.

### III. OPTICAL NETWORK STRUCTURE

This section will present a fully comprehensive discussion of the optical fiber network structure and its properties.

#### A. Properties of Optical Signal Distribution

As usual, the light is the main source of the fiber optics, which generates the optical signal, where the light is an electromagnetic wave as a part of the electromagnetic spectrum. The main characteristics of electromagnetic waves are wavelength, frequency, and energy. The electromagnetic spectrum contains light waves (visible light), radio waves, microwaves, infrared rays, UV rays, Gama rays, and x-rays (Gurevich et al., 2018). Fig. 2 shows the various bands of light waves, such as the ray (incoherent) or beam (coherent) (Zhang et al., 2019).

The propagation of the light distribution through the medium counts on Snell's Law, by describing the refraction relationship between two materials' different refractive indexes, as shown by equation (1) (Stigloher et al., 2016).

$$n_1 \sin \phi_1 = n_2 \sin \phi_2 \quad (1)$$

Where  $n_1$  and  $n_2$  are refractive index for incident medium1 and refracted medium2, respectively,  $\phi_1$  and  $\phi_2$  are incident angle and refracted angle, respectively, as shown in Fig. 3 (Xu et al., 2019). Hence, the light will be distributed among

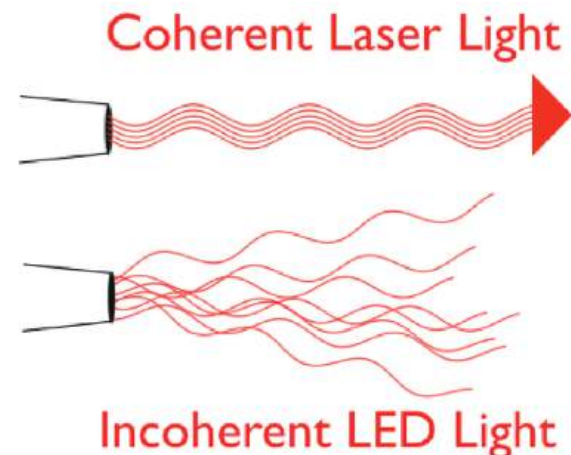


Fig. 2. Coherent versus incoherent light wave (Zhang et al., 2019).

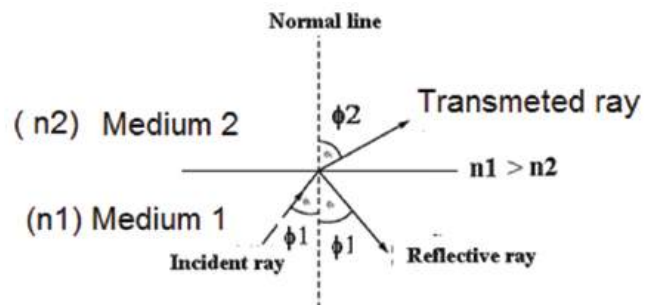


Fig. 3. Light ray behavior (refraction and reflection at a material surface (Xu et al., 2019)).

the several materials, and this distribution depends on the variable value of the incident angle of the light layers (material).

The principle of light travel in any material depends on how fast it travels, whether it is insulating or dielectric on entering. Hence, the light goes through any material at a



slow speed, and the percentage of this decrease depends on the value of the refractive index material of the medium. The speed of light in the material denoted by ( $v$ ) is less than the speed of light in a vacuum ( $c$ ). Moreover, the ratio of light speed in the vacuum over the light speed in the material will give a value of the refractive index ( $n$ ) of the material as given by equation (2) (11).

$$n = \frac{c}{v} \tag{2}$$

**B. Light Behavior and Dispersion**

When the incident angle increases, the refracted angle will also increase until the refracted ray is parallel to the horizontal axis, and any increase after that will result in total reflection and the angle called the critical angle. This case is called total internal reflection (Martin-Fernandez et al., 2013), as shown in Fig. 4.

This case happens in the fiber optics, whereas the light transmuting throws it; therefore, there will be multiple refractions and reflections that produce an aberration and dispersion in the optics signal. To understand the dispersion, we have to imagine two light rays incident on the fiber with different incident angles (ray B perpendicular on the fiber into the center of the fiber (core) and ray A inclined), whereas the fiber has multi-material (refractive index); therefore, the two rays will move inside the fiber, but with the various optical

paths, that means the ray A will reach the end fiber faster than ray B. Due to this, the different separation between ray A and ray B is called dispersion (Potsaid et al., Thorlabs Inc., 2015), as it is shown in Fig. 5.

The fiber optic has a different layer of refractive index, distributed as a radial distribution; therefore, when light is incident on the fiber, it will move inside the fiber (by multiple refractions) until it reaches the end with dispersion. Because each ray has its own optical path and they will not be reached (to the end of the fiber) at the same time, the difference in the time of the ray moving is equal to  $\Delta t$  (Keiser, 2006), so  $\Delta t$  is equal to:

$$\Delta t = \frac{Ln_1}{(cn_2)(n_1 - n_2)} \tag{3}$$

Where  $n_1$  and  $n_2$  are the refractive indexes of the first and second materials,  $L$  is the length of the fiber optics, and  $S$  is the speed of the light in the vacuum.

In general, the dispersion will be various in fiber optics, whether it is single-mode or multi-mode fiber (which are two types of fiber optics) (Sabitu et al., 2019), as shown in Fig. 6.

**C. Fiber-Optical Communication Network**

The components of fiber optics will be of two types: Active and passive, such as an optical amplifier, coupler, splitter, and multiplexer (Wavelength Division Multiplexing [WDM] and DE). The difference between passive optical

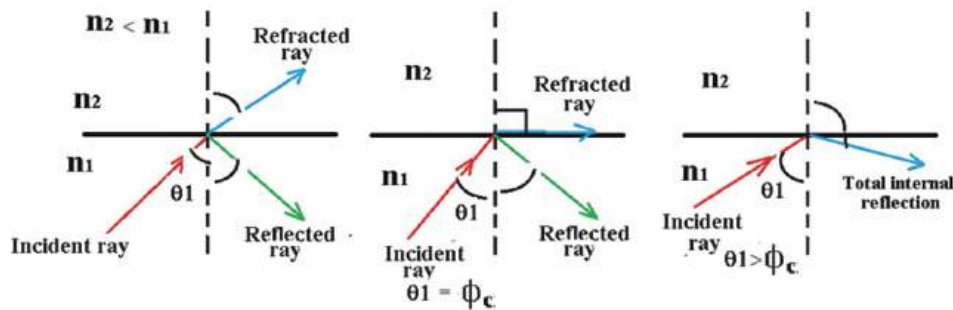


Fig. 4. A critical angle behavior (Martin-Fernandez et al., 2013).

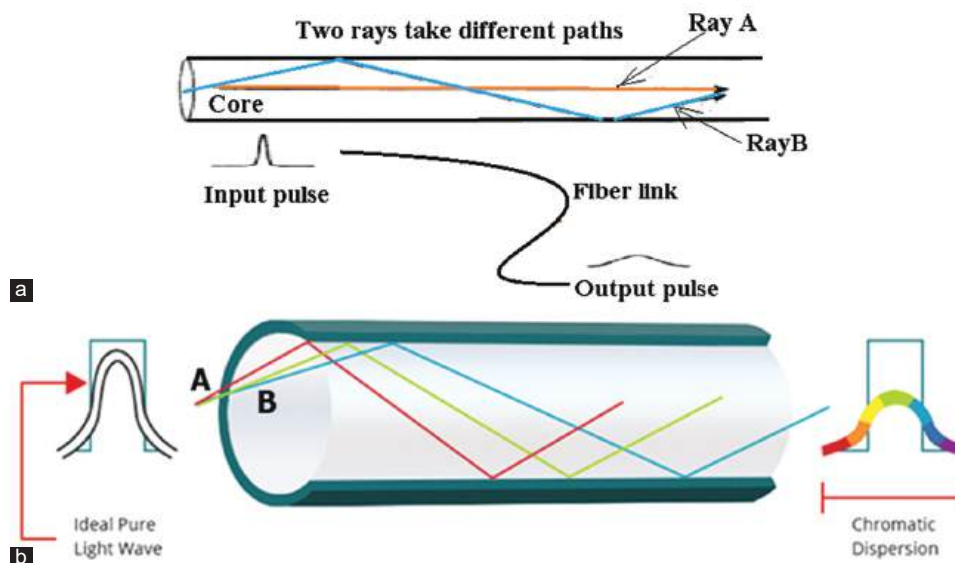


Fig. 5. Dispersion in fiber optics (Potsaid et al., Thorlabs Inc., 2015).

components and active optical components is that the passive will work without external power, whereas the action will not work without external power (Agrawal 2012).

The network is important to share resources and digital information (Marrogy, 2020). For a long period, a fiber-optic network is used to transmute large-capacity information. Moreover, backbone networks use optical fibers due to their ability to transmit high-speed data of more than 10,000 Mbps (10 Gbps) and provide very high spectrum bandwidth.

The network of fiber optics has been used across the countries to transmute huge amounts of information, as well as the fiber-optic network, which is used in many fields and areas such as broadcasting, military, space, and industry. Fig. 7 shows the optical fiber communication networks (Lam et al., 2010).

#### D. Fiber-Optic Routers

To connect networks with different local area networks, routers are needed to join and merge various subnets with IP addresses counting on the network. There are different types of routers depending on their purpose, such as core, enterprise, edge, branch, and routing protocols (Qasmarrogy and Almashhadani, 2020).

A router of fiber looks like a gateway that connects two or more networks. There is no limitation to using several routers; it may be possible to use 100 routers or repeaters in one package, such as the OSI model, and usually, a router will be in layer 3 of the optical link layers.

Mainly fiber routers connected to ISP modems. They are used to connect the backbone of the internet as they have fast port connections and can forward a huge amount of data between networks, whereas a wireless router can be connected to standard devices.

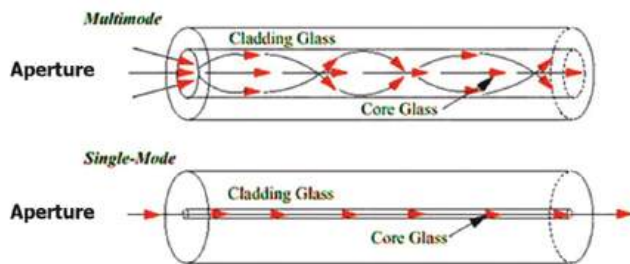


Fig. 6. Structure of fiber optics mode (Sabitu et al., 2019).

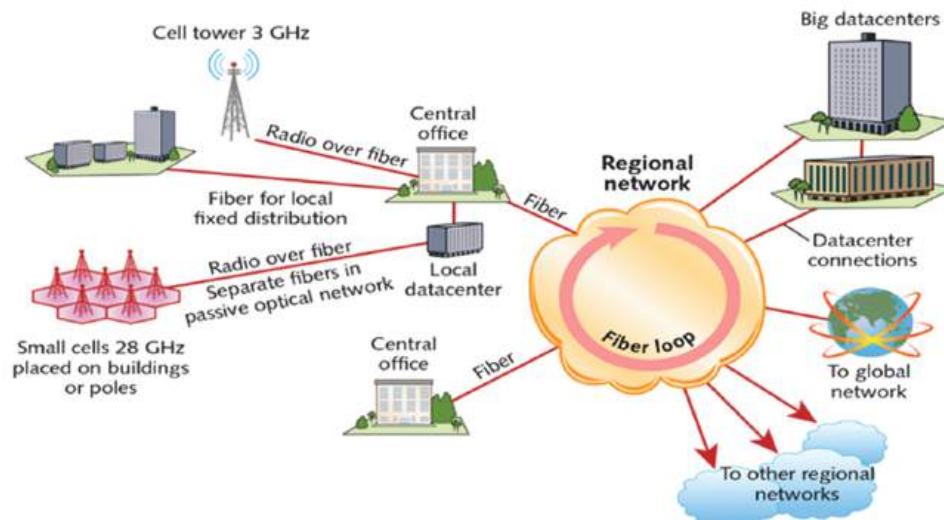


Fig. 7. Fiber optics networks (Lam et al., 2010).

#### E. WDM System

The WDM is a type of optical multiplexer that is a wavelength deviation multiplexer and is used with optical communication. Its basic structure is shown in Fig. 8. It offers a boost to the transmission capacity of the fiber. The function of WDM is to accept multiple independent wavelength sources (with a small difference between them) and then transmit them in one narrow spectral band in the same fiber without any effect on the information. Hence, this processing “sometimes” is called a dense WDM (DWDM).

The advantage of DWDM is that it is wavelength spaced properly to avoid channel interference adjusting because if interference occurs, it produces distortion in the optical signal. This distortion refers to the difference between the beam center wavelength of the light and the characteristics of spectral operating from other optical components (The reasons for this case are the time and temperature). Furthermore, the distortion produces the dispersion or drift in the pulse of the optical signal; if this dispersion is not treated, it will cause the wavelength to trespass into another spectral band region. (Richter et al., 2013). As shown in Fig. 9. The Chromatic WDM Application on FTTH with a Guard Band Between Wavelength Channels as an operations safety factor.

#### F. Fiber-Optic Cable

Fiber-optic cable contains several single fibers, whereas each single fiber structure is from the center (middle of the fiber) a core surrounded by cladding and then buffer coating (jacket). The core is made of a sort of glass (number of layers; each layer has a value of the refractive index ( $n$ ), distributed as radially as shown in Fig. 10), which illustrates a cable of optical fiber with six suboptical cables (called loose tubes) that contain six optical fibers with a diameter of  $250 \mu\text{m}$ . Hence, the light (with information) will be transmitted in every single optical fiber inside the core by optical carrier waves, whereas the cladding keeps the optical signal inside the core by processing what is called total internal reflection, as shown in Fig. 11 (Chang, Senko Advanced Components Inc., 2016).

When the light travels in fiber optics, some of the speed will be changed due to the rays' refraction during passing through the variable refractive index ( $n$ ) of the material, according to Snell's law (eq. (1)), where  $n$  is the ratio

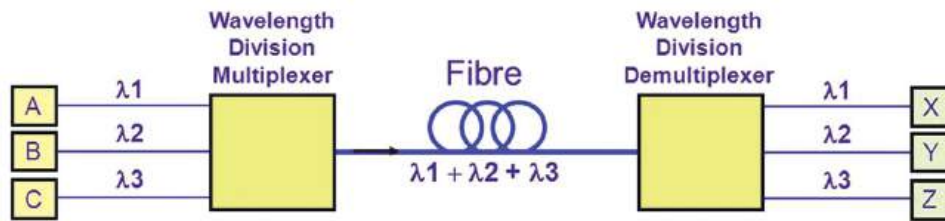


Fig. 8. WDM technology diagram (Winzer, 2012).

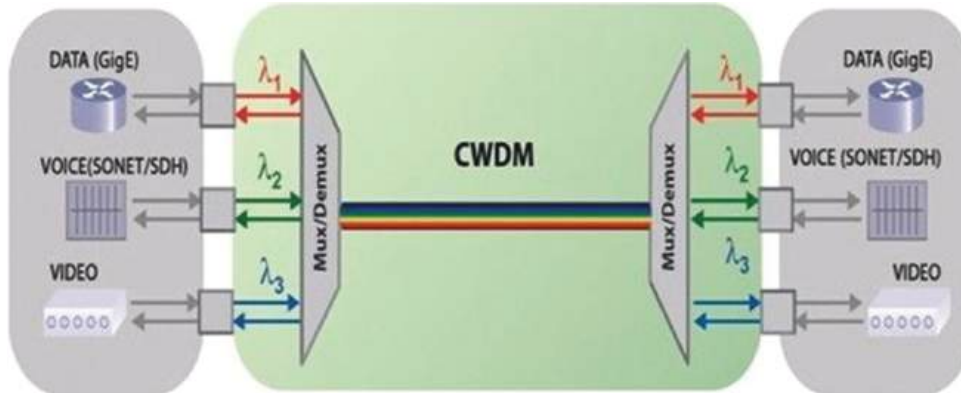


Fig. 9. CWDM application on FTTA (Richter et al., 2013).

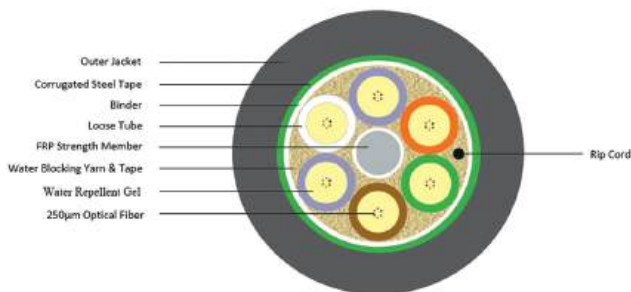


Fig. 10. Layers of pica fiber cable (Chang, Senko Advanced Components Inc., 2016).

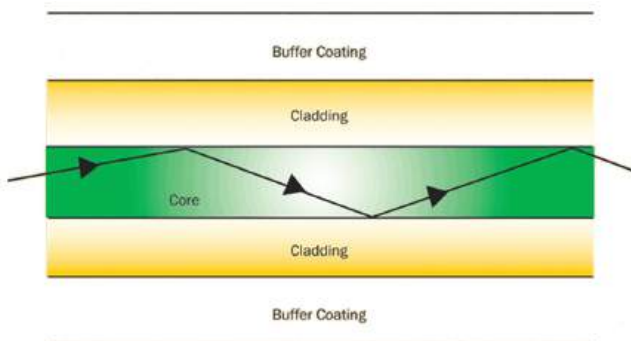


Fig. 11. Transmitting of optical signal in a fiber optic by applying refraction and reflection laws (Chang, Senko Advanced Components Inc., 2016).

between the speed of light in the vacuum ( $c$ ) and the speed of the light in the material ( $v$ ). As usual, the speed of the light will be reduced because the light will intersect with the particles (molecules) of the materials. This reason will produce some absorption, and the others will be scattered.

In this case, it is fair to treat it using an optical amplifier to raise the power and re-transmitting the optical signal again into the fiber optics, as shown in Fig. 11.

#### IV. FIBER OPTIC AND VARIABLE TEMPERATURE EFFECTS

The effect of variable temperature degrees will be on the thermal expansion value of the optical component material, that is, it affects the shape coefficient ( $q$ ) and position coefficient ( $p$ ) (Jamieson, 1981).

Whereas ( $q$ ) depends on the radius of curvature value for the optical component surface and ( $p$ ) depends on the value of the object and image distance (Li et al., 2020).

The change in the values of  $p$  and  $q$  will transfer indirectly to the focal length ( $f$ ) values because any change in the refractive index ( $n$ ) of the optical component material will change the values of  $p$  and  $q$ . Therefore,  $f$  can be calculated from the following equation (Jamieson, 1981):

$$f = \frac{K}{(n-1)} \tag{4}$$

Whereas  $K$  is a geometrical constant, for any variable in the ratio of the variable of refractive index to the variable of focal length, any variable in temperature ( $dT$ ) will be a variable in refractive index ( $dn$ ), which means a change in the speed of the light in the material, which causes more dispersion and distortion (Li et al., 2020). Therefore, (Jamieson, 1981)

$$\frac{\partial f}{\partial n} = \frac{K}{(n-1)^2} \tag{5}$$

Finally, any change in the value of focal length will be a change in the shape of the focal point (causing defocus or a distorted image), the variable in the focal length ( $f$ ) (Jamieson, 1981), as follows:

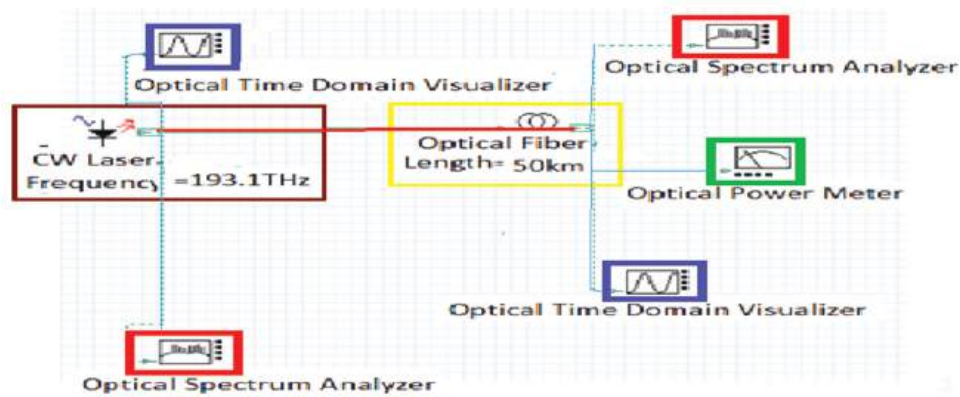


Fig. 12. Practical diagram of optical fiber connection (using Optisystem15).

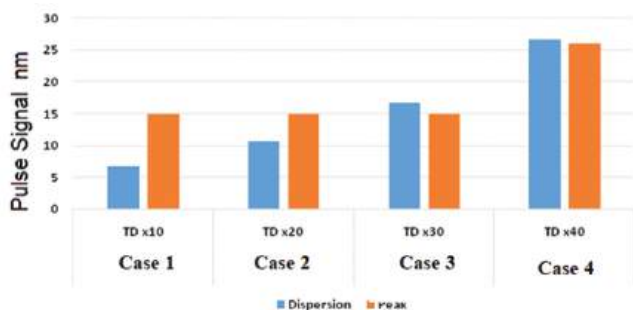


Fig. 13. Dispersion and peak power values.

$$\Delta f = \frac{\Delta n K}{(n-1)^2} \quad (6)$$

## V. RESULTS AND DISCUSSION

Using the simulation program (Optisystem 15) to setup the simulated circuit, as shown in Fig. 12, simulating the circuit with different random values of the dispersion according to variable values of temperature degree. For each run, the output was recorded for both Optical Time Domain Visualize and Optical Spectrum Analyzer, and the simulation parameters are shown in Table I.

Therefore, four main values of dispersions have been taken (according to the value of temperature), as shown in the following Table II.

Figs. 13–15 show the results histogram of Table II data. Fig. 13 shows the relation between dispersion value and peak power with pulse signal for each case (1, 2, 3, and 4). Whereas the Fig. 14 shows the behavior of bandwidth for variable temperatures, and Fig. 15 shows the relationship between pulse signals for variable temperatures.

Fig. 16 shows the spot diagram at the image plane of the fiber optics (we used the simulation program “ZEMAX OpoiticStudio”) for two cases: the first without the temperature effect and the second with the temperature effect. It is the effect of temperature on spot distribution (where the spot is defined as the interaction of the number of rays (output rays) with the image plane, and the size and intensity of the spot depend on the number of rays that interact with



Fig. 14. Bandwidth values.

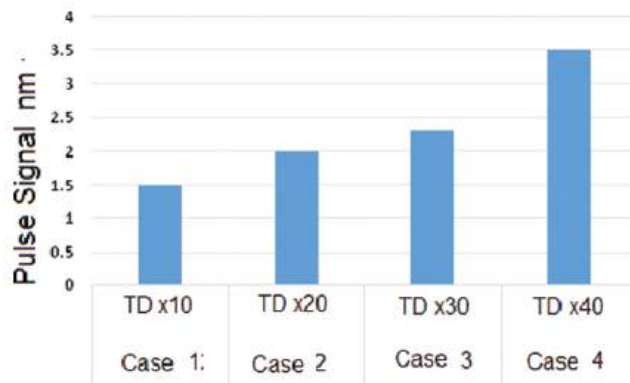


Fig. 15. Pulse signal values.

TABLE I  
SIMULATION PARAMETERS

Parameters	Values
Fiber-optic cable	Single-mode
Fiber-optic length	50 km
Signal frequency	193.1 THz
Sample rate	$64 \times 10^{10}$ H
Sequence length	128 bits
Sample per bit	64
Number of samples	8192
Linewidth	10 MHz

the image plane). Whereas Fig. 17 shows the behavior of spot distribution for cases without a temperature effect,

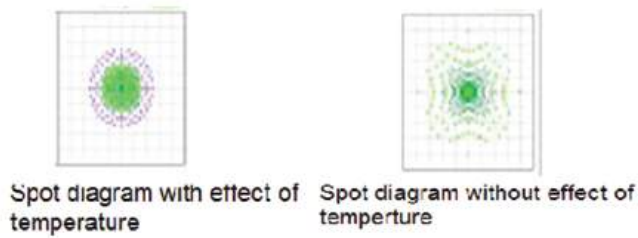


Fig. 16. Spot diagram at image plane (using the simulation ZEMAX).

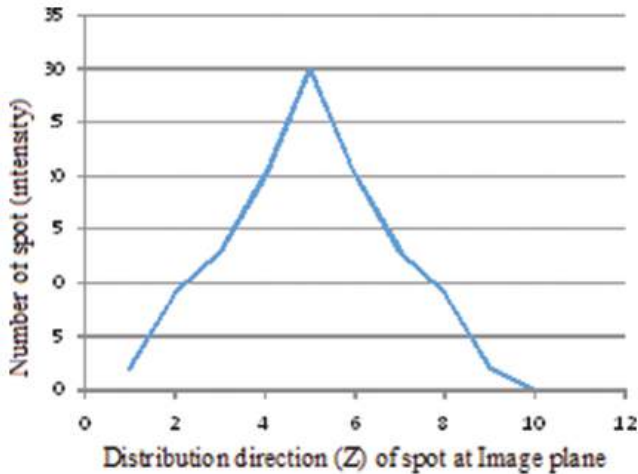


Fig. 17. The spot diagram distribution at image plane without effect of temperature.

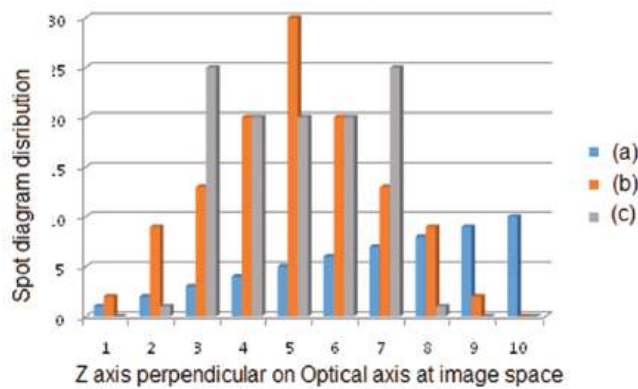


Fig. 18. Histogram shows the spot diagram distribution for (a) linear distribution, (b) normal distribution (without temperature effect), and (c) spot distribution (with temperature effect).

Fig. 18 shows the spot distribution for three cases: the first is for liner distribution, which means the distribution from the outer image plane to the center of it; the second is for a normal spot diagram without a temperature effect; and the third is for spot distribution with a temperature effect.

By analyzing the output of the Figs. 19–22, which are the result of using the simulation program (Optisystem 15). The figures displayed the output of (visualize instruments) “Optical Spectrum Analysis” and “Optical Time Domain.” In Fig. 19, the dispersion value is the minimum value, whereas it increases randomly until Fig. 22 has the maximum value of dispersion. The bandwidth of optical spectrum analysis

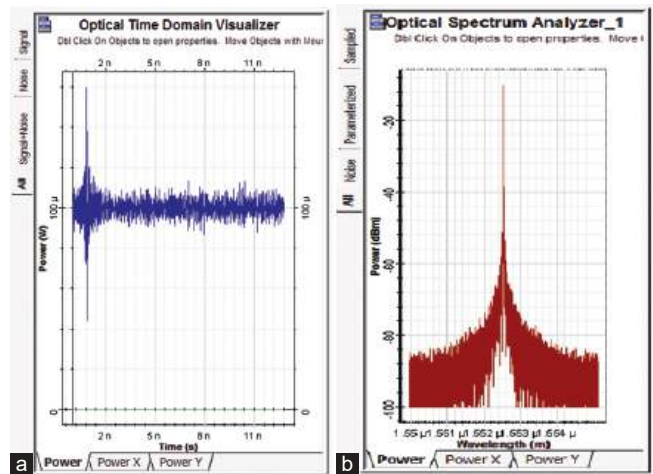


Fig. 19. Case 1 (a) optical time domain visualizer and (b) optical spectrum analyzer (Using Optisystem 15).

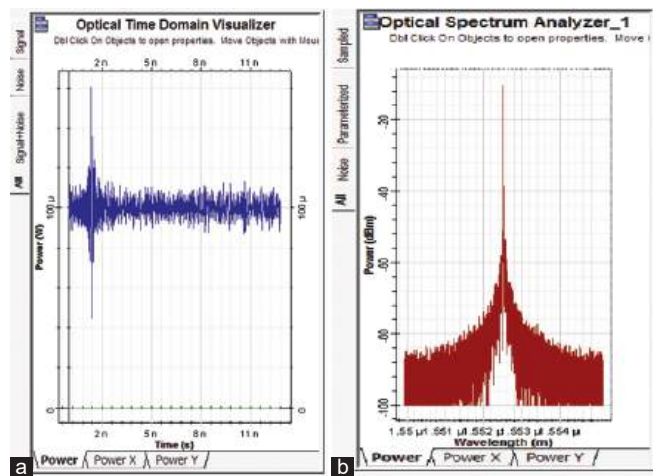


Fig. 20. Case 2 (a) Optical time domain visualizer and (b) optical spectrum analyzer.

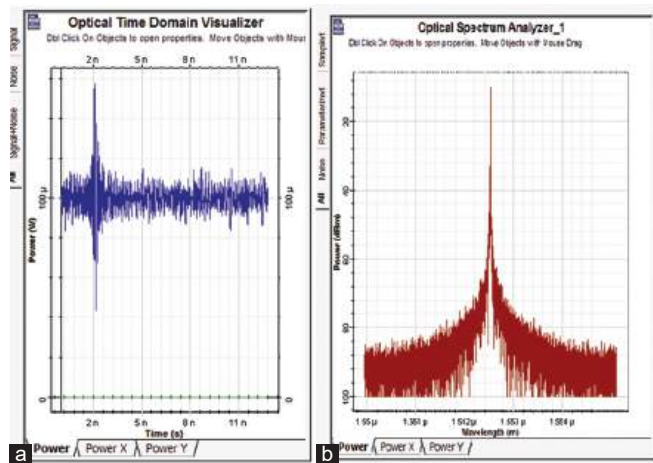


Fig. 21. Case 3 (a) Optical time domain visualizer and (b) optical spectrum analyzer.

is variable, depending on the dispersion value, which was affected by the thermal temperature. And for the “optical time domain,” the pulse of the signal was moved from the minimum value (1.5 nm), as shown in Fig. 19, to get the

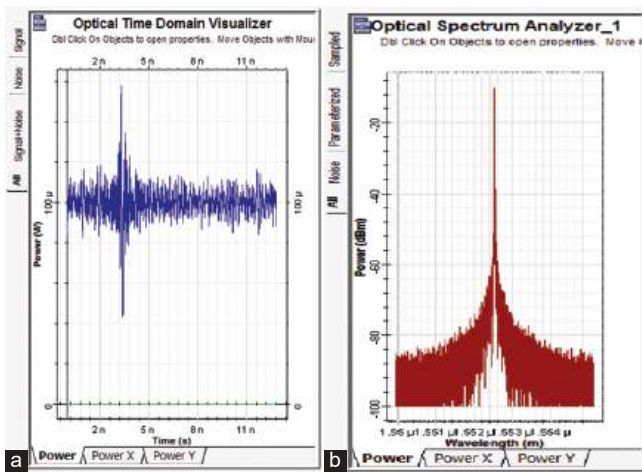


Fig. 22. Case 4 (a) Optical time domain visualizer and (b) optical spectrum analyzer.

TABLE II  
DISPERSION VALUES

Temp. K <sup>o</sup> T <sub>D</sub>	Dispersion	Bandwidth	Peak	Case number	Pulse signal
T <sub>D</sub> ×10	6.75	80%	15	1	1.5 nm
T <sub>D</sub> ×20	10.70	50%	15	2	2 nm
T <sub>D</sub> ×30	16.75	90%	15	3	2.3 nm
T <sub>D</sub> ×40	26.75	75%	26	4	3.5 nm

maximum value in Fig. 22 is 32.5 nm due to the variable value of dispersion.

## VI. CONCLUSION

1. As a conclusion, we can see that the thermal effect on the fiber optics signal takes place during the thermal expansion of the fiber optics material.
2. Of course, the effect of temperature variables on the optical signal distribution is clear during the distribution of the spot diagram.
3. The effect will transfer to the dispersion value of the fiber optics.
4. The effective value of thermal is not clear in fiber optics because there are different types of material (that means different refractive index and different thermal expansion for each one) in fiber optics. The reason for the thermal effect will be distributed between the material layers.
5. The amount of the temperature variable does not linearly affect the fiber optics signal because there are many productions against the extra effect, such as temperature and force.
6. The thermal effect will be less in fiber cable than in single fiber. Because there is a double jacket coating on the cable than in single fiber. Furthermore, there is an outer PVC jacket on the cable.
7. The variable in the dispersion value does not have the same effect on the optical image form as an optical signal. Because the tolerance value of imaging is higher than that of the optical signal. Furthermore, the effect of the dispersion

value (which happens due to the thermal effect) is not clear; for each fiber optics manufacturing, there will be some acceptance value of dispersion that does not affect the optical signal (which is within the manufacturing tolerance).

8. Using the Optisystem simulation program is useful for designing and analyzing optical fiber systems.

Using the ZEMAX optical simulation program is useful for designing and analyzing geometrical optics.

For future work, we suggest implementing all the work practically to test more values and get more realistic results.

## REFERENCES

- Agrawal, G.P., 2012. *Fiber-Optic Communication Systems*. Vol. 222. John Wiley and Sons, United States.
- Chang, J.J.F., and Senko Advanced Components Inc., 2016. *Cable Guide for Fiber Optic Cables*. U.S. Patent No 9, 360, 649.
- Clark, K.A., Chen, Y., Fokoua, E.R.N., Bradley, T., Poletti, F., Richardson, D.J., Bayvel, P., Slavik, R., and Liu, Z., 2019. Low Thermal Sensitivity Hollow-Core Fiber for Optically-Switched Data Center Applications. In: *45<sup>th</sup> European Conference on Optical Communication (ECOC 2019)*. IET, Stevenage, pp.1-4.
- Fokoua, E.N., Petrovich, M.N., Bradley, T., Poletti, F., Richardson, D.J., and Slavik, R., 2018. Ultralow Thermal Sensitivity of Phase and Propagation Delay in Hollow-Core Fibers. In: *2018 23<sup>rd</sup> Opto-Electronics and Communications Conference (OECC)*, United States, IEEE, pp.1-2.
- Fokoua, E.N., Zhu, W., Chen, Y., Ding, M., Poletti, F., Richardson, D.J., and Slavik, R., 2019. Thermally Insensitive Optical Fibres and their Applications. In: *2019 Asia Communications and Photonics Conference (ACP)*. United States: IEEE, pp.1-1.
- Ghassemlooy, Z., Popoola, W., and Rajbhandari, S., 2019. *Optical Wireless Communications: System and Channel Modelling with Matlab®*. CRC Press, United States.
- Gurevich, A.V., Garipov, G.K., Almenova, A.M., Antonova, V.P., Chubenko, A.P., Kalikulov, O.A., Karashtin, A.N., Kryakunova, O.N., Lutsenko, V.Y., Mitko, G.G., Mukashev, K.M., Nam, R.A., Nikolaevsky, N.F., Osedlo, V.I., Panasyuk, M.I., Ptitsyn, M.O., Piscal, V.V., Ryabov, V.A., Saduev, N.O., Sadykov, T.K., and Zybin, K.P., 2018. Simultaneous observation of lightning emission in different wave ranges of electromagnetic spectrum in Tien Shan mountains. *Atmospheric Research*, 211, pp.73-84.
- Jamieson, T.H., 1981. Thermal effects in optical systems. *Optical Engineering*, 20(2), p.202156.
- Keiser, G., 2006. *Optical Communications Essentials*. The McGraw-Hill Companies, United States.
- Lam, C.F., Liu, H., Koley, B., Zhao, X., Kamalov, V., and Gill, V., 2010. Fiber optic communication technologies: What's needed for datacenter network operations. *IEEE Communications Magazine*, 48(7), pp.32-39.
- Li, T., Zhang, C., Yuan, Y., Shuai, Y., and Tan, H., 2020. Effects of image positions on temperature reconstruction using light field camera. *Results in Physics*, 17, p.103146.
- Marrogy, G.A.Q., 2020. Enhancing video streaming transmission in 5 GHz fanet drones parameters. *Telecommunications and Radio Engineering*, 79(11), 997-1007.
- Martin-Fernandez, M.L., Tynan, C.J., and Webb, S.E.D., 2013. A 'pocket guide' to total internal reflection fluorescence. *Journal of Microscopy*, 252(1), pp.16-22.
- Potsaid, B.M., Taranto, J.J., Cable, A.E., and Thorlabs Inc, 2015. *Compact, Low Dispersion, and Low Aberration Adaptive Optics Scanning System*. U.S. Patent No 9,200,887.
- Qasmarrogy, G.A., and Almashhadani, Y.S., 2020. Ad Hoc on-demand distance vector inherent techniques comparison for detecting and eliminating the black

- hole attack nodes in mobile ad hoc network. *Cihan University-Erbil Scientific Journal*, 4(1), pp.77-81.
- Richter, T., Elschner, R., Schmidt-Langhorst, C., Kato, T., Watanabe, S., and Schubert, C., 2013. NARROW Guard-Band Distributed Nyquist-WDM Using Fiber Frequency Conversion. In: *2013 Optical Fiber Communication Conference and Exposition and the National Fiber Optic Engineers Conference (OFC/NFOEC)*. IEEE, United States, pp.1-3.
- Sabitu, R.I., Dong-Nhat, N., and Malekmohammadi, A., 2019. High dispersion four-mode fiber for mode-division multiplexing systems. *Optik*, 181, pp.1-12.
- Stigloher, J., Decker, M., Körner, H.S., Tanabe, K., Moriyama, T., Taniguchi, T., Hata, H., Madami, M., Gubbiotti, G., Kobayashi, K., and Ono, T., 2016. Snell's law for spin waves. *Physical Review Letters*, 117(3), p.037204.
- Winzer, P.J., 2012. Optical networking beyond WDM. *IEEE Photonics Journal*, 4(2), pp.647-651.
- Winzer, P.J., 2014. Spatial multiplexing in fiber optics: The 10x scaling of metro/core capacities. *Bell Labs Technical Journal*, 19, pp.22-30.
- Xu, Y., Bai, P., Zhou, X., Akimov, Y., Png, C.E., Ang, L.K., Knoll, W., and Wu, L., 2019. Optical refractive index sensors with plasmonic and photonic structures: Promising and inconvenient truth. *Advanced Optical Materials*, 7(9), p.1801433.
- Yang, H., Feng, G., and Zhou, S., 2011. Thermal effects in high-power Nd: YAG disk-type solid-state laser. *Optics and Laser Technology*, 43(6), pp.1006-1015.
- Zhang, Z., Wang, H., Satyan, N., Rakuljic, G., Santis, C.T., and Yariv, A., 2019. Coherent and Incoherent Optical Feedback Sensitivity of High-Coherence Si/III-V Hybrid Lasers. In: *Optical Fiber Communication Conference*. Optical Society of America, Washington, DC, pp. 1-3.
- Zhu, W., Fokoua, E.R.N., Taranta, A.A., Chen, Y., Bradley, T., Petrovich, M.N., Poletti, F., Zhao, M., Richardson, D.J., and Slavik, R., 2019. The thermal phase sensitivity of both coated and uncoated standard and hollow core fibers down to cryogenic temperatures. *Journal of Lightwave Technology*, 38(8), pp.2477-2484.

# New Thiazole Derivatives: Potent Antifungal against *Candida albicans*, with *silico* Docking Unveiling Key Protein Interactions

Rebaz A. Omer<sup>1,2†</sup>, Karzan M. Ahmed<sup>3</sup>, Khdir A. Othman<sup>1</sup>, Wali M. Hamad<sup>1</sup>, Rahman K. Faraj<sup>4</sup>, Ali J. Muhialdin<sup>5</sup> and Shalaw K. Salih<sup>1</sup>

<sup>1</sup>Department of Chemistry, Faculty of Science and Health, Koya University, Koya, KOY45, Kurdistan Region – F.R. Iraq

<sup>2</sup>Department of Pharmacy, College of Pharmacy, Knowledge University, Erbil 44001, Kurdistan Region – F.R. Iraq

<sup>3</sup>Department of Chemistry, College of Education, University of Garmian, Kalar 46021, Kurdistan Region – F.R. Iraq

<sup>4</sup>Department of Chemistry, College of Science, University of Garmian, Kalar 46021, Kurdistan Region – F.R. Iraq

<sup>5</sup>Department of Animal Production, College of Agricultural Engineering Sciences, University of Garmian, Kifri 46022, Kurdistan Region – F.R. Iraq

**Abstract**—While bacterial superbugs have garnered much attention, the rise of antifungal resistance poses a growing threat. This study explores the potential of newly synthesized 2,5-Bis(3,4-Dialkoxy Phenyl) Thiazolo[5,4-d] Thiazoles (DATn compounds) as antifungal agents. Notably, DATn compounds demonstrated significant fungicidal activity against *Candida albicans*, a major fungal pathogen, whereas remaining largely ineffective against common bacterial strains, such as *Staphylococcus aureus* and *Escherichia coli*. *In silico* docking simulations using Schrödinger suites unveiled the molecular basis for this selectivity, revealing strong interactions between DATn molecules and a crucial fungal protein (Portion Data Bank ID: 8JZN) in *C. albicans*. These findings highlight the potential of DATn compounds as promising leads for the development of novel antifungal therapies, particularly in light of escalating drug resistance concerns.

**Index Terms**—Antifungal activity, Bacterial resistance, *Candida albicans*, DATn compounds, Drug discovery, Molecular docking.

## I. INTRODUCTION

In recent years, the scientific community's fascination with heterocyclic mesomorphic compounds has surged, driven by

the remarkable mesomorphic properties exhibited by these molecules (Omer, et al., 2023b, Omer, Koparir and Koparir, 2023a). This growing interest is attributed not only to the potential for discovering novel mesogenic substances in heterocyclic chemistry but also to the profound influence of heteroatoms, including sulfur, oxygen, and nitrogen, on the formation and behavior of mesophases. These heteroatoms confer unique properties on heterocyclic compounds, making them versatile candidates for various applications (Salih, et al., 2023; Omar, et al., 2023b). This study focuses on a specific class of heterocyclic mesomorphic compounds known as 2,5-Bis(3,4-dialkoxy phenyl) Thiazolo[5,4-d] thiazoles, collectively referred to as DAT<sub>n</sub> compounds. These compounds have garnered attention not only for their inherent mesomorphic properties but also for their potential to revolutionize diverse scientific domains including materials science, liquid crystal displays, and antimicrobial research (Al-Mutabagani, et al., 2021; Atmaram and Roopan, 2022). In the context of antimicrobial research, pathogens such as *Staphylococcus aureus*, *Escherichia coli*, and *Candida albicans* present significant global challenges (Omar, Omar and Abdullah, 2016a, Omar, Smail and Omar, 2016b). *S. aureus*, responsible for a spectrum of infections from skin ailments to life-threatening diseases, necessitates targeted intervention strategies. *E. coli*, a notorious bacterium, plays a role in various infections, including urinary tract infections and foodborne illnesses. *C. albicans*, a fungal pathogen, is associated with conditions such as candidiasis, posing a particular challenge, especially for immunocompromised individuals (Omer, et al., 2019; Koparir, et al., 2022).

This research takes a multifaceted approach to evaluate the antimicrobial potential of newly synthesized compounds. *In*

ARO-The Scientific Journal of Koya University  
Vol. XII, No. II (2024), Article ID: ARO.11557. 13 pages  
DOI: 10.14500/aro.11557

Received: 29 February 2024; Accepted: 19 June 2024

Regular research paper: Published: 25 July 2024

†Corresponding author's e-mail: rebaz.anwar@koyauniversity.org  
Copyright © 2024 Rebaz A. Omer, Karzan M. Ahmed, Khdir A. Othman, Wali M. Hamad, Rahman K. Faraj, Ali J. Muhialdi and Shalaw K. Salih. This is an open-access article distributed under the Creative Commons Attribution License (CC BY-NC-SA 4.0).





*in vitro* experiments rigorously examine these compounds' ability to inhibit the growth of the mentioned pathogens *S. aureus*, *E. coli*, and *C. albicans*. Precise experimentation allows the determination of their minimum inhibitory concentrations (MIC) and minimum bactericidal concentrations (MBC), providing insights into their effectiveness against these pathogens. Furthermore, the *in silico* research involves molecular docking using the Schrödinger Suite, specifically the version released in 2023, to gain a deeper understanding how these compounds interact with specific proteins or molecular pathways intrinsic to the targeted pathogens. In the case of *S. aureus*, two critical targets, penicillin-binding protein 2a (PBP2a) and D-Ala: D-Ala ligase, have been selected for their roles in cell wall integrity. In *E. coli*, DNA gyrase, vital for DNA replication, is the target of interest. For *C. albicans*, beta-glucan synthase, a fundamental component of the fungal cell wall, is strategically addressed. Inhibition of these targets is aimed at weakening the pathogens, rendering them more susceptible to immune defenses and conventional antimicrobial agents.

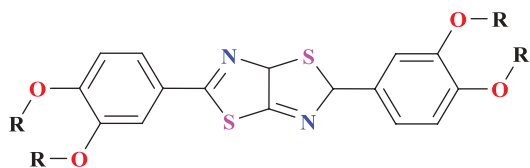
## II. EXPERIMENTAL AND METHODS

### A. In Vitro Section

Synthesis of 2,5-Bis(3,4-dialkoxy phenyl) Thiazolo[5,4-d] thiazoles (DAT<sub>T</sub><sub>n</sub>) was completed using the technique published in previous work (Salih, et al., 2023). Subsequently, its molecular structure was verified through Fourier-transform infrared spectroscopy, <sup>1</sup>H-NMR, and <sup>13</sup>C-NMR analysis (Hamad, Aziz, and Al-Dujaili, 2004), with the 3,4 positions of the two benzene rings substituted (R = C<sub>n</sub>H<sub>2n+1</sub>, n = 2–10) (Fig. 1). The materials used in the study as samples were (DAT<sub>T</sub><sub>n</sub> compounds), *S. aureus* is a multidrug-resistant Gram-positive bacterium, *E. coli* is a broad-spectrum beta-lactamase, and *C. albicans* is a fungal infection. Supporting materials are nutrient agar, nutrient broth, and dimethyl sulfoxide (DMSO) from Sigma Aldrich in Turkey.

### B. Preparing Serial Dilutions

The solution of each compound was prepared by adding 0.001 g of the compound into the 1 mL of DMSO solvent, drawn 0.1 mL of each compound (DAT<sub>T</sub><sub>2</sub>, 3, 4, 5, 6, 7, 8, 9, and 10), and added into 0.9 mL of nutrient broth (tube 1) and then 0.1 mL from tube 1 into the second tube, from it into the third tube, and so on. However, the final drawing mixture was discarded. Finally, serial dilutions of each compound in nutrient broth were prepared, as shown in Table I.



2,5-Bis(3,4-dialkoxy phenyl) Thiazolo[5,4-d] thiazoles (DAT<sub>T</sub><sub>n</sub>)

$$(R = C_nH_{2n+1} \quad n = 2-10)$$

Fig. 1. General molecular structure of study compounds.

### C. Microbial Inoculation

A loopful of each of the bacterial strain's colony and yeast colony was inoculated in a nutrient broth tube and incubated at 37°C for 24 h. After the visibility growth of each strain, and adjusted it to 0.5 McFarland by *DensiCHEK* device (BioMerieux/French), 10 μL of each strain was added into each dilution and then incubated for 24–48 h. After incubation time, a loopful of each tube contents was subcultures utilizing striking on nutrient agar and incubated for 24–48 h. The results were read to the end of the visible growth of colonies.

## III. RESULTS AND DISCUSSION

### A. In Vitro

The compound (DAT<sub>T</sub><sub>n</sub> compounds) has been synthesized and its antibacterial and fungicidal activity has been evaluated by serial dilution method (National Committee for Clinical Laboratory Standard, 2020). To determine the antimicrobial activity of the DAT<sub>T</sub><sub>n</sub> compounds, a serial concentration analysis (DAT<sub>T</sub><sub>2</sub>, 3, 4, 5, 6, 7, 8, 9, and 10) were conducted, as shown in Table I. This analysis aims to evaluate the antibacterial and fungicidal activity of the DAT<sub>T</sub><sub>n</sub> compounds against various strains, including Gram-positive *S. aureus*, Gram-negative *E. coli*.

To obtain accurate scientific results, tubes containing the final concentrations of the DAT<sub>T</sub><sub>n</sub> compounds were inoculated with a standard microbial suspension (10 μL of 10<sup>5</sup> CFU/mL strains of *S. aureus*, *E. coli*, and *C. albicans*) in tubes with nutrient broth to determine the MIC and MBC values for each strain. After making all the preparations, the tubes were incubated aerobically at 35°C for 24–48 h. After an overnight incubation period at 35°C, the tubes were examined for visible bacterial growth as indicated by turbidity. Three control tubes were maintained for each strain (media control, *in vivo* control, and extraction control). The lowest concentration (highest dilution) of a compound that did not result in visible growth (no turbidity) in the first 24 h when compared to control tubes is considered the initial MIC. Dilutions that showed no turbidity were incubated for an additional 24 h at 35°C. The lowest concentration that did not result in visible turbidity after a total incubation period of 48 h was considered the MIC. All concentration was determined by sub-cultivation (which showed no visible turbidity) on fresh nutrient agar medium. The plates were incubated for 24–48 h at 35°C. It is seen from the data presented in Table II that (DAT<sub>T</sub><sub>n</sub> compounds) exhibits antifungal activity with respect to the test cultures under study. It appears that the test culture of *C. albicans* demonstrated the same susceptibility level to DAT<sub>T</sub><sub>2</sub>, 3, 4, 5, 6, and 7 compound concentrations but moderately to DAT<sub>T</sub><sub>8</sub>, 9, and 10. *S. aureus* with coccus shape was resistant to all compound concentrations (DAT<sub>T</sub><sub>2</sub>, 3, 4, 5, 6, 7, 8, 9, and 10) by dilution method. Furthermore, *E. coli* was resistant to compound concentrations (DAT<sub>T</sub><sub>2</sub>, 3, 4, 5, 6, 7, 8, 9, and 10) by the dilution method. Through the experimental procedure, we found that the concentration

TABLE I  
CHEMICAL STRUCTURE AND MOLECULAR WEIGHT OF DATT<sub>n</sub> COMPOUNDS WITH DELUSIONS USED

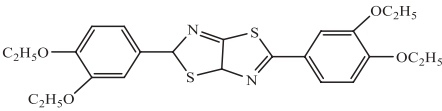
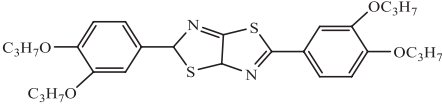
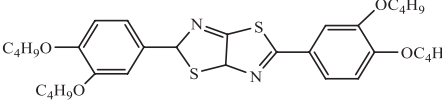
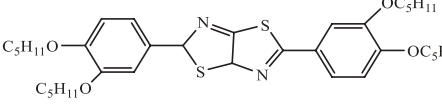
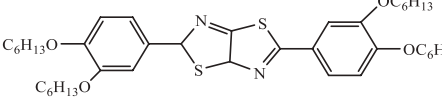
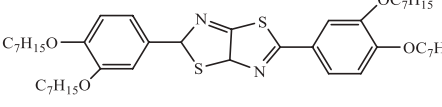
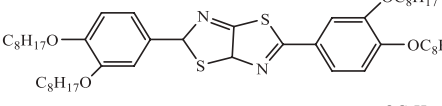
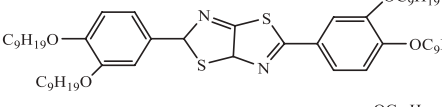
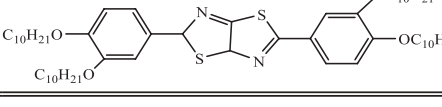
No.	Name of compounds	Chemical structures	Molecular weight	Molarity	Serial dilutions
1	DATT <sub>2</sub>		472.62	0.0021	0.0021–0.00052
2	DATT <sub>3</sub>		528.73	0.0019	0.0019–0.00047
3	DATT <sub>4</sub>		584.83	0.0017	0.0017–0.00042
4	DATT <sub>5</sub>		640.94	0.0015	0.0015–0.00037
5	DATT <sub>6</sub>		697.05	0.0014	0.0014–0.00035
6	DATT <sub>7</sub>		753.16	0.0013	0.0013–0.00032
7	DATT <sub>8</sub>		809.27	0.0012	0.0012–0.0003
8	DATT <sub>9</sub>		865.37	0.0011	0.0011–0.00027
9	DATT <sub>10</sub>		921.48	0.001	0.001–0.00025

TABLE II  
EFFECTS OF COMPOUNDS ON BACTERIAL AND FUNGAL GROWTH

No.	Name of compounds	<i>Staphylococcus aureus</i>	<i>Escherichia coli</i>	<i>Candida albicans</i>
1	DATT <sub>2</sub>	+	+	–
2	DATT <sub>3</sub>	+	+	–
3	DATT <sub>4</sub>	+	+	–
4	DATT <sub>5</sub>	+	+	–
5	DATT <sub>6</sub>	+	+	–
6	DATT <sub>7</sub>	+	+	–
7	DATT <sub>8</sub>	+	+	±
8	DATT <sub>9</sub>	+	+	±
9	DATT <sub>10</sub>	+	+	±

(+) growth of microbes or the compounds not effective, (–) not growth of microbes or the compounds kills the microbes, (±) low growth of microbes or the compounds effective moderately

of DATT<sub>7</sub>, did not result any growth after a total incubation, which is considered the MIC. Therefore, our results revealed the importance of DATT<sub>n</sub> compounds when associated with antifungal, to control resistance, which has become a threat to human health.

### B. Targeting Proteins across Pathogens

The pathogens *S. aureus*, *E. coli*, and *C. albicans* are causative agents of diverse infections in humans. The mitigation of these infections through molecular docking necessitates the precise targeting of specific proteins or molecular pathways intrinsic to these pathogens (Moravej, et al., 2018; Koparir, et al., 2023a; Khan, et al., 2023). Viable targets encompass enzymes implicated in cell wall biosynthesis, host cell adhesion, toxin production, and virulence factors. The molecular docking process encompasses target identification, 3D structure acquisition, compound screening for binding interactions, binding affinity prediction, and experimental compound validation. The study has focused on specific proteins of *E. coli*, and *S. aureus*, which have been carefully chosen for inhibition (Rementeria, et al., 2005; Ruer, et al., 2015; Anwar Omar, et al., 2023).

#### *S. aureus*

Identified two critical targets within the pathogenic bacterium *S. aureus* that are essential for cell wall integrity. The first target is PBP2a, labeled as 5M18 in the Protein Data Bank (PDB). PBP2a, a member of the Penicillin-Binding

Proteins (PBPs) family, is centrally involved in peptidoglycan synthesis. Inhibiting PBPs disrupts the cell wall, rendering *S. aureus* more susceptible to immune defenses and antibiotics. Protein 5M18 features a high-resolution structure (1.98 Å) (Fishovitz, et al., 2014; Verma, et al., 2022; Mahasenan, et al., 2017; Koparir, et al., 2023b). The second target was found in PDB entry 3N8D (crystal structure of *S. aureus* VRSA-9 D-Ala: D-Ala ligase), which offers the crystal structure of *S. aureus* VRSA-9 D-Ala: D-Ala ligase. This enzyme is a key contributor to cell wall synthesis. The structural data it provides are indispensable for potential antibiotic development, particularly when addressing antibiotic-resistant *S. aureus* strains. Protein 3N8D exhibits a reasonable resolution (2.3 Å) and solid refinement. Its lattice parameters and symmetry are well defined. Further analysis involves exploring the protein's three-dimensional structure and identifying potential ligand-binding sites (Lebreton and Cattoir, 2019; Paymal, et al., 2023; Omar, et al., 2023a). Together, these two targets present a multifaceted strategy for weakening *S. aureus* by compromising its cell wall integrity.

#### *E. coli*

We have chosen DNA gyrase as our docking target due to its pivotal role in DNA replication within *E. coli*. With good-resolution structure and well-defined parameters, such as those found in the DNA binding and cleavage domain (PDB ID: 6RKU), it serves as an ideal candidate for molecular docking studies. This selection enables us to precisely understand how our molecules interact with DNA gyrase, ultimately disrupting DNA replication and leading to the demise of bacterial cells (Nöllmann, et al., 2007; Jakhar, et al., 2022).

#### *C. albicans*

Beta-glucan synthase, denoted by PDB ID, has been strategically chosen with a resolution (2.47 Å) structure and well-defined parameters. This enzyme plays a pivotal role in the synthesis of beta-glucans, a fundamental constituent of the fungal cell wall. The inhibition of this enzyme significantly weakens the fungal cell wall, rendering *C. albicans* more susceptible to host immune defenses and antifungal agents (Liu and Balasubramanian, 2001; Zhao, et al., 2023).

#### *C. Docking Studies on Proteins*

Schrödinger's "LigPrep" tool in Maestro 13.5 was used to generate three-dimensional models of the synthesized compounds (DATT<sub>2-10</sub>). These models were prepared to create the chemical structures. To ensure accurate binding interactions, the "Protein Preparation Wizard" in Schrödinger's suite was utilized for proteins 5M18, 3N8D, 6RKU, and 8JZN. This process involved adding missing hydrogen atoms, correcting ionization states, formal charges, bond orders, and applying the OPLS4 force field (Chen, et al., 2023a). For a comprehensive evaluation of protein binding sites for DATT<sub>n</sub> molecules, the SiteMap panel within Maestro was employed. Following the identification of these binding sites, the Glide Grid tool was instrumental in configuring the docking environment, defining essential site characteristics. Subsequently, molecular docking with

DATT<sub>2-9</sub> molecules was conducted to predict their interactions within the protein's binding sites. The Glide Grid played a vital role in ensuring the accuracy of these calculations by providing critical site information for the evaluation of ligand-protein interactions and the identification of potential drug candidates (Farid, et al., 2006; Halgren, 2009). The structures of DATT<sub>n</sub> molecules, generated using "LigPrep," were systematically docked into various pockets within proteins 5M18, 3N8D, 6RKU, and 8JZN, based on their specific binding site characteristics, including sitescore, size, and Dscore. To achieve precise results, the "Glide" software with extra precision (XP) was utilized, and the Induced Fit Docking workflow within Maestro was incorporated for proteins exhibiting strong binding affinity with DATT<sub>n</sub> molecules.

#### *D. Site Selection for Effective DATT<sub>n</sub> Molecule Interactions*

In the study, the SiteMap panel within the Maestro software was leveraged to predict multiple binding pockets within the molecular models of four proteins: 5M18, 3N8D, 6RKU, and 8JZN. Each protein yielded a set of five binding sites, resulting in a total of 20 distinct binding pockets under scrutiny. The primary objective was to identify the binding pocket that offered the most favorable interactions with DATT<sub>n</sub> molecules. The ensuing data (Table III) provide an overview of the key characteristics of these binding pockets. Notably, the analysis revealed that when compounds were docked with site-4 in the 8JZN protein of *C. albicans*, it produced the most promising interaction with DATT<sub>n</sub> molecules compared to the other pockets in the remaining proteins (Table IV). This alignment with experimental results suggests the potential of these molecules to effectively inhibit the enzyme (Table II), leading to a significant weakening of the cell wall of *C. albicans*. This outcome holds the promise of halting microbial growth or even eradicating the microbes entirely, marking a significant advancement in antifungal research.

#### *E. Glide-dock\_XP\_8JZN-sit-4*

In the context of molecular docking simulations conducted within Schrödinger Maestro, this research scrutinizes molecular interactions by assessing docking scores and XP scores. These scores encompass various factors, including van der Waals interactions, electrostatic interactions, desolvation energies, and hydrogen bonding, all of which play a pivotal role in predicting binding affinity. Lower scores are indicative of more favorable interactions between ligands and proteins. Table V presents the docking scores and XP GlideScores for a range of DATT<sub>n</sub> molecules, shedding light on their respective binding affinities to the target protein. These scores span the spectrum from DATT<sub>10</sub>, which registers a score of -2.279, to DATT<sub>6</sub> and DATT<sub>8</sub>, both of which exhibit scores of -9.760. This variance underscores the diversity in binding strengths across the compounds. Notably, there is a remarkable concurrence between the docking and XP GlideScores for each DATT<sub>n</sub> molecule, with the exception of DATT<sub>10</sub>, which deviates as an outlier, implying potentially weaker binding. Conversely, DATT<sub>2</sub>, DATT<sub>3</sub>, DATT<sub>4</sub>, DATT<sub>5</sub>,

TABLE III  
OPTIMAL PROTEIN BINDING SITES WITH HIGHEST INTERACTION SCORES FOR DATT<sub>n</sub> MOLECULES

Title	5M18_site_1 <i>Staphylococcus aureus</i>	3N8D-site_2 <i>Staphylococcus aureus</i>	6RKU_site_2 <i>Escherichia coli</i>	8JZN_site_4 <i>Candida albicans</i>
Site score	1.003876	1.025507	1.043826	1.145268
Size	1001	256	620	300
D score	0.996551	0.970397	1.051778	1.224372
Volume	2722.391	879.109	1590.834	779.296
Exposure	0.559419	0.615038	0.479429	0.431818
Enclosure	0.703794	0.736137	0.763531	0.775485
Contact	0.891395	0.865776	0.965688	0.992804
Phobic	0.394444	0.261777	0.506718	2.2275
Philic	1.121856	1.261613	1.062394	0.554965
Balance	0.3516	0.207494	0.476959	4.013764
Don/acc	1.028832	0.816949	1.485156	0.857137

DATT<sub>7</sub>, and DATT<sub>9</sub> all manifest scores surpassing the  $-8.122$  threshold, signifying substantial promise in terms of binding affinities (Sandor, Kiss, and Keserű, 2010; Jays, Mohan, and Saravanan, 2019). Furthermore, the research delves into the assessment of ligand efficiency concerning DATT<sub>n</sub> molecules positioned within site-4 of the 8JZN protein. Ligand efficiency serves as a metric for gauging their binding effectiveness. The values encompass a spectrum from  $-0.036$  to  $-0.254$ , with DATT<sub>2</sub> showcasing the highest efficiency at  $-0.254$ , and DATT<sub>10</sub> recording the lowest efficiency at  $-0.036$ . These results cast DATT<sub>2</sub> as a compelling candidate characterized by a robust binding affinity. However, it is important to acknowledge that further studies are imperative to validate its suitability for drug development (Abad-Zapatero and Metz, 2005; Hopkins, et al., 2014). Analysis of “Glide EModel” and “Glide Energy” values reveals a close correspondence across the various molecules. DATT<sub>6</sub> emerges as the frontrunner with the highest Glide EModel value at  $-118.419$ , indicative of a robust and favorable binding profile. In contrast, DATT<sub>10</sub> reports the lowest value at  $-37.813$ , which signifies a relatively less favorable binding profile. The rest of the molecules exhibit values that fall within this range (Vass, Tarcsay, and Keserű, 2012; Tripathi, et al., 2012). Values pertaining to “Glide EInternal” exhibit significant variability. DATT<sub>8</sub> takes the lead with the highest value of  $21.881$ , signifying a substantial contribution of internal energy to the binding. Conversely, DATT<sub>4</sub>, DATT<sub>5</sub>, and DATT<sub>6</sub> display values of  $0.000$ , denoting that their internal energy exerts minimal influence on the binding energy (Gulcin, et al., 2022). The “glide evdw” parameter highlights DATT<sub>9</sub> as the compound with the lowest van der Waals energy value at  $-77.755$ , signifying robust non-polar interactions within the protein pocket. In contrast, DATT<sub>2</sub> reports the lowest value at  $-52.870$ , indicating relatively weaker interactions. The other molecules demonstrate varying strengths in their respective interactions (Naghiyev, et al., 2022). Analysis of “XP Electro” elucidates that DATT<sub>5</sub> boasts the most negative electrostatic energy at  $-0.209$ , underscoring robust interactions, whereas DATT<sub>4</sub> registers the highest positive energy at  $0.012$ . The other molecules exhibit differing electrostatic energies, exerting an impact on their respective binding within the protein pocket. Among

the molecules, DATT<sub>6</sub> stands out with a hydrogen bond interaction value of  $-0.350$ , whereas DATT<sub>8</sub> and DATT<sub>10</sub> exhibit comparatively weaker hydrogen bond interactions. In contrast, DATT<sub>2</sub>, DATT<sub>3</sub>, DATT<sub>4</sub>, DATT<sub>6</sub>, DATT<sub>7</sub>, and DATT<sub>9</sub> report no notable hydrogen bonding interactions, signifying values of  $0.000$  (Kaka, et al., 2024). The “XP RotPenal” parameter, employed to assess ligand rotational freedom within the protein pocket, yields analogous values ranging from  $0.330$  to  $0.342$  across all molecules. This uniformity implies consistent flexibility in ligand binding, with lower values indicating a lesser degree of rotational constraint (Beinat, 2014). In the context of “XP ExposPenal,” it is observed that DATT<sub>10</sub> incurs the highest penalty at  $1.860$  for exposed polar atoms, suggesting potential constraints on binding stability. In contrast, the other molecules are associated with lower or zero penalties, which allude to fewer constraints related to exposed polar atoms in the context of ligand binding (Sarafroz, Siddiqui, and Yar, 2020). Finally, scrutiny of “glide posenum” reveals that DATT<sub>5</sub> exhibits the highest conformational flexibility, offering  $30$  distinct binding poses. On the other hand, DATT<sub>10</sub> exhibits the least flexibility, characterized by a solitary binding pose. The remaining molecules present varying numbers of binding poses, underscoring their adaptability within the protein pocket (Erdoğan, Taslimi, and Tuzun, 2021). Table VI shows docking scores and binding characteristics for DATT<sub>n</sub> molecules at protein site 8JZN-sit-4.

In the conducted study, we explored the intricate interactions between DATT<sub>n</sub> molecules and the 8JZN-sit-4 protein in *C. albicans*. To visually represent these interactions, a comprehensive fingerprint interaction (Fig. 2) was generated. This figure effectively illustrates the diverse contacts occurring between DATT<sub>n</sub> molecules and the protein’s binding pocket, encompassing various interaction types, including backbone, sidechain, polar, hydrophobic, aromatic, and charged residues, providing a clear overview of the binding process. To quantitatively evaluate these interactions, computational analysis was performed and the results are summarized in Table V. This table offers a quantitative assessment of the similarity between DATT<sub>n</sub> molecules and the protein, enabling researchers to compare interaction patterns across different DATT<sub>n</sub> molecules

TABLE IV  
DOCKING PERFORMANCE METRICS FOR LIGAND EFFICIENCY AND SCORING (GLIDE-XP) IN DAT<sub>T</sub>N MOLECULE INTERACTIONS

5M18- <i>Staphylococcus aureus</i>									
Title	DAT <sub>T</sub> <sub>2</sub>	DAT <sub>T</sub> <sub>3</sub>	DAT <sub>T</sub> <sub>4</sub>	DAT <sub>T</sub> <sub>5</sub>	DAT <sub>T</sub> <sub>6</sub>	DAT <sub>T</sub> <sub>7</sub>	DAT <sub>T</sub> <sub>8</sub>	DAT <sub>T</sub> <sub>9</sub>	DAT <sub>T</sub> <sub>10</sub>
Glide ligand efficiency	-0.108	-0.131	-0.075	-0.077	-0.073	-0.024	-0.035	-0.015	-0.032
Docking score	-3.447	-4.720	-2.994	-3.392	-3.502	-1.237	-1.948	-0.892	-2.016
XP GScore	-3.447	-4.720	-2.994	-3.392	-3.502	-1.237	-1.948	-0.892	-2.016
Glide evdw	-38.679	-35.950	-53.513	-59.394	-51.745	-60.290	-69.386	-66.366	-69.030
Glide ecoul	-7.419	-0.949	-5.115	-5.633	-3.711	-3.503	-5.252	-6.902	-7.488
Glide energy	-46.098	-36.899	-58.628	-65.027	-55.456	-63.793	-74.638	-73.268	-76.518
Glide einternal	0.000	0.000	14.549	8.684	11.026	0.000	7.101	30.423	19.701
Glide emodel	-62.869	-65.495	-73.446	-92.087	-84.403	-101.019	-110.560	-93.079	-114.995
XP HBond	-1.427	-0.268	-0.019	0.000	0.000	0.000	0.000	0.000	-0.541
XP PhobEn	0.000	0.000	0.000	0.000	0.000	0.000	0.000	0.000	0.000
XP PhobEnHB	0.000	-1.500	0.000	0.000	0.000	0.000	0.000	0.000	0.000
XP LowMW	0.000	0.000	0.000	0.000	0.000	0.000	0.000	0.000	0.000
XP RotPenal	0.233	0.316	0.323	0.336	0.341	0.342	0.340	0.335	0.330
XP LipophilicEvdW	-1.838	-2.983	-3.085	-3.386	-5.397	-2.777	-3.191	-3.006	-3.508
XP Electro	-0.556	-0.071	-0.384	-0.422	-0.278	-0.263	-0.394	-0.518	-0.562
XP ExposPenal	0.142	0.563	0.171	0.080	0.832	0.461	1.297	1.296	1.264
glide posenum	5.000	1.000	14.000	5.000	15.000	10.000	35.000	1.000	7.000
3N8D- <i>Staphylococcus aureus</i>									
Title	DAT <sub>T</sub> <sub>2</sub>	DAT <sub>T</sub> <sub>3</sub>	DAT <sub>T</sub> <sub>4</sub>	DAT <sub>T</sub> <sub>5</sub>	DAT <sub>T</sub> <sub>6</sub>	DAT <sub>T</sub> <sub>7</sub>	DAT <sub>T</sub> <sub>8</sub>	DAT <sub>T</sub> <sub>9</sub>	DAT <sub>T</sub> <sub>10</sub>
Glide ligand efficiency	-0.120	-0.136	-0.087	-0.109	-0.071	-0.058	-0.037	-0.076	-0.006
Docking score	-3.825	-4.904	-3.499	-4.797	-3.406	-3.031	-2.078	-4.556	-0.401
XP GScore	-3.825	-4.904	-3.499	-4.797	-3.406	-3.031	-2.078	-4.556	-0.401
Glide evdw	-38.856	-34.421	-48.673	-55.916	-47.490	-56.718	-57.837	-61.914	-28.325
Glide ecoul	-8.955	-10.910	-7.660	-4.414	-5.321	-3.778	-2.763	-2.931	-1.953
Glide energy	-47.811	-45.331	-56.334	-60.330	-52.812	-60.496	-60.600	-64.845	-30.279
Glide einternal	9.591	10.785	11.031	19.182	8.949	16.441	16.736	17.774	9.544
Glide emodel	-58.857	-58.214	-77.045	-78.723	-68.386	-76.720	-80.318	-89.321	-1.856
XP HBond	-1.333	-1.876	-1.557	-0.773	-0.421	0.000	-0.350	-0.700	0.000
XP PhobEn	0.000	0.000	0.000	0.000	0.000	0.000	0.000	0.000	0.000
XP PhobEnHB	0.000	0.000	0.000	0.000	0.000	0.000	0.000	0.000	0.000
XP LowMW	0.000	0.000	0.000	0.000	0.000	0.000	0.000	0.000	0.000
XP RotPenal	0.233	0.316	0.323	0.336	0.341	0.342	0.340	0.335	0.330
XP LipophilicEvdW	-2.054	-2.525	-2.819	-4.029	-3.762	-4.474	-3.637	-5.330	-1.466
XP electro	-0.672	-0.818	-0.575	-0.331	-0.399	-0.283	-0.207	-0.220	-0.147
XP ExposPenal	0.000	0.000	0.129	0.000	0.834	0.384	0.777	0.358	0.882
glide posenum	72.000	3.000	7.000	1.000	21.000	7.000	30.000	2.000	1.000
6RKU- <i>Escherichia coli</i>									
Title	DAT <sub>T</sub> <sub>2</sub>	DAT <sub>T</sub> <sub>3</sub>	DAT <sub>T</sub> <sub>4</sub>	DAT <sub>T</sub> <sub>5</sub>	DAT <sub>T</sub> <sub>6</sub>	DAT <sub>T</sub> <sub>7</sub>	DAT <sub>T</sub> <sub>8</sub>	DAT <sub>T</sub> <sub>9</sub>	DAT <sub>T</sub> <sub>10</sub>
Glide ligand efficiency	-0.165	-0.086	-0.067	-0.071	-0.111	-0.093	-0.077	-0.013	-0.009
Docking score	-5.290	-3.088	-2.677	-3.110	-5.336	-4.811	-4.303	-0.759	-0.584
XP GScore	-5.290	-3.088	-2.677	-3.110	-5.336	-4.811	-4.303	-0.759	-0.584
Glide evdw	-52.633	-65.206	-61.157	-61.702	-58.950	-73.248	-65.615	-64.589	-74.283
Glide ecoul	-3.907	-2.179	0.282	-4.856	-3.214	-3.992	-4.051	-4.488	-4.374
Glide energy	-56.540	-67.385	-60.875	-66.558	-62.164	-77.240	-69.666	-69.077	-78.657
Glide einternal	8.603	10.345	0.000	17.200	8.961	15.148	18.866	12.609	17.759
Glide emodel	-66.950	-82.863	-79.753	-85.753	-99.824	-113.239	-98.092	-100.341	-114.929
XP HBond	-0.320	-0.257	-0.147	-1.251	-0.829	-1.385	-0.391	-0.700	0.000
XP PhobEn	0.000	0.000	0.000	0.000	-0.650	0.000	0.000	0.000	0.000
XP PhobEnHB	0.000	0.000	0.000	0.000	0.000	0.000	0.000	0.000	0.000
XP LowMW	0.000	0.000	0.000	0.000	0.000	0.000	0.000	0.000	0.000
XP RotPenal	0.233	0.316	0.323	0.336	0.341	0.342	0.340	0.335	0.330
XP LipophilicEvdW	-6.108	-6.984	-6.874	-5.993	-7.957	-7.469	-5.242	-5.129	-5.272
XP Electro	-0.293	-0.163	0.021	-0.364	-0.241	-0.299	-0.304	-0.337	-0.328
XP ExposPenal	0.199	0.000	0.000	0.162	0.000	0.000	1.294	1.071	0.686
glide posenum	3.000	95.000	7.000	2.000	7.000	7.000	1.000	1.000	1.000

(Sastry, et al., 2010; Chen, et al., 2023b). The data reveal intriguing insights into the properties and interactions of

DAT<sub>T</sub><sub>n</sub> molecules. DAT<sub>T</sub><sub>9</sub> emerges with the highest number of any contacts, indicating extensive interactions with other

TABLE V  
INTERACTIONS AND SIMILARITY MEASURES BETWEEN DATT<sub>n</sub> MOLECULES AND 8JZN-SIT-4 PROTEIN IN *CANDIDA ALBICANS*

Title	DATT <sub>2</sub>	DATT <sub>3</sub>	DATT <sub>4</sub>	DATT <sub>5</sub>	DATT <sub>6</sub>	DATT <sub>7</sub>	DATT <sub>8</sub>	DATT <sub>9</sub>	DATT <sub>10</sub>
SIFT any contact	16	19	20	22	21	23	26	27	21
SIFT backbone interaction	6	6	5	6	6	7	5	12	8
SIFT side chain interaction	15	18	20	20	21	21	26	23	18
SIFT polar residues	5	6	6	7	8	8	9	7	10
SIFT hydrophobic residues	10	12	14	13	13	13	17	16	8
SIFT hydrogen bond acceptor	0	0	0	0	0	0	0	0	0
SIFT hydrogen bond donor	0	0	0	0	0	0	0	0	1
SIFT aromatic residue	3	4	5	3	4	3	5	3	3
SIFT charged residue	2	2	2	2	2	2	3	2	3
Canvas means tanimoto similarity	0.513	0.58	0.548	0.553	0.518	0.464	0.425	0.467	0.4
Canvas max tanimoto similarity	1	1	1	1	1	1	1	1	1
Canvas max tanimoto similarity ID	129	128	127	126	123	125	122	124	130
Canvas min tanimoto similarity	0.265	0.337	0.286	0.355	0.312	0.273	0.254	0.349	0.254
Canvas min tanimoto similarity ID	130	130	130	130	130	122	130	129	122

TABLE VI  
DOCKING SCORES AND BINDING CHARACTERISTICS FOR DATT<sub>n</sub> MOLECULES AT PROTEIN 8JZN-SITE-4<sup>f</sup>

Title	DATT <sub>2</sub>	DATT <sub>3</sub>	DATT <sub>4</sub>	DATT <sub>5</sub>	DATT <sub>6</sub>	DATT <sub>7</sub>	DATT <sub>8</sub>	DATT <sub>9</sub>	DATT <sub>10</sub>
docking score	-8.122	-8.510	-9.248	-9.255	-9.760	-9.395	-9.760	-9.555	-2.279
XP GScore	-8.122	-8.510	-9.248	-9.255	-9.760	-9.395	-9.760	-9.555	-2.279
glide ligand efficiency	-0.254	-0.236	-0.231	-0.210	-0.203	-0.181	-0.174	-0.159	-0.036
glide emodel	-77.15	-89.46	-103.27	-103.81	-118.42	-112.64	-115.33	-112.43	-37.81
glide einternal	6.061	9.649	0.00	0.00	0.00	18.463	21.881	21.065	10.962
glide evdw	-52.87	-59.82	-62.33	-64.11	-67.38	-72.66	-76.96	-77.75	-65.03
XP Electro	-0.022	-0.051	0.012	-0.209	-0.200	-0.026	-0.070	-0.061	-0.105
XP HBond	0.00	0.00	0.00	0.00	-0.350	0.00	-0.160	0.00	-0.138
XP PhobEn	-0.850	-0.700	-0.840	-0.800	-0.556	-0.311	-0.625	-0.774	0.000
XP RotPenal	0.233	0.316	0.323	0.336	0.341	0.342	0.340	0.335	0.330
XP ExposPenal	0.000	0.143	0.00	0.00	0.314	0.00	0.065	0.859	1.860
Glide poseum	2	15	14	30	2	29	8	7	1

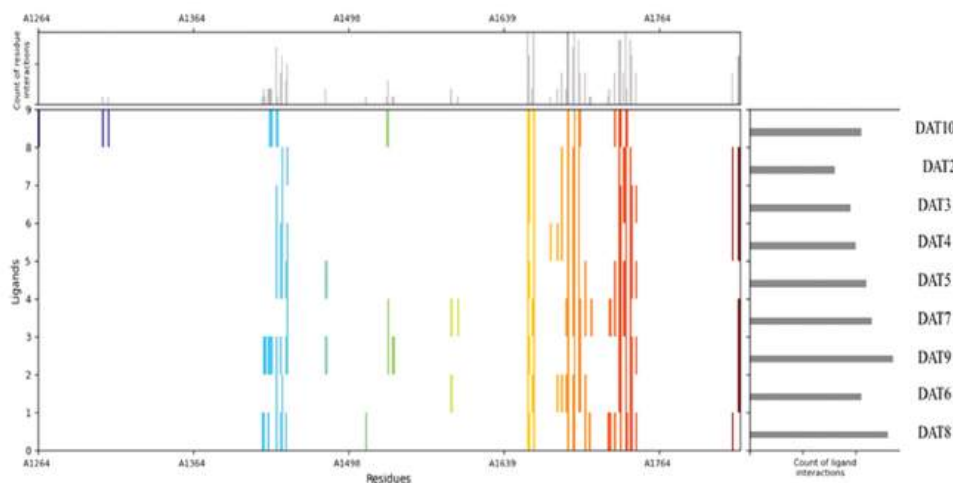


Fig. 2. Unveiling DATT<sub>n</sub> molecule interactions with 8JZN-sit-4 protein in *Candida albicans*, interaction fingerprint.

molecules. Meanwhile, DATT<sub>8</sub> leads in terms of side chain interactions and features a notable count of polar residues and hydrophobic residues, suggesting its versatility in molecular interactions. DATT<sub>10</sub> is distinctive for its hydrogen bond donor capabilities. Furthermore, the mean Tanimoto similarity score provides information on how structurally similar these molecules are to others in a chemical structure

database, with DATT<sub>3</sub> displaying the highest similarity. In contrast, DATT<sub>7</sub> exhibits the lowest similarity. These values collectively shed light on the molecular characteristics and interactions of the DATT<sub>n</sub> molecules, which may be pertinent in various biological and chemical contexts (Rajitha, et al., 2021; Mamad, et al., 2024). DATT<sub>9</sub> has been selected for further investigation due to its promising attributes, including

low docking scores, favorable XP GlideScores, robust van der Waals interactions, and significant conformational flexibility with multiple binding poses. These characteristics suggest strong binding within the protein pocket.

**F. Induced-Fit Docking (IFD): DATT<sub>9</sub> with 8JZN**

In Fig. 3, both the 3D and 2D interaction maps, derived from the Induced Fit docking of DATT<sub>9</sub> with the 8JZN-sit-4 protein in *C. albicans* using XP mode, clearly illustrate substantial alterations in the ligand's positioning and orientation within the binding site. These alterations reflect the adaptability of the protein pocket in response to induced fit docking. As a result of this flexibility, certain side

chains or residues shift to optimize binding, leading to the accommodation of the ligand in various poses. Furthermore, the binding site volume, particularly in the interaction map between the protein and DATT<sub>9</sub>, has also been modified due to the flexibility exhibited by both the protein and DATT<sub>9</sub>. This adaptability in the binding site plays a crucial role in enabling different binding poses and interactions, ultimately influencing the ligand's binding behavior. In comparison between DATT<sub>9</sub> obtained through Glide-Dock\_XP mode and DATT<sub>91</sub> to DATT<sub>96</sub> from InducedFit\_XP mode, several crucial observations emerge in Table VII. First, the Prime Energy of DATT<sub>9</sub> is notably higher, indicating a less favorable energy state, whereas DATT<sub>91</sub> to DATT<sub>96</sub> exhibit highly

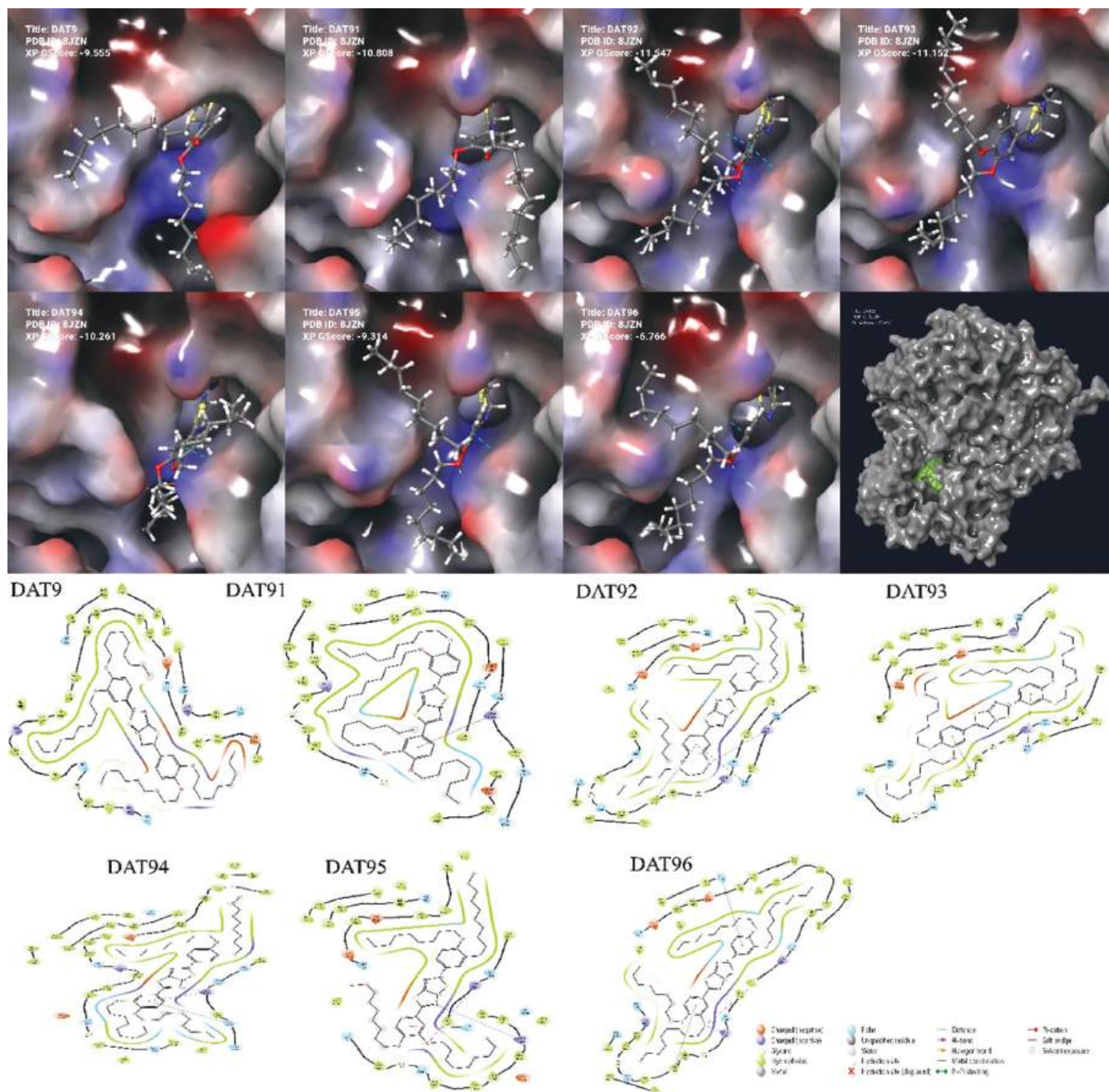


Fig. 3. 3D and 2D interaction maps of DATT<sub>9</sub> with 8JZN-sit-4 protein in *Candida albicans* using IFD-XP mode.

TABLE VII  
DOCKING AND INTERACTION SCORES OF DATT<sub>9</sub> WITH MULTIPLE POSES AGAINST 8JZN-SIT-4 PROTEIN IN *CANDIDA ALBICANS* USING (IFD-XP MODE)

Title	DATT <sub>9</sub>	DATT <sub>91</sub>	DATT <sub>92</sub>	DATT <sub>93</sub>	DATT <sub>94</sub>	DATT <sub>95</sub>	DATT <sub>96</sub>
Glide ligand efficiency	-0.159	-0.180	-0.192	-0.186	-0.171	-0.155	-0.113
Docking score	-9.555	-10.808	-11.547	-11.152	-10.261	-9.314	-6.766
XP GScore	-9.555	-10.808	-11.547	-11.152	-10.261	-9.314	-6.766
Glide evdw	-77.755	-87.116	-90.445	-89.558	-82.374	-82.197	-88.358
Glide ecoul	-0.807	-0.660	-4.439	-2.381	0.170	-3.713	-2.342
Glide energy	-78.562	-87.776	-94.884	-91.939	-82.204	-85.910	-90.701
Glide einternal	21.065	17.232	14.207	20.107	24.761	17.440	21.516
Glide emodel	-112.434	-131.887	-168.887	-153.724	-123.005	-148.729	-150.178
XP HBond	0.000	0.000	-0.660	0.000	0.000	-0.505	-0.428
XP PhobEn	-0.774	-0.799	-1.150	-0.950	-1.071	-1.075	-1.004
XP PhobEnHB	0.000	0.000	0.000	0.000	0.000	0.000	0.000
XP LowMW	0.000	0.000	0.000	0.000	0.000	0.000	0.000
XP RotPenal	0.335	0.335	0.335	0.335	0.335	0.335	0.335
XP LipophilicEvdW	-9.480	-11.450	-9.947	-10.194	-9.701	-9.198	-10.012
XP Electro	-0.061	-0.050	-0.333	-0.179	0.013	-0.278	-0.176
XP ExposPenal	0.859	0.721	0.781	0.106	0.405	0.714	1.030
Glide poseenum	7.000	6.000	2.000	7.000	1.000	1.000	1.000
Prime energy	3,224.8	-62,714.7	-62,698.9	-62,701.0	-62,706.4	-62,714.0	-62,714.7
Interaction map area	1627.451	1593.710	1594.665	1656.250	1560.356	1688.436	1528.935
IFD score		-3,146.540	-3,146.490	-3,146.200	-3,145.580	-3,145.010	-3,142.500

negative values, signifying a substantial reduction in energy during induced fit docking. This highlights the improved energetically favorable interactions between the ligand and protein in the induced fit poses. Glide Ligand Efficiency, although slightly lower in DATT<sub>91</sub> to DATT<sub>96</sub>, is a common trend in induced fit docking, where ligands adapt to precise protein pockets at the expense of higher energy penalties. Second, in terms of the Docking Score (XP GScore), DATT<sub>9</sub> presents a score of approximately -9.56, whereas DATT<sub>91</sub> to DATT<sub>96</sub> consistently exhibit lower, more negative scores. These lower scores represent enhanced binding affinity and energy minimization in the induced fit poses, showcasing the optimization of ligand-protein interactions. Moreover, the Van der Waals energy (Glide evdw) is reduced in DATT<sub>91</sub> to DATT<sub>96</sub>, implying improved Van der Waals interactions as ligands better fit protein binding sites, reducing steric clashes. In addition, the electrostatic energy (Glide ecoul) shows less negative values in DATT<sub>9</sub> compared to DATT<sub>91</sub> to DATT<sub>96</sub>, implying optimized electrostatic interactions in induced fit docking. Lower internal energy (Glide einternal) in DATT<sub>91</sub> to DATT<sub>96</sub> reflects improvements achieved in internal energy contributions through induced fit docking, which may be linked to favorable ligand conformations in binding sites. The variations in XP HBond values from DATT<sub>91</sub> to DATT<sub>96</sub> indicate changes in hydrogen bond formation or disruption during induced fit docking, which can significantly impact binding specificity and strength. Furthermore, the XP Lipophilic EvdW values in DATT<sub>91</sub> to DATT<sub>96</sub> are generally lower, demonstrating enhanced hydrophobic interactions typical of induced fit docking. Finally, XP ExposPenal values differ, reflecting changes in exposure energy penalties due to ligand or protein conformational alterations during induced fit docking. The varying number of generated poses among DATT<sub>91</sub> to DATT<sub>96</sub> underscores the conformational adaptability of ligands and proteins during the induced fit

docking process. This comprehensive comparison reveals the benefits of induced fit docking, resulting in improved binding affinity, energy minimization, and more optimized ligand-protein interactions. These parameter changes signify the ligand's capacity to conform more favorably to the specific binding site, ultimately achieving more energetically favorable poses.

#### G. Exploring Ligand-Protein Interactions (*S. aureus* and *E. coli*)

After conducting molecular docking simulations using Glide-Dock in XP mode, an advanced and highly accurate docking mode within the Schrödinger suite, with DATT<sub>n</sub> molecules in various binding pockets of the 5M18 and 3N8D proteins from *S. aureus* bacteria and the 6RKU protein in *E. coli*, we delved deep into the intricate molecular interactions at play (Fig. 4). Glide's XP mode acted, such as a magnifying glass, allowing us to scrutinize the ligand-protein binding with exceptional precision. This in-depth analysis provided us with valuable insights into the binding affinities and potential of these DATT<sub>n</sub> molecules as drug candidates. The data from all pockets were carefully analyzed. Subsequently, the most promising sites were identified and are referred to as "5M18\_site\_1," "3N8D-site\_2," and "6RKU\_site\_2" in Table III. However, it is important to note that the data obtained from docking DATT<sub>n</sub> molecules into these specific pockets (Table IV) do not indicate a strong interaction between the molecules and both proteins in *S. aureus* and the 6RKU protein of *E. coli*. This suggests that these molecules may not effectively bind to the proteins. This observation aligns with the *in vitro* results presented in Table II, which also suggest that the compounds are not effective in inhibiting the growth of *S. aureus* and *E. coli* microbes.



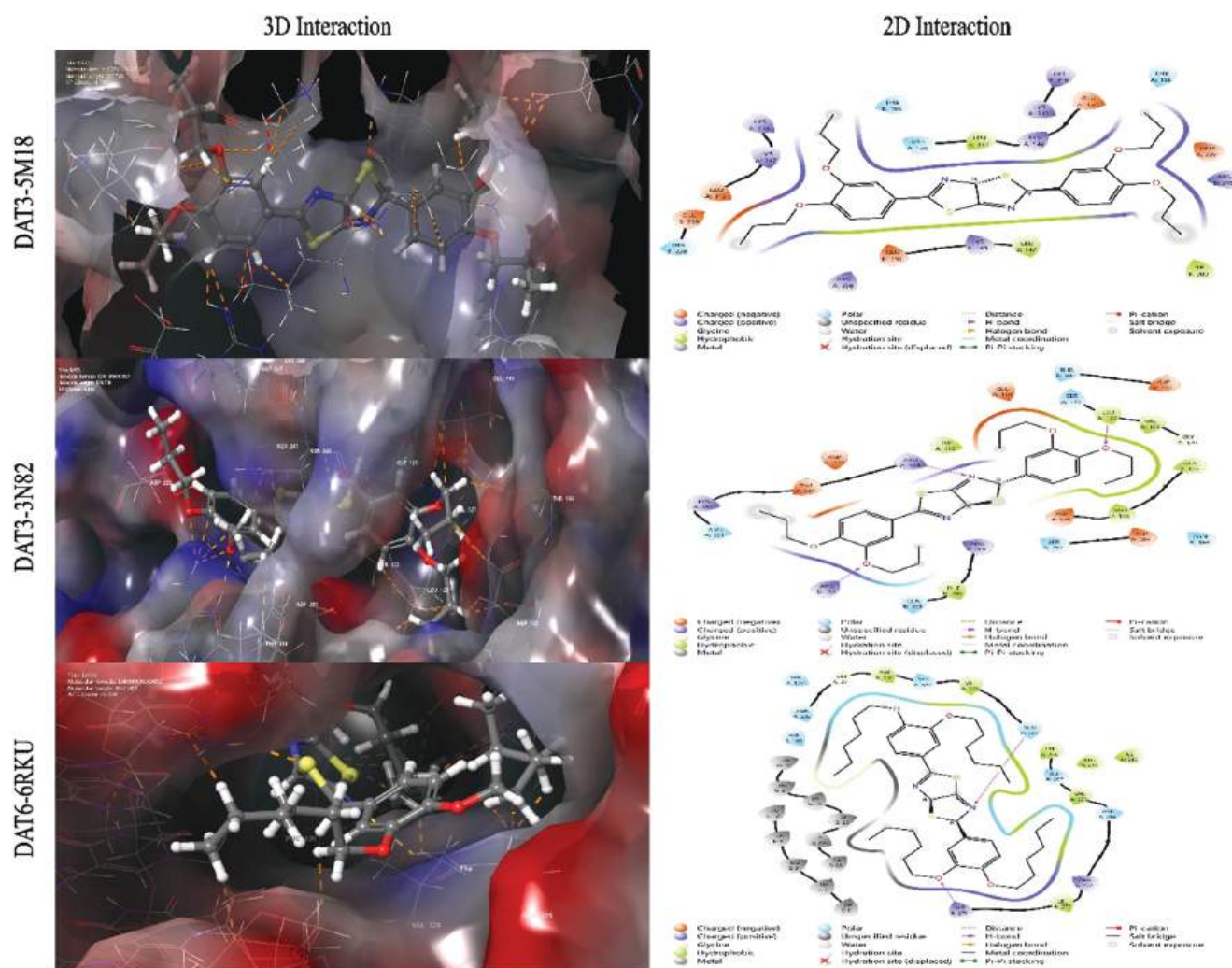


Fig. 4. Protein-ligand interaction maps and electrostatic surfaces for docked  $DATT_3$  on *Staphylococcus aureus* proteins (Portion Data Bank [PDB]: 3N82 and 5M18) and  $DATT_6$  on *Escherichia coli* protein (PDB: 6RKU) in 2D and 3D.

#### H. Molecular Descriptors $DATT_2$ - $DATT_{10}$

In Maestro Schrodinger software, molecular descriptors tool has been used for the prediction of topological descriptors, QikProp properties, semiempirical properties (method to use for SE calculation PM7) through geometry optimization and QikProp 4.4 user manual was employed to evaluate the descriptor values and determine recommended ranges for each descriptor (Hostaš, Řezáč, and Hobza, 2013), and several of these parameters have been shown in Table VIII. The analysis of  $DATT_n$  molecules in Table VIII offers crucial insights into their pharmaceutical characteristics. Notably, the molecular weights (ranging from 472.616 to 921.474 amu) deviate for some  $DATT_n$  molecules from the typical drug range, potentially influencing their suitability in drug development, particularly with regard to factors, such as drug absorption and distribution. In addition, the  $i_{qp}\#stars$  values indicate that  $DATT_4$  to  $DATT_{10}$  possess unique properties compared to established drugs. The  $i_{qp}\#rotor$  values, ranging from 8 to 40, indicate an increased structural flexibility in these molecules, potentially impacting their applicability. A uniform  $i_{qp}\#rtvFG$  value of 0 reduces the

risk of false positives in screening assays. In terms of central nervous system (CNS) activity ( $i_{qp}\#CNS$ ), most  $DATT_n$  molecules are inactive. Dipole moments, predominantly within the expected range of 1.0–12.5, suggest balanced charge distribution, while the absence of hydrogen bonding points to limited interaction with water. The analysis of the First Zagreb index ( $i_{desc}\#First\ Zagreb$ ) highlights size variations among these molecules, with  $DATT_{10}$  being the largest and  $DATT_2$  the smallest. Solvent-accessible surface area (SASA) values for  $DATT_5$  to  $DATT_{10}$  indicate larger-than-typical values, possibly impacting molecular interactions and biological activity. Furthermore,  $DATT_n$  molecules align with the recommended hydrophobic properties ( $r_{qp}\#FOSA$ ) for drugs. The  $\pi$  component of the SASA ( $r_{qp}\#PISA$ ) offers insights into surface area properties related to carbon and attached hydrogen atoms. Polar surface area (PSA) values fall within the expected range, indicating relatively small PSAs. Hydrophilic components remain within the recommended range. Finally, weakly PSA properties ( $r_{qp}\#WPSA$ ) exhibit variations among  $DATT_n$  molecules, presenting a comprehensive overview of their unique pharmaceutical

TABLE VIII  
DECIPHERING DATT<sub>n</sub> MOLECULES: TOPOLOGICAL, QIKPROP, AND SEMIEMPIRICAL REVELATIONS

No.	Property or descriptor	DATT <sub>2</sub>	DATT <sub>3</sub>	DATT <sub>4</sub>	DATT <sub>5</sub>	DATT <sub>6</sub>	DATT <sub>7</sub>	DATT <sub>8</sub>	DATT <sub>9</sub>	DATT <sub>10</sub>	Range or recommended values
1.	r_qp_mol_MW	472.62	528.72	584.83	640.94	697.05	753.15	809.26	865.37	921.47	130.0–725.0
2.	i_qp_#stars	1.00	3.00	6.00	9.00	10.00	11.00	11.00	12.00	12.00	0–5
3.	i_qp_#rotor	8.00	12.00	16.00	20.00	24.00	28.00	32.00	36.00	40.00	0–15
4.	i_qp_#rtvFG	0.00	0.00	0.00	0.00	0.00	0.00	0.00	0.00	0.00	0–2
5.	i_qp_CNS	0.00	0.00	0.00	−1.00	−2.00	−2.00	−2.00	−2.00	−2.00	−2.0–2
6.	r_mopac_Dipole	1.57	3.73	1.84	3.96	3.83	3.14	4.63	1.73	1.50	1–12
7.	r_qp_volume	1,489.67	1,677.13	1,886.26	2,051.56	2,380.64	2,616.12	2,836.69	3,074.95	3,339.37	500–2000
8.	i_desc_First_Zagreb	166.00	182.00	198.00	214.00	230.00	246.00	262.00	278.00	294.00	
9.	r_qp_SASA	836.48	915.65	995.33	1,064.24	1,279.87	1,389.27	1,519.60	1,633.93	1,787.42	300–1000
10.	r_qp_FOSA	527.46	620.98	733.70	802.52	1,012.32	1,124.63	1,230.41	1,370.91	1,515.75	0–750
11.	r_qp_PISA	198.61	183.21	157.90	158.37	177.55	146.32	168.02	175.75	162.88	0–450
12.	r_qp_PSA	43.94	43.67	47.57	46.42	42.48	47.89	45.43	47.79	43.69	7.0–200
13.	r_qp_FISA	31.54	29.18	32.03	26.51	21.28	33.64	34.72	19.67	31.46	7–330
14.	r_qp_WPSA	78.87	82.28	71.70	76.84	68.72	84.68	86.45	67.61	77.33	0.0–175.0
15.	r_qp_donorHB	0.00	0.00	0.00	0.00	0.00	0.00	0.00	0.00	0.00	0–6
16.	r_qp_accptHB	6.50	6.50	6.50	6.50	6.50	6.50	6.50	6.50	6.50	0.0–20.0
17.	r_qp_QPpolrz	50.22	55.01	60.57	64.62	75.41	81.96	88.43	95.47	103.36	13–70
18.	r_qp_QPlogPo/w	6.16	7.40	8.67	9.81	11.98	13.46	14.92	16.52	18.18	−2.0–6.5
19.	r_qp_QPlogS	−7.71	−8.57	−9.38	−10.06	−13.46	−14.95	−16.78	−18.21	−20.51	−6.5–0.5
20.	r_qp_QPlogKp	−0.63	−0.26	−0.02	0.47	1.02	1.06	1.51	2.19	2.32	−8.0–−1.0
21.	r_qp_QPPMDCK	7,577.53	8,365.19	6,843.61	8,317.08	8,494.52	7,761.02	7,734.32	8,701.66	7,445.97	<25 poor, >500 great
22.	r_qp_QPPCaco	4,975.04	5,238.45	4,922.62	5,552.44	6,224.53	4,752.50	4,641.00	6,447.90	4,983.75	<25 poor, >500 great
23.	r_qp_QPlogBB	−0.10	−0.31	−0.61	−0.78	−1.03	−1.43	−1.72	−1.78	−2.23	−3.0–1.2
24.	r_qp_PercentHumanOralAbsorption	100.00	100.00	100.00	100.00	100.00	100.00	100.00	100.00	100.00	>80% is high
25.	i_qp_RuleOfFive	1.00	2.00	2.00	2.00	2.00	2.00	2.00	2.00	2.00	Maximum is 4
26.	i_qp_RuleOfThree	2.00	2.00	2.00	2.00	2.00	2.00	2.00	2.00	2.00	Maximum is 3
27.	r_mopac_HOMO_Energy	−8.42	−8.41	−8.56	−8.43	−8.40	−8.72	−8.48	−8.56	−8.50	PM7
28.	r_mopac_LUMO_Energy	−0.96	−0.85	−0.92	−0.88	−0.89	−0.91	−0.86	−0.83	−0.95	PM7
29.	r_mopac_MOPAC_Total_Energy_EV	−5,231.4	−5,831.2	−6,431.0	−7,030.8	−7,630.6	−8,230.5	−8,830.3	−9,421.0	−10,030.1	PM7
30.	r_mopac_MOPAC_Heat_of_Formation	−70.23	−91.10	−113.18	−134.85	−150.92	−174.29	−192.48	−206.67	−234.73	PM7

SASA: Solvent-accessible surface area, WPSA: Weakly polar surface area, CNS: Central nervous system, HOMO: Highest occupied molecular orbital, LUMO: Lowest unoccupied molecular orbital

attributes. In the examination of the DATT<sub>n</sub> molecules (DATT<sub>2</sub> to DATT<sub>10</sub>), a spectrum of significant characteristics and descriptors emerges. Evidently, these molecules manifest limited propensity for hydrogen bonding with water, denoted by an estimated average of zero hydrogen bonds donated to water molecules, juxtaposed with their capacity to accept an average of 6.5 hydrogen bonds from water. Their polarizability values indicate variations in their interaction potential, with DATT<sub>6</sub> to DATT<sub>10</sub> exceeding the conventional range. Moreover, the r\_qp\_QPlogPo/w descriptor highlights deviations in their affinity for organic solvents over water, which may impact solubility and distribution. Their aqueous solubility levels suggest potential obstacles, with all DATT<sub>n</sub> molecules encountering difficulties in achieving aqueous solubility. Strikingly, these compounds exhibit elevated skin permeability and the ability to effectively transgress the blood–brain barrier, promising prospects for dermal drug delivery and CNS interaction. Their adherence to Lipinski’s rule of five underscores their drug-like attributes, although Jorgensen’s rule of three implies potential challenges in oral availability. The analysis of electronic structure unveils fluctuations in highest occupied molecular orbital and lowest unoccupied molecular orbital energy levels, signifying shifts in reactivity and stability (Omer, et al., 2020; Ahmed and

Omer, 2021). A progressive trend of stability, as indicated by diminishing MOPAC total energy and heat of formation values, positions DATT<sub>n</sub> molecules for multifaceted applications in the pharmaceutical and chemical domains.

#### IV. CONCLUSION

The synthesis and assessment of DATT<sub>n</sub> compounds have unveiled their potential as promising antimicrobial agents. Our *in vitro* experiments have unveiled their remarkable antifungal activity against *C. albicans*, offering a promising avenue for combatting fungal infections. Nevertheless, it is crucial to acknowledge the limited efficacy of these compounds against *S. aureus* and *E. coli*, two clinically significant bacterial strains. The *in silico* molecular docking studies, conducted using the Schrödinger suite, have yielded valuable insights into the interactions between DATT<sub>n</sub> compounds and specific target proteins within these pathogens. Particularly, the robust binding affinity observed between DATT<sub>n</sub> compounds and the 8JZN protein in *C. albicans* suggests their suitability as potential drug candidates for treating fungal infections. The combined results from our *in vitro* and *in silico* investigations underscore the multifaceted nature of DATT<sub>n</sub> compounds,

emphasizing their promise as antifungal agents. Subsequent research and clinical trials are imperative to fully explore their therapeutic potential, evaluate their safety profile, and establish their efficacy for clinical applications.

#### ACKNOWLEDGMENT

Authors would like to express our gratitude to Koya University's Chemistry Department for their assistance and support in our endeavor.

#### REFERENCES

- Abad-Zapatero, C., and Metz, J.T., 2005. Ligand efficiency indices as guideposts for drug discovery. *Drug Discovery Today*, 10, pp.464-469.
- Ahmed, L., and Omer, R., 2021. 1H-pyrrole, furan, and thiophene molecule corrosion inhibitor behaviors. *Journal of Physical Chemistry and Functional Materials*, 4, pp.1-4.
- Al-Mutabagani, L.A., Alshabanah, L.A., Gomha, S.M., Abolibda, T.Z., Shaban, M., and Ahmed, H.A., (2021). Synthesis and mesomorphic and electrical investigations of new furan liquid crystal derivatives. *Frontiers in Chemistry*, 9, p.711862.
- Anwar Omar, R., Koparir, P., Koparir, M., and Safin, D.A., 2023. A novel cyclobutane-derived thiazole-thiourea hybrid with a potency against COVID-19 and tick-borne encephalitis: Synthesis, characterization, and computational analysis. *Journal of Sulfur Chemistry*, 45, pp.1-18.
- Atmaram, U.A., and Roopan, S.M., 2022. Biological activity of oxadiazole and thiadiazole derivatives. *Applied Microbiology and Biotechnology*, 106, pp.3489-3505.
- Beinat, C., 2014. *The Design and Synthesis of Selective  $\alpha$ 7 Nicotinic Acetylcholine Receptor Agonists for the Treatment of Neurological Disease*. The University of Sydney, Sydney.
- Chen, W., Cui, D., Jerome, S.V., Michino, M., Lenselink, E.B., Huggins, D.J., Beaudrait, A., Vendome, J., Abel, R., Friesner, R.A., and Wang, L., 2023a. Enhancing hit discovery in virtual screening through absolute protein-ligand binding free-energy calculations. *Journal of Chemical Information and Modeling*, 63, pp.3171-3185.
- Chen, W., Cui, D., Jerome, S.V., Michino, M., Lenselink, E.B., Huggins, D.J., Beaudrait, A., Vendome, J., Abel, R., Friesner, R.A., and Wang, L., 2023b. Enhancing hit discovery in virtual screening through absolute protein-ligand binding free-energy calculations. *Journal of Chemical Information and Modeling*, 63, pp.3171-3185.
- Erdoğan, M., Taslimi, P., and Tuzun, B., 2021. Synthesis and docking calculations of tetrafluoronaphthalene derivatives and their inhibition profiles against some metabolic enzymes. *Archiv der Pharmazie*, 354, p.2000409.
- Farid, R., Day, T., Friesner, R.A., and Pearlstein, R.A., 2006. New insights about HERG blockade obtained from protein modeling, potential energy mapping, and docking studies. *Bioorganic and Medicinal Chemistry*, 14, pp.3160-3173.
- Fishovitz, J., Hermoso, J.A., Chang, M., and Mobashery, S., 2014. Penicillin-binding protein 2a of methicillin-resistant *Staphylococcus aureus*. *IUBMB Life*, 66, pp.572-577.
- Gulcin, İ., Petrova, O.V., Taslimi, P., Malysheva, S.F., Schmidt, E.Y., Sobenina, L.N., Gusarova, N.K., Trofimov, B.A., Tuzun, B., and Farzaliyev, V.M., 2022. Synthesis, characterization, molecular docking, acetylcholinesterase and  $\alpha$ -glycosidase inhibition profiles of nitrogen-based novel heterocyclic compounds. *ChemistrySelect*, 7, p.e202200370.
- Halgren, T.A., 2009. Identifying and characterizing binding sites and assessing druggability. *Journal of Chemical Information and Modeling*, 49, pp.377-389.
- Hamad, W.M., Aziz, H.J., and Al-Dujaili, A.H., 2004. Synthesis and liquid crystalline studies of some heterocyclic compounds with lateral long chain substituents. *ZANCO Journal of Pure and Applied Sciences*, 16, pp.63-69.
- Hopkins, A.L., Keserü, G.M., Leeson, P.D., Rees, D.C., and Reynolds, C.H., 2014. The role of ligand efficiency metrics in drug discovery. *Nature Reviews Drug Discovery*, 13, pp.105-121.
- Hostaš, J., Řezáč, J., and Hobza, P., 2013. On the performance of the semiempirical quantum mechanical PM6 and PM7 methods for noncovalent interactions. *Chemical Physics Letters*, 568, pp.161-166.
- Jakhar, R., Khichi, A., Kumar, D., Sura, K., Bhoomika, Dangi, M., and Chhillar, A.K., 2022. Development of pharmacophore model to identify potential DNA gyrase inhibitors. *Journal of Biomolecular Structure and Dynamics*, 41, pp.10125-10135.
- Jays, J., Mohan, S., and Saravanan, J., 2019. Molecular docking studies of novel aminopyrimidines as potent antifungal agents. *Chemical Methodologies*, 3, pp.442-450.
- Kaka, K.N., Omer, R.A., Mamand, D.M., and Qader, A.F., 2024. Bromination of chalcone: Study on synthesis, characterization, and optoelectronic properties. *Aro-The Scientific Journal of Koya University*, 12, pp.48-53.
- Khan, F., Jeong, G.J., Javaid, A., Thuy Nguyen Pham, D., Tabassum, N., and Kim, Y.M., 2023. Surface adherence and vacuolar internalization of bacterial pathogens to the *Candida* spp. cells: Mechanism of persistence and propagation. *Journal of Advanced Research*, 53, pp.115-136.
- Koparir, P., Anwar Omar, R., Sarac, K., Koparir, M., and Safin, D.A., 2023a. Novel 1, 2, 4-triazolethiol-thiophen Hybrids: Facile synthesis, characterization, ADMET prediction and molecular docking. *Polycyclic Aromatic Compounds*, 6, pp.1-15
- Koparir, P., Omar, R.A., Sarac, K., Ahmed, L.O., Karatepe, A., Taskin-Tok, T., and Safin, D.A., 2023b. Synthesis, characterization and computational analysis of thiophene-2, 5-diylbis ((3-mesityl-3-methylcyclobutyl) methanone). *Polycyclic Aromatic Compounds*, 43, pp.6107-6125.
- Koparir, P., Parlak, A.E., Karatepe, A., and Omar, R.A., 2022. Elucidation of potential anticancer, antioxidant and antimicrobial properties of some new triazole compounds bearing pyridine-4-yl moiety and cyclobutane ring. *Arabian Journal of Chemistry*, 15, p.103957.
- Lebreton, F., and Cattoir, V., 2019. Resistance to glycopeptide antibiotics. In: *Bacterial Resistance to Antibiotics: From Molecules to Man*. John Wiley and Sons, United States, pp.51-80.
- Liu, J., and Balasubramanian, M.K., 2001. 1,3-beta-Glucan synthase: A useful target for antifungal drugs. *Current Drug Targets-Infectious Disorders*, 1, pp.159-169.
- Mahasanen, K.V., Molina, R., Bouley, R., Batuecas, M.T., Fisher, J.F., Hermoso, J.A., Chang, M., and Mobashery, S., 2017. Conformational dynamics in penicillin-binding protein 2a of methicillin-resistant *Staphylococcus aureus*, allosteric communication network and enablement of catalysis. *Journal of the American Chemical Society*, 139, pp.2102-2110.
- Mamad, D.M., Azeez, Y.H., Kaka, A.K., Ahmed, K.M., Omer, R.A., and Ahmed, L.O., 2024. The inhibitor activity of some azo compound derivatives using density functional theory and molecular dynamics simulations. *Computational and Theoretical Chemistry*, 1237, p.114645.
- Moravej, H., Moravej, Z., Yazdanparast, M., Heiat, M., Mirhosseini, A., Moosazadeh Moghaddam, M., and Mirnejad, R., 2018. Antimicrobial peptides: Features, action, and their resistance mechanisms in bacteria. *Microbial Drug Resistance*, 24, pp.747-767.
- Naghiyev, F., Mamedov, I., Askerov, R., Taslimi, P., and Poustforoosh, A., 2022. Synthesis and biological activity of functionally substituted pyrimidine and pyran derivatives on the basis of isatylidene malononitriles. *ChemistrySelect*, 7, p.e202202006.
- Nöllmann, M., Crisona, N.J., and Arimondo, P.B., 2007. Thirty years of

*Escherichia coli* DNA gyrase: From *in vivo* function to single-molecule mechanism. *Biochimie*, 89, pp.490-499.

Omar, R.A., Koparir, P., Sarac, K., Koparir, M., and Safin, D.A., 2023a. A novel coumarin-triazole-thiophene hybrid: Synthesis, characterization, ADMET prediction, molecular docking and molecular dynamics studies with a series of SARS-CoV-2 proteins. *Journal of Chemical Sciences (Bangalore)*, 135, p.6.

Omar, R.A., Omar, K.A., and Abdullah, B.A., 2016a. Polyaniline: Synthesis, characterizations and study their antibacterial activity against *Escherichia coli*. *Journal of Chemical, Biological and Physical Sciences*, 6, p.510.

Omar, R.A., Smail, A.K., and Omar, K.A., 2016b. Study on the activity of Ag/Nylon 6, 10 nanocomposite against *Escherichia coli*. *International Journal of Current Microbiology and Applied Sciences*, 5, pp.935-941.

Omar, S.Y., Mamand, D.M., Omer, R.A., Rashid, R.F., and Salih, M.I., 2023b. Investigating the role of metoclopramide and hyoscine-N-Butyl bromide in colon motility. *ARO-The Scientific Journal of Koya University*, 11, pp.109-115.

Omer, R.A., Ahmed, L.O., Koparir, M., and Koparir, P., 2020. Theoretical analysis of the reactivity of chloroquine and hydroxychloroquine. *Indian Journal of Chemistry*, 59A, pp.1828-1834.

Omer, R.A., Gheni, A.I., Omar, K.A., and Ahmed, L.O., 2019. Antimicrobial activity of nylon nanocomposites against *Staphylococcus aureus* and *Escherichia coli* bacteria. *Science Journal of University of Zakho*, 7, pp.138-143.

Omer, R.A., Koparir, P., and Koparir, M., 2023a. Synthesis, experimental characterization, DFT and theoretical anticorrosion study for 1-(4-(3-Methyl-3-phenylcyclobutyl)thiazol-2-yl)-3-(p-tolyl)thiourea. *Protection of Metals and Physical Chemistry of Surfaces*, 59, pp.1315-1325.

Omer, R.A., Mustafa, R.A., Salih, S., Hamad, W., and Taher, S., 2023b. Synthesis of a new series of benzothiazole compounds and study of their liquid crystal properties. *Passer Journal of Basic and Applied Sciences*, 5, pp.78-84.

Paymal, S.B., Barale, S.S., Supanekar, S.V., and Sonawane, K.D., 2023. Structure based virtual screening, molecular dynamic simulation to identify the oxadiazole derivatives as inhibitors of *Enterococcus* D-Ala-D-Ser ligase for combating vancomycin resistance. *Computers in Biology and Medicine*, 159, p.106965.

Rajitha, G., Rani, M.V., Vankadoth, U.N., and Umamaheswari, A., 2021. Design of novel selective estrogen receptor inhibitors using molecular docking and protein-ligand interaction fingerprint studies. *Journal of Pharmaceutical*

*Research International*, 33, pp.470-483.

Rementeria, A., López-Molina, N., Ludwig, A., Vivanco, A.B., Bikandi, J., Pontón, J., and Garaizar, J., 2005. Genes and molecules involved in *Aspergillus fumigatus* virulence. *Revista Iberoamericana de Micología*, 22, pp.1-23.

Ruer, S., Pinotsis, N., Steadman, D., Waksman, G., and Remaut, H., 2015. Virulence-targeted antibacterials: Concept, promise, and susceptibility to resistance mechanisms. *Chemical Biology and Drug Design*, 86, pp.379-399.

Salih, S.K., Mustafa, R.M., Mamad, D.M., Kaka, K.N., Omer, R.A., and Hamad, W.M., 2023. Synthesis of liquid crystalline benzothiazole based derivatives: Theoretical and experimental study of their optical and electrical properties. *ZANCO Journal of Pure and Applied Sciences*, 35, pp.143-162.

Sandor, M., Kiss, R., and Keserű, G.R.M., 2010. Virtual fragment docking by Glide: A validation study on 190 protein-fragment complexes. *Journal of Chemical Information and Modeling*, 50, pp.1165-1172.

Sarafroz, M., Siddiqui, S.A., and Yar, M.S., 2020. Synthesis, antimicrobial, and molecular docking studies of 1, 3-thiazolidin-4-one analogs bearing benzothiazole. *Indian Journal of Heterocyclic Chemistry*, 30, pp.325-335

Sastry, M., Lowrie, J.F., Dixon, S.L., and Sherman, W., 2010. Large-scale systematic analysis of 2D fingerprint methods and parameters to improve virtual screening enrichments. *Journal of Chemical Information and Modeling*, 50, pp.771-784.

Tripathi, S.K., Selvaraj, C., Singh, S.K., and Reddy, K.K., 2012. Molecular docking, QPLD, and ADME prediction studies on HIV-1 integrase leads. *Medicinal Chemistry Research*, 21, pp.4239-4251.

Vass, M., Tarcsay, Á., and Keserű, G.M., 2012. Multiple ligand docking by Glide: Implications for virtual second-site screening. *Journal of Computer-Aided Molecular Design*, 26, pp.821-834.

Verma, A.K., Ahmed, S.F., Hossain, M.S., Bhojiya, A.A., Mathur, A., Upadhyay, S.K., Srivastava, A.K., Vishvakarma, N.K., Barik, M., and Rahaman, M.M., 2022. Molecular docking and simulation studies of flavonoid compounds against PBP-2a of methicillin-resistant *Staphylococcus aureus*. *Journal of Biomolecular Structure and Dynamics*, 40, pp.10561-10577.

Zhao, C.R., You, Z.L., Chen, D.D., Hang, J., Wang, Z.B., Ji, M., Wang, L.X., Zhao, P., Qiao, J., and Yun, C.H., 2023. Structure of a fungal 1, 3- $\beta$ -glucan synthase. *Science Advances*, 9, p.eadh7820.

# Assessment of Radioactivity in Building Materials: Implications for Health in Kurdistan Region of Iraq

Adeeb O. Jafir<sup>1†</sup>, Mohammed I. Hussein<sup>1</sup>, Idrees A. Nadir<sup>2</sup>, Barzan N. Sabr<sup>1</sup> and Ali H. Ahmed<sup>1</sup>

<sup>1</sup>Department of Physics, College of Science, Salahaddin University - Erbil, Erbil, Kurdistan Region – F.R. Iraq

<sup>2</sup>Department of Earth Sciences and Petroleum, College of Science, Salahaddin University - Erbil, Erbil, Kurdistan Region – F.R. Iraq

**Abstract**—This research investigates the radioactivity levels of various rock types used in construction within the Kurdistan region and assesses their potential impact on human health, the measurements were performed using an HPGe gamma-ray spectrometer. The measured activity concentrations of <sup>226</sup>Ra, <sup>232</sup>Th, and <sup>40</sup>K radionuclides varied from ND (Chromitite) to 78.68 ± 4.54 Bq/kg (Marly Limestone), ND (Chromitite) to 109.52 ± 10.23 Bq/kg (Mudstone), and ND (Chromitite) to 2973.6 ± 152.1 Bq/kg (Claystone), respectively. The obtained Ra<sub>eq</sub> values for all rock samples are well below the UNSCEAR, 2008 recommended value of 370 Bq/kg, 71.43% of D<sub>R</sub>, 66.66% of E<sub>out</sub>, 71.43% of E<sub>in</sub>, 100% of H<sub>in</sub> and H<sub>out</sub>, 71.43% of ELCR<sub>out</sub>, 71.43% of ELCR<sub>in</sub>, and 100% of activity utilization index of the rock samples are well below the recommended values declared by UNSCEAR, 2008. The radioactivity level of rock types that are prepared as building materials should be assessed by the producers and considered by the users to reduce the overall cancer risk. The outcomes of the RESRAD-BUILD computer code indicate that the maximum external and inhalation doses were calculated to be 19.7 and 0.105 μSv for R7 and R1 samples, respectively, over a period of 70 years.

**Index Terms** – Annual dose, Building materials, HPGe detector, Primordial radionuclides, Radiation indices, RESRAD-BUILD code, Rocks.

## I. INTRODUCTION

Radiation is present in the environment, and people are exposed to it in their natural environments through frequent sources of ionizing radiation. Background radiation typically comes from terrestrial and cosmic rays (Guidebook, 1989). The most common radionuclides in nature that produce

gamma radiation are thorium, uranium, and potassium. Potassium experiences a simple radioactive decay, but uranium and thorium go through a series of complex disintegrations (Hanfi, et al., 2021).

The fundamental source of radiological exposure that monitors interest is due to primordial radionuclides such as <sup>238</sup>U, <sup>232</sup>Th, and <sup>40</sup>K, which occur in minerals such as zircon and monazites (Gaafar, Cunej, Gawad, 2014).

Uranium and thorium produce oxygen-containing compounds. Typically, 2–4 ppm of uranium and 8–12 ppm of thorium can be found in the crust of the earth. The minerals with the highest thorium concentrations in rocks are monazite, orthite, zircon, sphere, epidote, and apatite (El Mezayen, et al., 2019).

Potassium is the major element and thorium is the minor element by weight content in the Earth's crust (2.83% and 9.6 ppm, respectively). The origin of radon in minerals in the crust of the earth is the decay of uranium and thorium; the concentration increases in fractures and veins (Gundersen, 2020).

The rocks are used for different building purposes, such as cement (limestone) and construction material (sandstone), which are both sedimentary sources; bath scrub (pumice) and kerb stone (granite), which are both of igneous sources; roofing material (slate), which is of metamorphic source; and statues, ornaments, and adornments (marble), which are all made from metamorphic rocks (Hossain, et al., 2020).

As the public's anxiety grows, numerous studies have been conducted recently to evaluate the natural primordial radionuclides present in different rock types used as building materials locally and internationally (Ahmed and Hussein, 2011; Legasu and Chaubey, 2022; Alshahrani, 2021; Salaheldin, et al., 2020; Abbas, Khattab and Abdel Azeem, 2018; Harb, et al., 2012a; Alnour, et al., 2012; Harb, et al., 2012b; Turhan, 2010; Rosianna, et al., 2020; Kuzmanović, et al., 2020; Oladunjoye, et al., 2022; Narloch, et al., 2019; Fallatah and Khattab, 2023).

In Iraq, especially within the Kurdistan area, there is no level of reference for radioactivity, and the majority of the population has constructed their dwellings from a variety of materials derived primarily from rocks.

ARO-The Scientific Journal of Koya University  
Vol. XII, No 2 (2024), Article ID: ARO.11545. 10 pages  
DOI: 10.14500/aro.11545

Received: 08 February 2024; Accepted: 25 June 2024

Regular research paper; Published: 25 July 2024

†Corresponding author's e-mail: adeeb.jafir@su.edu.krd

Copyright © 2024 Adeeb O. Jafir, Mohammed I. Hussein, Idrees A. Nadir, Barzan N. Sabr, and Ali H. Ahmed. This is an open access article distributed under the Creative Commons Attribution License.



The samples in the study area are composed of igneous, metamorphic, and sedimentary rocks (Table I), deposited at different geological ages from the Mesozoic to the Cenozoic. Tectonically, the study area is within the unstable shelf, and this zone is divided into subdivisions: thrust zone, imbricated zone, and high folded zone (Jassim and Goff, 2006).

In this study, the natural radioactivity of various rock types in the Kurdistan region of Iraq is determined using an HPGe gamma-ray spectrometer. Based on guidelines issued by UNSCEAR 2008, radium equivalent activities, the absorbed dose rate, annual effective dose, external and internal hazard index, activity utilization index (AUI), and excess lifetime cancer have been determined. In addition, the residents' inhalation and external doses have been computed using the simulation RESRAD BUILD computer code. Aiming to inform safety standards and mitigate health risks associated with prolonged exposure to natural radionuclides.

## II. GEOLOGICAL SETTING OF THE STUDY AREA

Tectonically, Iraq is divided into many NW-SE trending parallel zones, according to Jassim and Goff, 2006. Iraq is tectonically divided from the southwest to the northeast into two major units: The Arabian Platform and the Shalair (Sanandaj-Sirjan) Terrane. The Arabian Platform is divided into an inner and an outer platform. The inner platform corresponds to the southwestern part of the stable shelf, whereas the outer platform was divided into the Mesopotamia Foredeep and the Western Zagros Fold-Thrust Belt. The Western Zagros Fold-Thrust Belt is further divided into four zones: The Low-Folded Zone (equivalent to the Foothill Zone), the High-Folded Zone, the Imbricate Zone, and the

Suture Zone (Jassim and Goff, 2006). The geological map of the study area is shown in Fig. 1.

## III. MATERIALS AND PROCEDURES

### A. Collection and Processing of Samples

In this investigation, 21 different types of rocks (three samples from each position and taking the average reduce the statistical uncertainty and improve the stability) were gathered from different locations in Kurdistan, as depicted in Fig. 2. All of the samples were pulverized and ground to the proper grain size for a 100-mesh sieve, and then desiccated in a furnace at 110°C for approximately 24 h. To establish secular equilibrium among the parent and its progeny, the dried samples were set within a 1 L Marinelli beaker with a tightly taped and sealed neck to prevent radon gas from escaping and then stored for 4 weeks.

In addition to the longitude, latitude, and altitude obtained using the GPS model (GPS-72, GARMIN), the geological character and elevation above sea level at each location have been determined, as illustrated in Table I.

### B. Estimation of Primordial Radionuclides in Rock Samples

The activity concentration of radionuclides was obtained from the spectra. In this configuration, Princeton Gamma Tech (PGT) Corporation, United States, manufactured the high-purity germanium detectors consisting of a vertically closed-end p-type coaxial with the following features: The diameter and length of the crystal are 70.6 and 70.7 mm, respectively (Azeez, Ahmad and Mansour, 2018).

Both resolution and relative efficiency for the detector were 1.97 keV for the second photopeak of <sup>60</sup>Co and 73.8%, respectively. The system's energy was calibrated using man-

TABLE I  
GEOLOGICAL AND GEOGRAPHICAL INFORMATION ABOUT THE STUDY AREA

Sample code	Location	Rock type	Rock components	Longitude	Latitude	Elevation (m)
R1	Bastora	Mudstone	Clay minerals	36°19'58" N	44°10'07" E	620
R2	Banaman	Sandstone	Quartz, feldspar, and rock fragments	36°21'14" N	44°10'47" E	740
R 3	Banaman	Marly limestone	Claystone and calcite	36°21'14" N	44°10'55" E	750
R 4	Banaman	Chalky limestone	calcite	36°21'30" N	44°11'20" E	800
R 5	Banaman	Dolomitic limestone	Dolomite mineral and calcite	36°21'30" N	44°11'20" E	800
R 6	Kore	Gypsum	Gypsum minerals	36°23'59" N	44°15'12" E	820
R 7	Kore	Claystone	Clay minerals	36°23'59" N	44°15'12" E	820
R 8	Hujran	Siltstone	Quartz and feldspar	36°24'27" N	44°15'45" E	830
R 9	Hujran	Marlstone	Clay minerals and calcite	36°24'48" N	44°15'48" E	830
R 10	Hujran	Limestone	Calcite	36°25'12" N	44°15'54" E	860
R 11	Beklo	Gabbro	Pyroxene, Ca-plagioclase, and Olivine	36°07'13" N	45°16'20" E	1215
R 12	Qalandar	Chromitite	Chromite mineral and serpentine	36°48'33" N	44°27'00" E	1345
R 13	Beklo	Amphibolite	Hornblende and plagioclase	36°08'20" N	45°17'25" E	1421
R 14	Jinasan	Pyroxenite	Pyroxene 100%	36°37'08" N	44°55'07" E	1468
R 15	Penjween	Hornblendite	Hornblende 100%	35°34'56" N	45°58'02" E	1469
R 16	Qaladiza	Marble	calcite	36°07'54" N	45°16'42" E	915
R 17	Shler valley	Plagiogranite	Quartz, Na-plagioclase, and orthoclase	35°45'59" N	46°12'09" E	1400
R 18	Shler valley	Granite	Quartz, orthoclase and Na-plagioclase	35°48'02" N	46°13'46" E	1920
R 19	Shler valley	Metamorphosed granite	Quartz, orthoclase, and Na-plagioclase	35°46'07" N	46°16'58" E	1630
R 20	Shler valley	Metamorphosed granite with increasing iron deposits	Quartz, orthoclase, and Na-plagioclase+Iron	35°46'04" N	46°17'36" E	1840
R 21	Choman	Phyllite	Clay minerals	36°34'49" N	44°59'29" E	3288

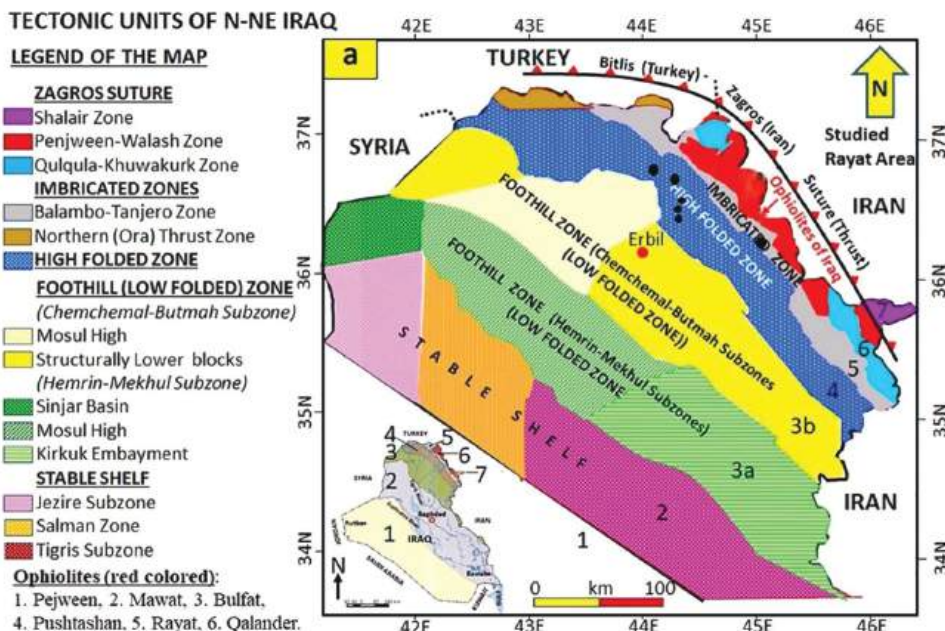


Fig. 1. Tectonic map of Iraq shows the study area (Ahmed, Kettanah and Ismail, 2020).

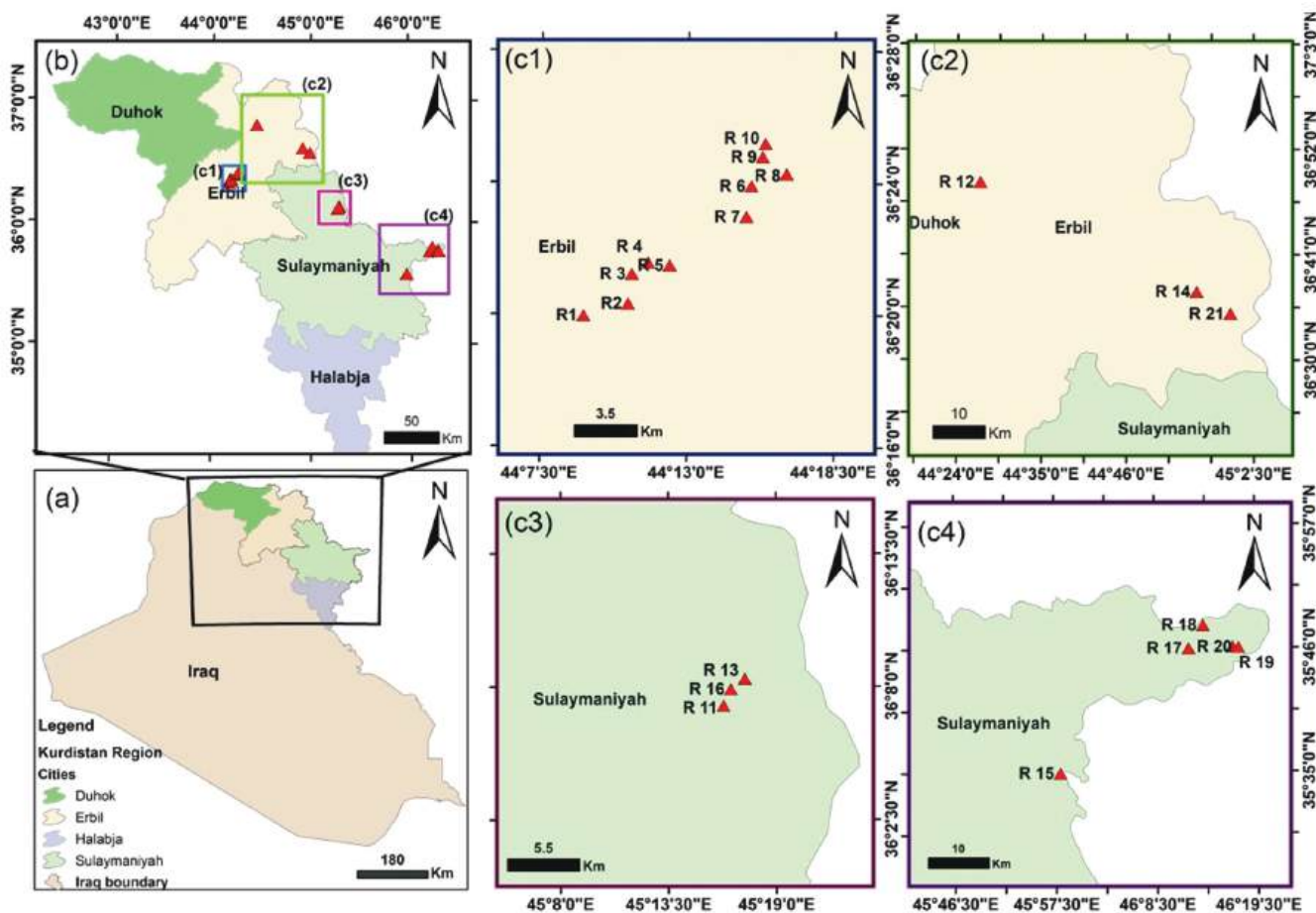


Fig. 2. Sampled position area in the Kurdistan Region.

made sources of  $^{60}\text{Co}$ ,  $^{137}\text{Cs}$ , and  $^{226}\text{Ra}$ . The standard sources used for the efficiency calibration must be under the same conditions as rock samples (Abdel-Rahman, et al., 2018; Bell, Judge and Regan, 2012).

The gamma spectroscopy technique of the HPGe detector at Koya University was used to obtain the spectra of rock samples. Both KCL and  $\text{UO}_2 \cdot (\text{OCOCH}_3)_2 \cdot 2\text{H}_2\text{O}$  in powder and solution form were applied to the volumetric efficiency

curves of Angle-3 with satisfaction (Azceez, Ahmad and Mansour, 2018).

To minimize the radiation that originates from the environmental background, the detector was enclosed in a lead that was 10 cm thick. The samples were left on the detector for 10 h. Using software developed for computers (Quantum-Gold for the PGT Corporation, 2001) and an 8000 multichannel analyzer, the spectra were obtained (Smail, Mansour and Ahmad, 2023). The activity concentration of  $^{226}\text{Ra}$  was obtained from the weighted average of both  $^{214}\text{Pb}$  and  $^{214}\text{Bi}$  decay with energies of 351.9 keV and 609.3 keV, respectively, whereas  $^{232}\text{Th}$  was obtained from  $^{212}\text{Pb}$ ,  $^{208}\text{Ti}$ , and  $^{228}\text{Ac}$  with energies of 583, 2614.5, and 911.2 keV, respectively. In addition,  $^{40}\text{K}$  was determined from 1460.8 keV (10.7%). For the activity concentrations ( $A_c$ ) of primordial radionuclides in rock samples, the following equation was used: (Jafir, 2023):

$$A_c (\text{Bq kg}^{-1}) = N (\varepsilon \times \gamma \times m \times t)^{-1} \pm SD (\varepsilon \times \gamma \times m \times t)^{-1} \quad (1)$$

Where  $N$ ,  $\varepsilon$ ,  $\gamma$ ,  $m$ ,  $t$ , and standard deviation are the net area under the photo peak after being subtracted from background, efficiency, branching ratio, mass, time, and standard deviation, respectively.

For primordial radionuclides, the minimum detectable activities (MDA) were obtained using the following formula (Dina, et al., 2022):

$$\text{MDA} = 1.645\sqrt{b} (\varepsilon \times \gamma \times m \times t)^{-1} \quad (2)$$

Where  $b$  and 1.645 are background counts and statistical coverage factors at a specified level of confidence of 95%, respectively. The calculated MDA for  $^{226}\text{Ra}$ ,  $^{232}\text{Th}$ , and  $^{40}\text{K}$  were found to be 0.54, 0.55, and 0.83 Bq/kg, respectively.

#### IV. RADIOLOGICAL INDICES

Measurement and evaluation of radiological indices are required to emphasize the radioactive dangers resulting from the presence of radionuclides in rocks.

##### A. Radium Equivalent ( $Ra_{eq}$ )

Due to the asymmetrical distribution of primordial natural radionuclides in rock samples (Legasu and Chaubey, 2022). It was established that the activity concentrations of  $^{226}\text{Ra}$ ,  $^{232}\text{Th}$ , and  $^{40}\text{K}$  may be mathematically expressed as a single parameter of ( $Ra_{eq}$ ).

$$Ra_{eq} (\text{Bq kg}^{-1}) = A_{Ra} + A_{Th} \times 1.41 + A_K \times 0.077 \quad (3)$$

Where  $A_{Ra}$ ,  $A_K$ , and  $A_{Th}$  represent the radium, thorium, and potassium-specific activities, respectively.

##### B. Absorbed Gamma Dose Rate ( $D_R$ )

The absorbed dose rate produced by evenly dispersed naturally existing radionuclides  $^{226}\text{Ra}$ ,  $^{232}\text{Th}$ , and  $^{40}\text{K}$  at a height of 1 m over the ground's surface was computed in accordance with the guidance stated by the UNSCEAR, 2000. The following relationship is used to calculate the absorbed gamma dose rate (on the Effects of Atomic Radiation and others, 2008) (Dina, et al., 2022):

TABLE II  
ACTIVITY CONCENTRATIONS OF PRIMORDIAL RADIONUCLIDES IN DIFFERENT ROCK SAMPLES

Sample code	Activity concentration (Bq/kg)		
	$^{226}\text{Ra}$	$^{232}\text{Th}$	$^{40}\text{K}$
R1	28.84±3.54	109.52±10.23	1382.10±75.12
R2	25.06±2.66	50.64±4.77	1544.90±67.19
R3	78.68±4.54	7.71±2.53	494.20±32.03
R4	22.83±2.53	ND±ND	181.9±19.41
R5	ND±ND	1.19±0.69	ND±ND
R6	ND±ND	ND±ND	4.06±0.76
R7	31.50±3.94	15.21±2.52	2973.60±152.1
R8	3.41±0.32	ND±ND	62.22±2.94
R9	36.49±3.47	13.58±3.52	683.60±43.74
R10	41.75±3.87	23.07±4.38	2559.60±120.80
R11	ND±ND	ND±ND	43.96±3.50
R12	ND±ND	ND±ND	ND±ND
R13	1.98±0.31	9.5±0.51	9.65±1.27
R14	5.77±1.35	13±1.59	52.64±6.57
R15	8.08±1.48	10.57±1.96	261.7±17.89
R16	2.38±0.81	ND±ND	ND±ND
R17	ND±ND	1.07±0.34	32.62±4.39
R18	23.16±3.04	58.43±5.94	1319.5±72.04
R19	32.74±3.36	65.82±5.89	2013.20±95.44
R20	11.71±1.77	12.18±2.08	423.80±24.9
R21	4.82±0.72	3.02±0.66	107.90±6.18

$$D_R (\text{nGy h}^{-1}) = A_{Ra} \times 0.462 + A_{Th} \times 0.604 + A_K \times 0.0417 \quad (4)$$

##### C. Annual Effective Dose Rate ( $E_{in}$ and $E_{out}$ )

The dose conversion factor (0.7) and the indoor occupancy factor (0.8), assuming 80% of the time is spent inside, are utilized for calculating the indoor annual effective dose rates (Qureshi, et al., 2014). This information comes from UNSCEAR. The annual effective dose (mSv/y) that a building resident would receive as a result of the activity within the rock materials was calculated using the following formula (Legasu and Chaubey, 2022):

$$E_{in} (\text{mSv/y}) = D_R \times 8760 \times 0.8 \times 0.7 \times 10^{-6} \quad (5)$$

In a similar way, the outdoor annual effective dose ( $E_{out}$ ) is derived from the total gamma radiation dose rate ( $D_R$ ) absorbed in rock samples by factoring in the outside occupancy factor of 0.2 and converting the factor from the rate of dose absorbed within air to the effective dose for individuals, which is 0.7 Sv.Gy<sup>-1</sup>. UNSCEAR (2000) provided the following equation for calculating  $E_{out}$ :

$$E_{out} (\text{mSv y}^{-1}) = D_R \times 8760 \times 0.2 \times 0.7 \times 10^{-6} \quad (6)$$

##### D. AUI

The AUI is an index that may be used to determine whether a material is suitable for building construction or not, given that the material has dual impacts and may be utilized as both a radiation shield and a source of radiation. It is an indicator of the mass percentage of construction materials in a building that is proportional to the fractional usage of those materials. (AUI) is computed using the formula below (Qureshi, et al., 2014; Jafir, Ahmed and Saridan, 2018):



$$AUI = \left( A_{Ra} / 50 \text{ Bq Kg}^{-1} \right) f_{Ra} + \left( A_{Th} / 50 \text{ Bq Kg}^{-1} \right) f_{Th} + \left( A_K / 500 \text{ Bq Kg}^{-1} \right) f_K \quad (7)$$

Where  $f_{Ra}$  (0.462),  $f_{Th}$  (0.604), and  $f_K$  (0.0417) represent the relative contributions of the three radionuclide activities to the gamma dose amount within air.

### V. RESULTS AND DISCUSSION

Table II displays the results of the gamma-ray activity concentrations of  $^{226}\text{Ra}$  and  $^{232}\text{Th}$ , as well as the single decay scheme of  $^{40}\text{K}$ . Concentrations of gamma-ray radionuclide activity are depicted in Fig. 3. Chromitite had the lowest concentrations of  $^{226}\text{Ra}$ ,  $^{232}\text{Th}$ , and  $^{40}\text{K}$ , all of which were below detection (ND). Maximum activity concentrations of  $^{226}\text{Ra}$ ,  $^{232}\text{Th}$ , and  $^{40}\text{K}$  were found in marly limestone ( $78.68 \pm 4.54 \text{ Bq/kg}$ ), mudstone ( $109.52 \pm 10.23 \text{ Bq/kg}$ ), and

clay stone ( $2973.6 \pm 152.1 \text{ Bq/kg}$ ), respectively. The absence of primordial radionuclides in chromitite rock types is related to the mineral composition, formation process, geological settings, and chemical differentiation.

When these results are compared to the global average value, the activity concentration of  $^{226}\text{Ra}$  for all studied samples is within the same range as the global average (32 Bq/kg) stated by the (on the Effects of Atomic Radiation and others, 2008), with the exception of 14.28%, which is found in marly limestone (R3), marlstone (R9), and limestone (R10). For  $^{232}\text{Th}$  activity concentration, 19% of the rock samples exceed the value of 45 Bq/kg, as in mudstone (R1), sandstone (R2), granite (R18), and metamorphosed granite (R19). Compared to UNSCEAR, 2008 (400 Bq/kg), it was found that 42.8% of the rock samples had higher  $^{40}\text{K}$  activity concentrations. Long-term inhalation exposure to uranium and thorium can cause several health problems, including anemia, acute leucopenia, chronic lung illnesses, and oral

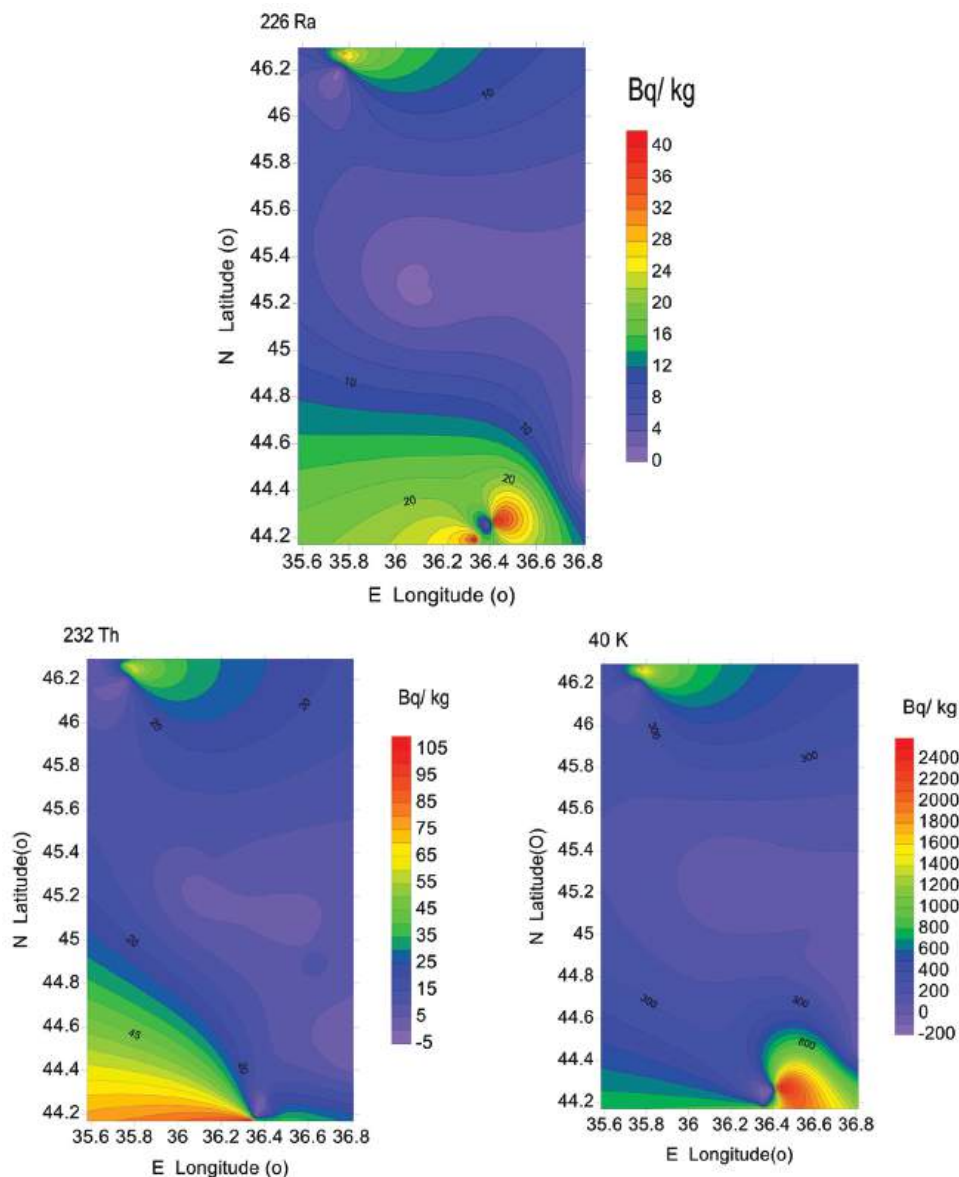


Fig. 3. Contour maps for activity concentrations of primordial radionuclides in rock samples.

necrosis. Cancers of the lungs, pancreas, liver, and kidneys can result from exposure to thorium (Taskin, et al., 2009).

Table III compares the obtained activity concentration values for  $^{226}\text{Ra}$ ,  $^{232}\text{Th}$ , and  $^{40}\text{K}$  with those observed in different countries. The radioactivity of sandstone samples is comparable to the same results reported in Bangladesh (Jaintapur region) (Dina, et al., 2022), but different from the same rock types in Egypt (Harb, et al., 2012a), the discrepancy in data between the two countries is due to the use of different detectors. For example, HPGe and NaI detectors are used. For the gypsum sample, our results are comparable to those reported in Turkey (Turhan, 2010) and Brazil (Narloch, et al., 2019) and lower than those in Iran (Imani, et al., 2021) and the use of gypsum in construction is safe and below the standard values in all of the countries mentioned. In the case of the siltstone samples, the results are completely different and considerably lower than those reported in Egypt (Harb, et al., 2012a). The results for limestone samples are completely inconsistent with those from Turkey (Turhan, 2010), particularly for the  $^{40}\text{K}$  concentrations. Inconsistent with prior measurements from the Western Alps in France (Malczewski and Žaba, 2012), the outcomes obtained in this study for marble samples fall within the limits stated in the UNSCEAR 2008, report. The activity concentrations in granite samples are less than those reported in Egypt (Harb, et al., 2012a)

and Malaysia (Alnour, et al., 2012) for  $^{226}\text{Ra}$ , comparable for  $^{232}\text{Th}$ , and greater than that for  $^{40}\text{K}$ , but less than those reported in Nigeria (Oladunjoye, et al., 2022) and Saudi Arabia (Fallatah and Khattab, 2023) for  $^{226}\text{Ra}$  and  $^{232}\text{Th}$  and greater than that for  $^{40}\text{K}$ . The activity concentrations for  $^{226}\text{Ra}$ ,  $^{232}\text{Th}$ , and  $^{40}\text{K}$  in chromitite are below the detection limit (ND), which is completely different from the results reported for the same rocks in India (Srinivasa, Rangaswamy and Sannappa, 2019). Chromite deposits (ultrabasic rocks) are found in the ultrabasic rocks of many ophiolites (Büchl, Brüggmann and Batanova, 2004). Potassium, uranium, and thorium content increase in igneous rocks with magmatic fractionation. This decreases in basic and ultrabasic rocks since these elements fall within the incompatible group, that is, they are related to components with large radii and high charges, which felsic rocks lack (Aydin, et al., 2006; Lasheen, et al., 2021). Considering the geological mineral composition of rock samples and the geographical conditions derived from different regions of the earth's crust, there is a wide variation in activity concentration in the same rock types around the earth.

#### A. Radiological Hazard Indices

The estimated radiological effects (radium equivalent, absorbed gamma dose rate, annual effective dose rate, and AUI are tabulated in Table IV and depicted in Fig. 4.

TABLE III  
COMPARES CURRENT STUDY ACTIVITY CONCENTRATIONS TO THOSE IN DIFFERENT COUNTRIES

Country	Rock type	Activity concentration (Bq/kg)			References
		$^{226}\text{Ra}$	$^{232}\text{Th}$	$^{40}\text{K}$	
Saudi Arabia	Pumice	79.03	73.13	521.91	(Alshahrani, 2021)
Saudi Arabia	Granite	102.5	486.8	726	(Fallatah and Khattab, 2023)
Iraq (Kurdistan)	Basalt	5.65±0.22	21.4±1.78	203.34±8.12	(Ahmed and Hussein, 2011)
Egypt	Granite	45.75±2.28	50.91±2.56	826.13±39.33	(Salaheldin, et al., 2020)
Egypt	Sand-siltstone	88.8	458.8	627.5	(Abbas, Khattab and Abdel Azeem, 2018)
Egypt	Gneiss	28.4±3	37.7±4	1167.6±42	(Harb, et al., 2012a)
	Granite	118±7	90.5±7	2208±91	
	Basalt	59.5±4	67.7±6	718.5±42	
	Sandstone	7.5±1.5	12.5±3	263.9±11	
	Siltstone	113±7	148.5±12	1672±55	
Brazil	Natural gypsum	1.91±0.10	1.14±0.06	ND	(Narloch, et al., 2019)
Malaysia	Granite	39±0.7	52±1	611±15	(Alnour, et al., 2012)
Iran	Gypsum	12	14	116	(Imani, et al., 2021)
	Granite	38	47	917	
	Marble	7	7	34	
Yemen	Basalt	21.79±3.1	19.5±2.6	399.3±16	(Harb, et al., 2012b)
Turkey	Gypsum	7.2	3.4	40.7	(Turhan, 2010)
	Limestone	19	4.3	55	
Indonesia	Volcanic	22882±16	33549±23	1909±134	(Rosianna, et al., 2020)
China	Granite	356	318	1636	(Tuo, et al., 2020)
Serbia	Granite	200±89	77±6	1280±78	(Kuzmanović, et al., 2020)
Nigeria	Granite	130±20	352±41	412±119	(Oladunjoye, et al., 2022)
Western Alps, France	Calcschist	14.4	14.4	392	(Malczewski and Žaba, 2012)
	Carbonaceousbreccia	22.5	4.26	111	
	Limestone dolomite	26.2	0.52	18	
	Dolomite	29.0	3.0	129	
	Marble	25.7	1.63	78	
	Quartzite	9.1	8.3	572	
India (Karnataka)	Chromite	51.9±1.3	79.4±1.6	423.9±9.6	(Srinivasa, Rangaswamy and Sannappa, 2019)
Bangladesh (Jaintapur area)	Sandstone	25±2	37±4	884±41	(Dina, et al., 2022)
World average	Background	32	45	400	(On the Effects of Atomic Radiation and others, 2008)

TABLE IV  
THE ESTIMATED RADIATION HAZARD INDICES FOR THE ROCK SAMPLES

Rock types	Ra <sub>eq</sub> Bq/kg	D <sub>R</sub> (nGy/h)	E <sub>out</sub> (mSv/y)	E <sub>in</sub> (mSv/y)	AUI
R1	291.87	137.11	0.17	0.67	1.70
R2	216.43	106.58	0.13	0.52	0.97
R3	127.75	61.61	0.08	0.30	0.86
R4	36.83	18.13	0.02	0.09	0.23
R5	1.70	0.72	0.00	0.00	0.01
R6	0.31	0.17	0.00	0.00	0.00
R7	282.21	147.74	0.18	0.72	0.72
R8	8.20	4.17	0.01	0.02	0.04
R9	108.54	53.56	0.07	0.26	0.56
R10	271.83	139.96	0.17	0.69	0.87
R11	3.38	1.83	0.00	0.01	0.00
R12	ND	ND	ND	ND	ND
R13	16.31	7.05	0.01	0.03	0.13
R14	28.42	12.72	0.02	0.06	0.21
R15	43.35	21.03	0.03	0.10	0.22
R16	2.38	1.10	0.00	0.01	0.02
R17	4.04	2.01	0.00	0.01	0.02
R18	208.32	101.02	0.12	0.50	1.03
R19	281.87	138.83	0.17	0.68	1.26
R20	61.76	30.44	0.04	0.15	0.29
R21	17.44	8.55	0.01	0.04	0.09
World average	370	59	0.07	0.41	2

In the current study, the Ra<sub>eq</sub> varied from ND (R12) to 291.87 Bq/kg (R1), as depicted in Fig. 4. The obtained values are lower than the suggested maximum of 370 Bq/kg (Annex, 2000).

The estimated absorbed dose rate ranges from ND (R12) to 147.74 nGy/h (R7); the maximum values are nearly twice the worldwide mean value of 59 nGy/h (Annex, 2000; Jafir, 2023), indicating that 28.57% of the calculated absorbed dose rate resulting from natural radioactive nuclides within the air for the studied area is above the allowed internationally recommended value. The outdoor annual effective doses of the public in the Kurdistan region due to exposure range from ND (R12) to 0.18 mSv/y (R7), whereas the indoor annual effective doses varied from ND (R12) to 0.72 mSv/y (R7), which indicates that 33.34% and 28.57% of the rock samples are outside the range of 0.07 mSv/y and 0.41 mSv/y for both types, respectively, as declared by (on the Effects of Atomic Radiation and others, 2008).

The obtained AUI values range from ND (R12) to 1.70 (R1). All are <2, implying an effective annual dose of a value below 0.3 mSv/y (Jafir, Ahmed and Saridan, 2018). The result demonstrates that these rocks are suitable for use in construction. Similar results were obtained by (Raghu, et al., 2017) regarding construction materials.

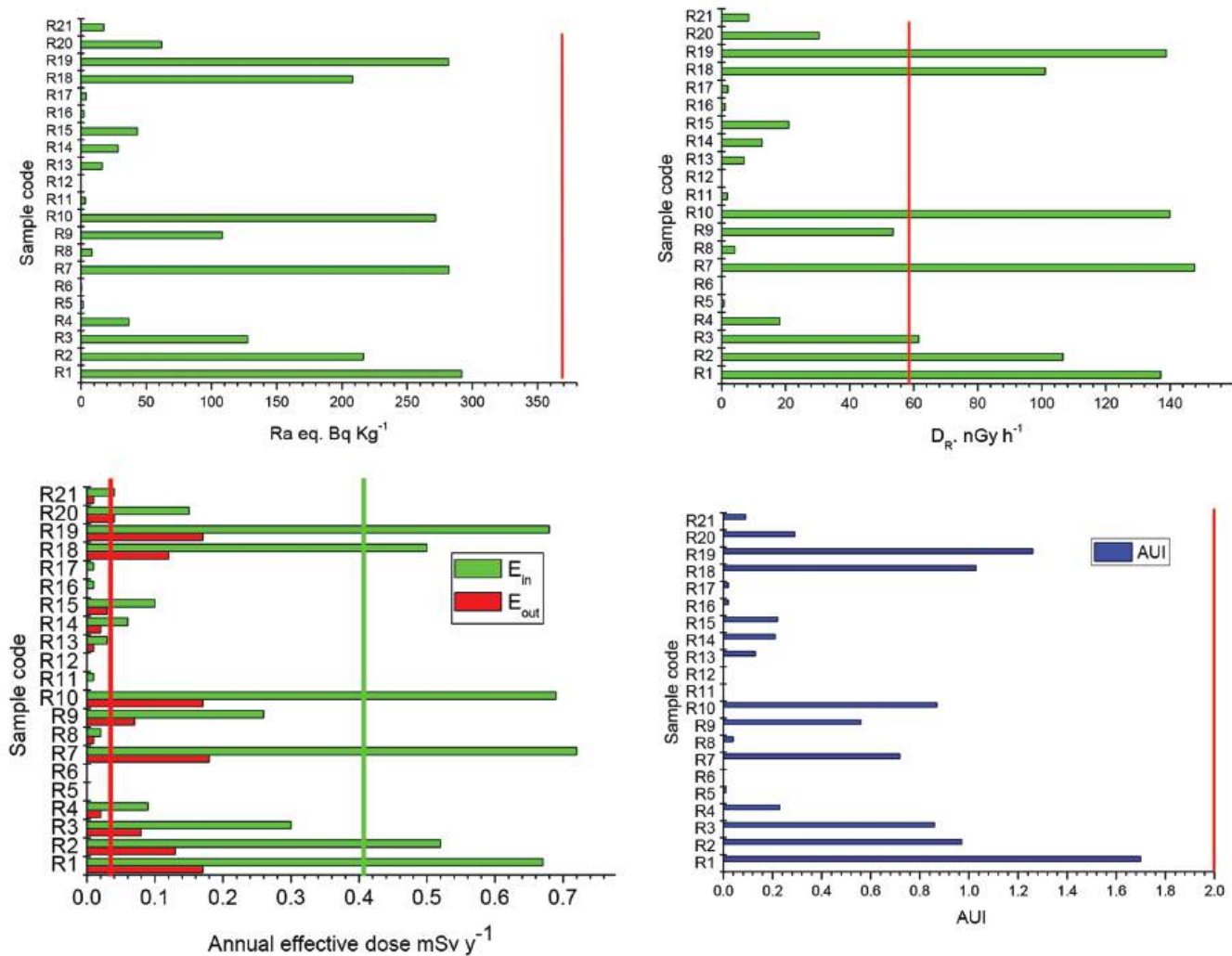


Fig. 4. The estimated radiation hazard indices for the rock samples.

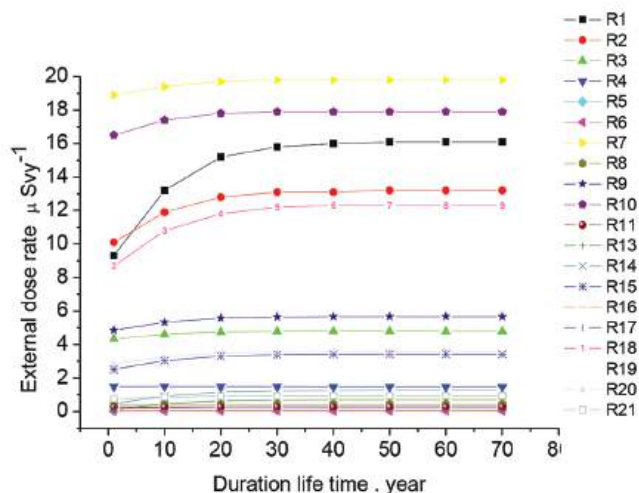


Fig. 5. Long-term variation in the external dose rate that individuals in a standard room are exposed to for all rock samples.

### B. RESRAD BUILD Simulation

About 80% of the inhabitants' time is spent indoors, so they might be significantly impacted by the natural radioactivity that emanates from the components of building materials. It is possible to calculate the radiological indoor dose of a resident of a radioactively contaminated building using the RESRAD-BUILD code (Yu, et al., 1994).

#### Room dimensions scenario

To investigate the impacts of the rocks used to construct the building's walls, the thickness of the walls was fixed at 20 cm, and the room dimensions were fixed at  $(3 \times 6 \times 3)$  m. The annual external and inhalation dose rates were computed over 70 years. The rocks' density was  $1.51 \text{ g/cm}^3$ . For this scenario, the default values for the inhalation rate of  $18 \text{ m}^3/\text{day}$ , deposition velocity of  $0.01/\text{ms}$ , ingestion rate of  $0.0001 \text{ m}^2/\text{h}$ , and resuspension rate of  $0.0000005/\text{s}$  were applied. The input activity concentrations of  $^{226}\text{Ra}$ ,  $^{232}\text{Th}$ , and  $^{40}\text{K}$  for RESRAD-BUILD simulations are listed in Table II.

#### External dose rate

Fig. 5 depicts the calculated external exposures for all samples over an average period of 70 years. During the first 30 years, the external indoor doses increased significantly before becoming reasonably saturated. Maximum external doses over 70 years were observed to be  $19.7 \text{ μSv}$  in the R7 sample; compared to the R10 sample, the activity concentrations of  $^{226}\text{Ra}$  and  $^{232}\text{Th}$  are lower in R10, whereas the activity concentration of  $^{40}\text{K}$  is higher, reflecting the fact that the cases were controlled by the high activity concentrations of  $^{40}\text{K}$ . All measured values are well below the UNSCEAR 2000 critical value of  $2.6 \text{ mSv/y}$ . This is consistent with the results of previous investigations (Adelikhah, et al., 2022).

#### Inhalation indoor dose rate

The calculated indoor inhalation doses for all samples and the average period of 70 years are presented in Fig. 6. During the first 30 years, indoor inhalation doses increased significantly before becoming relatively constant. The R1 exhibited the highest indoor inhalation doses due to the

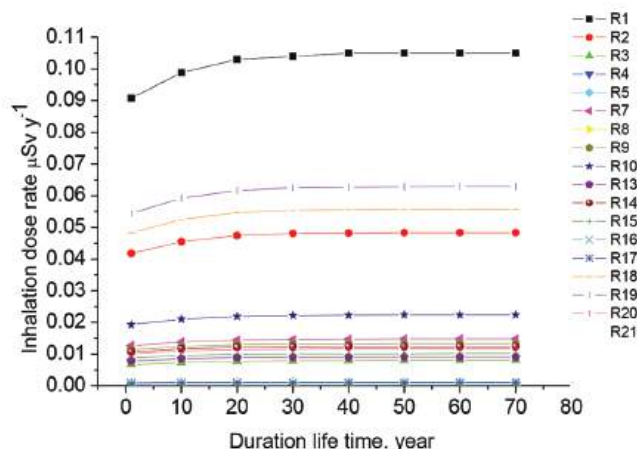


Fig. 6. Long-term variation in the inhalation dose rate that individuals in a standard room are exposed to for all rock samples.

high activity concentrations of  $^{226}\text{Ra}$  and  $^{232}\text{Th}$ , respectively. Compared to the activity concentration in R10 samples, radon originates from  $^{226}\text{Ra}$  ( $^{222}\text{Rn}$ ) and  $^{232}\text{Th}$  ( $^{220}\text{Rn}$ ), whereas  $^{40}\text{K}$  does not contribute to dose inhalation (Adelikhah, et al., 2022; Ndjana Nkoulou 2<sup>nd</sup>, et al., 2022). This inhalation dose range is lower than the global average of  $5.799 \text{ μSv/y}$  (Annex, 2000). The low level of radon concentration in building materials over 70 years is due to continuous changes in the air exchange rate. Mudstone (R1) has the greatest inhalation dose among the 21 studied rocks, while R12 has the lowest (zero) inhalation dose delivered to the inhabitants.

## VI. CONCLUSION

The calculated activity concentrations of primordial radionuclides  $^{226}\text{Ra}$ ,  $^{232}\text{Th}$ , and  $^{40}\text{K}$  fall within the range declared by UNSCEAR (2008), with the respective exception ratios of 14.28%, 19%, and 42.8% for the studied rock samples. The determined activity concentrations and radiological hazards in the rock types can be used as baseline data to determine any future radiological changes resulting from environmental and human activities. The lowest amount of  $\text{Ra}_{\text{eq}}$  was found in chromitite, whereas the greatest amount was identified in mudstone. A wide variation of activity concentration was observed in different rock types, the result of the present study indicates that individuals should be aware of the potential radiological risks of utilizing rocks as building materials before using them and that long-term exposure to low doses of radiation in rock samples can increase the overall risk of cancer. According to the results obtained from RESRAD simulations, the indoor dose was controlled by  $^{232}\text{Th}$  compared to  $^{226}\text{Ra}$  due to the homogenous condition for both  $^{222}\text{Rn}$  and  $^{220}\text{Rn}$  in the standard model of the room; the short lifetime of  $^{220}\text{Rn}$  (56 s) reflects the uncertainty in the homogeneity. Finally, because the RESRAD-BUILD takes into account both radionuclide decay and the ingrowth of the decay product, the ingrowth of the  $^{232}\text{Th}$  decay product may cause the dosage to look higher, but  $^{226}\text{Ra}$  is not an issue because it reaches equilibrium much faster. The results also show that  $^{40}\text{K}$  controlled the external

dose rate, but it did not contribute to the indoor dose due to its long half-lives. Furthermore, the rocks used in the building construction would not contain pure  $^{226}\text{Ra}$  or  $^{232}\text{Th}$ , although they can have a distributed decay chain.

#### REFERENCES

- Abbas, A.E.H.A., Khattab, M.R., and Abdel Azeem, M.M., 2018. Natural radionuclides distribution and environmental impacts of ferruginous sand-siltstone (raw material) and their manufactured Ahmer oxide used as wall paints. *Environmental Forensics*, 19, pp.217-224.
- Abdel-Rahman, M.A.E., El-Mongy, S.A., Farghal, A., and Sayed, M.S., 2018. Study of Some Parameters Affecting Efficiency of HpGe Detectors for Accurate Radionuclides Analysis. In: *The International Conference on Chemical and Environmental Engineering*. Military Technical College, Egypt, pp.371-388.
- Adelikhah, M., Imani, M., Hegedhus, M., and Kovács, T., 2022. Modelling of indoor external and internal exposure due to different building materials containing NORMs in the vicinity of a HNBRA in Mahallat, Iran. *Heliyon*, 8, p.e08909.
- Ahmed, A.A., and Hussein, M.I., 2011. Natural radioactivity measurements of basalt rocks in Sidakan district northeastern of Kurdistan region-Iraq. *International Journal of Geo-Engineering*, 5, pp.66-73.
- Ahmed, I.N., Kettanah, Y.A., and Ismail, S.A., 2020. Genesis and tectonic setting of high-Cr podiform chromitites of the Rayat ophiolite in the Zagros Suture Zone, Northeastern Iraq. *Ore Geology Reviews*, 123, p.103583.
- Alnour, I.A., Wagiran, H., Ibrahim, N., Laili, Z., Omar, M., Hamzah, S., and Idi, B.Y., 2012. Natural radioactivity measurements in the granite rock of quarry sites, Johor, Malaysia. *Radiation Physics and Chemistry*, 81, pp.1842-1847.
- Alshahrani, B.E., 2021. Natural radioactivity level in pumice rock, in Saudi Arabia and effect on human health. *International Journal of Environmental Analytical Chemistry*, 103(14), pp.3410-3421.
- Annex, A., 2000. *Dose Assessment Methodologies. Sources of Effects Ionizing Radiation*. UNSCEAR, Austria.
- Aydin, I., Aydoğan, M.S., Oksum, E., and Koçak, A., 2006. An attempt to use aerial gamma-ray spectrometry results in petrochemical assessments of the volcanic and plutonic associations of Central Anatolia (Turkey). *Geophysical Journal International*, 167, pp.1044-1052.
- Azeez, H.H., Ahmad, S.T., and Mansour, H.H., 2018. Assessment of radioactivity levels and radiological-hazard indices in plant fertilizers used in Iraqi Kurdistan Region. *Journal of Radioanalytical and Nuclear Chemistry*, 317, pp.1273-1283.
- Bell, S.J., Judge, S.M., and Regan, P.H., 2012. An investigation of HPGGe gamma efficiency calibration software (ANGLE V. 3) for applications in nuclear decommissioning. *Applied Radiation and Isotopes*, 70, pp.2737-2741.
- Büchl, A., Brüggmann, G., and Batanova, V.G., 2004. Formation of podiform chromitite deposits: implications from PGE abundances and Os isotopic compositions of chromites from the Troodos complex, Cyprus. *Chemical Geology*, 208, pp.217-232.
- Dina, N.T., Das, S.C., Kabir, M.Z., Rasul, M.G., Deeba, F., Rajib, M., Islam, M.S., Hayder, M.A., and Ali, M.I., 2022. Natural radioactivity and its radiological implications from soils and rocks in Jaintiapur area, North-east Bangladesh. *Journal of Radioanalytical and Nuclear Chemistry*, 331, pp.4457-4468.
- El Mezayen, A.M., Heikal, M.A., El-Feky, M.G., Shahin, H.A., Abu Zeid, I.K., and Lasheen, S.R., 2019. Petrology, geochemistry, radioactivity, and M--W type rare earth element tetrads of El Sela altered granites, south eastern desert, Egypt. *Acta Geochimica*, 38, pp.95-119.
- Fallatah, O., and Khattab, M.R., 2023. Evaluation of environmental radioactivity and hazard impacts saudi arabia granitic rocks used as building materials. *Minerals*, 13, p.165.
- Gaafar, I., Cuney, M., and Gawad, A.A., 2014. Mineral chemistry of two-mica granite rare metals: Impact of geophysics on the distribution of uranium mineralization at El Sela Shear Zone, Egypt. *Open Journal of Geology*, 4, p.137.
- Guidebook, A., 1989. *Measurement of Radionuclides in Food and the Environment*. International Atomic Energy Agency, Vienna.
- Gundersen, L.C.S., 2020. Radon in sheared metamorphic and igneous rocks. In: *Field Studies of Radon in Rocks, Soils, and Water*. Vol. 39. CRC Press, United States, pp.39-50.
- Hanfi, M.Y.M., Masoud, M.S., Sayyed, M.I., Khandaker, M.U., Faruque, M.R.I., Bradley, D.A., and Mostafa, M.Y.A., 2021. The presence of radioactive heavy minerals in prospecting trenches and concomitant occupational exposure. *PLoS One*, 16, p.e0249329.
- Harb, S., Abbady, A.E.B., El-Kamel, A.E.H., Saleh, I.I., and Abd El-Mageed, A.I., 2012a. Natural radioactivity and their radiological effects for different types of rocks from Egypt. *Radiation Physics and Chemistry*, 81, pp.221-225.
- Harb, S., El-Kamel, A.E.H., Abbady, A.E.B., Saleh, I.I., and Abd El-Mageed, A.I., 2012b. Specific activities of natural rocks and soils at quaternary intraplate volcanism north of Sana'a, Yemen. *Journal of Medical Physics*, 37, p.54.
- Hossain, M.F.A., Tasneem, N., Alam, A.B.M.R., and Hossain, A.S.M.F., 2020. Study on the properties and uses of rocks found in Bangladesh. *Soil Dynamics and Earthquake Engineering*, 3, pp.1-7.
- Imani, M., Adelikhah, M., Shahrokhi, A., Azimpour, G., Yadollahi, A., Kocsis, E., Toth-Bodrogi, E., and Kovács, T., 2021. Natural radioactivity and radiological risks of common building materials used in Semnan province dwellings, Iran. *Environmental Science and Pollution Research*, 28, pp.41492-41503.
- Jafir, A.O., 2023. Investigation of radioactivity level in drinking water resources and soil samples collected from the Hawraman villages, Iraq. *Applied Radiation and Isotopes*, 194, p.110665.
- Jafir, A.O., Ahmed, A.H., and Saridan, W.M., 2018. Estimation of radiological parameters from seasonal observations of primordial natural radionuclides in sediments of Darbandikhan Lake water resources at Kurdistan region, Northeastern Iraq. *Environmental Earth Sciences*, 77, p.334.
- Jassim, S.Z., and Goff, J.C., 2006. *Geology of Iraq*. DOLIN, s.r.o., distributed by Geological Society of London, p.5.
- Kuzmanović, P., Todorović, N., Filipović Petrović, L., Mrda, D., Forkapić, S., Nikolov, J., and Knežević, J., 2020. Radioactivity of building materials in Serbia and assessment of radiological hazard of gamma radiation and radon exhalation. *Journal of Radioanalytical and Nuclear Chemistry*, 324, pp.1077-1087.
- Lasheen, E.S.R., Rashwan, M.A., Osman, H., Alamri, S., Khandaker, M.U., and Hanfi, M.Y., 2021. Radiological hazard evaluation of some egyptian magmatic rocks used as ornamental stone: Petrography and natural radioactivity. *Materials (Basel)*, 14, p.7290.
- Legasu, M.L., and Chaubey, A.K., 2022. Determination of dose derived from building materials and radiological health related effects from the indoor environment of Dessie city, Wollo, Ethiopia. *Heliyon*, 8, p.e09066.
- Malczewski, D., and Žaba, J., 2012. Natural radioactivity in rocks of the Modane--Aussois region (SE France). *Journal of Radioanalytical and Nuclear Chemistry*, 292, pp.123-130.
- Narloch, D.C., Paschuk, S.A., Corrêa, J.N., Rocha, Z., Mazer, W., Torres, C.A.M.P., Del Claro, F., Denyak, V., and Schelin, H.R., 2019. Characterization of radionuclides present in portland cement, gypsum and phosphogypsum mortars. *Radiation Physics and Chemistry*, 155, pp.315-318.
- Ndjana Nkoulou, J.E. 2<sup>nd</sup>, Manga, A., German, O., Sainz-Fernandez, C., and Kwato Njock, M.G., 2022. Natural radioactivity in building materials, indoor radon measurements, and assessment of the associated risk indicators in some localities of the Centre Region, Cameroon. *Environmental Science and Pollution Research*, 29, pp.54842-54854.
- Oladunjoye, O.I., Yinusa, T.S., Ajekigbe, K.M., and Oketayo, O.O., 2022.

- Assessment of radiation hazard indices caused by naturally occurring radionuclides in granite samples from selected quarry Site in Kano State, Northwest Nigeria. *Radiochemistry*, 64, pp.656-664.
- Qureshi, A.A., Tariq, S., Din, K.U., Manzoor, S., Calligaris, C., and Waheed, A., 2014. Evaluation of excessive lifetime cancer risk due to natural radioactivity in the rivers sediments of Northern Pakistan. *Journal of Radiation Research and Applied Sciences*, 7, pp.438-447.
- Raghu, Y., Ravisankar, R., Chandrasekaran, A., Vijayagopal, P., and Venkatraman, B., 2017. Assessment of natural radioactivity and radiological hazards in building materials used in the Tiruvannamalai District, Tamilnadu, India, using a statistical approach. *Journal of Taibah University for Science*, 11, pp.523-533.
- Rosianna, I., Nugraha, E.D., Syaeful, H., Putra, S., Hosoda, M., Akata, N., and Tokonami, S., 2020. Natural radioactivity of laterite and volcanic rock sample for radioactive mineral exploration in Mamuju, Indonesia. *Geosciences*, 10, p376.
- Salaheldin, G., El-Gamal, H., Zahran, E.B., and Abdel, M., 2020. Assessment of radiation hazards of radionuclides for granite rocks from Gabal Ghareb, Eastern Desert of Egypt. *Assiut University Journal of Multidisciplinary Scientific Research*, 49, pp.1-16.
- Smail, J.M., Mansour, H.H., and Ahmad, S.T., 2023. Evaluation of radiological hazards in lower Zab river sediments. *Radiation Effects and Defects in Solids*, 178, pp.1252-1268.
- Srinivasa, E., Rangaswamy, D.R., and Sannappa, J., 2019. Assessment of radiological hazards and effective dose from natural radioactivity in rock samples of Hassan district, Karnataka, India. *Environmental Earth Sciences*, 78, p.431.
- Taskin, H., Karavus, M., Ay, P., Topuzoglu, A., Hidiroglu, S., and Karahan, G., 2009. Radionuclide concentrations in soil and lifetime cancer risk due to gamma radioactivity in Kirklareli, Turkey. *Journal of Environmental Radioactivity*, 100, pp.49-53.
- The United Nations Scientific Committee on the Effects of Atomic Radiation (UNSCEAR), 2008. *Effects of Ionizing Radiation, United Nations Scientific Committee on the Effects of Atomic Radiation (UNSCEAR) 2006 Report, Volume I: Report to the General Assembly, Scientific Annexes A and B. United Nations.*
- Tuo, F., Peng, X., Zhou, Q., and Zhang, J., 2020. Assessment of natural radioactivity levels and radiological hazards in building materials. *Radiation Protection Dosimetry*, 188, pp.316-321.
- Turhan, S., 2010. Radioactivity levels of limestone and gypsum used as building raw materials in Turkey and estimation of exposure doses. *Radiation Protection Dosimetry*, 140, pp.402-407.
- Yu, C., LePoire, D.J., and Jones, L.G., 1994. *RESRAD-BUILD: A Computer Model for Analyzing the Radiological doses Resulting from the Remediation and Occupancy of Buildings Contaminated with Radioactive Material*. The University of Chicago, Chicago.

# Toward Optimizing Coarse Aggregate Types and Sizes in High-strength Concrete

Madeh I. Hamakareem<sup>1†</sup>, Daban A. Muhedin<sup>2</sup>, Ahmed J. Hama Rash<sup>1</sup>, Sangar J. Qadir<sup>3</sup>,  
and Loghman Khodakarami<sup>4</sup>

<sup>1</sup>Department of Geotechnical Engineering, Faculty of Engineering, Koya University, Koya KOY45, Kurdistan Region-F.R, Iraq

<sup>2</sup>Department of Civil Engineering, Faculty of Engineering, Koya University, Koya KOY45, Kurdistan Region-F.R, Iraq

<sup>3</sup>Department of Civil Engineering, College of Engineering, University of Sulaimani, Sulaimani, Kurdistan Region-F.R, Iraq

<sup>4</sup>Department of Petroleum Engineering, Faculty of Engineering, Koya University, Koya KOY45, Kurdistan Region-F.R, Iraq

**Abstract**—The development of very effective coarse aggregate types and sizes can lead to a rapid increase in the production of high strength concrete (HSC). This research investigates the effects of five different coarse aggregate types and a range of maximum coarse aggregate sizes on the mechanical properties of concrete through experimental tests and numerical analysis. The workability of fresh concrete is examined using the slump cone test, whereas the mechanical performance of hardened concrete is assessed through compressive strength and splitting tensile strength tests. The experimental results are compared to the predicted results from the codes and design guidelines to assess their predictions. Both coarse aggregate types and sizes show a significant influence on the mechanical properties of HSC performance, especially the compressive strength of HSC, which could be increased on average by 25%. Moreover, the predictions of splitting tensile strength using the ACI 318 and ACI 363 equations are not very accurate, particularly at a high strength range. Therefore, this study develops a new equation for predicting splitting tensile strength based on both experimental test results conducted in this research and a significant amount of data collected from the literature. Evaluation metrics, including R2, RMSE, MAPE, and MAE, demonstrate the superior accuracy of the proposed equation compared to the design guidelines equations. The findings of this research can contribute toward the optimization of aggregate type and size in concrete mix design for enhanced performance and provide valuable insights into the relationship between compressive and splitting tensile strengths in HSC.

**Index Terms**—High-strength concrete, maximum aggregate size, compressive strength, splitting tensile strength, aggregate types

ARO-The Scientific Journal of Koya University  
Vol. XII, No.2 (2024), Article ID: ARO.11589. 11 pages  
Doi: 10.14500/aro.11589

Received: 28 March 2024; Accepted: 26 June 2024

Regular research paper; Published: 25 July 2024

<sup>†</sup>Corresponding author's e-mail: madeh.izat@koyauniversity.org

Copyright © 2024 Madeh I. Hamakareem, Daban A. Muhedin, Ahmed J. Hama Rash, Sangar J. Qadir, and Loghman Khodakarami.

This is an open-access article distributed under the Creative Commons Attribution License (CC BY-NC-SA 4.0).



## I. INTRODUCTION

High-strength concrete (HSC) has been used widely throughout the world, but its popularity has recently emerged in Iraq. It is defined as concrete with a compressive strength of 55 MPa or greater (ACI Committee 363, 2010). HSC production utilizes common materials such as cement, sand, and coarse aggregate, along with admixtures such as high-range water-reducing admixture, silica fume, and fly ash (Darwin and Dolan, 2021). However, achieving desired strength relies on a low water-to-cement ratio (Wu et al., 2001b) and strict quality control during production (Darwin and Dolan, 2021). The application of HSC is driven by its high uniform density, low permeability, and high durability. It has been used in the columns of high-rise buildings to reduce size, increase floor space, and permit longer spans in bridges (Gjørsv, 2008; ACI Committee 363, 2010).

The properties of HSC, and in particular compressive strength, which is one of the most significant criteria in the design of concrete structures, are influenced by parameters, namely: Cement type, supplementary cementitious materials, chemical admixtures, and curing regimes. However, the properties of coarse aggregate, especially its types and maximum particle size, significantly impact the strength behavior of HSC (Caldarone, 2009; Meddah, Zitouni and Belâabes 2010; Jin et al., 2021). The role of coarse aggregate in compressive strength is critical in HSC. This is due to the high matrix strength in HSC, which increases the likelihood of crack development through aggregates and consequently modifies cracking mechanisms compared to ordinary concrete (Neville and Brooks, 2010).

The relationship between maximum coarse aggregate size (MCAS) and the compressive strength of HSC has been studied by many researchers. For instance, Wu, Chen and Yao (2001a) reported that the compressive strength of HSC increases as MCAS increases but subsequently decreases beyond MCAS of 15 mm. Experimental investigations

conducted by Rao and Prasad (2002) and Akçaoğlu, Tokyay and Çelik (2002) emphasized a positive correlation between MCAS and compressive strength, with peak strength observed at a MCAS of 20 mm and 32 mm, respectively.

However, Meddah, Zitouni and Belâabes (2010) observed only a marginal increase in the compressive strength of HSC when MCAS was reduced from 25 mm to 15 mm. Moreover, Grabiec, Zawal and Szulc (2015) conducted a study to examine the influence of MCAS (8 mm and 16 mm), aggregate type (gravel, crushed basalt, and crushed granite), and cement content ( $600 \text{ kg/m}^3$  and  $700 \text{ kg/m}^3$ ) on the properties of HSC. They found that reducing MCAS increased compressive strength for both gravel and crushed granite but led to a significant reduction for crushed basalt at  $700 \text{ kg/m}^3$  cement content. At lower cement content, decreasing MCAS reduced compressive strength for gravel and crushed granite but improved it for crushed basalt. They also acknowledge that a wider range of MCAS needs to be explored to specify the relationship between aggregate size and the strength behavior of HSC. A more recent numerical and theoretical investigation by Jin et al. (2021) showed that the strength of concrete roughly increased as the MCAS was reduced. MCAS is also found to influence the tensile strength of HSC. According to studies conducted by Akçaoğlu, Tokyay and Çelik (2002) and Al-Oraimi, Taha and Hassan (2006), the tensile strength of HSC increases with decreasing MCAS, whereas Rao and Prasad (2002) reported the opposite trend. These conflicting results highlight the need for further investigation to clarify the effects of MCAS on the compressive strength and tensile strength of HSC.

Several researchers (Kılıç et al., 2008; Beushausen and Dittmer, 2015; Vishalakshi, Revathi and Sivamurthy Reddy 2018) have identified aggregate type (strength, shape, surface texture, and mineralogy) as a critical factor affecting the compressive strength of HSC. Their findings indicate that stronger aggregates contribute to an overall enhancement in the strength of concrete. Moreover, these studies reveal a similar relationship between aggregate strength and the splitting tensile strength of concrete. However, Beushausen and Dittmer (2015) reported that the effect of aggregate strength on the splitting tensile strength or flexural strength of concrete is limited. The investigation conducted by Grabiec, Zawal and Szulc (2015) provided valuable insights into the factors affecting the compressive strength of HSC, but it did not reach conclusive findings regarding the sole influence of the aggregate type. In their study, Góra and Piasta (2020) investigated the impact of six distinct types of coarse aggregates on the properties of both ordinary and high-performance concrete. The experimental results revealed that an increase in aggregate strength does not always result in a corresponding increase in the compressive strength or splitting tensile strength of high-performance concrete. These mixed findings underscore the complexity and the need for further exploration of the influence of coarse aggregate characteristics on the strength behavior of HSC.

As discussed above, the influence of MCAS size and coarse aggregate type on the compressive strength and splitting tensile strength of HSC concrete remains inconsistent

across various studies. Moreover, research on producing HSC without supplementary cementitious materials is also limited. In addition, previous investigations lack consensus regarding the optimum aggregate size and type for producing HSC. Thus, our research aims to systematically investigate the effects of five coarse aggregate types (crushed gravel [CG], crushed limestone [CL], crushed dolomitic limestone [DL], crushed high-calcium limestone [HCL], and natural gravel [NG]) and various MCAS (9.5 mm, 12.5 mm, 19 mm, and 25 mm) for CG on the compressive strength and splitting tensile strength of HSC. We seek to provide clearer insights into optimizing aggregate type and size in concrete mix for enhanced performance and contribute to the development of a more sustainable and potentially more cost-effective production of HSC. By combining experimental tests with numerical analysis, this study also aims to improve an equation based on existing ACI 363R-10 and ACI 319-14 equations for predicting splitting tensile strength based on the compressive strength of HSC.

## II. EXPERIMENTAL PROGRAM

### A. Materials and Test Methods

Ordinary Portland Cement (Type I) was consistently used in this investigation for all mixtures. A liquid polycarboxylic-based superplasticizer was utilized in this work to reduce mixing water and maintain concrete workability. Natural river sand with a smooth surface and rounded-shaped particles was used as fine aggregate. Its specific gravity and water absorption, determined based on ASTM C128-15 (2015), were 2.7 and 0.6%, respectively. The grading of fine aggregate complied with ASTM C 33/C33M-18 (2018), see Fig. 1.

In this experimental investigation, five different aggregate types, namely: CG, CL, DL, HCL, and NG, were utilized to examine the effect of aggregate types on the strength behavior of HSC. The aggregates were sourced from three different aggregate production plants within the Sulaymaniyah governorate/Iraq, see Fig. 2a.

The types of aggregates were identified using macroscopic observation and X-ray fluorescence (XRF) testing. The results of XRF tests for the five types of aggregates are presented

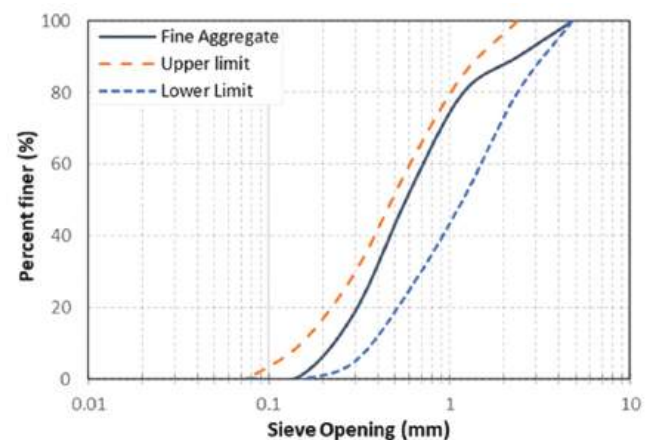


Fig. 1. Particle size distribution of fine aggregate.





Fig. 2. (a) Aggregate plant locations with respective aggregate types in brackets, (b) Coarse aggregate types: (a) crushed gravel, (b) crushed limestone, (c) crushed dolomitic limestone, (d) crushed high-calcium limestone, and (e) natural gravel.

in Table I. Visual observation showed that CG aggregate contained limited proportions of uncrushed particles and a small percentage of limestone aggregates. We conducted visual assessments on CG samples and differentiated between uncrushed and limestone particles. The separated particles were weighted differently, and the average percentage of different components was computed. The rationale behind using this technique was to determine major components quickly. The detailed physical characteristics of different coarse aggregates are summarized in Table II. To investigate the influence of MCAS on the compressive strength and splitting tensile strength of HSC, CG aggregates with different MCAS of 9.5 mm, 12.5 mm, 19 mm, and 25 mm were used.

In the selection of aggregate types and sizes, we prioritized local availability to reduce transportation impacts and costs. Not only does this strategy support the local economy, but it is also in line with environmental standards aimed at reducing carbon footprints related to construction materials. In addition, our choices met the requirements of relevant standards like ASTM C 33 for aggregates, which offer guidelines on the grading and quality of aggregates. Particle size analysis of various aggregate types and different sizes of CG considered in this study conformed to the requirements of ASTM C 33/C33M-18 (2018), as shown in TABLE III and presented graphically in Fig. 3. ACI 363R-10 sets ASTM C33 as the minimum requirement for aggregate to produce HSC.

*B. Mix Proportions and Sample Preparation*

The concrete mixture was designed following the guidelines outlined in ACI Committee 211 (2008) and was

TABLE I  
RESULTS OF X-RAY FLUORESCENCE (XRF) OF DIFFERENT TYPES OF COARSE AGGREGATE, %

Aggregate types	CaO	SiO <sub>2</sub>	Al <sub>2</sub> O <sub>3</sub>	MgO	Fe <sub>2</sub> O <sub>3</sub>	Others
Crushed gravel	16.20	70.51	6.89	0.98	2.60	2.82
Crushed limestone	67.42	19.75	4.96	3.76	1.85	2.26
Crushed dolomitic limestone	81.46	4.10	1.79	10.42	0.70	1.53
Crushed high-calcium limestone	83.07	8.69	4.21	1.43	0.95	1.63
Natural gravel	5.12	77.93	12.64	0.88	1.55	1.88

further refined through the use of trial mixes. The proportion of the mixture for all concrete specimens remained consistent throughout the experimental program and consisted of 560 kg/m<sup>3</sup> of cement, 175 kg/m<sup>3</sup> of water, 660 kg/m<sup>3</sup> of sand, 1027 kg/m<sup>3</sup> of coarse aggregate, and 4.48 kg/m<sup>3</sup> of superplasticizer. The concrete constituents were thoroughly mixed in a tilted concrete mixer, Fig. 4a. Initially, the coarse aggregate and a portion of the mixing water are blended. Then, sand, cement, and approximately 70% of the water are added to the mixer incrementally and mixed for about 5 min. Subsequently, the remaining water is combined with the superplasticizer and introduced into the mixture, followed by an additional 5 min of mixing.

After the mixing process, a slump test was conducted in accordance with ASTM C143/C143M-15a (2015) to assess the workability of fresh concrete. Standard steel cylinders with a diameter of 100 mm and a height of 200 mm were oiled, poured in three layers, and adequately compacted using a table vibrator, Fig. 4b.

The concrete specimens cast, as shown in Fig. 4c, for the assessment of both compressive strength and splitting tensile strength were moist-cured and tested after 7, 28, and 56 days.

TABLE II  
PHYSICAL PROPERTIES OF DIFFERENT COARSE AGGREGATES (CG, CL, DL, HCL, AND NG)

Properties of aggregate	CG	CL	DL	HCL	NG	Standards
Specific Gravity	2.68	2.72	2.71	2.50	2.65	(ASTM C127-15, 2015)
Water Absorption, %	1.22	0.8	1.0	1.72	1.46	(ASTM C127-15, 2015)
Flakiness and Elongation Index, %	7.1	7.8	9.3	8	6.6	(ASTM D4791-10, 2010)
Impact value, %	5.7	6.9	7.1	12.1	4.9	(BS 812-112:1990, 1990)
Unit weight, kg/m <sup>3</sup>	1600	1590	1530	1560	1600	(ASTM C29/C29M-17a, 2017)
Surface Texture	Mostly Rough	Rough	Rough	Rough	Smooth	-

CG: Crushed gravel, CL: Crushed limestone, DL: Dolomitic limestone, HCL: High-calcium limestone, NG: Natural gravel

TABLE III  
PARTICLE SIZE ANALYSIS OF DIFFERENT AGGREGATE SIZES OF CG AND AGGREGATE TYPES (CG, CL, DL, HCL, AND NG) AS PER ASTM C136/C136M-14 (2014)

Aggregate type	CG	CG	CG	CG	CL	DL	HCL	NG
Aggregate size, mm	25	19	12.5	9.5	12.5	12.5	12.5	12.5
% Passing 25 mm	100	-	-	-	-	-	-	-
% Passing 19 mm	67.45	100	-	-	-	-	-	-
% Passing 12.5 mm	20.41	40.77	97.5	-	100	98.9	100	97
% Passing 9.5 mm	5.34	7.34	40.4	100	44.5	45.4	69.7	65.8
% Passing 4.75 mm	-	0.06	13.1	19	11.2	0.7	14.60	2.5
% Passing 2.36 mm	-	-	0	4.6	1.4	0	0.49	0.1
% Passing 1.18 mm	-	-	-	2	-	-	-	-

CG: Crushed gravel, CL: Crushed limestone, DL: Dolomitic limestone, HCL: High-calcium limestone, NG: Natural gravel

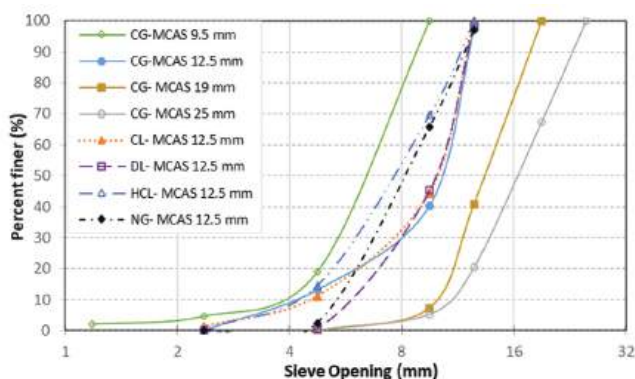


Fig. 3. Particle size distribution of different coarse aggregates.

A total of three specimens were formulated for each compressive strength and splitting tensile strength reading. The compression test was conducted based on ASTM C39/C39M-14 (2018) (Fig. 4d), whereas the splitting tensile test was carried out according to ASTM C496/C496M-11 (2011) (Fig. 4e).

### III. RESULTS AND DISCUSSIONS

#### A. Workability

The influence of MCAS on concrete workability, as indicated by the slump value, is illustrated in Fig. 5a. It can be observed that the workability of concrete increased with an increase in MCAS. For instance, concrete produced with a 9.5 mm MCAS obtained the lowest slump value (200 mm), whereas concrete made with a 25 mm MCAS yielded the highest slump value (230 mm). This effect is attributed to the larger particles, which result in a smaller surface area for a

given amount of aggregate mass, thereby reducing the water demand in a concrete mixture (Neville, 2011).

Fig. 5b demonstrates how aggregate types affect the workability of concrete in terms of slump value. The slump values of CG, CL, and DL concrete were similar and smaller when compared to the slump value of NG concrete. This is because the former concrete series was produced from angular, rough-surfaced, crushed aggregate, whereas the latter was produced from rounded and smooth-surfaced natural aggregate.

It was noticed that HCL concrete, despite sharing a similar shape and surface texture aggregates with CG, CL, and DL concrete, exhibited a lower slump value than its counterparts. This can be attributed to the aggregate gradation of HCL aggregate, which contained a higher proportion of smaller particles when contrasted with CG, CL, and DL aggregate, see Table III. This observation is supported by the test results reported by Uddin et al. (2017). Higher water absorption of HCL aggregate, as presented in Table I, could also contribute to the reduction of slump in HCL aggregate concrete.

Increasing MCAS improves workability, benefiting concrete placement and consolidation. However, this improvement comes at the cost of reducing compressive strength. To quantify this trade-off, this study explored the effect of MCAS on the compressive strength of HSC. For instance, both 9.5 mm and 12.5 mm MCAS yielded slump values of 200 mm and 215 mm, respectively. However, the 9.5 mm mix achieved a higher compressive strength of 67.07 MPa compared to the 60.56 MPa of the 12.5 mm mix. In addition, a 25 mm mix produced a slump value of 230, but compressive strength dropped to 50.01 MPa, which is not considered HSC. This highlights the significance of optimizing HSC mix design to ensure efficient construction and structural performance.

#### B. Compressive Strength

Coarse aggregate is a crucial parameter that affects the compressive strength of HSC. The compressive strength results of concrete specimens containing different coarse aggregate types (CG, CL, DL, HCL, and NG) and moist-cured for 7, 28, and 56 days are presented in Fig. 6.

Fig. 6 shows a significant variation in compressive strength among different aggregate types, highlighting the important role of aggregate characteristics (strength, shape, surface texture, and mineralogy) in determining the compressive strength of HSC. At 7 days of curing, the compressive strength of CG concrete was 1.2%, 13.2%, 17.3%, and



Fig. 4. (a) concrete mixer, (b) shaking table, (c) some of the cast samples, (d) compression testing, and (e) splitting tensile testing.

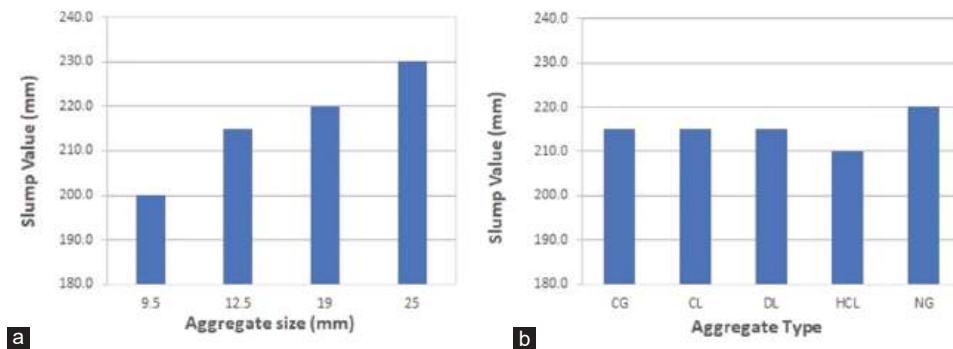


Fig. 5. Effect of (a) maximum coarse aggregate size, (b) aggregate type on concrete workability.

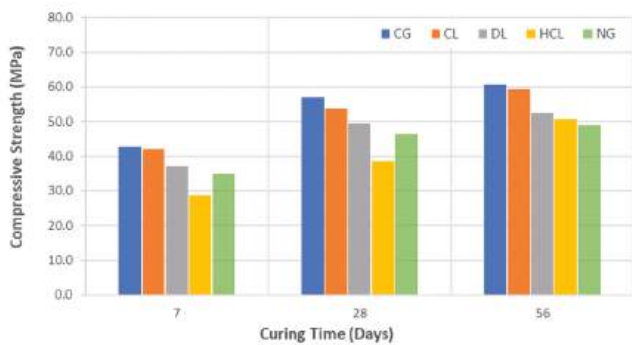


Fig. 6. Influence of different aggregate types on the compressive strength of HSC.

32.6% higher compared to CL, DL, NG, and HCL concrete, respectively. Similarly, at 28 days of curing, the CG concrete exhibited a 5.7% higher compressive strength compared to CL concrete, 13.3% higher than DL concrete, 18.56% higher than NG concrete, and 32.32% higher than HCL concrete. At 56 days of curing, CG concrete achieved the highest compressive strength, measuring 60.56 MPa, surpassing CL,

DL, HCL, and NG concrete by 2.1%, 13.3%, 16.1%, and 19.1%, respectively.

Despite having similar surface textures and a maximum aggregate size of 12.5 mm for the crushed aggregates, CG concrete consistently exhibited the highest compressive strength throughout all curing periods. CL concrete showed comparable compressive strength to CG concrete but was significantly higher compared to DL and HCL concrete. These variations are attributed to the differing strength characteristics and mineralogy of the crushed aggregates. The physical properties of the aggregates, as presented in Table II, indicate a stronger nature of CG and CL aggregates in comparison to DL and HCL aggregates. Moreover, the XRF test results in Table I reveal that CG and CL aggregates contain a higher proportion of quartz minerals compared to other crushed aggregates, and such aggregates generally demonstrate better mechanical properties (Liu et al., 2005). On the other hand, DL and HCL aggregates contain a significant amount of calcite minerals, as indicated in Table I. The presence of calcite minerals in these aggregates contributes to their inferior mechanical properties, as

evidenced by test results reported by Beshr, Almusallam and Maslehuddin (2003).

NG concrete showed the lowest compressive strength at 56 days of curing, which can be related to a smooth surface and rounded gravel particles, resulting in a reduced aggregate-cement paste bonding strength. The compressive strength of NG concrete was higher compared to HCL concrete after 7 and 28 days, but HCL concrete exhibited greater strength after 56 days. This reversal might be due to strong bonding strength at the HCL-cement paste interface at a high strength level.

Fig. 7 shows the failure of tested specimens, made from different aggregates, after compression tests. Cracks predominantly passed through aggregates in CG and CL concretes, indicating a good aggregate-cement paste bond (Fig. 7a and b). However, a few instances of debonding between uncrushed particles and cement paste were observed in CG concrete (Fig. 7a), highlighting the impact of aggregate surface texture on the interfacial bond. Both DL and HCL concrete exhibited similar failure patterns, with cracks propagating through the middle of the specimens from top to bottom (Fig. 7c and d). Despite comparable surface textures, DL concrete achieved higher compressive strength than HCL concrete, underscoring the role of aggregate strength in enhancing overall strength in HSC. The NG specimen showed sporadic cracks throughout its height (Fig. 7e), possibly indicating localized failure due to a weak interfacial bond, likely related to the smooth surface texture of the NG aggregate.

Fig. 8 illustrates the compressive strength of concrete made from CG with varying MCAS of 9.5 mm, 12.5 mm, 19 mm, and 25 mm, and moisture-cured for 7, 28, and 56 days. It is evident that the compressive strength results are influenced by MCAS and curing time. The compressive strength of cylinder specimens increased as the MCAS increased.

At 7 days of curing, the compressive strength of concrete with an MCAS of 9.5 mm was 48.01 MPa. In comparison, for concretes made with MCAS of 12.5 mm, 19 mm, and 25 mm, the corresponding strengths were 42.66 MPa,

35.86 MPa, and 30.29 MPa, respectively. At 28 days, the compressive strength of concrete made with MCAS of 9.5 mm, 12.5 mm, 19 mm, and 25 mm was 61.09 MPa, 56.93 MPa, 45.84 MPa, and 40.77 MPa, respectively.

For the 56-day curing period, concrete formulated with MCAS of 9.5 mm and 12.5 mm achieved compressive strengths of 67.07 MPa and 60.56 MPa, respectively. In contrast, the concrete specimens produced using MCAS of 19 mm and 25 mm demonstrated compressive strengths of 50.75 MPa and 50.21 MPa, respectively, falling short of the HSC criteria defined by ACI 363. The 56-day test results reveal that reducing MCAS from 25 mm to 9.5 mm led to an average increase in compressive strength of slightly over 25%.

Several factors contribute to the achievement of higher compressive strength with smaller MCAS: Greater aggregate surface area (Neville, 2011), lower stress concentration around particles (ACI Committee 363, 2010), and a thinner interfacial transition zone at the aggregate-cement paste interface. Smaller aggregates also tend to have fewer internal flaws, like microcracks (Price, 2003), resulting in good mechanical performance, which is favorable for attaining high concrete compressive strength (Caldarone, 2009).

Based on the HSC definitions outlined in the introduction, both CG and CL demonstrate suitability for HSC production. This can be achieved by limiting the MCAS to 12.5 mm or smaller, thereby eliminating the need for supplementary cementitious materials typically used in HSC production. This approach to HSC production offers significant economic advantages for countries that lack access to by-products such as fly ash and silica fume.

Both ACI 211.4R-08 and ACI 363R-10 state that crushed and natural aggregates are acceptable for HSC production, with crushed aggregates generally being more effective due to their ability to create a better bond with the cement paste. The codes also state that HSC can be produced using MCAS of up to 25 mm, but they recommend smaller sizes, preferably 13 mm or less. However, our findings show that only crushed aggregates with an MCAS of 12.5 mm are suitable for HSC production. It should be noted that the present study only



Fig. 7. Failure modes of tested concrete specimens: (a) Crushed gravel, (b) crushed limestone, (c) dolomitic limestone, (d) high-calcite limestone, and (e) natural gravel.

considered cement as the binder for HSC production, while these codes typically consider a combination of cement and supplementary cementitious materials.

### C. Splitting Tensile Strength

Fig. 9 presents the results of splitting tensile strength tests conducted on concrete specimens made with different types of aggregates and tested at 7, 28, and 56 days. As expected, the splitting tensile strength increased as the curing duration increased. It is observed that CL concrete recorded the highest splitting tensile strength across all curing periods, followed by DL, CG, HCL, and NG concrete. At 56 days, CL exceeded DL, CG, HCL, and NG by 10.08%, 11.31%, 12.55%, and 18.1%, respectively. These results emphasize the impact of aggregate type on the splitting tensile strength of concrete.

Several researchers (Kılıç et al., 2008; Beushausen and Dittmer, 2015; Vishalakshi, Revathi and Sivamurthy Reddy 2018) have reported that the influence of aggregate type on the compressive strength and splitting tensile strength in HSC is comparable. However, a comparison of the test results presented in Fig. 5 in the previous section and Fig. 9 contradicts this statement. The order of tested concrete specimens, in terms of splitting tensile strength from highest to lowest, was CL, DL, CG, HCL, and NG. In contrast, the order of tested specimens in relation to compressive strength, from highest to lowest, was CG, CL, DL, HCL, and NG.

It is worth noting that there was an exchange of positions between CG and both CL and DL regarding splitting tensile strength. This could be related to the presence of certain

particles in CG aggregate that retained a smooth surface texture, which is not desirable for a good mechanical bond between the cement paste and aggregate particles. This observation is supported by Neville (2011), who stated that the tensile strength of low water-to-cement concrete is greatly affected by variations in aggregate surface texture, as the aggregate-cement paste bond controls the tensile strength. The presence of smooth surface texture particles in CG aggregate can influence the compressive strength mainly by affecting the aggregate-cement paste bond. However, the extent of this influence may not be significant in the case of compressive strength results, as concrete made of CG still provided the highest compressive strength value compared to other aggregate types. This might be due to other factors, like aggregate strength, that could play a more dominant role than the surface texture of the aggregates.

Fig. 10 represents the splitting tensile test results of concrete specimens composed of CG with varying MCAS (9.5 mm, 12.5 mm, 19 mm, and 25 mm) and most cured for 7, 28, and 56 days. The results indicate that the splitting tensile strength of concrete decreases as MCAS increases. This trend is similar to the outcomes of the MCAS effect on compressive strength discussed in the previous section, see Fig. 6. Akçaoğlu, Tokyay and Çelik (2004) reported similar results, suggesting that the noted reduction in splitting tensile strength as MCAS increases, corresponds to a decrease in the strength of the aggregate-cement paste bond. Larger aggregate sizes increase the volume of aggregate in relation to cement paste, leading to a greater difference between the elastic moduli of the two constituent phases. This results in greater stress concentration and more microcracks around the aggregates.

### D. Relationship between Compressive Strength and Splitting Tensile Strength of HSC

The splitting tensile strength of specimens, incorporating various types and sizes of coarse aggregates and moist-cured at different ages, is graphically presented against the compressive strength results of concrete in Fig. 11. The data shown in Fig. 11 exhibits a notable degree of dispersion, especially beyond a compressive strength of 50 MPa, emphasizing the influence of various aggregate characteristics (types, sizes, shapes, surface texture, and mineralogy) and curing time on the strength behavior of HSC.

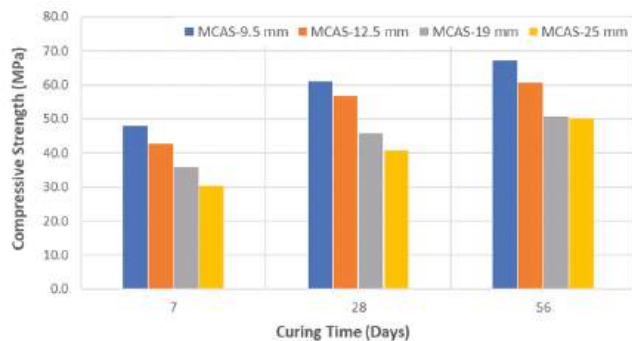


Fig. 8. Effect of various maximum coarse aggregate sizes on the compressive strength of HSC.

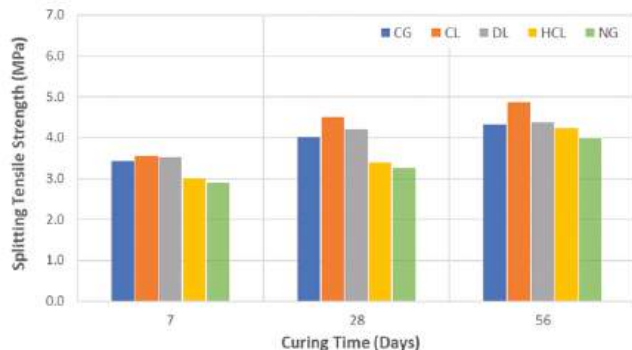


Fig. 9. Effect of aggregate type on the splitting tensile strength of HSC.

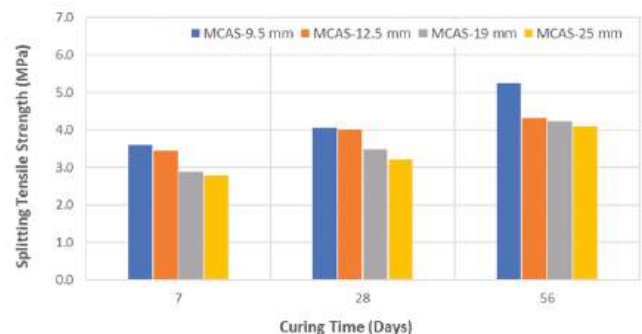


Fig. 10. Effect of various MCAS on the splitting tensile strength of HSC.

Several empirical equations are available to predict splitting tensile strength based on concrete compressive strength. For instance, (ACI Committee 363, 2010) and (ACI Committee 318, 2015) adopted (1) and (2), respectively.

$$f_{ct} = 0.59\sqrt{f'_c} \tag{1}$$

$$f_{ct} = 0.56\sqrt{f'_c} \tag{2}$$

Where  $f_{ct}$ : concrete tensile strength, MPa and  $f'_c$ : concrete compressive strength, MPa

However, the data from this study indicate that both equations seem to overestimate splitting tensile strength for compressive strengths below 50 MPa. Conversely, at higher strengths, they tend to underestimate splitting tensile strength values, as shown in Fig. 9. This result is consistent with the statement that the estimated values of splitting tensile strength using square root equations deviate from experimental splitting tensile strength results as concrete compressive strength increases (Rashid, Mansur and Paramasivam 2002; ACI Committee 363, 2010). In addition, concerns about accuracy and reliability may have factored into the ACI 318 committee's decision to remove (2) from the 2019 edition of ACI 318M.

The majority of researchers (Rashid, Mansur and Paramasivam 2002; Zain et al., 2002; Pul, 2008) who investigated the correlation between compressive strength and tensile strength of concrete predominantly employed the coefficient of determination  $R^2$  as a measure of accuracy for their equation and compared their results with those formulas presented in building standards or developed by previous scholars. However, in contrast to this prevailing approach, the authors of this study believed that the use of other error metrics such as root mean square error (RMSE), mean absolute percentage error (MAPE), and mean square error (MAE) can provide invaluable insights into the performance and accuracy of the equation under development. These metrics can be computed using (3) to (6) (Erdal, Karakurt and Namli 2013; Golafshani, Behnood and Arashpour 2020; Nguyen et al., 2022):

$$R^2 = 1 - \frac{\sum_{i=1}^n (y_i - \hat{y}_i)^2}{\sum_{i=1}^n (y_i - \bar{y})^2} \tag{3}$$

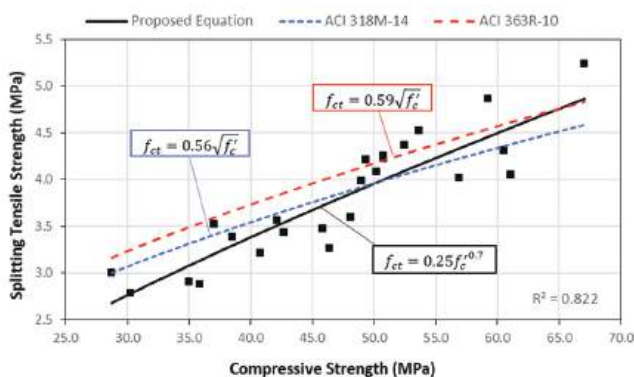


Fig. 11. Comparison between the experiment results (i.e., rectangular shape) and the prediction of splitting tensile strength based on the compressive strength of concrete for different equations.

$$RMSE = \sqrt{\frac{\sum_{i=1}^n (y_i - \hat{y}_i)^2}{n}} \tag{4}$$

$$MAPE = \frac{1}{n} \sum_{i=1}^n \left| \frac{y_i - \hat{y}_i}{y_i} \right| * 100 \tag{5}$$

$$MAE = \frac{1}{n} \sum_{i=1}^n |y_i - \hat{y}_i| \tag{6}$$

Where  $y_i$ : observed compressive strength value,  $\hat{y}_i$ : Predicted compressive strength value,  $\bar{y}$ : mean of the observed compressive strength values, and n: number of average tests.

In light of the preceding discussion, we introduce a new equation to estimate the splitting tensile strength of concrete based on its compressive strength, as presented in Fig. 9. The data in the present study are divided into two sets: 70% serves as a training dataset for model generation, while the remaining 30% constitutes the testing dataset for model validation. To assess the accuracy of the proposed equation, key error metrics such as  $R^2$ , RMSE, MAPE, and MAE were calculated for both the developed equation and those presented in (ACI Committee 363, 2010) and (ACI Committee 318, 2015) for comparison, see Table IV. The results demonstrate that the proposed formula outperforms both equations, with superior accuracy across all metrics. Interestingly, the ACI 363R-10 equation exhibits the lowest performance, underscoring the potential inaccuracy of conventional 0.5-power equations at higher concrete strengths.

For further generalization of the proposed equation, a dataset has been carefully compiled from pertinent literature (Al-Oraimi, Taha and Hassan 2006; Pul, 2008; Beushausen and Dittmer, 2015; Vishalakshi, Revathi and Sivamurthy Reddy 2018; Góra and Piasta, 2020). The compiled compressive strength data are plotted against splitting tensile strength, as depicted in Fig. 12. It is noticeable that the proposed equation provides a better estimation of splitting tensile strength, especially at higher compressive strengths. This observation underscores the potential of the developed equation to provide more reliable predictions in cases of high compressive strengths. The graphical representation in Fig. 12 visually supports and reinforces this noteworthy finding.

Fig. 13 shows the splitting tensile strength residuals of the proposed, ACI 363R-10, and ACI 318-15 equations. The

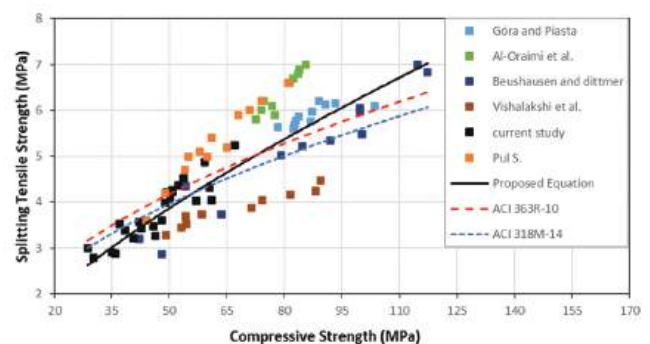


Fig. 12. Performance of the proposed equation, ACI 363R-10, and ACI 318M-14 to predict splitting tensile strength.

TABLE IV

EVALUATION RESULTS OF PROPOSED, ACI 363R-10, ACI 318M-14 EQUATIONS					
References	Equations	R <sup>2</sup>	RMSE	MAPE	MAE
Proposed Equation	$f_{ct} = 0.25f_c^{0.7}$	0.823	0.287	6.231	0.243
(ACI Committee 363, 2010)	$f_{ct} = 0.59\sqrt{f_c}$	0.810	0.485	13.537	0.472
(ACI Committee 318, 2015)	$f_{ct} = 0.56\sqrt{f_c}$	0.817	0.377	9.216	0.334

residual plot serves to illustrate the discrepancies between the actual and predicted values within the regression model. The plot features blue, orange, and gray points, which denote the residuals, while the red line signifies the zero-residual axis. Analyzing this plot necessitates consideration of three primary aspects: random scatter, patterns and trends, and heteroscedasticity. The following points provide a detailed examination of these aspects:

1. Random scatter: The residuals exhibit a random scatter around the horizontal axis (represented by the red line). This randomness suggests that the regression model provides an unbiased estimation of the dependent variable, as there is no discernible structure in the residuals.
2. Patterns and trends: The absence of specific patterns, such as curves or linear trends within the residual plot, implies that the chosen regression model is appropriate. A lack of discernible patterns indicates that the model does not suffer from specification errors and that it captures the underlying relationship between the variables effectively.
3. Heteroscedasticity: The uniform spread of residuals across the range of predicted values indicates homoscedasticity, meaning the variance of residuals is constant. This uniformity is crucial for the validity of the model's inferences, as heteroscedasticity could lead to inefficient estimates and affect the reliability of hypothesis tests.

In summary, the analysis of the residual plot suggests that the regression model accurately represents the data. The absence of random scatter, specific patterns, and heteroscedasticity supports the validity of the model, indicating that no further adjustments are necessary. This confirms that the regression model is well-suited for predicting the dependent variable based on the given independent variables.

*E. Correlation between Aggregate Impact Value (AIV) and Compressive Strength of HSC*

Fig. 14 shows the correlation between the AIV of CG, CL, DL, and HCL aggregates and the compressive strength of HSC at 7, 28, and 56 days of curing. A strong relationship between AIV and compressive strength is evident at 28 and 7 days of curing, with coefficient of determination (R<sup>2</sup>) values of 0.9147 and 0.8215, respectively. While the correlation weakens at 56 days (R<sup>2</sup>=0.6942), AIV remains relevant for early compressive strength assessment. This finding is crucial from a construction standpoint, as AIV can serve as an important criterion for predicting the quality of concrete in terms of compressive strength.

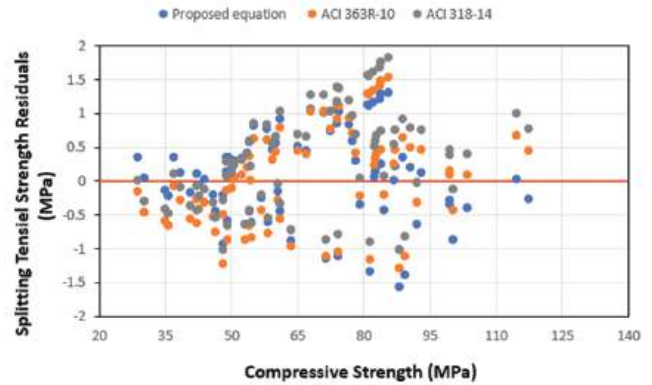


Fig. 13. Splitting tensile strength residual versus compressive of HSC for the proposed, ACI 363R-10, and ACI 318-15 equations.

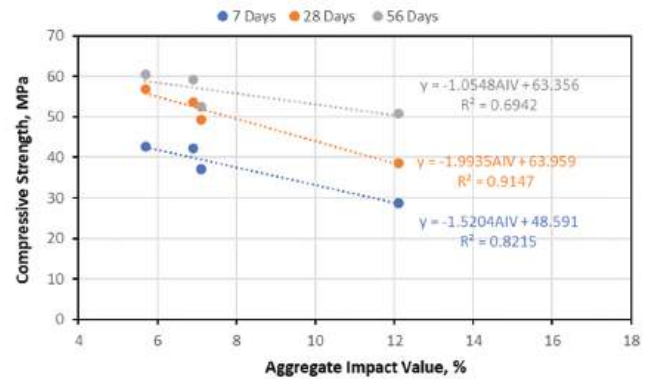


Fig. 14. Correlation between aggregate impact value and compressive strength of HSC.

AIV can be used as a rapid and reliable indicator of aggregate quality that increases the pace of the aggregate selection process. Incorporating AIV into aggregate selection criteria can help ensure that only aggregates with desirable impact values are used, leading to an overall improvement in concrete quality. However, it is important to note that the compressive strength of HSC is influenced by several factors, including aggregate type, size, and surface texture. Therefore, we recommend using AIV in combination with other parameters to provide a more comprehensive assessment of aggregate suitability for HSC production. In addition, further investigation on a wider range of aggregate types, water-cement ratios, and cementitious materials relevant to HSC will refine the AIV-compressive strength relationship, ensuring more reliable and consistent quality control in HSC production.

IV. CONCLUSION

This study investigated the effects of the types and maximum size of coarse aggregate on the mechanical properties of fresh and hardened concrete. In particular, the influence on the compressive strength and splitting tensile strength of HSC toward the optimization of aggregate type and size in concrete mix design for enhanced performance. The following conclusions can be drawn from the key findings of the present study:

1. The MCAS exerts a significant influence on the properties of fresh HSC. The workability of concrete showed an ascending trend as MCAS increased (i.e., increasing MCAS from 9.5 mm to 25 mm led to an increase in slump value from 200 mm to 230 mm). In addition, aggregates characterized by an angular morphology, such as CG, CL, and DL, resulted in a lower slump value compared to rounded-shape and smooth surface NG aggregate.
2. MCAS exerts a pronounced effect on the compressive strength and splitting tensile strength of HSC. Regardless of curing duration, a decrease in MCAS results in an observed increase in both compressive strength and splitting tensile strength of the HSC. Reducing MCAS from 25 mm to 9.5 mm yielded an average increase in compressive strength of slightly over 25%. HSC can be produced using locally available materials by limiting the MCAS of concrete mix to 9.5 mm and 12.5 mm, without the need for supplementary cementitious materials. However, this approach may present certain limitations, such as reducing workability due to a low water-to-cement ratio. This issue can be addressed to a great extent through careful mix design to optimize aggregate size, cement content, and the use of superplasticizers.
3. The compressive strength of concrete produced from CG exceeded that of CL, DL, and HCL aggregates. In contrast, the concrete created with NG aggregate exhibited the lowest compressive strength. This highlights the influence of aggregate type on the performance of HSC. The surface texture of coarse aggregates plays a significant role in influencing the splitting tensile strength of HSC. Among the tested concrete specimens, the ranking in terms of splitting tensile strength, from highest-to-lowest, follows the order of CL, DL, CG, HCL, and NG concrete specimens. However, when considering compressive strength, the sequence was CG, CL, DL, HCL, and NG concrete specimens. Interestingly, for splitting tensile strength, CG traded positions with both CL and DL, despite showing better mechanical properties. This variation may be associated with the presence of smooth surface texture retained by certain particles in NG aggregates, which is not desirable for a good mechanical bond at the aggregate-cement paste interface.
4. Existing empirical equations, such as those from ACI 363R-10 and ACI 318M-14, for predicting tensile strength based on compressive strength show limitations, particularly at high compressive strengths (>55 MPa). A new equation to predict the tensile strength from the compressive strength of HSC is proposed in this study. The evaluation metrics used, including  $R^2$ , RMSE, MAPE, and MAE, provided comprehensive insights into the equation's performance, suggesting its potential for more reliable tensile strength prediction in HSC.
5. The correlation between the AIV and compressive strength of HSC is strong at 7 and 28 days of curing, with  $R^2$  of 0.9147 and 0.8215, respectively. However, it moderately weakens at 56 days, with  $R^2= 0.69$ . Knowing concrete strength properties through AIV testing is indispensable in practical concrete production.
6. Using locally available materials eliminates the need to import aggregates and supplementary cementitious

materials over long distances. This significantly lowers transportation-related energy consumption and carbon emissions, thereby reducing the overall environmental footprint of the construction process. Moreover, sourcing construction materials close to construction sites makes the construction process more flexible and resilient. This is particularly important during global supply chain disruptions, guaranteeing the continuation of construction work without increased costs or delays related to material shortages. The reduction in material costs makes sustainable construction practices more feasible and appealing to local builders and developers.

Although XRF tests were used in this study to determine the chemical composition of aggregate types, a petrographical investigation can provide more detailed results. Therefore, we recommend conducting petrographical analyses in future research to gain a better understanding of the chemical compositions of aggregates. Further studies on the relationship between AIV and the strength properties of HSC concrete can be an interesting topic for researchers.

#### ACKNOWLEDGMENT

The authors would like to thank Koya University, the Faculty of Engineering, the Civil Engineering Department, and the Concrete Laboratory for supporting us in this study.

#### REFERENCES

- ACI Committee 211, 2008. *Guide for Selecting Proportions for High-strength Concrete Using Portland Cement and Other Cementitious Materials*. American Concrete Institute, United States.
- ACI Committee 318, 2015. *Building Code Requirements for Structural Concrete (ACI 318M-14) and Commentary (ACI 318RM-14)*. American Concrete Institute, United States.
- ACI Committee 363, 2010. *Report on High-Strength Concrete*. American Concrete Institute, United States.
- Akçaoğlu, T., Tokyay, M., and Çelik, T., 2002. Effect of coarse aggregate size on interfacial cracking under uniaxial compression. *Materials Letters*, 57(4), pp.828-833.
- Akçaoğlu, T., Tokyay, M., and Çelik, T., 2004. Effect of coarse aggregate size and matrix quality on ITZ and failure behavior of concrete under uniaxial compression. *Cement and Concrete Composites*, 26(6), pp.633-638.
- Al-Oraimi, S.K., Taha, R., and Hassan, H.F., 2006. The effect of the mineralogy of coarse aggregate on the mechanical properties of high-strength concrete. *Construction and Building Materials*, 20(7), pp.499-503.
- ASTM C127-15, 2015. *Standard Test Method for Relative Density (Specific Gravity) and Absorption of Coarse Aggregate*. ASTM International, United States.
- ASTM C128-15, 2015. *Standard Test Method for Density, Relative Density (Specific Gravity), and Absorption of Fine Aggregate*. ASTM International, United States.
- ASTM C136/C136M-14, 2014. *Standard Test Method for Sieve Analysis of Fine and Coarse Aggregates*. ASTM International, United States.
- ASTM C143/C143M-15a, 2015. *Standard Test Method for Slump of Hydraulic-Cement Concrete*. ASTM International, United States.



- ASTM C29/C29M-17a, 2017. *Test Method for Bulk Density (Unit Weight) and Voids in Aggregate*. ASTM International, United States.
- ASTM C33/C33M-18, 2018. *Specification for Concrete Aggregates*. ASTM International, United States.
- ASTM C39/C39M-14, 2018. *Standard Test Method for Compressive Strength of Cylindrical Concrete Specimens*. ASTM International, United States.
- ASTM C496/C496M-11, 2011. *Standard Test Method for Splitting Tensile Strength of Cylindrical Concrete Specimens*. ASTM International, United States.
- ASTM D4791-10, 2010. *Test Method for Flat Particles, Elongated Particles, or Flat and Elongated Particles in Coarse Aggregate*. ASTM International, United States.
- Beshr, H., Almusallam, A.A., and Maslehuddin, M., 2003. Effect of coarse aggregate quality on the mechanical properties of high strength concrete. *Construction and Building Materials*, 17(2), p.97.
- Beushausen, H., and Dittmer, T., 2015. The influence of aggregate type on the strength and elastic modulus of high strength concrete. *Construction and Building Materials*, 74, pp.132-139.
- BS 812-112, 1990. *Testing Aggregates - Method for Determination of Aggregate Impact Value (AIV)*.
- Caldarone, M.A., 2009. *High-Strength Concrete: A Practical Guide*. 1<sup>st</sup> ed., CRC Press, London.
- Darwin, D., and Dolan, C.W., 2021. *Design of Concrete Structures*. 16<sup>th</sup> ed., McGraw-Hill Education Asia, United States.
- Erdal, H.I., Karakurt, O., and Namli, E., 2013. High performance concrete compressive strength forecasting using ensemble models based on discrete wavelet transform. *Engineering Applications of Artificial Intelligence*, 26(4), pp.1246-1254.
- Gjørsv, O.E., 2008. 7 - High-strength concrete (Woodhead Publishing series in civil and structural engineering). In: S. Mindess, ed. *Developments in the Formulation and Reinforcement of Concrete*. 2<sup>nd</sup> ed. Woodhead Publishing, United Kingdom, pp.153-170.
- Golafshani, E.M., Behnood, A., and Arashpour, M., 2020. Predicting the compressive strength of normal and High-Performance Concretes using ANN and ANFIS hybridized with Grey Wolf Optimizer. *Construction and Building Materials*, 232, p.117266.
- Góra, J., and Piasta, W., 2020. Impact of mechanical resistance of aggregate on properties of concrete. *Case Studies in Construction Materials*, 13, p.e00438.
- Grabiec, A.M., Zawal, D., and Szulc, J., 2015. Influence of type and maximum aggregate size on some properties of high-strength concrete made of pozzolana cement in respect of binder and carbon dioxide intensity indexes. *Construction and Building Materials*, 98, pp.17-24.
- Jin, L., Yu, W., Li, D., and Du, X., 2021. Numerical and theoretical investigation on the size effect of concrete compressive strength considering the maximum aggregate size. *International Journal of Mechanical Sciences*, 192, p.106130.
- Kılıç, A., Atiş, C.D., Teymen, A., Karahan, O., Özcan, F., Bilim, C., and Özdemir, M., 2008. The influence of aggregate type on the strength and abrasion resistance of high strength concrete. *Cement and Concrete Composites*, 30(4), pp.290-296.
- Liu, H., Kou, S., Lindqvist, P.A., Lindqvist, J.E., and Åkesson, U., 2005. *Microscope Rock Texture Characterization and Simulation of Rock Aggregate Properties. SGU Project 60-1362/2004*. Sveriges Geologiska Undersökning, Sweden. Available from: <https://urn.kb.se/resolve?urn=urn:nbn:se:Itu:diva-25098> [Last accessed on 2023 Oct 11].
- Meddah, M.S., Zitouni, S., and Belâabes, S., 2010. Effect of content and particle size distribution of coarse aggregate on the compressive strength of concrete. *Construction and Building Materials*, 24(4), pp.505-512.
- Neville, A.M., 2011. *Properties of Concrete*. 5<sup>th</sup> ed., Pearson, Harlow.
- Neville, A.M., and Brooks, J.J., 2010. *Concrete Technology*. 2<sup>nd</sup> ed., Prentice Hall, Harlow.
- Nguyen, N.H., Abellán-García, J., Lee, S., Garcia-Castano, E., and Vo, T.P., 2022. Efficient estimating compressive strength of ultra-high performance concrete using XGBoost model. *Journal of Building Engineering*, 52, p.104302.
- Price, B., 2003. High strength concrete. In: J. Newman and B. S. Choo, eds. *Advanced Concrete Technology, Process*. Butterworth-Heinemann, Oxford, pp.1-16.
- Pul, S., 2008. Experimental investigation of tensile behaviour of high strength concrete. *Indian Journal of Engineering and Materials Sciences*, 15, pp.467-472.
- Rao, G.A., and Prasad, B.K.R., 2002. Fracture energy and softening behavior of high-strength concrete. *Cement and Concrete Research*, 32(2), pp.247-252.
- Rashid, M.A., Mansur, M.A., and Paramasivam, P., 2002. Correlations between mechanical properties of high-strength concrete. *Journal of Materials in Civil Engineering*, 14(3), pp.230-238.
- Uddin, M.T., Mahmood, A.H., Kamal, M.R.I., Yashin, S.M., and Zihan, Z.U.A., 2017. Effects of maximum size of brick aggregate on properties of concrete. *Construction and Building Materials*, 134, pp.713-726.
- Vishalakshi, K.P., Revathi, V., and Sivamurthy Reddy, S., 2018. Effect of type of coarse aggregate on the strength properties and fracture energy of normal and high strength concrete. *Engineering Fracture Mechanics*, 194, pp.52-60.
- Wu, K., Chen, B., and Yao, W., 2001a. Study of the influence of aggregate size distribution on mechanical properties of concrete by acoustic emission technique. *Cement and Concrete Research*, 31(6), pp.919-923.
- Wu, K.R., Chen, B., Yao, W., and Zhang, D., 2001b. Effect of coarse aggregate type on mechanical properties of high-performance concrete. *Cement and Concrete Research*, 31(10), pp.1421-1425.
- Zain, M.F.M., Mahmud, H.B., Ilham, A., and Faizal, M., 2002. Prediction of splitting tensile strength of high-performance concrete. *Cement and Concrete Research*, 32(8), pp.1251-1258.

# The Recovery of Historical Buildings in Post-war Aleppo

Yara Aboasfour<sup>†</sup> and Lígia Nunes

Department of Architecture, Lusófona University, Augusto Rosa Street,  
n° 24 4000-098 Porto - Portugal

**Abstract**—Throughout history, wars and armed conflicts have severely impacted cultural heritage, erased collective memories, and left entire populations seemingly non-existent. However, recognizing the significance of cultural heritage is the primary impetus for its subsequent reconstruction. Since the Syrian war outbreak in 2011, Aleppo, one of the world's oldest continuously inhabited urban centers, has suffered significant damage to its historic sites such as shrines, khans, and other architectural treasures due to bombings and clashes. In 2017, a study by the Directorate of Antiquities and Museums in Aleppo revealed that over 70% of the city's historic center was destroyed. As a result, the cultural heritage of Aleppo and its social and symbolic values have been threatened. This represents a huge loss not only to Syria but also to the international community. This paper explores the significant role that collective memories play in shaping a city's identity in the aftermath of war. The research aims to analyze the best approach for intervention during the reconstruction phase, whether it be preservation, restoration, enhancement, or eventual reconstruction by reviewing some international experiences. Furthermore, it explains the current situation of the old city of Aleppo and presents some cultural buildings that have been severely damaged or destroyed during the conflict. The study will compare the essential values of each case study and finally conclude with suggestions about the suitable intervention of different case studies that represent the values mentioned before.

**Index Terms**—Aleppo, Collective memory, Cultural heritage, Reconstruction.

## I. INTRODUCTION

Aleppo was once an economically significant and culturally rich hub that reflected the Syrian identity. However, the Syrian conflict that started in 2011 drastically altered this reality. Aleppo emerged as the most severely devastated city in the country (World Bank Group, 2017). Between 2012 and 2016, archaeological sites in Aleppo were severely targeted regardless of their significant value and partially or entirely

damaged. The destruction of Aleppo's cultural heritage resulted in social division and substantial economic threat (Abd-Alkarim, 2013). It posed severe losses to the local community's cultural identity and the global community, which paid little attention to these facts.

A few research studies are the only significant initiatives that have been taken to promote an understanding of this heritage's protection. The most relevant initiative is UNESCO's decision in 2013 to declare Aleppo a World Heritage Site in Danger, which means transferring it to the List of World Heritage in Danger, trying through this measure to alert experts (UNITAR, 2015). However, this measure had only symbolic results, without real impact. An additional disaster struck – the earthquake, which occurred on February 6, 2023 (OCHA, 2023). This seismic event has made it even more challenging for the city and its residents to reconstruct, recover, and protect their invaluable cultural heritage for future generations.

This study aims to apply a reconstruction approach to historical buildings in the old city of Aleppo. The ultimate goal is to develop standards and indicators for dealing with historic buildings damaged by wars or armed conflicts by producing results and recommendations aimed at directing the reconstruction of historical buildings in Syria in general and in the old city of Aleppo in particular, to restore the features of the old city and preserve the city's cultural identity.

## II. METHODOLOGY

This study delves into the crucial role that collective memories play in shaping the identity of a city, as seen in historical Aleppo. It examines the current state of the heritage through case studies and its comparisons, highlighting the need for a specific approach for each case during the reconstruction phase. This intervention must consider the building's physical condition, history, and values to prevent any damage to the collective memory and identity. In this research, case studies are chosen using the criteria of its history (including its age) and its relevance to Syrian culture, located along the axis between the Umayyad Mosque and the Citadel. The building's damages were assessed from light damage to severe damage in each case study, taking into consideration non-structural damage to partial or total collapse. The intervention approach is considered by

ARO-The Scientific Journal of Koya University  
Vol. XII, No. 2 (2024), Article ID: ARO.11488. 8 pages  
DOI: 10.14500/aro.11488

Received: 27 November 2023; Accepted: 01 July 2024  
Regular research paper; Published: 03 August 2024

<sup>†</sup>Corresponding author's e-mail: a22010155@alunos.ulht.pt  
Copyright © 2024 Yara Aboasfour and Lígia Nunes. This is an open-access article distributed under the Creative Commons Attribution License (CC BY-NC-SA 4.0).



analyzing international experiences and using the exposed local values as a reference, namely, their previous use and the number of interventions suffered before.

### III. COLLECTIVE MEMORY, IDENTITY, AND CULTURAL HERITAGE

According to Martin Heidegger (1971), the basic principle of human identity is that a person needs tangible elements to confirm his identity and the heritage the built environment represents. It is spiritually connected to the human being, and what is meant is not only the built part but also the unbuilt one. The city's urban voids, such as its streets and squares, in the words of Kostof (1992), are our means to a deeper understanding of the city. In his book *Genius Loci*, Norberg-Schulz (1980) states that nature invites humans to inhabit it when attractive factors are present, including water, view, or protection.

When people settle in the place, they begin to build and construct. Stability is usually accompanied by giving things meanings and values, and these meanings later turn into culture and heritage (Lynch, 1981). Therefore, the built heritage relates to the people, their habits, and their response to economic, climatic, and social needs. Lynch emphasizes that every city, with its architecture and function and people's values, customs, and beliefs, is only a unique phenomenon (Lynch, 1981).

Concepts regarding cultural heritage and understanding it have changed over the past two decades. Heritage contains material and non-material forms, including hopes, aspirations, emotions, values, interpretations, symbols, and narratives (Barakat, 2005). However, the essential and inclusive component is memory; without memory, everything related to time, continuity, change, and individual and collective identities becomes reduced to being only "old things" that can be collected. The built environment has gone beyond being a dwelling and a sanctuary to become a solid memory and cultural and historical symbolism, with all its forms and expressions (Barakat, 2021).

Within this framework, collective memory plays a pivotal role in shaping how cultural heritage is perceived, interpreted, and transmitted. It imbues historical sites, artifacts, and rituals with meaning, connecting present-day communities to their ancestral past and fostering a sense of continuity. Moreover, collective memory serves as a lens through which cultural heritage is understood, influencing perceptions of identity and belonging. By safeguarding and promoting collective memory, societies can ensure the preservation and appreciation of their identity for future generations.

### IV. HISTORIC BACKGROUND

The city's history dates back to at least the third millennium BCE, with archaeological evidence suggesting settlements during the Bronze Age. Over the centuries, Aleppo thrived as a critical center along the ancient trade routes, particularly the Silk Road, connecting the Mediterranean Sea with the lands of Asia and beyond. Its strategic location made it

a melting pot of cultures, religions, and ideas. The city began at the height of the citadel, the oldest archaeological witness, dating back to 3800 years; the citadel was the center of power and the sanctuary when the city had an external enemy. Important buildings, such as schools, khans, and bathrooms, gather around the nucleus. These structures witnessed their importance and the role played by the old city (Aboasfour, 2019).

The natural factors that characterize the city's topography have significantly impacted its emergence and continuation. The outline of the city of Aleppo can confirm the validity of this hypothesis; the presence of the city within the basin of the Quiq River, in addition to the plateau built the citadel above, can be considered one of the most critical factors that contributed to the continuity of the city and its revival after all that has been exposed over time of natural disasters in addition to the repeated destruction and burning (Al-Ghazzi, 1992). In Aleppo, the patterns and styles that make up the architectural and urban heritage mix in a unique model in which time and things overlap with the civilizations and antiquities that preceded it. These include Hittite, Hellenistic, Roman, Byzantine, and Ayyubid, residing in the memory in any corner from which we look at this city (UNESCO, 2018).

The area of the old city within the walls is 42 hectares and features tightly packed courtyard houses connected by networks of high-walled alleys. Aleppo's historical significance is deeply ingrained in the collective memory of its inhabitants, which has become integral to its identity. For example, the Great Mosque of Aleppo, dating back to the 8<sup>th</sup> century, stands as a symbol of the city's enduring religious and architectural heritage. Similarly, the Aleppo Citadel is a reminder of its strategic importance throughout history. To the west of the citadel, it is one of the largest and best-preserved covered bazaars (souqs) in the Middle East, extending for miles through narrow streets. Souqs and khans represent an exceptional reflection of the social, cultural, and economic aspects of what was once one of the wealthiest cities of all humanity (Mobaiyed, 2007).

In the summer of 2012, the city was subjected to the systematic destruction of its historical center to obliterate its identity and cultural value through the ages. Where the fighters were holed up in their old neighborhoods, and their leaders stressed that humans are more important than stone, but people were killed, and the stone destroyed. "More than 70% of the historic center of Aleppo was destroyed" (World Bank Group, 2017) due to the armed conflict in the city, where the sites suffered from the effects of bombing and clashes, which caused severe damage to a large number of historic and public buildings, burned the old markets as well as the exposure of the old city to looting and smuggling of antiquities out of the country.

Terrorist organizations blew up tunnels in the city of Aleppo since the summer of 2012, digging tunnels from areas under their control, blowing them up, or infiltrating them to carry out attacks. They detonated several tunnels around the fortress; the most notable was in May 2014, and another in 2015 caused the collapse of part of the citadel's wall, leading to significant damage in the area around the

citadel (UN-Habitat, 2014). Experts and researchers have actively evaluated the extensive impact inflicted on the old town and its cultural heritage. These studies aim to analyze the structural stability of buildings comprehensively, examine the state of archaeological sites, and determine the overall loss of cultural and historical significance. Despite the scars of conflict, Aleppo's architectural legacy is a testament to human resilience. Efforts to preserve and rebuild stand as a testament to the city's unwavering spirit, ensuring that future generations may glimpse the splendor of its storied past amidst the ruins of adversity.

## V. CASE STUDIES

Near the Citadel of Aleppo, several prominent buildings along the axis between the Umayyad Mosque and the Citadel were chosen according to their date of construction from the older to the most recent one: Sultaniyah School, Yalbga Bath, Khusrawiyah Mosque and School, The Carlton Hotel, and The New Serail, as they are located within an area that is the symbol of their city and one of the most active areas for the city's residents (Fig. 1). The main square in front of the castle was the scene of many cultural activities and surrounded by cultural cafés, restaurants, and entertainment centers. These buildings collectively represent a harmonious blend of cultural heritage, forming an integral part of the collective memory of Syrians, the city's cultural identity, and historical legacy (Aboasfour, 2019).

Damage is assessed according to the following levels:

- Light damage when the unit has only suffered non-structural damage.
- Medium damage occurs when the building has sustained moderate and more severe non-structural damage.
- Severe damage occurs when a building experiences critical structural damage, making it unstable or even causing a partial or total collapse.

Each case study is presented individually in the following sections:



Fig. 1. The Location of the study cases (B-tu, 2016). (A) Sultaniyah school (B) Yalbga bath (C) Khusrawiyah mosque and school (D) The Carlton Hotel (E) The new serial.

### A. Sultaniyah School

The Sultaniyah School, also the Royal School, is located toward the door of the Citadel of Aleppo. It is considered one of the most important Islamic monuments, as its construction dates to the Ayyubid era. King Al-Zahir Ghazi started the school construction, only completed in 1223 AD (Fig. 2). The school mosque was a square-shaped room roofed with a distinctive dome. The mosque also contains one of the rare niches regarding the installation and the marble's quality. With many types of stones and marble, it also contained entirely accurate carving works and columns with Corinthian capitals made of marble, standing on both sides of the mihrab (Al-Ghazzi, 1992).

Its physical condition is distorted because the building was bombed in December 2014. The school was destroyed except for remains on the northern side of the courtyard and the minaret as shown in Fig. 3, though they are also heavily ruined (UNITAR, 2015). It is historically significant as it contains the mausoleum of al-Zahir Ghazi, the famous ancient ruler of Aleppo. Architecturally, it was rich in inscriptions and included splendid architectural features representing the Ayyubid style. Consequently, the overall historical loss is categorized as severe and critical.

### B. Yalbga Bath

It is considered one of the most important historical sites due to its archeological, structural, artistic, and architectural features. As one of the few Mamluk public baths to have preserved its original function. It was still standing and preserving its original character until the bombing in April 2014. Taking this into consideration, the overall historical loss is categorized as severe (UNITAR, 2015).

It occupies a significant location at the foot of the Citadel's entrance and faces the street with a monumental façade built in polychrome masonry, of the Mamluk style. The façade of the bathroom is decorated with alternating bricks in black and yellow (Figs. 4 and 5 show the facade of the bath before and after the war). The dome of the outer section rests on the shoulders of the Iwan vaults with triangular spherical corners and is decorated with floral motifs inscribed in red and blue. The floor of the inner section is paved with small alternating stones in black and yellow in coordinated geometric styles (Al-Ghazzi, 1992).

### C. Khusrawiyah Mosque and School

The Khusrawiyah complex, designed by Mimar Sinan, was constructed in 1544 during the Ottoman reign. It was the first school in Aleppo, Syria, known as the religious secondary, and it was described as Azhar of Aleppo. It stood near the citadel to the west across its ring road (Al-Ghazzi, 1992). However, in 2014, the entire complex, except for the northern entrance, was destroyed during the Battle of Aleppo. The central mosque within the complex suffered extensive damage, causing its collapse and leaving behind a sizable crater (UNITAR, 2015).

The Al-Khusrawiyah complex in Aleppo has significant historical significance as it was the first example of Ottoman

architecture in the city. This complex introduced a new architectural and urban concept to Aleppo by blending Ottoman design principles with local building traditions and materials as shown in Fig. 6. The mosque's grand portal features two marble columns with engravings, a door under a dome, and a patterned decoration stone on each side. The ceramic tiles that adorn the windows, the mihrab (altar), and the pulpit within the prayer hall are examples of this fusion (Al-Ghazzi, 1992). From Fig. 7 it is essential to note that the overall loss of historical significance associated with the Khusrawiyah complex is severe and critical.

#### *D. The Carlton Hotel*

The construction of the hotel building, initially known as the Strangers Hospital, commenced in 1819 and spanned 48 years, culminating in its completion in 1897. In 1892, it was the seat of the municipality. The facility's inauguration officially took place in 1900 under the auspices of Governor Jamil Pasha. The primary purpose of the establishment was to provide medical treatment for poor people and strangers, and its establishment was made possible through subsidies and contributions from various benefactors (Al-Ghazzi, 1992). The building was transformed into the National Hospital, comprising 32 rooms, two spacious residences, two elongated salons, and a pharmacy. In 1988, it underwent further conversion into a health institute before being repurposed as a hotel (Fig. 8), capitalizing on its exceptional location and captivating view near the Aleppo Citadel (Al-Ghazzi, 1992). Arches, arcades, and a spacious lobby characterize the Ottoman building of the Carlton Hotel. It is considered one of the preeminent archaeological highlights in Aleppo. However as shown in Fig. 9, the hotel is currently suffering severe deterioration due to two bombing incidents in February 2014 and May 2014 (UNITAR, 2015).

#### *E. The New Serail*

In constructing the new serail, the concept of building a novel government edifice traces its origins back to the latter stages of the Ottoman era. Nonetheless, the construction process encountered interruptions and was recommenced in 1928 after establishing the State of Syria during the period of the French Mandate. On 15 April 1933, the New Serail was officially inaugurated, assuming the role of the customary headquarters for the governor and mayor of the city. It served as the governmental seat until 2008 when the new headquarters of the Aleppo City Council was inaugurated (Fig. 10). In 2011, the Serail underwent a renovation to transform it into a hotel. Positioned south of the Citadel and east of its primary entrance, the building featured a U-shaped design, encompassing three floors and a basement. Its central area comprises a spacious atrium flanked by rooms on both sides and a sizable garden to the south (Al-Ghazzi, 1992).

Between 2014 and 2015, the site witnessed complete structure demolition. The central section and the entire eastern wing suffered irreparable damage due to the excavation of a tunnel beneath the building, followed by the strategic placement of explosives, resulting in the formation

of a substantial crater (UNITAR, 2015). Considering the historical significance of the new serail as the established above for the city's governor and mayor since the nascent years of Syria, coupled with its noteworthy contribution to the local landscape of modern architectural expression, the loss incurred is deemed severe and critical (Fig. 11).

## VI. RESULTS AND DISCUSSION

### *A. The Value and Importance of Studied Cases*

The process of nominating buildings for preservation and reconstruction in Aleppo is based on previously specified criteria. These criteria have been classified into variable values such as architectural, aesthetic, historical, religious, and political. The importance of these values varies depending on their impact on the collective memory of the people of Aleppo. In addition, there are fixed values such as the building's age, location, uniqueness, and physical condition. These values can be compared (Table I), to provide a nuanced understanding of the diverse values of different structures. This comparison can help prioritize restoration and reconstruction efforts. Decision makers can then make choices based on the distinct values a building carries and its physical condition. This approach ensures that resources are allocated to preserve and restore structures that hold tremendous significance for Syria's cultural heritage.

### *B. Intervention Approaches*

From the several reconstruction approaches followed in destroyed cities worldwide, some were successful. Still, unfortunately, some results have caused an even more significant loss of the city's people and cultural heritage (Stanley-Price, 2009). However, each city adopts a unique reconstruction strategy to restore its prosperity and ensure its survival. For Aleppo, implementing targeted approaches inspired by international experiences and developing innovative solutions tailored to its specific context could prove highly effective.

The first approach aims to use the building as a witness to the events, and the lack of change is an approach that focuses on preserving the symbolic value of a building rather than its physical importance. This approach aims to maintain the building's condition as it serves as a witness to historic events. It preserves the building as a part of the city's memory, highlighting the horrors of war and their impact on human and historical values (Stanley-Price, 2009). This approach is suitable for buildings with special significance and a strong reason for preservation. Due to the decrease in land area and the increase in population density, these buildings are chosen by experts from various fields.

The case of the A-Dome in Hiroshima exemplifies this strategy, preserving the city's main ruins amidst a new park designed to engage the experience and understanding of the past. The A-Dome was one of the few structures left standing near the epicenter of the atomic bomb blast on August 6, 1945. In the aftermath of the bombing, there were debates about whether to demolish the A-Dome as a painful relic of the past or preserve it as a symbol of the horrors of



Fig. 2. Sultaniyah school before the war (UNESCO, 2018b).



Fig. 6. Khusrawiyah before the war (UNESCO, 2018b).



Fig. 3. Sultaniyah School after the war. Source: Author.



Fig. 7. Khusrawiyah after the war (UNESCO, 2018b).



Fig. 4. Yalbga Bath before the war (UNESCO, 2018b).



Fig. 8. The Carlton Hotel before the war (Aboasfour, 2019).



Fig. 5. Yalbga Bath after the war. Source: Author.



Fig. 9. The Carlton Hotel after the war (Aboasfour, 2019).

war. Ultimately, the decision was made to leave the building ruins standing. Over the decades, the A-Dome has become a global symbol of peace and reconciliation, attracting visitors worldwide who come to pay their respects and reflect on the consequences of nuclear warfare (Ide, 2007).

Other approaches of restoring/reconstructing the old are expected to be considered more, such as rebuilding the damaged historical building or part of it as it was in the past. These aspire to transcend the tragedy of the past by restoring/reconstructing the symbols of the past to preserve their existence. The restoration/reconstruction of the destroyed historical architecture keeps the memory and identity of the place (Al Aloul, 2007). Despite the difficulty of implementing this approach, it is sometimes considered reasonably necessary. Primarily, this type of reconstruction requires prior, accurate, and comprehensive documentation of the condition and form of the building before destruction; such documentation can be challenging and complicated if the building is not adequately documented before its destruction. Furthermore, reconstructing a historical building to its original form often requires skilled artisans and craftsmen capable of replicating traditional building techniques and materials. Finding experts with the necessary expertise can be difficult, especially for buildings with unique architectural features or historical significance. Finally, Restoring or reconstructing historical buildings can be prohibitively expensive and challenging.

Consequently, this approach is mainly concentrated in historical areas and buildings with a particular symbolic value whose presence is essential in the community's memory and identity. This approach aspires to overcome the tragedy of the past by rebuilding the symbols of the past. For example, the Church of Our Lady (Frauenkirche) in Dresden, Germany, represents an attempt to reconstruct the lost heritage and reformulate the culture of the past destroyed during World War II. Reduced to rubble during the bombing of Dresden, the church's restoration, initiated in the 1990s, painstakingly recreated its Baroque splendor using original plans, salvaged materials, and skilled craftsmanship. Today, it serves as a poignant reminder of Dresden's ability to overcome the scars of war and unite to preserve cultural heritage for future generations (Jäger and Burkert, 2001).

Another solution, an evolving approach that mixes the old and the new, aims to blend the identity and heritage of the old with the addition of the imprint of the contemporary time and the addition of an appropriate development that illustrates the development taking place in architecture without affecting the actual identity and memory of the site (Al Aloul, 2007). This approach solves the question by developing thoughts without abandoning the city's local identity by pairing the old building with a new design as a complementary part to keep pace with the spirit of the times and suit the rapid and urgent needs of the development and the difficulty of using old methods and patterns.

For example, the famous Berlin, Germany Reichstag case represents this approach. The Reichstag building holds significant historical and political importance. It served as the seat of the German Parliament until it was severely damaged by fire in 1933. After World War II, the building stood

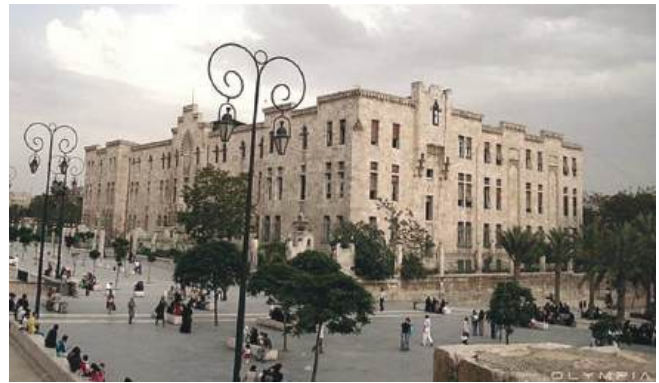


Fig. 10. The New Serail before the war (Aboasfour, 2019).



Fig. 11. The New Serail after the war (Aboasfour, 2019).

abandoned and in ruins within the divided city of Berlin. However, following German reunification in 1990, plans were made to restore and renovate the Reichstag as the seat of the German Parliament. In addition to the original monument, new technologies and materials (a new dome made of glass) were added while adding symbolic values. The iconic glass dome, designed by architect Norman Foster, symbolizes transparency and democracy and offers panoramic views of the city. Today, the Reichstag symbolizes Germany's democracy and commitment to openness and transparency (Filler, 2007).

International experience may contribute to Aleppo's cultural heritage after the conflict. It is urgent to discuss it as soon as possible with the global community, decide on the best way to help local experts and decision makers how to deal with the reconstruction phase after the conflict ends, choose appropriate approaches for reconstructing the affected buildings, respecting the old and ensuring that the resulting structure is a new significant point that highlights the historical value of the surrounding area. Therefore, intervention approaches in the old city at the level of a single building include the approach of preserving the demolished building as an archaeological landmark and a memorial to the devastation caused by war, the approach of reconstruction of an exact copy of ancient buildings, and finally, the approach of combining elements of the original building with modern impressions.

Referring to the case studies, all are severely or entirely damaged, and all of them are ancient, too. However, Sultaniyah School is the oldest among them, followed by Yalbga Bath and Khusrawiyah Mosque. All cases are essential regarding the

TABLE I  
VALUES COMPARISON BETWEEN THE STUDIED BUILDINGS

Name of building	Sultaniyah school	Yalbga bath	Khusrawiyah mosque and school	Carlton Hotel	The new serail
Building age	The founder of this school is King Al-Zaher Ghazi. It was completed in the period after his death in 1223	Created in the Mamluk era in 1495 by Prince Yelbga Naciri	It was designed by Mimar Sinan. Its construction was completed in 1544	The construction was completed in 1897	The construction was suspended for the duration of the French mandate until it was completed in 1933
Architectural and aesthetic values	It was rich in inscriptions and included splendid architectural features representing the Ayyubid style	The building's facades alternate with black and yellow panels typical of the Mamluk style	It was the first example of the Ottoman architectural style in the city	It is built in the Ottoman style characterized by arches and construction methods with a wide hallway and lobby	It is built in the Ottoman style. Its facades are inspired by the defensive balconies in the facing castle towers
Historical value	It contains the mausoleum of al-Zahir Ghazi	One of few Mamluk baths that preserved its function	The first example of Ottoman architecture in the city	The first public hospital in Aleppo to help the poor and strangers	One of few well-preserved Ottoman government buildings
Religious value	Several rooms around the central courtyard serve as a religious school		Known as the religious secondary (Azhar of Aleppo)		
Uniqueness and scarcity	An important religious landmark representing the Ayyubid era	It is one of the unique baths that were known in Aleppo	The first mosque influenced by the Byzantine style of Istanbul old churches	The hospital was built from donor funds	It combined traditional aesthetics with new engineering methods
Political value				In 1892 it was the seat of the municipality	It included the headquarters of the Governor of Aleppo

values discussed earlier in Table I, which range across all the buildings. Sultaniyah School, Yalbga Bath, and Khusrawiyah Mosque and School are religious and unique buildings whose functions have not and will not change. According to historical plans, they should be reconstructed as before, using original building materials as much as possible. The Carlton Hotel and the new serial can be assumed to be of different use from the original one. In this case, one can follow a different approach to reconstruction operations. In both cases, the resulting building is not expected to be completely similar to the old building.

## VII. CONCLUSION

The study delves into the reality of several historical buildings within Aleppo's old city, exploring potential approaches to preserving them as memory agents. The research shows that the criteria used to analyze case studies effectively determine the priorities and intervention principles for the listed buildings while considering international references. On the one hand, most historical buildings, particularly those still serving their original purpose, should be restored first. On the other hand, buildings that had already lost their original use could be expected to change their use once more and face a mix or contemporary intervention approach if the new additions represent new values for the ancient building and maintain its original values and memory. Therefore, developing a comprehensive and strategic reconstruction approach for Aleppo's historical buildings is paramount. This approach must consider historical use and current conditions, integrating traditional and contemporary methods. Furthermore, interdisciplinary research and discussions should strike a

balance between preserving collective memories and meeting modern functional needs, ensuring a harmonious fusion of old and new that honors and sustains cultural heritage for future generations.

## REFERENCES

- Abd-Alkarim, M., 2013. *Annual Report 2013*. Ministry of Culture, Directorate General of Antiquities and Museums, Syrian Arab Republic, Aleppo Old City.
- Aboasfour, Y., 2019. *Reconstruction after Conflicts: The Study Case of Aleppo*. Master Thesis. Lusófona do Porto University.
- Al Aloul, M., 2007. *The Destruction of Cultural Heritages by Warfare and Reconstruction Strategies: Lessons Learned from Case Studies of Rebuilt Cities*. Master Thesis. University of Florida.
- Al-Ghazzi, K., 1992. *Nahr Al-zahab fi Tarikh Halab (The Golden Age in the History of Aleppo)*. Dar al-Qalam al-Arabi, Aleppo. [Arabic].
- Barakat, S., 2005. *After the Conflict. Reconstruction and Development in the Aftermath of War*. I.B. Tauris, London.
- Barakat, S., 2021. Necessary conditions for integrated approaches to the post-conflict recovery of cultural heritage in the Arab world. *International Journal of Heritage Studies*, 27(5), pp.433-448.
- B-tu, 2016. *Plan of the Old City of Aleppo. Aleppo Archive in Exile. Plan of the Old City of Aleppo Project*. Archaeological Heritage Network, Cottbus.
- Filler, M., 2007. *Makers of Modern Architecture*. Vol. 1, The New York Review of Books, New York, p.226.
- Heidegger, M., 1971. *Poetry, Language, Thought*. Harper and Row, New York.
- Ide, K., 2007. A symbol of peace and peace education: The Genbaku Dome in Hiroshima. *The Journal of Aesthetic Education*, 41(4), pp.12-23.
- Jäger, W., and Burkert, T., 2001. *The Reconstruction of the Frauenkirche in Dresden*. In: *Proceedings of III. Seminar on Historical Constructions 7.-9.11.01*



in GUIMARÃES. Portugal.

Kostof, S., 1992. *The City Assembled*. Thames and Hudson, London.

Lynch, K., 1981. *A Theory of Good City Form*. 1<sup>st</sup> ed., The MIT Press, United States.

Mobaiyed, A.R., 2007. *Aleppo Monuments*. Ministry of Culture, Aleppo. [Arabic].

Norberg-Schulz, C., 1980. *Genius Loci: Towards A Phenomenology of Architecture*. Academy Editions Ltd., United Kingdom.

OCHA, 2023. *Earthquake: Türkiye and North-West Syria Flash Update No. 1 As of 6 February 2023*. Available from: <https://reliefweb.int/report/turkiye/earthquake-turkiye-and-north-west-syria-flash-update-no-1-6-february-2023> [Last accessed on 2024 Mar 01].

Stanley-Price, N., 2009. *The Reconstruction of Ruins: Principles and Practice*. Routledge, United Kingdom.

UNESCO, 2018. *Ancient City of Aleppo*. Available from: <https://bit.ly/3qikUvb>

[Last accessed on 2023 Jan 20].

UNESCO. 2018b. *Five Years of Conflict: The State of Cultural Heritage in the Ancient City of Aleppo: A Comprehensive Multi-temporal Satellite Imagery-based Damage Analysis for the Ancient City of Aleppo*. Available from: <https://unesdoc.unesco.org/ark:/48223/pf0000265826> [Last accessed on Feb 10].

UN-Habitat, 2014. *City Profile Aleppo: Multi-Sector Assessment*. Available from: <https://unhabitat.org/city-profile-aleppo-multi-sector-assessment> [Last accessed on 2023 Feb 01].

UNITAR, 2015. *Damage Assessment of Aleppo*. United Nations Institute for Training and Research, Geneva. Available from: <https://www.unitar.org/unosat/maps/syr> [Last accessed on 2023 Feb 20].

World Bank Group, 2017. *Syria Damage Assessment of selected cities Aleppo, Hama, Idlib*. International Bank for Reconstruction and Development, The World Bank, Washington. Available from: <https://documents1.worldbank.org/curated/en/530541512657033401/pdf/121943-wp-p161647-public-syria-damage-assessment.pdf> [Last accessed on 2023 Jan 12].

# Assessing E-Government Effectiveness: A Structural Equation Modeling Approach

Aso K. Ameen<sup>1,2†</sup>, Dler H. Kadir<sup>3,4</sup>, Dana A Abdullah<sup>2</sup>, Ismail Y. Maalood<sup>2</sup> and Hewir A. Khidir<sup>3</sup>

<sup>1</sup>Department of Computer Science, College of Science, Cihan University-Erbil,  
Kurdistan Region - F.R. Iraq

<sup>2</sup>Department of Information and Communication Technology Center (ICTC)-System Information, Ministry of Higher Education and  
Scientific Research,  
Erbil, Kurdistan Region - F.R. Iraq

<sup>3</sup>Department of Statistics and Informatics, College of Administration and Economics, Salahaddin University-Erbil,  
Kurdistan Region - F.R. Iraq

<sup>4</sup>Department of Business Administration, Cihan University-Erbil,  
Kurdistan Region - F.R. Iraq

**Abstract**—In this study, we address the pressing need to improve e-government services by conducting a comprehensive evaluation of document management practices within the Ministry of Higher Education in the Kurdistan Region of Iraq. Employing structural equation modeling and regression modeling techniques, we assess the effectiveness of key variables using the six factors (digitalization, utility, reliability, efficiency, user satisfaction, and accessibility) under the e-government assessment model. Our findings reveal that user satisfaction and ease of access are pivotal for the success of e-government services, with digitization and efficiency significantly impacting operational effectiveness. Furthermore, it also concerns that without improving the overall user satisfaction, the level of acceptance and use of e-government remains low. High user satisfaction can make a lot of difference in overall engagement besides improving service delivery among organizations. Through insights specific to the Kurdistan Region, we underscore the importance of balancing technical infrastructure with user experience. Our proposed six-factor model offers valuable guidance for policymakers and practitioners globally, aiming to enhance e-government services.

**Index Terms**—E-Government services, Kurdistan region, Regression modeling, Structural equation modeling, User satisfaction

## I. INTRODUCTION

Digitization has radically transformed the area of E-Government Service Delivery, in particular, the Ministry of Higher Education in the Kurdistan Region of Iraq (KRI).

ARO-The Scientific Journal of Koya University  
Vol. XII, No.2 (2024), Article ID: ARO.11601. 9 pages  
Doi: 10.14500/aro.11601

Received: 23 April 2024; Accepted: 15 July 2024  
Regular research paper; Published: 05 August 2024

†Corresponding author's e-mail: [aso.khaleel@mhe-krq.org](mailto:aso.khaleel@mhe-krq.org)  
Copyright © 2024 Aso K. Ameen, Dler H. Kadir, Dana A Abdullah,  
Ismail Y. Maalood, and Hewir A. Khidir. This is an open-access  
article distributed under the Creative Commons Attribution License  
(CC BY-NC-SA 4.0).



The Ministry has been in line with other governments across the world to create efficiencies, enhance transparency, and establish good governance with the use of digital technology. It started with an e-government system called [www.erp.mohe.gov.krd](http://www.erp.mohe.gov.krd), which was designed and established in the buildings of the ministry and government universities in 2017. The main elements of this e-government system are six, namely, accounts, scholarships, student records, language center, and document management. In that regard, the paper will describe document management incorporated into the system. User satisfaction is another important factor; indeed, satisfaction is at the core of e-government acceptance and performance. The degree of perceived user satisfaction has a positive relationship with the amount of usage and level of confidence in the system which is also a significant reason for the effectiveness of e-government services.

Assessing the level of satisfaction of users about the management of documents in e-government services helps in the enhancement and operation of the government processes. As the Ministry of Higher Education, it functions in a complex environment that is keenly sensitive to advances in technology and changes in the citizens' expectations. Hence, it is important for policy makers, administrators, and stakeholders to know and measure satisfaction benchmarks about document management in e-government services. Document management in the context of this paper refers to the processes involved in creating, storing, accessing, and sharing documents and other forms of documentation that are critical for effective functioning and to ensure that the institutions of the government are efficient, credible, and reliable (Al-Musawi, 2020). The research of this study is to undertake a general investigation on e-government document management satisfaction among the Ministry of Higher Education of the KRI.

Using structural equation modeling (SEM) as a methodological framework, the study aims to clarify the complicated interactions between various elements that influence satisfaction levels. This study uses SEM to provide

a deeper knowledge of the causes of document management satisfaction by simultaneously examining several variables and their interactions. This work has significance beyond theoretical research, as its findings have practical consequences for policymakers and administrators responsible for improving the efficiency of e-government services. By identifying the primary factors that contribute to satisfaction with document management, policymakers can develop focused interventions and strategies to enhance the functioning and user experience of e-government platforms within the Ministry of Higher Education in the KRI. Furthermore, the findings from this study can provide guidance for larger efforts focused on establishing digital governance strategies and improving public participation and contentment in the higher education sector in the Kurdistan Region.

This means that the literature has emphasized the need to monitor and review progress and setbacks in the process of e-government implementation at different stages (Moon, 2002; Heeks, 2006; Nawafleh and Fares, 2024). Regarding the assessment model applied in this research, it is important to note that it focuses on six efficiency standards: Digitalization, Utility, Reliability, Efficiency, User Satisfaction, and Accessibility forming the e-government assessment model (EGOVSAT). By exploring these standards, the research seeks to find out the extent of efficacy of services and understand how the e-government systems can be fine-tuned to enhance performance and satisfaction levels.

The rest of the article is organized as follows: In Section II, related literature on e-government services and document management area is discussed. Section III of the study highlights the design of the research together with the ways of data gathering and analysis. The findings of the study are laid down in Section IV of the paper, while the discussion of the results is provided in Section V of the paper only. Finally, Section VI consists of the conclusion of the paper and implementation of recommendations for policy and practice.

## II. LITERATURE REVIEW

The integration of e-government services is continuously growing in recognition as an essential element of innovation in the public sector, ensuring easy access by citizens and stakeholders to information, transactions, and government services through e-government services (Moon, 2002). It also offers many benefits related to efficiency, transparency, citizen participation, and speed of access and use of data (Heeks, 2006). This is of particular importance in the Kurdistan Region, where e-government initiatives promise to transform the mechanisms used in providing public services. A key element of this transformation lies in improving document management systems, which play a crucial role in enhancing user satisfaction and overall service quality.

The characteristics that impact user satisfaction with e-government services include accessibility, ease of use, quality, and security. Recently, Muttaqin and Susanto emphasized the importance of trust and perceived ease of use in determining user satisfaction (Muttaqin and Susanto,

2019). Furthermore, new articles show an increase in the focus of e-government services on the user perspective and discuss the significance of the personalization factor in enhancing the efficiency of services, users' participation, and satisfaction levels (Maksimova, Solvak and Krimmer, 2021).

The application of SEM in e-government research allows for a comprehensive analysis of the relationship between user satisfaction and its determinants and shows how SEM can be used to investigate the impact of service innovation on user satisfaction (Nawafleh and Fares, 2024). They show that this method can deal with complex interactions of variables. Similarly, apply a SEM study to examine the impact of digital divide factors on the adoption of e-government services, providing in-depth insights into social, economic, and demographic influences (Muhammad and Kaya, 2023). However, certain limitations can be identified in these studies, which include restricted demographic factors, and the concentration on geographical areas only. In addition, according to improvements to the electronic government, service delivery system increase user satisfaction by positively influencing perceptions of ease of use and usefulness (Sachan, Kumar and Kumar, 2018).

Moreover, the use of blockchain as a tool for the improvement of security and openness of e-government services has been described in the works. Thus, current challenges are observed in the adoption of blockchain technology for various purposes because of legal and technical hurdles (Ølnes and Jansen, 2017).

The literature also addresses specific challenges and opportunities for implementing e-government in the KRI. It discusses the structural and political barriers to the adoption of e-government services (Doski, 2015). While emphasizing the role of public-private partnerships in accelerating the development of e-government services (Al-Taie and Kadry, 2013), E-government in the region, in addition, examines the impact of user perceptions and cultural factors on the adoption of e-government services in Iraqi Kurdistan, providing a comprehensive look at the local dynamics that influence e-government success (Yahia and Miran, 2022). These papers despite completing a vast coverage of the subject fail to capture the dynamism of the technological environment within which Content Delivery Networks exist and operate as well as the consequences thereof on the users' perceptions of satisfaction.

The usefulness of the EGOVSAT model for evaluating e-government services has been highlighted through its application in several studies that confirm its effectiveness in evaluating service quality and user satisfaction. Describes the model's adaptability and impact in a broader context, and emphasizes its importance in evaluating service quality and user satisfaction (Hassan, et al., 2021). While describing its adaptability and impact in a broader context and emphasize its importance in global e-government research (Nawafleh, 2021; Ahmed, et al., 2016). However, for the model to apply in other cultural contexts, further research is needed to prove the pertinent cross-cultural utility.

Extensive literature reviews have identified complex factors that influence satisfaction with e-government

services, with document management systems proving to be an essential component of effective service delivery. Implementing an electronic document management system can provide valuable insight into these complex dynamics and interrelationships that lead to user satisfaction. A deeper understanding can be gained. As e-government initiatives are implemented, especially in regions such as the KRI, it is important to address unique challenges and leverage the latest innovations to realize the full potential of e-government services. Future research should design the experiments to include more recent technological structures and take into account other organizational demographics.

### III. RESEARCH MODEL

This study utilized the “Six Factor Model” to evaluate the document management performance of e-government services, particularly at the Ministry of Higher Education and Scientific Research KRI. This comprehensive framework, which comprises six major dimensions that start with digitalization, utility, reliability, efficiency, user satisfaction, and accessibility, is required to assess the quality of e-government services from the end-user viewpoint.

Digitization is defined as the conversion of old services into digital representations, which is necessary for updating service delivery (Di Giulio and Vecchi, 2023). Moreover, we focus on five questions. Utility assesses the practical value and application of e-government services, ensuring that they satisfy users’ demands successfully (Dunayev, et al., 2023). Also here, we are using five questions. Reliability assesses the consistency and dependability of these services, which is critical for ensuring user confidence (AL-Kaabi, 2023). As well, we focus on three questions. Moreover, efficiency in the context of e-government services refers to the extent to which these services effectively use time and resources, hence demonstrating operational efficiency (AL-Kaabi, 2023). Moreover, we are working on three questions. User Satisfaction is a direct indicator of service success as it reflects consumers’ overall acceptance of the services offered (Lee, Lee and Lee, 2023.). Our attention is centered on five specific questions. Last but not least, accessibility assesses the ease with which services may be accessed, with an emphasis on the significance of accommodating all individuals (Othman, et al., 2023.).

By combining these characteristics, our study model seeks to give a thorough assessment of the present level of e-government services in the KRI’s higher education sector. The use of SEM will enable a sophisticated study of user data, identifying critical aspects that impact customer happiness and service quality. The six factors are shown in Fig. 1.

### IV. METHODOLOGY (MATERIALS AND METHODS)

#### A. Data Collection

Questionnaires were distributed to users of document management systems at public universities operating

under the auspices of the Ministry of Higher Education and Scientific Research in the KRI for the purposes of this research. Based on the constructs of the SEM model, these questionnaires sought to comprehensively assess the e-government services as perceived by the consumers.

A combination of qualitative and quantitative inquiries was used to collect information relating to efficiency, accessibility, reliability, facilities, digitalization, and user satisfaction with the system. The total number of questions distributed was 25. The dataset of the distribution of questions across sections is shown in Fig. 1. The total response collected was 369. After the completion of data collection, a comprehensive analysis was conducted using SPSS and R language, which unveiled noteworthy patterns, trends, and possible improvements for the e-government services.

The aforementioned methodical approach underscores our commitment to conducting a thorough assessment of the efficacy of e-government services in the higher education sector of KRI by means of methodical data collection and analysis.

#### B. Reliability Test

Cronbach’s alpha can be used to measure internal consistency, and its purpose adorns itself as the extent of the internality of Consistency tested among a set of items (Bonett and Wright, 2015). It is an index of reliability as well as consistency of scale measurements. This coefficient is ascertainable geometrically by the number of the items of the test and their mean inter-correlation. The general and standardized formula to calculate Cronbach’s alpha is shown in Equation (1).

$$\alpha = \frac{N * \bar{c}}{\bar{v} + (N - 1) * \bar{c}} \quad (1)$$

#### C. Confirmatory Factor Analysis (CFA) - Construct Validity

CFA is a statistical method that verifies the validity of a hypothesized factor structure in SEM, analyzing the relationships between observed variables based on a theoretical model. It is mainly used in social science, psychology, and education when scientists investigate an underlying structure about a set of observed variables. This statistical test has been declared to be done in various fields (Brown, 2015).

#### D. Basic Concepts

##### Latent variables

Latent variables are unobservable constructs or factors that are hypothesized to underlie the observed variables. In CFA, we assume that there are latent variables that influence the observed variables.

##### Observed variables

These are the measurable variables that are directly observed or measured in a study.

##### Factor loadings

Factor loadings represent the strength and direction of the relationship between a latent variable and an observed variable. Denoted as  $\lambda$  (lambda), the formula for the relationship between the latent variable (F) and the observed variable (X) is:

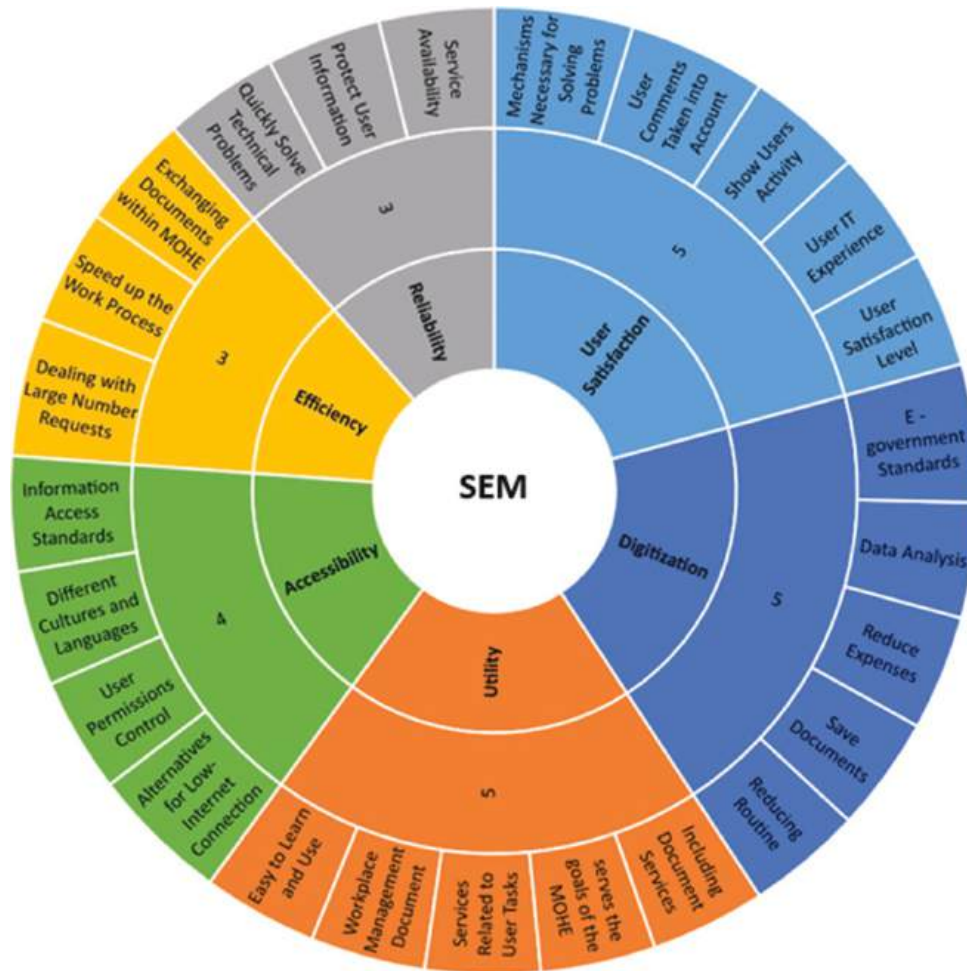


Fig. 1. Strategic Enterprise Management (SEM) model organized into several key domains: The sixS's of service dominant logic are Efficiency, Accessibility, Reliability, User Satisfaction, Utility and Digitization. Each domain is broken down into detailed goals and tasks, showing this broad and extensive system applied to the enhancement of the extent and quality of services as well as the satisfaction of the end-user within an organization.

$$X_i = \lambda_i * F + \epsilon \tag{2}$$

Where

- $X_i$ : Observed variable i
- $\lambda_i$ : Factor loading for observed variable i
- $F$ : Latent factor
- $\epsilon$ : Error term for observed variable i

Where:

- $Y$ : The dependent variable.
- $X_1, X_2, X_3, \dots, X_n$ : The independent variables.
- $\beta_0, \beta_1, \beta_2, \dots, \beta_n$ : the regression coefficients, representing the change in  $Y$  for a one-unit change in each independent variable, holding all other variables constant.
- $\epsilon$  is the error term, representing the difference between the observed and predicted values of  $Y$ .

This equation allows us to estimate the value of the dependent variable  $Y$  based on the values of the independent variables  $X_1, X_2, X_3, \dots, X_n$ , with each independent variable contributing to the prediction of  $Y$  to some extent.

Multiple regression analysis is a powerful tool for understanding the relationships between multiple variables and predicting outcomes based on those relationships.

### V. REGRESSION MODELING ANALYSIS

Multiple regression analysis extends ordinary least squares linear regression to predict the value of a dependent variable using two or more independent variables. While simple linear regression involves predicting the dependent variable from just one independent variable, multiple regression allows for more complex relationships to be modeled. In multiple regression, the relationship between the dependent variable and each independent variable is considered simultaneously (Cohen, et al., 2013).

The multiple regression equation is represented as follows:

$$Y = \beta_0 + \beta_1 X_1 + \beta_2 X_2 + \dots + \beta_n X_n + \epsilon \tag{3}$$

### VI. STATISTICAL RESULTS

#### A. Descriptive Statistics

Before diving into the statistical tests, it was essential to provide a brief description of some of the respondent's

demographics. The findings regarding the respondent's gender reveal a notable gender distribution within the study. With 63.86% of respondents identifying as female and 36.14% as male, it suggests a higher participation rate among females in the evaluation of document management satisfaction in e-government services within the Ministry of Higher Education as seen in (Fig. 2a).

Moreover, the majority of responses are between the ages of 36–45 (48.10%) and 25–35 (30.98%), indicating a strong representation of people in their prime working years. While, less percentage of users were found within the age group (46–55) and above 55 years old with 16.85% and 4.08%, respectively as provided in (Fig. 2b).

The education background of respondents reveals that the majority (64.40%) hold undergraduate degrees, followed by post-graduate qualifications (30.16%). A lesser proportion (4.89%) claimed to possess a high school diploma, while only 0.54% fell into the “others” group. This distribution implies that people involved in rating document management satisfaction in e-government services within the Ministry of Higher Education are more likely to have higher education qualifications. Understanding respondents' educational backgrounds is critical for developing communication and training materials that enable effective engagement and understanding across the ministry's various educational levels which is shown in (Fig. 2c).

In addition to the above demographical variables, other information was also necessary to understand how the system can be improved based on their responses on the technical part. Participant's occupation was recorded and based on (Fig. 3a), the majority of responders (68.48%) work as administrative personnel, followed by academic staff (28.53%). A small minority of respondents identified as visitors (0.82%), with 2.17% falling into the category of “others.”

In (Fig. 3b), the breakdown of specialists' areas of work as users of the platform reveal that the majority (48.10%) come from science backgrounds, followed closely by those from social backgrounds (43.21%). A smaller percentage (8.70%) indicated that they do not have a specialized area. Understanding the distribution of specialists' areas of work helps in tailoring platform features and functionalities to cater to the specific needs and preferences of users from different disciplinary backgrounds within the Ministry of Higher Education.

The breakdown of respondents' computer skill levels shows that the majority (55.86%) had a medium level of proficiency, with 39.51% having an advanced level. A lesser percentage (4.63%) falls within the primary skill level as illustrated in (Fig. 3c). This distribution indicates a predominantly capable user population, with a significant number of advanced abilities, which is critical for

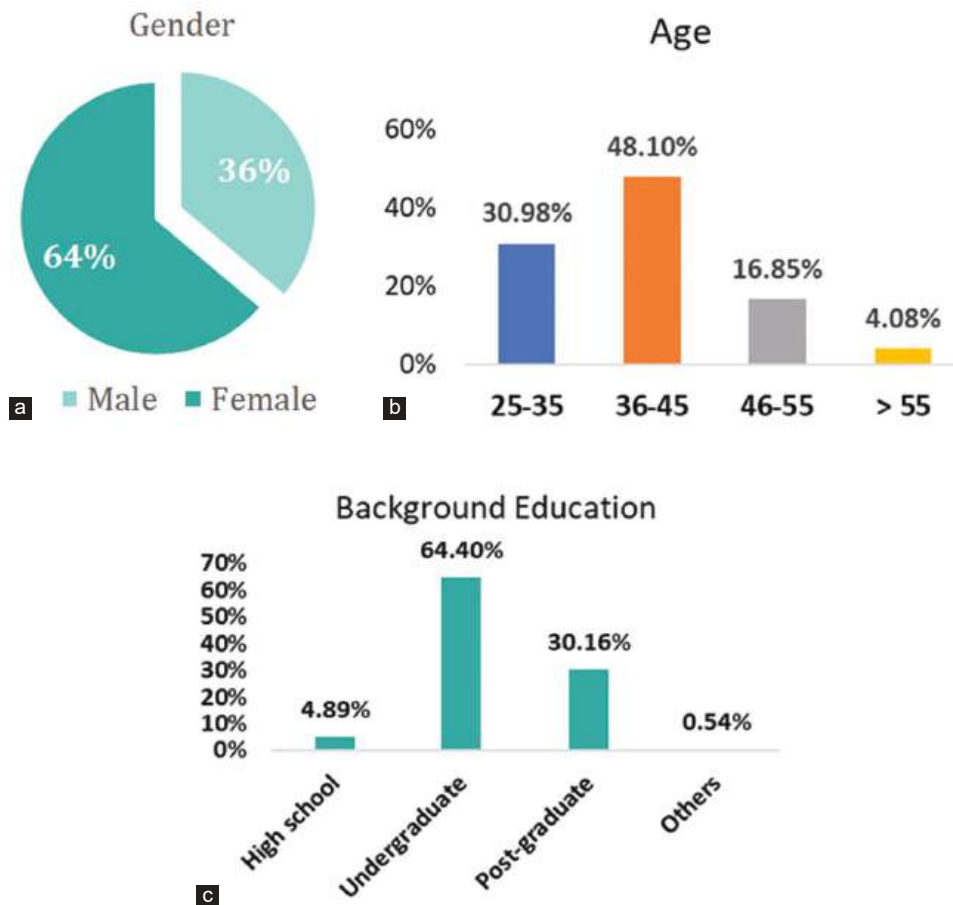


Fig. 2. (a) Pie-Chart illustration of participant's gender, (b) Age distribution bar-chart of the respondents and (c) Background Education bar-chart demonstration.

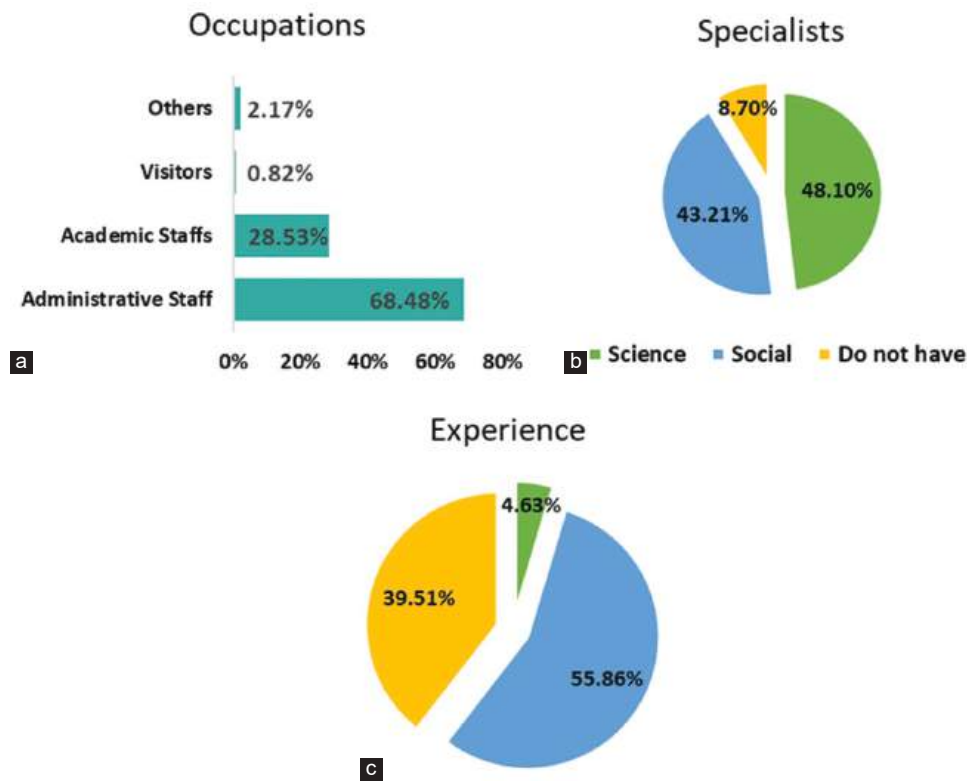


Fig. 3. (a) Pie-chart illustration of participant’s occupation, (b) Specialist’s distribution bar-chart of the respondents and (c) Experience bar-chart demonstration.

properly employing the platform for evaluating document management satisfaction in e-government services within the Ministry of Higher Education. Understanding skill levels allows you to adapt training and support materials to match the various needs of users with varying levels of proficiency.

### VII. SEM RESULTS

Six latent factors were studied to evaluate the platform from the view of the users and they were digitalization, utility, efficiency, reliability, user satisfaction, and accessibility. As part of implementing the construct validity which demonstrates the relationships between the latent factor and observed variables, regression modeling was also built to present how user satisfaction and reliability of the system are affected by other factors separately.

Cronbach’s alpha revealed good results across all aspects of the scale as provided in Table I. Reliability had the lowest score (0.751), while utility recorded the greatest consistency across the observed variables on this latent factor with a value of 0.849 as shown in Table I. Furthermore, the mean values of all latent factors indicated above are acceptable and all contributed to leveling up the performance of the system.

The corrected item-total correlations in the six-factor model showed values of 0.585–0.695 for Digitalization, 0.607–0.681 for Utility, 0.537–0.607 for Reliability factor, 0.650–0.713 for Efficiency, 0.556–0.700 for User Satisfaction and 0.606–0.657 for Accessibility as shown

TABLE I  
CRONBACH’S ALPHA OUTCOMES

Scale	Mean	SD	Cronbach’s alpha
Digitalization	3.9319	0.756	0.827
Utility	4.0556	0.7195	0.849
Reliability	3.6883	0.8181	0.751
Efficiency	3.9982	0.7888	0.827
User satisfaction	3.7204	0.7878	0.839
Accessibility	3.6901	0.8039	0.811
Total	3.876	0.7795	0.956

in Table II. Importantly, none of the items showed correlations <0.3 on either observed variables with their latent factors. Despite these findings, deleting any item did not increase Cronbach’s alpha which means that all observed variables measured, had significant contributions with their related latent factors, hence, demonstrating the relevance of each question in sustaining the scale’s integrity.

In terms of factor loading values, they denote the strength of the association between a latent factor and its indicators while considering the scale of measurement. Values closer to 1 imply a stronger correlation between the latent factor and the observed variable, with larger values indicating that the observed variable serves as a reliable indicator of the latent factor where all values were greater than the cut-off value of 0.3. In addition, all items for all six latent factors were statistically significant ( $p < 0.05$ ), signifying a substantial relationship between the latent factor and each observed variable. However, the R-square values for the

TABLE II  
FACTOR LOADING, CORRECTED ITEM-TOTAL CORRELATION, CRONBACH'S ALPHA IF ITEM DELETED, AND R-SQUARE RESULTS

Scales	Items	Factor loading (SE)	Corrected item-total correlation	Cronbach's alpha if the item deleted	p-value	R-square
Digitalization	D1	0.548 (0.020)	0.698	0.772	0.000	0.566
	D2	0.511 (0.024)	0.585	0.803	0.000	0.464
	D3	0.536 (0.033)	0.596	0.803	0.000	0.408
	D4	0.523 (0.023)	0.605	0.798	0.000	0.492
	D5	0.557 (0.022)	0.640	0.788	0.000	0.541
Utility	U1	0.461 (0.022)	0.607	0.831	0.000	0.432
	U2	0.536 (0.019)	0.677	0.813	0.000	0.55
	U3	0.514 (0.018)	0.681	0.812	0.000	0.551
	U4	0.565 (0.021)	0.662	0.817	0.000	0.56
	U5	0.539 (0.019)	0.665	0.816	0.000	0.559
Reliability	R1	0.563 (0.026)	0.607	0.638	0.000	0.516
	R2	0.561 (0.025)	0.605	0.643	0.000	0.535
	R3	0.626 (0.036)	0.537	0.729	0.000	0.535
Efficiency	E1	0.603 (0.022)	0.691	0.755	0.000	0.605
	E2	0.649 (0.023)	0.713	0.732	0.000	0.634
	E3	0.603 (0.022)	0.650	0.795	0.000	0.607
User satisfaction	US1	0.602 (0.021)	0.691	0.792	0.000	0.596
	US2	0.691 (0.026)	0.685	0.794	0.000	0.618
	US3	0.652 (0.026)	0.700	0.789	0.000	0.575
	US4	0.424 (0.026)	0.556	0.828	0.000	0.344
	US5	0.462 (0.021)	0.586	0.821	0.000	0.444
Accessibility	A1	0.553 (0.021)	0.636	0.762	0.000	0.565
	A2	0.609 (0.031)	0.657	0.750	0.000	0.508
	A3	0.607 (0.034)	0.630	0.765	0.000	0.473
	A4	0.542 (0.022)	0.606	0.775	0.000	0.538

observed variables were relatively modest, ideally falling within the range of 0.60–0.90, indicating that the latent factors effectively explained the variability in the observed variables.

In addition to the SEM findings, the CFA conducted on the hypothesized constructed questionnaire involving all six factors and demonstrated a satisfactory fit with the data ( $n = 368$ ):  $\chi^2 = 618.69$  (260),  $p < 0.001$ ; Comparative fit index (CFI) = 0.932; Tucker-Lewis index (TLI) = 0.921; root mean square error of approximation (RMSEA) = 0.061. In addition, it is advisable to achieve a CFI above 0.90 which was the case. Fortunately, both root mean square of residuals (RMSR) and RMSEA values were below 0.08, suggesting an acceptable fit to support the CFI.

As shown in Table III, all six latent factors showed a significant effect in evaluating the ERP system by the respondents, and it was important to measure the reliability and user satisfaction factors. Referencing the multiple regression model shown in Table IV, it can be noticed that all four latent factors were statistically significant in improving the system's reliability as well as satisfaction by the users and the variability of reliability was measured with 45.40% was due to the collective effect of digitalization, utility, efficiency, and accessibility, whereas these factors had an impact by 56.30% on user satisfaction. These findings suggested that one can pay attention to these factors to improve or increase the reliability and user satisfaction level. The values of R-square which were not very high indicate a good sign of not suffering from overfitting and can lead us to an accurate and reliable conclusion in reference to the independent's influences.

TABLE III  
CONSTRUCT VALIDITY RESULTS

Scales	X2	df	P	CFI	TLI	RMSR	RMSEA
Six factors model	618.69	260	<0.001	0.932	0.921	0.042	0.061

CFI: Comparative fit index, TLI: Tucker-lewis index, RMSR: Root mean square of residuals, RMSEA: Root mean square error of approximation

TABLE IV  
MULTIPLE REGRESSION MODELING ANALYSIS FINDINGS

Dependent	Independents	Unstandardized coefficients		p-value	Adjusted R-square	VIF
		B	SE			
		Reliability	(Constant)			
	Digitalization	0.194	0.066	0.003		2.006
	Utility	0.250	0.071	0.001		2.382
	Efficiency	0.267	0.059	0.000		2.237
	Accessibility	0.181	0.056	0.001		1.777
User satisfaction	(Constant)	0.137	0.174	0.030	56.30%	-
	Digitalization	0.166	0.055	0.002		2.006
	Utility	0.194	0.059	0.001		2.382
	Efficiency	0.156	0.049	0.001		2.237
	Accessibility	0.397	0.046	0.000		1.777

## VIII. DISCUSSION

This study used the EGOVSAT to assess the effectiveness of e-government document management systems at the Ministry of Higher Education in Iraq's Kurdistan Region. It utilizes a six-factor model that includes digitalization, utility, reliability, efficiency, user satisfaction, and accessibility. Utilizing SEM and regression analyses has provided valuable understanding regarding the factors



that improve user satisfaction and the dependability of the system.

The SEM analysis revealed that accessibility and user satisfaction play a significant role in the success of e-government services. This implies that, despite advances in digital infrastructure, the ease of access and extent to which these services meet user needs remain critical to their effectiveness. Furthermore, the study identifies digitization and efficiency as critical drivers of operational excellence, implying that continued efforts to improve these areas could result in significant improvements in service delivery.

The regression analysis confirms the impact of the aforementioned factors, demonstrating that digitalization, utility, efficiency, and accessibility all account for significant differences in reliability and user satisfaction. This demonstrates the interconnected nature of these factors, with improvements in one area potentially improving others, ultimately leading to better user experiences and service reliability.

Importantly, although the result is based on a moderate Cronbach's Alpha score of 0.695, which indicates sufficient reliability without significant multicollinearity among variables, it also confirms the independence of predictors in the regression model (Hassan, et al., 2021). Moreover, the proposed dimensions and the proposed dimensions in the EGOVSAT explained 53.2% of the variation in citizens' satisfaction with e-government services (Nawafleh, 2021). Accessibility, information, security, reliability, trust, and perceived ease of use all have a positive impact on service quality and customer satisfaction (AL-Kaabi, 2023). In addition, improvements to the electronic government service delivery system increase user satisfaction by positively influencing perceptions of ease of use and usefulness, as validated by SEM (Sachan, et al., 2018). However, our results show that the study is highly reliable (Cronbach's Alpha = 0.956), users are satisfied (56.30%), and the model fits well (CFI = 0.932; TLI = 0.921; RMSEA = 0.061). This shows that the research was done correctly, and the results may be useful in other places where e-government programs are being used, not just the Kurdistan Region.

This study makes a significant contribution to the e-government literature by identifying the critical factors influencing user satisfaction and system reliability. The findings advocate for a balanced approach that takes into account both technical infrastructure and user experience, and they provide a road map for policymakers looking to improve e-government service delivery. Future research could delve deeper into the dynamic interactions between these factors, as well as test the model in a variety of contexts, to broaden the findings.

## IX. CONCLUSION

This study evaluates e-government services provided by the Ministry of Higher Education of KRI using the EGOVSAT and a "six-factor" framework, emphasizing the significance of accessibility, utility, reliability, efficiency, digitization, and

user satisfaction. By analyzing user responses with SEM, we find that accessibility and user satisfaction are critical to the success of e-government, whereas operational efficiency is significantly impacted by digitization and efficiency and there was a significant relationship between latent factors and observed variables where all factor loading values were statistically significant. Our research findings suggest that continuous improvements are necessary to align with changing user demands, even in the face of progress in service digitization and accessibility, and the SEM of all six factors, demonstrated a satisfactory fit with the data ( $n = 368$ ):  $\chi^2 = 618.69$  (260),  $p < 0.001$ ; CFI = 0.932; TLI = 0.921; RMSEA = 0.061. Fortunately, both RMSR and RMSEA values were below 0.08, suggesting an acceptable fit to support the CFI. The application of the EGOVSAT offers profound insights into user requirements in KRI and promotes a well-rounded approach that takes into account user experience and technical infrastructure. In addition, we also reached a conclusion that both reliability and user satisfaction were significantly affected by other latent factors with R-square 45.40% and 56.30%, respectively. Furthermore, a comprehensive examination reaffirms that the six latent factors have a substantial effect on service dependability and user satisfaction. This study adds to the body of e-government literature by providing specific insights into the context of KRI. It also acts as a starting point for future research by advocating for an approach to e-government service provision that is user-centric, effective, and inclusive.

## REFERENCES

- Ahmed, A.M., Hassan, B., Saeed, S., and Saeed, A.A. 2016. Evaluating e-Government services in Kurdistan institution for strategic studies and scientific research using the EGOVSAT model. *Journal of Applied Research*, 1(2), pp.1-7.
- AL-Kaabi, R. 2023. The impact of e-government services on customer satisfaction in the private sector: A case study of the Kingdom of Bahrain (SIJILAT) an online commercial registration. *The Electronic Journal of Information Systems in Developing Countries*, 89(6), p.e12275.
- Al-Musawi, M.M. 2020. Transforming One-stop E-services in Iraq: Focusing on Perception of Blockchain Technology in Digital Identity System. In: *IEEE Global Humanitarian Technology Conference (GHTC)*. IEEE, pp.1-4.
- Al-Taie, M.Z., and Kadry, S. 2013. E-government: Latest trend and future perspective the Iraq case. *European Journal of Scientific Research*, 99(2), pp.307-323.
- Bonett, D.G., and Wright, T.A. 2015. Cronbach's alpha reliability: Interval estimation, hypothesis testing, and sample size planning. *Journal of Organizational Behavior*, 36(1), pp.3-15.
- Brown, T.A. 2015. *Confirmatory Factor Analysis for Applied Research*. Guilford Publications, New York.
- Cohen, J., Cohen, P., West, S.G., and Aiken, L.S. 2013. *Applied Multiple Regression/Correlation Analysis for the Behavioral Sciences*. Routledge, United Kingdom.
- Di Giulio, M., and Vecchi, G. 2023. Implementing digitalization in the public sector. Technologies, agency, and governance. *Public Policy and Administration*, 38(2), pp.133-158.
- Doski, S. 2015. Implementation of E-government in Kurdistan Regional Government (KRG): Political, Social and Economic Constraints. In:

- European Conference on Digital Government*. UK: Academic Conferences International Ltd, p.386.
- Dunayev, I., Byelova, L., Kud, A., and Rodchenko, V. 2023. Implementing the “government as a platform” concept: The assessment method and an optimal human-centered structure to address technological challenges. *Eastern-European Journal of Enterprise Technologies*, 122(13), pp.6-16.
- Hassan, B.A., Ahmed, A.M., Saeed, S.A., and Saeed A.A., 2021. *Evaluating E-government Services in Kurdistan Institution for Strategic Studies and Scientific Research Using the EGOVSAT Model*. [arXiv preprint] arXiv:2105.02697.
- Heeks, R. 2006. Understanding and Measuring eGovernment: International benchmarking Studies. In: *UNDESA Workshop “E-participation and E-government: Understanding the Present and Creating the Future”*. Budapest, Hungary, pp.27-28.
- Lee, B.K., Lee, E.H., and Lee, T. 2023. The effect of E-Government website evaluation on user satisfaction and intention to use: The mediating role of warmth and competence judgment on government. *Information Communication and Society*, 26(9), pp.1868-1889.
- Maksimova, M., Solvak, M., and Krimmer, R. 2021. Data-driven Personalized E-Government Services: Literature Review and Case Study. In: *International Conference on Electronic Participation*. Springer International Publishing, Cham, pp.151-165.
- Moon, M.J. 2002. The evolution of E-government among municipalities: Rhetoric or reality? *Public Administration Review*, 62(4), pp.424-433.
- Muhammad, A.S., and Kaya, T. 2023. Factors affecting the citizen’s intention to adopt E-government in Nigeria. *Journal of Information Communication and Ethics in Society*, 21(3), pp.271-289.
- Muttaqin, M.H., and Susanto, T.D. 2019. The Effect of Website Components on User Trust in Increasing the Interest to Use Public Administration Service on E-government Website. In: *2019 International Conference on Computer Science, Information Technology and Electrical Engineering (ICOMITEE)*. IEEE, pp.30-36.
- Nawafleh, S. 2021. E-government and citizen satisfaction in Jordan: EGOVSAT testing using SEM approach. *International Journal of Productivity and Quality Management*, 34(1), pp.20-32.
- Nawafleh, S., and Fares, A.M.S. 2024. UTAUT and determinant factors for adopting E-government in Jordan using a structural equation modelling approach. *Electronic Government an International Journal*, 20(1), pp.20-46.
- Ølnes, S., and Jansen A. 2017. Blockchain Technology as a Support Infrastructure in E-Government. In: *Electronic Government: 16<sup>th</sup> IFIP WG 8.5 International Conference Proceedings, EGOV 2017*. Springer International Publishing, St. Petersburg, Russia, pp.215-227.
- Othman, A., Al Mutawaa, A., Al Tamimi, A., and Al Mansouri, M. 2023. Assessing the readiness of government and semi-Government institutions in Qatar for inclusive and sustainable ICT accessibility: Introducing the MARSAD Tool. *Sustainability*, 15(4), p.3853.
- Sachan, A., Kumar, R., and Kumar, R. 2018. Examining the impact of E-government service process on user satisfaction. *Journal of Global Operations and Strategic Sourcing*, 11(3), pp.321-336.
- Yahia, H., and Miran, A. 2022. Evaluating the electronic government implementation in the Kurdistan region of Iraq from citizens’ perspective. *Humanities Journal of University of Zakho*, 10(2), pp.594-601.

# Transmission Power Reduction Based on an Enhanced Particle Swarm Optimization Algorithm in Wireless Sensor Network for Internet of Things

Moneer A. Lilo<sup>1</sup>, Abidulkarim K. Yasari<sup>1</sup>, Mustafa M. Hamdi<sup>2†</sup>, Abdulkareem D. Abbas<sup>3</sup>

<sup>1</sup>Department of Electronic and Communication Engineering, College of Engineering, Al-Muthanna University, Al-Muthanna, Iraq

<sup>2</sup>Department of Computer Science, College of Computer Science and IT, University of Anbar, Al-Anbar, Iraq

<sup>3</sup>Department of Computer Engineering Techniques, Al-Maarif University College, Al-Anbar, Iraq

**Abstract**—A wireless sensor network (WSN) consists of several sensor nodes; all these nodes can sense physical events, including light, heat, and pressure. These networks are essential in smart homes, smart agriculture, and smart water management, swelling with the concept of the Internet of Things. However, WSN needs to address the challenges of energy issues; thus, energy-conserving techniques have been pursued for communication. Optimization of energy is normally solved using the Particle Swarm Optimization (PSO) algorithm since it offers high accuracy but is prone to local optima, thus resulting in early convergence. To tackle this challenge, this paper proposes the development of an enhanced particle swarm optimization for the node power estimation (EPSO-NPE) model. EPSO-NPE calculates distinct transmission powers for each node, preventing the formation of isolated areas within a sensor cluster. Unlike the original PSO, the EPSO algorithm enhances exploration capabilities by avoiding stagnation on search space boundaries. A comparative analysis with the original PSO-based model (PSO-NPE), where nodes adopt maximum power for connectivity, reveals superior performance by EPSO-NPE. The enhanced model exhibits heightened energy-saving capabilities, ultimately extending the network's lifetime.

**Index Terms**—IoT, Power estimation, PSO, Transmission power reduction, WSN.

## I. INTRODUCTION

Nowadays, the Internet of Things (IoT) is one of the extensive areas that allow data collection and sharing, and it is rapidly engaging our daily life (Abdalkafor and

Aliesawi, 2022) (Gardašević et al., 2020). Mainly, the advanced technologies involving smart sensors, advanced communication technologies, and internet protocols are the critical elements of enabling IoT (Mohammed et al., 2024; Haseeb et al., 2020; Al-Rami and Alheeti, 2022). The number of connected devices to the IoT environment is growing (Al Zakitat et al., 2023; Abdaljabar, Ucan and Alheeti, 2021). It depicts a vast global network of thousands of physical machine devices around the world connected to the internet, collecting and sharing data and interacting with each other (Abdul-Qawy, Almurisi and Tadisetty, 2020). Thus, it has a significant impact on several sectors such as medical, industries, agriculture, home automation, and smart cities environments (Tao et al., 2024; Rani et al., 2020; Nafea et al., 2024). Furthermore, the establishment of IoT-based mesh networks and sensor nodes is dramatically increased, which is the issue that inherits the problem of energy constraints depicted by the transmission power of the network's nodes (Wasmi et al., 2021; Hamdi, Rashid and Nafea, 2024). Thus, network clustering and beamforming have been used to avoid inefficient transmission power (Heinzelman and Younis, 2000; Khediri et al., 2021; Ismael et al., 2023). However, the evolution of the IoT leads to remain this field an open area for more required correlated research.

Consequently, the power supply charge powers the three distinct subsystems: the sensor unit, the central processing unit, and the communication unit (Abdelaal and Theel, 2014; Haseeb et al., 2020). On another side, the mitigation of wasting power of a particular sensor node can be accomplished by several wireless node events such as packet overhead, overhearing, collisions, idle listening, and state transitions. This research aims to continuously link each of all of the nodes that are sensors in one cluster without triggering any state changes by the ideal amount of transmission power for each node in the network. At this time, we will not consider the other instances of energy waste. While switching between states would use up some of the battery

ARO-The Scientific Journal of Koya University  
Vol. XII, No. 2 (2024), Article ID: ARO.11554. 9 pages  
DOI: 10.14500/aro.11554

Received: 25 February 2024; Accepted: 27 July 2024

Regular research paper: Published: 18 August 2024

†Corresponding author's e-mail: mustafa.maad.hamdi@uoanbar.edu.iq

Copyright © 2024 Moneer A. Lilo, Abidulkarim K. Yasari, Mustafa M. Hamdi, and Abdulkareem D. Abbas. This is an open-access article distributed under the Creative Commons Attribution License (CC BY-NC-SA 4.0).



life of the sensor, it could also be a way to conserve power. To save energy, the nodes can enter a sleep state and disable most of their functions (Mendes, Rodrigues and Chen, 2010; Del-Valle-Soto et al., 2020). The focus of this research is on network connectivity, therefore various node statuses will not be handled. The next step for stationary sensors is to gain network connectivity, subsequently, the goal of the network may change to a different mode.

Despite, calculating the least power level for each node placed on the network edge to connect its closer neighboring, or a group of nodes to reach the edges, in the case of the intermediate nodes, would be the ideal solution to detect the minimum required power to connect every wireless sensor network (WSN) node. As the node number in the cluster increased, finding out the closest neighboring nodes while maintaining the entire network connection would cause an elevation in computational overhead. For that, a sub-ideal solution, with a minimal computing-intensive might be utilized.

The particle swarm algorithm (PSO) algorithm is the most popular swarm-based algorithm used by several studies of WSN and energy estimation (Sun et al., 2020). This algorithm was proposed by Eberhart and Kennedy (1995) to cope with the non-linear functions with optimization issues. The PSO algorithm has become a widespread technique utilized to solve optimization issues in WSNs because of its simplicity and ability to provide high-quality solutions and fast convergence (Kulkarni and Venayagamoorthy, 2010; Ling et al., 2020). Thereafter, utilizing a PSO for power estimation is one of the potential solutions. However, the PSO algorithm is easy to dive into local optima, Thus, the model would neglect to get the correct results and bring about premature convergence. Consequently, this study sheds light on this issue and proposes an enhanced particle swarm optimization (PSO) for node power estimation named EPSO-NPE. This algorithm avoids the local optima problem to some extent by avoiding the stuck on the boundaries that occur in the original PSO and at the same time, it is supposed to enhance the exploration and exploitation procedure of the algorithm. The rest of the paper is structured as follows; Section 2 provides a literature review related to the proposed system and related methods and technologies. Therefore, Section 3 depicts the methodology of this study, while sections 4 provide the results of the taken experiments. Finally, Sections 5 and 6 provide discussion and conclusion, respectively.

## II. LITERATURE REVIEW

### A. WSN Clustering and Energy Consumption

Recently, WSNs have obtained the researcher's attention in many disciplines (Afsar and Tayarani-N, 2014) (Mohapatra et al., 2020). WSNs have originated as a new robust paradigm that can be utilized in lots of applications for generating various types of parameter reports, such as pressure, temperature, light, chemical activity, and humidity (Tyagi and Kumar, 2013; Khalifeh et al., 2021). Therefore, the WSN system can be assessed based on several

parameters including, (i) the lifetime of a network, in which every network node has to be designed to control the local energy supply to get the maximum limit of network lifetime. (ii) Network Coverage, in which network nodes must be effectively distributed in all monitored areas to hit the coverage standards. (iii) Scalability in which it is supposed that any potential addition of new nodes to the network in the future must not cause any change in the network performance. (iv) Response time, in which the WSNs should respond to alarm-oriented risk situations like fire detection timely and quickly, and (v) Security, which is considered as one of the crucial measures of the WSNs, especially if the WSN is designed for security-oriented purposes (Mahajan and Dhiman, 2016; Mohapatra et al., 2020).

Therefore, to enhance the effectiveness of WSNs and increase network lifetime, energy efficiency, and scalability, as well as decrease routing delay, clustering is applied to WSNs (Afsar and Tayarani-N, 2014; Mahajan and Dhiman, 2016; Mohapatra et al., 2020). Clustering refers to dividing the network nodes into sets based on particular mechanisms (Afsar and Tayarani-N, 2014) (Mohapatra et al., 2020). In clustering, a group of nodes composed the clusters, some nodes are chosen to be cluster-heads and other nodes are called regular nodes. The cluster head (CH) receives data from regular nodes. Then, CH collects data and transmits them to the base station (Afsar and Tayarani-N, 2014; Ilyas et al., 2020). As clusters in WSN aid in data aggregation, this could assist in decreasing the energy consumption and transmission overhead (Mohapatra et al., 2020), Fig. 1 shows the flow of data in a networked cluster.

On another side, there are some design challenges associated with WSN clustering, include (i) Storage, in which sensors have storage limitations that can lead to some constraints on satisfying the query and storage requirement. (ii) Security, in which WSNs may incur too many threats and security issues that lead to the need to provide security protocols and measures. (iii) Communication, which should cover the entire WSNs area to maximize reliability and also enhance network coverage. (iv) Limited Energy, which is one of the most crucial challenges, where the energy forms a constraint to the sensor networks. Thus, decreasing the consumption of energy is one of the critical clustering

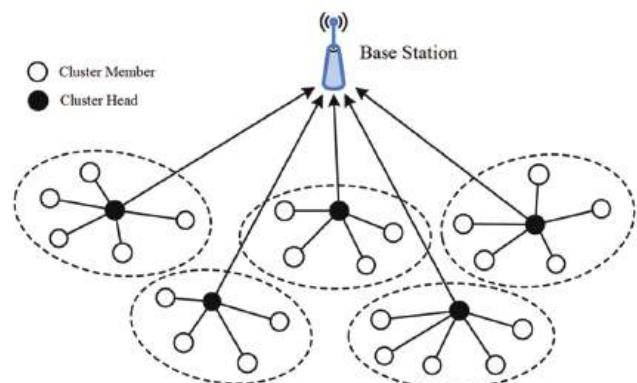


Fig. 1. Network Architecture of Clustered WSNs (Gui, Zhou and Xiong, 2016).

issues. (iv) Network Lifetime, in which one of the clustering design concerns is represented in the possible limitations of a network lifetime, while the sensor node is a low amount of energy. (vi) Quality of service (QoS), whereby quality is an important issue regarding clustering. Occasionally, clustering concentrates on energy efficiency rather than quality which can cause some clustering obstacles (Vyas and Chouhan, 2014; Mohapatra et al., 2020; Khediri et al., 2021).

Consequently, based on the aforementioned challenges, energy efficiency represents an important measure of WSNs' effectiveness. Hence, researchers proposed numerous protocols and approaches that may help in enhancing the energy consumption in clustering WSNs. Sensors can be split into several small sets named clusters to support the aggregation of data through an efficient network organization (Younis, Krunz and Ramasubramanian, 2006; Mohapatra et al., 2020). Thus, it would cause reliability enhancement, decrease the network communication overhead, and lead to considerable savings in energy. On another side, some Authors utilized clustering to select a group of network nodes. They institute an effective topology for prolonging the lifetime improve energy saving of battery-powered WSNs (Abd Aziz et al., 2012; Khediri et al., 2021).

### B. PSO

PSO is an optimization algorithm inspired biologically by birds' social behavior or fishes' swarms and their ability to exploit or explore a d-dimensional search area for shelter or food (Jain and Sharma, 2013; Rao, Jana and Banka, 2017; Freitas, Lopes and Morgado-Dias, 2020). In a d-dimensional area, the PSO algorithm finds the optimal solution for a specific issue by utilizing an iterative operation (Kaur and Kumar, 2018; Freitas, Lopes and Morgado-Dias, 2020). In PSO, the swarm is formed of a group of individual particles. Each particle in the swarm owns a specific fitness measured by the fitness function. The particle is (flown) over the d-dimensional search area (Rini, Shamsuddin and Yuhaniz, 2011; Freitas, Lopes and Morgado-Dias, 2020). The particles interact with each other, constituting a particular social behavior. The particles are estimated regarding their fitness function, and then their speeds and positions are updated in every step of the PSO algorithm. Each particle's role and rate are updated based on its experience and the neighboring particles. The superior work might be the minimum or maximum values. The updates of particles depend on the tracking of two extreme values. The first one is the best (optimal) solution of the (individual extremum pbest) particles. The second is the best (optimal) solution for the whole population, called the (global extremum gbest). Therefore, several parameters control the searching behavior of the PSO algorithm including (i) coefficient of inertia weight  $w$ , which controls the algorithm's tendency to expand search space and explore new areas within it. (ii) accelerate constants  $c_1$  and  $c_2$ , in which it functions as the weight of accelerating statistically when each particle is forwarded to the position of pbest and gbest, (iii) and  $r_1$  and  $r_2$ , which are random numbers between  $[0,1]$ . In the original PSO

algorithm, the updating equations of the particle's velocity and position are as follows:

$$v_i^{t+1} = w^t v_i^t + c_1 r_1^t (p_{ibest}^t - x_i^t) + c_2 r_2^t (gbest - x_i^t) \quad (1)$$

$$x_i^{(t+1)} = x_i^t + v_i^{(t+1)} \quad (2)$$

Where  $t$  represents the number of iterations,  $v_i$  represent the speed of the particle and  $x_i$  is the position of the particle.

In literature, several studies addressed some issues related to WSNs designation, such as energy constraint, limited capabilities, and bandwidth unavailability, and generally routing protocol optimization. Thus, the issue can be modeled as an optimization problem, which allows metaheuristic algorithms to be used in their solution. From a central point of view, several studies produced the PSO algorithm as an optimization solution in WSNs. Some of these studies examined the optimization algorithms such as the PSO algorithm functioning to reduce the energy consumption of WSN, enhance the convergence of WSN, and increase its lifetime. Next are some related studies that were reviewed.

A study by da Silva Fré et al., (2015) utilized PSO to calculate the nodes' transmission powers in related areas of a WSN. This work's findings indicated that the suggested PSO algorithm allowed the saving of sensors' energy significantly by at least, 1 dBm of the overall transmission power of the network compared with a simplistic method. Meanwhile, Rao, Jana, and Banka proposed an approach consisting of a combination of energy-efficient CHs selection and PSO (PSO-ECHS). This approach takes various parameters into account as the sink distance, intra-cluster distance, and sensor nodes' residual energy. The findings affirmed the suggested approach's superiority compared with the other existing approaches regarding the network lifetime and energy consumption. As they could run the algorithms by changing the sensor node number from 300 to 500, CHs number from 30 to 50, and calculated overall consumption of energy at the end of 5000 rounds.

Kaur and Kumar, (2018) have utilized the PSO-UFC protocol to handle the imbalance of inter-cluster and intra-cluster energy consumption between Master CHs. The simulation results manifested that the proposed protocol increases the lifetime of the network and enhances energy consumption. In the FND criteria, the used protocol enhanced the network lifetime by 86%, and in the HDN criteria the network lifetime was enhanced by 68%. In addition, Latiff, Tsimenidis and Sharif, (2007) proposed PSO-C as an energy-aware clustering algorithm for WSN. The proposed approach operated to select the best (k-CHs) that can reduce the cost through routing. The approach was a centralized and distance-based approach that takes into consideration the extreme distance between CH and other nodes and the residual CH candidates' energy. Nodes with adequate energy are chosen to be CHs, while nodes with an energy higher than the average are qualified to be a CCH in each round.

On the other hand, Tam et al., (2018) suggested an algorithm based on PSO and fuzzy clustering to minimize network energy consumption and decrease network disconnects. The proposed model resolved the clustering limitations of 3D WSN. Moreover, fuzzy clustering enables more easily to determine the optimal structure of clustering in 3D WSN. Meanwhile, Wang, (2020) applied PSO for optimizing the deployment of WSN nodes. The results revealed that PSO could optimize WSN layout optimally and effectively, coped with the fixed sensor nodes' impact on optimization, realized rapid convergence speed, and enhanced the efficacious WSN coverage.

Furthermore, a study by Jain and Sharma, (2013) sought to solve the coverage issues in distributed WSN. Whereby, they proposed a modified discrete binary PSO algorithm for the WSN nodes' placement to obtain the maximum coverage. The proposed algorithm fixed the coverage problem by setting a finite sensor number, optimizing the sensor's deployment, and considering the sensor deployment scheme factor. On another side, Sahoo, Amgoth and Pandey, (2020) integrated the PSO algorithm with the energy-efficient clustering and sink mobility (ECSM) technique to address the sink mobility and cluster head (CH) selection issues. This study covered the node degree, residual energy distance, and energy consumption rate (ECR) as CH selection factors. The results indicated that the PSO-ECSM enhanced the stability period and improved the network's lifetime and throughput.

### III. METHODOLOGY

#### A. The System and Network Connectivity

This research only considers scripts that have one cluster and  $N$  wireless sensors. Using the newly formed mesh network, they must transmit measurement packets to a sink node. This means that an L-sided square would contain the locations of the sinks and sensors. In addition, the subsequent calculation of the global neighbors' matrix  $\Gamma_\gamma$  is based on the transmitted power vector  $\gamma$ , as expressed in equation (3):

$$r_{ij}(\gamma) = \begin{cases} 0, & \text{if } P_j < P_{th} \\ 1, & \text{if } P_j \geq P_{th} \end{cases} \quad (3)$$

where  $P_j$  is the power which it is received at node  $j$ , when  $i$  is transmitting with a power  $\gamma_i$ , and  $P_{th}$  is representing the sensitivity of the receiver. Therefore, a connection is established between two nodes when the first node broadcasts a strong enough signal to exceed the sensitivity of the receiver. According to Fig. 2, the distance from the node is depicted by the circles at its center, and the measured power is precisely  $P_{th}$ . This indicates that its signal can be received by another node within the circle.

Moreover, according to the Friis formula, equation (4), There is a direct correlation between the received power and both the transmitted power and the physical distance between the nodes:

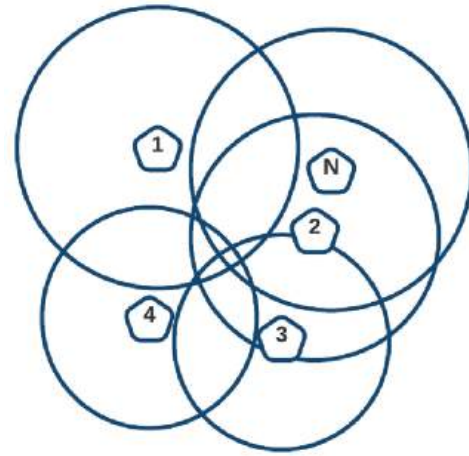


Fig. 2. Structure model.

$$\frac{P_R}{P_t} = \frac{A_r A_t}{d^2 \lambda^2} \quad (4)$$

Where,  $P_R$  stands for the received power,  $P_t$  for the transmitted power,  $d$  for the transmitting and receiving antenna's effective areas, and  $\lambda$  for the wavelength, which is acquired by dividing the light's speed  $c$  by the frequency  $f$  of the signal. The focus of this work is therefore on a power transfer optimization model rather than a particular hardware architecture of sensor nodes. Therefore, to represent the effective antenna regions, the simplest possible antenna model would be chosen. Accordingly, the following are the effective areas given by equation (5) when each sensor node is equipped with a single isotropic antenna for transmission and reception:

$$A_{isotropic} = \frac{\lambda^2}{4\pi} \quad (5)$$

And making  $A_r = A_t = A_{isotropic}$ , the power ratio (i.e., equation 4) simplifies to equation (6) as follows:

$$\frac{P_R}{P_t} = \left( \frac{\lambda}{4\pi d} \right)^2 \quad (6)$$

Furthermore, after computing the neighbors matrix using equation 3, to find out whether the network is linked or not, a method is employed. When each of the nodes in a network possesses at least one link to each other and can form a path that includes all of the nodes, we define it as a fully connected network.

Determining the fully connected condition of a particular network is harder when the number of nodes is large, but easier when a network has a smaller number of nodes or/and a smaller AoI. Whereby, in the first case, a large number of nodes linked in one network makes its management essential. When determining connectedness, the initial step is to compute the Laplacian Matrix of the neighboring matrix, which is provided by equation (7)

where  $n_i$  is the  $i^{\text{th}}$  node and  $n$  is the total number of nodes (GROSS, 2004).

$$L = (l_{ij})_{n \times n} \quad (7)$$

$$l_{ij} = \begin{cases} \text{deg}(n_i) & \text{if } i = j \\ -1 & \text{if } i \neq j \text{ and } \Gamma_{ij} = 1 \\ 0 & \text{otherwise} \end{cases} \quad (8)$$

where  $\text{deg}(n_i)$  is the number of connected nodes to the node  $n_i$ , and this value can be determined using equation (9), as shown below:

$$\text{deg}(n_i) = (r^2)_{ij} \leftrightarrow i = j \quad (9)$$

Therefore, for  $i=j$ , the number of connections to  $n_i$  is the same as the square of the neighbor matrix. Determining the eigenvalues  $\psi$  of the Laplacian matrix  $L$ , using equation (10), is the second step after calculating the Laplacian matrix. The process is as follows:

$$L.E = \psi.E \quad (10)$$

where  $E$  is an eigenvector, which is a column vector with  $n$  elements that have to be equal to and match every possible Laplacian eigenvalue  $\psi$ . The eigenvalues linked to each eigenvector are the values of  $\psi$  that satisfy equation (10) and can be set up inside a vector  $\Psi$  in the following way:

$$\Psi = [\psi_1, \psi_2, \psi_3, \dots, \psi_n]^T \quad (11)$$

with  $\psi_1 < \psi_2 < \psi_3 < \dots < \psi_n$

The fully connected requirement can only be met if the second smallest Laplacian eigenvalue  $\psi_2$ , also known in the Neighbor Matrix as the algebraic connectivity, is positive. Finally, in the neighbor matrix, there must be a positive second smallest Laplacian eigenvalue and a minimum of one connection per node to determine if a network is fully connected. Under these conditions, a fully connected cluster can be initiated using the transmission power of individual nodes (Wormald, Gross and Yellen, 2004).

### B. The EPSO-NPE Model

In this study, the EPSO-NPE model is proposed. In the original PSO algorithm, the algorithms start with the exploration task and then further for the exploitation task depending on the particle's speed. However, in the velocity and position update equation, if a particular particle exceeds the velocity or/and its position out of boundaries, the algorithm forces the particle to determine boundaries where the particle is mostly stuck on there. Thus, this behavior is considered as one of the main reasons behind the degradation in local optima of the original PSO algorithm. The node power estimation based on PSO is as Algorithm 1.

Consequently, to solve this problem and enhance the PSO, the particle involved on out of velocity bounds problem

### ALGORITHM 1: PSO-NPE

---

```

Initialize algorithm's parameters include  $c1, c2$ ; the value of inertia weight  $\omega_{min}, \omega_{max}$ , the maximum number of iterations, the population size  $Pop$  and the, lower bound  $lb$ , upper bound  $ub$ , and minimum velocity  $Vmin$ , maximum velocity  $Vmax$ .
for  $i \in \{1, 2, \dots, N\}$  do
 $x_i \leftarrow rand(lb, ub)$ 
 $v_i \leftarrow rand(Vmin, Vmax)$ 
endfor
for  $i \in \{1, 2, \dots, Pop\}$  do
 $fitness_i \leftarrow f(x_i, position_{script})$ 
 $f(pbest)_i \leftarrow fitness_i \triangleright individualfitness$ 
 $pbest_i \leftarrow x_i$ 
endfor
for  $(gbest) \leftarrow \min(f(pbest)) \triangleright globalfitness$ 
 $gbest \leftarrow pbest$ 
 $\omega \leftarrow \omega * \omega_{damp}$ 
for  $t \in \{1, 2, \dots, t_{max}\}$  do
for  $i \in \{1, 2, \dots, N\}$  do
according to Equation (1) update the speed of particle  $i$ 
for  $j \in \{1, 2, \dots, N\}$  do
if  $(v_{ij} > vMax)$ 
 $(v_{ij} \leftarrow vMax)$ 
endif
if  $(v_{ij} < vMin)$ 
 $(v_{ij} \leftarrow vMin)$ 
endif
endif
endfor
endfor
for  $i \in \{1, 2, \dots, N\}$  do
according to Equation (2) update the position of particle  $i$ 
for  $j \in \{1, 2, \dots, N\}$  do
if  $(x_{ij} > xMax)$ 
 $(x_{ij} \leftarrow xMax)$ 
endif
if  $(x_{ij} < xMin)$ 
 $(x_{ij} \leftarrow xMin)$ 
endif
endif
endfor
endfor
for  $i \in \{1, 2, \dots, N\}$  do
 $fitness_i \leftarrow f(x_i, position_{script})$ 
if  $(fitness_i < f(pbest)_i)$  then
 $f(pbest)_i \leftarrow fitness_i$ 
 $pbest_i \leftarrow x_i$ 
endif
if  $(f(pbest)_i < f(gBest))$  then
 $f(gBest) \leftarrow f(pbest)_i$ 
 $gbest \leftarrow pbest_i$ 
endif
endif
endfor
Output optimal solution by  $gbest$ .

```

---

takes a new value of velocity within the velocity range as following equation 1:

$$P_{out}^v = (v_{up} - v_{low}) \times rand(1,1) + v_{low} \quad (12)$$

Where  $v_{up}$  and  $v_{low}$  are the maximum and minimum limits of velocity.

Meanwhile, the particle involved in the position out of bounds problem is updated to a new position within the search space range as in the following equation 2:

$$P_{out}^{pos} = (pos_{up} - pos_{low}) \times rand(1,1) + pos_{low} \quad (13)$$

To implement the proposed model, the algorithm's parameters were set as follows; population size set to 30, in which each particle presents a solution for its corresponding transmission power of a node. Learning coefficients  $c1$  and  $c2$  are set at 2, and the value of inertia weight  $\omega$  and inertia weight damping ratio are set to 1 and 0.7, respectively. The maximum number of iterations is set to 100, and the population size  $Pop$  is set to 20. Finally, the lower bound  $lb$  and upper bound  $ub$  are set to  $-30$  and  $0$ , and minimum velocity  $Vmin$ , and maximum velocity  $Vmax$  are set to  $-4$  and  $4$ , respectively, as illustrated in Table I.

Therefore, the PSO algorithm according to the fitness function will decide whether all nodes are associated with the estimations of the transmission power of every node. In the event of all nodes connection, then the fitness function restores the amount of the power of the nodes. Otherwise, it restores a limitless value represented by an infinite value. The pseudocode of this technique is illustrated in Algorithm 2. The next section provides the experimental results. Moreover, the node transmitted power estimations that outcomes in the smallest amount (i.e., energy saving), is acquired from the stored  $gbest$  values.

#### IV. RESULTS AND DISCUSSION

This section provides the results of the performed experiments. The transmission power optimization was performed one by implementing the original PSO-NPE method that is illustrated in Algorithm 1, and the other one is by implementing the proposed method (i.e., EPSO-NPE) that is illustrated in Algorithm 2. Moreover, to get a robust result, the algorithms were run 10 times for each. The algorithms were tested over 15 scripts, each script includes the transmitter and receiver positions of 20 nodes, in which the area of random sensors distribution is identified to  $20 \times 20$  length of meter, and sensor sensitivity and transmission frequency are  $-60$  dbm and  $915$  MHz, respectively.

Fig. 3 illustrates the summation of the transmission power of nodes for 15 taken scripts by the PSO-NPE and EPSO-NPE methods. Generally, the graph shows that the estimated power determined by the proposed method is less than the one determined by the PSO-NPE over all 15 scripts. Moreover, it is clear that in script 8 the PSO-NPE failure to provide a solution, while the EPSO-NPE succeeded to provide a solution with approximate power  $-4.95$ dBm. This indicates that the proposed algorithm (i.e. EPSO) has a higher capability to search the search space and find a solution compared with the original PSO. On another side, it can be observed that in comparison with PSO-NPE, the use of EPSO-NPE has saved, at minimum, approximately  $1$ dBm

#### ALGORITHM 2: EPSO-NPE

Initialize algorithm's parameters include  $c1$ ,  $c2$ ;  $\omega_{min}$ ,  $\omega_{max}$ , the maximum number of iterations, the population size  $Pop$  and the, lower bound  $lb$ , upper bound  $ub$ , and minimum velocity  $Vmin$ , maximum velocity  $Vmax$ .

```

for  $I \in \{1,2,\dots,N\}$  do
 $x_i \leftarrow rand(lb, ub)$ 
 $v_i \leftarrow rand(Vmin, Vmax)$ 
endfor
for  $i \in \{1,2,\dots,Pop\}$  do
 $fitness_i \leftarrow f(x_i, position_{script})$ 
 $f(pbest)_i \leftarrow fitness_i \triangleright individualfitness$ 
 $pbest_i \leftarrow x_i$ 
endfor
for ( $gbest$ )  $\leftarrow \min f(pbest) \triangleright globalfitness$ 
 $gbest \leftarrow pbest$ 
 $gbest \leftarrow pbest$ 
 $\omega \leftarrow \omega * \omega_{damp}$ 
for  $t \in \{1,2,\dots,t_{max}\}$  do
for  $i \in \{1,2,\dots,N\}$  do
according to Equation (1) update speed of particle  $i$ 
for  $j \in \{1,2,\dots,N\}$  do
if ( $v_{ij} > vMax$ ) or ( $v_{ij} < vMin$ )
according to Equation (12) update speed of particle  $i$ 
endif
endif
endif
for  $i \in \{1,2,\dots,N\}$  do
according to Equation (2) update the position of particle  $i$ 
for  $j \in \{1,2,\dots,N\}$  do
if ( $x_{ij} > xMax$ ) or ( $x_{ij} < xMin$ )
according to Equation (13) update speed of particle  $i$ 
endif
endif
endif
for  $i \in \{1,2,\dots,N\}$  do
 $fitness_i \leftarrow f(x_i, position_{script})$ 
if ( $fitness_i < f(pbest)_i$ ) then
 $f(pbest)_i \leftarrow fitness_i$ 
 $pbest_i \leftarrow x_i$ 
endif
if ( $f(pbest)_i < f(gBest)$ ) then
 $f(gbest) \leftarrow f(pbest)_i$ 
 $gbest \leftarrow pbest_i$ 
endif
endif
endif
Output optimal solution by  $gbest$ 

```

of power, and at maximum approximately  $2$  dBm of Power as it can be seen in script number three.

On another side, Figs. 4 and 5 illustrate the distribution of the estimated power values and the medians, for the undertaken 15 scripts by PSO-NPE and EPSO-NPE, respectively. Regardless of the difference between the boxes resulting from the same method. Comparably between the two methods, the box plots for PSO-NPE are lower than the



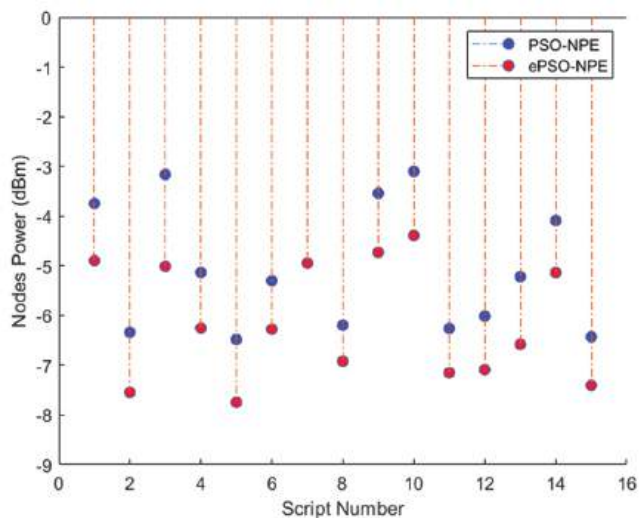


Fig. 3. Nodes power estimation for the PSO-NPE and ePSO-NPE methods.

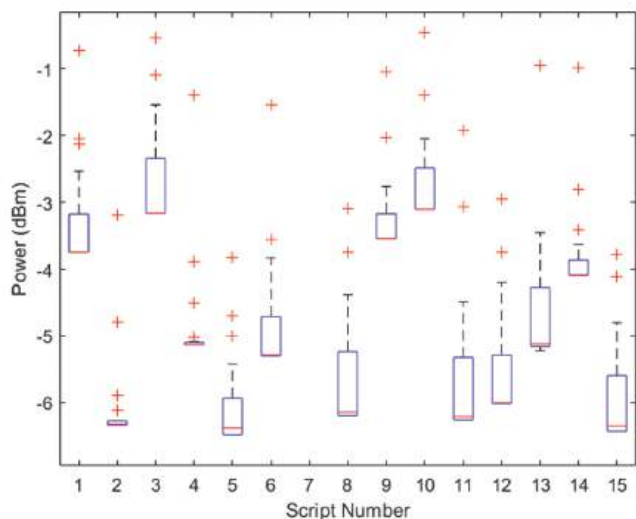


Fig. 4. Nodes powers by each script using PSO-NPE.

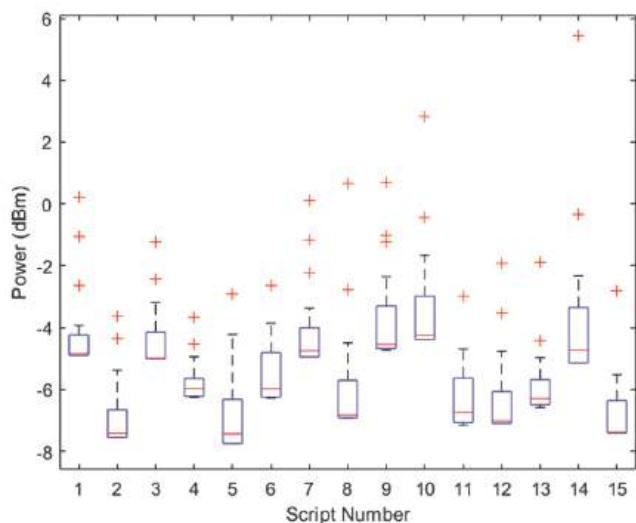


Fig. 5. Nodes powers by each script using ePSO-NPE.

TABLE I  
PARAMETER/FACTOR SETUP OF PSO AND EPSO

Parameter/Factor	value
Population size	20
Dimension	20
Iterations	1000
runtime	10
C1	2
C2	2
$\omega_{min}-\omega_{max}$	0.4, 0.9
Vmin- Vmax	-4, 4
lb-ub	-30, 0

equivalent plots for EPSO-NPE over all scripts. Moreover, node power estimations based on the EPSO-NPE are much lower than the PSO-NPE within several scripts such as in script 3 and script 5. On another side, it can be observed that some of the box plots regarding PSO-NPE are short compared with the ones by the EPSO-NPE, such as in scripts 2, 4, and 14. This indicates that there is an obvious difference between the two methods' performances, where the latter outperforms the one by the original PSO in which, unlike the EPSO, the overall estimated power based on PSO has a high level of agreement over all iterations. As a result, this is sufficient evidence that proves the better exploration ability of the proposed method.

### V. CONCLUSION

This paper proposed a new method named as EPSO-NPE to enhance the performance of the node transmission power estimation, thus to save the energy of sensor nodes within the connected state. Consequently, compared with the method based on the original PSO, the use of EPSO-NPE has saved, at minimum and maximum 1dBm and 2dBm, respectively, of the total transmitting power of the network. Moreover, unlike the PSO-NPE, the EPSO-NPE could provide superior solutions for all the scripts. As a result, the outperforming of the proposed method could be proven by several results, and this superior performance I showed overall undertaken scripts. Moreover, while the exploration behavior of the algorithm is boosted, the proposed EPSO algorithm has proven a better searching ability with high exploration and exploitation capabilities. For future work, more empirical analysis will be established on node placements and its power, and with a higher number of scripts. Technically, more studies will be established on the PSO algorithm and the possibility to enhance its performance from other aspects, and extend the comparison range to evolve more methods, techniques, and other frequencies such as ZigBee and WiFi.

### REFERENCES

Abd Aziz, A., Sekercioglu, Y.A., Fitzpatrick, P., and Ivanovich, M., 2012. A survey on distributed topology control techniques for extending the lifetime of battery powered wireless sensor networks, *IEEE Communications Surveys and Tutorials*, 15(1), pp.121-144.

- Abdjalbar, Z.H., Ucan, O.N., and Alheeti, K.M.A., 2021. An intrusion Detection System for IoT using KNN and Decision-Tree Based Classification. In *2021 International Conference of Modern Trends in Information and Communication Technology Industry (MTICTI)*. IEEE, United States, pp.1-5.
- Abdalkafor, A.S., and Aliasawi, S.A., 2022. Efficient Data Aggregation Strategy in Wireless Sensor Networks: Challenges and Significant Applications. In: *Proceedings of International Conference on Computing and Communication Networks: ICCCN 2021*. Springer, Germany, pp.131-139.
- Abdelaal, M., and Theel, O., 2014. Recent Energy-Preservation Endeavours for Longlife Wireless Sensor Networks: A Concise Survey. In: *2014 Eleventh International Conference on Wireless and Optical Communications Networks (WOCN)*. IEEE, United States, pp.1-7.
- Abdul-Qawiy, A.S.H., Almurisi, N.M.S., and Tadisetty, S., 2020. Classification of energy saving techniques for IoT-based heterogeneous wireless nodes. *Procedia Computer Science*, 171, pp.2590-2599.
- Afsar, M.M., and Tayarani-N, M.H., 2014. Clustering in sensor networks: A literature survey. *Journal of Network and Computer Applications*, 46, pp.198-226.
- Al Zakitat, M.A.S., Abdulrazzaq, M.M., Ramaha, N.T.A., Mukhlif, Y.A., and Ismael, O.A., 2023. Harnessing Advanced Techniques for Image Steganography: Sequential and Random Encoding with Deep Learning Detection. In: *International Conference on Emerging Trends and Applications in Artificial Intelligence*. Springer, Germany, pp.456-470.
- Al-Rami, B., and Alheeti, K., 2022. A new classification method for drone-based crops in smart farming. *International Journal of Interactive Mobile Technologies*, 16, pp.164-174.
- Da Silva Fré, G.L., De Carvalho Silva, J., Reis, F.A., and Mendes, L.D.P., 2015. Particle Swarm Optimization Implementation for Minimal Transmission Power Providing a Fully-Connected Cluster for the Internet of Things. In *2015 International Workshop on Telecommunications (IWT)*. IEEE, United States, pp.1-7.
- Del-Valle-Soto, C., Mex-Perera, C., Nolzco-Flores, J.A., Velázquez, R., and Rossa-Sierra, A., 2020. Wireless sensor network energy model and its use in the optimization of routing protocols. *Energies*, 13(3), p.728.
- Eberhart, R., and Kennedy, J., 1995. Particle Swarm Optimization. In: *Proceedings of the IEEE International Conference on Neural Networks*. Citeseer, New Jersey, pp.1942-1948.
- Freitas, D., Lopes, L.G., and Morgado-Dias, F., 2020. Particle swarm optimisation: A historical review up to the current developments. *Entropy (Basel)*, 22(3), p.362.
- Gardašević, G., Katzis, K., Bajić, D., and Berbakov, L., 2020. Emerging wireless sensor networks and internet of things technologies-foundations of smart healthcare. *Sensors (Basel)*, 20(13), p.3619.
- Gui, J., Zhou, K., and Xiong, N., 2016. A cluster-based dual-adaptive topology control approach in wireless sensor networks. *Sensors (Basel)*, 16(10), p.1576.
- Hamdi, M.M., Rashid, S.A., and Nafea, A.A., 2024. Resource allocation and edge computing for dual hop communication in satellite assisted UAVs enabled VANETs. *Iraqi Journal For Computer Science and Mathematics*, 5(3), pp.108-127.
- Haseeb, K., Ud Din, I., Almogren, A., and Islam, N., 2020. An energy efficient and secure IoT-based WSN framework: An application to smart agriculture. *Sensors (Basel)*, 20(7), p.2081.
- Heinzelman, W.R., and Younis, M., 2000. Energy-Scalable Algorithms and Protocols for Wireless Microsensor Networks. In: *2000 IEEE International Conference on Acoustics, Speech, and Signal Processing. Proceedings (Cat. No. 00CH37100)*. IEEE, United States, pp.3722-3725.
- Ilyas, M., Ullah, Z., Khan, F.A., Chaudary, M.H., Malik, M.S.A., Zaheer, Z., and Durrani, H.U.R., 2020. Trust-based energy-efficient routing protocol for internet of things-based sensor networks. *International Journal of Distributed Sensor Networks*, 16(10), p.1550147720964358.
- Ismael, O.A., Abdulrazzaq, M.M., Ramaha, N.T.A., Mukhlif, Y.A., and Al Zakitat, M.A.S., 2023. Exploring Lightweight Blockchain Solutions for Internet of Things. In: *International Conference on Emerging Trends and Applications in Artificial Intelligence*. Springer, Germany, pp.437-455.
- Jain, N., and Sharma, K., 2013. Modified discrete binary PSO based sensor placement for coverage in WSN networks. *International Journal of Electronics and Computer Science Engineering (IJECSSE)*, 1, pp.1549-1553.
- Kaur, T., and Kumar, D., 2018. Particle swarm optimization-based unequal and fault tolerant clustering protocol for wireless sensor networks. *IEEE Sensors Journal*, 18(11), pp.4614-4622.
- Khalifeh, A., AlQammaz, A., Darabkh, K.A., Abu Sha'ar, B., and Ghatasheh, O., 2021. A framework for Artificial Intelligence Assisted Smart Agriculture utilizing lorawan Wireless Sensor Networks. In: *Soft Computing Applications: Proceedings of the 8th International Workshop Soft Computing Applications (SOFA 2018)*. Vol. 2. Springer, Germany, pp.408-421.
- Khediri, S.E., Nejah, N., Khan, R.U., and Kachouri, A., 2021. An improved energy efficient clustering protocol for increasing the life time of wireless sensor networks. *Wireless Personal Communications*, 116, pp.539-558.
- Kulkarni, R.V., and Venayagamoorthy, G.K., 2010. Particle swarm optimization in wireless-sensor networks: A brief survey. *IEEE Transactions on Systems, Man, and Cybernetics, Part C (Applications and Reviews)*, 41(2), pp.262-267.
- Latiff, N.M.A., Tsimenidis, C.C., and Sharif, B.S., 2007. Energy-Aware Clustering For wireless Sensor Networks Using Particle Swarm Optimization. In: *2007 IEEE 18th International Symposium on Personal, Indoor and Mobile Radio Communications*. IEEE, United States, pp.1-5.
- Ling, H., 2020. Coverage optimization of sensors under multiple constraints using the improved PSO algorithm. *Mathematical Problems in Engineering*, 2020(1), p.8820907.
- Mahajan, S., and Dhiman, P.K., 2016. Clustering in wireless sensor networks: A review. *International Journal of Advanced Research in Computer Science*, 7(3), pp.198-201.
- Mendes, L.D.P., Rodrigues, J.J.P.C., and Chen, M., 2010. A Cross-Layer Sleep and Rate Adaptation Mechanism for Slotted ALOHA Wireless Sensor Networks. In: *2010 International Conference on Information and Communication Technology Convergence (ICTC)*. IEEE, United States, pp.213-217.
- Mohammed, N.S., Dawood, O.A., Sagheer, A.M., and Nafea, A.A., 2024. Secure smart contract based on blockchain to prevent the non-repudiation phenomenon. *Baghdad Science Journal*, 21(1), p.234.
- Mohapatra, H., Rath, A., Landge, P., Bhise, D., Panda, S., and Gayen, S., 2020. A comparative analysis of clustering protocols of wireless sensor network. *International Journal of Mechanical and Production Engineering Research and Development*, 10(3), pp.2249-6890.
- Nafea, A.A., Ibrahim, M.S., Mukhlif, A.A., AL-Ani, M.M., and Omar, N., 2024. An ensemble model for detection of adverse drug reactions. *ARO-The Scientific Journal of Koya University*, 12(1), pp.41-47.
- Rani, S., Rajagopal, M., Kanagachidambaresan, G.R., and Parimanam, J., 2020. *Integration of WSN and IoT for Smart Cities*. Springer, Germany.
- Rao, P.C.S., Jana, P.K., and Banka, H., 2017. A particle swarm optimization based energy efficient cluster head selection algorithm for wireless sensor networks. *Wireless Networks*, 23, pp.2005-2020.
- Rini, D.P., Shamsuddin, S.M., and Yuhaziz, S.S., 2011. Particle swarm optimization: Technique, system and challenges. *International Journal of Computer Applications*, 14(1), pp.19-26.
- Sahoo, B.M., Amgoth, T., and Pandey, H.M., 2020. Particle swarm optimization based energy efficient clustering and sink mobility in heterogeneous wireless sensor network. *Ad Hoc Networks*, 106, p.102237.
- Sun, W., Tang, M., Zhang, L., Huo, Z., and Shu, L., 2020. A survey of using

- swarm intelligence algorithms in IoT. *Sensors*, 20(5), p.1420.
- Tam, N.T., Hai, D.T., Son, L.H., and Vinh, L.T., 2018. Improving lifetime and network connections of 3D wireless sensor networks based on fuzzy clustering and particle swarm optimization. *Wireless Networks*, 24, pp.1477-1490.
- Tao, H., Alawi, O.A., Kamar, H.M., Nafea, A.A., AL-Ani, M.A., Abba, S.I., Salami, B.A., Oudah, A.Y., and Mohammed, M.K., 2024. Development of integrative data intelligence models for thermo-economic performances prediction of hybrid organic rankine plants. *Energy*, p.130503.
- Tyagi, S., and Kumar, N., 2013. A systematic review on clustering and routing techniques based upon LEACH protocol for wireless sensor networks. *Journal of Network and Computer Applications*, 36(2), pp.623-645.
- Vyas, P., and Chouhan, M., 2014. Survey on clustering techniques in wireless sensor network. *International Journal of Computer Science and Information Technologies*, 5(5), pp.6614-6661.
- Wang, Y., 2020. Optimization of Wireless Sensor Network for Dairy Cow Breeding Based on Particle Swarm Optimization. In: *2020 International Conference on Intelligent Transportation, Big Data and Smart City (ICITBS)*. IEEE, United States, pp.524-527.
- Wasmi, M.H., Aliesawi, S.A., Jasim, W.M., Mishlish, S.M., Hammad, J.A., and Mahdi, G.O., 2021. Energy-Efficient Cluster-Based Routing Protocol for Solving Data Route Selection Problem in Wireless Sensor Networks. In *2021 IEEE 12<sup>th</sup> Energy Conversion Congress and Exposition-Asia (ECCE-Asia)*. IEEE, United States, pp.1-7.
- Wormald, N.C., Gross, J.L., and Yellen, J., 2004. *Handbook of Graph Theory*. CRC Press, United States.
- Younis, O., Krunz, M., and Ramasubramanian, S., 2006. Node clustering in wireless sensor networks: Recent developments and deployment challenges. *IEEE Network*, 20(3), pp.20-25.

# Synthesis Development and Molecular Docking Study of New Azo Chalcone Derivatives

Myasar Kh. Ibrahim<sup>1†</sup> and Shireen R. Mohammed<sup>2</sup>

<sup>1</sup>Department of Basic Science, College of Agricultural Engineering Sciences, University of Duhok, Duhok, Kurdistan Region – F.R. Iraq

<sup>2</sup>Department of Chemistry, College of Science, University of Zakho, Duhok, Kurdistan Region – F.R. Iraq

**Abstract**—This work is divided into two main parts. The first part involves the synthesis of new azo chalcone compounds through a two-step process. Initially, azo compounds are synthesized by diazotizing 3-nitroaniline, followed by a coupling reaction with 4-hydroxyacetophenone, which has a terminal ketone group. Subsequently, the resulting product undergoes a Claisen–Schmidt condensation reaction with various aromatic aldehyde substrates to produce new  $\alpha$ ,  $\beta$ -unsaturated ketones, known as azo chalcone compounds. The successful synthesis of these compounds is confirmed using Fourier-transform infrared spectroscopy, <sup>1</sup>H NMR, and <sup>13</sup>C NMR spectral analyses. The second part of this study explores the theoretical biological activity of the synthesized compounds against severe acute respiratory syndrome coronavirus 2 through molecular docking studies. The results indicate potential antiviral properties for each compound, with compounds B5 and B8 exhibiting the most promising results. These compounds achieved higher docking scores ( $\Delta G$  -6.235 kcal/mol and -5.832 kcal/mol, respectively) and each formed four hydrogen bonds with the target protein.

**Index Terms**—Antiviral activity, Azo chalcone compounds, Molecular docking, Severe acute respiratory syndrome coronavirus 2, Synthesis.

## I. INTRODUCTION

Azo chalcone compounds contain two significant functional groups: (-CH=CHCO-) and (-N=N-) and have two isomers, *trans* and *cis*; the *trans* isomer is more common. Therefore, they are widely used for dyeing in industries (Vollheim, 1993), the final product in pharmaceuticals (Mezgebe and Mulugeta, 2022), and they have biological activity such as anticancer “antitumor breast cancer cells” (Baper and Mohamm, 2023), antimicrobial “against *Staphylococcus aureus* and *Bacillus subtilis*”, and antioxidant “Ferrous ion-chelating activity” (Okolo, et al., 2021; Rohini, Devi and Devi, 2015).

Different modifications and routes are made to obtain azo chalcones with desired properties (Kadhium, Mohammed and Baper, 2023; ALKazmi, Hawais and Alasadi, 2023; Baper and Mohamm, 2023). The most common synthesis method for preparing azo compounds is amine diazotization, which was reported first by the German organic chemist Peter Griess in 1858 (Yates and Yates, 2016). The diazotization consists of nitrosation of primary aromatic amines with nitrous acid to produce diazonium salts then coupling with nucleophiles such as *ortho*- or *para*-phenol or aniline. These compounds can be identified by their functional group (-N=N-), which has particular interest due to their strong bioactivities (Yates and Yates, 2016; Abbas, Al-Hamdani and Shaker, 2011), such as antimicrobial (Gür, 2019; Kofie, Dzidzoramengor and Adosraku, 2015), anti-bacterial (Mamand, et al., 2024), anti-fungal (Mezgebe and Mulugeta, 2022), anti-inflammatory (Mamand, et al., 2024), anti-viral (Mezgebe and Mulugeta, 2022), and anti-tubercular and anti-cancer (Kofie, Dzidzoramengor and Adosraku, 2015). Furthermore, azo compounds are used in pharmacological applications (Mezgebe and Mulugeta, 2022) such as HIV inhibitors of viral replication, including Evans blue and Congo red (Kozlowski and Watson, 1992). It is thought that the binding of azo dyes to this virus’s reverse transcriptase and protease is what causes this effect. Various compounds have demonstrated antibacterial and pesticidal properties due to the presence of an azo moiety (Katritzky, Chen and Tala, 2009; Hawaiz and Samad, 2012); azo-imine (Hussein and Aziz, 2011); azo-pyrazoline derivatives (Hawaiz, Hussein and Samad, 2014); pyrimidine derivatives (Mamand, et al., 2024); moreover, azo compounds were used as dyes more than half of all commercial colorants (Benkhaya, M’rabet and El Harfi, 2020). Azo benzene derivatives with active functional groups such as formyl or acetyl groups are produced by the most significant reaction, azo linkage, which links highly activated aromatic rings through an electrophilic aromatic substitution reaction. For these reasons, azo-compounds have huge literature publications.

Claisen–Schmidt condensation reaction (crossed-aldol reaction) is a powerful tool for the synthesis  $\alpha$ , $\beta$ -unsaturated ketones (chalcones) which have a general formula  $C_6H_5CH=CHCOPh$ . Acetophenone and benzaldehyde, or their

ARO-The Scientific Journal of Koya University  
Vol. XII, No. 2 (2024), Article ID: ARO.11522. 9 pages  
DOI: 10.14500/aro.11522

Received: 17 January 2024; Accepted: 02 August 2024  
Regular research paper: Published: 18 August 2024

<sup>†</sup>Corresponding author’s e-mail: myasar.ibrahim@uod.ac  
Copyright © 2024 Myasar Kh. Ibrahim and Shireen R. Mohammed.  
This is an open-access article distributed under the Creative Commons Attribution License (CC BY-NC-SA 4.0).



modified form, can undergo this reaction in the occurrences of sodium hydroxide in ethanol to produce chalcone (Kaka, Dabbagh and Hamad, 2016; Calvino, et al., 2005; Hsieh, et al., 2012; Aksöz and Ertan, 2012). Furthermore, the azo compound that contains terminal ketone reacts with different aromatic aldehyde substrates through Claisen–Schmidt condensation to obtain chalcones attached to an azo compound called azo chalcone compounds (ALKazmi, Hawais and Alasadi, 2023; Hawaiz, Samad and Aziz, 2015). This process involves the formation of a carbon–carbon new bond and holds great significance in the field of organic synthesis (Zweifel, Nantz and Somfai, 2017). Chalcone compounds have several different names such as methyl styryl ketone (Sivasankerreddy, et al., 2018) and benzylideneacetophenone benzalacetone (Tawfiq, 2016). Because chalcone derivatives have a ketoethylenic moiety (CO–CH=CH–), they are a valued species (Elkanzi, et al., 2022).

Our current work builds upon our ongoing efforts to design, synthesize, and identify new molecules derived from azo chalcone. This is achieved through two main processes. First, the reaction between 3-nitroaniline and 4-hydroxyacetophenone takes place under basic conditions in a coupling reaction step. Second, the coupling product is reacted with various aromatic aldehyde substrates under basic conditions using the Claisen–Schmidt condensation protocol. This ultimately yields new azo chalcone products, as shown in Fig. 1.

## II. EXPERIMENTAL

### A. Materials and Methods

The chemicals and solvents used in this work were purchased from Scharlau, Merck, and Fluka Companies and were used without any further purification. Melting points were measured with an uncorrected measuring device of melting point (melting point type: Electrothermal 12372). Fourier-transform infrared spectra were recorded using Thermo Scientific Nicolet iS 20 Fourier-transform infrared spectroscopy (FT-IR) Spectrometer station (4000–400  $\text{cm}^{-1}$ ) used for attenuated total reflectance (ATR) vibration measurements with (4  $\text{cm}^{-1}$ ) resolution. The software Omnic 9.2.86, Firmware version 1.02 by Thermo Fisher Scientific, was used for data collection, drawing, and interpretation of FT-IR (ATR) spectra. NMR spectra were recorded by Bruker NMR spectrometer, operating at (400 MHz) with an internal standard; tetramethylsilane, and all NMR spectra were measured at the Department

of Chemistry/College of Education/University of Basra. Preparative thin layer chromatography (TLC) silica gel 60, F254 Glass used for clean-up compounds.

### B. Synthesis

#### Preparation of hydroxy-3-((3nitrophenyl)diazenyl)phenyl-ethan-1-one (B1)

The compound (**B1**) was synthesized according to the patent (Botros and Creek, 1977), with some development as shown: In a 1 L, 3-Nitroaniline (8.28 g, 60 mmol, 1.0 eq.) was dissolved in 25 mL of distilled water and concentrated hydrochloric acid (HCl) (23 mL), the solution was cool down to 0–5°C in ice-bath with stirring. A cold solution of sodium nitrate (8.28 g, 120 mmol, 2eq.) in 15 mL distilled water was added drop by drop to the content of the flask, stirring for (1 h) while keeping the same temperature. The final cold aqueous mixture in the above flask, which contains the product of diazonium salt, was added dropwise to the basic phenolic solution with stirring in an ice bath for (4 h). The phenolic solution consists of; sodium carbonate (22 g, 207 mmol, 3.45 eq.), distilled water (220 mL) and 4-hydroxy acetophenone (8.209 g, 60.3 mmol, 1.005 eq.). The cold mixture was filtered using Buchner under vacuum; the precipitant was washed with distilled water and acidified with 2N, HCl and filtered, then washed with boiling distilled water twice and followed by purification using preparative TLC to give the expected product as shown in Table I.

#### General procedure for the synthesis of azo chalcones (B2-B12)

Azo chalcones were prepared from compound (B1) after converting it (B1) to Enolate form, which was prepared by dissolving NaOH (0.6 g, 15 mmol, 4.28eq.) in ethanol (15 mL) then 1 g, 3.5 mmol, 1eq. of azo compound **B1** was added with stirring for 48 h in 28°C. Aromatic aldehyde substrates (5 mmol, 1.4eq.) were dissolved in ethanol (25 mL) and added drop by drop to the Enolate solution, then stirred for (4–48 h), then filtered, acidify by (2M, HCl) and filtered, then washed with boiling distilled water and hot ethanol, to give the expected products as shown in Table I. All monitoring compounds were using TLC and preparative TLC with eluents (toluene/ethyl acetate [EtOAc] 3:1).

### C. Molecular Docking Study

Molecular docking is commonly used to detect the best binding direction of a molecule linked to the molecule of a protein to calculate binding energy and predict biological activity depending on  $\Delta G$  [Kcal/mol] as shown in Table II.

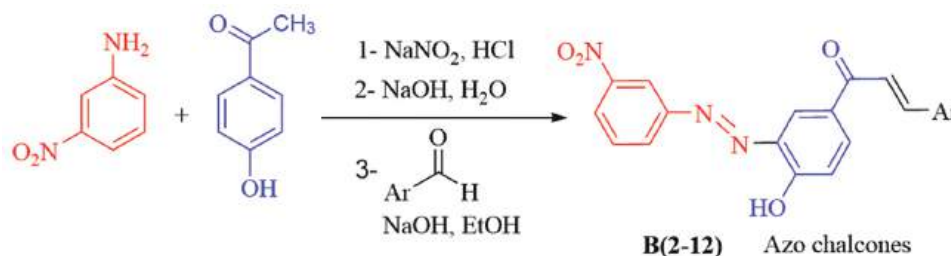


Fig. 1. Synthetic route of azo chalcone products.

TABLE I  
THE PHYSICAL PROPERTIES OF THE SYNTHESIS COMPOUNDS

Compound - Ar	M.P.	Color	TLC R <sub>f</sub>	Yield %
<b>B1</b>	181–184	Brown	0.7	94
<b>B2</b>	195–196	Brown	0.8	68
<b>B3</b>	228–229	Yellow	0.85	94
<b>B4</b>	226–227	Yellow	0.83	97
<b>B5</b>	222–223	Yellow	0.82	93
<b>B6</b>	142–145	Dark brown	0.8	68
<b>B7</b>	227–228	Light brown	0.75	96
<b>B8</b>	218–220	Brown	0.8	94
<b>B9</b>	183–185	Brown	0.6	82
<b>B10</b>	182–184	orange	0.78	95
<b>B11</b>	193–194	Light brown	0.7	96
<b>B12</b>	175–177	Brown	0.78	86

TLC: Thin layer chromatography

The template of severe acute respiratory syndrome coronavirus 2 (SARS-CoV-2) 3CL protease was collected from the protein bank which is shown in Fig. 2, before the docking process. Then, setups of 12 different ligands were built in by ChemDraw, and the Chem3D software was used to transform the 2D structure into the 3D structure. Through energy minimization, the best ligand three-dimensional (3D) structure was chosen, to predict the strength of the bond; optimum conformation was chosen and used. The receptor of the virus (SARS-CoV-2 3CL protease) was significantly reduced utilizing protein preparation and reduction techniques from the PyRx libraries, which is a powerful molecular docking tool that is used to find the binding ability lies between the receptor and ligand. A molecular docking program that gives effective docking results (Chawsheen and Al-Bustany, 2019) called AutoDock Vina, PyRx, and PyMol software were used for all newly synthesis compounds **B2-B12** with the crystallographic structure of SARS-CoV-2 as a molecule target Fig. 2. The active site of the receptor SARS-CoV-2 3CL protease contains the amino acid residues shown in Fig. 3a and b.

### III. RESULTS AND DISCUSSION

Our protocol of the synthesis consists of two general lines; first, preparation of a new azo compound (**B1**) through a diazotization reaction at a low temperature, of 3-nitroaniline with nitrous acid to produce diazonium salts, followed by one-pot coupling the diazonium salt with 4-hydroxyacetophenone in basic ethanolic solution of NaOH. Second, the compound **B1** reacts with various aromatic aldehyde substrates (–Ar) Table I in an ethanolic solution of NaOH at room temperature to produce new azo chalcone compounds **B2-B12**, as shown in Fig. 4. The final expected products were easily isolated through preparative TLC and purification as shown in Fig. 5, giving acceptable yields (68–97%).

The physical properties of the prepared compounds were studied and are shown in Table I.

#### A. FTIR (ATR) Spectra Measurements

The resulting compounds were identified using FTIR technology, the ATR was used with novel ZnSe crystal to

TABLE II  
MOLECULAR DOCKING SCORES FOR THE SYNTHESIS COMPOUNDS

Compound	Name	Docking score (ΔG)
<b>B1</b>	1-(4-hydroxy-3-(((3-nitrophenyl) diazenyl) phenyl) ethan-1-one	–5.54
<b>B2</b>	1-(4-hydroxy-3-(((3-nitrophenyl) diazenyl) phenyl)-3-(naphthalene-1-yl) prop-2-en-1-one	–5.324
<b>B3</b>	3-(2,3-dichlorophenyl)-1-(4-hydroxy-3-(((3-nitrophenyl) diazenyl) phenyl) prop-2-en-1-one	–5.657
<b>B4</b>	3-(2,4-dichlorophenyl)-1-(4-hydroxy-3-(((3-nitrophenyl) diazenyl) phenyl) prop-2-en-1-one	–5.432
<b>B5</b>	3-(2,6-dichlorophenyl)-1-(4-hydroxy-3-(((3-nitrophenyl) diazenyl) phenyl) prop-2-en-1-one	–6.235
<b>B6</b>	3-(3-bromophenyl)-1-(4-hydroxy-3-(((3-nitrophenyl) diazenyl) phenyl) prop-2-en-1-one	–5.823
<b>B7</b>	3-(4-bromophenyl)-1-(4-hydroxy-3-(((E)-(3-nitrophenyl) diazenyl) phenyl) prop-2-en-1-one	–5.789
<b>B8</b>	3-(4-chlorophenyl)-1-(4-hydroxy-3-(((3-nitrophenyl) diazenyl) phenyl) prop-2-en-1-one	–5.832
<b>B9</b>	3-(4-(dimethylamino) phenyl)-1-(4-hydroxy-3-(((3-nitrophenyl) diazenyl) phenyl) prop-2-en-1-one	–5.456
<b>B10</b>	1-(4-hydroxy-3-(((3-nitrophenyl) diazenyl) phenyl)-3-(p-tolyl) prop-2-en-1-one	–5.654
<b>B11</b>	1-(4-((5-acetyl-2,4-dihydroxyphenyl) diazenyl) phenyl) ethan-1-one	–5.325
<b>B12</b>	1-(4-hydroxy-3-(((3-nitrophenyl) diazenyl) phenyl)-5-phenylpenta-2,4-dien-1-one	–5.364

analyze the synthesis compounds, and all results are shown in Table III spectrum of the compounds, the bands that appear at  $1600\text{--}1670\text{ cm}^{-1}$  are due to stretching (str.) vibration (vib) of carbonyl group ( $\text{-C=O}$ ). The bands at  $(950\text{--}1000)\text{ cm}^{-1}$ ,  $(1600\text{--}1660)\text{ cm}^{-1}$ , and  $(3060\text{--}3085)\text{ cm}^{-1}$  belong to str. vib. of (C-H) alkene, aliphatic, and aromatic, respectively. The moderate bands appear at  $1250\text{--}1335\text{ cm}^{-1}$  and belong to str. vibrations of C-N. The bands at  $1350\text{ cm}^{-1}$  and  $1530\text{ cm}^{-1}$  belong to  $(\text{NO}_2)$  str. symmetric and asymmetric vib., respectively. The band that appears at  $3100\text{--}3320$  is attributed to str. vibration of O-H. The band at  $1035\text{--}1100\text{ cm}^{-1}$  is attributed to C-Cl str. vib. for chloro-substituted

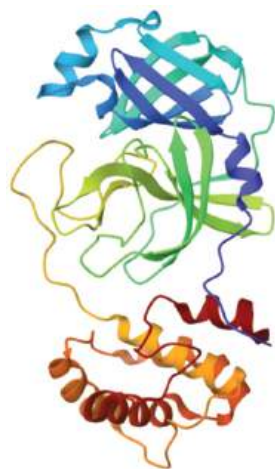


Fig. 2. 3D image severe acute respiratory syndrome coronavirus 2 3CL.

compounds (Shriner, et al., 2004; Pretsch, Bühlmann and Badertscher, 2000; Clayden, Greeves and Warren, 1995).

The overlay IR spectrum in Fig. 6 shows the confirmation of producing the **B1** compound by disappearing  $\text{NH}_2$  peak from 3-Nitroaniline and appearing N=N and C-N peaks in product **B1**. Furthermore, ATR overlay spectrums in Fig. 7 illustrate the difference between reactant B1 and product B8, which provided evidence of producing azo chalcone compound B8.

#### B. $^1\text{H}$ NMR and $^{13}\text{C}$ NMR Spectrums of Compounds

The  $^1\text{H}$  NMR spectra of synthesized azo compound **B1** showed the following characteristic chemical shifts ( $\delta$ ), as a singlet at 12.86 ppm for the OH group, singlet at 2.68 ppm for  $\text{CH}_3$ . The  $^{13}\text{C}$  NMR appears singlet at 195.89 and 26.52 ppm for C=O and OH groups, respectively. The  $^1\text{H}$ -NMR spectrum of synthesized azo chalcone compound **B3** is shown in Fig. 8. All  $^1\text{H}$ -NMR spectra of the synthesized azo compounds showed the following characteristic chemical shifts ( $\delta$ ), the significant doublet peaks of the AB system for each proton of ( $\text{-HC=CH-}$ ) appear in two regions: first at  $(8.18\text{--}7.4)$  ppm, with J coupling at 15.60 Hz for all compounds except B2 and B6, at 15.20 Hz. While the second peak appeared at  $(7.94\text{--}7.38)$  with J coupling at 15.60 Hz for all compounds except B2 and B6, it was at 15.20 Hz. This is very important evidence of the formation of the double bond for chalcones. Furthermore, extra peaks at 7.00-8.84 which belong to the aromatic system. The  $^{13}\text{C}$  NMR spectrum of synthesized azo

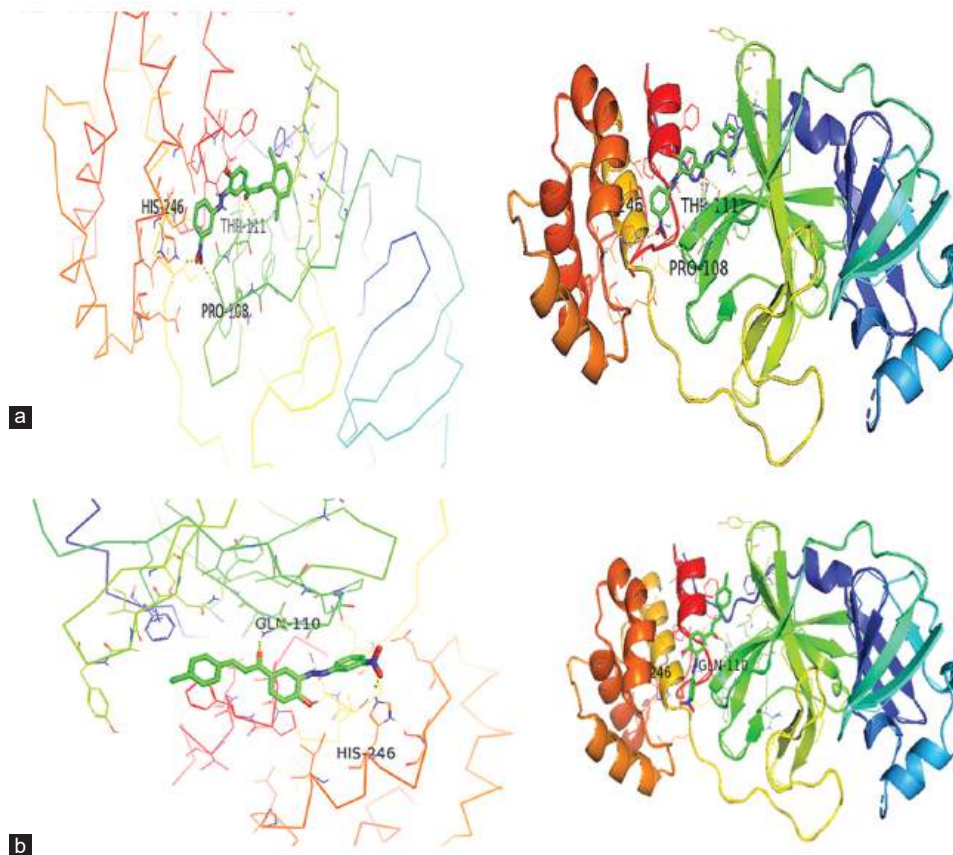


Fig. 3. Binding and docking interaction between severe acute respiratory syndrome coronavirus 2 3CL and compound: (a) **B5**, (b) **B8**.

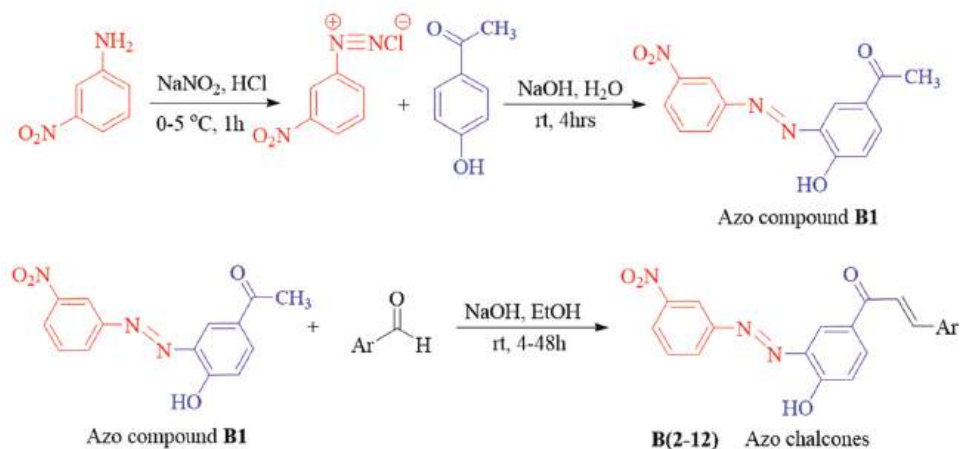


Fig. 4. Synthesis of azo chalcone compounds.

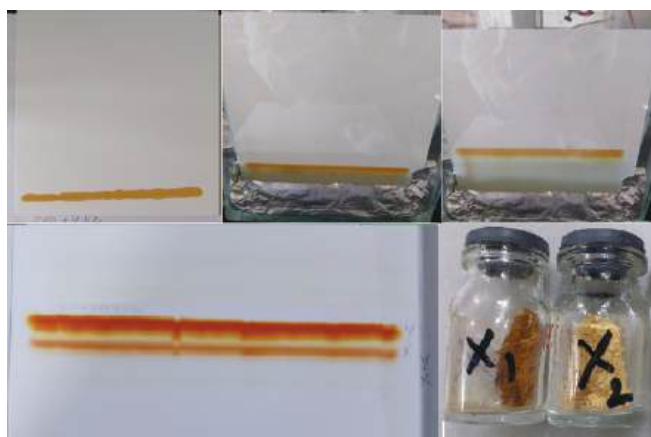


Fig. 5. Purification process of the azo compound using preparative thin-layer chromatography.

chalcone compound **B3** is shown in Fig. 9. The  $^{13}\text{C}$  NMR for all synthesized azo compounds appears with two significant peaks at 136–145 ppm and 125.41–125.93 ppm for two carbons of C=C. The following data illustrates  $^1\text{H}$  NMR interpretation for synthesized compounds.

**(B1)**  $^1\text{H}$  NMR (400 MHz,  $\text{CDCl}_3$ )  $\delta$  12.90 (s, 1H, OH), 8.77 (t,  $J = 2.4$  Hz, 1H,  $\text{CH}_{\text{ar}}$ ), 8.73 (d,  $J = 2.4$  Hz, 1H,  $\text{CH}_{\text{ar}}$ ), 8.38 (ddd,  $J = 8.4$ , 2.4 and 1.2 Hz, 1H,  $\text{CH}_{\text{ar}}$ ), 8.25 (ddd,  $J = 8.0$ , 2 and 1.2 Hz, 1H,  $\text{CH}_{\text{ar}}$ ), 8.19 (dd,  $J = 8.8$  and 2.4 Hz, 1H,  $\text{CH}_{\text{ar}}$ ), 7.90 (d,  $J = 15.6$  Hz, 1H, CH=CH), 7.76 (t,  $J = 8.0$  Hz, 1H,  $\text{CH}_{\text{ar}}$ ), 7.74–7.7 (m, 2H,  $\text{CH}_{\text{ar}}$ ), 7.65 (d,  $J = 15.6$  Hz, 1H, CH=CH), 7.45–7.44 (m, 3H,  $\text{CH}_{\text{ar}}$ ), and 7.18 (d,  $J = 8.8$  Hz, 1H,  $\text{CH}_{\text{ar}}$ ).

**(B2)**  $^1\text{H}$  NMR (400 MHz,  $\text{CDCl}_3$ )  $\delta$  12.91 (s, 1H, OH), 8.80–8.72 (m, 3H,  $\text{CH}_{\text{ar}}$ ), 8.36 (ddd,  $J = 8.3$ , 2.4, 1.1 Hz, 1H,  $\text{CH}_{\text{ar}}$ ), 8.29 (d,  $J = 8.4$  Hz, 1H,  $\text{CH}_{\text{ar}}$ ), 8.23 (dd,  $J = 8.7$ , 2.1 Hz, 2H,  $\text{CH}_{\text{ar}}$ ), 7.99–7.87 (m, 3H,  $\text{CH}_{\text{ar}}$ ), 7.74–7.52 (m, 5H,  $\text{CH}_{\text{ar}}$  and CH=CH), and 7.20 (d,  $J = 8.8$  Hz, 1H,  $\text{CH}_{\text{ar}}$ ).

**(B3)**  $^1\text{H}$  NMR (400 MHz, DMSO)  $\delta$  11.68 (s, 1H, OH), 8.79 (t,  $J = 2.1$  Hz, 1H,  $\text{CH}_{\text{ar}}$ ), 8.50–8.47 (m, 2H,  $\text{CH}_{\text{ar}}$ ), 8.38 (dd,  $J = 8.2$ , 2.4 Hz, 1H,  $\text{CH}_{\text{ar}}$ ), 8.27 (t,  $J = 9.1$  Hz, 2H,  $\text{CH}_{\text{ar}}$ ), 8.02 (d,  $J = 15.6$  Hz, 1H, CH=CH), 7.95–7.87 (m, 2H,  $\text{CH}_{\text{ar}}$  and CH=CH), 7.72 (d,  $J = 2.2$  Hz, 1H,  $\text{CH}_{\text{ar}}$ ), 7.53 (dd,  $J = 8.5$ , 2.2 Hz, 1H,  $\text{CH}_{\text{ar}}$ ), and 7.23 (d,  $J = 8.7$  Hz, 1H,  $\text{CH}_{\text{ar}}$ ).

**(B4)**  $^1\text{H}$  NMR (400 MHz, DMSO)  $\delta$  11.71 (s, 1H, OH), 8.81 (t,  $J = 2.1$  Hz, 1H,  $\text{CH}_{\text{ar}}$ ), 8.52–8.48 (m, 2H,  $\text{CH}_{\text{ar}}$ ), 8.40 (dd,  $J = 8.2$ , 2.3 Hz, 1H,  $\text{CH}_{\text{ar}}$ ), 8.34–8.26 (m, 2H,  $\text{CH}_{\text{ar}}$ ), 8.06 (d,  $J = 15.6$  Hz, 1H, CH=CH), 7.97–7.88 (m, 2H,  $\text{C}_{\text{ar}}$  and CH=CH), 7.74 (d,  $J = 2.1$  Hz, 1H,  $\text{CH}_{\text{ar}}$ ), 7.55 (dd,  $J = 8.5$ , 2.2 Hz, 1H,  $\text{CH}_{\text{ar}}$ ), and 7.24 (d,  $J = 8.7$  Hz, 1H,  $\text{CH}_{\text{ar}}$ ).

**(B5)**  $^1\text{H}$  NMR (400 MHz, DMSO)  $\delta$  11.70 (s, 1H, OH), 8.81 (s, 1H,  $\text{CH}_{\text{ar}}$ ), 8.51–8.41 (m, 3H,  $\text{CH}_{\text{ar}}$ ), 8.20 (d,  $J = 8.7$  Hz, 1H), 7.91 (t,  $J = 8.0$  Hz, 1H,  $\text{CH}_{\text{ar}}$ ), 7.81 (d,  $J = 15.6$  Hz, 1H, CH=CH), 7.70–7.6 (m, 3H,  $\text{CH}_{\text{ar}}$  and CH=CH), 7.45 (t,  $J = 8.4$  Hz, 1H,  $\text{CH}_{\text{ar}}$ ), and 7.28 (d,  $J = 8.6$  Hz, 1H,  $\text{CH}_{\text{ar}}$ ).

**(B6)**  $^1\text{H}$  NMR (400 MHz, DMSO)  $\delta$  11.70 (s, 1H, OH), 8.81 (t,  $J = 2.1$  Hz, 1H,  $\text{CH}_{\text{ar}}$ ), 8.51–8.48 (m, 1H,  $\text{CH}_{\text{ar}}$ ), 8.39 (dd,  $J = 8.2$ , 2.3 Hz, 1H,  $\text{CH}_{\text{ar}}$ ), 8.30 (dd,  $J = 8.6$ , 2.3 Hz, 1H,  $\text{CH}_{\text{ar}}$ ), 8.22 (d,  $J = 7.8$  Hz, 1H,  $\text{CH}_{\text{ar}}$ ), 7.99–7.88 (m, 4H,  $\text{CH}_{\text{ar}}$ ), 7.73 (d,  $J = 8.0$  Hz, 1H,  $\text{CH}_{\text{ar}}$ ), 7.49 (t,  $J = 7.5$  Hz, 1H, C=C), 7.41–7.35 (m, 1H, C=C), and 7.25 (d,  $J = 8.6$  Hz, 1H,  $\text{CH}_{\text{ar}}$ ).

**(B7)**  $^1\text{H}$  NMR (400 MHz, DMSO)  $\delta$  11.65 (s, 1H, OH), 8.81 (t,  $J = 2.1$  Hz, 1H,  $\text{CH}_{\text{ar}}$ ), 8.52–8.47 (m, 2H,  $\text{CH}_{\text{ar}}$ ), 8.39 (dd,  $J = 8.3$ , 2.3 Hz, 1H,  $\text{CH}_{\text{ar}}$ ), 8.30 (dd,  $J = 8.7$ , 2.3 Hz, 1H,  $\text{CH}_{\text{ar}}$ ), 7.99 (d,  $J = 15.5$  Hz, 1H, CH=CH), 7.95–7.85 (m, 3H,  $\text{CH}_{\text{ar}}$ ), 7.72 (d,  $J = 15.5$  Hz, 1H, CH=CH), 7.52 (d,  $J = 8.4$  Hz, 2H,  $\text{CH}_{\text{ar}}$ ), and 7.24 (d,  $J = 8.7$  Hz, 1H,  $\text{CH}_{\text{ar}}$ ).

**(B8)**  $^1\text{H}$  NMR (400 MHz, DMSO)  $\delta$  11.66 (s, 1H, OH), 8.84 (t,  $J = 2.0$  Hz, 1H,  $\text{CH}_{\text{ar}}$ ), 8.54–8.49 (m, 2H,  $\text{CH}_{\text{ar}}$ ), 8.41 (dd,  $J = 8.1$ , 2.3 Hz, 1H,  $\text{CH}_{\text{ar}}$ ), 8.32 (dd,  $J = 8.7$ , 2.2 Hz, 1H,  $\text{CH}_{\text{ar}}$ ), 8.02 (d,  $J = 15.6$  Hz, 1H, CH=CH), 7.97–7.9 (m, 3H,  $\text{CH}_{\text{ar}}$ ), 7.75 (d,  $J = 15.5$  Hz, 1H, CH=CH), 7.54 (d,  $J = 8.1$  Hz, 2H,  $\text{CH}_{\text{ar}}$ ), and 7.26 (d,  $J = 8.7$  Hz, 1H,  $\text{CH}_{\text{ar}}$ ).

**(B9)**  $^1\text{H}$  NMR (400 MHz,  $\text{CDCl}_3$ )  $\delta$  12.85 (s, 1H, OH), 8.74 (t,  $J = 2.1$  Hz, 2H,  $\text{CH}_{\text{ar}}$ ), 8.63 (d,  $J = 2.2$  Hz, 2H,  $\text{CH}_{\text{ar}}$ ), 8.37 (dd,  $J = 8.4$ , 2.3 Hz, 2H,  $\text{CH}_{\text{ar}}$ ), 8.24 (d,  $J = 8.5$  Hz, 1H,  $\text{CH}_{\text{ar}}$ ), 8.07 (dd,  $J = 8.8$ , 2.2 Hz, 2H,  $\text{CH}_{\text{ar}}$ ), 7.76 (t,  $J = 8.1$  Hz, 2H,  $\text{CH}_{\text{ar}}$  and CH=CH), 7.13 (d,  $J = 8.8$  Hz, 2H,  $\text{CH}_{\text{ar}}$  and CH=CH), and 2.67 (s, 6H,  $\text{CH}_3$ ).

**(B10)**  $^1\text{H}$  NMR (400 MHz, DMSO)  $\delta$  11.63 (s, 1H, OH), 8.82 (t,  $J = 2.1$  Hz, 1H,  $\text{CH}_{\text{ar}}$ ), 8.51 (d,  $J = 8.1$  Hz, 1H,  $\text{CH}_{\text{ar}}$ ), 8.46 (d,  $J = 2.2$  Hz, 1H,  $\text{CH}_{\text{ar}}$ ), 8.39 (dd,  $J = 8.0$ , 2.3 Hz, 1H,  $\text{CH}_{\text{ar}}$ ), 8.30 (dd,  $J = 8.7$ , 2.3 Hz, 1H,  $\text{CH}_{\text{ar}}$ ), 7.93–7.88 (m, 2H,  $\text{CH}_{\text{ar}}$  and CH=CH), 7.79 (d,  $J = 7.8$  Hz, 2H,  $\text{CH}_{\text{ar}}$ ),



TABLE III  
THE FTIR SPECTRUM ASSIGNMENT FOR SYNTHESIS COMPOUNDS

Compound	str. Ar. C-N	str. C=O ketone or $\alpha$ , $\beta$ ketone	str. C=C	str. C=C-H	str. Ar=C-H	str. sym. NO <sub>2</sub>	str. asy. NO <sub>2</sub>	C-H str. asy. (CH <sub>3</sub> )	C-H ben. sym. (CH <sub>3</sub> )	O-H str.	C-Cl str.
<b>B1</b>	1279	1681	1603	956	3067	1348	1530	2927	2861	3103	
<b>B2</b>	1288	1654, 1681	1593	971	3048	1347	1523			3089	
<b>B3</b>	1296	1664	1664	976	3063	1349	1527			3085	1049, 1075
<b>B4</b>	1296	1664	1614	977	3061	1349	1529			3086	1050, 1075
<b>B5</b>	1293	1663	1614	987	3082	1348	1527			3094	1042, 1072
<b>B6</b>	1270	1657	1600	975	3078	1345	1530			3100	Br 1075
<b>B7</b>	1276, 1288	1658	1599	977	3085	1348	1525			3099	Br 1093
<b>B8</b>	1275, 1287	1658	1600	977	3085	1347	1525			3099	1092
<b>B9</b>	1279	1681	1603	956	3068	1347	1530	2977	2865, 2872	3103	
<b>B10</b>	1281	1654	1654	981	3057	1345	1523	2924	2861	3103	
<b>B11</b>	1282	1658	1612	978	3079	1349	1522			3097	
<b>B12</b>	1279	1681	1603	956	3066	1347	1530			3103	

Ar. Aromatic, str. Stretching, bn. Bending. FTIR: Fourier-transform infrared spectroscopy

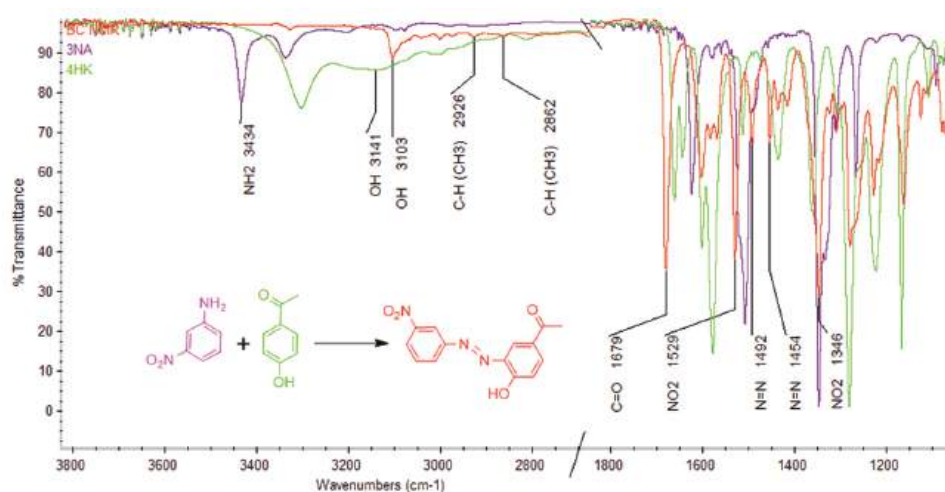


Fig. 6. Overlay of attenuated total reflectance spectrum of reactant and product **B1** compound.

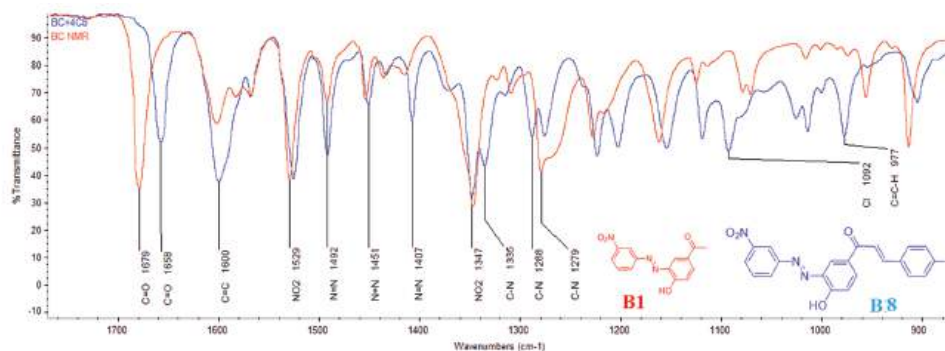


Fig. 7. Attenuated total reflectance overlay spectrum of compounds **B1** and **B8**.

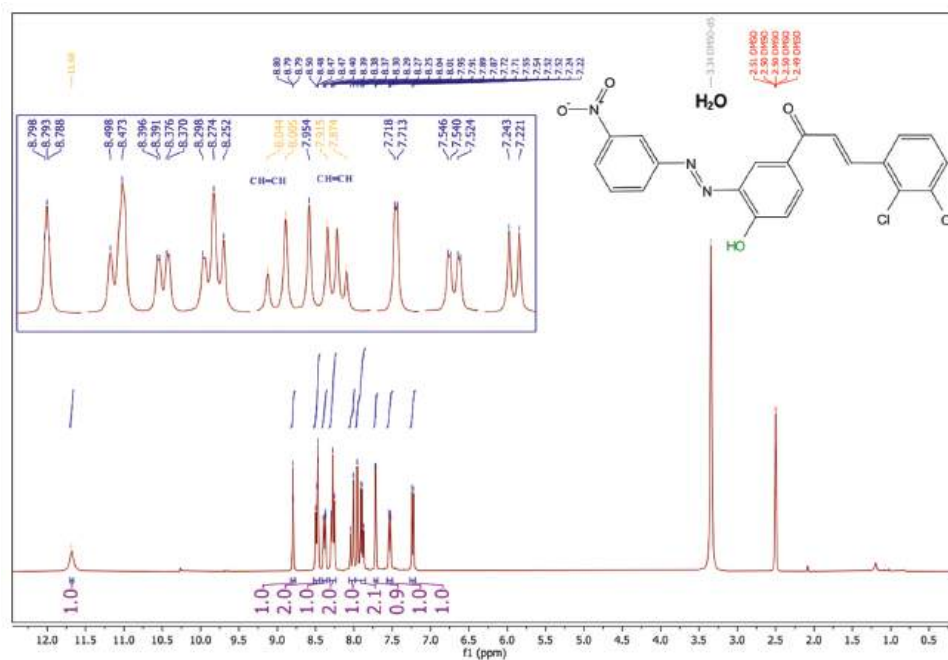
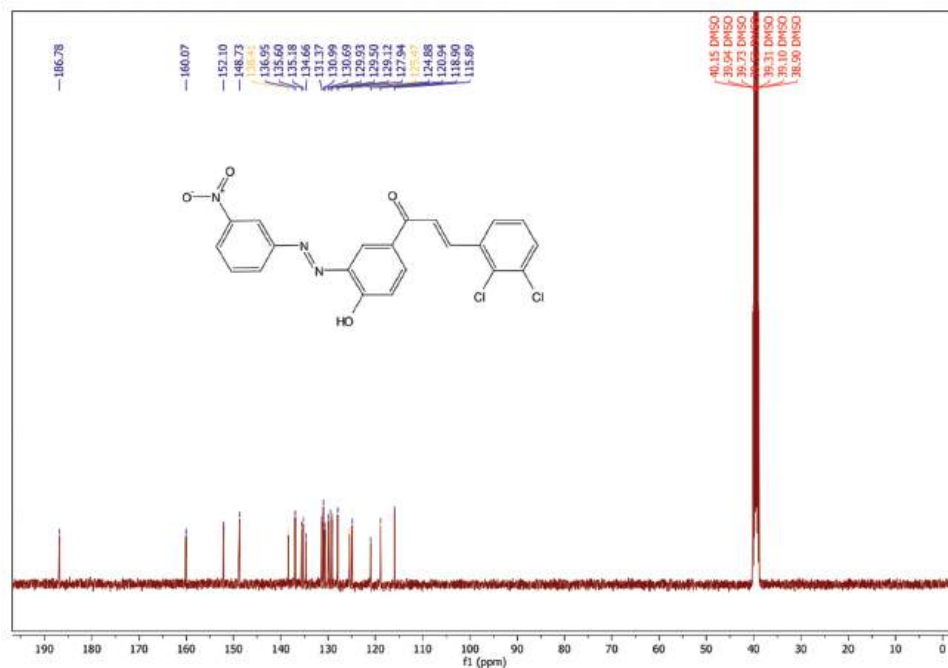
7.72 (d,  $J = 15.6$  Hz, 1H, CH=CH), 7.25 (dd,  $J = 14.0$ , 8.2 Hz, 3H, CH<sub>ar</sub>), and 2.35 (s, 3H, CH<sub>3</sub>).

(**B11**) <sup>1</sup>H NMR (400 MHz, CDCl<sub>3</sub>)  $\delta$  12.90 (s, 1H, OH, CH<sub>ar</sub>), 8.77 (t,  $J = 2.4$  Hz, 1H, CH<sub>ar</sub>), 8.73 (d,  $J = 2.4$  Hz, 1H, CH<sub>ar</sub>), 8.38 (ddd,  $J = 8.4$ , 2.4, 1.2 Hz, 1H, CH<sub>ar</sub>), 8.25 (ddd,  $J = 8.0$ , 2, 1.2 Hz, 1H, CH<sub>ar</sub>), 8.19 (dd,  $J = 8.8$ , 2.4 Hz, 1H, CH<sub>ar</sub>), 7.90 (d,  $J = 15.6$  Hz, 1H, CH=CH), 7.76 (t,  $J = 8.0$  Hz, 1H, CH<sub>ar</sub>), 7.74–7.7 (m, 2H, CH<sub>ar</sub>), 7.65 (d,  $J = 15.6$  Hz, 1H, CH=CH), 7.45–7.44 (m, 3H, CH<sub>ar</sub>), and 7.18 (d,  $J = 8.8$  Hz, 1H, CH<sub>ar</sub>).

(**B12**) <sup>1</sup>H NMR (400 MHz, DMSO)  $\delta$  11.53 (s, 1H, OH), 8.72 (d, 3H, CH<sub>ar</sub>), 8.59–8.18 (m, 5H, CH<sub>ar</sub> and CH=CH), 8.11–7.76 (m, 3H, CH<sub>ar</sub> and CH=CH), and 7.50–7.06 (m, 5H, CH<sub>ar</sub> and CH=CH).

The following data illustrates <sup>13</sup>C NMR interpretation for synthesized compounds.

(**B1**) <sup>13</sup>C NMR (101 MHz, CDCl<sub>3</sub>)  $\delta$  187.65 (C=O), 156.88 (C<sub>OH</sub>), 151.03 (C<sub>ar</sub>), 149.38 (C<sub>ar</sub>), 145.20 (C<sub>ar</sub>), 144.31 (C<sub>ar</sub>), 136.41 (C=C), 135.20 (C<sub>ar</sub>), 134.93 (C<sub>ar</sub>), 131.21 (C<sub>ar</sub>), 130.86

Fig. 8. <sup>1</sup>H NMR spectrum of synthesized azo chalcone product **B3**.Fig. 9. <sup>13</sup>C NMR spectrum of synthesized azo chalcone product **B3**.

(C<sub>ar</sub>), 130.65 (C<sub>ar</sub>), 129.17 (2C<sub>ar</sub>), 129.05 (C<sub>ar</sub>), 128.72 (2C<sub>ar</sub>), 125.69 (C=C), 121.06 (C<sub>ar</sub>), 119.35 (C<sub>ar</sub>), 116.50 (C<sub>ar</sub>).

(**B2**) <sup>13</sup>C NMR (101 MHz, CDCl<sub>3</sub>) δ 187.35 (C=O), 156.91 (C<sub>-OH</sub>), 150.93 (C<sub>ar</sub>), 149.29 (C<sub>ar</sub>), 141.97 (C<sub>ar</sub>), 136.38 (C=C), 135.26 (C<sub>ar</sub>), 134.93 (C<sub>ar</sub>), 133.86 (C<sub>ar</sub>), 132.31 (C<sub>ar</sub>), 131.91 (C<sub>ar</sub>), 131.13 (C<sub>ar</sub>), 130.59 (C<sub>ar</sub>), 129.22 (C<sub>ar</sub>), 128.94 (C<sub>ar</sub>), 127.17 (C<sub>ar</sub>), 126.48 (C<sub>ar</sub>), 125.67 (C<sub>ar</sub>), 125.61 (C=C), 125.29 (C<sub>ar</sub>), 125.01 (C<sub>ar</sub>), 123.58 (C<sub>ar</sub>), 123.53 (C<sub>ar</sub>), 119.37 (C<sub>ar</sub>), 116.52 (C<sub>ar</sub>).

(**B3**) <sup>13</sup>C NMR (101 MHz, DMSO) δ 186.78 (C=O), 160.07 (C<sub>-OH</sub>), 152.10 (C<sub>ar</sub>), 148.73 (C<sub>ar</sub>), 138.41 (C=C), 136.95 (C<sub>ar</sub>), 135.60 (C<sub>ar</sub>), 135.18 (C<sub>ar</sub>), 134.66 (C<sub>ar</sub>), 131.37

(C<sub>ar</sub>), 130.99 (C<sub>ar</sub>), 130.69 (C<sub>ar</sub>), 129.93 (C<sub>ar</sub>), 129.50 (C<sub>ar</sub>), 129.12 (C<sub>ar</sub>), 127.94 (C<sub>ar</sub>), 125.47 (C=C), 124.88 (C<sub>ar</sub>), 120.94 (C<sub>ar</sub>), 118.90 (C<sub>ar</sub>), 115.89 (C<sub>ar</sub>).

(**B4**) <sup>13</sup>C NMR (101 MHz, DMSO) δ 186.84 (C=O), 160.15 (C<sub>-OH</sub>), 152.14 (C<sub>ar</sub>), 148.76 (C<sub>ar</sub>), 138.47 (C=C), 136.97 (C<sub>ar</sub>), 135.62 (C<sub>ar</sub>), 135.19 (C<sub>ar</sub>), 134.68 (C<sub>ar</sub>), 131.39 (C<sub>ar</sub>), 131.02 (C<sub>ar</sub>), 130.72 (C<sub>ar</sub>), 129.96 (C<sub>ar</sub>), 129.52 (C<sub>ar</sub>), 129.11 (C<sub>ar</sub>), 127.97 (C<sub>ar</sub>), 125.48 (C=C), 124.95 (C<sub>ar</sub>), 120.81 (C<sub>ar</sub>), 118.94 (C<sub>ar</sub>), 115.90 (C<sub>ar</sub>).

(**B5**) <sup>13</sup>C NMR (101 MHz, DMSO) δ 187.21 (C=O), 160.49 (C<sub>-OH</sub>), 152.53 (C<sub>ar</sub>), 149.16 (C<sub>ar</sub>), 138.84 (C=C),

137.38 (C<sub>ar</sub>), 136.03 (C<sub>ar</sub>), 135.61 (C<sub>ar</sub>), 135.09 (C<sub>ar</sub>), 131.80 (C<sub>ar</sub>), 131.42 (C<sub>ar</sub>), 131.12 (C<sub>ar</sub>), 130.36 (C<sub>ar</sub>), 129.93 (C<sub>ar</sub>), 129.55 (C<sub>ar</sub>), 128.37 (C<sub>ar</sub>), 125.90 (C<sub>ar</sub>), 125.31 (C=C), 121.37 (C<sub>ar</sub>), 119.33 (C<sub>ar</sub>), 116.32 (C<sub>ar</sub>).

(B6) <sup>13</sup>C NMR (101 MHz, DMSO) δ 186.99 (C=O), 160.11 (C<sub>-OH</sub>), 152.15 (C<sub>ar</sub>), 148.75 (C<sub>ar</sub>), 147.49 (C<sub>ar</sub>), 141.00 (C<sub>ar</sub>), 138.47 (C=C), 134.63 (C<sub>ar</sub>), 134.00 (C<sub>ar</sub>), 133.31 (C<sub>ar</sub>), 132.15 (C<sub>ar</sub>), 130.98 (C<sub>ar</sub>), 130.70 (C<sub>ar</sub>), 129.17 (C<sub>ar</sub>), 128.88 (C<sub>ar</sub>), 128.24 (C<sub>ar</sub>), 125.43 (C=C), 124.59 (C<sub>ar</sub>), 120.71 (C<sub>ar</sub>), 118.94 (C<sub>ar</sub>), 115.89 (C<sub>ar</sub>).

(B7) <sup>13</sup>C NMR (101 MHz, DMSO) δ 187.06 (C=O), 159.91 (C<sub>-OH</sub>), 152.14 (C<sub>ar</sub>), 148.75 (C<sub>ar</sub>), 142.28 (C<sub>ar</sub>), 138.44 (C=C), 135.08 (C<sub>ar</sub>), 134.59 (C<sub>ar</sub>), 133.71 (C<sub>ar</sub>), 130.98 (C<sub>ar</sub>), 130.68 (2C<sub>ar</sub>), 129.41 (C<sub>ar</sub>), 128.96 (2C<sub>ar</sub>), 125.44 (C=C), 122.39 (C<sub>ar</sub>), 120.66 (C<sub>ar</sub>), 118.83 (C<sub>ar</sub>), 115.90 (C<sub>ar</sub>).

(B8) <sup>13</sup>C NMR (101 MHz, DMSO) δ 187.10 (C=O), 159.92 (C<sub>-OH</sub>), 157.14 (C<sub>ar</sub>), 152.17 (C<sub>ar</sub>), 148.76 (C<sub>ar</sub>), 142.29 (C<sub>ar</sub>), 138.48 (C=C), 138.15 (C<sub>ar</sub>), 134.59 (C<sub>ar</sub>), 133.70 (C<sub>ar</sub>), 130.99 (C<sub>ar</sub>), 130.68 (2C<sub>ar</sub>), 129.41 (C<sub>ar</sub>), 128.95 (2C<sub>ar</sub>), 125.45 (C=C), 122.42 (C<sub>ar</sub>), 120.53 (C<sub>ar</sub>), 118.84 (C<sub>ar</sub>), 115.90 (C<sub>ar</sub>).

(B9) <sup>13</sup>C NMR (101 MHz, DMSO) δ 187.18 (C=O), 159.84 (C<sub>-OH</sub>), 159.64 (C<sub>ar</sub>), 152.11 (C<sub>ar</sub>), 148.71 (C<sub>ar</sub>), 143.74 (C<sub>ar</sub>), 138.41 (C=C), 136.11 (C<sub>ar</sub>), 134.60 (C<sub>ar</sub>), 130.93 (C<sub>ar</sub>), 130.69 (C<sub>ar</sub>), 129.92 (C<sub>ar</sub>), 129.48 (C<sub>ar</sub>), 125.39 (C=C), 121.93 (C<sub>ar</sub>), 121.64 (C<sub>ar</sub>), 120.65 (C<sub>ar</sub>), 118.76 (C<sub>ar</sub>), 116.55 (C<sub>ar</sub>), 115.86 (C<sub>ar</sub>), 113.62 (C<sub>ar</sub>), 55.31 (C<sub>ar</sub>).

(B10) <sup>13</sup>C NMR (101 MHz, DMSO) δ 187.14 (C=O), 159.80 (C<sub>-OH</sub>), 152.17 (C<sub>ar</sub>), 148.75 (C<sub>ar</sub>), 143.84 (C<sub>ar</sub>), 140.69 (C<sub>ar</sub>), 138.44 (C=C), 134.52 (C<sub>ar</sub>), 132.01 (C<sub>ar</sub>), 130.97 (C<sub>ar</sub>), 130.69 (C<sub>ar</sub>), 129.61 (C<sub>ar</sub>), 129.56 (2C<sub>ar</sub>), 129.01 (2C<sub>ar</sub>), 125.41 (C=C), 120.59 (C<sub>ar</sub>), 120.46 (C<sub>ar</sub>), 118.80 (C<sub>ar</sub>), 115.91 (C<sub>ar</sub>), 21.15 (CH<sub>3</sub>).

(B11) <sup>13</sup>C NMR (100.2 MHz, CDCl<sub>3</sub>) δ 187.65 (C=O), 156.88 (C<sub>-OH</sub>), 151.03 (C<sub>ar</sub>), 149.38 (C<sub>ar</sub>), 145.20 (C<sub>ar</sub>), 144.31 (C<sub>ar</sub>), 136.41 (C=C), 135.20 (C<sub>ar</sub>), 134.93 (C<sub>ar</sub>), 131.21 (C<sub>ar</sub>), 130.86 (C<sub>ar</sub>), 130.65 (C<sub>ar</sub>), 129.17 (C<sub>ar</sub>), 129.05 (C<sub>ar</sub>), 128.72 (2C<sub>ar</sub>), 125.69 (C=C), 121.06 (C<sub>ar</sub>), 119.35 (C<sub>ar</sub>), 116.50 (C<sub>ar</sub>).

(B12) <sup>13</sup>C NMR (101 MHz, CDCl<sub>3</sub>) δ 187.60 (C=O), 156.89 (C<sub>-OH</sub>), 151.03 (C<sub>ar</sub>), 145.30 (C<sub>ar</sub>), 136.43 (C=C), 135.24 (C<sub>ar</sub>), 134.97 (C<sub>ar</sub>), 134.60 (C<sub>ar</sub>), 133.50 (C<sub>ar</sub>), 132.42 (C<sub>ar</sub>), 131.29 (C<sub>ar</sub>), 131.09 (C<sub>ar</sub>), 130.66 (C<sub>ar</sub>), 129.05 (C<sub>ar</sub>), 128.96 (C<sub>ar</sub>), 128.85 (C<sub>ar</sub>), 127.98 (C<sub>ar</sub>), 127.63 (C<sub>ar</sub>), 126.98 (C=C), 125.71 (C=C), 123.82 (C<sub>ar</sub>), 121.10 (C<sub>ar</sub>), 119.38 (C<sub>ar</sub>), 116.52 (C<sub>ar</sub>).

### C. Molecular Docking

Drug molecules' interactions with proteins can be seen using molecular docking. The goal of molecular docking calculations is to predict which mode of interaction between a given protein and ligand is most likely. These results are shown in Table II formerly known as C30 endopeptidase or 3-chymotrypsin-like protease, and the primary protease found in coronaviruses is referred to as 3C-like protease (3CLpro) or main protease (Mpro). It breaks down eleven conserved sites on the coronavirus polyprotein. It is a cysteine protease

and a member of the PA clan of proteases. At its active site, it has a cysteine-histidine catalytic dyad that cleaves a Gln-(Ser/Ala/Gly) peptide bond (Ahmad, et al., 2021).

This family is known as the SARS coronavirus main proteinase, according to the Enzyme Commission. Nonstructural protein 5 (nsp5) of the coronavirus is correlated with the 3CL protease. The 3C protease (3Cpro), a homologous protease present in picornaviruses, is denoted by the letter "3C" in the common name. There are two hydrogen bonding (H. B.) links between compound **B2** and the protein. The two bonds link with the active sites THR 111 and HIS 246 of the protein. Compound **B3** forms only one H.B. link with the active site HIS246 of the protein. Compound **B4** interacts with the residues of the protein's active sites, GLN 110 and HIS 246 to form two linkages. Compound **B5** interacts with the residues of the protein's active sites, PRO108, THR 111, and HIS 246 to form three links, which are shown in Fig. 3a. These three interactions provide evidence of the higher activity of compound **B5** toward the protein. Compound **B6** is linked with the protein's active sites, ARG298 and ALA7 by two H. B. Compound **B7** linked with protein's active sites, GLN110 and HIS 246 through two H. B. Compound **B8** linked with protein's active sites, GLN110 and HIS 246 by two H. B. Fig. 3b. Compound **B9** forms two H. B. connections with the protein residues in their active sites GLN110 and HIS 246. Compound **B10** establishes three connections with the protein residues GLY15, GLY120, and GLY71 in the active site. These three interactions provide evidence of the higher activity of compound **B10** like compound **B5** toward the protein. Compound **B11** linked with protein's active sites, SER158, LYS102 by two H. B. Finally, the compound **B12** establishes three H. B. connections with the active site residues of proteins ASN 151, THR 111, and PRO 108. Furthermore, these three interactions provide evidence of the higher activity like compounds **B5** and **B10**. The results of molecular docking scores for synthesized compounds in Table II showed that the best compounds with higher binding ability were **B5** and **B8** because they had a high docking score ( $\Delta G$  -6.235 kcal/mol) and (-5.832 kcal/mol), respectively (Mohamed, Mahmoud and Refaat, 2020). Although compound **B8** had two H. B.s, it shows a high docking score. It is worth mentioning that, compounds **B10** and **B12** each had three H. B.s with protein, but they showed lower activity than **B5** and **B8** due to the low docking scores ( $\Delta G$  -5.654 kcal/mol) and (-5.364 kcal/mol) of **B10** and **B12**, respectively.

### IV. CONCLUSION

The synthesis of novel azo and azo chalcones (**B1-B12**) was performed. All the synthesized compounds were completely identified by FTIR (ATR) and NMR. The <sup>1</sup>H NMR spectrum shows significant doublet peaks of the AB system at 8.18–7.3 ppm with J coupling at 15.60 Hz for all compounds except B2 and B6 at 15.20 Hz whereas <sup>13</sup>C NMR appears with two significant peaks at 136–145 and 125.41–125.93 ppm for two carbons of C=C. All these compounds were evaluated for

antiviral potential against SARS-CoV-2 3CL. Among them, compounds **B5** ( $\Delta G$   $-6.235$  kcal/mol) and **B8** ( $\Delta G$   $-5.832$  kcal/mol) showed more potential activity or binding ability toward the virus.

#### ACKNOWLEDGMENT

The author would like to appreciate Barcopharma Co. (agent of Thermo Fisher Co.) for their support that made this work easy and possible.

#### REFERENCES

- Abbas, S., Al-Hamdani, A.L.I., and Shaker, S.A., 2011. Synthesis, characterization, structural studies and biological activity of a new schiff base-Azo ligand and its complexation with selected metal ions. *Oriental Journal of Chemistry*, 27(3), pp.835-845.
- Ahmad, B., Batoool, M., Ul Ain, Q., Kim, M.S., and Choi, S., 2021. Exploring the binding mechanism of PF-07321332 SARS-CoV-2 protease inhibitor through molecular dynamics and binding free energy simulations. *International Journal of Molecular Sciences*, 22(17), p.9124.
- Aksöz, B.E., and Ertan, R., 2012. Spectral properties of chalcones II. *Fabad Journal of Pharmaceutical Sciences*, 37(4), pp.205-216.
- AlKazmi, A.A., Hawais, F.E., and Alasadi, Y.K., 2023. Synthesis and characterization of some pyrazoline derivatives from Chalcones containing azo and ether groups. *Tikrit Journal of Pure Science*, 22(9), pp.69-75.
- Baper, S.H., and Mohammd, M.S., 2023. Synthesis, characterization and study anticancer activity of new Azo-Chalcone with mix Ligand of some divalent metal chelate complexes. *Journal of Kufa for Chemical Sciences*, 2(9), pp.390-408.
- Benkhaya, S., M'rabet, S., and El Harfi, A., 2020. Classifications, properties, recent synthesis and applications of azo dyes. *Heliyon*, 6(1), p.e03271.
- Botros, R., and CreeK, B., 1977. Azomethine dyes derived from an O-Hydroxy aromaticaldehyde and A 2-Ammopyrone', United State Patent 405119A. Available from: <https://patentimages.storage.googleapis.com/aa/21/3e/16ceb20dd9212f/US4051119.pdf>.
- Calvino, V., Picallo, M., López-Peinado, A.J., Martín-Aranda, R.M., and Durán-Valle, C.J., 2005. Ultrasound accelerated Claisen-Schmidt condensation: A green route to chalcones. *Applied Surface Science*, 252(17), pp.6071-6074.
- Chawsheen, M.A., and Al-Bustany, H.A., 2019. Docking study to predict the efficacy of phosphatidylinositol 3-kinase  $\alpha$  inhibitors. *Aro-The Scientific Journal of Koya University*, 7(2), pp.47-52.
- Clayden, J., Greeves, N., and Warren, S., 1995. *Organic Chemistry*. 2<sup>nd</sup> ed. Oxford University Press Inc., New York.
- Elkanzi, N.A.A., Hrichi, H., Alolayan, R.A., Derafa, W., Zahou, F.M., and Bakr, R.B., 2022. Synthesis of chalcones derivatives and their biological activities: A review. *ACS Omega*, 7(32), pp.27769-27786.
- Gür, M., 2019. Synthesis, characterization, and antimicrobial properties of new 1,3,4-thiadiazoles derived from azo dyes. *Journal of Heterocyclic Chemistry*, 56(3), pp.980-987.
- Hawaiz, F.E., and Samad, M.K., 2012. Synthesis and spectroscopic characterization of some new biological active azo-pyrazoline derivatives. *European Journal of Chemistry*, 9(3), pp.1613-1622.
- Hawaiz, F.E., Hussein, A.J., and Samad, M.K., 2014. One-pot three-component synthesis of some new azo-pyrazoline derivatives. *European Journal of Chemistry*, 5, pp.233-236.
- Hawaiz, F.E., Samad, M.K., and Aziz, M.Y., 2015. Synthesis of some new heterocyclic compounds derived from 4-(4-hydroxy-3-chlorophenyl) azoacetophenone. *Journal of Zankoy Sulaimani-Part A*, 17(2), pp.85-92.
- Hsieh, C.T., Hsieh, T.J., El-Shazly, M., Chuang, D.W., Tsai, Y.H., Yen, C.T., Wu, S.F., Wu, Y.C., and Chang, F.R., 2012. Synthesis of chalcone derivatives as potential anti-diabetic agents. *Bioorganic and Medicinal Chemistry Letters*, 22(12), pp.3912-3915.
- Hussein, A.J., and Aziz, H.J., 2011. Synthesis and spectroscopic characterization of some new azo-thiazolidinone derivatives. *Pelagia Research Library*, 2(5), pp.136-146.
- Kadhium, A.J., Mohammed, M.S., and Baper, S.H., 2023. Design, preparation some transition metal complexes of Chalcone-Azo with Paracetamol ligand and Evaluation anti-biological activity of some complexes. *Journal of Kufa for Chemical Sciences*, 3(1), pp.55-67.
- Kaka, K.N., Dabbagh, A.M., and Hamad, W.M., 2016. Kinetics study of the formation of pyrimidine thione from the reaction of 2,6-dibenzylidinedicyclohexanone and its derivatives with thiourea. *ARO-The Scientific Journal of Koya University*, 4(2), pp.37-42.
- Katritzky, A.R., Chen, Q.Y., and Tala, S.R., 2009. Convenient and efficient preparations of azodye-labeled peptides. *Chemical Biology and Drug Design*, 73(6), pp.611-617.
- Kofie, W., Dzidzoramengor, C., and Adosraku, R.K., 2015. Synthesis and evaluation of antimicrobial properties of AZO dyes. *International Journal of Pharmacy and Pharmaceutical Sciences*, 7(4), pp.398-401.
- Kozlowski, M.R., and Watson, A., 1992. Inhibition of gp120 binding to the CD4 antigen by dyes: Mechanism of effect and contribution to anti-HIV activity. *Antiviral Chemistry and Chemotherapy*, 3(1), pp.49-53.
- Mamand, S.O., Abdul, D.A., Ayoob, M.A., Hussein, A.J., Samad, M.K., and Hawaiz, F.E., 2024. Traditional, one-pot three-component synthesis and anti-bacterial evaluations of some new pyrimidine derivatives. *Inorganic Chemistry Communications*, 160, p.111875.
- Mezgebe, K., and Mulugeta, E., 2022. Synthesis and pharmacological activities of azo dye derivatives incorporating heterocyclic scaffolds: A review. *RSC Advances*, 12(40), pp.25932-25946.
- Mohamed, G.G., Mahmoud, W.H., and Refaat, A.M., 2020. Nano-azo ligand and its superhydrophobic complexes: Synthesis, characterization, DFT, contact angle, molecular docking, and antimicrobial studies. *Journal of Chemistry*, 2020, pp. 19.
- Okolo, E.N., Ugwu, D.I., Ezema, B.E., Ndefo, J.C., Eze, F.U., Ezema, C.G., Ezugwu, J.A., and Ujam, O.T., 2021. New chalcone derivatives as potential antimicrobial and antioxidant agent. *Scientific Reports*, 11(1), pp.1-13.
- Pretsch, E., Bühlmann, P., and Badertscher, M., 2000. *Structure Determination of Organic Compounds: Tables of Spectral Data*. Springer, Berlin.
- Rohini, R.M., Devi, K., and Devi, S., 2015. Synthesis of novel phenyl azo chalcone derivatives for antitubercular, antiinflammatory and antioxidant activity. *Der Pharma Chemica*, 7(1), pp.77-83.
- Shriner, R.L., Hermann, C.K.F., Morrill, T.C., Curtin, D.Y., and Fuson, R.C., 2004. *The Systematic Identification of Organic Compounds*. John Wiley & Sons, Inc., United States.
- Sivasankerreddy, L., Nagamani, B., Rajkumar, T., Babu, M.S., Subbailah, N.Y., Harika, M.S., and Nageswarao, R., 2018. Novel diazenyl containing phenyl styryl ketone derivatives as antimicrobial agents. *Anti-Infective Agents*, 17(1), pp.28-38.
- Tawfiq, M.T., 2016. Synthesis and characterization of some new azo dyes derivatives via chalcone and study some of their biological activity. *Baghdad Science Journal*, 13(1), p.0122.
- Vollheim, T., 1993. Survey of industrial chemistry. *Advanced Materials*, 5(5), p.400.
- Yates, E., and Yates, A., 2016. Johann Peter Griess FRS (1829-88): Victorian brewer and synthetic dye chemist. *Notes and Records*, 70(1), pp.65-81.
- Zweifel, G.S., Nantz, M.H., and Somfai, P., 2017. *Modern Organic Synthesis: An Introduction, Modern Organic Synthesis*. John Wiley & Sons, United States.

# Graphical User Authentication Algorithms Based on Recognition: A Survey

Zena M. Saadi<sup>1†</sup>, Ahmed T. Sadiq<sup>1</sup> and Omar Z. Akif<sup>2</sup>

<sup>1</sup>Department of Computer Science, University of Technology,  
Baghdad, Iraq

<sup>2</sup>Department of Computer Science, College of Education for Pure Science (Ibn al-Haitham), University of Baghdad,  
Baghdad, Iraq

**Abstract**—In cyber security, the most crucial subject in information security is user authentication. Robust text-based password methods may offer a certain level of protection. Unfortunately, extensive use of strong passwords is barely feasible since people who use them tend to write them on paper or store them in a computer file. Many computer systems, networks, and internet-based environments have tried adopting graphical authentication methods in the past few years for user identification. It is significant to note that security and usability are the two main attributes of all graphical passwords. Unfortunately, none of these methods can effectively solve both of these issues at the same time. The aspects of the discussion included the ISO usability standards and characteristics of graphical user authentication and possible pre-attacks on 19 recognition-based authentication systems. In the current analysis, the differentiation table of attack patterns for all recognition-based techniques is revealed. Finally, the nineteen methods' positive and negative aspects were explained in a detailed table.

**Index Terms**—Graphical Password, Graphical User Authentication, ISO usability, Possible attacks, Recognition, Security.

## I. INTRODUCTION

Information security refers to the practices, technologies, and processes designed to protect sensitive information from unauthorized access, use, disclosure, disruption, modification, or destruction. This includes protecting information in various forms, such as electronic, physical, or verbal, from threats, vulnerabilities, and risks, Encryption is the process of converting plaintext (readable data) into unreadable ciphertext to protect it from unauthorized access. This is done using an encryption algorithm and a secret key. The utilization of alphanumeric passwords has traditionally been

employed to ensure the authenticity of a user. Many people tend to remember visuals more easily than text; graphical authentication has been suggested as a potential replacement for text-based authentication (Farid, et al., 2021). Despite the availability of alternative identification techniques, such as biometrics and smart card technology in the present time, it is highly likely that the password system will remain dominant due to the concerns surrounding dependability, privacy, simplicity of use, and security associated with alternative methods (Siddiqui, et al., 2018; Latee, et al., 2023). The majority commonly used method for authenticating a user within a system is the textual password. This method is currently commonly used for user authentication in computer systems, internet-based contexts, and networks (Gao, et al., 2010; Nagothu, et al., 2019; Furkan, Ant and Stephen, 2006). However, the vulnerabilities of this approach are widely recognized. Most passwords can be easily guessed or cracked. For example, the dictionary attack is a frequently employed method for hacking into an alphanumeric password (Susan, et al., 2005). This attack is highly efficient, as it requires minimal time to uncover the user's password (Amna, Kenz and Wafa, 2021; Leon and Boštjan, 2020). Moreover, another shortcoming of this strategy is the challenge of maintaining password memory. Recent studies have demonstrated that humans have a limited capacity to remember multiple passwords (Zhao and Li, 2007; Lashkari, et al., 2011). An inherent challenge with alphanumeric passwords is that users must recall them when logging into systems where they have been employed. Nevertheless, humans frequently forget their passwords, especially if they are not used continuously. As a result, people frequently write down their passwords or choose readily guessed passwords, such as the names of their pets, close friends, or birthdays (Nicholas, Andrew and Robert, 2012). Another form of password strategy that has been proposed for many security systems is the graphical password technique. Graphical passwords are potentially simpler to recall and offer enhanced security in contrast to conventional alphanumeric passwords, as they leverage humans' ability to memorize and recall images more effectively (Erlich and Zviran, 2009).

This methodology was devised to tackle the challenges linked with traditional passwords utilizing alphanumeric

ARO-The Scientific Journal of Koya University  
Vol. XII, No. 2 (2024), Article ID: ARO.11603. 15 pages  
Doi: 10.14500/aro.11603

Received: 24 April 2024; Accepted: 08 August 2024  
Regular review paper; Published: 23 August 2024

<sup>†</sup>Corresponding author's e-mail: cs.22.15@grad.uotechnology.edu.iq  
Copyright © 2024 Zena M. Saadi, Ahmed T. Sadiq and Omar Z. Akif. This is an open-access article distributed under the Creative Commons Attribution License (CC BY-NC-SA 4.0).



structures. It not only enhances memorization and user-friendliness but also offers enhanced security (Lazar, et al., 2011; Biddle, Chiasson and Oorschot, 2012). Grounded on the premise that individuals possess superior image retention abilities in comparison to numbers and words and that a single image carries more significance than multiple passwords, both software firms and behavioral scientists appear to endorse this methodology (Komanduri and Hutchings, 2008). Searchmetric or Cognometric systems, also referred to as Recognition-Based systems, necessitate users to memorize and recognize image collections when setting passwords, and subsequently (Constantine, et al., 2023), when logging in, and detecting images among distractors. Put differently, in the Recognition-Based approach, users are shown a series of images, and validation is accomplished by recollecting and picking out the designated image during the initial enrollment phase. Diverse categories of images are employed by the proposed recognition-based systems, such as symbols, abstract art, facial features, and common objects (Gao, et al., 2010).

A graphical password, also known as an image-based password or pictorial password, is a password scheme that uses an image, logo, or gesture instead of or in addition to text to verify an identity or validate authentication. However, due to the limited implementation of recognition-based graphical password systems, the vulnerabilities associated with these schemes are not yet fully comprehended. In general, the current techniques employed in recognition-based graphical passwords are still in their nascent stage. Extensive research and user studies are imperative to enhance the maturity and utility of these techniques. This study encompasses a comprehensive investigation into the existing recognition-based graphical password scheme, evaluating both its strengths and weaknesses (Komanduri and Hutchings, 2008). Moreover, it analyzes and identifies the usability characteristics and potential threats to recognition-based graphical passwords. In addition, a comprehensive and comparative evaluation of the usability attributes, attacks that occur and the pros and cons of each of the various recognition-based graphical password techniques are listed, aspects that have not received sufficient attention in prior studies (Brostoff and Sasse, 2000).

## II. SCHEMES BASED ON RECOGNITION

This section enumerates and elucidates a selection of recognition-focused frameworks that were examined from the years 2000 to 2023, emphasizing their limitations.

### A. The Passface Scheme

In 2000, the Passface scheme was developed by the Real User Corporation (Brostoff and Sasse, 2000). A commercial product known as Passfaces was introduced by the Real User Corporation, based on the premise that individuals possess superior memory retention for faces as opposed to other types of images. Users of Passfaces are required to choose a human face from a collection of nine options, where only

one face is recognizable to them while the rest function as distractors. This iterative process continues until all four faces are correctly identified. A comparative analysis of Passfaces passwords indicated that users exhibited greater ease in remembering Passfaces in contrast to text-based passwords. Moreover, users displayed significant susceptibility to factors such as the characteristics of the faces used, such as their ethnicity, gender, and attractiveness (Sabzevar and Stavrou, 2008). As a result, the predictability of Passfaces passwords could potentially be compromised. One potential resolution to this challenge is the random assignment of faces to users, although this approach would heighten the difficulty for users to memorize their passwords. Furthermore, the use of Passfaces for login and registration processes can be time-consuming in comparison to text-based password systems. Further studies were conducted to assess the security features of PassFaces, particularly its susceptibility to social engineering threats where hackers attempt to manipulate users into revealing their chosen image (Khan, Din and Almogren, 2023; Levin, 2000). This study revealed that if a decoy image is carefully chosen to resemble the user's selection, it is not possible for another individual to accurately enter the password solely based on the description of the image they have heard in the Fig. 1.

### B. Déjà vu Scheme

This strategy, which was introduced in 2000, allows consumers to choose a predetermined number of photographs from a big portfolio. The images were created using random art, one of the hash visualization algorithms, because the designer wished to lessen the possibility of a description attack. The color value of each pixel in the image is defined by a random mathematical formula that is generated when one initial seed is provided. One random abstract image will be the result, as seen in Fig. 2. Since the image is solely dependent upon only a seed and must be kept on the trusted server; it is not required to retain the images pixel by pixel for the first seed. The user must successfully navigate a difficult sequence of photos during the authentication step, some of which are spoof images mixed in with his portfolio.



Fig. 1. Passface Scheme by Brostoff and Sasse.

The user will be verified if he or she is able to successfully select their whole portfolio (Rachna and Adrian, 2000).

There are various issues with this approach. First off, it takes the user more than 60 s to create a portfolio using this method a longer period than it takes to create a text password which is 25 s. Compared to using a text password, the login process using this method takes the user longer (Khan, Din and Almogren, 2023). However, the user may find the procedure of choosing an image from the database to be time-consuming and laborious. The requirement to save the seeds in each user’s plain text portfolio image could be another disadvantage (Nagothu, et al., 2019).

*C. Triangle Scheme*

A group presented the Triangle algorithm in 2002, and it produced numerous techniques that can thwart a shoulder surfing attack. Triangle, their initial scheme, is depicted in Fig. 3. Using this strategy, a set of N objects that could number in the hundreds or thousands is randomly displayed on the screen by the system. A subset of K previously selected and memorized objects are also present. Stated otherwise, these K objects represent the user passwords.

The user must locate three of its password objects, then click inside the invisible triangle formed through these three objects, or click inside a convex hull of the displayed scroll

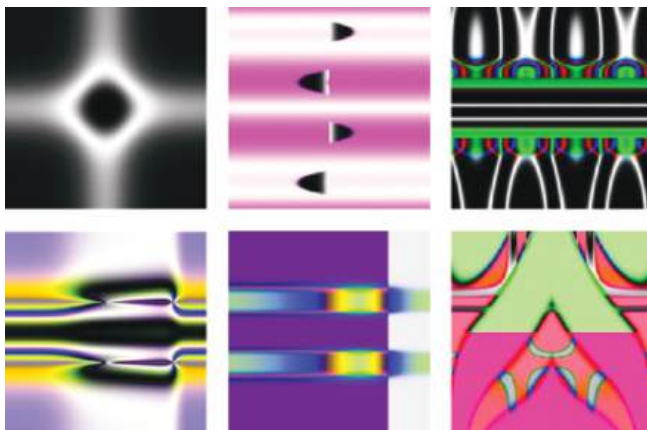


Fig. 2. Déjà vu Scheme by Rachna and Adrian.

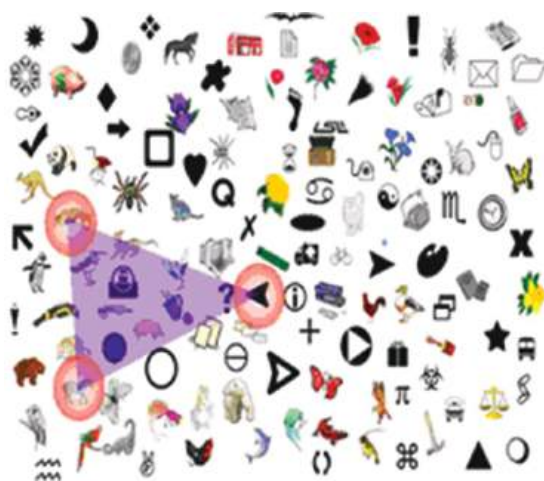


Fig. 3. Triangle Scheme by Sobrado and Birget.

objects, after a system randomly selects a placement object N after login. In addition, this task is replayed several times for each login, utilizing different displays for some N objects. As a result, there is very little chance that you will coincidentally click in the right area in each task (Sobrado and Birget, 2002).

There are various issues with this approach. To make this method resistant against shoulder surfing attacks, the method’s designer recommended using one thousand objects throughout the login process. However, the use of so many objects makes the display extremely congested and the objects themselves nearly indistinguishable. On the other hand, employing fewer objects will result in a smaller password space and a larger convex hull (Nagothu, et al., 2019).

*D. Movable Frame Scheme*

This model was created in 2002 using the same designers and based on the same concepts and presumptions as a triangle scheme. Using this method, the user has to find three things out of K; these three objects are their passwords. As Fig. 4 illustrates, only three pass objects are ever exhibited at once, and only one of those things is ever housed in a movable frame.

To align the password object is on the frame with the other two pass objects, the user must drag the mouse around the frame and the objects inside it during the login process. The process is carried out several times to reduce the possibility of the frame being moved at random (Rachna and Adrian, 2000). Due to the excessive number of objects, this approach has the disadvantage of being a tedious, complicated, and time-consuming process, this schema has used in some applications as

1. Robotics: The scheme is used to model and control robotic arms, humanoid robots, and other complex robots.
2. Computer vision: The scheme is used to track moving objects and estimate their trajectories.
3. Biomechanics: The scheme is used to model and analyze human movement, including gait analysis and motion simulation (Furkan, Ant, and Stephen, 2006).

*E. Picture Password Scheme*

This algorithm was created in 2003 specifically for handheld devices such as PDAs (personal digital assistants).

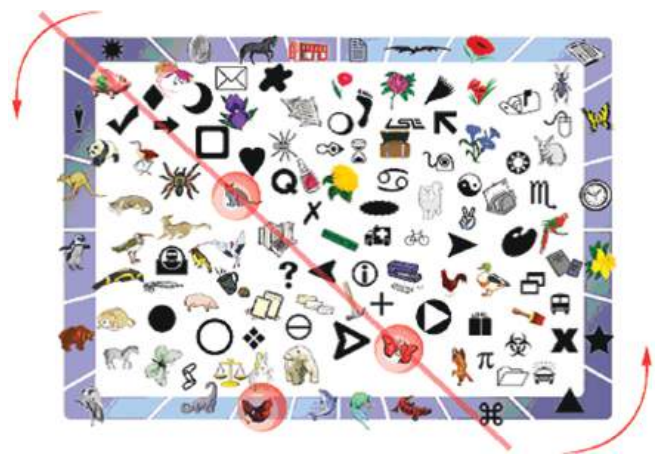


Fig. 4. Moveable Frame Scheme Furkan, Ant and Stephen.

As illustrated in Fig. 5, a user registers a series of thumbnail images that will be used as a password in the future after choosing a theme that indicates the thumbnail photos to be applied. The user needs to enter the currently enrolled image sequence for verification on turning on the PDA to access the device. On successful authentication, the user has the option to modify their password and choose an alternative theme or sequence.

The password space is deemed small because there is a 30-photo limit on thumbnail images. Therefore, the designer included a second way to choose the thumbnail item to guarantee that a password space is equivalent to the alphanumeric. In addition to choosing individual thumbnail components as previously, it is also possible to choose two thumbnail items together to create a new alphabet item. Previously, this was accomplished by using a shift key on a conventional keyboard to pick uppercase or special letters; however, in this case, each thumbnail item acts as a shift key for all other items, including it. The password space increases from thirty to nine hundred and thirty items with this modification, which is comparable to the 95 printable ASCII characters that are accessible from a conventional keyboard. However, doing so will increase the complexity and difficulty of the generated password's memorability (Jansen, et al., 2003). This model's disadvantage is that the shift key adds complexity and difficulty to the algorithm.

*F. Where is Waldo (WIW) Scheme*

This algorithm was presented by Man, et al. as a technique for making graphical password shoulder surfing resistant in 2003. Every image in this algorithm has been given a distinct code. As illustrated in Fig. 6, the user is presented with multiple scenes during authentication, each containing multiple password objects and multiple decoy ones. The user will input the code string that corresponds to his password since every password object has a distinct code. Even if the complete authentication procedure is recorded; it is extremely difficult for a shoulder surfer to crack this type of password. Users still need to commit the code to memory for every password object variation when using this method, though.



Fig. 5. Picture Password Scheme by Jansen, et al.

In the event that four photos are presented, each with four variations, the user must commit sixteen codes to memory.

The disadvantage of this approach is that it is cumbersome for the user to memorize all case-varying passwords, even though the password objects offer some clues for remembering the codes (Tu, Dahai and Yun, 2021).

*G. Story Scheme*

The story concept from 2004 divided the pictures that were accessible into nine categories: vehicles, women, food, animals, kids, men, objects, nature, and sports. To create an easily remembered story, users must choose their passwords from a mixed picture of nine different categories, as seen in Fig. 7. Some people employed this technique without coming up with their own narrative (Darren, Fabian, and Michael, 2004).

According to this study, remembering the story scheme was more difficult than using Passface authentication.

*H. Jetafida Scheme*

This approach was introduced in 2008 in an attempt to compile all the usability features such as design and layout acceptability, ease of use, ease of creation, ease of memorization, and ease of learning into a single algorithm.



Fig. 6. Man et al. Scheme by Tu, Dahai and Yun.

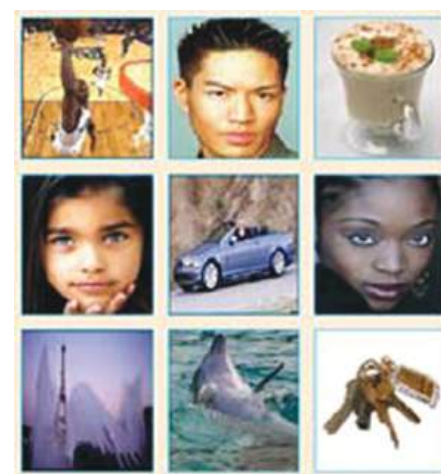


Fig. 7. Story Scheme by Darren, Fabian, and Michael.



As illustrated in Fig. 8, the user will choose three images as a password during registration and arrange them in the order he desires during the login process.

To improve usability during the login process, the user's password will be combined with seventeen-colored graphics. Thirty or so individuals use the trial version. They stated that 53% of users thought the design and screen layout were appropriate, 40% thought the algorithm was easy to use, 50% thought it was easy to create, 55% thought the new algorithm was easy to memorize, and 57% of users agreed the algorithm is easy to learn (Ali and Norafida, 2008). Since the method is so young, no survey has yet found a unique disadvantage.

*I. WYSWYE ("Where You See is What You Enter") Scheme*

Khot, Kumaraguru, and Srinathan (2012) presented a secure scheme to counteract shoulder-surfing attacks in recognition-



Fig. 8. Jetafida Scheme by Ali and Norafida.

based graphical passwords (Khot, Kumaraguru and Srinathan, 2012). The technique utilized the WYSWYE scheme, as shown in Fig. 9 which requires users to select image-based password patterns from an image grid and replicate them on another grid. WYSWYE symbolizes on "Where You See (the password) is What You Enter (the position)". This scheme, based on the concept of tabular reductions and identification of patterns, is both straightforward and efficient. It involves identifying the pattern of N password images within an M×M grid and mapping them onto an independent N×N grid. During the login process, the Challenge grid is displayed next to an empty, randomly generated image grid created by the system, which consists of the M×M grid with N password pictures and M2-N decoy pictures. However, the users do not directly interact with this grid. Instead, they use a distinct N×N grid called the Response grid, which is positioned on the right-hand side of the screen, to enter their input. To successfully log in, the users need to accurately recognize the patterns of the password images and replicate them in the Response grid.

*J. Ho et al.'s Scheme*

In 2014, Ho et al. introduced an approach (Ho, et al., 2014) that permits the challenge set's input to consist of both registered and decoy images. The user must register multiple photos during the registration process. The order of the registered photographs must be retained by the user. Using the initial picture, the cued image, and the suggested method, a pass-image is produced during the authentication process. The initial image marked at the start and the prompted image corresponds to the first and second images that have been registered, respectively. The pass-image is then obtained by applying the suggested technique. The user must decide if the

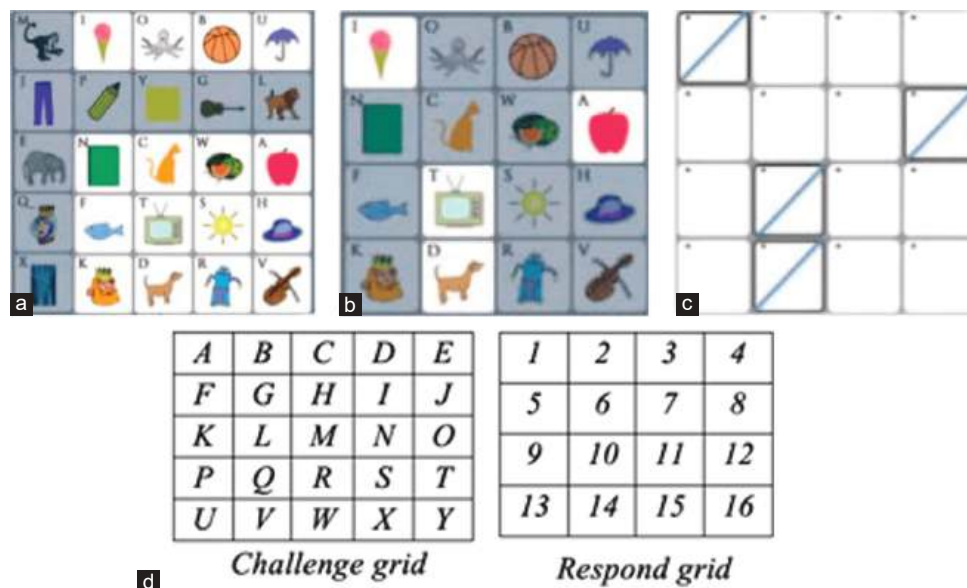


Fig. 9: Where You See is What You Enter (WYSWYE; adapted from Nagothu et al.) user interface by Khot, Kumaraguru, and Srinathan. (a) Users must mentally cross out each row and column from the challenge grid that doesn't have the password images in this example, an apple, a dog, ice cream, and television. (b) Users must determine where the password images are located in the grid with less challenge. (c) Users must click where the password images are located in the response grid. (d) Sample notations that are used in the challenge and respond grids to highlight WYSWYE's shortcomings.



Fig. 10. The Gokhale and Waghmare system’s user interface by Gokhale and Waghmare.



Fig. 11. The system’s user interface by Por, et al.

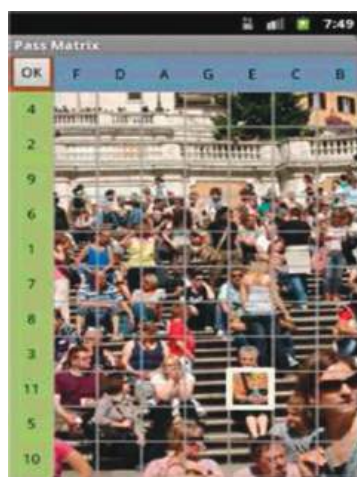


Fig. 12. The system’s user interface by Sun, et al.

cued picture is on half the imaginary line in the suggested technique. The amount of offset is determined at one in the event that the cued picture is not on half the imaginary line. The pass-image is therefore the picture that follows the



Fig. 13. Displaying an alphanumeric characters registration screen by Nizamani, Hassan, and Shaikh.

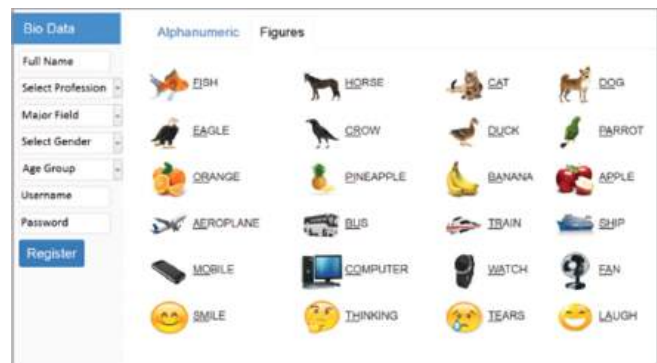


Fig. 14. Registration screen with visual representations by Nizamani, Hassan, and Shaikh.

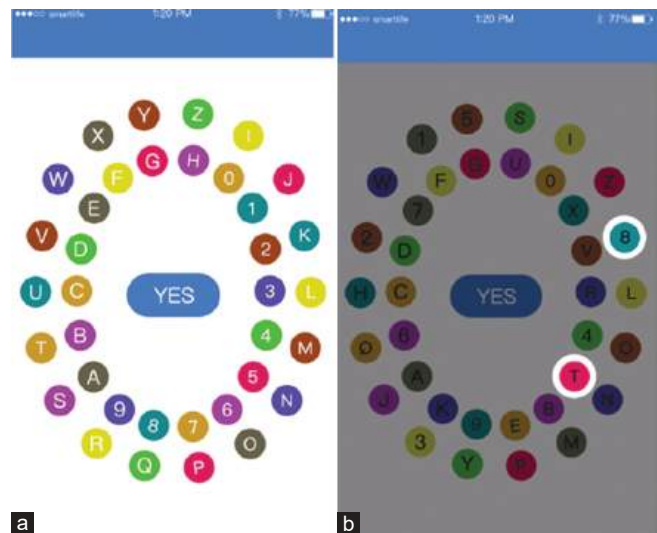


Fig. 15. The first stage of login verification by Li, et al. (a) Primary interface. (b) The system passes implicitly “8,T” as a user login indicator.

beginning image immediately along the imaginary half-line. It is necessary for the user to verify whether the cued picture is the final image on the half imaginary line if it is on it. The highest offset is used if the cued picture is not the final image on the hypothetical half-line. Consequently, the pass-image is last picture along the hypothetical half-line (Por, Ku and Ang, 2019). The quantity offset is lowered by one if the cued picture appears last on the hypothetical half-line.

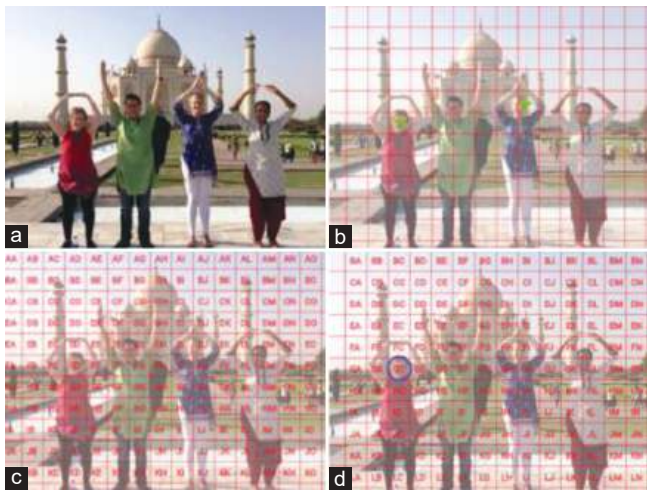


Fig. 16. Aligned over the first click point (Rajarajan and Priyadarsini). (a) User’s password image. (b) Click points chosen by user indicated by circles. (c) Image presented with grid of alphabets. (d) Secret token ‘GC’.



Fig. 17. Select 2-digit secret number and one secret image by Kausar, et al.



Fig. 18. Select arithmetic operation, secret position, and security question by Gao, et al.

Consequently, the pass-image is the picture that comes before the final image along the hypothetical half-line. The identical procedure is utilized to identify the next pass-image; the only differences are that the cued picture is the second registered image and the beginning image is the current pass-image.



Fig. 19. Selection of verification grids and password path in registration phase.

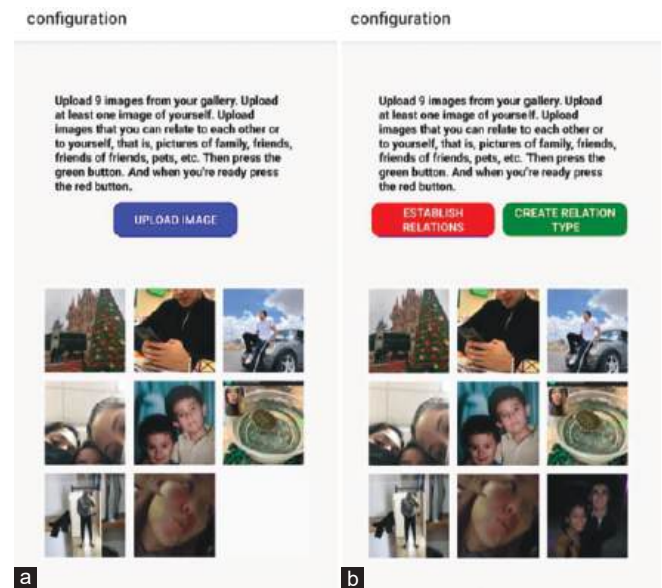


Fig. 20. Multi-Factor Authentication Scheme. (a) Image loading screen. (b) The Image upload screen once the user has uploaded nine images by Kausar, et al.

Up until the last pass-image is achieved, this procedure is repeated. The user must click the last pass-image to log in.

This technique can stop direct observation attacks, suggests (Ho, et al., 2014). Nevertheless, the system is susceptible to reverse engineering assaults when numerous sessions are videotaped (Por, Ku and Ang, 2019). Attacks using reverse engineering take advantage of the constancy of the registered photos utilized in a challenge set. One way to conduct a reverse engineering attack is to exclude certain images that are not possible to be the final cued image. By determining the final beginning image or eliminating more photos, an attacker can then get the remaining registered images. As a result, attackers can identify the registered photos and log in using those identities.

*K. Gokhale and Waghmare’s Scheme*

A graphical password technique was presented by Gokhale and Waghmare in 2016 (Gokhale and Waghmare, 2016). A user

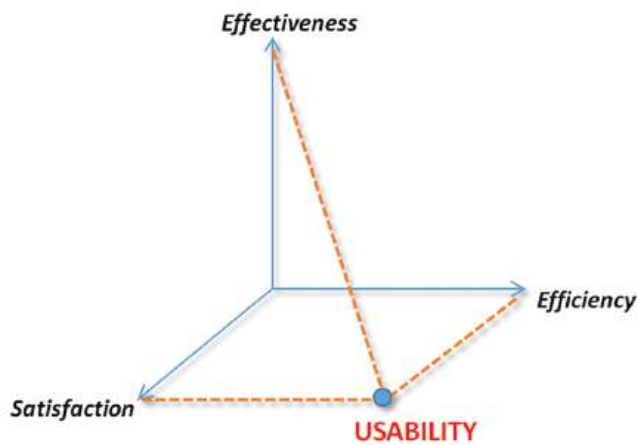


Fig. 21. The main part in IOS-9241.

must register multiple photographs from a set of 25 images during the registration process. It is required that the user register a minimum of six photographs, and the total number of images registered must be even. The order of the registered photographs must be retained by the user. The selected registered photographs are shown on a panel for the user's convenience. However, these pictures will vanish in 5 s. The user must then select a question from the pool of questions. There is a number assigned to each question. The user is needed to enter a place as the response to the question after choosing it. To help the user remember the chosen place, the user has the option to pick one of the 25 backdrop images provided by the system or upload their own image from local storage. Three locations must be registered by the user, and each place needs to be connected to a question. The user must use the registered photos to get multiple pass-images during the authentication process. Row information from the first registered image and column information from the second registered image are utilized to calculate the position of the first pass-image. The first pass-image is the intersection image. For every pair of registered photos, this procedure is repeated. Subsequently, the three sets of recorded questions are shown to the user at random. During registration, the user must click on the places linked to the questions to respond to them as shown in Fig. 10.

This technique is simple to implement and can stop shoulder-surfing attacks, claims (Gokhale and Waghmare, 2016). Attackers can readily shoulder-surf the clicked spots, though, because the locations are set (Islam, Por and Othman, 2019). In addition, after making several observations, the attackers can remove the registered photographs. This indicates that shoulder-surfing assaults can still be made against this scheme.

#### L. Por et al.'s scheme

A technique utilizing digraph substitution rules was presented by Por, et al. (2017). The user must register two photos throughout the registration process. After that, to log in using the first or second pass-image, the user must register. The user must choose a pass-image during authentication to log in utilizing digraph substitution rules as shown in Fig. 11.

This strategy can stop shoulder-surfing attacks, according to Por, et al. (2017). Nonetheless, through numerous

shoulder-surfer sessions, attackers can simply track the clicked photos and gather details regarding the registered images provided they are aware of the underlying technique (Khot, Kumaraguru and Srinathan, 2012).

#### M. Sun et al.'s scheme

In 2018 (Sun, et al., 2018), Sun et al. presented PassMatrix, which makes advantage of the picture discretization algorithm, as shown in Fig. 12. The registration process requires the user to choose many photos. Every choice has a corresponding letter on the horizontal bar and a corresponding number on the vertical bar. For every pre-selected puzzle, the user must move the letter to the column on the horizontal bar and the number to the row on the vertical bar. This procedure is iterated for every chosen image. The first chosen image's random problems are then displayed. Every problem has a number at the vertical bar and a letter at the horizontal bar. For every pre-selected puzzle, the user must move the letter to the column on the horizontal bar and the number to the row on the vertical bar. Each chosen image undergoes this process once more.

This technique is capable of thwarting shoulder-surfing attacks, as per (Ho, et al., 2014). The fact that the problems and the chosen photos are fixed, however, leads us to conclude that this system is still susceptible to shoulder-surfing attacks. After several observations, an attacker may shoulder-surf the selected in advance puzzle in each of the chosen images to log in.

#### N. A Hybrid Textual-Graphical Authentication Scheme

In 2021, S. Z. Nizamani et al. introduced a hybrid authentication system that incorporates both text and graphic elements. This scheme encompasses a multitude of mechanisms to address the shortcomings of current security schemes. Both easy login and secure login represent two different types of password inputs that can be dynamically chosen within this framework. The primary goal of the methodologies used in this study is to create a harmonious balance between data protection and ensuring user convenience. Moreover, the framework includes a unique graphical style for password creation, which enhances memorability. Furthermore, it integrates a multi-step verification process that focuses on the idea of one-time passwords (OTPs). Furthermore, this approach takes advantage of basic arithmetic operations to enhance security measures and assigns random numerical values to password components, organizing them in a randomized order (Nizamani, et al., 2021) as shown in the Fig. 13 and 14.

The efficiency of this framework was evaluated through its implementation and evaluation of its security flexibility against various cyber threats, in addition to its ease of use and ease of retrieval. Therefore, a comparison was made between the reliability and authentication speed of this approach and eight other authentication mechanisms (Nizamani, et al., 2021).

#### O. PinWheel Scheme

In 2021, PinWheel was presented by Li et al. as a login authentication system. This system combines graphical passwords with biometrics. In Fig. 15. each login using this new

technique accompanies a unique challenge value that has been derived from the fixed bead chosen by the user at registration. To achieve a secure authentication, legitimate users have to enter this challenge value into the specific field to authenticate their identity. Developers can mitigate some types of attacks, such as shoulder-surfing, smudge attacks, and video analysis, by merging a local password with a text password. This effectively prevents unauthorized access to the user credentials. Furthermore, restricting login permeation for achieving reliable administrators, PinWheel combined an optional user feature-based authentication approach, for this end, improving the security of the device and protecting data privacy over an additional security layer.

PinWheel underwent rigorous testing against various attack scenarios to evaluate its security efficacy. The outcomes of these assessments were affirmative, signaling the resilience of the system. Furthermore, an extensive user evaluation of PinWheel was executed, gathering insights on long-term password retention and authentication duration from individuals who tested a trial version of PinWheel on their mobile devices. A questionnaire was formulated to facilitate data collection in the latter phases of the trial. The findings of the investigation underscored the remarkable user-friendliness of PinWheel (Li, et al., 2021).

#### *P. SelfiePass Scheme*

The SelfiePass scheme, proposed by Rajarajan et al. in 2021, presents a remedy for the susceptibility of graphical passwords in the presence of shoulder surfing threats. By allowing users to input click points on images without direct contact with the image cells, the scheme employs a grid consisting of permutations of two alphabets, accompanied by a secret token transmitted through headphones to guide users in selecting the click points as shown in Fig. 16.

During the process, the user manipulates the grid columns horizontally and vertically to position the secret token (password) on the designated column for the first click point. The system then determines the click point based on the token's placement. This procedure is repeated for the entry of the second click point, ensuring that even if an attacker records a video of the authentication process, they are unable to ascertain the actual click points. In this manner, SelfiePass establishes a secure and resilient graphical password scheme for user authentication (Rajarajan and Priyadarsini, 2021).

#### *Q. GRA-PIN scheme*

In 2022, Kausar et al. presented a hybrid authentication approach for Smart Devices. This approach combines text and graphical-based techniques, requiring users to determine four distinct options to generate a password. The four selections of GRA-PIN consist of choose of two-digit numbers, choose one secret image, choose the swipe-up/down position for arithmetic operation, and finally, choose the password position in the final four-digit PIN. In addition, the user is required to provide a secret answer in the event of forgetting the password as shown in Figs. 17 and 18. To enhance security against shoulder surfing, guessing, and

camera attacks, a new password is generated each time the user logs in. Overall, this authentication technique offers enhanced reliability, security, and user-friendliness, all while maintaining usability and security (Kausar, et al., 2022).

#### *R. VGMSGP Scheme*

In 2022, Wang, et al. introduced a graphical password scheme as shown in Fig. 19 that amalgamates a verification grid and map slipping strategy to enhance the security and usability of the authentication process. During the authentication process, the user is mandated to manipulate the map to align every point on the password path within the predetermined verification grid. This particular approach thwarts shoulder-surfing attempts by complicating the task for malicious individuals in pinpointing the exact verification grid selected by the user. Across integrating the password pathway with the verification grid and employing the technique of map slipping, the system enhances the security of the authentication procedure and boosts the effectiveness of protecting against shoulder-surfing attacks by a range of 37% to 56%. In addition, the utilization of the map slipping technique enhances the user-friendliness of passwords in the system, increasing it by 3% to 6%.

In addition, using a map slipping strategy, combined with representing password points as coordinates on the map, helps reduce the storage burden of the system. This scheme successfully achieves a harmonious balance between usability and security by incorporating a map-slipping strategy as a defense mechanism against shoulder-surfing attacks (Wang, et al., 2022).

#### *S. Multi-Factor Authentication (MFA) Scheme*

In the year 2023, Carrillo-Torres et al. put forward an innovative MFA mechanism as shown in Fig. 20 that relies on image recognition and user-established connections, thus eliminating the need for supplementary hardware and ensuring simplicity of use. The integration of textual and graphical elements within the suggested mechanism increases the password space, rendering it more resilient and impervious to security threats.

The process of authentication entails users discerning specific images from a collection of randomly chosen images and establishing a self-pre-configured relationship between two specific images. A functional model of the suggested system was developed and deployed, and it underwent testing by users from various backgrounds. The algorithm underwent testing on users through the utilization of a mobile application available on both the Android and iOS platforms. The suggested system demonstrated a 100% accuracy rate in identifying and authenticating users, provided that authentication items and credentials have not been forgotten, and was discovered to be user-friendly and preferable to common MFA mechanisms (Carrillo-Torres, et al., 2023).

### III. ISO STANDARD USABILITY

The biggest developer and publisher of international standards globally is the International Organization for

Standardization or ISO for short. As the ISO worked on developing methods for usability evaluation, it defined several models; however, none of these models was suitable for evaluating all the schemes. All the ISO techniques provide information on the method, its features and usability only in several cases. In this section, we shall be discussing about ISO 9241. The main part of IOS 9241 is the HERE (Human Ergonomics Requirements in Environment) part that Fig. 21. describes the user and environment requirements. (Ali and Norafida, 2008):

- *Effectiveness*: Describes the transactional level that entails how users engage with a process to achieve predetermined goals with great accuracy and detail. In other words, how effective the users are in using the system to complete the tasks meant to accomplish the laid down objectives.
- *Efficiency*: is the ratio of resources used to the accuracy and thoroughness with which users accomplish their objectives.
- *Satisfaction*: The absence of discomfort and favorable perspectives toward the product's usage. Speaks of a user's perspective or their feelings regarding the system they are using such as (Use the mouse or Pen simply, Some of the GUI qualities include: Easy generation of password, clear steps of registration and login, and attractive layout, among others (Muhammad, et al., 2015). Thus, Table I shows the comparative usability of the graphical schemes used above methods was attained.

Table I collected all of the effectiveness, efficiency, and satisfaction usability attributes. Then, the characteristics of each one of them are created based on previous research. For example, using the mouse makes the user more satisfied compared to using the keyboard. Thus, it turned out that the methods mentioned 1, 2, 3, 4, and 19 received the property of effectiveness but did not receive efficiency. It was also not pointed out that the researcher actually employs it in real-life situations. In regards to methods 13, 14, 15, 16, and 17, they managed to satisfy the effectiveness characteristic, furthermore, they are utilized in the real world with a different satisfaction characteristic.

#### IV. POSSIBLE VULNERABILITIES IN SYSTEMS FOR GRAPHICAL PASSWORDS BASED ON RECOGNITION

In the subsequent section, an extensive investigation into the potential assaults on recognition-based graphical password methods has been carried out and the assaults have been recognized and ascertained. The potential assaults have been correlated to the recognition-based schemes. The potential assaults have been categorized into four types of assaults, spyware, guessing, shoulder surfing, and SQL injection. These represent the current active assaults on recognition-based schemes (Khodadadi, et al., 2016; Xiaoyuan, Ying and Scott, 2005).

- *Spyware attack*  
This is a specific type of attack where sensitive data are first recorded on the user's machine through the installation of

software tools. The malware records every key or mouse movement, unbeknownst to the user, and then transmits the recorded data outside of the computer. However, it is generally not possible to use key listening spyware or key logging alone to crack graphical passwords, as the effectiveness of mouse spyware in this regard has not been proven. Even if mouse tracking is successfully captured, it is insufficient to discover and crack the graphical password. Further information, including window size and position, as well as timing information, is required to fully exploit this specific threat.

- *Guessing attack*  
Users typically determine their passwords based on personal information such as the names of their pets, passport numbers, and last names. In response, hackers employ password guessing techniques to attempt to deduce passwords by trying out various possibilities. Password guessing attacks can be sorted into two primary forms: offline dictionary attacks and online password guessing attacks. In an offline dictionary attack, the attacker widely looks up the password by manipulating the inputs using one or more oracles tools. On the other hand, in an online password guessing attack, the attacker attempts an already guessed password by manipulating the inputs using one or more oracles tools. However, it seems that even graphical passwords can be easily guessed, similar to textual passwords.
- *Shoulder surfing attack*  
Shoulder surfing is the practice of attackers discovering users' credentials by either direct observation or external recording using video cameras while the actual user computes the information. Shoulder-surfing becomes extremely dangerous when attackers are able to pinpoint the precise location of users and make use of surveillance equipment and high-resolution cameras with telescopic lenses. While this poses a greater risk in a private setting, it is especially problematic in a public one. Most graphical passwords are susceptible to shoulder surfing, much like text passwords. There are now just a few recognition-based methods available to address the problem of shoulder-surfing. Table II demonstrates the comparative schemes based on recognition, in response to prevalent attacks.

As we can see in this table three schemes named, Ho et al.'s, Gokhale and Waghmare and PassMatrix do bad provide resistance against spyware attacks, guessing attacks, and shoulder surfing. For Por et al., A Hybrid Textual-Graphical Authentication and GRA-PIN provide resistance against spyware attacks in a good level, guessing attacks, and shoulder surfing. However, each method in the above table is not against SQL inject attack, for any attacker can enter the database and steal all information as passwords that must in future work design approach against this. In Table III, the most important positive and negative aspects of the mentioned recognition-based methods will be reviewed (Adebimpe, et al., 2023).

TABLE I  
THE USABILITY FEATURES IN RECOGNITIONBASED SCHEMES

Ref	Recognition-Based Schemes	Usability Features										Efficiency		Effectiveness	
		Use the mouse or Pen simply	Simple Way to Create Password	Memorability	Simple Steps of Registration and Login	Esthetically pleasant Design	Easy to Understand	Easy to Implement and Deployment	Server and Browser Compatible	Change the User Interface according to the device	Easy to Correct	The Utilization in Real World	Reliability and Accuracy		
1.	Passface Scheme	Yes	Yes	Yes	Yes	Yes	Yes	Yes	Yes	Yes	Yes	Yes	No	Yes	Yes
2.	Déjà vu Scheme	Yes	Yes	No	Yes	No	Yes	No	No	Yes	No	No	No	Yes	Yes
3.	Triangle Scheme	Yes	Yes	Yes	Yes	No	Yes	No	No	Yes	Yes	No	No	Yes	Yes
4.	Movable Frame Scheme	Yes	Yes	Yes	Yes	No	Yes	No	No	Yes	Yes	No	No	Yes	Yes
5.	Picture Password Scheme	Yes	Yes	Yes	Yes	Yes	Yes	Yes	No	Yes	Yes	No	Yes	No	No
6.	Where is Waldo (WIW) Scheme	No	Yes	Yes	Yes	Yes	No	No	No	No	Yes	Yes	Yes	Yes	No
7.	Story Scheme	Yes	Yes	Yes	Yes	No	Yes	No	No	No	No	No	Yes	Yes	No
8.	Jetafida Scheme	Yes	Yes	Yes	Yes	Yes	Yes	Yes	No	No	No	No	Yes	Yes	No
9.	WYSWYE Scheme	Yes	Yes	Yes	Yes	Yes	Yes	Yes	No	Yes	Yes	No	Yes	No	No
10.	Ho et al.'s Scheme	No	Yes	Yes	No	No	No	No	No	No	No	No	No	No	No
11.	Gokhale and Waghmare Scheme	No	Yes	No	No	No	Yes	No	No	No	No	No	No	No	No
12.	Por et al. Scheme	Yes	Yes	Yes	Yes	Yes	Yes	Yes	Yes	No	No	No	No	No	No
13.	PassMatrix Scheme	Yes	Yes	Yes	Yes	Yes	Yes	Yes	Yes	No	No	No	Yes	Yes	Yes
14.	A Hybrid Textual-Graphical Authentication Scheme	Yes	Yes	Yes	Yes	Yes	Yes	Yes	Yes	Yes	Yes	No	Yes	Yes	Yes
15.	PinWheel Scheme	No	Yes	Yes	Yes	Yes	Yes	Yes	No	No	No	No	Yes	Yes	Yes
16.	SelfPass Scheme	No	Yes	Yes	Yes	Yes	Yes	Yes	Yes	Yes	Yes	Yes	Yes	Yes	Yes
17.	GRA-PIN Scheme	Yes	Yes	Yes	Yes	Yes	Yes	Yes	No	No	No	No	Yes	Yes	Yes
18.	VGMSP Scheme	Yes	Yes	Yes	Yes	No	No	No	No	No	No	No	No	No	No
19.	Multi-Factor Authentication (MFA) Scheme	No	Yes	No	No	No	No	No	Yes	Yes	Yes	No	No	No	Yes

The "Yes" word refers to a present feature of an approach in these references while the "No" word means that the technique is not mentioned in the provided in these references

TABLE II  
THE ATTACKS ON RECOGNITION \_BASED SCHEMES

Ref	Recognition _Based Schemes	Spyware Attack	Guessing Attack	Shoulder Surfing Attack	SQL injection
1.	Passface Scheme	Bad	Good	Good	Bad
2.	Déjà vu Scheme	Bad	V.Good	V.Good	Bad
3.	Triangle Scheme	Bad	Good	Bad	Bad
4.	Movable Frame Scheme	Bad	V.Good	Bad	Bad
5.	Picture Password Scheme	Bad	Good	V.Good	Bad
6.	Where is Waldo (WIW) Scheme	V.Good	Bad	Bad	Bad
7.	Story Scheme	Bad	Good	Bad	Bad
8.	Jetafida Scheme	Bad	Bad	V.Good	Bad
9.	WYSWYE Scheme	V.Good	Bad	V.Good	Bad
10.	Ho et al.'s scheme	Bad	Bad	Bad	Bad
11.	Gokhale and Waghmare scheme	Bad	Bad	Bad	Bad
12.	Por et al. scheme	Good	Good	V.Good	Bad
13.	PassMatrix scheme	Bad	Bad	Bad	Bad
14.	A Hybrid Textual-Graphical Authentication Scheme	V.Good	Good	Good	Bad
15.	PinWheel scheme	Bad	V.Good	V.Good	Bad
16.	SelfiePass scheme	Bad	Good	Good	Bad
17.	GRA-PIN scheme	V.Good	Good	Good	Bad
18.	VGMSGP scheme	Bad	Bad	V.Good	Bad
19.	Multi-factor authentication (MFA) scheme	V.Good	V.Good	Bad	Bad

The "V.Good, Good" word refers to resistance to attack while the "Bad" word means that the technique is non-resistance to attacks

TABLE III  
A SUMMARY OF THE STRENGTHS AND WEAKNESSES OF THE CHOSEN RECOGNITION-BASED SCHEMES

Ref.	Author	Methodology	Positive aspects	Negative aspects	Year
1.	Brostoff and Sasse	Passface Scheme	Easy to use, create and recognize	Because this system uses a keyboard or mouse to navigate across multiple faces, it may be vulnerable to guessing and shoulder surfing attacks	2000
2.	Rachna and Adrian	Déjà vu Scheme	Reduce the chance of description attack	During the login process, choosing an image from the database can be time-consuming and laborious for the user	2000
3.	Sobrado and Birget	Triangle Scheme	Can overcome shoulder surfing attacks	Using this amount of objects makes the screen very crowded and the objects almost indistinguishable	2002
4.	Sobrado and Birget	Movable Frame Scheme	Provides an additional layer of security, offers a unique and visually appealing authentication method	Unpleasant, confusing, and time-consuming	2002
5.	Bye Janesen	Picture Password Scheme	Suitable for handheld devices such as a Personal Digital Assistant (PDA)	Little password area because there are only thirty total images	2003
6.	Man, et al.	Where is Waldo (WIW) Scheme	Shoulder surfing resistant.	The user finds it difficult to remember all of the passwords in their various instances	2003
7.	Davis, Monroe and Reiter	Story Scheme	Easy to remember	More complex to remember in comparison to Passface authentication	2004
8.	Ali Mohamed and Norafida	Jetafida Scheme	Ease of use, create, Memorize and learn	Users may face additional difficulties in recalling and replicating their selected graphical passwords	2008
9.	Khot, Kumaraguru and Srinathan	WYSWYE Scheme	Possessed higher login success rates than typical unprotected recognition-based graphical passwords, with no authentication failures, and were much more secure against shoulder surfing	Still susceptible to shoulder-surfing attacks since, after several observations, attackers can filter out the bogus pictures and log in as authentic users	2012
10.	Ho et al.	Ho et al.'s Scheme	Preventing the recurrence of analysis attacks	Because the recorded images used in the challenge set stay consistent, the system is susceptible to reverse engineering assaults when numerous sessions are video-recorded	2014
11.	Gokhale and Waghmare	Gokhale and Waghmare Scheme	It can prevent shoulder-surfing attacks and is easy to put into practice	Prone to repeated observations of attacks involving shoulder surfing (MOSSAs)	2016
12.	Por et al.	Por et al. Scheme	SSAs can be mitigated without compromising the strength of the password	Not strong enough to withstand multi-session observational attacks	2017

(Contd...)



TABLE III  
(CONTINUED)

Ref.	Author	Methodology	Positive aspects	Negative aspects	Year
13.	Sun et al.	PassMatrix scheme.	To lessen the impact of the direct observation assault, use the login indication	Tolerant of potential compromises including numerous observations and video recording	2018
14.	Nizamani et al.	A Hybrid Textual-Graphical Authentication Scheme	Provides better usability, its security against seven different security attacks	A High number of steps may affect the ease of use of the scheme, including login time Not be suitable for all users and may not improve security in all scenarios	2021
15.	Li et al.	PinWheel scheme	Prevent shoulder-surfing attacks, smudge attacks, or video analysis attacks PinWheel has good usability	Requires additional device support for the login authentication process, which limits its usability Limitations in terms of convenience and user satisfaction	2021
16.	Rajarajan and Priyadarsini	SelfiePass scheme	Resistant to shoulder surfing attacks Enhancing usability	The sources do not explicitly mention any vulnerability in the SelfiePass scheme	2021
17.	Kausar, et al.	GRA-PIN scheme	It is more reliable, robust, and user-friendly for smart devices Resistant for shoulder surfing, guessing, and camera attacks	The sources do not explicitly mention any vulnerability in the GRA-PIN scheme but many future trends can enhance the security: for example, using a touch or fingerprint sensor, GPS, microphone, etc.,	2022
18.	Wang et al.	VGMSGP scheme	Can effectively defend against shoulder-surfing attacks and reasonable usability simultaneously The use of Google Maps API helps to reduce the storage pressure of the system in a networked environment	Not resistant the strong shoulder-surfing attacks, i.e., multiple camera recordings while users are logged in	2022
19.	Carrillo-Torres et al.	Multi-factor authentication (MFA) scheme	Not require additional hardware, making it cost-effective and easy to implement Easy to use and preferable over common MFA mechanisms	It may still face usability challenges in terms of user acceptance and ease of use There may be failed authentication attempts because the user forgets the relationships between images	2023

## V. DISCUSSION

This investigation has brought to light the fact that various proposed graphical authentication schemes based on recognition have both advantages and disadvantages. It is not surprising that the majority of these schemes are intended to be memorable, as the primary objective of graphical passwords is to relieve the cognitive burden associated with textual passwords. The relationship between usability and security is commonly perceived as a trade-off, where enhancing one aspect tends to have a corresponding impact on the other.

Effective and safe graphical password schemes allow for passwords that are both easy to remember and complex enough to withstand attacks such as shoulder-surfing and spyware attacks. The procedure for logging in must be uncomplicated and efficient, as it is the most ordinary task performed by users of authentication systems. Our inquiry has proven this; memorability is a critical factor in login performance since it is the primary predictor of successful logins. The problem of remembering passwords over varying lengths of time and with varying login frequencies is addressed by memorability measures. While increasing memorability has been the main focus of research on graphical passwords, new usability issues have also surfaced. For example, it typically takes longer to authenticate using these methods. Users often complain that the procedure for logging in and creating a password are time-consuming,

specifically when using recognition-based approaches. During registration, for instance, users must select pictures from a range of options.

In adopting the use of pass-images, during the authentication, users are required to scan through many pictures in a process that might turn out to be tiresome. Moreover, it is established that most users are ignorant about the graphical passwords and therefore, are not as flexible as the text passwords. Since text-based passwords are smaller in size as compared to graphical passwords, there is a clear indication that a lot of images are required to be stored within one database. The network transfer delay is another problem; this is mainly due to recognition-based techniques, which require the display of numerous images at every verification phase. The observed case on current schemes of visual passwords does not involve password modification or reset even though there is usually a requirement for such procedures when a password cannot be remembered.

## VI. CONCLUSION AND FUTURE RESEARCH

This study has examined nineteen contemporary recognition-based graphical password systems. The security and usability characteristics of these systems have been further analyzed and discussed in depth. Subsequently, comparative tables of algorithms based on recognition were constructed, focusing on usability aspects and potential security attacks. Ultimately,

it was observed that since the inception of graphical image authentication methods, researchers have continuously strived to introduce novel techniques or enhance existing ones, particularly aiming at improving usability and security. Regrettably, efforts to enhance usability often lead to a reduction in security measures, while prioritizing security compromises usability features. Table II highlights that numerous recognition-based graphical password protocols, believed to be resilient against common attacks, such as shoulder-surfing, exhibit notable usability limitations, particularly in terms of prolonged login times, high success rates required for authentication, and issues with memorability, rendering them less practical for daily use. It is considered one of the most important types of attacks, SQL injection and the design of any model must be taken into account to avoid the attack and data theft, this challenge is particularly evident in recognition-based graphical password systems, where users are tasked with selecting specific images visible on the screen. Consequently, the design community faces the ongoing challenge of devising a method that effectively balances security and usability. Further research is warranted to substantiate the claim that individuals are more adept at remembering graphical passwords than textual ones, as existing user studies are scarce and inconclusive in supporting this assertion. Emphasizing the usability perspective, it is imperative to investigate the impact of using specific images as graphical passwords, assess the efficiency of proficient users, and identify common insecure practices users employ when creating graphical passwords.

## REFERENCES

- Adebimpe, L.A., Ng, I.O., Idris, M.Y.I., Okmi, M., Ku, C.S., Ang, T.F., and Por, L.Y., 2023. Systemic literature review of recognition-based authentication method resistivity to shoulder-surfing attacks. *Applied Sciences*, 13, p.10040.
- Ali Mohamed, E., and Norafida, I., 2008. Graphical Password: Prototype Usability survey. In: *International Conference on Advanced Computer Theory and Engineering*, pp.351-355.
- Ali, M.E., and Norafida, I., 2008. Graphical password: Comprehensive study of the usability features of the recognition base graphical password methods. In: *3<sup>rd</sup> International Conference on Convergence and Hybrid Information Technology*, pp.1137-1143.
- Amna, J.A., Kenz, A.B., and Wafa, I.E., 2021. Develop Graphical Passwords Authentication System Resistant To Shoulder Surfing Attacks. In: *The 7<sup>th</sup> International Conference on Engineering and MIS 2021 (ICEMIS'21)*. Association for Computing Machinery, New York, USA, p.55.
- Biddle, R., Chiasson, S., and Oorschot, P., 2012. Graphical passwords: Learning from the first twelve years. *ACM Computing Surveys (CSUR)*, 44, pp.1-41.
- Brostoff, S., and Sasse, M.A., 2000. Are passfaces more usable than passwords? A field trial investigation. In: McDonald, S., Waern, Y., and Cockton, G., (eds) *People and Computers XIV - Usability*. Springer, London.
- Carrillo-Torres, D., Pérez-Díaz, J.A., Cantoral-Ceballos, J.A., and Vargas-Rosales, C., 2023. A novel multi-factor authentication algorithm based on image recognition and user established relations. *Applied Sciences*, 13, p.1374.
- Constantine, S., Margherita, A., Stavroula, N., and Gavriel, S., 2023. HCI International 2023 Posters. In: *25<sup>th</sup> International Conference on Human-Computer Interaction, HCII, Copenhagen, Denmark, July 23-28, Proceedings, Part IV: Communications in Computer and Information Science*. Vol. 1835, Springer, Cham.
- Davis, D, Monrose, F., and Reiter, M.K., 2004. On User Choice in Graphical Password Schemes. In: *Proceedings of the 13<sup>th</sup> USENIX Security Symposium*.
- Erlich, Z., and Zviran, M., 2009. Authentication methods for computer systems security. In: *Encyclopedia of Information Science and Technology*. 2<sup>nd</sup> ed., Vol. 1. IGI Global, United States, pp.288-293.
- Farid, B., Mat, M.L., Lip, Y., and Zaidan, A.A., 2021. A systematic review of PIN-entry methods resistant to shoulder-surfing attack. *Computers and Security*, 101, p.102116.
- Furkan, T., Ant, O., and Stephen, H., 2006. A Comparison of Perceived and Real Shoulder-Surfing Risks between Alphanumeric and Graphical Passwords. In: *Proceedings of the Second Symposium on Usable Privacy and Security (SOUPS '06)*. Association for Computing Machinery, New York, USA, pp.56-66.
- Furkan, T., Ant, O., and Stephen, H., 2006. *Symposium on Usable Privacy and Security (SOUPS)*. Pittsburgh, PA, USA, pp.56-66.
- Gao, H., Ren, Z., Chang, X., Liu, X., and Aickelin, U., 2010. A New Graphical Password Scheme Resistant to Shoulder-Surfing. In: *Proceedings International Conference on Cyberworlds*, CW Network, United States.
- Gao, H., Xiyang, L., Wang, S., Liu, H., and Dai, R., 2010. Design and Analysis of a Graphical Password Scheme. In: *2009 4<sup>th</sup> International Conference on Innovative Computing, Information and Control, (ICICIC)*, pp.675-678.
- Gokhale, M., and Waghmare, V., 2016. The shoulder surfing resistant graphical password authentication technique. *Procedia Computer Science*, 79, pp.875-884.
- Ho, P.F., Kam, Y.H.S., Wee, M.C., Chong, Y.N., and Por, L.Y., 2014. Preventing shoulder-surfing attack with the concept of concealing the password objects' information. *ScientificWorldJournal*, 2014, p.838623.
- Islam, A., Por, L., and Othman, F., 2019. A review on recognition-based graphical password techniques. In: *Computational Science and Technology, Lecture Notes in Electrical Engineering*. Springer, Singapore.
- Jansen, W., Gavril, S., Korolev, V., Ayers, R., and Swanstrom, R., 2003. *Picture Password: A Visual Login Technique for Mobile Devices*. National Institute of Standards and Technology, Gaithersburg, MD.
- Kausar, N., Din, I.U., Khan, M.A., Almogren, A., and Kim, B.S., 2022. GRA-PIN: A graphical and PIN-based hybrid authentication approach for smart devices. *Sensors (Basel)*, 22, p.1349.
- Khan, M.A., Din, I.U., and Almogren, A., 2023. Securing access to internet of medical things using a graphical-password-based user authentication scheme. *Sustainability*, 15, p.5207.
- Khodadadi, T., Muzahidul Islam, A.K.M., Baharun, S., and Komaki, S., 2016. Evaluation of recognition-based graphical password schemes in terms of usability and security attributes. *International Journal of Electrical and Computer Engineering*, 6, pp.2939-2948.
- Khot, R.A., Kumaraguru, P., and Srinathan, K., 2012. WYSWYE: Shoulder Surfing Defense for Recognition based Graphical Passwords. In: *Proceedings of the 24<sup>th</sup> Australian Computer-Human Interaction Conference*, pp.285-294.
- Komanduri, S., and Hutchings, D., 2008. Order and Entropy in Picture Passwords. In: *Proceedings - Graphics Interface*, pp.115-122.
- Lashkari, A.H., Abdul Manaf, A., Masrom, M., and Daud, S.M., 2011. Security evaluation for graphical password. In: Cherif, H., Zain, J.M., and El-Qawasmeh, E., (eds) *Digital Information and Communication Technology and Its Applications: Communications in Computer and Information Science*. Vol. 166. Springer, Berlin, Heidelberg.
- Latee, F., Ian, O., Mohd, Y., Mohammed, O., Chin, S., and Tan, F., 2023. Systemic literature review of recognition-based authentication method resistivity to shoulder-surfing attacks. *Applied Sciences*, 13(18), p.10040.
- Lazar, L., Tikolsky, O., Glezer, C., and Zviran, M., 2011. Personalized cognitive passwords: An exploratory assessment. *Information Management and Computer Security*, 19, pp.25-41.

- Leon, B., and Boštjan, B., 2020. Shoulder surfing experiments: A systematic literature review. *Computers and Security*, 99, p.102023.
- Levin, D.T., 2000. Race as a visual feature: Using visual search and perceptual discrimination tasks to understand face categories and the cross-race recognition. *Journal of Experimental Psychology: General*, 129, pp.559-74.
- Li, Y., Yun, X., Fang, L., and Ge, C., 2021. An efficient login authentication system against multiple attacks in mobile devices. *Symmetry*, 13, p.125.
- Muhammad, D., Abdul, H., Norafida, I., and Hazinah, K., 2015. Towards Identifying Usability and Security Features of Graphical Password in Knowledge based Authentication Technique. In: *Second Asia International Conference on Modeling and Simulation*, pp.396-403.
- Nagothu, D., Chen, Y., Blasch, E., Aved, A., and Zhu, S., 2019. Detecting malicious false frame injection attacks on surveillance systems at the edge using electrical network frequency signals. *Sensors (Basel)*, 19, p.2424.
- Nicholas, W., Andrew, S., and Robert, B., 2012. Do you see Your Password? Applying Recognition to Textual Passwords. In: *Proceedings of the Eighth Symposium on Usable Privacy and Security (SOUPS '12)*. Association for Computing Machinery, New York, USA, p8.
- Nizamani, S.Z., Hassan, S.R., Shaikh, R.A., Abozinadah, E.A., and Mehmood, R., 2021. A novel hybrid textual-graphical authentication scheme with better security, memorability, and usability. *IEEE Access*, 9, pp.51294-51312.
- Por, L., Ku, C., Islam, A., and Ang, T., 2017. Graphical password: Prevent shoulder-surfing attack using digraph substitution rules. *Frontiers of Computer Science*, 11, pp.1098-1108.
- Por, L.Y., Ku, C.S., and Ang, T.F., 2019. Preventing shoulder-surfing attacks using digraph substitution rules and pass-image output feedback. *Symmetry*, 11, p.1087.
- Rachna, D., and Adrian, P., 2000. Deja Vu--a user study: Using Images for Authentication. In: *Proceeding of the 9th USENIX Security Symposium*.
- Rajarajan, S., and Priyadarsini, P.L.K., 2021. SelfiePass: A Shoulder Surfing Resistant Graphical Password Scheme. In: *International Conference on Recent Trends on Electronics, Information, Communication and Technology (RTEICT)*. Bangalore, India, pp.563-567.
- Sabzevar, A.P., and Stavrou, A., 2008. Universal Multi-factor Authentication Using Graphical Passwords. In: *Proceedings of the 2008 IEEE International Conference on Signal Image Technology and Internet Based Systems*, pp.625-632.
- Siddiqui, N., Misbah, U., Mohd, S., and Miftah, S., 2018. A Novel Shoulder-Surfing Resistant Graphical Authentication Scheme. In: *2018 4th International Conference on Computing Communication and Automation (ICCCA)*. IEEE, pp.1-5.
- Sobrado, L., and Birget, J., 2002. Graphical passwords. The Rutgers Scholar. An Electronic Bulletin for Undergraduate Research, 4, pp.1-9.
- Sun, H., Chen, S., Yeh, J., and Cheng, C., 2018. A shoulder surfing resistant graphical authentication system. *IEEE Transactions on Dependable and Secure Computing*, 15, pp.180-193.
- Susan, W., Jim, W., Jean, C., Alex, B., and Nasir, M., 2005. PassPoints: Design and longitudinal evaluation of a graphical password system. *International Journal of Human-Computer Studies*, 63(1-2), pp.102-127.
- Tu, J., Dahai, T., and Yun, W., 2021. An active-routing authentication scheme in MANET. *IEEE Access*, 9, pp.34276-34286.
- Wang, Z., Lingzhi, L., Ruohan, M., Ching-Nung, Y., Zhili, Z., and Hengfu, Y., 2022. Verification Grid and map slipping based graphical password against shoulder-surfing attacks. *Security and Communication Networks*, 2022, p.6778755.
- Xiaoyuan, S., Ying, Z., and Scott, G., 2005. Graphical Passwords: A Survey. In: *Proceedings of the 21st Annual Computer Security Applications*, pp.463-472.
- Zhao, H., and Li, X., 2007. S3PAS: A Scalable Shoulder-Surfing Resistant Textual-Graphical Password Authentication Scheme. In: *21st International Conference on Advanced Information Networking and Applications Workshops (AINAW'07)*, Niagara Falls, ON, Canada, pp.467-472.

# Flexible Job Shop Scheduling Problem-Solving Using Apiary Organizational-Based Optimization Algorithm

Mais A. Al-Sharqi<sup>1†</sup>, Ahmed T. Sadiq<sup>2</sup> and Safaa O. Al-mamory<sup>3</sup>

<sup>1</sup>Informatics Institute for Postgraduate Studies, Iraqi Commission for Computers and Informatics, Baghdad, Iraq

<sup>2</sup>Department of Computer Science, University of Technology, Baghdad, Iraq

<sup>3</sup>Department of Cybersecurity, College of Information Technology, University of Babylon, Babylon, Iraq

**Abstract**—Flexible job shop scheduling problem (FJSSP) is a complex and challenging problem that plays a crucial role in industrial and manufacturing production. FJSSP is an expansion of the standard job shop scheduling problem (JSSP). One of FJSSP's objectives that the manufacturing system competing for is minimizing the makespan. This paper uses a new nature-inspired metaheuristic optimization algorithm called the Apiary Organizational-Based Optimization algorithm (AOOA) to solve the FJSSP. This Algorithm simulates the organizational behavior of honeybees inside the apiary and translates their activities and vital processes during their lifecycle into phases that can solve such NP-hard problems. Two benchmark datasets, Brandimarte and Hurink, with 10 MK instances and 24 (edata, rdata, and vdata) instances respectively, were used to demonstrate the ability of AOOA to solve FJSSP. Moreover, the results of AOOA were compared with a set of state-of-the-art algorithms and statistically measured using the paired samples t-test and p-value, RPD, and group-based superiority statistical analysis to test its performance. AOOA outperformed Elitism GA, Enhanced GA, Improved GA, and MOGWO in solving all 10 MK instances and HICSA in solving 9 MK instances out of 10. Moreover, AOOA overcame CS, CS-BNG, CS-ILF, CHA, and MCA in solving 24, 12, 12, 23, and 24 instances of edata, rdata, and vdata, respectively. AOOA proved its robustness, showing promising outcomes.

**Index Terms**—Apiary Organizational-Based Optimization Algorithm, Flexible job shop scheduling, Makespan, Metaheuristic nature-inspired.

## I. INTRODUCTION

In the era of advanced technology and intelligence, time is important in manufacturing companies' competition. Production systems' scheduling is the means to utilize

available resources and achieve more productivity in less time (Meng, et al., 2024). The flexible job shop scheduling problem (FJSSP) is an expansion of the standard job shop scheduling problem (JSSP) which was debuted by Burcker and Schlie in 1990 (Jiang, Yu and Chen, 2023). FJSSP is a more difficult nondeterministic polynomial hard (NP-hard) problem compared to JSP (Wang, et al., 2024). This is because every job operation can be allocated to more than one machine and might have variable processing times (Song, et al., 2022). FJSSP is a single objective and multiobjective based on the optimization problem and the aim of the researcher. Reducing the entire processing time, or makespan, is one of the most important objective functions.

The FJSS has significant applications and advantages that gained the researchers' attention (Xie, et al., 2019). Some of these are: (1) Maximizing resource utilization by allocating machines, tools, and labor in the best possible way. (2) Minimizing makespan or the total time needed to finish all tasks to maximize time efficiency. (3) Meeting client delivery criteria and deadlines by effectively scheduling jobs and resources. (4) Handling intricate production processes because jobs in such industries may involve several procedures and call for various resources at different times. (5) Scheduling systems are meant to be flexible to adapt to unexpected changes such as machine failures, urgent orders, and job priority shifting. and (6) Cost reduction via FJSS effective scheduling which not only saves cost but also enhances competitiveness.

Nature-inspired metaheuristic algorithms are commonly used to address NP-hard problems. The Organizational-Based Optimization Algorithm (AOOA) proposed by Al-Sharqi, Al-Obaidi and Al-mamory (2024) is a new nature-inspired optimization algorithm that takes its steps from the organizational behavior of honeybees inside the apiary. The contribution of this paper is to employ the concept of multiple populations of the apiary to solve the NP-hard FJSSP and minimize the makespan using the AOOA. A benchmark function of thirty-four instances distributed on four datasets was used to test AOOA's ability to solve FJSSP. AOOA performance was compared with several well-known

ARO-The Scientific Journal of Koya University  
Vol. XII, No. 2 (2024), Article ID: ARO.11609. 13 pages  
Doi: 10.14500/aro.11609

Received: 28 April 2024; Accepted: 02 August 2024  
Regular research paper; Published: 24 August 2024

<sup>†</sup>Corresponding author's e-mail: Phd202110697@iips.edu.iq  
Copyright © 2024 Mais A. Al-Sharqi, Ahmed T. Sadiq and Safaa O. Al-mamory. This is an open-access article distributed under the Creative Commons Attribution License (CC BY-NC-SA 4.0).



metaheuristic algorithms and showed superiority in the results of scheduling time reduction (i.e., makespan).

The rest of this research is structured as follows. In Section 2, the related works are reviewed. Problem definition and an elucidating example are discussed in Section 3. Section 4 explains the AOOA used to solve FJSSP. In Section 5, the experimental results of FJSSP are presented and discussed. Finally, Section 6 concludes the key points of this work and highlights its possible future directions.

## II. RELATED WORK

Many metaheuristic algorithms were proposed to solve FJSSP. In FJSSP, time is the most crucial factor represented by makespan where the objective function is used to minimize it. As the proposed algorithm in this present research is inspired by the organizational behavior and lifecycle of honeybees in the apiary, there is no similar related literature. Accordingly, earlier works that were conducted to solve FJSSP are outlined here. Previous literature can be categorized into five groups based on natural operations; so many types of metaheuristic algorithms were proposed (Rajwar, Deep and Das, 2023). These algorithms can be categorized based on their underlying precept into four essential groups.

The first group can refer to evolutionary algorithms. They adopt Charles Darwin's theory of natural selection or survival of the fittest individuals. These algorithms are population-based such as Genetic Algorithms (GA), Differential Evolution (DE), Evolutionary Strategies (ES), Genetic Programming (GP), and Gene Expression Programming (GEP).

Xie and Chen (2018) designed the elitism genetic algorithm (ELGA) that was paired with the elitism strategy in external memory to define inaccurate time quota as interval grey processing time. The proposed algorithm solved FJSSP by minimizing the interval grey makespan.

Saving energy through production scheduling is a complicated nonlinear programming problem in flexible manufacturing systems with resource flexibility and complex constraints. This led Dai, et al. (2019) to utilize intelligent scheduling techniques to reduce energy consumption. Accordingly, a multi-objective optimization model for FJSSP with transportation restrictions was developed to decrease energy usage and makespan. This was integrated with the enhanced genetic algorithm (EHGA) in which the results supported decision-makers in flexible manufacturing systems.

In another research study, an improved genetic algorithm (IGA) was proposed by (Zhang, et al., 2020). This was performed by combining the setup and transportation times with the processing time. This was to minimize the makespan time, total setup time, and total transportation time. The research introduced three various methods to improve the quality and diversity of the initial population. The crossover was improved by artificial pairing to keep reasonable solutions and improve poor solutions effectively. Furthermore, a method for adaptive weighting was executed to modify mutation probability and search ranges for individuals within the population. Standard datasets were used to support the efficacy of the proposed methodology.

Another group of metaheuristics is the physical law-based algorithms. These algorithms depend on physical phenomena such as Simulated Annealing (SA), Tabu Search (TS), Variable Neighborhood Search (VNS), and Iterated Local Search (ILS) or chemical reactions such as ions motion optimization algorithm (IMOA), and thermal exchange optimization (TEO). A research study examined the benefits and drawbacks of using variable-size batching in manufacturing scheduling (Li, et al., 2022). It was noticed that besides the flexibility of this technique, it can increase not only energy consumption but also scheduling searches. To solve this difficulty, both the makespan and the total energy consumption were taken into account. Hence, a two-stage multi-objective hybrid algorithm (HICSA) was proposed. It combined the simulated annealing algorithm (SAA) with the imperialist competitive algorithm (ICA). Through various stages, the task sequence optimization and lot-splitting approach were enhanced by performing SAA with an iterated column generation algorithm. Experiments demonstrate the efficiency of the proposed HICSA algorithm.

The third group is miscellaneous algorithms (Rajwar, Deep and Das, 2023). These algorithms have influenced various theories on human behavior, game theory, mathematical theorems, politics, artificial thought, and other subjects. Zeidabadi and Dehghani proposed the Puzzle Optimization Algorithm (POA) to solve different optimization problems. The basic idea of the proposed POA is the mathematical simulation of solving a puzzle process (Zeidabadi and Dehghani, 2022). They considered that each member of the population is a puzzle that can be updated based on the guidance of other members and tried to complete its puzzle using the pieces suggested by other members.

The fourth group is represented by the nature-inspired and swarm intelligence algorithms. The nature-inspired algorithms are primarily based on animals' natural organizational behavior or biological processes during the lifecycle. This can help them survive and adapt to their environment to achieve their task efficiently. Swarm intelligence is a decentralized and self-organized system in which individuals perform tasks via collective and cooperative behavior. This is a population-based system that reflects the primary characteristics of a swarm system in adaptability (learning by doing), effective communication, and knowledge-sharing. Examples of such algorithms are Particle Swarm Optimization (PSO), Grey Wolf Optimizer (GWO), Firefly Algorithm (FA), Bat Algorithm (BA), Cuckoo Search (CS), and Artificial Bee Colony (ABC).

Al-Obaidi and Hussein, (2016) enhanced the Cuckoo Search algorithm (CS). The initial modification was made on the Best Neighbors Generation (CS-BNG) prediction, whereas the second was based on the utilization of Iterative Levy Flight (CS-ILF). Adjustments were made to the defining characteristics of the CS algorithm to improve search performance in the discrete state space. The proposed algorithms enhanced the solutions' quality and convergence rate. Several FJSSP benchmark situations were tested to evaluate the performance of the enhanced algorithms where they outperformed the original cuckoo search method.

To make a balance between production competence and environmental leverage, energy-efficient scheduling was

prioritized for green manufacturing (Luo, Zhang and Fan, 2019). The research addressed the multi-objective flexible job shop scheduling problem (MOFJSP) by employing variable processing speed to minimize makespan and total energy usage simultaneously. A multi-objective grey wolf optimization (MOGWO) algorithm, which utilizes a three-vector chromosomal encoding form, was introduced. The proposed algorithm takes into consideration the assignment of machines, speeds, and operation order. Extensive numerical experiments on thirty-five different scale benchmarks were conducted to verify the effectiveness of the suggested algorithm.

Based on the behavior of meerkats in the Kalahari Desert, Sadiq Al-Obaidi, Abdullah and Ahmed (2018) introduced the meerkat clan algorithm (MCA) as a new swarm intelligence algorithm. By utilizing meerkat behavior such as sentry, foraging, and babysitter, the algorithm partitions solution sets and executes operations specifically on the foraging set. It was found that the sentry identified the best solution. MCA was used in solving FJSSP where the experimental results showed better efficiency than the original Cuckoo Search, Artificial Fish Search, and Camel Herd algorithms.

Al-Obaidi et al. proposed a new nature-inspired algorithm that mimics camel herds' behavior (Sadiq Al-Obaidi, Abdullah and Ahmed, 2017). The role of the leader of each herd was considered, which guided the herd to the source of food and water depending on humidity value with neighboring strategy. FJSSP was undertaken as a case study to verify the proposed algorithm, Camel Herds Algorithm (CHA) in which the results proved the ability of CHA to find the optimal solution in the problem space. Table I summarizes the metaheuristic algorithms that tackle the FJSSP.

The Apiary Organizational-Based Optimization algorithm (AOOA) is a new nature-inspired algorithm that adopts the concept of multiple populations by introducing the apiary concept. AOOA simulates the organizational behavior of honeybees (the queen, drones, and workers) inside the apiary and the biological activities of workers' bees during their lifecycle. In this work, AOOA is employed to solve the FJSSP where the concept of multiple populations is utilized to minimize the makespan.

### III. PROBLEM DEFINITION

FJSSP is widely regarded as an NP-hard problem because of (i) deciding which operation can be served by the machine, which is known as the routing problem, and (ii) decisions on

the sequence of operations on each machine, which is known as the sequence problem (Alzaqebah, et al., 2022). According to Wu and Cai (2021); Jedrzejowicz and Wierzbowska (2022), the n multiplies m FJSSP is described as:

A set of  $n$  jobs  $J = \{J_1, J_2, \dots, J_n\}$  must be handled on a set of  $M$  machines  $M = \{M_1, M_2, \dots, M_n\}$ . Each job  $j \in J$  is characterized by a sequence of  $n_j$  operations  $O_j = \{O_{j,1}, O_{j,2}, \dots, O_{j, n_j}\}$ . Each task might have a unique sequence of operations. These operations must be executed in the specified order. The following constraints characterize the problem (Bissoli, et al., 2018; Amirteimoori, et al., 2022):

1. For every operation  $o \in O_j$  of job  $j$ , there is a subset  $MS_o$  of machines that execute the operation  $o$  with the duration  $dr$  for each  $r \in MS_o$ .
2. Each operation  $o$  must be processed on precisely one machine  $r \in MS_o$  and each machine can process exactly one operation at a time.
3. For each operation  $o$  processed on  $r$  machine, an uninterrupted duration  $dr$  is assigned.
4. Similar tasks adhere to a predetermined order.
5. Only one machine can be selected for each operation.
6. All jobs can be executed at the beginning of the work, and all machines are available.
7. As the processing proceeds, no preemptions or cancellations are permitted.
8. Each operation  $o$  has its beginning and end time  $co$ . A schedule is a set of all completion times  $\{co \mid o \in O_j, 1 \leq j \leq n\}$  that satisfies all aforementioned constraints.
9. The time necessary to complete whole tasks is known as makespan:  $C_{max} = \max_{o \in O_{j, 1 \leq j \leq n}} c_o$

The makespan is an optimization criterion which means identifying the schedule that minimizes it. Some constraints that may be considered with makespan finding in FJSSP:

- (i) All machines are obtainable at time zero, and job groups are launched.
- (ii) Machine setup time and the transportation time between operations are included in the processing time (Lu et al., 2019; Şahman, 2021; Zhang, et al., 2021; Zhu, et al., 2022)

#### A. An Elucidation Example

An example is provided here to explain FJSSP. Given a set of three jobs ( $J=3$ ) and three machines ( $M=3$ ). Each job consists of a sequence of operations ( $O_{j,i}$ , and  $i$  is the number of operations for the job), which must be processed

TABLE I  
OPTIMIZATION OBJECTIVE OF DIFFERENT ALGORITHMS FOR SOLVING FJSSP

Algorithm	Objective	Classification
ELGA	Minimize process time and makespan.	Evolutionary algorithm
IGA	Minimize processing time, set-up time, and transportation time.	Evolutionary algorithm
EHGA	Minimize Makespan	Evolutionary algorithm
HICSA	Minimize makespan and the total energy consumption	Physical law-based algorithms
CS, CS-BNG, CS-ILF	Minimize Makespan	Nature-inspired and swarm intelligence algorithms
MOGWO	Minimize Makespan and total energy usage	Nature-inspired and swarm intelligence algorithms
MCA	Minimize Makespan	Nature-inspired and swarm intelligence algorithms
CHA	Minimize Makespan	Nature-inspired and swarm intelligence algorithms

consecutively. As shown in Table I,  $J1$  has  $O11$ ,  $O12$ , and  $O13$ . Every operation can be assigned to at least one elected machine out of a predefined subset of machines with a specific operation processing time on that machine. In other words, it can be suggested that  $M1$  or  $M3$  for  $O11$  with times 3 or 6,  $M2$  or  $M3$  for  $O12$  with times 9 or 2, and  $M1$  or  $M2$  for  $O13$  with times 1 or 4, respectively.

$J2$  also consists of three operations:  $O21$ ,  $O22$ , and  $O23$ . Each has a subset of machines that can be allocated for each operation within the determined time.  $O21$  can be implemented on  $M1$ ,  $M2$  or  $M3$  with time =3, 7 or 1, respectively. Correspondingly,  $O22$  can be implemented on  $M2$  or  $M3$  with time = 7 or 1.  $O23$  can be performed on  $M1$  or  $M3$  with time = 8 or 5, respectively.

$J3$  has only two operations,  $O31$  and  $O32$ , with a subset of machines  $M1$  or  $M2$  for  $O31$  with times 3 or 6, and  $M2$  or  $M3$  for OS with times 5 or 9, respectively as they can be processed within the associated time. The details of the explained example are depicted in Table II.

#### IV. THE USE OF AOOA FOR FJSSP SOLVING

To employ AOOA for FJSSP solving, the population representation and the AOOA phases were determined and the phases were adapted to be convenient for FJSSP.

##### A. AOOA Stages

AOOA is a new nature-inspired metaheuristic optimization algorithm proposed by Al-Sharqi, Al-Obaidi and Al-mamory (2024). Its concept depends on organizational behavior and biological processes of honeybees inside the apiary. Moreover, AOOA simulates the activities of hives' members (queen, drone, and workers) during their lifecycle. AOOA consists of seven phases corresponding to honeybees' different activities inside the apiary. These phases are initialization, drone exchange, Fertilization and Bees Breeding, Worker Lifecycle, Queen Investiture, Fading out, and Swarming. Fig. 1 illustrates the AOOA phases.

In the AOOA first phase, the population is randomly initiated considering the constraints of each job. The population consists of ( $h$ ) numbers of hives each hive has a ( $b$ ) number of bees. The population size is calculated according to Equation (1).

$$N = h \times b \tag{1}$$

TABLE II  
THE PROCESSING TIME AND OPERATION ASSIGNMENT FOR A SET OF JOBS

Job	Operation	Machine		
		$M1$	$M2$	$M3$
$J1$	$O11$	3	-	6
	$O12$	-	9	2
	$O13$	1	4	-
$J2$	$O21$	3	7	1
	$O22$	-	7	1
	$O23$	8	-	5
$J3$	$O31$	3	6	-
	$O32$	-	5	9

For FJSSP, the population consists of ( $N$ ) numbers of hives and each hive has ( $r$ ) jobs and ( $m$ ) machines with ( $k$ ) operations for each machine. The population was represented as a set of hives, each with a three-dimensional array of jobs ( $job$ ), operations ( $op$ ), and machines ( $M$ ). Each 2D array (i.e. an individual) represents a possible scheduling solution as a sequence of different operations of jobs for each machine. Fig. 2 shows the population representation of FJSSP.

Drone exchange is the second phase of AOOA in which a randomly selected drone of one hive is exchanged with a drone from another hive as shown in Fig. 3.

In the third phase, the queen of each hive is fertilized with a list of fittest drones (those who have the minimum makespan) to produce ( $k$ ) new bees according to the fertilization equation shown in (2) under the control of  $fert_{ratio}$ .

$$New\_b_{H_i} = \begin{cases} Q_{H_i} + rand(d_{H_i} - Q_{H_i}), & \text{if } \left( \frac{d_{H_i} - Q_{H_i}}{d_{H_i}} \right) < 0.5 \\ \frac{1}{2}(Q_{H_i}) + rand \frac{1}{2}(d_{H_i}), & O.W \end{cases} \tag{2}$$

Where  $Q_{H_i}$ ,  $d_{H_i}$  represent the queen and drone of the  $i^{th}$  hive, respectively. At the same time, ( $rand$ ) represents a random number within [0,1].

To adapt AOOA to the FJSSP, a random number of machines (i.e., columns) is selected for each drone to fertilize the queen. The queen is searched for each job and operation ( $J_{n, nj}$ ) pair in the selected machine of the drone. If found, it will be the first index of the newly generated bee. If it is not found, search for the next pair. The remaining pairs of ( $J_{n, nj}$ ) will be given the rest of the indices as depicted in Fig. 4.

The newly generated bees are either drones or workers according to randomly generated value ( $rand$ ).

The worker lifecycle is the fourth phase. This phase simulates the behavior of workers bees. Each worker is assigned an age representing the likelihood of transforming an existing bee into a new one. From a biological standpoint, the lifespan of workers spans from a minimum of 1 day to a maximum of 60 days. The worker's life cycle is defined as the duration of the worker's life in terms of the number of days to perform simple or 1-opt (i.e., one-optima), 2-opt, and 3-opt based on the worker's age translocation as follows:

- 1–10: applying simple translocation on the worker (i),
- 11–25: applying 2-opt worker (i),
- 26–50: applying 3-opt worker (i),
- 51–60: applying 2-opt worker (i),
- Otherwise, dropping worker (i).

As noted in (3), each period involves a certain number of modifications on the chosen worker to generate a new bee.

$$NW_{H_i} = W_{H_i} + rand \cdot \left( \frac{W_{H_i}^{max\_g} - W_{H_i}^g}{W_{H_i}^{max\_g}} \right) \times W_{H_i} \tag{3}$$

Where  $W_{H_i}$  is the worker of the  $i^{th}$  hive, ( $rand$ ) is a random number within [0,1), and  $w^{max\_g}$  is the maximum age of the

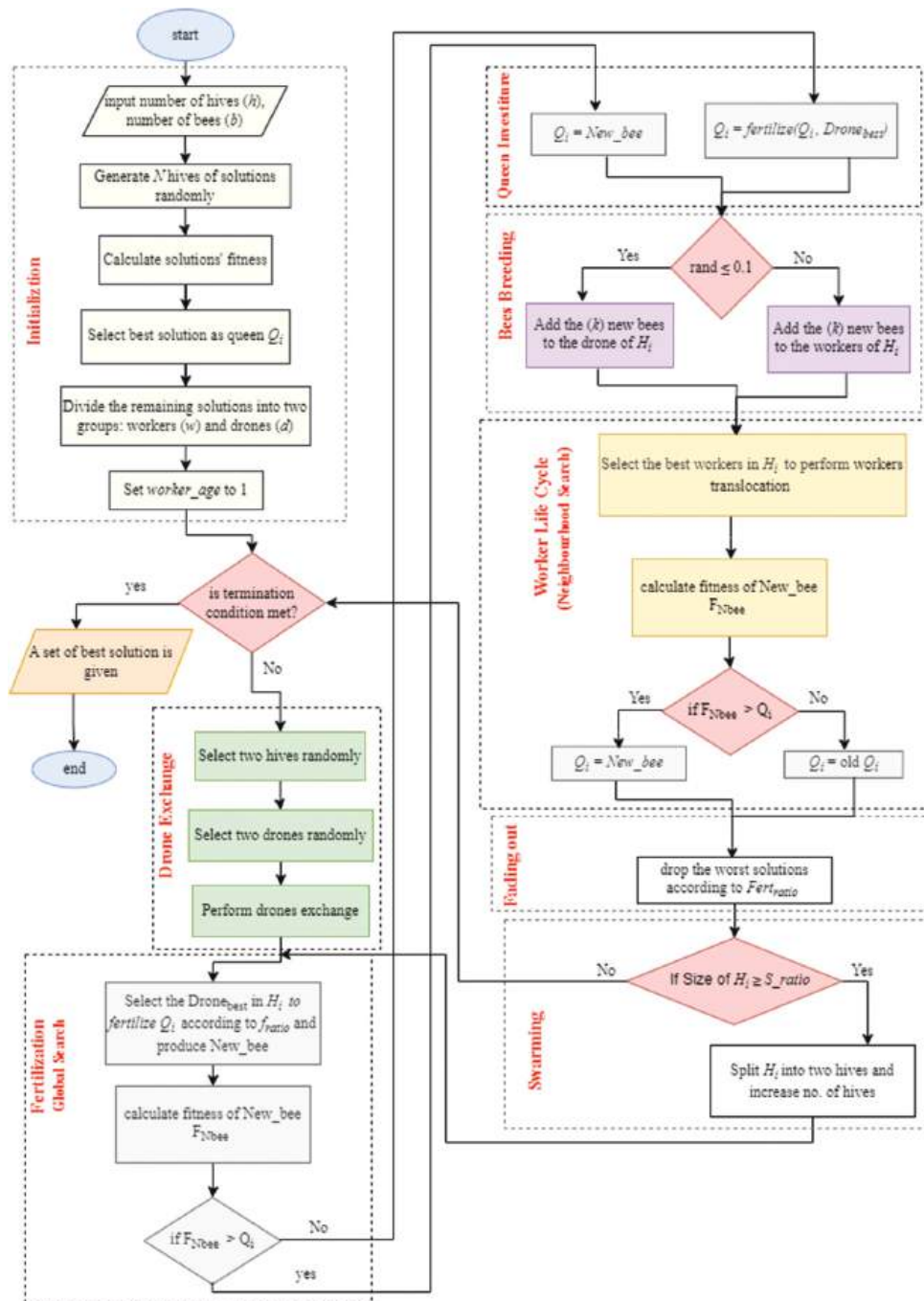


Fig. 1. Apiary Organizational-Based Optimization algorithm phases.

worker. To adopt AOOA for FJSSP, some columns are selected randomly where each column represents a specific machine. According to (*rand*), one, two, or three positions are randomly chosen to perform simple, 2-opt, or 3-opt translocations, respectively. An example of the worker translocation process is illustrated in Fig. 5, where the selected worker consists of five machines M1, M2, M3, M4, and M5. The randomly selected machines M1, M2, and M4 perform 3-opt, 2-opt, and simple (1-opt) respectively to generate a new bee. The fitness of new bees is calculated and it will be added to the population.

In the fifth phase, queen investiture, if the fitness of the new bee is better than the queen then the newly generated bee will be invested as the queen of this hive. This step

guides the search toward enhanced solutions by exploiting good ones to find the optimal solution(s).

Naturally, bees' max age is 60 days (sometimes less because of climate or diseases). They die at the end of their lifecycle. On the other hand, drones fade out after the queen fertilization process. AOOA simulates this behavior into the sixth phase, the fading out phase. AOOA controls the increasing size of populations in each hive of the apiary by adding a control parameter called  $fd_{ratio}$  which dominates the number of dying bees. The  $fd_{ratio}$  is ranged between 10% and 30% of bees (a nature-inspired ratio).

The last phase of AOOA's phases is the swarming phase. This phase mimics the swarming phenomenon of honeybee



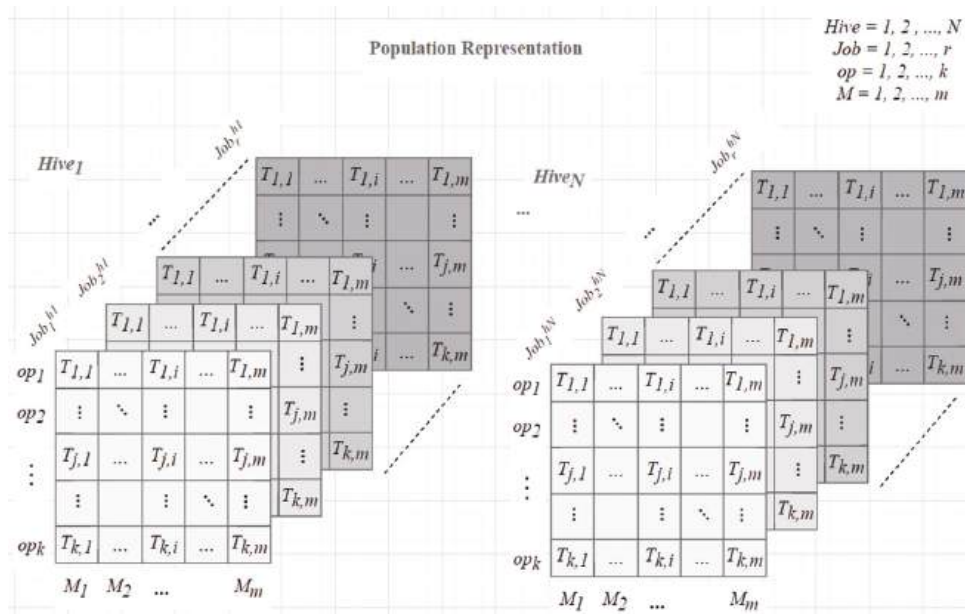


Fig. 2. Flexible job shop scheduling problem population representation.

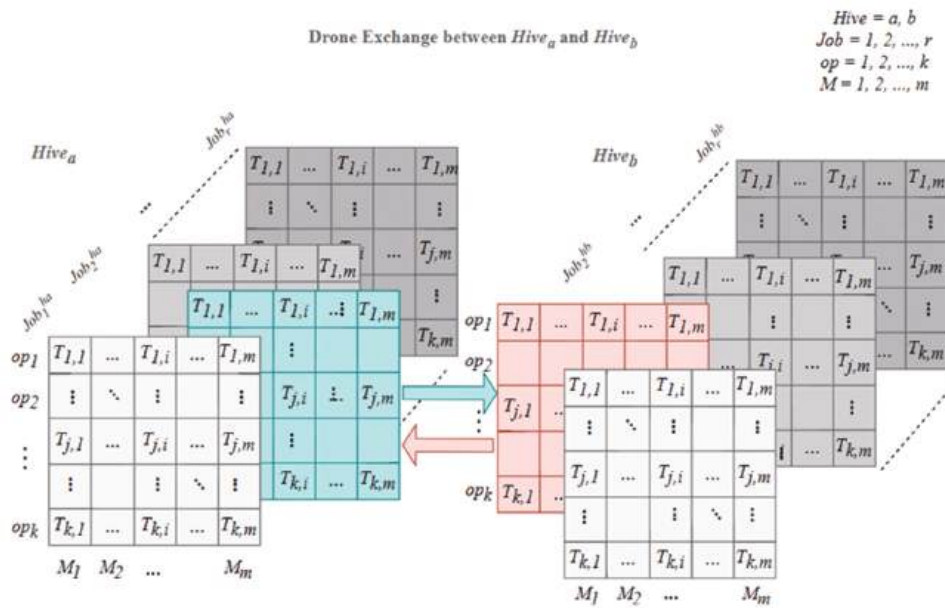


Fig. 3. Drone exchange between two randomly selected hives.

behavior in which the bees split the crowded hive into two hives.  $S_{ratio}$  is a control parameter added to manage the hive separation process. AOOA assumed that  $S_{ratio}$  is a user-defined value tuned based on the problem.

## V. EXPERIMENTS AND RESULTS

### A. Comparison of the AOOA Performance with the Competing Algorithms

To confirm the efficacy and resilience of the suggested AOOA, it was compared to some competing metaheuristic algorithms using a total of 34 benchmark instances, with different sizes (small, medium, and large) scales, were used in the experiments. These benchmark instances consist of

Brandimarte Data (BRdata) (MK01-MK10) (Brandimarte, 1993) and Hurink edata (la01-la08), rdata (la01-la08), and vdata (la01-la08) (Hurink, Jurisch and Thole, 1994).

The first test was to investigate the AOOA Performance of MK01-MK10 Instances. The effectiveness of AOOA's performance was validated by comparing the FJSSP results with other metaheuristic algorithms, namely, the ELGA, EHGA, IGA (Zhang et al., 2020), MOGW0 (Luo, Zhang and Fan, 2019), and HICSA (Li, et al., 2022). The experiments were performed through 10 independent runs and 50 iterations for each run. The experimental results were evaluated statistically using the relative percentage difference (RPD) and compared to the lower bound (LB). FJSSP has a known LB to which the results would be comparable. The calculation method of RPD is shown in (4)

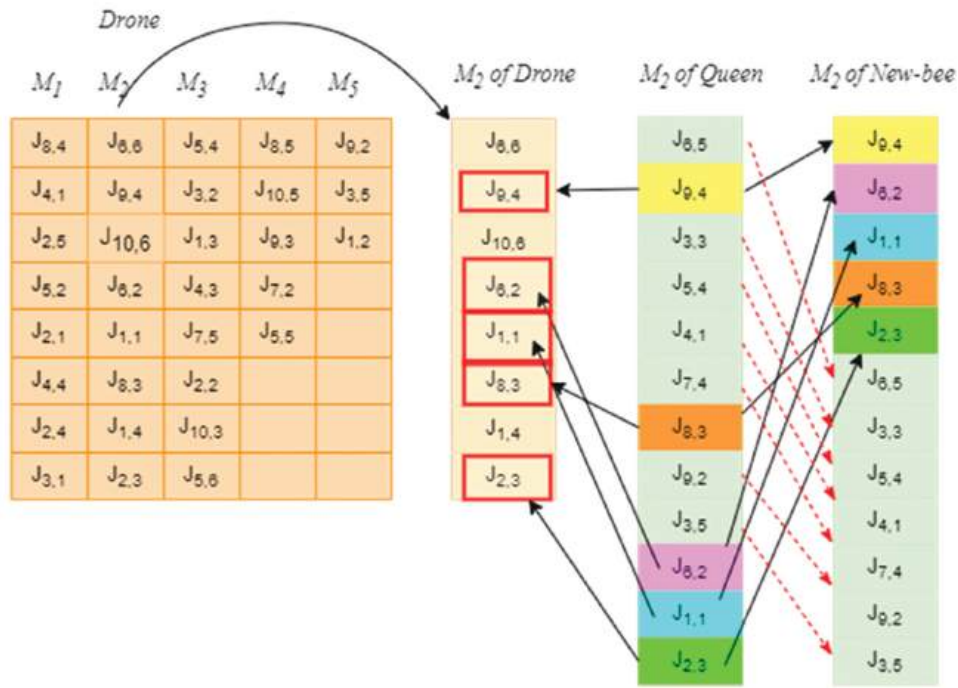


Fig. 4. Queen fertilization with the best drone.



Fig. 5. Worker translocation process.

$$RPD = \frac{Best C_{max} - LB}{\left(\frac{Best C_{max} + LB}{2}\right)} \times 100\% \quad (4)$$

Where Best \$C\_{max}\$ denotes the optimal makespan value produced by the algorithm, and LB denotes each instance's known lower bound value. Based on Equation 4, it can be noticed that a decrease in the RPD value could correspond to a reduction in the gap between an algorithm solution result and LB, indicating a closer match between the two values. Hence, if the optimal solution found by AOOA matches LB, the result of RPD equals zero. Table III displays the problem instance, its size, the LB, the minimum makespan (best \$C\_{max}\$),

RPD, and Rank which ranks the AOOA and the competing algorithms according to the RPD value. The optimal value acquired by AOOA has lower RPD values than other algorithms for MK01-MK09 and a competitive near-lower value for MK10. This reflects the excellent performance of AOOA. Best RPD results are denoted in bold and a zero-value means achieving LB. The optimal values that match LB are highlighted in bold with the (\*) symbol.

The outcomes confirm that AOOA achieves first rank in comparison with ELGA, EHGA, IGA, MOGWO, and HICSA in MK01-MK09 and comes in second rank in MK10. AOOA successfully found the optimal solution for MK08. This validates the superiority of the proposed algorithm in

TABLE III

COMPARISON RESULTS OF MAKESPAN FOR INSTANCES (MK01-MK10) WITH OTHER ALGORITHMS OF (LUO, ZHANG AND FAN, 2019) AND (LI, ET AL., 2022)

Instance	Size	LB	Parameter	ELGA	EHGA	IGA	MOGW	HICSA	AOOA
MK01	10×6	36	Best C <sub>max</sub>	82	68	65	70	87	<b>45</b>
			RPD	78	61.5	57.4	64.2	82.9	<b>22.2</b>
			Rank	5	3	2	4	6	<b>1</b>
MK02	10×6	24	Best C <sub>max</sub>	63	57	52	61	80	<b>41</b>
			RPD	62.9	89.7	81.5	73.7	87.1	<b>52.3</b>
			Rank	5	3	2	4	6	<b>1</b>
MK03	15×8	204	Best C <sub>max</sub>	350	330	313	322	445	<b>247</b>
			RPD	27.8	52.7	47.2	42.2	44.9	<b>19.1</b>
			Rank	2	6	5	3	4	<b>1</b>
MK04	15×8	48	Best C <sub>max</sub>	120	112	107	106	162	<b>65</b>
			RPD	85.7	80	76.1	75.3	108.6	<b>30.1</b>
			Rank	5	4	3	2	6	<b>1</b>
MK05	15×4	168	Best C <sub>max</sub>	314	284	276	287	447	<b>197</b>
			RPD	60.6	51.3	48.6	52.3	90.7	<b>15.9</b>
			Rank	5	3	2	4	6	<b>1</b>
MK06	10×15	33	Best C <sub>max</sub>	174	158	129	159	207	<b>121</b>
			RPD	136.2	130.9	118.5	131.3	145	<b>114.3</b>
			Rank	5	3	2	4	6	<b>1</b>
MK07	20×5	133	Best C <sub>max</sub>	311	265	267	255	418	<b>197</b>
			RPD	80.2	66.3	67	62.9	103.4	<b>38.8</b>
			Rank	5	3	4	2	6	<b>1</b>
MK08	20×10	523	Best C <sub>max</sub>	805	783	781	792	543	<b>523*</b>
			RPD	42.5	39.8	39.6	40.9	3.8	<b>0</b>
			Rank	6	4	3	5	2	<b>1</b>
MK09	20×10	299	Best C <sub>max</sub>	615	566	567	548	480	<b>424</b>
			RPD	69.1	61.7	61.9	58.8	46.5	<b>34.6</b>
			Rank	6	4	5	3	2	<b>1</b>
MK10	20×15	165	Best C <sub>max</sub>	474	494	424	457	304	357
			RPD	96.7	99.8	87.9	93.9	59.3	73.6
			Rank	5	6	3	4	1	2

exploring the search region and guiding the search toward optimal solutions.

The second test was to verify the robustness and effectiveness of AOOA on 24 instances of the Hurink dataset. The test was partitioned into three subtests: edata, rdata, and vdata with (la1- la8) for each. A set of five metaheuristic optimization algorithms: CS, CS-BNG, CS-ILF (Al-Obaidi and Hussein, 2016), CHA (Al-Obaidi, Abdullah and Ahmed, 2017), and MCA (Al-Obaidi, Abdullah and Ahmed, 2018) was selected for comparison with AOOA. Table IV illustrates the comparison results of Hurink datasets for the compared algorithms. The comparison was based on the RPD and ranked the competing algorithms accordingly. The best values are identified in bold type and the optimal values that match LB are highlighted in bold with the (\*) symbol.

The results show the superiority of AOOA rank in edata la1-la8 over other algorithms. In rdata, AOOA was superior in la2 and came in the second rank in la3 while it came in the third rank in la1, la4, la5, la6, la7, and la8. For the vdata, the results proved the supremacy of AOOA in la1, la3, and la7 instances while it came in the second rank in la4 and la5. AOOA came in the third rank in la6 and la7. For la2, AOOA is in the fourth rank of RPD.

TABLE IV

COMPARISON RESULTS OF MAKESPAN FOR HURINK WITH COMPETING ALGORITHMS

Instance	Size	LB	Parameter	CS	CS-BNG	CS-ILF	CHA	MCA	AOOA
edata-la1	10×5	609	Best C <sub>max</sub>	729	636	634	888	780	<b>614</b>
			RPD	17.9	4.3	4	37.3	24.6	<b>0.8</b>
			Rank	4	3	2	6	5	<b>1</b>
edata-la2	10×5	655	Best C <sub>max</sub>	783	707	694	823	724	<b>655*</b>
			RPD	17.8	7.6	5.8	22.7	10	<b>0</b>
			Rank	5	3	2	6	4	<b>1</b>
edata-la3	10×5	550	Best C <sub>max</sub>	663	593	588	732	706	<b>550*</b>
			RPD	18.6	7.5	6.7	28.4	24.8	<b>0</b>
			Rank	4	3	2	6	5	<b>1</b>
edata-la4	10×5	568	Best C <sub>max</sub>	709	620	619	830	703	<b>568*</b>
			RPD	22.1	8.8	8.6	37.5	21.2	<b>0</b>
			Rank	5	3	2	6	4	<b>1</b>
edata-la5	10×5	503	Best C <sub>max</sub>	605	525	526	681	655	<b>522</b>
			RPD	18.4	4.3	4.5	30.1	26.3	<b>3.7</b>
			Rank	4	2	3	6	5	<b>1</b>
edata-la6	15×5	833	Best C <sub>max</sub>	976	864	861	1332	1229	<b>833*</b>
			RPD	15.8	3.7	3.3	46.1	38.4	<b>0</b>
			Rank	4	3	2	6	5	<b>1</b>
edata-la7	15×5	762	Best C <sub>max</sub>	960	818	819	1255	1136	<b>785</b>
			RPD	23	7.1	7.2	48.9	39.4	<b>3</b>
			Rank	4	2	3	6	5	<b>1</b>
edata-la8	15×5	845	Best C <sub>max</sub>	1001	880	868	1257	1129	<b>852</b>
			RPD	16.9	4.1	2.7	39.2	28.8	<b>0.8</b>
			Rank	4	3	2	6	5	<b>1</b>
rdata-la1	10×5	570	Best C <sub>max</sub>	723	607	609	665	789	621
			RPD	23.7	6.3	6.6	15.4	32.2	8.6
			Rank	5	1	2	4	6	3
rdata-la2	10×5	529	Best C <sub>max</sub>	680	573	567	633	770	<b>554</b>
			RPD	25	8	6.9	17.9	37.1	<b>4.6</b>
			Rank	5	3	2	4	6	<b>1</b>
rdata-la3	10×5	477	Best C <sub>max</sub>	621	518	512	590	708	514
			RPD	26.2	8.2	7.1	21.2	39	7.5
			Rank	5	3	1	4	6	2
rdata-la4	10×5	502	Best C <sub>max</sub>	646	542	538	623	720	551
			RPD	25.1	7.7	6.9	21.5	35.7	9.3
			Rank	5	2	1	4	6	3
rdata-la5	10×5	457	Best C <sub>max</sub>	577	484	480	568	667	489
			RPD	23.2	5.7	4.9	21.7	37.4	6.8
			Rank	5	2	1	4	6	3
rdata-la6	15×5	799	Best C <sub>max</sub>	974	832	821	1044	1252	857
			RPD	19.7	4	2.7	26.6	44.2	7
			Rank	4	2	1	5	6	3
rdata-la7	15×5	749	Best C <sub>max</sub>	917	779	776	1005	1123	802
			RPD	20.2	3.9	3.5	29.2	40	6.8
			Rank	4	2	1	5	6	3
rdata-la8	15×5	765	Best C <sub>max</sub>	938	793	790	1061	1203	823
			RPD	20.3	3.6	3.2	32.4	44.5	7.3
			Rank	4	2	1	5	6	3
vdata-la1	10×5	570	Best C <sub>max</sub>	728	613	609	671	815	<b>607</b>
			RPD	24.3	7.3	6.6	16.3	35.4	<b>6.3</b>
			Rank	5	3	2	4	6	<b>1</b>
vdata-la2	10×5	529	Best C <sub>max</sub>	675	565	564	560	770	574
			RPD	24.3	6.6	6.4	5.7	37.1	8.2
			Rank	5	3	2	1	6	4
vdata-la3	10×5	477	Best C <sub>max</sub>	627	515	520	574	706	<b>515</b>
			RPD	27.2	7.7	8.6	18.5	38.7	<b>7.7</b>
			Rank	4	1	2	3	5	<b>1</b>
vdata-la4	10×5	502	Best C <sub>max</sub>	652	534	531	641	706	534

(Contd...)

TABLE IV  
(CONTINUED)

Instance	Size	LB	Parameter	CS	CS-BNG	CS-ILF	CHA	MCA	AOOA
vdata-la5	10×5	457	RPD	26	6.2	5.6	24.3	33.8	6.2
			Rank	4	2	1	3	5	2
			Best $C_{max}$	587	485	499	531	645	499
vdata-la6	15×5	799	RPD	24.9	5.9	8.8	15	34.1	8.8
			Rank	4	1	2	3	5	2
			Best $C_{max}$	981	826	821	1042	1212	839
vdata-la7	15×5	749	RPD	20.4	3.3	2.7	26.4	41.1	4.9
			Rank	4	2	1	5	6	3
			Best $C_{max}$	941	774	773	968	1130	796
vdata-la8	15×5	765	RPD	22.7	3.3	3.2	25.5	40.6	6.1
			Rank	4	2	1	5	6	3
			Best $C_{max}$	952	779	787	908	1181	<b>777</b>
			RPD	21.8	1.8	2.8	17.1	42.8	<b>1.6</b>
			Rank	5	2	3	4	6	<b>1</b>

### B. Sensitivity Analysis

AOOA population consists of two critical parameters: the number of hives ( $h$ ) and bees ( $b$ ). As the number of machines and jobs vary in FJSSP, the population size of AOOA should also vary to fit the search space. Therefore, it makes sense to inspect the impact of different ( $h$ ) and ( $b$ ). For this reason, two scales were used to fit all sizes of  $N \times M$  where  $N$  is the number of jobs and  $M$  is the number of machines. SSA and MSA apiary were tested for each instance of benchmark data with small, medium, and large-sized jobs and machines. This can disclose whether SSA can find the best results, so there is no need to increase computational complexity by increasing population size and its consequent computations using MSA. Table V illustrates the apiary scales of FJSSP. Each instance was tested against all hive sizes with all bees' numbers. However, experiments manifest that increasing ( $h$ ) and ( $b$ ) to be convenient for LSA yields increasing computational time at a dramatic rate. Therefore, MSA was adopted to include both medium and large-scale FJSS problem sizes.

By observing the results of all 34 instances illustrated in Table VI, it is clear that the minimum makespan was found using SSA for small factories with small-scale jobs and machines of MK instances (i.e., MK1 and MK2). When the size of factories increases, the minimum makespan was found in MSA, MK3, MK5, MK7, MK10. In MK4 and MK6, there was a slight difference in SSA and MSA results in both best and average makespan where the best was found in SSA. In MK8 and MK9 both SSA and MSA gave the same results. Larger values than eight and seventy for  $h$  and  $b$ , respectively failed to achieve closer results to the optimal solution but this significantly increased the implementation time. Moreover, most optimal solutions (i.e., minimum makespan) appeared in the early iterations, and the ultimate solution appeared in iteration 50.

It was evident in the results of edata, rdata, and vdata that 70% of best  $C_{max}$  was found using MSA in edata (la1, la6, la7, and la8), rdata (la1, la4, la6, la7, and la8), and vdata (la2, la4, la5, la7, and la8). Edata la2, la3, and la4, SSA, and MSA gave the same results, but the mean  $C_{max}$  of MSA was better than the  $C_{max}$  of SSA. Therefore, edata la2, la3, and

TABLE V  
APIARY PARAMETER VALUES ACCORDING TO FJSSP PROBLEM SIZE

Problem size		Apiary Scale		Number of Hives	Number of Bees
Job	Machines				
Small	10	5	Small-scale	3	30
	10	6	apiary (SSA)	4	40
Medium	15	4		5	50
	15	5	Medium scale	6	50
Large	15	8	apiary (MSA)	7	60
	20	5		8	70
	10	15			
	20	10			
	20	15			

la4 results were counted within the 17 instances of the best  $C_{max}$  of MSA (i.e. 70%). The best  $C_{max}$  resulting from SSA was 7 instances with 30% in edata (la5), rdata (la2, la3, and la5), and vdata (la1, la3, and la6). The results proved that the effect of increasing population size using MSA on enhancing the minimum and mean makespan is bigger for MS factories than for SS factories. The best values of (Best  $C_{max}$ ) and (Mean  $C_{max}$ ) are identified in bold type.

### C. Performance Analysis

In this section, the results and findings analysis will be discussed. The discussion is divided into two parts: statistical performance analysis of AOOA with the competing algorithms and limitations.

The first part is divided into two subparts. The first subpart investigates the relationship between the AOOA and the five competing algorithms using a paired samples t-test. We analyzed the data from samples of the six participant algorithms, categorizing them based on (ELGA, EHGA, IGA, MOGWO, HICSA, and AOOA) for MK instances and (CS, CS-BNG, CS-ILF, CHA, MCA, and AOOA) for Hurink dataset. Table VII shows the p-values for the MK01-MK10, edata, rdata, and vdata instances of the AOOA vs. the competing algorithms with degrees of freedom ( $df=8$ ), sample size ( $N=9$ ), and significance level ( $\alpha = 0.05$ ). The p-values  $\geq (\alpha)$  are highlighted in bold type.

The paired samples t-test yielded a  $t$  statistic and the calculated p-value shown in Table VII, indicating an extremely statistically significant difference between AOOA and other algorithms at the  $\alpha = 0.05$  level. The low p-values of AOOA (except for edata5, rdata2 - rdata5 of CS-BNG, and CS-ILF) indicate strong evidence against the null hypothesis proving that the results are significant.

The second subpart measures the AOOA performance for the 34 instances compared to the competing algorithms using group-based superiority in finding the best makespan. AOOA outperformed ELGA, EHGA, IGA, and MOGWO in 10 MK instances with 100% superiority. On the other hand, it outperformed HICSA in 9 MK instances (MK1-MK9) and competed with HICSA on MK10. For edata, AOOA was superior to all competing algorithms: CS, CS-BNG, CS-ILF, CHA, and MCA with 100% superiority. In rdata and vdata, AOOA was superior to CS and MCA in all 16 instances while it was superior to CHA in all eight rdata instances and seven

TABLE VI  
BEST AND MEAN MAKESPAN RESULTS USING SSA AND MSA OF MK1-MK10

Instance	Apiary Scale	Best C <sub>max</sub>	Mean C <sub>max</sub>	Instance	Apiary Scale	Best C <sub>max</sub>	Mean C <sub>max</sub>
MK1	SSA	<b>45</b>	54.1	edata-la8	SSA	854	<b>878.7</b>
	MSA	46	53.9		MSA	<b>852</b>	888.2
MK2	SSA	<b>41</b>	47.8	rdata-la1	SSA	632	678.9
	MSA	43	<b>46</b>		MSA	<b>621</b>	<b>667.2</b>
MK3	SSA	257	274.3	rdata-la2	SSA	<b>554</b>	640
	MSA	<b>247</b>	<b>270.2</b>		MSA	588	<b>622.3</b>
MK4	SSA	<b>65</b>	85.2	rdata-la3	SSA	<b>514</b>	592.4
	MSA	70	<b>81.1</b>		MSA	525	<b>573.9</b>
MK5	SSA	199	213.4	rdata-la4	SSA	562	611.1
	MSA	<b>197</b>	<b>209.7</b>		MSA	<b>551</b>	<b>595.3</b>
MK6	SSA	<b>121</b>	138.8	rdata-la5	SSA	<b>489</b>	549.1
	MSA	125	<b>135.5</b>		MSA	517	<b>548.2</b>
MK7	SSA	203	228.6	rdata-la6	SSA	894	927.9
	MSA	<b>197</b>	<b>227.1</b>		MSA	<b>857</b>	<b>914.73</b>
MK8	SSA	523	523	rdata-la7	SSA	814	863.9
	MSA	523	523		MSA	<b>802</b>	<b>852.8</b>
MK9	SSA	424	454.5	rdata-la8	SSA	834	885.4
	MSA	424	<b>450.8</b>		MSA	<b>823</b>	<b>884.2</b>
MK10	SSA	363	<b>378.6</b>	vdata-la1	SSA	<b>607</b>	685.2
	MSA	<b>357</b>	381.6		MSA	644	<b>677.4</b>
edata-la1	SSA	637	672.9	vdata-la2	SSA	576	637.3
	MSA	<b>614</b>	<b>650</b>		MSA	<b>574</b>	<b>627.6</b>
edata-la2	SSA	655	673.9	vdata-la3	SSA	<b>515</b>	573.7
	MSA	655	<b>663.2</b>		MSA	539	<b>565.1</b>
edata-la3	SSA	550	566.3	vdata-la4	SSA	545	603.7
	MSA	550	<b>563.9</b>		MSA	<b>534</b>	<b>586.4</b>
edata-la4	SSA	568	597.5	vdata-la5	SSA	503	557.8
	MSA	568	<b>587.8</b>		MSA	<b>499</b>	<b>538.2</b>
edata-la5	SSA	<b>522</b>	560.3	vdata-la6	SSA	<b>839</b>	<b>911.3</b>
	MSA	524	<b>551.9</b>		MSA	870	920.4
edata-la6	SSA	849	909.3	vdata-la7	SSA	810	871.4
	MSA	<b>833</b>	<b>892.4</b>		MSA	<b>796</b>	<b>866.7</b>
edata-la7	SSA	795	844.7	vdata-la8	SSA	834	902.2
	MSA	<b>785</b>	<b>826.7</b>		MSA	<b>777</b>	<b>874.5</b>

TABLE VII

PAIRED SAMPLES T-TEST AND P VALUE FOR AOOA VERSUS OTHER ALGORITHMS OF INSTANCES MK01-10, EDATA01-08, RDATA01-08, AND VDATA01-08, DF=8, N=9, A=0.05

PI	AOOA VS.	t	Sig. (2-tailed) p-value	PI	AOOA VS.	t	Sig. (2-tailed) p-value
MK1	ELGA	26.407	4.54629E-09	MK6	ELGA	21.964	1.94932E-08
	EHGA	18.141	8.75736E-08		EHGA	55.763	1.18696E-11
	IGA	15.656	2.76462E-07		IGA	7.069	0.00011
	MOGWO	20.346	3.56036E-08		MOGWO	26.382	4.58033E-09
	HICSA	26.328	4.65453E-09		HICSA	52.178	2.01724E-11
MK2	ELGA	20.084	3.94225E-08	MK7	ELGA	35.207	4.63615E-10
	EHGA	17.605	1.10756E-07		EHGA	17.519	1.15079E-07
	IGA	9.197	1.57994E-05		IGA	18.973	6.16255E-08
	MOGWO	10.670	5.22089E-06		MOGWO	14.493	5.02867E-07
	HICSA	27.086	3.71812E-09		HICSA	69.046	2.15518E-12
MK3	ELGA	27.721	3.09392E-09	MK8	ELGA	149.000	4.60432E-15
	EHGA	28.156	2.73463E-09		EHGA	229.399	1.45963E-16
	IGA	20.616	3.20934E-08		IGA	188.259	7.09268E-16
	MOGWO	23.233	1.25126E-08		MOGWO	155.568	3.26094E-15
	HICSA	46.764	4.83285E-11		HICSA	19.228	5.54874E-08
MK4	ELGA	66.287	2.98493E-12	MK9	ELGA	70.795	1.76492E-12
	EHGA	31.825	1.03469E-09		EHGA	39.941	1.69834E-10
	IGA	33.942	6.20127E-10		IGA	40.510	1.51749E-10

(Contd...)

TABLE VII  
(CONTINUED)

PI	AOOA VS.	t	Sig. (2-tailed) p-value	PI	AOOA VS.	t	Sig. (2-tailed) p-value
MK5	MOGWO	22.277	1.74305E-08	MK10	MOGWO	40.827	1.42600E-10
	HICSA	92.655	2.05504E-13		HICSA	16.397	1.92877E-07
	ELGA	83.326	4.79935E-13		ELGA	33.070	7.62695E-10
	EHGA	45.667	5.84033E-11		EHGA	36.765	3.28452E-10
	IGA	59.713	6.87372E-12		IGA	21.805	2.06362E-08
edata-la1	MOGWO	50.579	2.58547E-11	edata-la5	MOGWO	43.756	8.21037E-11
	HICSA	153.139	3.69824E-15		HICSA	-9.330	1.42094E-05
	CS	23.465	1.15698E-08		CS	13.496	8.71455E-07
	CS-BNG	1.982	0.08280		CS-BNG	1.197	<b>0.26552</b>
	CS-ILF	2.366	0.04555		CS-ILF	0.965	<b>0.36276</b>
edata-la2	CHA	38.736	2.16744E-10	edata-la6	CHA	37.789	2.63954E-10
	MCA	18.805	6.60635E-08		MCA	25.873	5.34432E-09
	CS	73.041	1.37505E-12		CS	39.804	1.74550E-10
	CS-BNG	39.179	1.98018E-10		CS-BNG	11.994	2.15235E-06
	CS-ILF	21.290	2.49111E-08		CS-ILF	6.337	0.00022
edata-la3	CHA	97.054	1.41831E-13	edata-la7	CHA	133.905	1.08180E-14
	MCA	74.046	1.23295E-12		MCA	132.679	1.16434E-14
	CS	131.109	1.28065E-14		CS	64.626	3.65552E-12
	CS-BNG	23.170	1.27823E-08		CS-BNG	6.818	0.00014
	CS-ILF	36.156	3.75183E-10		CS-ILF	7.230	8.98005E-05
edata-la4	CHA	231.587	1.35290E-16	edata-la8	CHA	95.006	1.68205E-13
	MCA	130.255	1.34932E-14		MCA	81.851	5.53566E-13
	CS	44.260	7.49525E-11		CS	57.522	9.26340E-12
	CS-BNG	20.171	3.81019E-08		CS-BNG	14.661	4.60020E-07
	CS-ILF	14.648	4.63250E-07		CS-ILF	6.058	0.00030
rdata-la1	CHA	54.677	1.38874E-11	rdata-la5	CHA	137.617	8.69330E-15
	MCA	45.279	6.25117E-11		MCA	104.127	8.08257E-14
	CS	46.593	4.97624E-11		CS	8.074	4.08754E-05
	CS-BNG	-3.386	0.00956		CS-BNG	-1.584	<b>0.15175</b>
	CS-ILF	-3.146	0.01369		CS-ILF	-1.460	<b>0.18245</b>
rdata-la2	CHA	4.441	0.00217	rdata-la6	CHA	7.829	5.09974E-05
	MCA	31.532	1.11355E-09		MCA	20.961	2.81675E-08
	CS	14.019	6.50345E-07		CS	16.055	2.27228E-07
	CS-BNG	1.609	<b>0.14633</b>		CS-BNG	4.677	0.00159
	CS-ILF	0.192	<b>0.85243</b>		CS-ILF	4.191	0.00303
rdata-la3	CHA	6.378	0.00021	rdata-la7	CHA	9.994	8.52846E-06
	MCA	25.276	6.42756E-09		MCA	4.314	0.00257
	CS	9.365	1.38234E-05		CS	25.866	5.35586E-09
	CS-BNG	-0.487	<b>0.63925</b>		CS-BNG	-7.338	8.08969E-05
	CS-ILF	-1.953	<b>0.08656</b>		CS-ILF	-11.057	3.99117E-06
rdata-la4	CHA	6.789	0.00014	rdata-la8	CHA	61.686	5.30169E-12
	MCA	16.631	1.72711E-07		MCA	85.750	3.81619E-13
	CS	11.872	2.32641E-06		CS	34.023	6.08574E-10
	CS-BNG	-0.527	<b>0.61264</b>		CS-BNG	-7.780	5.33524E-05
	CS-ILF	-0.192	<b>0.85272</b>		CS-ILF	-14.344	5.44727E-07
vdata-la1	CHA	8.752	2.27471E-05	vdata-la5	CHA	57.098	9.82709E-12
	MCA	17.356	1.23754E-07		MCA	112.547	4.34061E-14
	CS	17.314	1.26166E-07		CS	32.655	8.43151E-10
	CS-BNG	4.825	0.00131		CS-BNG	4.206	0.00297
	CS-ILF	4.851	0.00127		CS-ILF	5.145	0.00088
vdata-la2	CHA	10.120	7.76489E-06	vdata-la6	CHA	7.075	0.00010
	MCA	7.542	6.66079E-05		MCA	8.051	4.17167E-05
	CS	17.408	1.20921E-07		CS	11.565	2.83930E-06
	CS-BNG	4.513	0.00197		CS-BNG	4.736	0.00147
	CS-ILF	4.529	0.00193		CS-ILF	4.664	0.00161
vdata-la3	CHA	4.489	0.00203	vdata-la7	CHA	8.006	4.34181E-05
	MCA	7.665	5.93336E-05		MCA	4.348	0.00245
	CS	14.976	3.90236E-07		CS	17.341	1.24636E-07
	CS-BNG	5.267	0.00076		CS-BNG	4.316	0.00256

(Contd...)

TABLE VII  
(CONTINUED)

PI	AOOA VS.	t	Sig. (2-tailed) p-value	PI	AOOA VS.	t	Sig. (2-tailed) p-value
vdata-la4	CS-ILF	5.827	0.00039	vdata-la8	CS-ILF	4.138	0.00326
	CHA	8.835	2.12313E-05		CHA	14.593	4.76762E-07
	MCA	8.721	2.33440E-05		MCA	5.555	0.00054
	CS	20.845	2.94166E-08		CS	11.476	3.01076E-06
	CS-BNG	5.574	0.00053		CS-BNG	4.787	0.00138
	CS-ILF	5.513	0.00057		CS-ILF	5.662	0.00047
	CHA	18.180	8.61057E-08		CHA	14.528	4.93665E-07
	MCA	8.517	2.77472E-05		MCA	5.558	0.00054

TABLE VIII  
GROUP-BASED SUPERIORITY OF AOOA

Dataset	Number of Instances Where AOOA is Better				
	ELGA	EHGA	IGA	MOGWO	HICSA
MK1-10	8	8	8	8	7
	CS	CS-BNG	CS-ILF	CHA	MCA
edata	8	8	8	8	8
rdata	8	2	1	8	8
vdata	8	2	3	7	8
Total instances	24	12	12	23	24

vdata instances (la1, la3-la8). AOOA outperformed CS-BNG in two rdata instances (la2, la3) while overcame CS-ILF algorithm in la2. However, AOOA overcame CS-BNG in two vdata instances (la1, la8) and was equal to it in rank in la3 and la4, while overcame CS-ILF in three vdata (la1, la3, and la8) and was equal to it in rank in la2. Finally, it was found that AOOA achieved better results over CS, CS-BNG, CS-ILF, CHA, and MCA in solving 24, 12, 12, 23, and 24 FJSSP instances, respectively. Table VIII shows the AOOA superiority over competing algorithms for edata, rdata, and vdata datasets.

We believe that there are several factors behind the superiority of AOOA which can be summarized in (i) The concept of multiple populations generating a large diverse population, (ii) good exploration and exploitation mechanisms, (iii) two sources to generate new solutions represented in queen fertilization and worker lifecycle, and (iv) drone exchange, fading out, and swarming increase diversity and prevent stagnation.

Although AOOA presented a superior performance, it still has some limitations. AOOA used classical 34 instances of FJSS benchmark datasets while other benchmark datasets can be used such as (Kacem, Hammadi and Borne, 2002; Fattahi, Saidi Mehrabad and Jolai, 2007), etc. More objective functions and constraints can be considered such as maximizing the profit by resource utilization or machine performance, minimizing transportation time, process time, job delay, and energy consumption. Furthermore, enhancement can be made to AOOA so that better results are obtained.

VI. CONCLUSION

This paper introduced a solution to one of the NP-hard real-world problems, namely the FJSSP using AOOA, a

new nature-inspired metaheuristic optimization algorithm. Its main structure was based on the organizational behavior of honey bees inside the apiary. Benchmark datasets of thirty-four instances of various sizes (small, medium, and large) scales were employed in the experiments to find the minimum makespan ( $C_{max}$ ). The results were compared to ten of the state-of-the-art algorithms, five for BRdata and five for Hurink edata, rdata, and vdata. They were statistically assessed using the paired samples t-test and p-value, RPD, and group-based superiority statistical analysis to prove the AOOA performance. The p-values of AOOA at  $\alpha = 0.05$  level (except for MK09 and edata02) indicate strong evidence against the null hypothesis proving that the results are significant. AOOA outperformed ELGA, EHGA, IGA, and MOGWO in solving all 10 MK instances and HICSA in solving 9 MK instances. Moreover, AOOA overcame CS, CS-BNG, CS-ILF, CHA, and MCA in solving 24, 12, 12, 23, and 24 instances of edata, rdata, and vdata, respectively. In many instances, AOOA achieved LB or near-optimal solutions to compete with other algorithms. The research demonstrated that the new nature-inspired algorithm can solve NP-hard problems effectively and efficiently. The overall findings were promising in comparison with some metaheuristic optimization algorithms.

REFERENCES

Al-Obaidi, A.T.S., Abdullah, H.S., and Ahmed, Z.O., 2017. Camel herds algorithm: A new swarm intelligent algorithm to solve optimization problems. *International Journal on Perceptive and Cognitive Computing*, 3(1), pp.6–10.

Al-Obaidi, A.T.S., Abdullah, H.S., and Ahmed, Z.O., 2018. Meerkat clan algorithm: A new swarm intelligence algorithm. *Indonesian Journal of Electrical Engineering and Computer Science*, 10(1), pp.354-360.

Al-Obaidi, A.T.S., and Hussein, S.A., 2016. Two improved Cuckoo search algorithms for solving the flexible job-shop scheduling problem. *International Journal on Perceptive and Cognitive Computing*, 2(2), pp.25-31.

Al-Sharqi, M.A., Al-Obaidi, A.T.S., and Al-mamory, S.O., 2024. Apiary organizational-based optimization algorithm: A new nature-inspired metaheuristic algorithm. *International Journal of Intelligent Engineering and Systems*, 17(3), pp.783-801.

Alzaqebah, M., Jawarneh, S., Alwohaibi, M., Alsmadi, M.K., Almarashdeh, I., and Mohammad, R.M.A., 2022. Hybrid brain storm optimization algorithm and late acceptance hill climbing to solve the flexible job-shop scheduling problem. *Journal of King Saud University -Computer and Information Sciences*, 34(6), pp.2926-2937.

Amirteimoori, A., Mahdavi, I., Solimanpur, M., Ali, S.S., and Tirkolaei, E.B.,

2022. A parallel hybrid PSO-GA algorithm for the flexible flow-shop scheduling with transportation. *Computers and Industrial Engineering*, 173, p.108672.
- Bissoli, D.C., Altoe, W.A.S., Mauri, G.R., and Amaral, A.R.S., 2018. A Simulated Annealing Metaheuristic for the Bi-objective Flexible Job Shop Scheduling Problem. In: *2018 International Conference on Research in Intelligent and Computing in Engineering (RICE)*. pp.1-6.
- Brandimarte, P., 1993. Routing and scheduling in a flexible job shop by Tabu search. *Annals of Operations Research*, 41(3), pp.157-183.
- Dai, M., Tang, D., Giret, A., and Salido, M.A., 2019. Multi-objective optimization for energy-efficient flexible job shop scheduling problem with transportation constraints. *Robotics and Computer-Integrated Manufacturing*, 59, pp.143-157.
- Fattahi, P., Saidi Mehrabad, M., and Jolai, F., 2007. Mathematical modeling and heuristic approaches to flexible job shop scheduling problems. *Journal of Intelligent Manufacturing*, 18(3), pp.331-342.
- Hurink, J., Jurisch, B., and Thole, M., 1994. Tabu search for the job-shop scheduling problem with multi-purpose machines. *OR Spektrum*, 15(4), pp.205-215.
- Jiang, M., Yu, H., and Chen, J., 2023. Improved self-learning genetic algorithm for solving flexible job shop scheduling. *Mathematics*, 11(22), p.4700.
- Kacem, I., Hammadi, S., and Borne, P., 2002. Approach by localization and multiobjective evolutionary optimization for flexible job-shop scheduling problems. *IEEE Transactions on Systems, Man and Cybernetics Part C: Applications and Reviews*, 32(1), pp.1-13.
- Li, Y., Yang, Z., Wang, L., Tang, H., Sun, L., and Guo, S., 2022. A hybrid imperialist competitive algorithm for energy-efficient flexible job shop scheduling problem with variable-size sublots. *Computers and Industrial Engineering*, 172, p.108641.
- Lu, C., Gao, L., Pan, Q., Li, X., and Zheng, J., 2019. A multi-objective cellular grey wolf optimizer for hybrid flowshop scheduling problem considering noise pollution. *Applied Soft Computing Journal*, 75, pp.728-749.
- Luo, S., Zhang, L., and Fan, Y., 2019a. Energy-efficient scheduling for multi-objective flexible job shops with variable processing speeds by grey wolf optimization. *Journal of Cleaner Production*, 234, pp.1365-1384.
- Luo, S., Zhang, L., and Fan, Y., 2019b. Energy-efficient scheduling for multi-objective flexible job shops with variable processing speeds by grey wolf optimization. *Journal of Cleaner Production*, 234, pp.1365-1384.
- Meng, L., Duan, P., Gao, K., Zhang, B., Zou, W., Han, Y., and Zhang, C., 2024. MIP modeling of energy-conscious FJSP and its extended problems: From simplicity to complexity. *Expert Systems with Applications*, 241, p.122594.
- Piotr Jedrzejowicz, I.W., 2022. Implementation of the Mushroom Picking Framework for Solving Flexible Job Shop Scheduling Problems in Parallel. In: *26<sup>th</sup> International Conference on Knowledge-Based and Intelligent Information and Engineering 26<sup>th</sup> International Conference on Knowledge-Based and Intelligent Information and Engineering Systems (KES 2022)*. pp.292-298.
- Rajwar, K., Deep, K., and Das, S., 2023. An exhaustive review of the metaheuristic algorithms for search and optimization: Taxonomy, applications, and open challenges. *Artificial Intelligence Review*, 56(11), pp.13187-13257.
- Sadiq Al-Obaidi, A.T., Abdullah, H.S., and Ahmed, Z.O., 2018. Solving flexible job shop scheduling problem using meerkat clan algorithm. *Iraqi Journal of Science*, 59(2A), pp.754-761.
- Şahman, M.A., 2021. A discrete spotted hyena optimizer for solving distributed job shop scheduling problems. *Applied Soft Computing*, 106, p.107349.
- Song, L., Liu, C., Shi, H., and Zhu, J., 2022. An improved immune genetic algorithm for solving the flexible job shop scheduling problem with batch processing. *Wireless Communications and Mobile Computing*, 2022, p.2856056.
- Wang, Y., Xia, T., Xu, Y., Ding, Y., Zheng, M., Pan, E., and Xi, L., 2024. Joint optimization of flexible job shop scheduling and preventive maintenance under high-frequency production switching. *International Journal of Production Economics*, 269, p.109163.
- Wu, L., and Cai, H., 2021. Energy-efficient adaptive sensing scheduling in wireless sensor networks using Fibonacci tree optimization algorithm. *Sensors (Basel)*, 21(15), p.55002.
- Xie, J., Gao, L., Peng, K., Li, X., and Li, H., 2019. Review on flexible job shop scheduling. *IET Collaborative Intelligent Manufacturing*, 1, p.67-77.
- Xie, N., and Chen, N., 2018. Flexible job shop scheduling problem with interval grey processing time. *Applied Soft Computing Journal*, 70, pp.513-524.
- Zeidabadi, F.A., and Dehghani, M., 2022. POA: Puzzle optimization algorithm. *International Journal of Intelligent Engineering and Systems*, 15(1), pp.273-281.
- Zhang, C., Tan, J., Peng, K., Gao, L., Shen, W., and Lian, K., 2021. A discrete whale swarm algorithm for hybrid flow-shop scheduling problem with limited buffers. *Robotics and Computer-Integrated Manufacturing*, 68, p.102081.
- Zhang, G., Hu, Y., Sun, J., and Zhang, W., 2020. An improved genetic algorithm for the flexible job shop scheduling problem with multiple time constraints. *Swarm and Evolutionary Computation*, 54, p.100664.
- Zhu, N., Zhao, F., Wang, L., Ding, R., Xu, T., and Jonrinaldi, 2022. A discrete learning fruit fly algorithm based on knowledge for the distributed no-wait flow shop scheduling with due windows. *Expert Systems with Applications*, 198, p.116921.



# Strategies for Sustainable Water Management: Hydrochemical Profiling and Protection Zone Design in Rania Basin, Iraq

Ata O. Salih<sup>1</sup> and Diary A. Al-Manmi<sup>2†</sup>

<sup>1</sup>Department of General Science, Charmo University, Sulaimani, Kurdistan Region – F.R. Iraq

<sup>2</sup>Department of Petroleum and Energy, Technical College of Engineering, Sulaimani Polytechnic University, Sulaimani, Kurdistan Region – F.R. Iraq

**Abstract**—Groundwater in the Rania basin, Iraqi Kurdistan region, has been under intensive exploitation in the last two decades, where quantity and quality are both affected. Hence, any attempt to protect the aquifers has become an urgent need. Saruchawa, Qulai Rania, and Qulai Kanimaran are the three large springs, among dozens of others in the area, that are heavily relied on as the sole or main source of water supply. Hydrochemical analysis, the first and most practical step to evaluating the water quality, was carried out through 60 water samples collected from 13 springs and 17 wells in both dry and wet seasons (October 2018 and May 2019). Laboratory results show a high calcium bicarbonate concentration with weak acids' dominance. Protection zones are delineated for these springs using aquifer susceptibility to contamination and analysis of the recession part of the spring curves. The equivalent relationship between the protection factor (Fp) produced by the Epikarst, protective cover, infiltration condition, and Karst network development mapping method and the groundwater protection zone (S) is considered. Qulai Rania and Kanimaran Springs are mapped to be in S2 (a highly vulnerable area), whereas Saruchawa Spring is located in S1 (very highly vulnerable). Based on the second method results (recession curve analyses), all three selected springs fall under the (D-type) vulnerability category. As a result, the immediate protection zone was going to be surrounded by the inner protection zone, and both are enclosed within the outer protection zone, which covers the remainder of the catchment area.

**Index Terms**—Groundwater quality, Hydrochemical analysis, Rania basin, Vulnerability assessment, Water security.

## I. INTRODUCTION

Groundwater is mainly extracted through wells or by utilizing the discharge from springs – natural outlets for

groundwater (U.S. Department of Agriculture Natural Resources Conservation Service, 2010). In mountainous regions, springs usually provide high-quality, gravity-fed water because there are fewer human impacts on the groundwater system than in urban or coastal areas (Filippini, et al., 2024). Groundwater from springs in northern Iraq in general, and in the Rania basin, in particular, has recently raised unprecedented concern among land users and related authorities. This has been caused by a severe drop in quantity and deterioration in quality which is mainly attributed to the rapid growth in urbanization and agricultural and industrial projects in the area in the last two decades. Despite the natural barriers provided by Earth's protective layers, recent decades have seen a significant increase in the risks facing groundwater, both in terms of its quality and quantity. This growing threat underscores the need for more rigorous protection and sustainable management of these critical water resources (Hamed Masoud, Dara Rebwar and Kirlas Marios, 2024). In urban regions, the presence of impermeable surfaces, modifications to natural streams, and built infrastructure can change how water infiltrates the ground, create new routes for subsurface water flow, and influence the quality of groundwater (Fryar, Currens, and Alvarez, 2023). It is well known that despite its significance as a vital source of water supply, groundwater may pose a significant health hazard if polluted due to difficulties in remediation. A balance between human activities such as urbanization, agriculture, and industry with groundwater protection could still be achieved if reasonable planning in land use is embraced (Meerkhan, et al., 2022). The physical and chemical properties of water must be investigated to decide on its suitability for different purposes as its not only quantity that is important but also its quality is important as well. The majority of past research on groundwater resilience has concentrated on analyzing trends in aquifer recharge, groundwater storage, hydraulic heads, and discharge. Only a small number of studies have examined the reality aspect of proposing protection strategies such as the delineation of source protection zones and aquifer features such as

ARO-The Scientific Journal of Koya University  
Vol. XII, No. 2 (2024), Article ID: ARO.11435. 12 pages  
Doi: 10.14500/aro.11435

Received: 08 October 2023; Accepted: 20 August 2024  
Regular research paper; Published: 05 September 2024

†Corresponding author's e-mail: diary.amin@spu.edu.iq  
Copyright © 2024 Ata O. Salih and Diary A. Al-Manmi. This is an open-access article distributed under the Creative Commons Attribution License (CC BY-NC-SA 4.0).



lithology, permeability, saturated thickness, transmissivity, and geometric properties of the fracture network (Filippini, et al., 2024; Zeydalinejad, 2023).

The Source Protection Zone is described as an area including surface and subsurface that surrounds a source of water, that is, a spring, or a wellfield through which pollutants may enter groundwater and reach the aquifer storage (US EPA, 2021).

According to Adams and Foster, 1992; Foster, Hirata, and Andreo, 2013, better ways of using the lands surrounding the source, coupled with delineating protection zones are vital to ensure the economic use of this important resource. Although many countries in Europe have already established three types of protection zones, a unified description on which all related authorities agreed has yet to be reached. The immediate zone, which occasionally includes swallow holes – natural depressions or sinkholes where surface water is drained into the ground, often disappearing into an underground river system – inside the catchment, is typically a region of 10 m wide surrounding a source (Doerfliger and Zwahlen, 1998). Zone (II) can also include certain places with favored infiltration and is regularly established on water passage time, 10–100 days depending on the member state (Doerfliger and Zwahlen, 1998). The remainder of the watershed or a minimum of 2 km or 400-day travel time restriction is bounded and referred to as the Outer Protection Zone (OPZ). (Doerfliger and Zwahlen, 1998; Al-Manmi and Saleh, 2019). The aim of this procedure, according to (Tarazi, 2009), is to protect potable water from pollution through the identification of specific zones that can be sources of potential harm around the water abstraction point.

Springhead/(zone I) immediate protection zone (IMPZ), (zone II) inner protection zone (IPZ), and (zone III) OPZ are subareas that accompany most groundwater protection schemes (Fig. 1). Some other programs add resource protection zone that covers the entire aquifer and often wider than the OPZ but not as wide as the whole catchment.

According to Al-Manmi and Saleh (2019), data availability and required precision are the two most influential factors when deciding on the extent of an area that needs protection

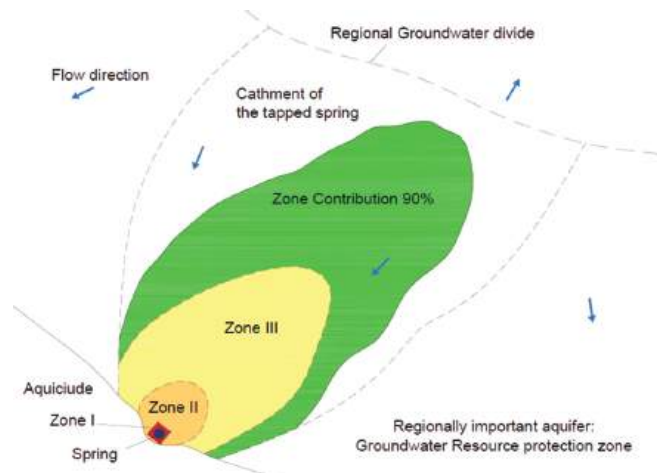


Fig. 1. Illustration of the protection areas around a spring (Goldscheider, 2005).

from contamination and selecting the most suited method to delineate protection zones. Most of these standards and policies differ from one country to another. This difference is mirrored in zone numbers, the minimum required dimensions, and land-use regulations (Marín, et al., 2015). In places where karst aquifers are predominant, assessment models such as E epikarst, P protective cover, I infiltration, and K karst network (EPIK) (Doerfliger, et al., 1999; Hamdan, et al., 2016); COP (Vias, et al., 2006); VULK (Jeannin, et al., 2001); PI (Goldscheider, et al. 2010); and CPO + K (Marín, et al., 2015) have been tested to obtain a measurable vulnerability index of groundwater and assist in the allocation of protected areas. The most specific methods to identify protective zones and delineate the vulnerability around springs in karst aquifers are EPIK vulnerability mapping and spring recession curve analysis (Doerfliger, et al., 1999; Al-Manmi and Saleh, 2019). The hydrograph's recession curve is thought to convey the geometrical and hydraulic properties of aquifers and is typically more stable (Filippini, et al., 2024; Abirifard, et al., 2022; Segadelli, et al., 2021; Fiorillo, 2014). It is a combination of the discharge from individual blocks, which comes from water infiltration through diffusion, and the discharge from focused recharging through conduits (Rusjan, Lebar and Bezak, 2023; Kovacs and Perrochet, 2008).

This paper aims to present a hydrochemical analysis of the basin's groundwater and delineate protection zones around three major springs of Saruchawa, Qulai Rania, and Kani Maran in the Rania basin using recession curve analysis and EPIK vulnerability mapping methods.

## II. MATERIALS AND METHODS

### A. Study Area

The area of interest is located in Iraq's northeastern region of Kurdistan. It stretches from the northeastern part to the southwestern area in the Sulaimani province and is bounded by latitudes ( $36^{\circ}05'15''$ ,  $36^{\circ}28'13''$ ) and longitudes ( $44^{\circ}25'38''$ ,  $44^{\circ}58'51''$ ). The area of the Rania basin covers something close to 1269.3 km<sup>2</sup>. The town of Rania is 131 km away from Sulaimani city in the northeast direction (Fig. 2). Apart from Rania district, the basin extends to engulf Chwarqurrna, Hajiwawa, Betwata, and Hiran sub-districts as well as 100 s of villages scattered among the mountain valleys (Al-Manmi, 2008). In Table I below, the three major springs that are delineated in this study, together with their main characteristics, are tabulated:

A 35-year (1984–2019) average of climatological parameters taken from Dokan Meteorological Station at longitude ( $44^{\circ}57'10''$ ) and latitude ( $35^{\circ}57'15''$ ) was calculated. The rainy season spans from October to May. The maximum average monthly temperature is 34.1°C recorded in July, whereas the lowest monthly average is 6.2°C recorded in January. This considerable difference in temperature is one of the main characteristics of continental climate. Nearly, 53% of the yearly precipitation precipitates in the cold season (December to February) and about 30% in spring (March to May). Over the years (1984–2019), there

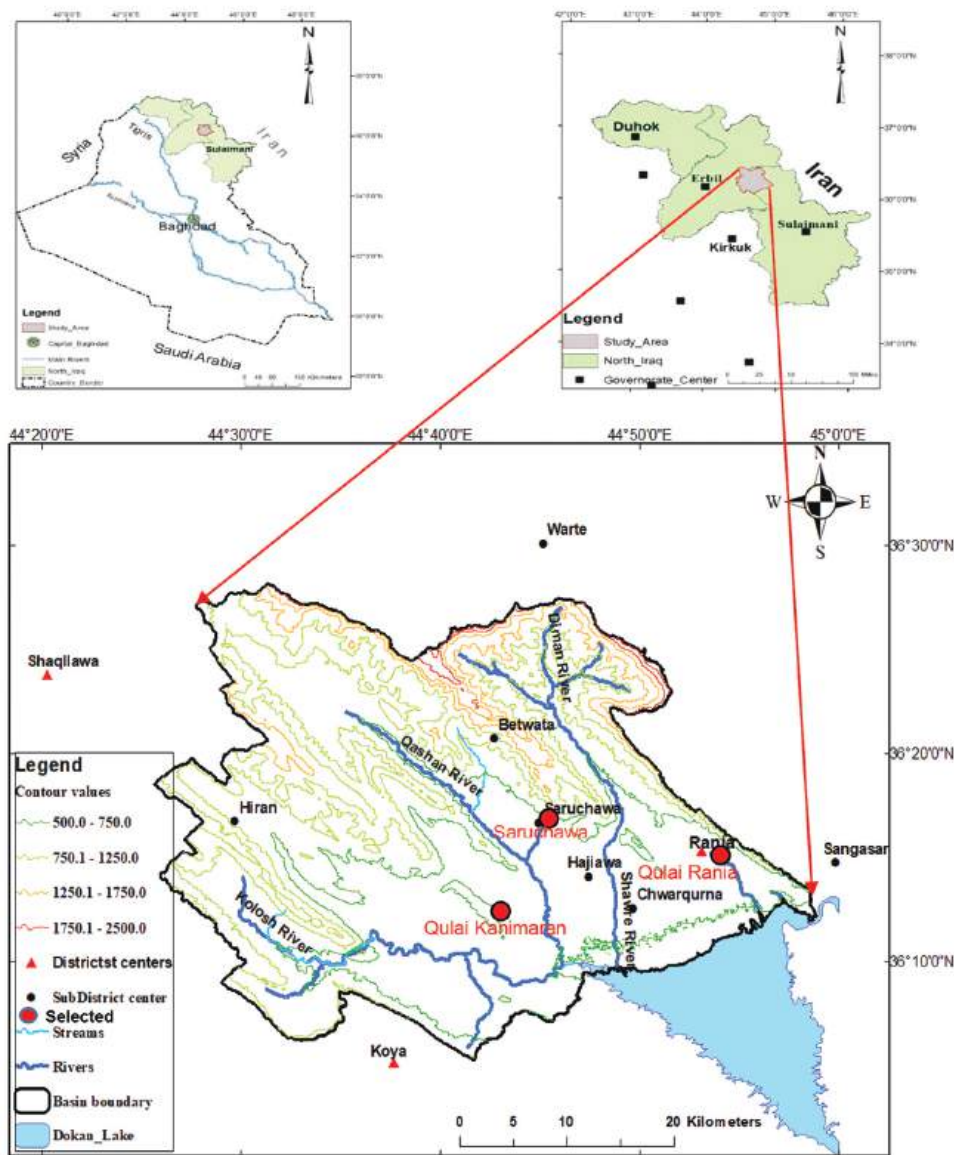


Fig. 2. Location of the selected springs and study area.

TABLE I  
INFORMATION ON THE THREE SPRINGS SELECTED FOR DELINEATION

Spring name	Location	Coordinates	Elevation (m.a.s.l)	Yield (l/s)	Usage
Saruchawa Spring	Saruchawa sub-district	36°16'30"N, 44°45'18"E	582	6514	Largest spring in the basin
Qulai Rania Spring	Rania's inner district	36°15'20"N, 44°53'8"E	Not specified	780	Supplies two-thirds of Rania district's water
Kani Maran Spring	Kani Maran village	36°12'28"N, 44°43'34"E	541	513	Used primarily for agricultural purposes

has been an average of 682.5 mm of precipitation annually, whereas the maximum average monthly rainfall is 125.1 mm for December.

*B. Geological Setting and Hydrogeology*

The exposed geological units in the Rania basin, as surveyed by (Bolton, 1958; Bellen, et al., 1959; Buday, 1980; Buday and Jassim, 1987; and Jassim and Goff, 2006), are represented by 17 formations, starting from the Sarki formation of the lower Jurassic all the way up to Gercus formation of Middle Eocene, as well as recent deposits from Pleistocene,

(Fig. 3a and b). In terms of water supply, quaternary deposits including floodplains, alluvial fans, and river terraces are considered the best units. The area of interest is situated in the lower Zab basin which itself is a part of the Dokan sub-basin.

According to Al-Manmi (2008) and as shown in (Fig. 4), there are four distinct aquifer systems; Quaternary, Early-Late Cretaceous, Late Cretaceous Limestone, and Jurassic systems, but the main is Quaternary. The direction of groundwater movement is from northwest to southeast.

The performed pumping tests of wells discharging from the studied basin showed that the transmissivity of the

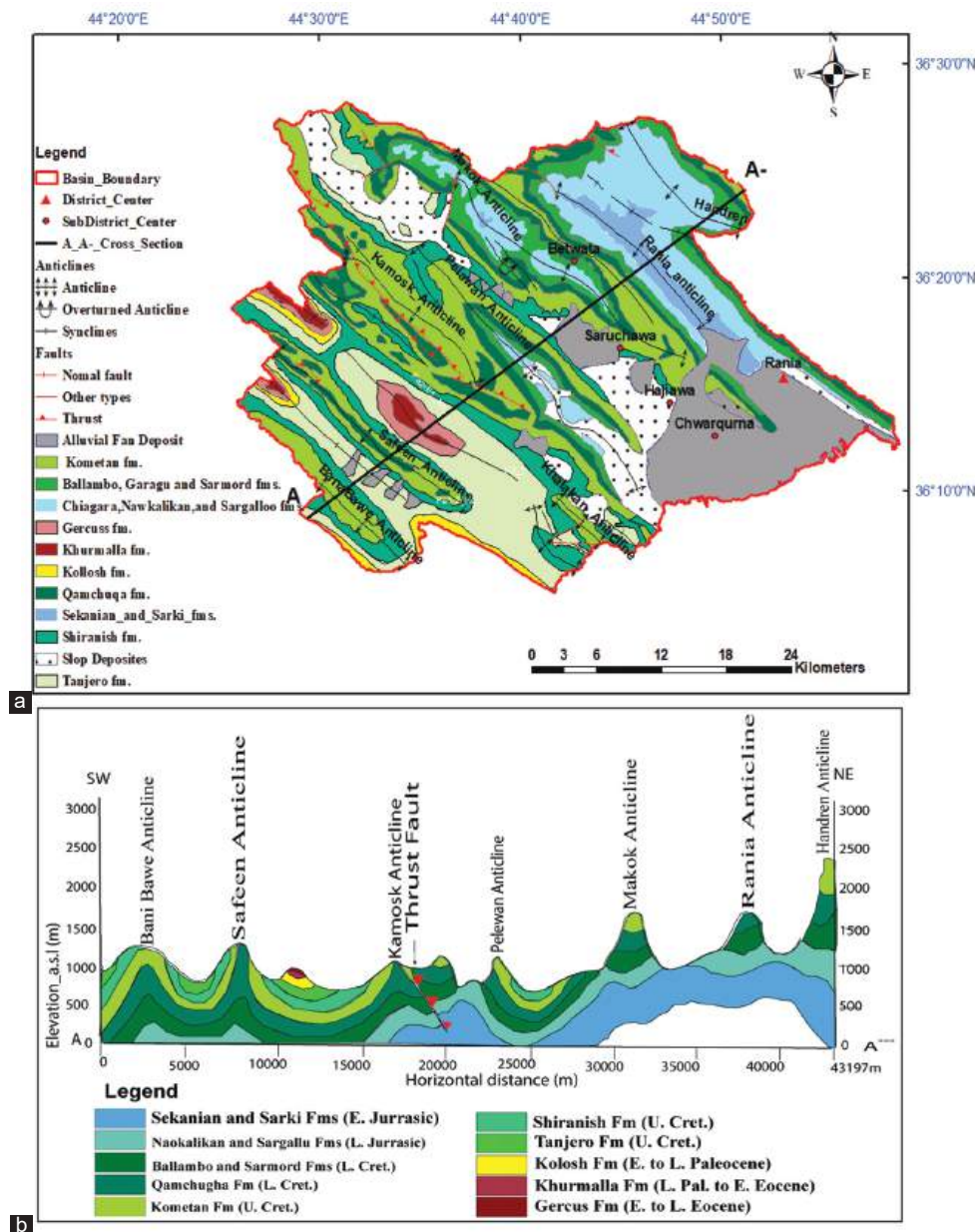


Fig. 3: (a) Rania basin's geology and (b) Geological cross section through line (A–A–), modified from (Sissakian, 1997).

aquifers ranges between 15 and 864 m<sup>2</sup>/day, hydraulic conductivity ranges between 0.2 and 12.8 m/day, discharge of wells ranges between 3 and 1616 m<sup>3</sup>/day and the static water level ranges between 5 and 60 m below ground surface. Recovery tests carried out in a neighboring area show a very high transmissivity value of  $6-9 \times 10^{-2}$  m<sup>2</sup>/s (Stevanovic and Markovic, 2004). Aquifer's names, lithology, and their geological ages are all tabulated in Table II.

### C. Quality Analyses for Hydrochemical Profiling

*In situ* measurements of temperature, electrical conductivity, and pH in 17 wells and 13 springs were recorded by a waterproof CyberScan PC 300 Portable pH/Conductivity/TDS Meter after calibration (Fig. 5). Small polyethylene containers of 500 mL were used to collect 60 water samples from 30 water sources penetrating the main

aquifers in October 2018 (dry season) and May 2019 (wet season). They were then transported in a container surrounded by ice packs at 4°C till reaching the laboratory for analyses.

Laboratory-based analyses were carried out in the Sulaimani Health Protection Directorate based on guidelines of the American Public Health Association (APHA, 2012). The reason for conducting two rounds of sampling was to detect seasonal variations. For each analysis, a charge balance was calculated to check for analytical error.

### D. Thematic Maps and Software

Geographic information system (GIS) ArcMap 10.5 was used to digitize previously drawn geological maps and cross-sections and construct shape files for geological, hydrogeological, and soil maps required for EPIK parameters in the delineation of the protection zones. After completing

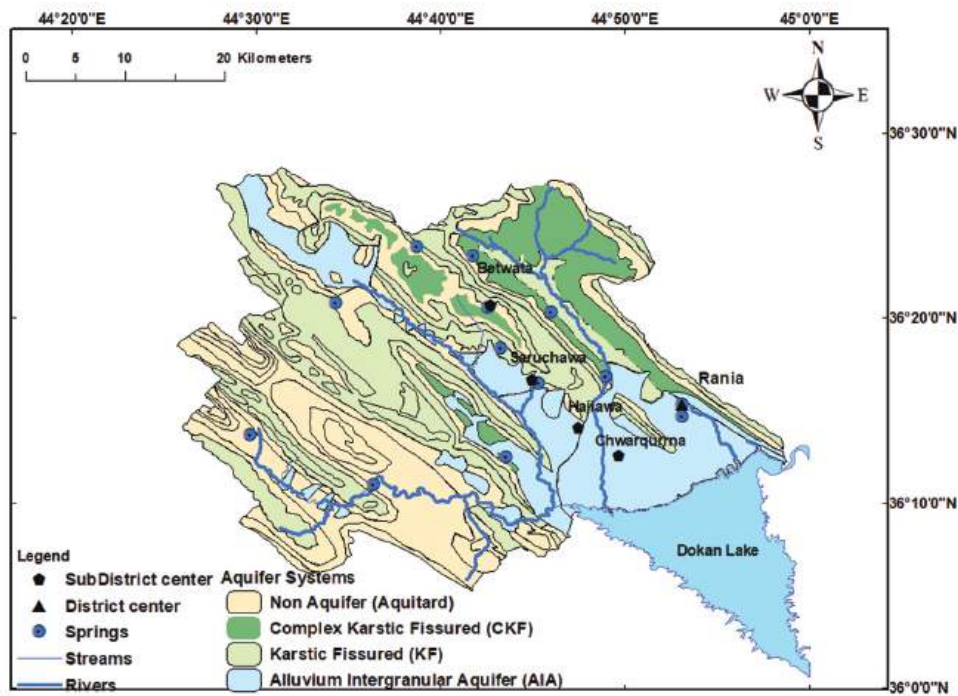


Fig. 4. Hydrogeological map, modified from (Al-Manmi, 2008).

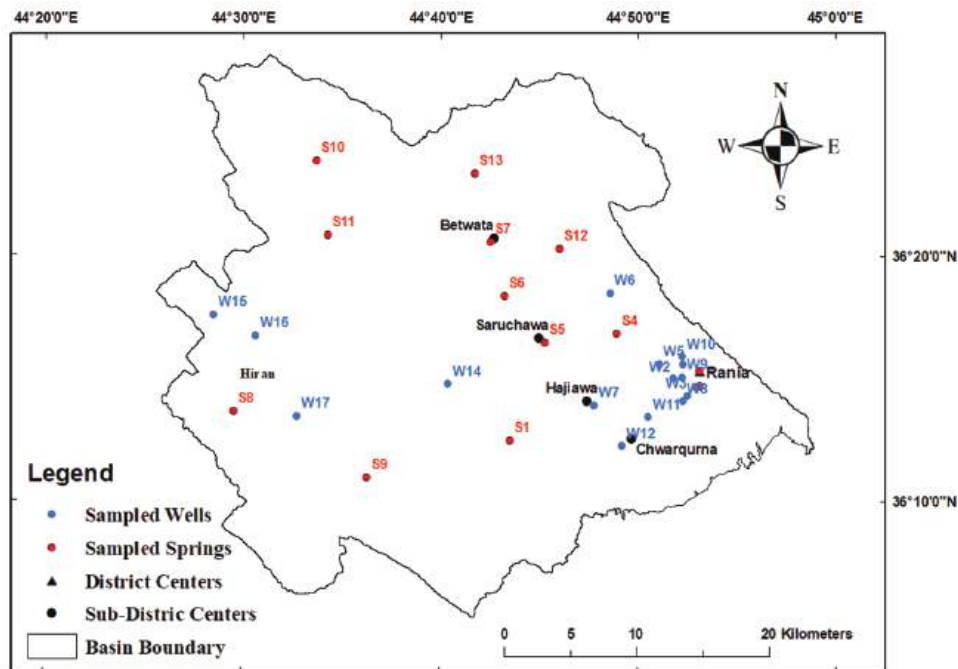


Fig. 5. Location map of wells and springs used for hydrochemical analyses.

TABLE II

LITHOLOGY, AGE, AND THICKNESS OF THE MAIN AQUIFERS IN THE STUDY AREA, MODIFIED FROM (STEVANOVIC AND MARKOVIC, 2004B; AZIZ, 2002; BABAN AND ALI, 2002)

Aquifer names	Geological formations	Aquifer Types	Lithology	Av. Thickness (m)
Lower Jurassic aquifer	E. Jurassic: Sarki and Sekanian	Karstic Fissured	Limestone, cherty shale, and dark dolomite	300
Upper Jurassic aquifer	U. Jurassic: Chia gara, Naokalikan, Barsarin and Sargallu	Complex Karstic Fissured	Dolomite, limestone, marl, and organic matter-rich limestone	385
Bekhma Aquifer	E. to L. Creat. Bekhma, Kometan and Qamchuqa	Karstic Fissured	Limestone and dolomite	450
Quaternary Aquifer	Quaternary: Alluvial Fans and Slope Deposits	Intergranular	Gravel, sand, silt, and clay	100

the individual layers as shape files, (GIS) ArcMap 10.5 was also used to express the four EPIK variables as thematic layers before converting them into raster. Each factor was attributed weighting factor as per the EPIK equation, and a summation of the four layers yielded the final EPIK vulnerability map.

*E. Conceptual Framework*

Models that are commonly used in allocating protection zones for water wells are not necessarily adaptable in the delineation of spring protection zones, especially karst springs. This is attributed to the very little natural attenuation capacity karstic flowing water wells may have.

Required steps to ensure a secure and safe drinking water supply from a groundwater source are:

1. Identification of areas where pollutants can enter the aquifer and change the water quality
2. Prioritize such areas by assigning protective measures
3. Constant source monitoring and water treatment through filtration and disinfection.

These security procedures, if properly observed, will eventually ensure the provision of a safe-to-drink water supply (Goldscheider, 2005).

Hydrogeological techniques such as recession curve analysis and vulnerability mapping such as the EPIK model are the most widely used methods to identify features that control groundwater flow to springs and assist in delineating spring protection zones (Fig. 6).

*Recession curve analysis*

System characterization through time-dependent functions (recession function) has been continuously investigated since the early days of contemporary hydrology (Civita, 2008). Decomposing of the spring hydrograph reveals that the first steep part of the falling curve represents the contribution from the vadose zone, whereas the depletion curve represents the aquifer’s input to the spring through its saturated zone. Furthermore, one of the functions of the recession curve is the pollutant’s time of travel (TOT), with the infiltrated water to the spring. This (TOT) varies inversely with the natural attenuation factors and the recession curve’s gradient, that is, the steeper the slope, the shorter the TOT and hence, the less attenuation capacity (Civita, 2008). To reach a recordable parameter to distinguish between different scenarios of hydrodynamic spring discharges and identify the pollutant’s maximum displacement velocity in the spring-supplying aquifer, the spring’s maximum discharge half-time (MDHT) is proposed and can be calculated through Eq. (1) (Civita, 2008).

$$MDHT = \frac{Q_{max}}{2} \cong t_i \tag{1}$$

Where:  $Q_{max}$  is the maximum spring discharge in the year, that is, the days from the maximum annual discharge moment ( $Q_{max}$ ) to the time when it is equal to  $Q_{max}/2$ . The depletion curves of the springs are plotted using their daily discharge rates on a nomogram to identify the corresponding range of flow velocity after computing MDHT (Fig. 7).

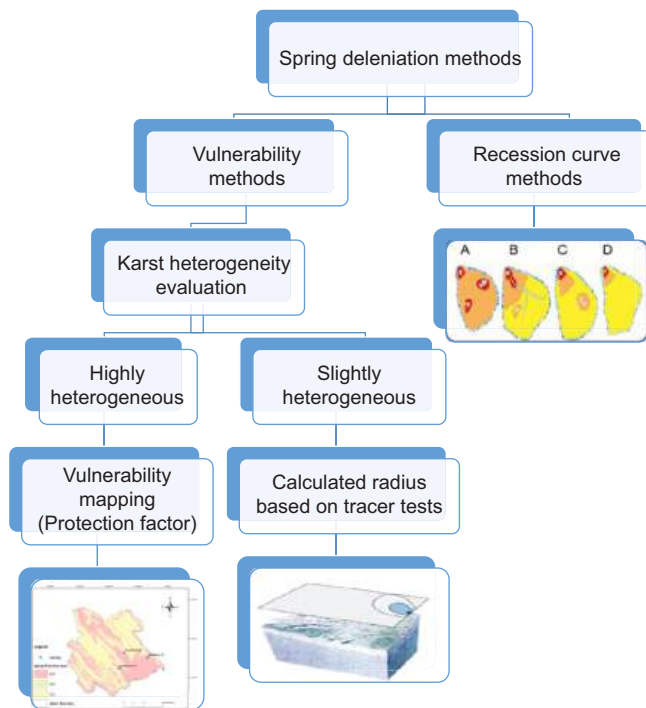


Fig. 6. Flowchart of common methods to delineate spring protection zones (Al-Manmi and Saleh, 2019).

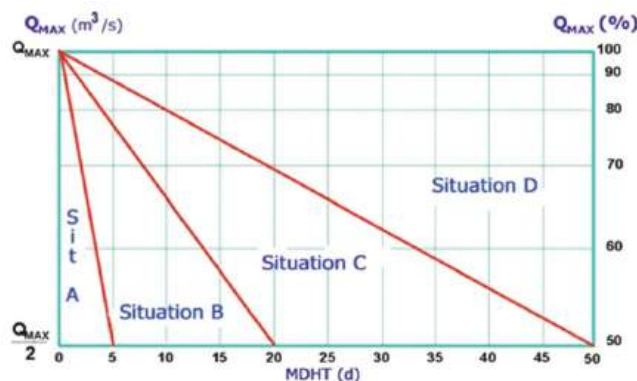


Fig. 7. A nomogram identifying basic A to D scenarios of pollution hazards of a karst spring (Civita and De Regibus, 1995; Civita, 2008).

Since the application of this model needs continuous daily readings of spring discharge to determine water’s travel time in the saturated zone, the researcher resorted to the archived data of the selected springs. Recordings taken by FAO staff in the previous hydrologic years for Saruchawa, Qulai Rania, and Kani Maran springs were utilized in drawing hydrographs, analyzing recession curves, calculating MDHT, designating pollution hazards, and subsequently delineating protection zones for the interested springs.

The depletion curves of the springs are plotted using their daily discharge rates, and a nomogram is used to identify the corresponding range of flow velocity after computing MDHT. Delay time determines the MDHT in a way that the longer delay time produces a larger depletion and, therefore, a higher MDHT. However, a greater rate of discharge increases pollutant dilution capacity in contrast to smaller aquifers with a small outflow and a weaker dilution capacity. Therefore, a spring

with a lower discharge should be considered more vulnerable. Thus, having considered all the aforementioned principles and pollution hazard scenarios, the designation standards for each protection zone around the springs are obtained (Table III).

*Vulnerability mapping method (EPIK Model)*

As this model is specially developed for karst aquifers (Awawdeh and Nawafleh, 2008), its application was also tried to delineate protection zones of the three springs of interest:

EPIK is an abbreviation composed of the first letters of epikarst (E), protective cover (P), infiltration conditions (I), and karst network development (K). Each of which is mapped and sub-sectioned into a series of divisions that are given a rating importance ranging from 1 to 4 and weighting values between 1 and 3 (Table IV).

According to SAEFL (2000), this model generates a color-coded map showing places relatively more susceptible to pollution from above the ground. The protection factor (Fp) is subsequently determined by adding the scores for each

class of any particular parameter and multiplying by the allocated weight, as indicated in the equation below:

$$Fp = 3E + 1P + 3I + 2K \tag{2}$$

The Fp value could range between 9 and 34 and the greater the Fp value is, the better protection the area has, that is, the area is less vulnerable because the vulnerability rating and the protection factor are opposites. It can also be categorized into four susceptibility grades: Very high, high, moderate, and low (Table V).

*A. Epikarst (E)*

Epikarst, according to Tripet, Doerfliger, and Zwahlen (1997), is defined as a zone of intensively karstified and highly permeable near the surface and under any consolidated soil if there is any. A map of Iraq's geology with a 1:250 000 scale which was compiled by Sissakian (1997) plus a geomorphological description with information on solution features in the studied basin also by Sissakian and Fouad (2014) were all used to surrogate for Epikarst as represented in (Table IV) and mapped in (Fig. 8a).

*B. Protective cover (P)*

This attribute is normally defined as upper unconsolidated or other non-karstic layers overlying the water-storing strata. To classify the protective cover in the studied basin and rate accordingly, detailed information on land cover and land

TABLE III  
IDENTIFIED SETTINGS BASED ON POLLUTION HAZARDS (CIVITA, 2008)

MDHT (d)	Scenario	Groundwater's velocity (m <sup>3</sup> /day)
<5	A	>1000
5-20	B	≈100
20-50	C	≈10
>50	D	≈1

TABLE IV  
APPRAISAL OF E, P, I, AND K FACTORS (DOERFLIGER AND ZWAHLEN, 1998)

Status	Code	Score	Description
<b>Epikarst</b>			
Karstic morphology observed (pertaining to epikarst)	E1	1	Caves, swallow holes, dolines, karren field, ruined-like relief, and cuestas.
Karstic morphology absent	E2	2	Intermediate zones in the orientation dolines, dry of valleys. Outcrops with medium fracturing
	E3	3	No karst morphological phenomena. A smaller number of fractures.
<b>Protective Cover</b>			
Protective cover absent	P1	1	A. Soil that is immediately resting on limestone or detrital deposits with extremely high hydraulic conductivity
		2	B. Soil found on more than 20 cm of any unit of low hydraulic conductivity**
	P2	2	0-20 cm of soil
	P3	3	20-100 cm of soil
Protective cover important	P3	3	>1 m of soil and low hydraulic conductivity formations
Protective cover important	P4	4	>8 m of very low hydraulic conductivity formations or >6 m of very low hydraulic conductivity formations with >1 m of soil (point measurements necessary)
<b>Infiltration Condition</b>			
Concentrated infiltration Diffuse infiltration	I1	1	Temporary swallow hole – bands and beds of temporary or permanent rivers – parts of the tributary catchment having non-natural drainage
	I2	2	Parts of a waterway catchment that are not artificially drained and where the slope is higher than 25% for meadows and pastures
	I3	3	Regions of a waterway catchment that are not artificially drained and where the slope is lower than 10% for cultivated regions and lower than 25% for meadows and pastures. External regions to the watershed of a surface waterway: bases of slopes and steep slopes, where runoff water penetrates.
	I4	4	Other parts of the watershed.
<b>Karst Development</b>			
Well-built karstic network	K1	1	A well-built karstic system with decimeter to meter-sized conduits with little fill and well interlocked
Unwell-developed karstic network	K2	2	Ill-developed karstic net with poorly interconnected drains of decimeter or minor size
Mixed or fissured aquifer	K3	3	The existence of a spring developing through the porous territory only fissured aquifer.

\*Cases: Scree, lateral glacial moraine, \*\*Cases: silts, clays

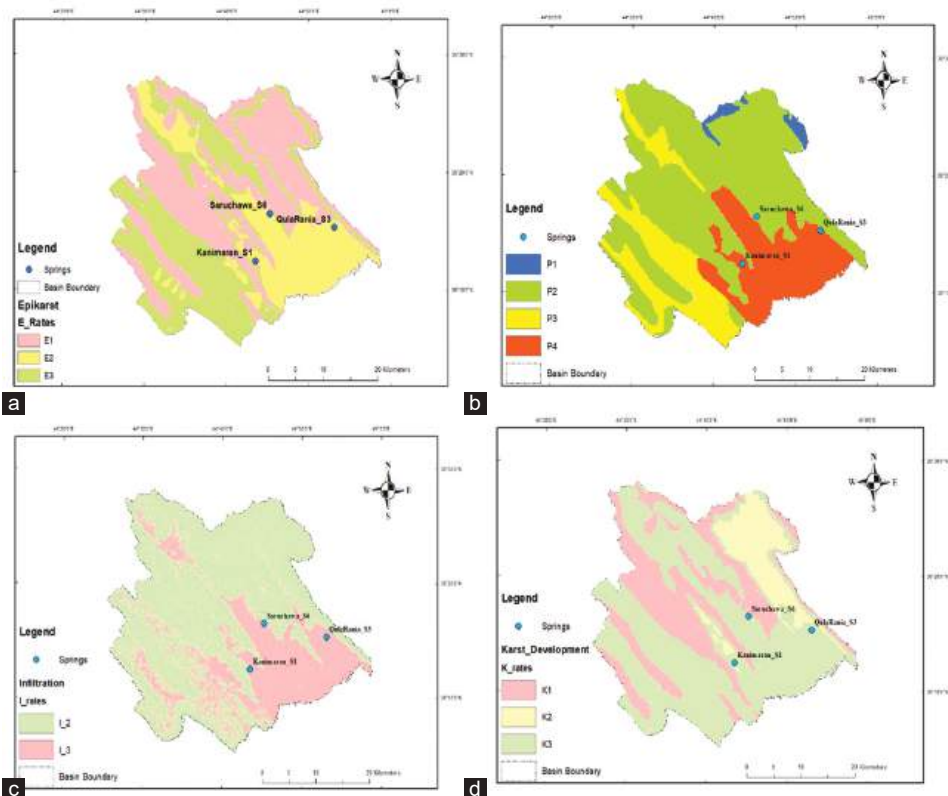


Fig. 8. (a) Epikarst rating map, (b) protective cover rating map, (c) infiltration rating map, (d) karst network rating map of the study area.

TABLE V  
VULNERABILITY ZONES AND PROTECTION FACTOR

Protection factor (F)	Susceptibility grades
9–19	Very high
20–25	High
26–34	Moderate
More than 25 and in the presence of both $P_4$ and $I_3$ , 4	Low

use (LULC map), soil cover description coupled with soil classification, and hydraulic conductivity of different parts of the basin were all utilized (Fig. 8b).

C. Infiltration attribute (I)

The important aspect of this parameter is related to the type-specific effect of recharge in the karstic system. The studied basin, as shown in Fig. 8c, is divided into two zones of I2 and I3 only, since no perennial streams feeding swallow holes were reported in the basin.

D. Karst development attribute (K)

Ratings from (Table IV) were used to subdivide the studied basin into three categories ranging from K1 up to K3. K1 was assigned to areas where the well-developed karstic network is reported in outcrops of cretaceous formations such as Bekhme (locally Kometan) and Qamchuqa. K2 is given to Jurassic formation where a karstic network exists but is not well developed and K3 to the absence of karstic features in the quaternary alluvial fan and slope deposits and aquitards units such as Tanjero, Shiranish, and Gercus formations (Fig. 8d).

III. RESULTS AND DISCUSSION

A. Pollution Scenarios Based on Recession Curve Analysis

The protection area surrounding a spring is composed of three zones. Zone (I) or IMPZ, Zone (II) or IPZ, and Zone (III) or OPZ as shown in Fig. 9. Assigned distances and their restricted practices are represented in Table VI.

Recordings for the three selected springs of Saruchawa, Qulai Rania, and Qulai Kanimaran taken in the past by FAO staff have been used to draw hydrographs, analyze recession curves, calculate MHDT, designate pollution hazards, and subsequently delineate protection zones (Table VII and Fig. 10). Thus, all of the three springs; Saruchawa, Qulai Rania, and Kanimaran fit the scenario of D-type. Therefore, The IPZ encloses IMPZ zones, whereas the OPZ includes the entire remaining catchment area.

B. Pollution level based on EPIK Protection Factor (Fp)

On completing the shape files for each parameter in ArcMap GIS 10.5, they were all converted to raster data with a 30 m grid. Each factor was assigned a weighting coefficient according to equation (2) and a summation of the four layers was obtained using the spatial analyst tool of the raster calculator. The final calculated protection factor produced by applying the EPIK model in the studied basin ranged from 12 to 28. Thus, the produced comprehensive EPIK map classified the vulnerability of the studied basin into moderate, high, and very high.

Areas categorized as having very high vulnerability (41.6%) are located in the northern parts of the studied basin



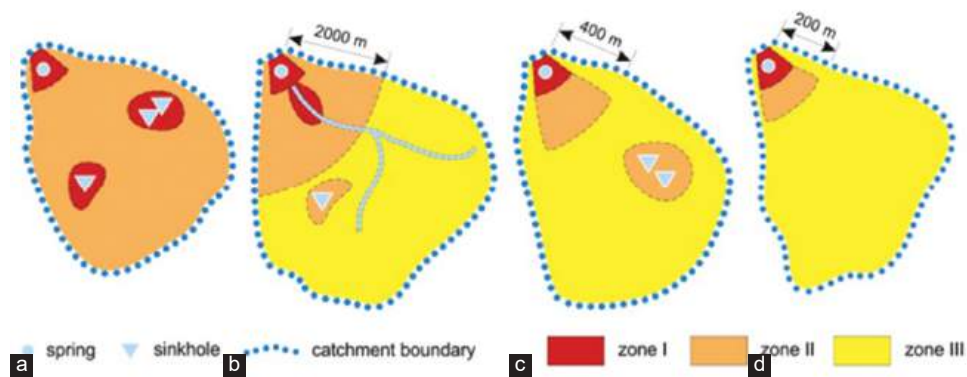


Fig. 9. (a-d) Pollution hazard scenarios and protection zoning (Civita, 2008).

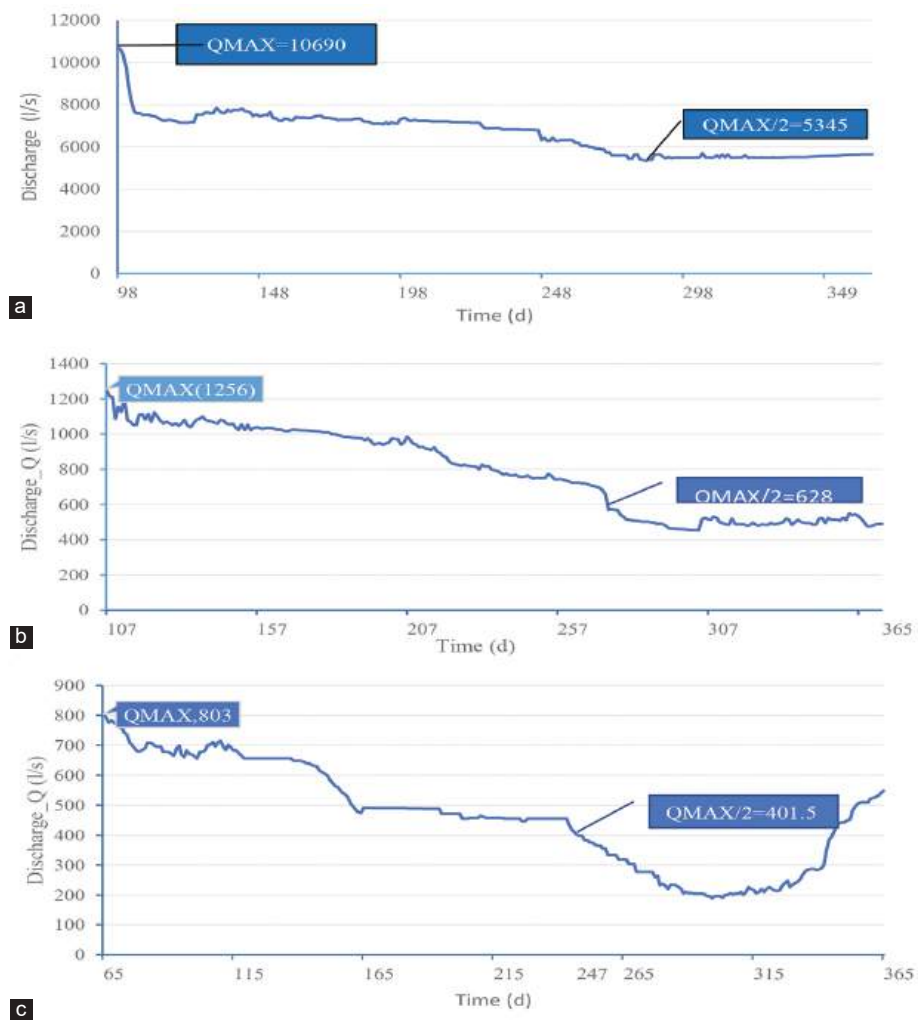


Fig. 10. Spring recession curve analyses (a – Saruchawa, b – Qulai Rania, c – Kanimaran).

TABLE VI  
ENCLOSED AREAS AND RESTRICTED PRACTICES FOR PROTECTION ZONES

Protection zones	Enclosed area (distance from the source) (m)	Remarks
Immediate (zone 1)	(10–40 m) upstream and (2–10 m) downstream	limited human activities except tree planting
Inner (zone 2)	- The whole catchment for (A and B) scenarios but decreased to (2 km) upstream for (B) scenario Upstream distance of (400–600 m) for C and (200–300 m) for D scenarios.	In case of a thick protective cover or aquitards One zone higher if sinkholes exist!
Outer (zone 3)	Remaining of the whole catchment area	Restricted settlement and land use but safeguarding strategies are still needed.

where karstic features are not only present but also well developed, and the protective cover is absent or very thin, especially in the rocky outcrops of the mountainous regions.

It is also worth mentioning that Makok anticline, which is a karst system itself and is home to most of the major springs including Saruchawa spring, is situated in this vulnerability zone as represented in (Table VIII) and shown also in Fig. 11.

### C. Final Spring Protection Zones Based on the EPIK Model

As represented in Table VIII, the protection factors obtained from the EPIK vulnerability model are used to designate specific spring protection zones. Fig. 12 illustrates that protection factors (Fp) ranging from 12 to 19 that may include dolines, swallow holes, and supplying watercourses are mostly categorized as S1, that is, least naturally protected

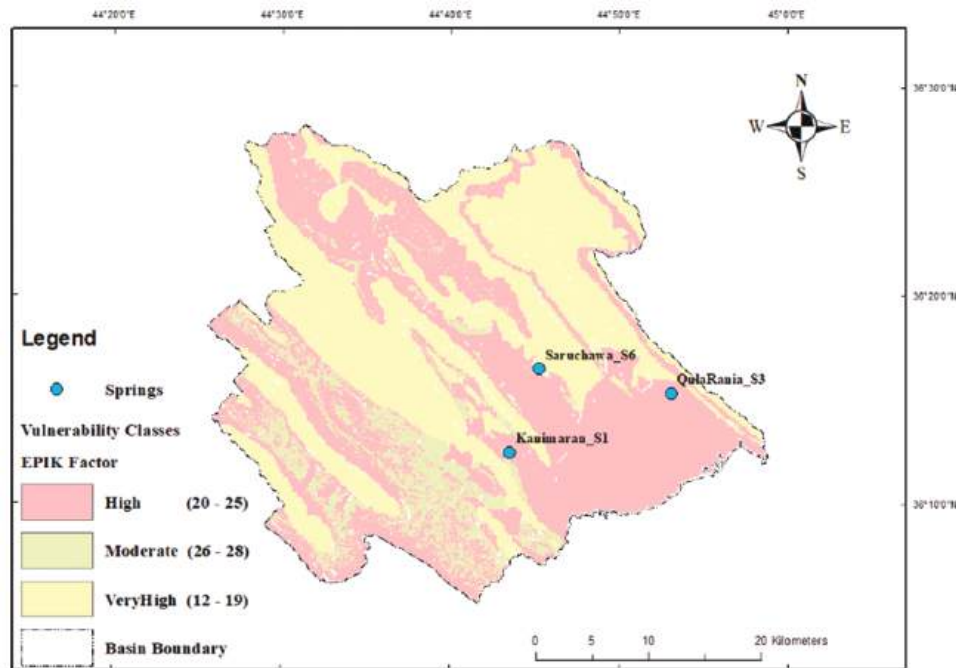


Fig. 11. EPIK vulnerability assessment map of the studied basin.

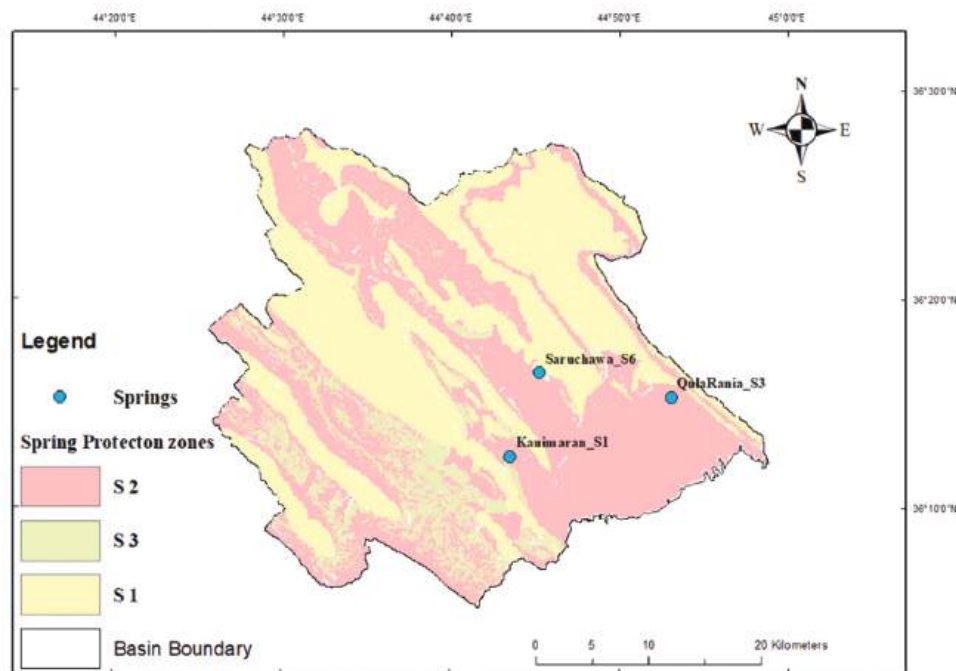


Fig. 12. Spring protection zones in the studied basin based on EPIK vulnerability.

TABLE VII  
DISCHARGE AND MDHT ASSESSMENT USING RECESSON CURVE ANALYSIS

Spring	Qmax (L/s)	Qmax/2 (L/s)	MDHT (day)	Scenario
Saruchawa	10690	5345	187	D
Qulai Rania	1256	628	166	D
Kanimaran	803	401.5	182	D

TABLE VIII  
AREA OF VULNERABILITY CLASSES OF THE STUDIED AREA USING EPIK

Vulnerability	Protection factor (Fp)	Area (km <sup>2</sup> )	Area (%)
Very high	12–19	528.52	41.63
High	20–25	621.25	48.94
Moderate	26–28	119.51	9.41

zone and has to be prioritized in terms of restricting certain activities such as extensive application of fertilizers and pesticides as well as dumping industrial refusals or untreated sewage water (SAEFL, 2000). Areas classed as having high vulnerability through the EPIK mapping model are given S2, whereas S3 is applied to those areas that have moderate vulnerability with a protection factor of 26–28.

The areas designed as zones of protection in the paper issued by the relevant authority in Switzerland adhere to the same constraints as the demarcated protection zones in EPIK (SAEFL, 2000). S2 and S3 include most of the drainage region for the springs, so certain operations such as installing gas stations, storing fuel, and infrastructural developments should be avoided. This is due to the limitations required by SAEFL (2000), connected with using each protection zone.

#### IV. CONCLUSIONS

This study presents a comprehensive hydrochemical analysis and vulnerability assessment for the Rania Basin's groundwater, focusing on three major springs: Saruchawa, Qulai Rania, and Kani Maran. The findings highlight the significant impact of intensive groundwater exploitation on both water quality and quantity, underscoring the urgent need for protective measures.

Hydrochemical analyses of 30 water sources, comprising 17 wells and 13 springs, reveal that the groundwater within the basin predominantly exhibits a calcium bicarbonate composition, characterized by alkalinity and a prevalence of weak acids. The physicochemical parameters measured across these samples align with the potability criteria established by the World Health Organization (WHO) and Iraqi standards, affirming the suitability of the basin's groundwater for consumption.

The delineation of protection zones using the EPIK vulnerability mapping method and recession curve analysis revealed varying levels of susceptibility across the springs, with Saruchawa being the most vulnerable. The results demonstrate the importance of implementing effective management strategies to safeguard these critical water resources. Areas categorized as having very high vulnerability (41.6%) of the entire basin are located in the northern parts of the studied basin (colored in yellow) where

karstic features are not only present but also well developed and the protective cover is absent or very thin, especially in the rocky outcrops of the mountainous regions and around Makok anticline, which is a karst system itself and is home to most of the major springs including Saruchawa spring is least protected naturally and hence require prioritization for robust environmental planning in terms of restriction certain industrial and agricultural activities. Immediate and IPZs were recommended for each spring, with the aim of reducing contamination risks and ensuring sustainable water supply for the region.

Future efforts should focus on continuous monitoring, public awareness, and the integration of these findings into regional water management policies to mitigate potential threats to groundwater sustainability in the Rania Basin.

#### REFERENCES

- Abirifard, M., Birk, S., Raeisi, E., and Sauter, M., 2022. Dynamic volume in karst aquifers: Parameters affecting the accuracy of estimates from recession analysis. *Journal of Hydrology*, 612, p.128286.
- Adams, B., and Foster, S.S.D., 1992. Land-surface zoning for groundwater protection. *Water and Environment Journal*, 6(3), pp.312-319.
- Al-Manmi, D.A., 2008. *BolWater Resources Management in Rania Area, Sulaimaniyah NE-Iraq*. Ph.D. Thesis, University of Baghdad, Baghdad, Iraq.
- Al-Manmi, D.A.M.A., and Saleh, K.A., 2019. Delineation of spring protection zone and vulnerability mapping of selected springs in Sulaymaniyah area, Kurdistan, Iraq. *Environmental Earth Sciences*, 78(21), p.622.
- APHA., 2012. In: Rice, E.W., Baird, R.B., Eaton, A.D., and Clesceri, L.S., Eds. *Standard Methods for the Examination of Water and Wastewater*. 22<sup>nd</sup> ed., American Public Health Association (APHA), American Water Works Association (AWWA) and Water Environment Federation (WEF), Washington, DC, USA.
- Awawdeh, M., and Nawafleh, A., 2008. A GIS-based EPIK model for assessing aquifer vulnerability in Irbid Governorate, North Jordan. *Jordan Journal of Civil Engineering*, 2(3), pp.267-278.
- Bellen, R.V., Dunnington, H.V., Wetzel, R., and Morton, D., 1959. Congrès géologique international. Lexique Stratigraphic International. Paris, p.333.
- Bolton, C.M.G., 1958. *The Geology of the Ranya Area*. Manuscript Report, (271). GEOSURV, Baghdad.
- Buday, T., 1980. The Regional Geology of Iraq. Stratigraphy and Palaeogeography. GEOSURV, Baghdad, Iraq, p.445.
- Buday, T., and Jassim, S.Z., 1987. In: Abbas, M.J., and Jassim, S.Z., Eds. *The Regional geology of Iraq: Tectonism, Magmatism and Metamorphism*. GEOSURV, Baghdad, Iraq, p.445.
- Civita, M., and De Regibus, C., 1995. Experimentation of some methodologies for assessing the vulnerability of aquifers. *Pitagora Bologna*, 3, pp.63-71.
- Civita, M.V., 2008. An improved method for delineating source protection zones for karst Springs based on analysis of recession curve data. *Hydrogeology Journal*, 16(5), pp.855-869.
- Doerfliger, N., and Zwahlen, F., 1998. *Groundwater Vulnerability Mapping in Karstic Regions (EPIK), Practical Guide*. Swiss Agency for the Environment, Forests and Landscape (SAEFL), Berne, p.56.
- Doerfliger, N., Jeannin, P.Y., and Zwahlen, F., 1999. Water vulnerability assessment in karst environments: A new method of defining protection areas using a multi-attribute approach and GIS tools (EPIK method). *Environmental Geology*, 39(2), pp.165-176.
- Filippini, M., Segadelli, S., Dinelli, E., Failoni, M., Stumpp, C., Vignaroli, G.,

- Casati, T., Tiboni, B., and Gargini, A., 2024. Hydrogeological assessment of a major Spring discharging from a calcarenitic aquifer with implications on resilience to climate change. *Science of the Total Environment*, 913, p.169770.
- Fiorillo, F., 2014. The recession of spring hydrographs, focused on karst aquifers. *Water Resources Management: An International Journal*, 28, pp.1781-1805.
- Foster, S., Hirata, R., and Andreo, B., 2013. The aquifer pollution vulnerability concept: Aid or impediment in promoting groundwater protection? *Hydrogeology Journal*, 21(7), pp.1389-1392.
- Fryar, A.E., Currens, B.J., and Alvarez, C.S., 2023. Hydrochemical delineation of Spring recharge in an urbanized karst basin, Central Kentucky. *Environmental and Engineering Geoscience*, 29(3), pp.203-216.
- Goldscheider, N., 2005. Karst groundwater vulnerability mapping: Application of a new method in the Swabian Alb, Germany. *Hydrogeology Journal*, 13, pp.555-564.
- Goldscheider, N., Klute, M., Sturm, S., and Hötzl, H., 2010. The PI method-a GIS-based approach to mapping groundwater vulnerability with special consideration of karst aquifers. *Zeitschrift für Angewandte Geologie*, 46(3), pp.157-166.
- Hamdan, I., Margane, A., Ptak, T., Wiegand, B., and Sauter, M., 2016. Groundwater vulnerability assessment for the karst aquifer of Tanour and Rasoun springs catchment area (NW-Jordan) using COP and EPIK intrinsic methods. *Environmental Earth Sciences*, 75, p.1474.
- Hamed Masoud, H., Dara Rebwar, N., and Kirlas Marios, C., 2024. Groundwater vulnerability assessment using a GIS-based DRASTIC method in the Erbil Dumpsite area (Kani Qirzhala), Central Erbil Basin, North Iraq. *Journal of Groundwater Science and Engineering*, 12(1), pp.16-33.
- Jassim, S.Z., and Goff, J.C., Eds., 2006. *Geology of Iraq*. Dolin, Prague and Moravian Museum, Brno, p.341.
- Jeannin, P.Y., Cornaton, F., Zwahlen, F., and Perrochet, P., 2001. *VULK: A Tool for Intrinsic Vulnerability Assessment and Validation*. In: 7<sup>th</sup> Conference on Limestone Hydrology and Fissured Media, Besanc. Vol. 13. pp.185-188.
- Kovacs, A., and Perrochet, P., 2008. A quantitative approach to Spring hydrograph decomposition. *Journal of Hydrology*, 352(1-2), pp.16-29.
- Marín, A.I., Andreo B., and Mudarra, M., 2015. Vulnerability mapping and protection zoning of karst springs. Validation by multitracer tests. *Science of the Total Environment*, 532, pp.435-446.
- Meerkhan, H., Freitas, L., Pereira, A.J.S.C., Rocha, F., and Chaminé, H.I., 2022. Delineating Springs safeguard zones with disco-urban Index: A valuable tool for groundwater vulnerability mapping in local-scale urban areas. *Discover Water*, 2, p.2.
- Rusjan, S., Lebar, K., and Bezak, N., 2023. Insight into heterogenous karst catchment by dynamical system approach. *Advances in Water Resources*, 180, p.104524.
- SAEFL., 2000. *Groundwater Vulnerability Mapping in Karstic Regions (EPIK). Practical Guide. Environment in Practice*. SAEFL, Berne, pp.56-57.
- Segadelli, S., Filippini, M., Monti, A., Celico, F., and Gargini A., 2021. Estimation of recharge in mountain hard-rock aquifer based on discrete spring discharge monitoring during base flow recession. *Hydrogeology Journal*, 29, pp.949-961.
- Sissakian, V.K., 1997. Geological map of Arbeel and Mahabad Quadrangles, scale 1:250000. In: *State Establishment of Geological Survey and Mining-Iraq's Geological Survey Publication*, Iraq-Baghdad.
- Sissakian, V., and Fouad, S.F., 2014. Geological Map of Sulaimaniyah Kirkuk Quadrangle, Scale 1: 250000. 2nd ed. Iraq Geological Survey Publications, Baghdad, Iraq.
- Mogheir, Y. and Tarazi, G., 2010. Comparative identification of wellhead protection areas for municipal supply wells in gaza. *Journal of Water Resource and Protection*, 2, pp.105-114.
- Tripet, J.P., Doerfliger, N., and Zwahlen, F., 1997. Vulnerability mapping in karst areas and its uses in Switzerland. *Hydrogeologie (France)*, 3, pp.51-57.
- U.S. Department of Agriculture Natural Resources Conservation Service, 2010. Springs and wells. In: *National Engineering Handbook*, Part 631, Ch. 32. USDA, Washington, DC, p.51.
- US EPA., 2021. Delineate the Source Water Protection Area. US EPA. Available from: <https://www.epa.gov/sourcewaterprotection/delineate-source-water-protection-area#:~:text=delineate%20the%20source%20water%20protection%20area%20the%20first%20step%20in,threat%20to%20source%20water%20quality> [Last accessed on 2023 Oct 01].
- Vias, J.M., Andreo, B., Perles, M.J., Carrasco, F., Vadillo, I., and Jimenez, P. 2006. A proposed method for groundwater vulnerability mapping in carbonate (karstic) aquifers: The COP method. *Hydrogeology Journal*, 14. pp.912-925.
- Zeydalinejad, N., 2023. An overview of the methods for evaluating the resilience of groundwater systems. *MethodsX*, 10, p.102134.

# Time Series-based Spoof Speech Detection Using Long Short-term Memory and Bidirectional Long Short-term Memory

Arsalan R. Mirza<sup>1†</sup> and Abdulbasit K. Al-Talabani<sup>2</sup>

<sup>1</sup>Department of Computer Science, Faculty of Science, Soran University,  
Soran, Kurdistan Region - F.R. Iraq

<sup>2</sup>Department of Software Engineering, Faculty of Engineering, Koya University,  
Koya KOY45, Kurdistan Region - F.R. Iraq

**Abstract**—Detecting fake speech in voice-based authentication systems is crucial for reliability. Traditional methods often struggle because they cannot handle the complex patterns over time. Our study introduces an advanced approach using deep learning, specifically long short-term memory (LSTM) and bidirectional LSTM (BiLSTM) models, tailored for identifying fake speech based on its temporal characteristics. We use speech signals with cepstral features such as mel-frequency cepstral coefficients (MFCC), constant Q cepstral coefficients, and open-source speech and music interpretation by large-space extraction to directly learn these patterns. Testing on the ASVspoof 2019 Logical Access dataset, we focus on metrics such as min-tDCF, equal error rate, recall, precision, and F1-score. Our results show that LSTM and BiLSTM models significantly enhance the reliability of spoof speech detection systems.

**Index Terms** – Bidirectional long short-term memory, Constant Q cepstral coefficients, Countermeasure spoofing, Long short-term memory, Mel-frequency cepstral coefficients, Open-source speech and music interpretation by large-space extraction.

## I. INTRODUCTION

Automatic Speaker Verification (ASV) (Bai and Zhang, 2021) is a popular biometric method that identifies a person by analyzing their recorded speech. The main idea is that everyone has a unique voice, similar to unique faces, irises, or fingerprints (Kamble et al., 2020).

Spoofing methods, such as voice conversion (VC), replay attacks, impersonation, and artificial speech can trick devices that use ASV (Wang et al., 2020) (Adiban Sameti and

Shehnepoor, 2020). Impersonation means copying someone's voice to access their account. VC changes the sound of a voice without changing what is said, whereas text-to-speech (TTS) creates fake speech. Replay attacks play recordings of a real voice to trick the system (Kinnunen et al., 2020). Combining these spoofing countermeasures with ASV makes the system more resistant to attacks (Wu et al., 2017).

By understanding, the need for effective countermeasures, several anti-spoofing challenges have emerged (Wu et al., 2015) (Kinnunen et al., 2017) (Todisco et al., 2019). To effectively detect spoof attacks, it is crucial to extract accurate data from speech signals. Choosing effective features is key in detecting spoofed speech. Features covering longer time spans across many frames are needed to detect these artifacts effectively (Tian et al., 2017).

### A. Proposed Work Contribution and Organization of the Paper

This paper investigates hand-crafted spectro-temporal representations, using deep learning and feature extraction, for detecting spoofed speech. The paper's contributions are (1) investigating well-known features with sequence-based representations, (2) suggesting deep learning with long short-term memory (LSTM) and bidirectional long short-term memory (BiLSTM) for spoofed speech detection instead of traditional methods, and (3) proposing a new feature by converting open-source speech and music interpretation by large-space extraction's (OpenSMILE's) 88 global representations into time series features.

The paper is organized as follows: Section 2 describes previous related work. Section 3 explains the background of ASVspoof 2019 for logical access, the types of attacks in the ASVspoof 2019 dataset, the feature extraction process, and the model used. Section 4 details the deep learning methodology. Sections 5 and 6 discuss the experimental setup, analyze results, and compare the proposed approach to current systems. The conclusion and directions for future research are covered in Section 7.

ARO-The Scientific Journal of Koya University  
Vol. XII, No. 2 (2024), Article ID: ARO.11636. 11 pages  
Doi: 10.14500/aro.11636

Received: 31 May 2024; Accepted: 23 August 2024  
Regular research paper; Published: 12 September 2024

<sup>†</sup>Corresponding author's e-mail: arsalan.mirza@soran.edu.iq  
Copyright © 2024 Arsalan R. Mirza and Abdulbasit K. Al-Talabani.  
This is an open-access article distributed under the Creative Commons Attribution License (CC BY-NC-SA 4.0).



## II. LITERATURE REVIEW

Spoofing speech detection has become increasingly important because of the growth in deceiving activities such as voice impersonation, conversion, synthetic speech attacks, and deepfake technology. To resolve this, researchers have investigated numerous methods for distinguishing genuine speech from fake speech (Nautsch et al., 2021).

A typical method for spoofing speech detection is extracting the acoustic feature from the speech signal (Rahmeni, Aicha, and Ayed, 2020) (Dave, 2013). The primary focus of early research was on conventional acoustic characteristics, however, the development of machine/deep learning approaches encouraged the researchers to focus on more complex to enhance the deep learning-based features/models (Jiang et al., 2009) (Kumari and Jayanna, 2015) (Ahmed et al., 2022).

Recent studies have used deep learning architectures such as recurrent neural networks (RNNs) and convolutional neural networks (CNN) to extract discriminative features from speech signals. A 1D-CNN+LSTM approach (Ahmed et al., 2022) was proposed on the ASVspooF 2019 dataset, achieving an equal error rate (EER) of 31.9%. A hybrid data augmentation technique using the synthetic minority over-sampling technique was implemented (Chakravarty and Dua, 2023) by employing an LSTM and support vector machine classifier, achieving EERs of 5.1% and 7.4% with 93% and 92% accuracy, respectively. A similar approach was used (Zhou et al., 2022) for the ASVspooF 2019 PA subset, using GTCC and mel-frequency cepstral coefficients (MFCC) features. The BiLSTM network achieved an accuracy of 97% and an EER of 2.97% through consistent implementation across multiple approaches.

Researchers have enhanced the accuracy of identifying fake speech by combining multiple acoustic features. As suggested by Karo, Yeredor, and Lapidot, 2022, they applied new methods based on probability mass function estimation to audio waveforms in the ASVspooF 2019 LA subset. They focused on two types of filter banks (MFCC and GTCC) and used diffusion maps to reduce dimensionality, measuring similarity through diffusion distance. Their evaluation of this subset achieved an EER of 12.09% for males and 12.99% for females. Similarly, Hassan and Javed, 2021 proposed an effective synthetic speech detector by combining spectral features including MFCC, GTCC, spectral flux, and spectral centroid. Their model, trained on 15,981 samples and tested on 14,161 samples, achieved an impressive EER of 3.05%.

Moreover, researchers have explored domain-specific knowledge, such as adopting different speech representations of the front-end model and the fusion of different temporal segments. Another research (Wei, Pang and Kuo, 2024) proposed a Green ASVspooF detector based on pre-trained speech representations by extracting the probability vectors, probability histograms, and probability patterns of fusion of three XGBoost classification stages and achieved 1.82% EER for the 2019 LA evaluation subset and lead to lower model sizes and inference complexity per input speech sample.

In addition to employing acoustic and deep features, various methods and platforms exist for extracting features from speech signals. For instance, according to Devesh et al., 2022, an 88-dimensional OpenSMILE feature set was applied to LJ speech, CMU-arctic, and LibreTTS datasets.

### A. Research Gap

Recent reviews of ASV and countermeasure systems highlight the ongoing need for improvement in this critical area. Both ASV and CM systems traditionally use acoustic and deep features for extracting features. Deep features (non-handcrafted features) are extracted from the multiple layers of a neural network. These features, which do not have explicit, pre-defined meanings, are learned during the training process. Neural networks capture complex patterns and hierarchical structures in the data through these deep features. However, few studies explore the effects of MFCC and constant Q cepstral coefficient (CQCC) features, especially in their time-series formats such as separate, concatenated, and fused forms. In addition, there has been limited focus in related research on time-series representations of speech, possibly due to the complexity of handling large amounts of data. Furthermore, as far as we know, the application of time-series OpenSMILE features with different time intervals has not been explored before.

## III. BACKGROUND

### A. ASVspooF 2019 Logical Access Subset

The ASVspooF 2019 project's logical access subset is part of its third version. It includes fake speech made by TTS or VC models. This subset contains 12,483 real utterances and 108,978 fake ones created by 19 different methods, such as 11 TTS techniques, 5 VC techniques, and three hybrid approaches. ASVspooF 2019 covers both logical access and physical access scenarios with a wider variety of spoofing methods and a larger dataset.

The ASVspooF 2019 logical access subset is part of the third version of the ASVspooF project. Spoofed samples are generated using TTS or VC models. The ASVspooF 2019 LA subset comprises 12,483 bonafide utterances and 108,978 spoofed utterances. These spoofed utterances are created using 19 different algorithms, including 11 TTS techniques, five VC techniques, and three hybrid approaches (as detailed in Table I).

The logical access subset of the ASVspooF 2019 dataset is divided into three subsets: training, development, and evaluation. The training subset is used to train spoofing countermeasures, whereas the development subset is used

TABLE I  
A SUMMARY OF THE ASVSPOOF 2019 LOGICAL ACCESS DATASET

ASVspooF 2019 LA Subset	Speaker		Utterance	
	Male	Female	Bonafide	Spoof
Train	8	12	2,580	22,800
Development	8	12	2,548	22,296
Evaluation	30	30	7,355	63,882

to optimize these countermeasures. Finally, the evaluation subset assesses the performance of the developed models.

The spoofing algorithms that are present in the evaluation data are not present in the training and development subsets. Out of 19 different spoofing algorithms, six (A01–A06) of them have been used for generating the utterance of the train and development subset whereas the remaining 13 (A07–A19) have been used for generating the evaluation subset.

*B. MFCC, CQCC, and OpenSMILE Feature*

MFCC are crucial features widely used in voice signal processing. The process of extracting MFCC involves dividing the signal into frames, calculating the energy spectrum, applying Mel filter banks, computing logarithms for each filter bank output, and performing discrete cosine transform (Novoselov et al., 2016). The computation and extraction steps are depicted in Fig. 1.

Short-term spectral features such as MFCC are commonly used in speech recognition systems (Abdul and Al-Talabani, 2022). The higher frequency filters in the Mel-scale filter bank used by MFCC have wider bandwidths compared to lower frequency filters, but they maintain the same temporal resolutions (Patel and Patil, 2015).

Studies have shown that CQCC features perform well in utterance and speaker verification (Todisco, Delgado and Evans, 2016). CQCC extraction involves using the constant-Q transform (CQT), which provides enhanced frequency resolution for lower frequencies and improved temporal resolution for higher frequencies (Todisco et al., 2019).

Fig. 2 illustrates how CQCC features are extracted. According to Todisco, Delgado, and Evans (2016), studies have used three different dimensions of CQCC features: 12, 19, and 29, all including C0. In the context of CQCC features, C0 represents the average energy across frequency bands after applying the CQT to the signal. The initial choice of 12 and 19 dimensions is based on their common use in

speech and speaker recognition. The 29 dimension aims to explore whether higher coefficients provide additional information useful for detecting spoofing.

In the opposite, Yang, Das and Li, 2020, claimed that the CQT feature, more precisely the log power spectrum of the CQT, does not have the phase information of the signal. To further generate the CQCC, even more information will be discarded. From a hand-crafted feature engineering point of view, a good feature must capture discriminative information between classes and must also be compact in size.

Moreover, there is another feature that has received relatively little attention in the area of research for spoof detection, which is the OpenSMILE feature. Open Speech and Music Interpretation by Large Scale (OpenSMILE) (Eyben, Wöllmer and Schuller, 2010) is an innovative open-source tool designed for extracting features in speech processing and music information retrieval. Its main purpose is to facilitate audio feature extraction. OpenSMILE offers a straightforward, scriptable console application where modular feature extraction components can be easily configured, allowing researchers to take advantage of features across various domains. The OpenSMILE<sup>1</sup> features are an open-source toolkit that extracts essential speech features. OpenSMILE features include three standard support features – ComParE 2016, GeMAPS, and eGeMAPS. ComParE 2016 (Eyben, Wöllmer and Schuller, 2010) is the largest in terms of size and each feature can be extracted in the low-level descriptor (LLD) or functional. The contribution of every feature including MFCC, CQCC, and OpenSMILE has been investigated in detecting fake speech, this motivated us to use the eGeMAPSv02 (Eyben et al., 2016) contains 88 functional parameters. The LLD contains 25 feature-level parameters for each 20 ms and with a hop length of 10 ms.

1. <http://www.audeering.github.io/opensmile>

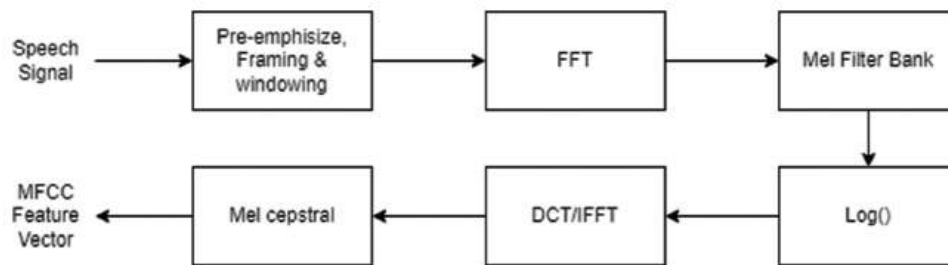


Fig. 1. Mel-frequency cepstral coefficient feature extraction process.

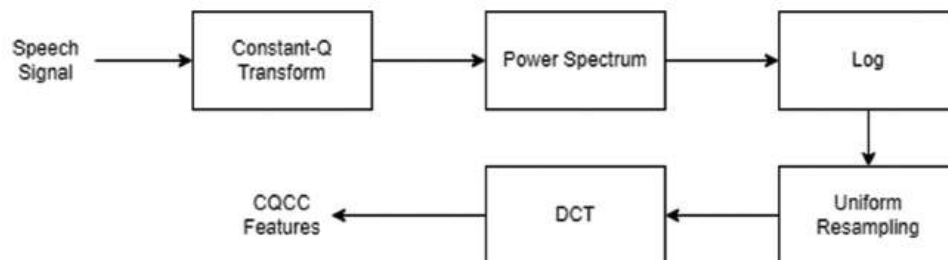


Fig. 2. Constant Q cepstral coefficients feature extraction process.

### C. LSTM and BiLSTM

LSTM is a specialized form of RNN widely utilized in natural language processing and time series prediction tasks. Unlike a standard LSTM, where the input flows only in one direction, a BiLSTM processes input in both forward and backward directions, allowing it to capture important contextual information from both past and future states. Fig. 3 illustrates the cell state of an LSTM model, highlighting its internal mechanisms.

The cell state is a crucial component in LSTM networks, responsible for maintaining long-term dependencies and preserving relevant information across extended sequences. Serving as the memory within the LSTM unit, it plays a vital role in capturing and retaining data from previous time steps (illustrated in Fig. 4, left). The cell state is updated and modified through three primary gates: the forget gate, the input gate, and the output gate. These gates work together to determine which information should be remembered or discarded, ensuring the LSTM effectively manages data throughout the sequence.

LSTM is specifically designed to update information across different time steps, overcoming the limitations of traditional RNNs. Unlike RNNs, LSTMs excel at capturing long-term dependencies in sequential data (as shown in Fig. 4, left). This capability makes LSTMs highly effective for time series prediction and other tasks involving sequential data in deep learning architectures. The BiLSTM network, illustrated in Fig. 4, right, enhances this functionality by processing data in both forward and backward directions, thereby integrating information from both past and future time steps for more comprehensive modeling.

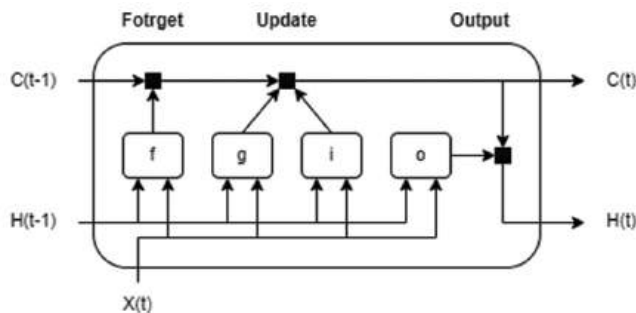


Fig. 3. Cell state used in long short-term memory.

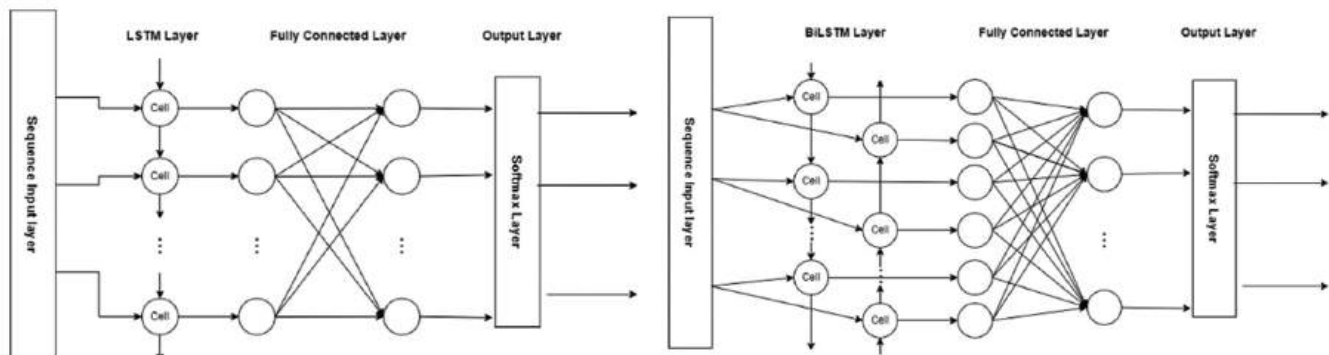


Fig. 4. The structure of long short-term memory (left) and bidirectional long short-term memory (right).

### IV. DEEP LEARNING APPROACH METHODOLOGY

This study primarily aimed to create a countermeasure to work alongside the proposed ASV system, which was included in the ASVspooF 2019 challenge. In this section, the architecture of the proposed CM system is presented. Regarding the feature extraction from the speech signal, the paper adopts the use of the CQCC, MFCC, and OpenSMILE features toolkit which will be described in section 4.1. At the classifier level, LSTM (Hochreiter and Schmidhuber, 1997) and BiLSTM are utilized to evaluate the data of the ASVspooF 2019 LA subset to build different CM systems. Fig. 5, shows an illustration of the proposed CM block diagram. The suggested model operated in sequence-based phases and each phase had several processes carrying out distinct tasks.

As illustrated in Fig. 5, the proposed method comprises several tasks of the deep learning model. The model is trained using the ASVspooF 2019 logical access subset. The main components of a spoofing detection system are feature extraction and decision-making modules. In front-end features extraction, time series-based features such as (MFCC, CQCC, and OpenSMILE) have been used, For the back-end speech spoofing countermeasure module, we explore the LSTM and BiLSTM classifiers for training the model, and the posterior probability is used for decision making. In our model the structure is a sequence-to-label classification, we have created a sequence input layer, followed by an LSTM layer, then a fully connected layer, and a Softmax layer at the end.

#### A. Feature Extraction

In this phase, we will discuss the used features and the extraction process. Feature extraction involves transforming raw speech data into a set of attributes or characteristics that can be used for analysis. This process includes selecting and transforming data to create informative, non-repetitive features that enhance model performance.

##### MFCC features

Feature extraction aims to provide a clear representation of the vocal tract based on its response characteristics. By leveraging the capabilities of the human auditory system (HAS), MFCC can accurately capture key parameters of speech signals across different voice transformation scenarios.



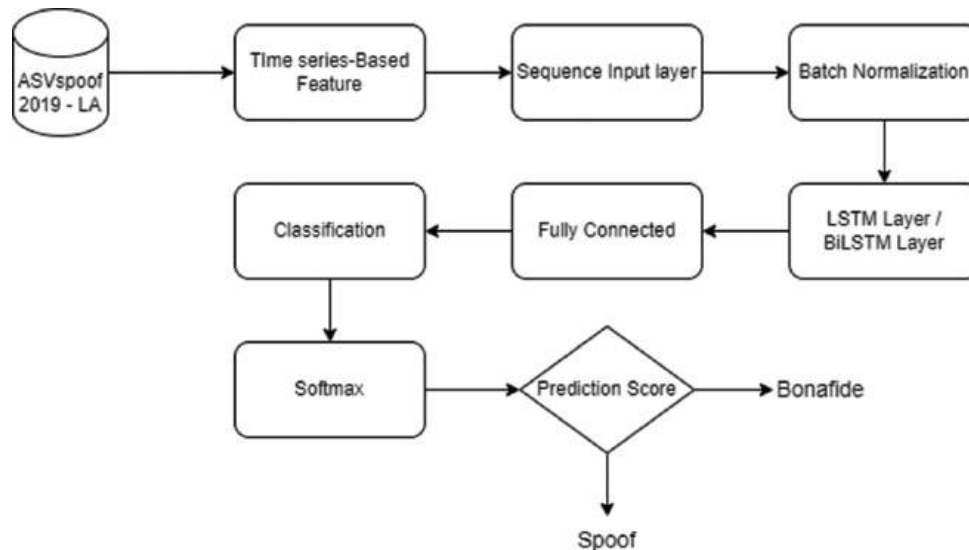


Fig. 5. The structure of the main approach of the proposed countermeasure.

In this study, the Librosa (McFee et al., 2015) library was used to extract a sequence of 12-dimensional MFCC feature vectors with log energy for each spoken sentence. MFCC and log power magnitude spectra (LPMSs) are obtained using a pre-emphasis with a coefficient of 0.97. Each frame is acquired by applying a 30 ms Hamming window with a step size of 15 ms.

#### CQCC features

CQCC is derived from CQT, which creates a time-frequency representation for speaker recognition and spoofing detection (Todisco, Delgado and Evans, 2016). CQCCs are adept at capturing distinct spectral features across various frequency levels, making them effective in distinguishing between different types of audio signals (Todisco, Delgado and Evans, 2017).

The CQCC feature was extracted with a time step of 12 ms, covering nine octaves with 96 bins per octave. Each feature vector includes 19 cepstral coefficients, including the 0<sup>th</sup> coefficient, along with their delta and double delta coefficients. Hence, each feature vector is 60-dimensional. In addition, we have extracted another CQCC feature set with different parameters. This new feature is extracted with nine octaves with 171 bins per octave and 12 static cepstral coefficients including 0<sup>th</sup> coefficient.

#### OpenSMILE features

The OpenSMILE features are an open-source toolkit that enables to the extraction of essential speech features such as auditory formants spectral, signal energy, MFCC, Shimmer, Jitter, linear predictive coding, pulse code modulation, and line spectral pairs. While the ComParE 2016 and GeMAPS can be used as a global representation of speech samples with 6373 and 88 features, respectively, we have used eGeMAPSv02 with LLDs as a feature set with 25 time-step parameters for each 20 ms and with a hop length of 10 ms.

Using the OpenSMILE feature, the global representation of each speech sample with eGeMAPSv02 which contains 88 functional parameters has been extracted. For a new time, series-based feature we have created a new feature by

splitting the speech signal into different frames and extracting the functional features for each frame. For this feature set, the hamming window has a size of 100 ms, and a step size of 40 ms is applied to extract the features.

#### B. Combined Feature

Combining features in the context of deep learning and data processing is the process of integrating multiple types or sets of features to create a more comprehensive and informative representation of the data. We have concatenated MFCC with CQCC to improve the accuracy and robustness of the system by providing diverse perspectives on the audio signal's characteristics. In this paper, we have used a combined feature set that consists of 13 MFCC and 13 CQCC to construct a new feature set with 26 dimensions of time steps whereas the length of utterance remains the same.

## V. EXPERIMENTAL SETUP

The implementation of the proposed deep learning approaches is carried out using Python version 3.9.13. We evaluated our models on the ASVspooof 2019 evaluation part for the logical access subset.

The proposed countermeasure models (LSTM and BiLSTM) have been implemented using MATLAB 2023b and Python on the Windows 10 operating system with 64GB of RAM and Processor Intel(R) Core (TM) 3.6GHz 16 CPUs and a Single GPU with 10 GB of size. Data extraction and preprocessing have been conducted using Jupyter Notebook within the Anaconda environment.

#### A. LSTM and BiLSTM Parameters Tuned

We used 1000 hidden states across all feature types in both models, even though most speech samples have fewer than 1000 time steps per sample. Our approach included training on the ASVspooof 2019 Train subset and testing on the development subset. We tested various layer numbers and configurations to optimize model

performance. Each model was trained for 100 epochs with a fixed learning rate of 0.001 and a batch size of 128 for efficient improvement.

### B. Experiments

Table II provides a detailed overview of the feature sets used in our investigation, including the number of features linked to each time step for LSTM and BiLSTM models. This systematic approach enables us to explore the efficiency of these models in extracting the artifact within the different types of features.

During the training of the models, the BiLSTM was slower than the LSTM model. This observation suggests that BiLSTM models can capture additional features in the data. In this regard, Siami-Namini, Tavakoli and Namin, 2019, recommended using BiLSTM instead of LSTM for forecasting problems in time series analysis.

### C. Fusion of Models

Fusion can occur at various levels, including feature-level fusion, decision-level fusion, or model-level fusion, depending on the specific application and context. In this set of experiments, model-level fusion, also known as late fusion, was used by combining the results from different models through averaging their outputs. This method allows for the creation of fusion models that use either the same classifier with different features or the same features with different classifiers to improve overall performance. Different model-level fusions were conducted, selecting the best-performing models based on various evaluation criteria to achieve more robust and effective results.

## VI. RESULTS AND DISCUSSION

In this section, we present the findings of our experimental analysis and engage in a comprehensive discussion of the observed results. We begin by summarizing the outcomes of our model implementations and highlighting key performance metrics.

### A. Feature-Level Fusion

Feature-level fusion is used for merging different types of features to enhance the performance of models. By combining multiple feature sets, enables more accurate and robust predictions and leveraging the strengths of each feature set.

TABLE II  
EXPERIMENTAL SETUP TIME SERIES-BASED FEATURE

Feature ID	Time series-based feature	Dimension
CQCC_60	CQCC	60
CQCC_13	CQCC	13
MFCC_13	MFCC	13
MFCC_CQCC_26	MFCC+CQCC	26
OS_25	OpenSMILE	25
OS_88	OpenSMILE	88

CQCC: Constant q cepstral coefficients, MFCC: Mel-frequency cepstral coefficients

### LSTM

With the LSTM model, we conducted the experiments using six different types of time series-based features, without employing any data augmentation process. The results of our analysis, as detailed in Table III, reveal significant insights into the performance of the LSTM models across various feature sets. Notably, the LSTM model with CQCC\_60 and OS\_25 features outperformed other features in all evaluation metrics.

As shown in Table III, the model with the CQCC with 60 dimensions of time step feature obtained the best EER (6.15%), Min-tDCF (0.1917), and Recall (99.91%) among other types of features. From the OpenSMILE time series-based feature (OS25 and OS88), we can conclude that the higher number of time step features does not guarantee to have a better result.

In experiment 5, with OS (25), an outstanding result was achieved in terms of accuracy, precision, and f1-score whereas the OS (25) has been extracted in the LLD of the OpenSMILE feature<sup>2</sup>. Furthermore, in experiment 6, the OpenSMILE with 88 time series-based features did not perform better than experiment 5 with OpenSMILE 25.

### BiLSTM

The result of the same features has been used with the BiLSTM model and the result is shown in Table IV. As we can see, in experiment 9, the 13 MFCCs time series-based features outperform all other features. In addition, this feature achieved the best result in terms of accuracy (93.05%).

The BiLSTM models outperformed their unidirectional LSTM in terms of accuracy, precision, recall, and f1-score whereas on the other hand, the LSTM model obtained outstanding results for EER (6.15%) and min-tDCF (0.1917). While the BiLSTM model is capable of capturing complex temporal dependencies as shown in Table IV, these findings underscore the enhanced capability of BiLSTM models in leveraging bidirectional context (Table IV).

Experiments 4 and 10, where a combination of CQCC and MFCC is performed, did not lead to improving the result of both LSTM and BiLSTM models.

## B. FUSION MODELS RESULT

In this section, the fusion models focus on combining the best-performing LSTM and/or BiLSTM experiments. A total of 12 experiments were carried out 6 for each model with the top performers identified using various evaluation metrics. Initially, the two best experiments from both LSTM and BiLSTM models were selected, followed by the selection of the best metrics between the two. Eventually, the selection was expanded to include the top three and four experiments for each model. To ensure a comprehensive analysis, experiments were selected from Tables III and IV. An averaging technique was applied to merge the results from the selected experiments in these fusion models.

A fusion model of the top two experiments, 1 and 9, produced the best results (Table V) in terms of EER and

2. <https://audeering.github.io/opensmile-python/usage.html#process-signal>

TABLE III  
LONG SHORT-TERM MEMORY RESULTS WITH DIFFERENT TYPES OF FEATURES

Experiment ID	Feature	Equal error rate %	Min-tDCF	Accuracy %	Precision %	Recall %	F1-score %
1	CQCC (60)	6.15	0.1917	80.51	78.33	99.91	87.82
2	CQCC (13)	13.06	0.4476	58.60	54.10	99.51	70.09
3	MFCC (13)	9.35	0.2456	81.60	79.63	99.81	88.59
4	MFCC_CQCC (26)	11.52	0.3475	58.22	53.47	99.88	69.66
5	OS (25)	8.25	0.2292	88.55	87.50	99.69	93.20
6	OS (88)	9.80	0.2344	86.74	85.39	99.78	92.03

CQCC: Constant q cepstral coefficients, MFCC: Mel-frequency cepstral coefficients

TABLE IV  
BiLSTM RESULTS WITH DIFFERENT TYPES OF FEATURES AND DIFFERENT TIME STEP

Experiment ID	Feature	Equal error rate %	Min-tDCF	Accuracy %	Precision %	Recall %	F1-score %
7	CQCC (60)	9.74	0.3090	81.87	80.13	99.56	88.80
8	CQCC (13)	21.46	0.6325	62.03	58.60	98.42	73.46
9	MFCC (13)	6.29	0.1937	93.05	92.71	99.50	95.99
10	MFCC_CQCC (26)	11.02	0.3748	82.25	80.90	99.14	89.10
11	OS (25)	8.93	0.2380	89.39	88.62	99.49	93.74
12	OS (88)	8.33	0.2333	87.99	86.89	99.68	92.84

CQCC: Constant q cepstral coefficients, MFCC: Mel-frequency cepstral coefficients

TABLE V  
FUSION MODEL RESULT OF COMBINING DIFFERENT TYPES OF EXPERIMENTS

Fusion models	Equal error rate %	Min-tDCF	Accuracy %	Precision %	Recall %	F1-score %
1,4	4.28	0.17766	85.66	84.05	99.94	91.31
1,5	5.54	0.19461	88.32	87.03	99.93	93.03
1,9	4.06	0.15862	91.64	90.75	99.92	95.11
1,12	5.88	0.19494	88.45	87.20	99.91	93.12
5,6	8.26	0.21688	88.00	86.78	99.81	92.84
5,9	5.98	0.18099	92.04	91.32	99.79	95.37
7,12	8.71	0.21638	87.33	85.99	99.86	92.41
9,11	6.25	0.19408	92.21	91.60	99.69	95.47
9,12	6.07	0.18543	91.66	90.90	99.78	95.13
1,3,4	4.73	0.18489	77.03	74.41	99.97	85.31
1,3,5	4.86	0.17893	87.01	85.56	99.95	92.19
1,5,6	6.06	0.19496	89.08	87.97	99.84	95.53
3,5,6	7.39	0.20877	87.46	86.13	99.87	92.49
7,9,12	6.02	0.19064	88.65	87.45	99.88	93.25
9,11,12	6.11	0.20110	89.73	88.77	99.75	93.94
1,3,5,6	5.18	0.19382	87.53	86.14	99.95	92.53
7,9,11,12	6.02	0.19872	88.99	87.83	99.87	93.46
1,3,5,6,7,8,11,12	5.87	0.19818	87.71	86.34	99.93	92.64

min-tDCF. The obtained results are 0.15862 for min-tDCF and 4.06% of EER. Consequently, in experiments 9 and 11, the best fusion model improved its accuracy and precision to 92.21% and 91.60%, respectively.

Based on the findings in Table V, the fusion model that combines CQCC and MFCC features (specifically fusion [1,4] and fusion [1,9]) shows that using the fusion of these features results in improved performance, particularly by achieving lower EER and min-tDCF values. It can also be inferred that combining different types of features and classifiers enhances the model's overall performance. However, unlike the EER, the fusion models did not outperform the single model in terms of accuracy (93.05%) and precision (95.99%) when compared to the single model in experiment 9.

### C. ATTACK-BASED ANALYSIS RESULT

The ASVspoof 2019 logical access dataset comprises 13 unseen attacks within the evaluation subset. The attack-based analysis section aims to identify the attack type with the most noticeable effect on the overall result. Within the LA subset, attack types range from A07 to A19. Each attack type consists of a total of 4914 samples, whereas 7355 samples are categorized as bonafide.

Fig. 6 offers insights into the performance of both the LSTM (left) and BiLSTM (right) models utilizing CQCC (60) in detecting spoofs created by various attack types (including A07, A09, A16, and A19) within the LA subset, showcasing the percentage of missed samples for each attack type.

The LSTM model demonstrates superior performance in detecting bonafide, A07, A09, A12, A16, and A19. In contrast, the BiLSTM model surpasses the LSTM in identifying attacks A10, A11, A14, and A15, yielding better results. However, it also struggles with misclassifications for attacks A13, A17, and A18.

Fig. 7 shows that utilizing CQCC with 13 dimensions did not yield improved results when compared to using CQCC with 60 dimensions. Despite the lower dimensionality, the performance of both LSTM and BiLSTM models did not significantly improve. Interestingly, among the attacks, only A07, A16, and A19 were consistently identified correctly by both models, irrespective of the dimensionality of the CQCC feature. This suggests that while reducing the dimensionality of the feature may offer computational advantages, it does not necessarily enhance the models' ability to accurately classify certain attack types.

Fig. 7. Miss classification of samples for each attack type of constant Q cepstral coefficients feature of 13 dimensions with long short-term memory (left) and bidirectional long short-term memory (right) models.

Even though the BiLSTM model demonstrated a higher misclassification rate of bonafide samples at 3.97%, the LSTM model showcased improved performance with a lower misclassification rate of 1.27%, as illustrated in Fig. 8. Moreover, it is noteworthy that despite this difference, the BiLSTM model exhibited superior performance in detecting all attack types when utilizing MFCC features, outperforming the LSTM models employing the same features. This suggests that while the LSTM model may excel in certain aspects, such as accurately classifying bonafide samples, the BiLSTM model shows promise in overall attack detection when leveraging MFCC features.

Fig. 8. Miss classification of samples for each attack type of mel-frequency cepstral coefficients feature of 13 dimensions with long short-term memory (left) and bidirectional long short-term memory (right) model.

In the LSTM model (depicted in Fig. 9), although the results differ from those of the BiLSTM model for attack types A07 to A16, the misclassification rate of bonafide samples is lower with LSTM at 0.53% compared to the BiLSTM models.

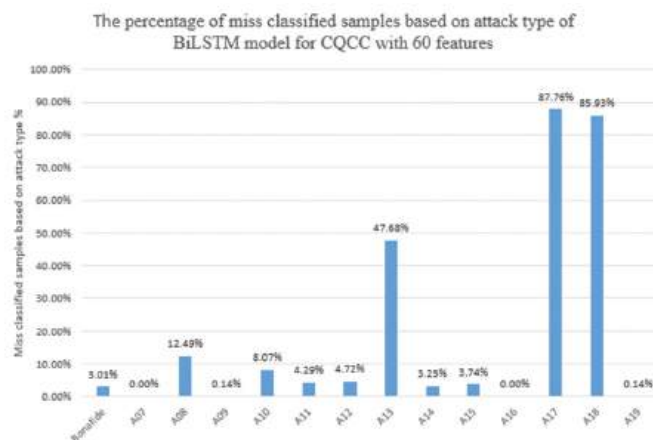
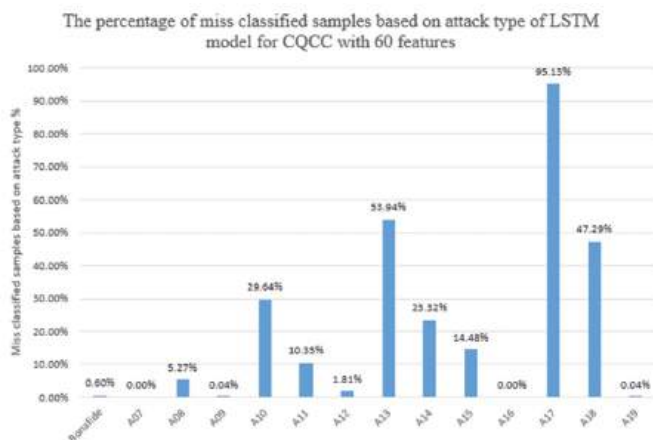


Fig. 6. Miss classification of samples for each attack type of constant Q cepstral coefficients feature of 60 dimensions with long short-term memory (left) and bidirectional long short-term memory (right) models.

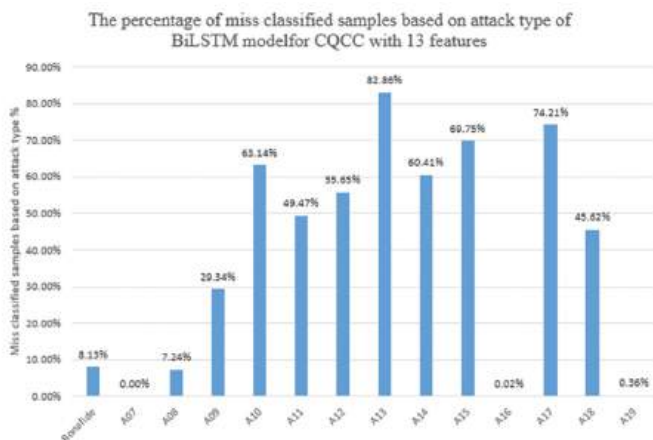
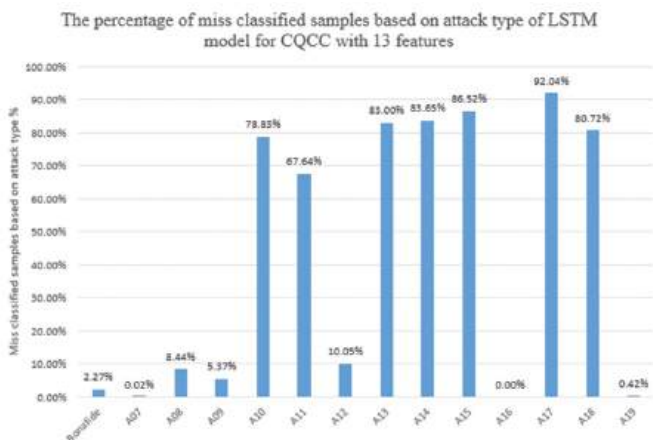


Fig. 7. Miss classification of samples for each attack type of constant Q cepstral coefficients feature of 13 dimensions with long short-term memory (left) and bidirectional long short-term memory (right) models.

Fig. 10 shows the misclassification outcomes based on attack types using OpenSMILE with 25 time series-based features. While both the LSTM and BiLSTM models demonstrate similar overall performance, they both notably enhance the identification of A07, A09, A10, A11, A12, A13,

A14, A15, and A16 attack types. However, both models exhibit a significantly higher rate of misclassification for A18, A17, A08, and A19 attacks, as well as bonafide samples.

Fig. 11 illustrates the percentage of misclassified samples by both LSTM and BiLSTM models across various attack

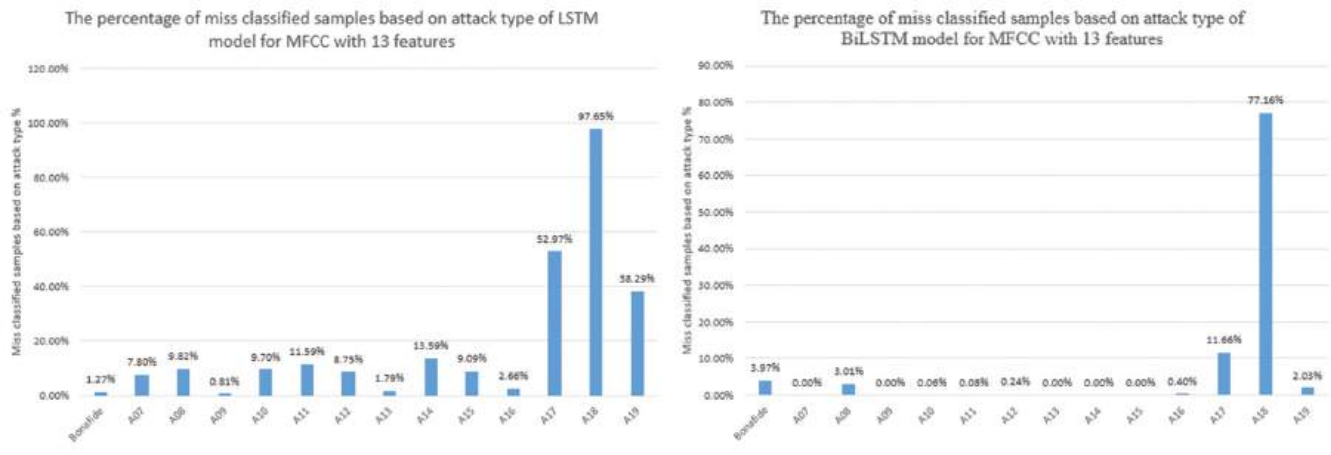


Fig. 8. Miss classification of samples for each attack type of mel-frequency cepstral coefficients feature of 13 dimensions with long short-term memory (left) and bidirectional long short-term memory (right) model.

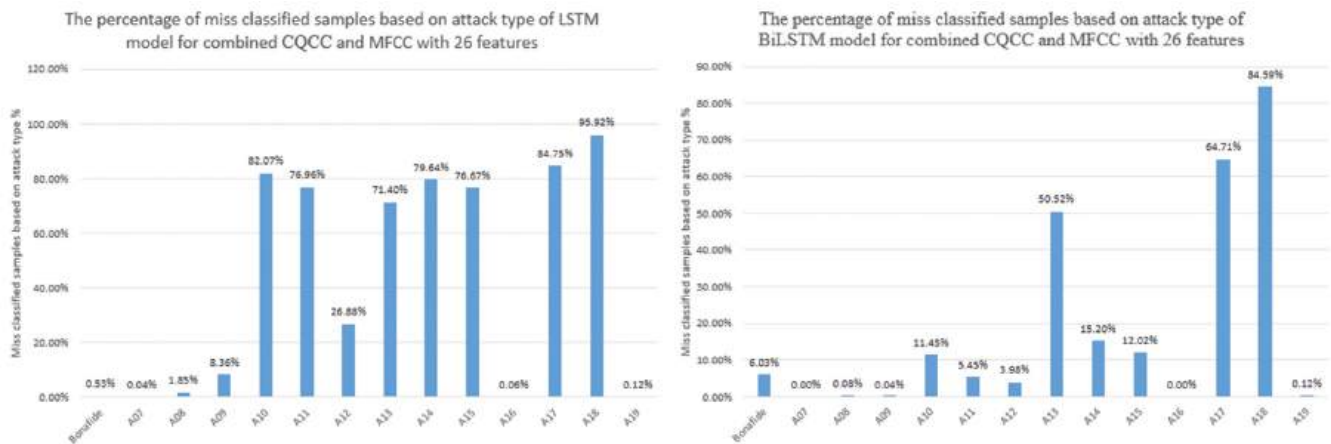


Fig. 9. Miss classification of samples for mel-frequency cepstral coefficients and constant Q cepstral coefficients combined features of 26 dimensions with long short-term memory (left) and bidirectional long short-term memory (right) model.

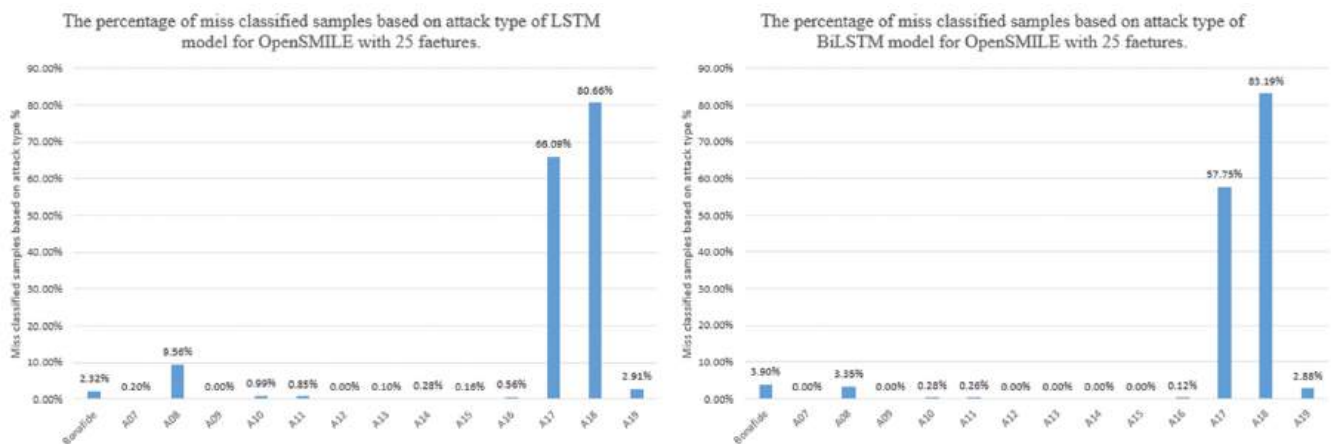


Fig. 10. Miss classification of samples for open-source speech and music interpretation by large-space extraction of 25 dimensions with long short-term memory (left) and bidirectional long short-term memory (right) model.

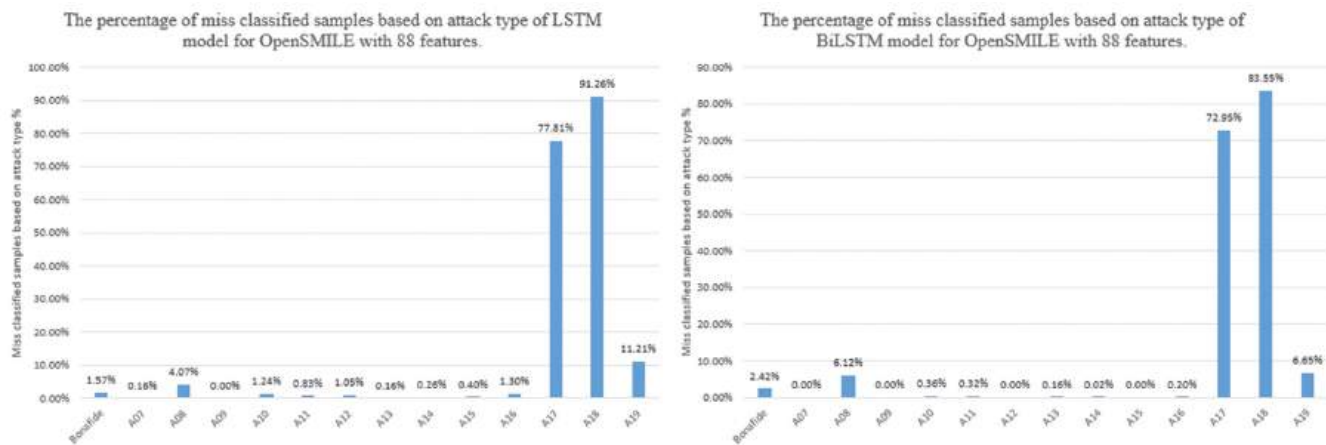


Fig. 11. Miss classification of samples for open-source speech and music interpretation by large-space extraction of 88 dimensions with long short-term memory (left) and bidirectional long short-term memory (right) model.

types, utilizing OpenSMILE features with 88 dimensions. Figs. 10 and 11 yield comparable results for OpenSMILE features with 25 dimensions and 88 dimensions, respectively. Although the misclassification rate for all attack types (excluding A17, A18, and A19) remains below 7% for both features with LSTM and BiLSTM, challenges arise in accurately detecting attacks A17 and A18.

Notably, all models with CQCC, MFCC, and OpenSMILE features succeeded in detecting the attack types but exhibited higher rates of misclassification for A17 and A18. The BiLSTM model had the lowest misclassification rate for attack A17 of 11.66% with 13 features of MFCC. Subsequently, the BiLSTM model with 13 features of CQCC obtained 45.62% with the lowest misclassification rate among all other types of features. The findings from Figs. 6-11 lead to the conclusion that detecting attack types A17, A18, and A19 poses greater difficulty compared to other attack types. While the BiLSTM model excels in detecting attacks A17, A18, and A19, the LSTM model achieves superior results in the term of EER and min-tDCF.

## VII. CONCLUSION

In this paper, an extensive investigation has been conducted on the effect of LSTM and BiLSTM model of the ASVspoof 2019 logical access dataset with a time series-based feature. The use of single and fusion versions of features on unseen attacks affects the spoof detection model. The investigations lead to the conclusion that having a higher number feature of time steps cannot guarantee improvement in the model's performance. In addition, the BiLSTM model outperforms the LSTM almost in all types of features. This indicates the usefulness of the BiLSTM model for time series-based features in contributing the spoof detection. Furthermore, within the logical access subset, the attacks A17, A18, and A19 are more challenging to detect. However, the CQCC feature achieved the lowest EER of 6.15% as a single system and an EER of 4.06% of the fusion model and the highest accuracy among all other features with 93.05% gained with the MFCC feature as a single system.

## VIII. ACKNOWLEDGMENT

The work was supported by Soran University. We appreciate the Faculty of Science at Soran University for their financial support, access to resources, and facilitation of the completion of this research.

## REFERENCES

- Abdul, Z.K., and Al-Talabani, A.K., 2022. Mel frequency cepstral coefficient and its applications: A review. *IEEE Access*, 10, pp. 122136-122158.
- Adiban, M., Sameti, H., and Shehnepoor, S., 2020. Replay spoofing countermeasure using autoencoder and siamese networks on ASVspoof 2019 challenge. *Computer Speech and Language*, 64, pp. 1-10.
- Ahmed, N., Khan, J., Sheta, N., Tarek, R., Zualkernan, I., and Aloul, F., 2022. Detecting Replay Attack on Voice-Controlled Systems using Small Neural Networks. In: *2022 IEEE 7th Forum on Research and Technologies for Society and Industry Innovation, RTSI 2022*, pp.50-54.
- Bai, Z., and Zhang, X.L., 2021. Speaker recognition based on deep learning: An overview. *Neural Networks*, 140, pp. 65-99.
- Chakravarty, N., and Dua, M., 2023. Data augmentation and hybrid feature amalgamation to detect audio deep fake attacks. *Physica Scripta*, 98(9), p. 096001.
- Dave, N., 2013. Feature extraction methods LPC, PLP and MFCC in speech recognition. *International Journal for Advance Research in Engineering and Technology*, 1(6), pp. 1-5.
- Devesh, K., Pavan, K.V., Ayush, A., and Mahadeva Prasanna, S.R., 2022. *Fake Speech Detection Using OpenSMILE Features*. Springer International Publishing, Berlin.
- Eyben, F., Scherer, K.R., Schuller, B.W., Sundberg, J., Andre, E., Busso, C., Devillers, L.Y., Epps, J., Laukka, P., Narayanan, S.S., and Truong, K.P., 2016. The Geneva minimalistic acoustic parameter set (GeMAPS) for voice research and affective computing. *IEEE Transactions on Affective Computing*, 7(2), pp. 190-202.
- Eyben, F., Wöllmer, M., and Schuller, B., 2010. OpenSMILE - The Munich Versatile and Fast Open-Source Audio Feature Extractor. In: *MM'10-Proceedings of the ACM Multimedia 2010 International Conference*, pp.1459-1462.
- Hassan, F., and Javed, A., 2021. Voice Spoofing Countermeasure for Synthetic Speech Detection. In: *2021 International Conference on Artificial Intelligence, ICAI 2021*, pp. 209-212.
- Hochreiter, S., and Schmidhuber, J., 1997. Long short-term memory. *Neural*

*Computation*, 9(8), pp. 1735-1780.

Jiang, Z., Huang, H., Yang, S., Lu, S., and Hao, Z., 2009. Acoustic Feature Comparison of MFCC and CZT-Based Cepstrum for Speech Recognition. In: *5<sup>th</sup> International Conference on Natural Computation, ICNC 2009*, 1(200808003), pp.55-59.

Kamble, M.R., Sailor, H.B., Patil, H.A., and Li, H., 2020. Advances in anti-spoofing: From the perspective of ASVspoof challenges. *APSIPA Transactions on Signal and Information Processing*, 9, e2.

Karo, M., Yeredor, A., and Lapidot, I., 2024. Compact time-domain representation for logical access spoofed audio. *IEEE/ACM Transactions on Audio Speech and Language Processing*, 32, pp.946-958.

Kinnunen, T., Delgado, H., Evans, N., Lee, K.A., Vestman, V., Nautsch, A., Todisco, M., Wang, X., Sahidullah, M., Yamagishi, J., and Reynolds, D.A., 2020. Tandem assessment of spoofing countermeasures and automatic speaker verification: Fundamentals. *IEEE/ACM Transactions on Audio Speech and Language Processing*, 28, pp. 2195-2210.

Kinnunen, T., Sahidullah, M., Delgado, H., Todisco, M., Evans, N., Yamagishi, J., and Lee, K.A., 2017. The ASVspoof 2017 Challenge: Assessing the Limits of Replay Spoofing Attack Detection. In: *Proceedings of the Annual Conference of the International Speech Communication Association, Interspeech, 2017-August*, pp.2-6.

Kumari, T.R.J., and Jayanna, H.S., 2015. Comparison of LPCC and MFCC Features and GMM and GMM-UBM Modeling for Limited Data Speaker Verification. In: *2014 IEEE International Conference on Computational Intelligence and Computing Research, IEEE ICCIC 2014*, pp. 95-103.

McFee, B., Raffel, C., Liang, D., Ellis, D.P.W., McVicar, M., Battenberg, E., and Nietok, O., 2015. *Librosa: Audio and Music Signal Analysis in Python*. In: *Proceedings of the 14<sup>th</sup> Python in Science Conference, (Scipy)*, pp.18-24.

Nautsch, A., Wang, X., Evans, N., Kinnunen, T., Vestman, V., Todisco, M., Delgado, H., Sahidullah, M., Yamagishi, J., and Lee, K.A., 2021. ASVspoof 2019: Spoofing countermeasures for the detection of synthesized, converted and replayed speech. *IEEE Transactions on Biometrics, Behavior, and Identity Science*, 3(2), pp. 252-265.

Novoselov, S., Kozlov, A., Lavrentyeva, G., Simonchik, K., and Shchemelinin, V., 2016. STC Anti-Spoofing Systems for the ASVspoof 2015 Challenge. In: *ICASSP, IEEE International Conference on Acoustics, Speech and Signal Processing - Proceedings*, pp.5475-5479.

Patel, T.B., and Patil, H.A., 2015. Combining Evidences from Mel Cepstral, Cochlear Filter Cepstral and Instantaneous Frequency Features for Detection of Natural vs. Spoofed Speech. In: *Proceedings of the Annual Conference of the International Speech Communication Association, INTERSPEECH*, pp.2062-2066.

Rahmeni, R., Aicha, A.B., and Ayed, Y.B., 2020. Acoustic features exploration

and examination for voice spoofing counter measures with boosting machine learning techniques. *Procedia Computer Science*, 176, pp. 1073-1082.

Siami-Namini, S., Tavakoli, N., and Namin, A.S., 2019. The Performance of LSTM and BiLSTM in Forecasting Time Series. In: *Proceedings - 2019 IEEE International Conference on Big Data, Big Data 2019*, pp.3285-3292.

Tian, X., Xiao, X., Chng, E.S., and Li, H., 2017. Spoofing Speech Detection using Temporal Convolutional Neural Network. In: *2016 Asia-Pacific Signal and Information Processing Association Annual Summit and Conference, APSIPA 2016*.

Todisco, M., Delgado, H., and Evans, N., 2016. A New Feature for Automatic Speaker Verification Anti-Spoofing: Constant Q Cepstral Coefficients. In: *Odyssey 2016: Speaker and Language Recognition Workshop*, pp.283-290.

Todisco, M., Delgado, H., and Evans, N., 2017. Constant Q cepstral coefficients: A spoofing countermeasure for automatic speaker verification. *Computer Speech and Language*, 45, pp. 516-535.

Todisco, M., Wang, X., Vestman, V., Sahidullah, M., Delgado, H., Nautsch, A., Yamagishi, J., Evans, N., Kinnunen, T., and Aik Lee, K., 2019. ASVspoof 2019: Future Horizons in Spoofed and Fake Audio Detection. In: *Proceedings of the Annual Conference of the International Speech Communication Association, INTERSPEECH, 2019*, pp.1008-1012.

Wang, X., Yamagishi, J., Todisco, M., Delgado, H., Nautsch, A., Evans, N., Sahidullah, M., Vestman, V., Kinnunen, T., Lee, K.A., Juvela, L., Alku, P., Peng, Y.H., Hwang, H.T., &... Ling, Z.H., 2020. ASVspoof 2019: A large-scale public database of synthesized, converted and replayed speech. *Computer Speech and Language*, 64, 101114.

Wei, C., Pang, R., and Kuo, C.C.J., 2024. A Green Learning Approach to Spoofed Speech Detection. In: *ICASSP 2024 - 2024 IEEE International Conference on Acoustics, Speech and Signal Processing (ICASSP)*, pp.12956-12960.

Wu, Z., Kinnunen, T., Evans, N., Yamagishi, J., Hanilci, C., Sahidullah, M., and Sizov, A., 2015. ASVspoof 2015: The First Automatic Speaker Verification Spoofing and Countermeasures Challenge. In: *Proceedings of the Annual Conference of the International Speech Communication Association, INTERSPEECH*, pp.2037-2041.

Wu, Z., Yamagishi, J., Kinnunen, T., Hanilci, C., Sahidullah, M., Sizov, A., Evans, N., Todisco, M., and Delgado, H., 2017. ASVspoof: The automatic speaker verification spoofing and countermeasures challenge. *IEEE Journal on Selected Topics in Signal Processing*, 11(4), pp. 588-604.

Yang, J., Das, R.K., and Li, H., 2020. Significance of subband features for synthetic speech detection. *IEEE Transactions on Information Forensics and Security*, 15(c), pp. 2160-2170.

Zhou, J., Hai, T., Jawawi, D.N.A., Wang, D., Ibeke, E., and Biamba, C., 2022. Voice spoofing countermeasure for voice replay attacks using deep learning. *Journal of Cloud Computing*, 11(1), 51.

# Micropollutant Control in Wastewater Treatment: A Review of Harnessing Nitrification and Denitrification Biotransformation of Micropollutant

Hanaa A. Muhammad<sup>1†</sup>, Hikmat M. Masyab<sup>1</sup>, Bakhtyar A. Othman<sup>2</sup>, Yaseen N. Mahmood<sup>1</sup>

<sup>1</sup>Department of Biology, Faculty of Science and Health, Koya University, Koya, KOY45, Kurdistan Region-F.R. Iraq

<sup>2</sup>Department of Public Health, College of Health Sciences, Hawler Medical University, Erbil, Kurdistan Region-F.R. Iraq

**Abstract** – Micropollutants, an array of organic compounds such as pharmaceuticals, personal care products, and agrochemicals, are pervasive in contemporary ecosystems, posing significant threats to environmental health even in trace concentrations. Therefore, exploring an efficient and effective technique to remediate these pollutants is essential. Nitrification–denitrification (ND) have emerged as one of the most sustainable treatment methods that effectively mitigate micropollutants while facilitating their biotransformation. This review provides a comprehensive analysis of the intricate interactions fundamentally and mechanically between the ND process and the influencing factors, such as dissolved oxygen (DO) concentration and pH optimization, which are vital to the success of micropollutant biotransformation. Insights gained from this examination contribute to a deeper understanding of microbial strategies, which offer potential avenues for sustainable environmental management and the protection of ecosystem integrity.

**Index Terms** – Biotransformation, Denitrification, Micropollutant, Nitrification, Wastewater treatment

## I. INTRODUCTION

Nitrification and denitrification (ND) are crucial processes in wastewater treatment and environmental sciences, playing a significant role in the fate and transformation of micropollutants such as pharmaceuticals, personal care products, and agrochemicals, are typically present in wastewater at concentrations ranging from a few nanograms per liter to several micrograms per liter (Suneethi et al., 2015). Despite their low concentrations, these compounds can be toxic, mutagenic, genotoxic, and disruptive to

endocrine systems, raising concerns about their impact on environmental and human health (Alzate Marin, Caravelli and Zaritzky, 2016; Miao et al., 2019). Conventional wastewater treatment plants (WWTPs) primarily focus on removing pathogens, total suspended solids (TSS), biochemical oxygen demand (BOD), and chemical oxygen demand (COD) (James and Vijayanandan, 2023), whereas nitrogen and micropollutants are left behind in the discharged of the so-called treated wastewater (Phan et al., 2014). This partially treated wastewater discharge is a significant global concern, with an estimated 80% of wastewater worldwide being inadequately treated (WWAP, 2017). This underscores the urgent need for sustainable and cost-effective solutions for nitrogen and micropollutant removal.

Biological treatment methods, particularly those involving ND, are crucial in eliminating the amount of existing nitrogen and the majority of the micropollutants. Because ND processes utilize microbial activity to convert ammonia (NH<sub>3</sub>) into nitrogen gas (N<sub>2</sub>), simultaneously reducing nitrogen levels and transforming micropollutants. However, the efficiency of ND processes is influenced by various factors, including the types of pollutants, microbial community composition (the variety of microorganisms and their food [M/F]), and operational conditions such as DO concentration, pH, and hydraulic retention time (HRT), the retention time of the sludge (SRT), aeration time, temperature, salinity, the sludge characteristics, and reactor configuration (Smith, 1978; Wang et al., 2020). Because the sensitivity of the microorganisms increases exponentially with various sources of pollutants; hence, microbial sensors could be used to quantify nitrifiable compounds and detect the effects of nitrification inhibiting (Hammar, 2002). Reid (1907) explained that the efficiency of this system is indirectly related to the pore size of the used filter particles, so the finer the particles are the better the effluent will be to discharge. In addition, dissolved oxygen concentration (DO), the ratio of carbon to nitrogen (C:N), the variety of microorganisms and their food (M/F), the retention SRT, the retention time for the hydraulic (HRT), pH, aeration time, temperature, salinity, the sludge characteristics, and reactor configuration contribute in

ARO-The Scientific Journal of Koya University  
Vol. XII, No. 2 (2024), Article ID: ARO.11661. 9 pages  
Doi: 10.14500/aro.11661

Received: 21 June 2023; Accepted: 04 September 2024

Regular review paper: Published: 17 September 2024

†Corresponding author's e-mail: [hanaa.muhammad@koyauniversity.org](mailto:hanaa.muhammad@koyauniversity.org)  
Copyright© 2024 Hanaa A. Muhammad, Hikmat M. Masyab, Bakhtyar A. Othman and Yaseen N. Mahmood. This is an open-access article distributed under the Creative Commons Attribution License (CC BY-NC-SA 4.0).





the efficiency determination (Smith, 1978; Wang et al., 2020). Each one of the mentioned factors has its contribution to the system efficiency, for example, existing DO is crucial in the ND process as it directly proportioned to removing efficiency of total nitrogen (91.17% total nitrogen removal at 1 mg/L DO concentration) (Huang et al., 2022).

$\text{NO}_3^-$ -N is not the only pollution that needs attention, micropollutants, such as pharmaceuticals, personal care products, industrial chemicals, and pesticides that are anthropogenic compounds (Luo et al., 2014) as well are vital in the cleaning process. The concentration of these micropollutants varies from a few ng/L to several  $\mu\text{g/L}$  (Wang and Wang, 2016). Even though these micropollutants exist in very low concentrations, they can be toxic, mutagenic, genotoxic, resistant to antibiotics, and disruptive to endocrine (Marti et al., 2014).

This review aims to synthesize current research on the effectiveness of ND in wastewater treatment, with a particular focus on the factors that enhance the process for both nitrogen and micropollutant removal. Therefore, by analyzing existing knowledge, the process's adaptability can be assessed in diverse treatment scenarios and explores the fate of micropollutants in these systems. The goal is to provide insights that will inform the development of more efficient and sustainable wastewater treatment strategies.

## II. MECHANISM AND PATHWAY OF ND

According to Liu et al. (2010), depending on the existing microbial populations and the achieved redox conditions with the flocs' physical nature, the mechanisms in this process can be categorized into several pathways: direct conversion of ammonia into di-nitrogen gas, and autotrophic nitrification,

heterotrophic denitrification, heterotrophic nitrification, and aerobic denitrification (Liu et al., 2010; James and Vijayanandan, 2023) (Fig. 1). Besides, the production of various microbial enzymes contributes to the biological degradation pathways. The floc size and density are essential contributors to the DO diffusion, Aeration rate and time, organic matter, and nitrogen concentration (He, Xue and Wang, 2009). The key factor in biological treatment is the microbial community, therefore enhancing the existence of the vital microorganisms based on the types of micropollutants through optimizing the environmental condition, such as carbon source, temperature, pH, aeration pattern, DO concentration, and free ammonia is crucial (Xiao and Tang, 2014). For example, autotrophic and heterotrophic bacteria grow in two different environments depending on the DO concentration, therefore, for these two different bacteria to coexist, enhancement should be the priority (Chang et al., 2019).

### A. Conventional Autotrophic Nitrification and Heterotrophic Denitrification

All the sources of nitrogen (total nitrogen) when it reaches the sewer system immediately naturally undergo a series of transformations starting with the hydrolysis of organic nitrogen to ammonia ( $\text{NH}_3$ ), then it automatically converts into ammonium ( $\text{NH}_4^+$ ) depending on the pH of the water (American Water Works Association, 2013). The amount of  $\text{NH}_4$  increases when the pH is low (acidic water) and vice versa (Bueno et al., 2018). The presence of novel bacteria in conventional nitrification is involved mostly in the establishment of the nitrification and denitrification of hydrolyzed sewage (Chai et al., 2019; Jia et al., 2020); thus, process will take place in mainly two stages; nitrification and then denitrification (Alzate Marin, Caravelli and Zaritzky, 2016).

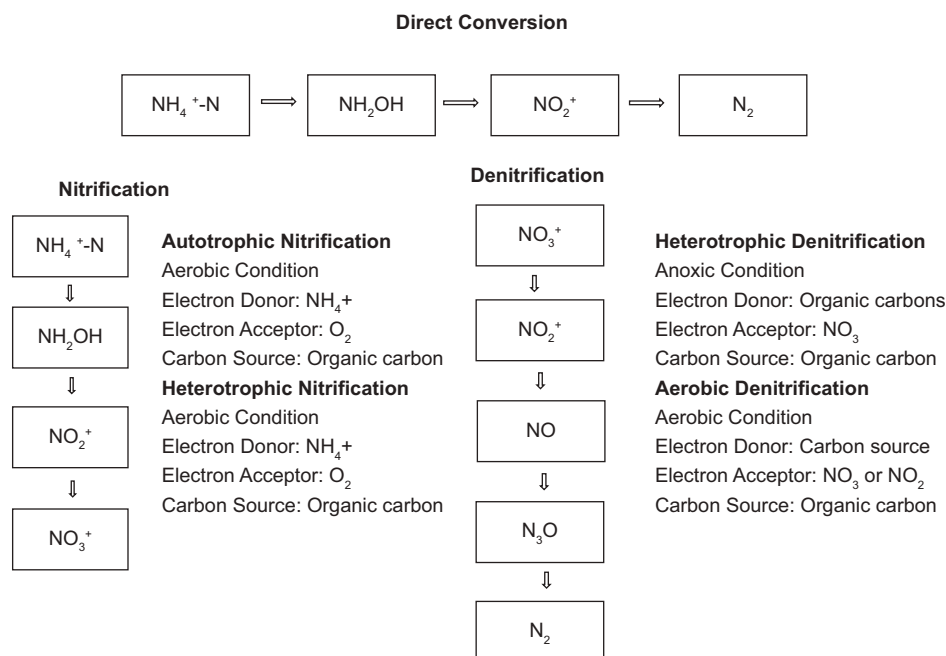


Fig. 1: Pathways of nitrogen transformation (James and Vijayanandan, 2023).

### First: Autotrophic nitrification

The autotrophic bacteria (nitrifiers) using ammonia monooxygenase (AMO) and nitrite reductase enzymes convert the existing ammonium ( $\text{NH}_4^+$ -N) into nitrite ( $\text{NO}_2^-$ -N) and then oxidize the latter into nitrate ( $\text{NO}_3^-$ -N) in various biological processes using DO (Smith, 1978). In this stage, most total organic carbon is reduced compared to the anaerobic zone (50% of COD is removed) (Khin and Annachhatre, 2004; Alzate Marin et al., 2016). Furthermore, research indicates that nitrifying enzymes significantly contribute to the cometabolic biotransformation of organic micropollutants. This process involves the simultaneous oxidation of ammonia and the degradation of various pollutants, including pharmaceuticals, under nitrifying conditions (Kennes-Veiga, et al., 2022). In addition, micropollutant degradation can be enhanced by certain phosphorus-accumulating organisms (PAOs) during nitrification (Kolakovic et al., 2022).

The nitrification process is sensitive to environmental factors such as the depth of the wastewater, pH, temperature, and the presence of specific chemicals, for example, nitrification can be enhanced by adding CaO, which maintains a pH of 8–9, whereas inhibitory substances such as chlorine lime and aluminum sulfate can hinder the process (Smith, 1978; Thakur and Medhi, 2019). In addition, the stability of nitrification is often challenged by the accumulation of nitrite-oxidizing bacteria (NOB) in nitrite-rich conditions (Li et al., 2013), which can be mitigated by optimizing the growth environment for nitrifiers (Di Capua et al., 2022). However, this could be enhanced through optimum conditions provision for the microorganisms, which leads to a significant increase in the efficiency of the process hence overcoming the limitations (Abu Bakar et al., 2018; Ma et al., 2017) which also make the structure cost-effective (Yan et al., 2019; Yang and Yang, 2011).

### Second: Heterotrophic denitrification

This is a key process in environmental engineering, that is performed by many different groups of microbes, such as *Bacillus cereus* and *Bacillus tequilensis* (Saïd et al., 2014). Following nitrification, when oxygen is depleted (under anoxic conditions), where heterotrophic bacteria use nitrate as an electron acceptor in the absence of oxygen for their respiration and the creation of nitrogen gas ( $\text{N}_2$ ) which bubbles out of the water (Zhang, Yang and Furukawa, 2010). This process not only reduces nitrogen levels but also decreases biochemical oxygen demand (BOD) by up to 80% as declared by Zhang, Yang and Furukawa, 2010. Interestingly, denitrification might occur even in well-oxygenated conditions within particulate matrices, where microcolonies of denitrifying bacteria metabolically shade each other (Smruga et al., 2021). Besides, Xu et al., (2015) explained that simultaneous nitrification and denitrification are more efficient and promising in removing nitrogen, chemical oxygen demand, sulfide, and micropollutants. Although stimulated nitrification–denitrification (ND) are cost-effective, consumes low energy, produces little sludge, and has a small footprint as elucidated by James

and Vijayanandan in 2023, it cannot be applied to treat mainstream wastewater. During this process, nitrite and nitrate, nitrous oxide, and nitric oxide reductase are produced by denitrifiers to catalyze the reactions (Singh et al., 2022).

### B. Heterotrophic Nitrification and Aerobic Denitrification

Denitrification can occur by different types of aerobic heterotrophic bacteria that produce  $\text{N}_2$  gas using  $\text{NO}_3^-$ -N as oxidizing agents; however, the vital enzyme that is essential in this process is periplasmic nitrate reductase, which is normally found in aerobic nitrifiers (Bucci et al., 2021; Ji et al., 2015; Qu et al., 2015); therefore, aerobic denitrifiers (heterotrophic nitrification) utilize organic carbon to perform nitrification (Rout et al., 2017; Song et al., 2021). Removing nitrogen under saline conditions using isolated halophilic stains, and *Halomonas campisalis* ha3 was efficient (Guo et al., 2013). This process is particularly efficient in environments with low temperatures or high salinity, where traditional nitrification and denitrification processes might be less effective (Song et al., 2021).

### C. Direct Conversion of Ammonia into Di-nitrogen Gas

In this process, some microorganisms, such as *Cupriavidus*, and *Thiosphaera pantotropha*, convert  $\text{NH}_4^+$  to  $\text{N}_2$  directly by first, producing hydroxylamine ( $\text{NH}_2\text{OH}$ ) by AMO under aerobic conditions through hydroxylation of  $\text{NH}_4^+$ -N, and next, oxidizing  $\text{NH}_2\text{OH}$  to  $\text{NO}_2^-$ -N by hydroxylamine oxidase, then the latter is directly transferred to  $\text{N}_2$  (figure 1) (James and Vijayanandan, 2023). This pathway, while less common, highlights the diversity of microbial strategies available for nitrogen removal in wastewater treatment.

## III. FACTORS AFFECTING ND

Physicochemical and operational parameters are the key factors that control the efficiency of this process; therefore, optimizing these factors helps in treating wastewater using the ND process. The essential factors that play a role in the procedure are as follows:

### A. pH

In general, the performance of the ND system can be evaluated using pH as an indicator, because pH in the reactor controls the amount of the existing microorganisms and their types as well (Hayatsu, Katsuyama and Tago, 2021; Huang et al., 2023) 3.5 g alkalinity is produced due to the reduction of 1 g  $\text{NO}_3^-$ -N in denitrification, whereas 7.14 g of alkalinity is consumed due to the oxidation of 1 g  $\text{NH}_4^+$ -N in nitrification; thus, pH can be maintained without any chemical additions (He, Xue and Wang, 2009). In addition, lead and copper are released from their bearing materials due to the reduction in pH and DO by nitrification (Zhang, Yang and Furukawa, 2010). Lead release increased from lead piping when pH was  $>7.5$  (100 mg/L alkalinity as  $\text{CaCO}_3$ ); however, soluble lead release increased 65 times more when pH was  $< 6.5$  (American Water Works Association, 2013). Maintaining an optimal pH is critical for both processes,

generally within the range of 6.5–7.5 for denitrification (Gan et al., 2019; Hayatsu, Katsuyama and Tago, 2021; Huang et al., 2023) and 8–8.4 for nitrification (He, Xue and Wang, 2009). For the highest specific rate of nitrate reduction, a pH of 10.5 may be required (Dhamole et al., 2008), whereas a range of 7–7.5 is optimal for overall ammonium and total nitrogen removal (Hossini et al., 2015). However, the acidophilic partial nitrification process recently has been developed for nitrification to occur effectively at a pH of lower than 6 even achieving stable nitrogen removal rates at 5.36 (Qian et al., 2019; F. Zhang et al., 2024). Therefore, the biotransformation of micropollutants' efficiency is determined significantly by the pH (Zhou et al., 2023)

### B. Temperature

Temperature controls microbial growth, as it affects enzyme denaturation, metabolism rate, and the overall efficiency of the ND process (Zhang et al., 2009). This parameter is directly proportioned to the micropollutant biotransformation and ammonia oxidation rate; however, it is inversely proportional to DO concentration (Fernandez-Fontaina et al., 2012). Hence, inhibited denitrification occurs when the temperature gets lowered (around 15°C) (Kanda et al., 2016), while the removal efficiencies drop from 98.0% at 18°C to 78.1% at 13°C for nitrification (Zhang et al., 2019). The optimum temperature for nitrifiers is 22–27°C, whereas it is 20–40°C for denitrifiers (He, Xue and Wang, 2009). Nitrate nitrogen removal was nearly 99.26% at 40°C (Qu et al., 2022). The activity of certain microbial pathways increases at higher temperatures causing the N<sub>2</sub>O gas emission which leads to a potent greenhouse gas (Nair et al., 2021). Hence, enhancing the ND process requires maintaining a temperature range of 18–35°C (James and Vijayanandan, 2023).

### C. Free Ammonia and Salinity

Free ammonia and salinity can significantly limit the existence of both the growth of ammonia-oxidizing bacteria (AOB) and NOB (Xiao and Tang, 2014; Zhu et al., 2015). The efficacy of AOB in degrading pharmaceutical compounds has been documented, as the broad substrate specificity of AOB allows them to metabolize a variety of micropollutants, thereby improving their removal from wastewater (Sharma et al., 2023).

It has been indicated that nitrification can be promoted when the concentration of free ammonia is nearly 10–15 mg/L, whereas *Nitrosomonas* which is essential for the effective nitrification processes becomes abundant the higher levels (Statiris et al., 2022; Sun et al., 2012).

Besides, salinity is inversely proportional to the ammonium oxidation rate; higher salinity levels decrease the ammonium oxidation rate, with a reduction by half observed when salinity increases from 2% to 1% (She et al., 2018). In addition, within high saline wastewater, halophilic or halotolerant species that are not that efficient at removing nitrogen will increase (Arumugham et al., 2024a; Zhou et al., 2023). At high salinity, ND can be enhanced through the NO<sub>2</sub><sup>-</sup>-N pathway, because NOB are more sensitive to the salinity (Corsino et al., 2016).

### D. DO Concentration

The existence of DO is a crucial factor that determines the type of bacteria that work on the nitrification (needs >2 mg/L) and denitrification (<0.2 mg/L) process (Pochana and Keller, 1999). High DO is necessary for the maximum removal of COD and NH<sub>4</sub><sup>+</sup>-N, as the availability of organic carbon is low in the flocs (James and Vijayanandan, 2023). However, nitrogen removal efficiency decreases when DO levels are higher than 3 mg/L, this also leads to increased nitrous oxide emissions (Li et al., 2020).

Sarioglu et al. (2009) manifest that around 1.8 mg O<sub>2</sub> per liter is sufficient to remove about 85–95% nitrogen for sustaining simultaneous ND in a membrane bioreactor. On the contrary, the persistence of certain micropollutants increases in the oxygen-activated sludge ND process (Levine, Meyer and Kish, 2006). Besides, the proliferation of heterotrophic bacteria is promoted due to the organic carbon utilization that leads to less organic carbon penetration into flocs (Liu et al., 2010), thus, with a high rate of DO, the electron acceptors shift from NO<sub>3</sub><sup>-</sup>-N/NO<sub>2</sub><sup>-</sup>-N to oxygen for denitrifies. Therefore, to improve the breakdown of micropollutants, recent advancements in wastewater treatments have focused on optimizing DO levels (Zhang et al., 2024).

### E. Food/Microorganism (F/M)

The F/M ratio is essential for reducing competition between heterotrophic and autotrophic nitrifiers. Besides, the provision of a sufficient amount of carbon substrates for denitrification is important (James and Vijayanandan, 2023). A low C/N ratio typically enhances nitrification, whereas denitrification gets suppressed; thus, it is essential for micropollutants to be metabolized and transformed by microorganisms (Arumugham et al., 2024a). F/M can be increased due to the maintenance of a high concentration of mixed liquor volatile suspended solids in the membrane bioreactor, leading to an increase in NH<sub>4</sub><sup>+</sup>-N Removal (He, Xue and Wang, 2009).

### F. HRT

The contact time between microorganisms and pollutants is important because the removal efficiency lowers once the contact time is insufficient (Wang et al., 2017a). HRT also impacts the diversity and richness of microbial communities, which are crucial for effective denitrification (Liu et al., 2010). Chang et al., (2019) explain that removing NH<sub>4</sub><sup>+</sup>-N and total nitrogen (TN) decreases by 42.11%, and 49.5% when the retention time was lowered from 12 h to 4 h, respectively. Even with low HRT, the availability of carbon substrate can maintain high denitrification efficiency (Pous et al., 2017a; Wang et al., 2017a). Song et al., (2020) declared that, for maximizing nitrogen removal, it is necessary to have an optimal HRT of around 5–6 h, based on the influent nitrate concentration, whereas denitrification performance improves when HRT get increased, however, excessively long HRTs cause nitrite accumulation and decrease treatment efficiency (Wang et al., 2017b). A study highlighted that increasing HRT can improve denitrification

performance by providing sufficient contact time between substrates and denitrifying bacteria. Optimized HRT ensures efficient hydraulic shear, which helps in forming denitrifying granular sludge. However, excessively long HRTs may lead to decreased treatment efficiency and nitrite accumulation, indicating a need for careful management of HRT to balance performance and efficiency (Pous et al., 2017b). In general, HRT through ND processes enhances the biotransformation of micropollutants (Ilies and Mavinic, 2001).

#### G. SRT

SRT is a critical loading parameter that influences the growth rate of microorganisms, nutrient transformations involved in ND, effluent concentrations, and treatment efficiency (Clara et al., 2005), especially in the secondary clarifier, where it can impact effluent quality (James et al., 2015). Longer retention times may provide microbes with more time to perform these processes, whereas shorter retention times could potentially limit their effectiveness; thus, optimizing SRT is essential in managing and enhancing the efficiency of ND systems. In general, SRT is longer than HRT to allow sufficient time for microbial reproduction (Clara et al., 2005). It has been indicated that for nitrification to be effective and efficient, 10–20 days is vital, whereas the optimal SRT is 10–30 days for efficient denitrification (Li and Wu, 2014).

#### H. Aeration Time

Ammonia-nitrogen oxidation is affected by the aeration rates and patterns, for instance, 99% nitrification efficiency was achieved with the aeration rates of 9 L-air/min (Mota et al., 2005). Besides, the removal and the composition of nitrifying bacterial communities greatly lie on lengths of aeration and non-aeration periods, for example, higher levels of certain AOB were achieved at short aeration times (e.g., 30 minutes), but for effective denitrification longer non-aeration periods (up to 4 h) was essential (Landi and Lu, 2022). Thus, oxidizing  $\text{NH}_4^+ \text{-N}$  completely is based on the aeration time (Abbassi, et al., 2014); however, temperature plays an important role as well, which is inversely proportioned with aeration (Zhang et al., 2009). Over-aeration can lead to  $\text{NO}_2^- \text{-N}$  accumulation and the deterioration of nitrification efficiency (Peng et al., 2004). Recently, the importance of aeration has been interconnected with ND processes to achieve the most effective treatment of wastewater containing micropollutants (Ghasemi, Hasani Zonoozi and Hoseini Shamsabadi, 2024).

### IV. REACTOR CONFIGURATION

Two factors control the efficiency of the configuration: the gradient of DO concentration, and the creation of an anoxic microenvironment inside the flocs (Yan et al., 2019). Besides, the intermittent feeding and microbial community composition represent the reactor conditions that significantly influence the removal efficiency of micropollutants (Gonzalez-Gil, Carballa and Lema, 2017).

The reactor should be designed in a way that guarantees the coexistence of nitrifiers and denitrifiers at a gradient concentration of DO; furthermore, the formation of flocs that have optimum size and density is essential in the reactor (James and Vijayanandan, 2023). For instance, in the Closed Down-Flow Hanging Sponge Reactor, DO concentration should be 1.2 mg- $\text{O}_2$ /L to achieve significant nitrite production while maintaining high ammonium removal rates (Landi and Lu, 2022).

Zhang et al., in 2009, claimed that the thickness of biofilm in the attached growth system affects total nitrogen removal and organic carbon significantly. The thicker the biofilm is, first; the more diffusion of organic carbon occurs using less oxygen (Li and Irvin, 2007), second; a favorable anoxic environment denitrifying bacteria can be developed due to the penetration of oxygen (0.20–0.25 mm depth) into the thicker biofilm (Gieseke et al., 2002). Besides the thickness, aeration time is vital as well, for example, the penetration increases up to 1.5 mm when the time is increased up to 3hrs (James and Vijayanandan, 2023). To optimize and enhance, this process, prediction, and prevention of interferences of biotransforming micropollutants with a focus on the biodegradability of potential inhibitory compounds is essential (Pagga, Bachner and Strotmann, 2006). This can be simulated by a computer model (Sanz et al., 1996). For example, a model in continuous up-flow filters, which has been validated in a semi-scale filtration plant for nitrification was stimulated by Qi in 2009; while a kinetic model highlighted the role of carbon sources and the potential for nitrite accumulation in the denitrification process (Michioku et al., 2016).

### V. BIOTRANSFORMATION

Biotransformation in the environment refers to how living organisms, particularly microorganisms, chemically modify or break down pollutants, toxins, or other organic compounds into less harmful or more easily degradable substances. This process plays a critical role in the natural detoxification of ecosystems and can involve various metabolic pathways, often leading to the complete mineralization of pollutants into basic inorganic compounds such as water, carbon dioxide, and minerals (Schwarzenbach, Gschwend and Imboden, 2017). Because all biological reactions are enzyme-catalyzed, biotransformation includes the *in vitro* enzymatic reactions, metabolism of the compounds, and biosynthetic pathways in the plants (Doble, Kruthiventi and Gaikar, 2004). Recently, complete ammonia oxidizers (comammox), these bacteria are the complete ammonia oxidizers have been discovered that can oxidize ammonia to nitrate in a single step, hence enhancing micropollutant biotransformation (Han et al., 2019).

Biotransformation seems to be the key to developing eco-friendly methods, in which enzymes are mostly in control. They elucidate that there are six groups of enzymes: ligases catalyze, oxidoreductases catalyze oxidation-reduction, transferases mediate, hydrolases catalyze the hydrolysis, lyases catalyze, and isomerases (Radley et al., 2023). There

are plenty of different micropollutants that have been treated using biotransformation, for instance, anti-cancer drugs (Gao et al., 2013). Every aspect of pesticide biotransformation in plants and microorganisms concludes that the persistent variation of pollutants in the process (Hall, Hoagland and Zablotowicz, 2000).

## VI. FATE OF MICROPOLLUTANTS

Micropollutants are emerging contaminants found in wastewater at low concentrations but with potentially harmful effects. Consuming water bodies that contain micropollutants is harmful to humans, therefore, removing them is vital (Phan et al., 2014). In general, the fate of micropollutants in WWTPs is governed by various processes, including biotransformation, photo-degradation, volatilization, and sorption which are commonly used in reducing micropollutants in treated effluent (Lakshminarasimman et al., 2018). However, the physicochemical properties of micropollutants and the treatment conditions determine the removal efficiency (Jonas et al., 2015).

Cometabolism is a primary degradable substrate used in this process, which produces biomass and acts as a source of electron donors (James and Vijayanandan, 2023). Besides the organic matter, micropollutants can act as an energy and carbon source for microbes; however, the ratio and concentration of both primary substrates and the micropollutants are essential (Dawas-Massalha et al., 2014; Tiwari et al., 2017).

In tandem with these, aeration, hydraulic, solid retention time, and redox condition are also critical operational parameters to determine the success of the process (Arumugham et al., 2024b). Nitrification helps the degradation of micropollutants through cometabolism (Dorival-García et al., 2013), for instance, ethinylestradiol, naproxen, and roxithromycin were transformed in a nitrification process (Suarez, Lema and Omil, 2010). This transformation is done through the production of the AMO enzymes by AOB (Dorival-García et al., 2013; Alvarino et al., 2018). That enzyme contributes to the degradation depending on the micropollutant's diffusion across the cell membrane, and their structure as well (Fernandez-Fontaina et al., 2012). Although not all micropollutants are degradable in nitrifying conditions, redox is the best condition for this purpose, due to mono- and di-oxygenase enzymes that are produced by both nitrifying and denitrifying bacteria (Dawas-Massalha et al., 2014; Hammer and Palmowski, 2021).

The redox conditions are vital in secreting various enzymes by microbial communities and the structure of the micropollutants is of great importance when it comes to biotransformation (Tiwari et al., 2017), for example, sulfamethoxazole, trimethoprim, and atenolol degrade perfectly in any condition (anaerobic, anoxic, and aerobic conditions); atenolol and trimethoprim were removed efficiently at anaerobic reactor (Alvarino et al., 2018; Lakshminarasimman et al., 2018); however, some others such as carbamazepine, diazepam, and diclofenac

were not undergoing any biotransformation at all (Sipma et al., 2010). In general, biodegradation makes simpler, less toxic, or completely mineralized into CO<sub>2</sub> products (Tiwari et al., 2017). It is worth mentioning that during nitrification, microplastics affect negatively on ammonia oxidation rate, but positively on denitrification (Li et al., 2020).

## VII. CONCLUSIONS

Nitrification and denitrification processes can help in biotransforming micropollutants and removing total nitrogen by harnessing the inherent capabilities of microorganisms to safeguard water quality. Recent research has highlighted the critical role of nitrifying enzymes in the cometabolic biotransformation of organic micropollutants. Besides, the discovery of comammox that are capable of oxidizing ammonia to nitrate in a single step, presents new opportunities for improving the efficiency of micropollutant biotransformation in wastewater treatment systems. Furthermore, enhanced biological phosphorus removal systems show a great contribution to micropollutant degradation by certain PAOs.

This process can be enhanced to make the process more efficient by controlling the gradient of DO in the same reactor within the flocs to co-exist with auto and heterotroph bacteria. Shifting from one mechanism to another depends on the microbial community, which can be influenced by operational parameters (e.g., DO, SRT, and HRT).

The efficiency of this system depends strongly on microbial diversity, environmental conditions (For example, the concentration of DO, the C:N ratio, microorganisms' food, the retention time for the hydraulic, pH, aeration time, temperature, salinity, the sludge retention ratio and sludge characteristics, and reactor configuration), and the specific nature of micropollutants. However, among the environmental factors, optimizing DO, and pH are the most critical parameters to the success of the process of micropollutant biotransformation. Besides, controlling sludge production caused by freeing N<sub>2</sub> into the atmosphere is challenging as well, thus innovating and adjusting a proper system is vital. ND process for micropollutant biotransformation was reviewed as a potential biological treatment process in removing carbon, nitrogen, and micropollutants from wastewater, which holds immense promise for sustainable and environmentally friendly solutions.

## REFERENCES

- Abbassi, R., Kumar Yadav, A., Huang, S., and Jaffé, P.R., 2014. Laboratory study of nitrification, denitrification and anammox processes in membrane bioreactors considering periodic aeration. *Journal of Environmental Management*, 142, pp.53-59.
- Abu Bakar, S.N.H., Abu Hasan, H., Mohammad, A.W., Sheikh Abdullah, S.R., Haan, T.Y., Ngtani, R., and Yusof, K.M.M., 2018. A review of moving-bed biofilm reactor technology for palm oil mill effluent treatment. *Journal of Cleaner Production*, 171, pp.1532-1545.
- Alvarino, T., Suarez, S., Lema, J., and Omil, F., 2018. Understanding the sorption and biotransformation of organic micropollutants in innovative biological

- wastewater treatment technologies. *Science of the Total Environment*, 615, pp.297-306.
- Alzate Marin, J.C., Caravelli, A.H., and Zaritzky, N.E., 2016. Nitrification and aerobic denitrification in anoxic-aerobic sequencing batch reactor. *Bioresource Technology*, 200, pp.380-387.
- American Water Works Association, 2013. *Nitrification Prevention and Control in Drinking Water*, 2<sup>nd</sup> ed., AWWA Manual. American Water Works Association, Denver, CO.
- Arumugham, T., Khudzari, J., Abdullah, N., Yuzir, A., Iwamoto, K., and Homma, K., 2024a. Research trends and future directions on nitrification and denitrification processes in biological nitrogen removal. *Journal of Environmental Chemical Engineering*, 12, p.111897.
- Arumugham, T., Khudzari, J., Abdullah, N., Yuzir, A., Iwamoto, K., and Homma, K., 2024b. Research trends and future directions on nitrification and denitrification processes in biological nitrogen removal. *Journal of Environmental Chemical Engineering*, 12, p.111897.
- Bucci, P., Coppotelli, B., Morelli, I., Zaritzky, N., and Caravelli, A., 2021. Heterotrophic nitrification-aerobic denitrification performance in a granular sequencing batch reactor supported by next generation sequencing. *International Biodeterioration and Biodegradation Society*, 160, p.105210.
- Bueno, R.F., Piveli, R.P., Campos, F., and Sobrinho, P.A., 2018. Simultaneous nitrification and denitrification in the activated sludge systems of continuous flow. *Environmental Technology*, 39, pp.2641-2652.
- Chai, H., Xiang, Y., Chen, R., Shao, Z., Gu, L., Li, L., and He, Q., 2019. Enhanced simultaneous nitrification and denitrification in treating low carbon-to-nitrogen ratio wastewater: Treatment performance and nitrogen removal pathway. *Bioresource Technology*, 280, pp.51-58.
- Chang, M., Wang, Y., Pan, Y., Zhang, K., Lyu, L., Wang, M., and Zhu, T., 2019. Nitrogen removal from wastewater via simultaneous nitrification and denitrification using a biological folded non-aerated filter. *Bioresource Technology*, 289, p.121696.
- Clara, M., Kreuzinger, N., Strenn, B., Gans, O., and Kroiss, H., 2005. The solids retention time-a suitable design parameter to evaluate the capacity of wastewater treatment plants to remove micropollutants. *Water Research*, 39, pp.97-106.
- Corsino, S.F., Capodici, M., Morici, C., Torregrossa, M., and Viviani, G., 2016. Simultaneous nitrification-denitrification for the treatment of high-strength nitrogen in hypersaline wastewater by aerobic granular sludge. *Water Research*, 88, pp.329-336.
- Dawas-Massalha, A., Gur-Reznik, S., Lerman, S., Sabbah, I., and Dosoretz, C.G., 2014. Co-metabolic oxidation of pharmaceutical compounds by a nitrifying bacterial enrichment. *Bioresource Technology*, 167, pp.336-342.
- Di Capua, F., Iannacone, F., Sabba, F., and Esposito, G., 2022. Simultaneous nitrification-denitrification in biofilm systems for wastewater treatment: Key factors, potential routes, and engineered applications Author links open overlay panel. *Bioresource Technology*, 361, p.127702.
- Doble, M., Kruthiventi, A.K., and Gaikar, V.G., 2004. *Biotransformations and Bioprocesses, Biotechnology and Bioprocessing Series*. Marcel Dekker, New York.
- Dorival-García, N., Zafra-Gómez, A., Navalón, A., González-López, J., Hontoria, E., and Vilchez, J.L., 2013. Removal and degradation characteristics of quinolone antibiotics in laboratory-scale activated sludge reactors under aerobic, nitrifying and anoxic conditions. *The Journal of Environmental Management*, 120, pp.75-83.
- Fernandez-Fontaina, E., Omil, F., Lema, J.M., and Carballa, M., 2012. Influence of nitrifying conditions on the biodegradation and sorption of emerging micropollutants. *Water Research*, 46, pp.5434-5444.
- Fernandez-Fontaina, E., Omil, F., Lema, J.M., and Carballa, M., 2012. Influence of nitrifying conditions on the biodegradation and sorption of emerging micropollutants. *Water Research*, 46, pp.5434-5444.
- Gao, F., Zhang, J.M., Wang, Z.G., Peng, W., Hu, H.L., and Fu, C.M., 2013. Biotransformation, a promising technology for anti-cancer drug development. *Asian Pacific Journal of Cancer Prevention*, 14, pp.5599-5608.
- Ghasemi, M., Hasani Zonoozi, M., and Hoseini Shamsabadi, M.J., 2024. Simultaneous nitrification and denitrification pattern in aerated moving-bed sequencing batch reactor: Choosing appropriate SRT for different COD/N ratios. *Water Practice and Technology*, 19, pp.1920-1935.
- Gieseke, A., Arnz, P., Amann, R., and Schramm, A., 2002. Simultaneous P and N removal in a sequencing batch biofilm reactor: Insights from reactor- and microscale investigations. *Water Research*, 36, pp.501-509.
- Gonzalez-Gil, L., Carballa, M., and Lema, J.M., 2017. Cometabolic enzymatic transformation of organic micropollutants under methanogenic conditions. *Environmental Science and Technology*, 51, pp.2963-2971.
- Guo, Y., Zhou, X., Li, Y., Li, K., Wang, C., Liu, J., Yan, D., Liu, Y., Yang, D., and Xing, J., 2013. Heterotrophic nitrification and aerobic denitrification by a novel *Halomonas campisalis*. *Biotechnology Letters*, 35, pp.2045-2049.
- Hall, J.C., Hoagland, R.E., and Zablotowicz, R.M., 2000. *Pesticide Biotransformation in Plants and Microorganisms Similarities and Divergences*. American Chemical Society, UAS.
- Hammar, F., 2002. History of modern genetics in Germany, In: Dutta, N.N., Hammar, F., Haralampidis, K., Karanth, N.G., König, A., Krishna, S.H., Kunze, G., Nagy, E., Orlich, B., Osbourn, A.E., Raghavarao, K.S.M.S., Riedel, K., Sahoo, G.C., Schomäcker, R., Srinivas, N.D., and Trojanowska, M. (Eds.), *History and Trends in Bioprocessing and Biotransformation, Advances in Biochemical Engineering/Biotechnology*. Springer, Berlin, Heidelberg, pp.1-29.
- Hammer, L., and Palmowski, L., 2021. Fate of selected organic micropollutants during anaerobic sludge digestion. *Water Environment Research*, 93, pp.1910-1924.
- Han, P., Yu, Y., Zhou, L., Tian, Z., Li, Z., Hou, L., Liu, M., Wu, Q., Wagner, M., and Men, Y., 2019. Specific micropollutant biotransformation pattern by the commensal bacterium *Nitrospira inopinata*. *Environmental Science and Technology*, 53, pp.8695-8705.
- Hayatsu, M., Katsuyama, C., and Tago, K., 2021. Overview of recent researches on nitrifying microorganisms in soil. *Soil Science and Plant Nutrition*, 67, pp.619-632.
- He, S., Xue, G., and Wang, B., 2009. Factors affecting simultaneous nitrification and de-nitrification (SND) and its kinetics model in membrane bioreactor. *Journal of Hazardous Materials*, 168, pp.704-710.
- Huang, R., Meng, T., Liu, G., Gao, S., and Tian, J., 2022. Simultaneous nitrification and denitrification in membrane bioreactor: Effect of dissolved oxygen. *Journal of Environmental Management*, 323, p.116183.
- Huang, S., Fu, Y., Zhang, H., Wang, C., Zou, C., and Lu, X., 2023. Research progress of novel bio-denitrification technology in deep wastewater treatment. *Frontiers in Microbiology*, 14, p.1284369.
- Ilies, P., and Mavinic, D.S., 2001. Biological nitrification and denitrification of a simulated high ammonia landfill leachate using 4-stage Bardenpho systems: System startup and acclimation. *Canadian Journal of Civil Engineering*, 28, pp.85-97.
- James, O.O., Cao, J.S., Kabo-Bah, A.T., and Wang, G., 2015. Assessing the impact of solids retention time (SRT) on the secondary clarifier capacity using the State Point Analysis. *KSCE Journal of Civil Engineering*, 19, pp.1265-1270.
- James, S.N., and Vijayanandan, A., 2023. Recent advances in simultaneous nitrification and denitrification for nitrogen and micropollutant removal: A review. *Biodegradation* 34, pp.103-123.
- Ji, B., Yang, K., Zhu, L., Jiang, Y., Wang, H., Zhou, J., and Zhang, H., 2015. Aerobic denitrification: A review of important advances of the last 30 years. *Biotechnology and Bioprocess Engineering*, 20, pp.643-651.
- Jia, Y., Zhou, M., Chen, Y., Hu, Y., and Luo, J., 2020. Insight into short-cut of simultaneous nitrification and denitrification process in moving bed biofilm reactor: Effects of carbon to nitrogen ratio. *Chemical Engineering Journal*, 400, p.125905.

- Jonas, M., Luca, R., Barry, D.A., and Christof, H., 2015. *A Review of the Fate of Micropollutants in Wastewater Treatment Plants*. Wiley Period. Inc CORE Metadata Citation and Similar Papers at. Coreacuk Provided Infoscience École Polytechnique. Fédérale Lausanne. Wiley, United States.
- Kanda, R., Kishimoto, N., Hinobayashi, J., and Hashimoto, T., 2016. Effects of recirculation rate of nitrified liquor and temperature on biological nitrification-denitrification process using a trickling filter. *Water and Environment Journal*, 30, pp.190-196.
- Kennes-Veiga, D.M., González-Gil, L., Carballa, M., and Lema, J.M., 2022. Enzymatic cometabolic biotransformation of organic micropollutants in wastewater treatment plants: A review. *Bioresource Technology*, 344, p.126291.
- Khin, T., and Annachhatre, A.P., 2004. Novel microbial nitrogen removal processes. *Biotechnology Advances*, 22, pp.519-532.
- Kolakovic, S., Salgado, R., Freitas, E.B., Bronze, M.R., Sekulic, M.T., Carvalho, G., Reis, M.A.M., and Oehmen, A., 2022. Diclofenac biotransformation in the enhanced biological phosphorus removal process. *Science of the Total Environment*, 806, p.151232.
- Lakshminarasimman, N., Quiñones, O., Vanderford, B.J., Campo-Moreno, P., Dickenson, E.V., and McAvooy, D.C., 2018. Biotransformation and sorption of trace organic compounds in biological nutrient removal treatment systems. *Science of the Total Environment*, 640-641, pp.62-72.
- Landi, A.I., and Lu, J., 2022. Effects of aeration rates and patterns on shortcut nitrification and denitrification. *Journal of Environmental Protection*, 13, pp.640-656.
- Levine, A.D., Meyer, M.T., and Kish, G., 2006. Evaluation of the persistence of micropollutants through pure oxygen activated sludge nitrification and denitrification. *Water Environment Research*, 78, pp.2276-2285.
- Li, A.J., Li, X.Y., Quan, X.C., and Yang, Z.F., 2013. Aerobic sludge granulation for partial nitrification of ammonia-rich inorganic wastewater. *Environmental Engineering and Management Journal*, 12, pp.1375-1380.
- Li, B., and Irvin, S., 2007. The comparison of alkalinity and ORP as indicators for nitrification and denitrification in a sequencing batch reactor (SBR). *Biochemical Engineering Journal*, 34, pp.248-255.
- Li, B., and Wu, G., 2014. Effects of sludge retention times on nutrient removal and nitrous oxide emission in biological nutrient removal processes. *International Journal of Environmental Research and Public Health*, 11, pp.3553-3569.
- Li, L., Song, K., Yeerken, S., Geng, S., Liu, D., Dai, Z., Xie, F., Zhou, X., and Wang, Q., 2020. Effect evaluation of microplastics on activated sludge nitrification and denitrification. *Science of the Total Environment*, 707, p.135953.
- Li, Y., Guo, J., Li, H., Song, Y., Chen, Z., Lu, C., Han, Y., and Hou, Y., 2020. Effect of dissolved oxygen on simultaneous removal of ammonia, nitrate and phosphorus via biological aerated filter with sulphur and pyrite as composite fillers. *Bioresource Technology*, 296, p.122340.
- Liu, Y., Shi, H., Xia, L., Shi, H., Shen, T., Wang, Z., Wang, G., and Wang, Y., 2010. Study of operational conditions of simultaneous nitrification and denitrification in a Carousel oxidation ditch for domestic wastewater treatment. *Bioresource Technology*, 101, pp.901-906.
- Luo, Y., Guo, W., Ngo, H.H., Nghiem, L.D., Hai, F.I., Zhang, J., Liang, S., and Wang, X.C., 2014. A review on the occurrence of micropollutants in the aquatic environment and their fate and removal during wastewater treatment. *Science of the Total Environment*, 473-474, pp.619-641.
- Ma, W., Han, Y., Ma, W., Han, H., Zhu, H., Xu, C., Li, K., and Wang, D., 2017. Enhanced nitrogen removal from coal gasification wastewater by simultaneous nitrification and denitrification (SND) in an oxygen-limited aeration sequencing batch biofilm reactor. *Bioresource Technology*, 244, pp.84-91.
- Marti, E., Huerta, B., Rodríguez-Mozaz, S., Barceló, D., Jofre, J., and Balcázar, J.L., 2014. Characterization of ciprofloxacin-resistant isolates from a wastewater treatment plant and its receiving river. *Water Research*, 61, pp.67-76.
- Miao, L., Yang, G., Tao, T., and Peng, Y., 2019. Recent advances in nitrogen removal from landfill leachate using biological treatments - a review. *Journal of Environmental Management*, 235, pp.178-185.
- Michioku, K., Taniura, H., and Inoue, K., 2016. Optimization of Nitrification/Denitrification Process in Landfill Leachate Treatment. In: *International Symposium on Ecohydraulics*. 11<sup>th</sup> ed Engineers Australia, Barton ACT, Melbourne, pp.342-349.
- Mota, C., Head, M., Ridenoure, J., Cheng, J., and De Los Reyes, F., 2005. Effects of aeration cycles on nitrifying bacterial populations and nitrogen removal in intermittently aerated reactors. *Applied and Environmental Microbiology*, 71, pp.8565-8572.
- Nair, D., Abalos, D., Philippot, L., Bru, D., Mateo-Marín, N., and Petersen, S.O., 2021. Soil and temperature effects on nitrification and denitrification modified N<sub>2</sub>O mitigation by 3,4-dimethylpyrazole phosphate. *Soil Biology and Biochemistry*, 157, p.108224.
- Pagga, U., Bachner, J., and Strotmann, U., 2006. Inhibition of nitrification in laboratory tests and model wastewater treatment plants. *Chemosphere*, 65, pp.1-8.
- Peng, Y.Z., Chen, Y., Peng, C.Y., Liu, M., Wang, S.Y., Song, X.Q., and Cui, Y.W., 2004. Nitrite accumulation by aeration controlled in sequencing batch reactors treating domestic wastewater. *Water Science and Technology*, 50, 35-43.
- Phan, H.V., Hai, F.I., Kang, J., Dam, H.K., Zhang, R., Price, W.E., Broeckmann, A., and Nghiem, L.D., 2014. Simultaneous nitrification/denitrification and trace organic contaminant (TrOC) removal by an anoxic-aerobic membrane bioreactor (MBR). *Bioresource Technology*, 165, pp.96-104.
- Pochana, K., and Keller, J., 1999. Study of factors affecting simultaneous nitrification and denitrification (SND). *Water Science Technologies*, 39, pp.61-68.
- Pous, N., Puig, S., Balaguer, M.D., and Colprim, J., 2017a. Effect of hydraulic retention time and substrate availability in denitrifying bioelectrochemical systems. *Environmental Science: Water Research and Technology*, 3, pp.922-229.
- Pous, N., Puig, S., Balaguer, M.D., and Colprim, J., 2017b. Effect of hydraulic retention time and substrate availability in denitrifying bioelectrochemical systems. *Environmental Science: Water Research and Technology*, 3, pp.922-229.
- Qian, W., Ma, B., Li, X., Zhang, Q., and Peng, Y., 2019. Long-term effect of pH on denitrification: High pH benefits achieving partial-denitrification. *Bioresource Technology*, 278, pp.444-449.
- Qu, D., Wang, C., Wang, Y., Zhou, R., and Ren, H., 2015. Heterotrophic nitrification and aerobic denitrification by a novel groundwater origin cold-adapted bacterium at low temperatures. *RSC Advances*, 5, pp.5149-5157.
- Qu, W., Suo, L., Liu, R., Liu, M., Zhao, Y., Xia, L., Fan, Y., Zhang, Q., and Gao, Z., 2022. Influence of temperature on denitrification and microbial community structure and diversity: A laboratory study on nitrate removal from groundwater. *Water*, 14, p.436.
- Radley, E., Davidson, J., Foster, J., Obexer, R., Bell, E.L., and Green, A.P., 2023. Engineering enzymes for environmental sustainability. *Angewandte Chemie International Edition*, 62, p.e202309305.
- Reid, G., 1907. Nitrification of sewage. *Proceedings of the Royal Society of London. Series B, Containing Papers of a Biological Character*, 79, pp.58-74.
- Rout, P.R., Bhunia, P., and Dash, R.R., 2017. Simultaneous removal of nitrogen and phosphorus from domestic wastewater using *Bacillus cereus* GS-5 strain exhibiting heterotrophic nitrification, aerobic denitrification and denitrifying phosphorus removal. *Bioresource Technology*, 244, pp.484-495.
- Saïd, M., Ezzahra, A.F., Jamal, A., Mohammed, R., and Omar, A., 2014. Heterotrophic denitrification by Gram-positive bacteria: *Bacillus cereus* and *Bacillus tequilensis* 4. *International Journal of Scientific and Research Publications*, 4.
- Sanz, J.P., Freund, M., and Hother, S., 1996. Nitrification and denitrification in continuous upflow filters - process modelling and optimization. *Water Science and Technology*, 34, pp.441-448.

- Sarioglu, M., Insel, G., Artan, N., and Orhon, D., 2009. Model evaluation of simultaneous nitrification and denitrification in a membrane bioreactor operated without an anoxic reactor. *Journal of Membrane Science*, 337, pp.17-27.
- Schwarzenbach, R.P., Gschwend, P.M., and Imboden, D.M., 2017. *Environmental Organic Chemistry*, 3<sup>rd</sup> ed. Wiley, Hoboken, NJ.
- Sharma, P., Kanta Pandey, K., Lepcha, A., Sharma, S., Maurya, N., Kumar Sharma, S., Pradhan, R., and Kumar, R., 2023. Elucidating the potential of nitrifying bacteria in mitigating nitrogen pollution and its industrial application. *Microsphere*, 2, pp.246-259.
- She, Z., Wu, L., Wang, Q., Gao, M., Jin, C., Zhao, Y., Zhao, L., and Guo, L., 2018. Salinity effect on simultaneous nitrification and denitrification, microbial characteristics in a hybrid sequencing batch biofilm reactor. *Bioprocess and Biosystems Engineering*, 41, pp.65-75.
- Singh, V., Ormeci, B., Mishra, S., and Hussain, A., 2022. Simultaneous partial Nitrification, ANAMMOX and denitrification (SNAD) - A review of critical operating parameters and reactor configurations. *Chemical Engineering Journal*, 433, p.133677.
- Sipma, J., Osuna, B., Collado, N., Monclús, H., Ferrero, G., Comas, J., and Rodriguez-Roda, I., 2010. Comparison of removal of pharmaceuticals in MBR and activated sludge systems. *Desalination*, 250, pp.653-659.
- Smith, A.G., 1978. *Nitrification-Denitrification of Wastewater using a Single-Sludge System, Research Report - Research Program for the Abatement of Municipal Pollution "Project no. 71-1-20."* Environment Canada : Obtained from Training and Technology Transfer Division (Water), Environmental Protection Service, Fisheries and Environment Canada, Ottawa.
- Smriga, S., Ciccarese, D., and Babbin, A.R., 2021. Denitrifying bacteria respond to and shape microscale gradients within particulate matrices. *Communications Biology*, 4, p.570.
- Song, T., Zhang, X., Li, J., Wu, X., Feng, H., and Dong, W., 2021. A review of research progress of heterotrophic nitrification and aerobic denitrification microorganisms (HNADMs). *Science of the Total Environment*, 801, p.149319.
- Song, X., Yang, X., Hallerman, E., Jiang, Y., and Huang, Z., 2020. Effects of hydraulic retention time and influent nitrate-N concentration on nitrogen removal and the microbial community of an aerobic denitrification reactor treating recirculating marine aquaculture system effluent. *Water*, 12, p.650.
- Statiris, E., Dimopoulos, T., Petalas, N., Noutsopoulos, C., Mamais, D., and Mamais, S., 2022. Investigating the long and short-term effect of free ammonia and free nitrous acid levels on nitrification biomass of a sequencing batch reactor treating thermally pre-treated sludge reject water. *Bioresource Technology*, 362, p.127760.
- Suarez, S., Lema, J.M., and Omil, F., 2010. Removal of pharmaceutical and personal care products (PPCPs) under nitrifying and denitrifying conditions. *Water Research*, 44, pp.3214-3224.
- Sun, H., Jiang, T., Zhang, F., Zhang, P., Zhang, H., Yang, H., Lu, J., Ge, S., Ma, B., Ding, J., and Zhang, W., 2012. Understanding the effect of free ammonia on microbial nitrification mechanisms in suspended activated sludge bioreactors. *Environmental Research*, 200, 111737.
- Suneethi, S., Keerthiga, G., Soundhar, R., Kanmani, M., Boobalan, T., Krithika, D., and Philip, L., 2015. Qualitative evaluation of small scale municipal Wastewater Treatment Plants (WWTPs) in South India. *Water Practice and Technology*, 10, pp.711-719.
- Thakur, I.S., and Medhi, K., 2019. Nitrification and denitrification processes for mitigation of nitrous oxide from waste water treatment plants for biovalorization: Challenges and opportunities. *Bioresource Technology*, 282, pp.502-513.
- Tiwari, B., Sellamuthu, B., Ouarda, Y., Drogui, P., Tyagi, R.D., and Buelna, G., 2017. Review on fate and mechanism of removal of pharmaceutical pollutants from wastewater using biological approach. *Bioresource Technology*, 224, pp.1-12.
- Wang, J., and Wang, S., 2016. Removal of pharmaceuticals and personal care products (PPCPs) from wastewater: A review. *Journal of Environmental Management*, 182, pp.620-640.
- Wang, J., Rong, H., Cao, Y., and Zhang, C., 2020. Factors affecting simultaneous nitrification and denitrification (SND) in a moving bed sequencing batch reactor (MBSBR) system as revealed by microbial community structures. *Bioprocess and Biosystems Engineering*, 43, pp.1833-1846.
- Wang, Z., Fei, X., He, S., Huang, J., and Zhou, W., 2017a. Effects of hydraulic retention time and ratio on thiosulfate-driven autotrophic denitrification for nitrate removal from micro-polluted surface water. *Environmental Technology*, 38, pp.2835-2843.
- Wang, Z., Fei, X., He, S., Huang, J., and Zhou, W., 2017b. Effects of hydraulic retention time and ratio on thiosulfate-driven autotrophic denitrification for nitrate removal from micro-polluted surface water. *Environmental Technology*, 38, pp.2835-2843.
- Xiao, J., and Tang, J.H., 2014. Nitrogen removal with nitrification and denitrification via nitrite. *Advanced Materials Research*, 908, pp.175-178.
- Xu, G., Feng, C., Fang, F., Chen, S., Xu, Y., and Wang, X., 2015. The heterotrophic-combined-with-autotrophic denitrification process: performance and interaction mechanisms. *Water Science and Technology*, 71, pp.1212-1218.
- Yan, L., Liu, S., Liu, Q., Zhang, M., Liu, Y., Wen, Y., Chen, Z., Zhang, Y., and Yang, Q., 2019. Improved performance of simultaneous nitrification and denitrification via nitrite in an oxygen-limited SBR by alternating the DO. *Bioresource Technology*, 275, pp.153-162.
- Yang, S., and Yang, F., 2011. Nitrogen removal via short-cut simultaneous nitrification and denitrification in an intermittently aerated moving bed membrane bioreactor. *Journal of Hazardous Materials*, 195, pp.318-323.
- Zhang, F., Du, Z., Wang, J., Du, Y., and Peng, Y., 2024. Acidophilic partial nitrification (pH<6) facilitates ultra-efficient short-flow nitrogen transformation: Experimental validation and genomic insights. *Water Research*, 260, 121921.
- Zhang, L., Wei, C., Zhang, K., Zhang, C., Fang, Q., and Li, S., 2009. Effects of temperature on simultaneous nitrification and denitrification via nitrite in a sequencing batch biofilm reactor. *Bioprocess and Biosystems Engineering*, 32, pp.175-182.
- Zhang, L., Yang, J., and Furukawa, K., 2010. Stable and high-rate nitrogen removal from reject water by partial nitrification and subsequent anammox. *Journal of Bioscience and Bioengineering*, 110, pp.441-448.
- Zhang, Q., Chen, X., Luo, W., Wu, H., Liu, X., Chen, W., Tang, J., and Zhang, L., 2019. Effects of Temperature on the characteristics of nitrogen removal and microbial community in post solid-phase denitrification biofilter process. *International Journal of Environmental Research and Public Health*, 16, p.4466.
- Zhang, X.Y., Zeng, Y.W., Tao, R.D., Zhang, M., Zheng, M.M., Qu, M.J., and Mei, Y.J., 2024. Analysis of the microbial diversity and the mechanism of simultaneous nitrification and denitrification in high nitrogen environments. *International Journal of Environmental Science and Technology*, 21, pp.1-14.
- Zhou, Y., Zhu, Y., Zhu, J., Li, C., and Chen, G., 2023. A comprehensive review on wastewater nitrogen removal and its recovery processes. *International Journal of Environmental Research and Public Health*, 20, p.3429.
- Zhu, S.M., Deng, Y.L., Ruan, Y.J., Guo, X.S., Shi, M.M., and Shen, J.Z., 2015. Biological denitrification using poly(butylene succinate) as carbon source and biofilm carrier for recirculating aquaculture system effluent treatment. *Bioresource Technology*, 192, pp.603-610.



# Data Envelopment Analysis-based Scenario Selection for Sequencing Pattern in a Simulated Robotic Cell

Bahareh Vaisi<sup>1†</sup>, Hiwa Farughi<sup>2</sup> and Sadigh Raissi<sup>3</sup>

<sup>1</sup>Young Researchers and Elite Club, South Tehran Branch, Islamic Azad University, Tehran, Iran

<sup>2</sup>Department of Engineering, University of Kurdistan, Sanandaj, Iran

<sup>3</sup>School of Industrial Engineering, South Tehran Branch, Islamic Azad University, Tehran, Iran

**Abstract**—In this study, the performance of suggested scenarios for part input sequences in a 3-machine robotic cell producing different parts is determined through the application of data envelopment analysis (DEA) and the Banker–Charnes–Cooper model. A single gripper robot supports the manufacturing process by loading and unloading products and moving them inside the system. This study addresses random machine failures and repairs to minimize cycle time based on two robot move cycles in a three-machine robotic cell and overall production costs. Here, simulation assists in the modeling of uncertainty and a simulation-based optimization approach is applied to find the best scenarios for sequencing patterns in the cell through several numerical examples using DEA. The results displayed that, efficient scenarios satisfying minimum time and cost, are those, in which the percentages of operations assigned to the machines are close to each other. This enables decision-makers in manufacturing systems to make precise selections of the optimal part sequencing pattern with the lowest production cost and cycle time for robotic cells.

**Index Terms**—Data envelopment analysis, Part sequencing, Robotic cell, Scenario design, Simulation.

## I. INTRODUCTION

The dominance of robotic systems has arisen as a pivotal point of both academic and industrial consideration, obtaining considerable attention (Ali, 2024). A robotic manufacturing cell consists of computer numerical control (CNC) machines with at least one robot (to pick up products and load/unload the machines). Consideration is given to the problem of part sequencing in a robotic cell served by a single gripper robot and three machines that produce different parts. We are interested in minimizing cycle time and production

costs. Cycle time is the average time required to process a component in a system. In the majority of published studies, cycle time minimization has served as the objective function for part sequencing problems. (Vaisi, Farughi and Raissi, 2022) Surveyed recent developments in the problems of robotic manufacturing systems between 2005 and 2021, including the problem of determining optimal part sequencing in robotic manufacturing cells.

Simultaneous optimization of the robotic move sequence and part input sequence was studied by (Zhao and Guo, 2018), and an effective chemical reaction optimization (ECRO) was proposed as an encoding solution method. How to incorporate machine breakdowns into robotic manufacturing cells is an unanswered question in the part sequencing problem. By using a simulation-based optimization strategy, (Vaisi, Farughi, and Raissi, 2018) demonstrated that it is possible to determine the optimal part input sequence in an unreliable two-machine robotic cell. In another study, the performance of different layouts in two-machine robotic cells that produce non-identical parts was compared (Foumani and Tavakkoli Moghaddam, 2019). (Vaisi, Farughi and Raissi, 2020) demonstrated the robustness of three-machine robotic cells using simulation-based optimization and multi-criteria decision-making techniques. In a recent study, (Vaisi, Farughi and Raissi, 2021) simulated the sequencing problem of a three-machine robotic cell under  $S_0$  cycle, where it produces different parts to obtain minimum cycle time/operational cost and maximum throughput. Then, response surface methodology and goal programming approach were utilized on the simulation results to optimize the sequencing problem. In a different study, a robotic cell was simulated to improve the reliability of the cell. By means of a supervised machine learning model, the faulty behavior of the critical component was classified (Mourtzis, Tsubou and Angelopoulos, 2023). To find the optimal cycle time in two-machine circular robotic cells with swap ability to maximize the output, a study has recently been conducted by (Khebouche and Boudhar, 2024). However, optimal sequencing of parts in the case of an existing unreliable robotic cell with three machines through data envelopment analysis (DEA) is also on appeal.

ARO-The Scientific Journal of Koya University  
Vol. XII, No.2 (2024), Article ID: ARO.11668. 9 pages  
Doi: 10.14500/aro.11668

Received: 23 June 2024; Accepted: 07 September 2024  
Regular research paper; Published: 21 September 2024

<sup>†</sup>Corresponding author's e-mail: st\_b\_vaisi@azad.ac.ir  
Copyright © 2024 Bahareh Vaisi, Hiwa Farughi and Sadigh.

Raissi. This is an open-access article distributed under the Creative Commons Attribution License (CC BY-NC-SA 4.0).



Unreliable robotic cells are those that are subject to random failure and maintenance.

Complex decisions regarding sequencing issues in robotic manufacturing cells, as a result of uncertainty, can be supported by computer simulation models. The development of simulation techniques dates back to the early 1960s, and simulation may be the most widely used analytical tool (Pidd, 1986). Although simulation methods are commonly referred to as descriptive modeling techniques, it has been demonstrated that computer simulation is an effective interface between operations research and computer science (Fu, 2002). The use of simulation in manufacturing from 2002 to 2013 was examined by (Negahban and Smith, 2014). The major milestones in the development of simulation tools were analyzed by (Mourtzis, Doukas and Bernidaki 2014) through a comprehensive study. In the context of the manufacturing system, they examined recent industrial simulation practices, their evolution, advances, and future trends. Using computer simulation in manufacturing systems has been considered by a number of researchers, such as the simulation of a chain store as a service sector by (Vaisi, Raissi and Vaisi, 2015); the simulation of a flexible manufacturing system by (Florescu, Barabaş and Sârbu, 2017); the simulation of an assembly line by (Yang, Chen and Lin, 2017); the simulation of capacitated assembly systems by (Woerner, Laumanns and Wagner, 2018); the simulation of a material handling system by (Leung and Lau, 2019), and so on. Furthermore, to support the strategic maintenance development in a production system, simulation-based optimization was done by (Linnéusson, Ng and Aslam, 2020). Simulation was also applied to train operators in a study done by (Karagiannis et al., 2021). The furniture manufacturing and assembly process in a furniture company were recently simulated through Arena software by (Kolny, Kaczmar-Kolny and Dulina, 2023). One more fresh study was done to simulate an automobile assembly manufacturing line and analyze bottlenecks in the manufacturing system, (Mohammed, Abdulghafour and AL-Enzi, 2024).

Following the aforementioned literature review, solution methods for the part sequencing problem primarily consisted of the Gilmore and Gomory algorithm, heuristics, and formulations based on the traveling salesman problem. A review of the relevant literature reveals that scenario design and scenario evaluation in three-machine robotic cells using DEA have not been previously conducted. Therefore, a scenario concept is being developed to bridge this gap. Two cycles are considered robot move cycles in 3-machine robotic manufacturing cells, which contributes to the novelty of the present study. The cycles are compared to determine the optimal sequencing pattern for the parts, in which each of the move cycles simultaneously minimizes cycle time and total production cost. It should be noted that there are six cycles for robot movements in three-machine robotic cells, and in "Table I", all the cycles will be presented. In the current study, two of the cycles are selected because few researches have been focused on them as their complexity is high.

DEA as a nonparametric mathematical programming technique has been evaluated as one of the most notable

TABLE I  
ROBOT ACTIVITY SEQUENCES IN THREE-MACHINE ROBOTIC CELLS

Cycles	Encoding of robot activity sequences
$S_1$	$A_{01} A_{12} A_{23} A_{34}$
$S_2$	$A_{01} A_{12} A_{23} A_{34}$
$S_3$	$A_{01} A_{12} A_{23} A_{34}$
$S_4$	$A_{01} A_{12} A_{23} A_{34}$
$S_5$	$A_{01} A_{12} A_{23} A_{34}$
$S_6$	$A_{01} A_{12} A_{23} A_{34}$

methods for measuring the performance of homogeneous units, i.e., decision-making units (DMUs) that transform inputs into outputs. A study of DEA applications from 1978 to August 2010 by (Liu et al., 2013) revealed that DEA is applicable in a variety of contexts for measuring efficiency. Furthermore, in another paper, (Emrouznejad and Yang, 2018) conducted a survey related to the theory and applications of DEA, reporting published papers from 1978 to 2017. Here are some recent studies demonstrating the practical applications of DEA in various industries: (Vaisi and Raissi, 2014) in Pride's spare parts manufacturing system; (Banker et al., 2017) in electric distribution firms; (Pjevcevic et al., 2017) in a port container terminal; (Vaisi, 2017) in a production system; (Vaisi et al., 2018) in a two-machine robotic cell; (Solgi et al., 2019) in complex product systems; (Wen et al., 2020) in the construction sector; (Zhu, Zhu and Emrouznejad, 2020) in manufacturing companies; (Vaisi, 2023) in a manufacturing system with a transport robot; and (Sinha, Vaisi and Edalatpanah, 2024) in the banking industry. With the exception of (Vaisi et al., 2018; Vaisi et al., 2023), there are no known published studies on the part sequencing problem utilizing DEA, which were done for a two-machine robotic cell. The current study seeks to fill this gap by considering a three-machine robotic manufacturing cell. It should be highlighted that the use of DEA to select the best sequencing patterns in robotic cells has been unparalleled in its field, and the current study is entirely distinct from our previous work due to the differences in terms of the nature of complexity for movement cycles in the two-machine and three-machine robotic cells.

Thus, the contribution of the current study is summarized as:

- Application of a simulation-based optimization approach to solve the part input sequencing problem in unreliable three-machine robotic cells.
- Presenting the DEA-based performance measurement of  $S_2$  and  $S_6$  cycles as two movement cycles for robots in three-machine robotic cells.

The structure of the paper is as follows: In the following section, the problem is defined, and assumptions and numerical examples are provided. In section III, the problem is modeled using a computer simulation technique. For the purpose of solving the problem, proposed scenarios are presented and DEA is utilized to determine the optimal part entrance sequence to the cell in section IV. In section V, the conclusion is presented.

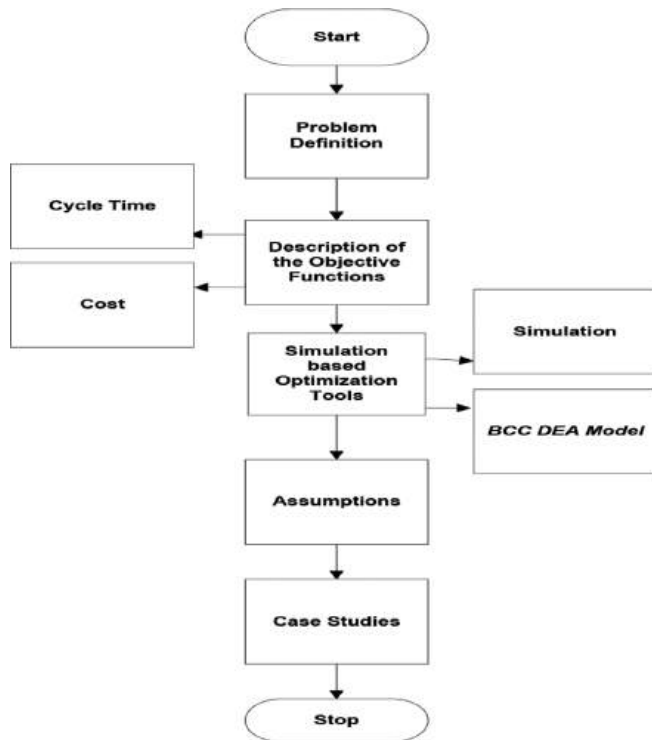


Fig. 1. Flowchart for the problem statement and optimization tools presentation.

## II. PROBLEM STATEMENT

In this section, the problem and solution tools are defined as they come in Fig. 1. Hence, the problem is defined in A, objective functions are described in B and C, the simulation-based optimization approach and its tools are represented in D and E, assumptions are summarized in F, and numerical examples are denoted in sub-section G of the existing section.

### A. Robotic Cell

In this study, an in-line robotic cell encompasses three similar CNC machines with no priority in operation, and a single gripper robot is assumed. A robotic cell is a manufacturing system composed of a number of CNC machines, a material-handling robot, and other relevant systems. The processing of each component begins in the input buffer and concludes in the output buffer (Vaisi et al., 2020; Vaisi et al., 2023). “Fig. 2” depicts an in-line three-machine robotic cell. It should be noted that different colors for the parts in “Fig. 2” represents that the cell produces different parts.

In-line robotic cells are a type of robotic cell layout. Based on this layout, robot movement between machines and buffers is linear. All machines are capable of performing the operations simultaneously. In addition, a single gripper robot is responsible for loading and unloading parts to and from the selected machine. In the current study, the output of this system consists of various part types and operates continuously. Each component requires processing by the machines, and there is no buffer storage between the machines. For the production of each part, multiple

types of operations must be performed on the machines; by percentage, some of these operations are performed on machine one, while the remaining ones are performed on machines two and three, respectively.

The primary objective of this study is to determine the sequence of entering parts into an unreliable three-machine robotic cell that experiences random failure and repair times while minimizing cycle time ( $S_2/S_6$  cycles) and total production cost.

### B. Cycle time

Six cycles, designated  $S_1, S_2, S_3, S_4, S_5$  and  $S_6$  cycles, may be utilized for part displacements in a 3-machine robotic cell. Here, we focused on the  $S_2$  and  $S_6$  cycles because they are well-known and commonly used cycles, but they have received less modeling attention than the other robot move cycles since they are more complicated. The move cycles  $S_2$  and  $S_6$  are described in the following paragraphs.

Based on the  $S_6$  cycle, the robot begins following operations sequentially from the input buffer. (1) picking part  $i$ , (2) proceeding to the first machine, (3) loading the first machine, (4) transferring to the third machine, (5) Waiting for the completion of the process on part  $(i-2)$  (if required), (6) unloading the part from the third machine, (7) transferring the item to the output buffer, (8) loading the output buffer, (9) moving to the second machine, (10) If necessary, waiting for the completion of the process on the part  $(i-1)$ , (11) unloading the part from the second machine, (12) moves the part to the third machine, (13) loads the part onto the third machine, (14) transferring to the first machine, (15) if necessary, waiting until the part  $i$  's process is complete, (16) unloading the initial machine, (17) transferring the part from the first machine to the second machine, (18) loading the part on the second machine, and (19) returning to the input buffer. The activity sequence of the  $S_6$  cycle is encoded by  $A_{01} A_{34} A_{23} A_{12}$  and it is a one-unit cycle, as shown by (Sethi et al., 1992; Gultekin, Akturk and Karasan, 2007).

Equation (1) could be used to calculate the  $S_6$  cycle time based on Table II’s key cycle time calculation parameters and according to (Gultekin, Akturk and Karasan, 2008).

$$T_{S_6} = \max \{8\epsilon + 12\delta, t(1) + 4\epsilon + 4\delta, t(2) + 4\epsilon + 4\delta, t(3) + 4\epsilon + 4\delta\} \quad (1)$$

The general process of  $S_2$  cycle in a three-machine cell is as follows. Once more, the input buffer is the initial location of the robot. Then, the robot performs the subsequent operations in succession. (1) The robot picks up part  $i$ , (2) moves to the first machine, (3) loads part  $i$  onto the first machine, (4) moves to the second machine, (5) Waits for the completion of the process on part  $(i-1)$  (if necessary), (6) unloads the component from the second machine  $(i-1)$ , (7) moves the part  $(i-1)$  to the third machine, (8) loads the part onto the third machine, (9) returns to the first machine, (10) If necessary, wait until the process on part  $i$  is complete, (11) unload the part from the first machine, (12) transfer it to the second machine, (13) load the part  $i$  onto the second machine, (14) proceeds to the third machine, (15) if necessary, waits until the third machine’s process is complete, (16) unloads the part  $(i-1)$  from the third machine,

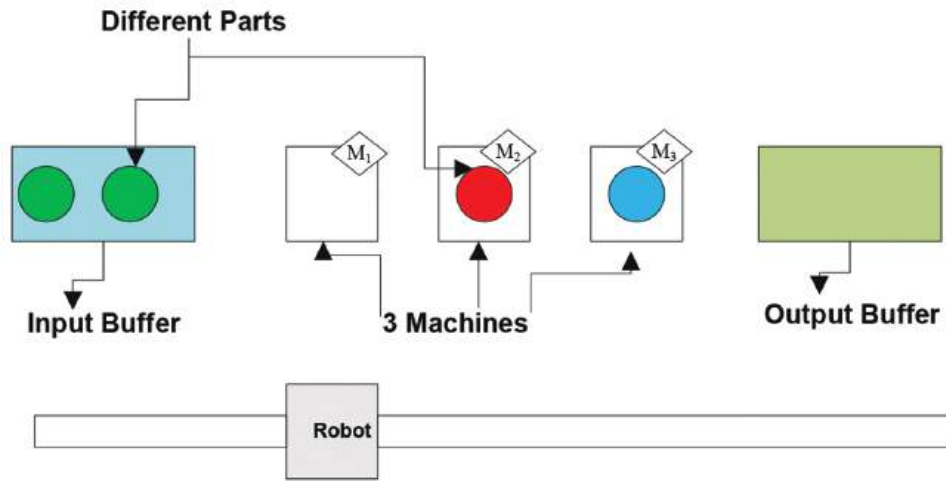


Fig. 2. A typical layout for an in-line robotic manufacturing cell comprising 3 machines.

TABLE II  
CYCLE TIME PARAMETERS

Parameters	Expression
$\epsilon$	Loading/unloading time
$\delta$	Robot's movement time between two consecutive locations
$T_{S_0}$	Cycle time based on $S_0$ robot move cycle
$T_{S_2}$	Cycle time based on $S_2$ robot move cycle
$A_{pq}$	Robot activity sequence from station, $p$ , to station, $q$ , for $p=0,1,2,3$ and $p=0,1,2,3$ .
$t_i(j)$	Processing times of part $i$ based on the Percentage of operations done by each machine $j$ ; $i=1, \dots, n$ ; $j=1,2,3$ .

$CM$	Machining cost (\$/min)
$CPM$	Cost of a PM visit (\$/visit) without considering any setup cost
$CT$	Cost of tool (\$/tool) Tool replacement prohibited in an operating cycle
$DR_j$	Expected down rate of machine $j$
$OP$	Observation period
$n$	The number of produced parts by type based on the percentage of operations done by each machine during the simulation period
$N$	Number of throughput products in the simulation period
$F$	Total cost (\$/times unit)
$TTF$	Time to failure (times unit)
$TTR$	Time to repair (times unit)
$t_i(j)$	Processing times of part based on the Percentage of operations done by each machine $j$ ; $i=1, \dots, n$ ; $j=1,2,3$

(17) transports the product to the output buffer; (18) deposits the product at the output buffer; and (19) returns to the input buffer. As a general rule, the activity sequence of the  $S_2$  cycle is encoded by  $A_{01} A_{23} A_{12} A_{34}$ , and this cycle produces one product in each cycle; see (Sethi et al., 1992). Equation (2) reveals the  $S_2$  cycle time based on "Table II" and in accordance with (Gultekin, Akturk and Karasan, 2008).

$$T_{S_2} = \max\{8\epsilon + 12\delta, t(1) + 6\epsilon + 8\delta, t(2) + 4\epsilon + 4\delta, t(3) + 6\epsilon + 8\delta, \frac{(t(1) + t(2) + t(3))}{2 + 4\epsilon + 4\delta}\} \quad (2)$$

The encoding of the movement cycles for three-machine robotic cells is tabulated in Table I.

### C. Total Production Cost

Total production cost is the second objective function of this study. The components of the total cost of production are machining, tooling, and preventive maintenance (Akturk and Gurel, 2007). Although tool switching has been measured in several studies, such as (Kamalabadi, Sadeghi and Maihami, 2012), (Farughi et al., 2017), and (Moradi, Yousefi Nejad Attari and Farughi, 2018), in the present study, it was ignored and the cost of tooling is considered to be a constant value. The following are the main parameters for calculating the total production cost:

Consequently, the total cost per operating cycle could be calculated by Eq. (3).

$$F = \sum_{i=1}^n n CM t_i(j) + \sum_{j=1}^3 CPM DR_j OP + N CT; \quad (3)$$

### D. Simulation

Simulation-based optimization approaches have become efficient measures for decision-makers to find near-optimal solutions within a reasonable time. In this research, a simulation model of different scenarios for parts sequencing in a three-machine robotic cell is developed using discrete-event simulation software. In the simulation model, each unique sequence of parts entering the robotic cell is considered a scenario, and a simulation model is developed to simulate the scenarios and generate output data for each one.

Simulation builds a real-process model of a system over time and conducts experiments to determine the system's behavior (Shannon, 1998). The procedure for doing a simulation in a robotic cell (as an example) briefly includes formulating the problem and objectives; presenting a conceptual model for the cell or a series of mathematical equations regarding the context of the robotic cell; collecting data; developing the simulated model of the robotic cell; confirming the simulated model; designing experiments;

performing simulation runs; and analyzing and documenting results (Banks, 1998).

After a certain period of simulation run, the system could reach a stable state. This period is known as a warm-up period and is typically set to 10% of the observation period in simulation software configurations. The beginning of the observation period coincides with the conclusion of the warm-up period. The simulation model is developed in Section III.

*E. Banker–Charnes–Cooper (BCC) DEA model*

As mentioned earlier, the use of simulation in connection with optimization may assist decision-makers in developing efficient scenarios. Using DEA as the optimization tool to evaluate and classify the scenarios is a distinctive aspect of three-machine robotic cells that have not been done yet. DEA is one of the most distinguished methods for measuring the performance of homogeneous DMUs. A DMU is an entity responsible for converting inputs into outputs. This method’s strengths are that it permits the use of multiple inputs and outputs, and the dimensions of input/output do not need to be converted. However, this method’s weakness is that outliers may affect the results.

In this study, one of the classical DEA models is used to evaluate the designed scenarios. Scenarios are treated as DMUs due to their output and input characteristics. We obtain DMU data through scenario execution. Here, DEA utilizes the BCC model to select the most effective scenarios.

The BCC DEA model can be described as follows (Banker et al., 1984): suppose there are “*n*” DMUs to be measured with “*m*” different inputs and “*s*” different outputs. DMU<sub>0</sub> consumes the input value *x*<sub>0</sub> and produces the output value *y*<sub>0</sub>. Under the assumption *x*<sub>0</sub> ≥ 0, *y*<sub>0</sub> ≥ 0, the efficiency formula is 
$$\frac{\text{weighted sum of outputs}}{\text{weighted sum of inputs}}$$
. Equation (4) represents the

efficiency of DMU<sub>0</sub> as a fractional linear program based on the BCC Ratio Model (Input Orientation). “*u<sub>r</sub>*”, and “*v<sub>i</sub>*” are the assigned output and input weights, while “*W*” is a free variable. In this study, the inputs/outputs will be determined, explained in detail, and implemented in sections III and IV.

$$\max E_0 = \frac{\sum_{r=1}^s u_r y_{r0} + W}{\sum_{i=1}^m v_i x_{i0}} \tag{4}$$

*S.t.*

$$\frac{\sum_{r=1}^s u_r y_{rj} + W}{\sum_{i=1}^m v_i x_{ij}} \leq 1 \quad j=1,2,\dots,n$$

*W; free variable*

$$u_r \geq 0$$

$$v_i \geq 0$$

$$r=1,2,\dots,s$$

$$i=1,2,\dots,m$$

*F. Assumptions*

Assume that machines in this robotic cell have two independent states: active and inactive. Failure and repair

rates may be constant or time-dependent; λ(*t*) and μ(*t*) separately. The study’s basic assumptions are summarized:

1. The availability of components at the input buffer and an empty position at the output buffer are both true.
2. The processing time for parts on the machines has been specified, despite breakdowns, etc.
3. The machines are subject to random failures and require maintenance.
4. The statistical density functions of TTF and TTR have accepted reliable parameters.
5. Setup times are insignificant.
6. Pre-emption in the processing of any operation is prohibited.

*G. Cases*

The issue is investigated using an example derived from prior work (Batur, Karasan and Akturk, 2012). In the following examples, each color corresponds to a distinct type of part.

Example 1. A three-machine robotic cell produces three different products separately, including Blue (B): 57, Red (R): 84, and Purple (P): 87, with their respective process times (in minutes), ε=1 and δ=2 time units, see (Batur, Karasan and Akturk, 2012).

Example 2. A three-machine robotic cell is assumed to produce a product in 57 minutes (a Blue colored product). ε and δ separately are 1 and 2 min; see (Batur, Karasan and Akturk, 2012).

Table III contains the cost parameters and their corresponding values for these three-machine robotic cells (Examples 1 and 2). These parameter values are assumed to be constant.

III. DEVELOPING SIMULATION MODEL

For the purpose of analyzing the existing robotic cell, the integration of computer simulation and linear programming optimization is used to control different sources of uncertainty. Enterprise dynamics (ED) is used to model the sequence of components in the presented robotic cell for simulation purposes. This simulation tool employs drag-and-drop technology and has a user-friendly interface to facilitate the modeling of anticipatory layouts.

“Fig. 3” illustrates the system’s simulation model. In this model, three dissimilar products flow through the system based first on the move the cycle of the robot and then on the S<sub>2</sub> move cycle, utilizing the ED special elements.

To obtain unbiased estimates, simulation models were run for long periods of time (>10000 h) following a 50-h warm-up period. In addition, the definition of performance measures (PFM) is as follows. The desired input and output variables of the DEA method are comprised PFMs.

Y<sub>1</sub>: The average time for each S<sub>6</sub> (S<sub>2</sub>) cycle in the simulation period

Y<sub>2</sub>: The average operating cost per part in the simulation period

TABLE III  
CHARACTERISTICS OF COST PARAMETERS

Characteristics of Cost Parameters	CM=50	CT=45
TTF=NegExp (10)	TTR=NegExp (2)	

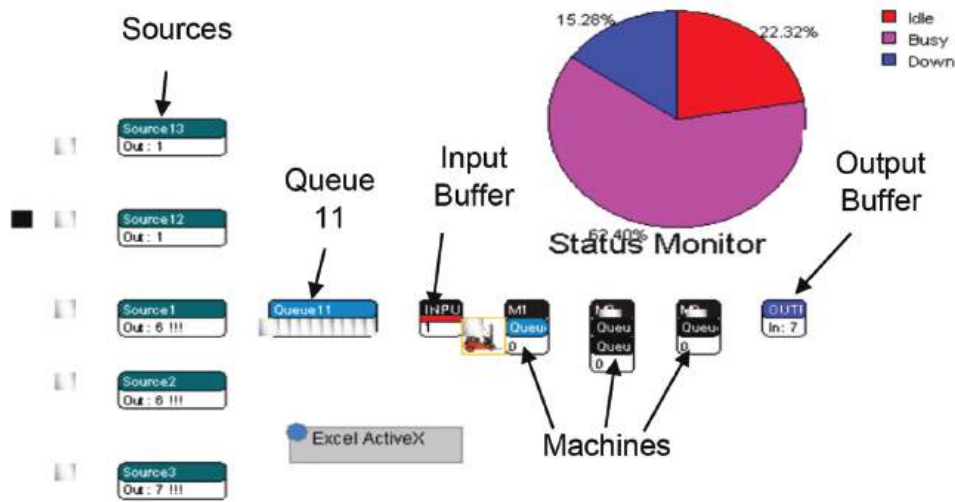


Fig. 3. A simulated model for the 3-machine robotic cell layout using ED.

$Y_3$ : Number of generative throughout the simulation period  
 To select the inputs/outputs of the system, a fundamental understanding of the production system and data analysis is required. In general, the major resources that enter the manufacturing system are the inputs, and the primary output is the production quantity (Jain, Triantis and Liu, 2011). This is also true for the robotic cell. Therefore, cycle time and cost are the typical inputs, and the operational output of the current robotic cell is the produced throughput.

IV. RESULTS

Simulation-based optimization methods were used to find the best sequencing patterns in a three-machine robotic cell. In this section, first, the validity of the simulation model is evaluated in A. Then, by defining the scenarios in B, DEA as the optimization tool will classify the scenarios in C. Discussion over the results will come in D.

A. Validation of the Simulated Model

Example 2 was simulated as a three-machine robotic cell (machine failures were ignored) based on the  $S_6$  cycle and the  $S_2$  cycle, respectively. After running the simulation model, it was determined with a confidence level of 95% that the average  $S_6$  cycle time and operating cost are 86.719 seconds and 187.5, respectively. ED software also reports that the average  $S_2$  cycle time and operating cost are 68.948 and 187.5, respectively.

Mann-Whitney Hypothesis testing is used to compare the statistical differences between the simulated model dataset and the real dataset. This is performed to validate the simulation model. The results of Equations (1) and (2) are referred to as the real dataset. The simulated model data includes the mean daily production after 25 replications of the simulation model. A P-value >0.85 indicates that there is no significant difference to reject the equality of two means, and the simulation model’s validity is confirmed.

In the next step, several scenarios are created to determine the optimal sequence for the part’s entrance into the robotic cell.

B. Scenario Design

In this step, various sequencing patterns for the part’s entrance to the robotic cell are formed. Each sequence pattern is simulated by ED software as a scenario. Table IV depicts the designed scenarios derived from Example 1. B-P-R and B-R-P are two possible sequences for case study 1 which come in the right part of “Table IV,” and the percentage of operations performed by each machine is defined in the left part of the table. Example 1 was simulated twice, once according to the  $S_6$  cycle and the second time according to the  $S_2$  cycle. The results according to the definable PFMs for the  $S_6$  cycle and the  $S_2$  cycle are separately summarized in Tables V and VI. After adjusting the simulation time, it is possible to obtain the average cycle time ( $S_2/S_6$ ), average cost, and number of generative throughput. The objective is to maximize throughput while minimizing cost and cycle time.

Let us discuss scenario 7 as an example. Consequently, scenario 7 indicates that 60% of the operations are done on Machine1 and Machine3, equally. The rest of the operations to produce a part are performed by Machine2. Meanwhile, the first part to be allocated to machines 2 and 3 is Blue (B) and the sequencing pattern for entering the parts to the cell is B-P-R, meaning Blue-Purple-Red; see (Cases in Section II). Results for this scenario show that based on the  $S_6$  cycle outcomes in “Table V,” the cycle time is 48.841, the cost is 15959.735, and the throughput is 40539. Whereas based on the  $S_2$  cycle results in “Table VI,” the cycle time is 69.862, the cost is 22782.198, and the robotic cell can produce 28341 parts during the simulation period.

On the dataset, the DEA tool is utilized to identify the optimal scenarios and the results will be displayed in C.

C. DEA Results

The optimal sequence is determined using a simulation-based optimization approach and the DEA method. DMUs in this case have two inputs and one output. As previously mentioned, the inputs consist of average cycle time ( $S_6/S_2$ ) and average cost, while the output is the number of produced throughput. The DEA method based on the “Equation (4)” is applied to compare the proposed scenarios.

TABLE IV  
DESIGNED SCENARIOS FOR THE EXAMPLE 1

Scenario Group (SG)	Sequence			Seq. 1 B-P-R			Seq. 2 B-R-P		
	The Percentage of operations performed by each machine			The first allocated part to the Second and Third machine			The first allocated part to the Second and Third machine		
SG	M <sub>1</sub>	M <sub>2</sub>	M <sub>3</sub>	B	P	R	B	P	R
Scenario Number									
A	33.3%	33.3%	33.3%	1	2	3	16	17	18
B	20%	40%	40%	4	5	6	19	20	21
C	30%	40%	30%	7	8	9	22	23	24
D	25%	25%	50%	10	11	12	25	26	27
E	60%	20%	20%	13	14	15	28	29	30

TABLE V  
DEFINABLE PFM VALUES BASED ON THE SCENARIOS OF S<sub>6</sub> CYCLE IN EXAMPLE 1

PFMs	Scenario Number (SN)					
	1	2	3	4	5	6
Y <sub>1</sub>	47.915	43.587	43.586	49.155	58.234	49.154
Y <sub>2</sub>	15659.37	15669.16	15668.785	17657.079	20898.394	17657.076
Y <sub>3</sub>	41322	41296	41297	36618	30909	36618
SN	7	8	9	10	11	12
Y <sub>1</sub>	48.841	44.406	44.367	54.779	54.744	60.157
Y <sub>2</sub>	15959.735	15961.3	15947.624	19665.213	19652.724	19632.534
Y <sub>3</sub>	40539	40535	40570	32858	32879	32913
SN	13	14	15	16	17	18
Y <sub>1</sub>	76.917	69.965	70.047	43.594	59.893	59.872
Y <sub>2</sub>	25071.426	25085.985	25115.143	15671.424	21490.558	21482.735
Y <sub>3</sub>	25742	25727	25697	41290	30053	30064
SN	19	20	21	22	23	24
Y <sub>1</sub>	49.221	49.196	64.08	48.819	44.382	44.365
Y <sub>2</sub>	17680.594	17671.95	20905.797	15952.7	15952.7	15946.842
Y <sub>3</sub>	36569	36587	30898	40557	40557	40572
SN	25	26	27	28	29	30
Y <sub>1</sub>	54.629	54.716	54.695	69.989	70.115	70.04
Y <sub>2</sub>	19611.201	19642.028	19635.499	25094.724	25139	25113.195
Y <sub>3</sub>	32949	32897	32908	25718	25672	25699

TABLE VI  
DEFINABLE PFM VALUES BASED ON THE SCENARIOS OF S<sub>2</sub> CYCLE IN EXAMPLE 1

PFMs	Scenario Number (SN)					
	1	2	3	4	5	6
Y <sub>1</sub>	73.967	67.268	67.238	78.605	71.531	78.708
Y <sub>2</sub>	24114.609	24123.581	24112.815	25620.482	25645.829	25653.953
Y <sub>3</sub>	26768	26758	26770	25188	25163	25155
SN	7	8	9	10	11	12
Y <sub>1</sub>	69.862	69.865	69.876	81.572	81.649	89.89
Y <sub>2</sub>	22782.198	22783.799	22787	29231.379	29257.8	29282.941
Y <sub>3</sub>	28341	28339	28335	22065	22045	22026
SN	13	14	15	16	17	18
Y <sub>1</sub>	114.033	92.838	102.153	67.222	67.3	73.919
Y <sub>2</sub>	37118.066	33252.545	33262.809	24106.54	24135.253	24099.373
Y <sub>3</sub>	17363	19388	19382	26777	26745	26785
SN	19	20	21	22	23	24
Y <sub>1</sub>	71.498	78.633	91.69	69.816	69.862	69.881
Y <sub>2</sub>	25633.656	25629.602	29866.601	22767.807	22782.199	22788.601
Y <sub>3</sub>	25175	25179	21594	28359	28341	28333
SN	25	26	27	28	29	30
Y <sub>1</sub>	92.862	89.778	92.878	92.825	92.797	102.132
Y <sub>2</sub>	33261.095	29245.905	33266.227	33247.419	33237.167	33255.967
Y <sub>3</sub>	19383	22054	19380	19391	19397	19386

Tables VII and VIII summarize the efficiency scores for each scenario, as well as the S<sub>6</sub> and S<sub>2</sub> cycles, in that order. Using the Lingo software, calculations were performed.

According to the results for scenario 7 (as an example), this scenario is more efficient based on the S<sub>2</sub> movement cycle of the robot than S<sub>6</sub>. The efficiency scores of this scenario confirm this fact which is a 0.963 score based on the S<sub>6</sub> cycle and 0.999 scores based on the S<sub>2</sub> cycle. However, none of them is efficient, since the efficiency score is one.

### V. DISCUSSION

The relative score of an efficient scenario is one, according to DEA logic. Thus, scenarios numbered “1” and “3” will be the most efficient for Example 1 under S<sub>6</sub>. Concerning the foregoing, as shown in Example 1, the sequence Blue-Purple-Red is preferred over any other sequence pattern when the Blue or Red part is the first one to be produced on the second and third machines. This applies to three different part types. Scenario “3” with 43.586-time units has a lower average S<sub>6</sub> cycle time score than scenario “1” with 47.915 time units. In contrast, scenario “1” has lower production costs than scenario “3.” During the observation period, the output rate for scenario “1” is 41322 versus 41297 for scenario “3”.

In a three-machine robotic cell operating on the S<sub>2</sub> cycle, the “22” scenario has the optimal part sequence pattern for Example 1. The Blue-Red-Purple sequence when Blue part is the first part on the second and third machines is the optimal part sequence pattern for these three different part types, robotic cell under S<sub>2</sub>.

In optimal scenarios, although the average cycle time and cost under S<sub>6</sub> are less than those values under S<sub>2</sub>, the number of total products produced during the simulation period under S<sub>6</sub> exceeds that of S<sub>2</sub>. Among the efficient scenarios, scenario coded “1” (which is under S<sub>6</sub>) has the highest throughput, which is just over 41,300 during the simulation period.

Figs. 4 and 5 compare the average efficiency of each scenario group based on the two candidate sequences for the move cycles (S<sub>6</sub>/S<sub>2</sub>). Clearly, the efficiency scores of the two sequences based on both cycles follow a nearly identical trend.

Scenario number 7 till 15 and scenario number 22 till 30 for the S<sub>6</sub> movement cycle in both sequence patterns have comparable amounts of efficiency, whereas the trends of both sequence patterns based on the S<sub>2</sub> cycle are volatile, fluctuating between 0.375 and 1. Nevertheless, on average, sequence pattern 1 has more efficient scenarios in both cycles.

Overall, the comparison demonstrates that the scenarios, as DMUs in the DEA method, are more efficient when the percentage of operations assigned to machines is closer to one another. Moreover, due to the similarity of the machines and their TTF/TTR, the optimal assignment of operations to machines occurs when the number of operations allocated to each machine is close. Consider the characteristics of scenarios 1, 2, 3, 7, 8, 9, 22, 23, and 24 as the near-optimal scenarios in both cycles.

TABLE VII  
EFFICIENCY SCORES OF SCENARIOS BASED ON THE BCC MODEL FOR  $S_6$  CYCLE  
IN EXAMPLE 1

SN	Scenario Number (SN) Efficiency Scores (ES) (Below comes)					
	1	2	3	4	5	6
ES	<b>1</b>	0.999	<b>1</b>	0.786	0.56	0.786
SN	7	8	9	10	11	12
ES	0.963	0.963	0.965	0.633	0.634	0.635
SN	13	14	15	16	17	18
ES	0.39	0.388	0.387	0.999	0.529	0.529
SN	19	20	21	22	23	24
ES	0.784	0.785	0.56	0.963	0.964	0.965
SN	25	26	27	28	29	30
ES	0.63656	0.634	0.635	0.388	0.386	0.387

TABLE VIII  
EFFICIENCY SCORES OF SCENARIOS BASED ON THE BCC MODEL FOR  $S_2$  CYCLE  
IN THE EXAMPLE 1

SN	Scenario Number (SN) Efficiency scores (ES) (Below comes)					
	1	2	3	4	5	6
ES	0.891	0.979	0.98	0.789	0.866	0.787
SN	7	8	9	10	11	12
ES	0.999	0.998	0.998	0.666	0.665	0.603
SN	13	14	15	16	17	18
ES	0.375	0.514	0.467	0.981	0.978	0.892
SN	19	20	21	22	23	24
ES	0.867	0.788	0.579	<b>1</b>	0.998	0.998
SN	25	26	27	28	29	30
ES	0.514	0.605	0.514	0.514	0.515	0.467

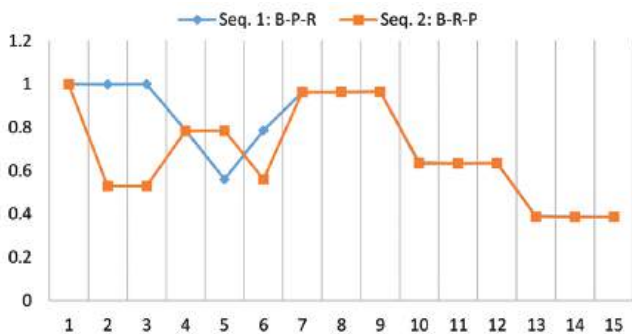


Fig. 4. Comparing the average efficiency of each scenario group based on the two candidate sequence patterns for the  $S_6$  cycle.

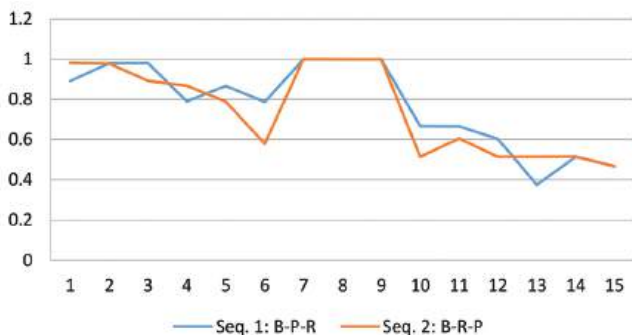


Fig. 5. Comparing the average efficiency of each scenario group based on the two candidate sequence patterns for the  $S_2$  cycle.

V. CONCLUSION

Simulation-based optimization, as a novel practice, was demonstrated in this study to determine the sequencing pattern of the parts in a robotic cell under breakdowns resulting from random failures. The cell consists of three machines that produce dissimilar parts and follow a  $S_6$  or  $S_2$  cyclic pattern for the robot. For the production of a part, multiple types of operations are performed on the machines. By percentage, some of these operations are done on machine one, while the remainder are performed on machines two and three separately. Optimal scenarios for the part's entrance into the robotic manufacturing cell are evidence of the simultaneous minimization of cycle time and cost. Using the DEA method, the proposed scenarios, which have been designed based on different sequences for entering the parts of the cell, were compared in numerical examples. Furthermore, the comparison reveals that the efficient scenarios are those, in which the percentages of operations assigned to the machines are close to each other, due to the similarity of the machines and their TTF/TTR. The results endorse the practicality of applying the DEA approach in robotic cell problems, which can be a helpful tool for decision-makers in robotic manufacturing systems. There is a range of robotic cells available to any industry, such as the automotive industry, to fabricate, finish, weld, transfer, or assemble parts. This depends on the size, weight, or type of the robots used. It is possible to extend the results of this study to include robotic cells with robot failures or robotic cells with dual gripper robots instead of single ones. Consequently, evaluating parts sequencing in unreliable m-machine robotic cells with the above features using simulation and other DEA models is an excellent practical topic for future study.

REFERENCES

Akturk, M.S., and Gurel, A.S., 2007. Machining conditions-based preventive maintenance. *International Journal of Production Research*, 45(8), pp.1725-1743.

Ali, A.K., 2024. A comprehensive framework for integrating robotics and digital twins in façade perforation. *Aro-the Scientific Journal of Koya University*, 12(1), pp.191-202.

Banker, R.D., Charnes, A., and Cooper, W.W., 1984. Some models for estimating technical and scale inefficiencies in data envelopment analysis. *Management Science*, 30(9), pp.1078-1092.

Banker, R., Førsund, F.R., and Zhang, D., 2017. Use of data envelopment analysis for incentive regulation of electric distribution firms. *Data Envelopment Analysis Journal*, 3(1-2), pp.1-47.

Banks, J., Ed. 1998. *Handbook of Simulation: Principles, Methodology, Advances, Applications, and Practice*. John Wiley and Sons, United States.

Batur, G.D., Karasan, O.E., and Akturk, M.S., 2012. Multiple part-type scheduling in flexible robotic cells. *International Journal of Production Economics*, 135(2), pp.726-740.

Emrouznejad, A., and Yang, G.L., 2018. A survey and analysis of the first 40 years of scholarly literature in DEA: 1978-2016. *Socio-Economic Planning Sciences*, 61, pp.4-8.



- Farughi, H., Dolatabadiazadeh, M., Moradi, V., Karbasi, V., and Mostafayi, S., 2017. Minimizing the number of tool switches in flexible manufacturing cells subject to tools reliability using genetic algorithm. *Journal of Industrial and Systems Engineering*, 10(special issue on Quality Control and Reliability), pp.17-33.
- Florescu, A., Barabaş, S., and Sârbu, F., 2017. Operational parameters estimation for a flexible manufacturing system. A case study. *MATEC Web of Conferences*, 112, p.05008.
- Foumani, M., and Tavakkoli Moghaddam, R., 2019. A scalarization-based method for multiple part-type scheduling of two-machine robotic systems with non-destructive testing technologies. *Iranian Journal of Operations Research*, 10(1), pp.1-17.
- Fu, M.C., 2002. Optimization for simulation: Theory vs. practice. *INFORMS Journal on Computing*, 14(3), pp.192-215.
- Gultekin, H., Akturk, M.S., and Karasan, O.E., 2007. Scheduling in a three-machine robotic flexible manufacturing cell. *Computers and Operations Research*, 34(8), pp.2463-2477.
- Gultekin, H., Akturk, M.S., and Karasan, O.E., 2008. Bicriteria robotic cell scheduling. *Journal of Scheduling*, 11, pp.457-473.
- Jain, S., Triantis, K.P., and Liu, S., 2011. Manufacturing performance measurement and target setting: A data envelopment analysis approach. *European Journal of Operational Research*, 214(3), pp.616-626.
- Kamalabadi, I.N., Sadeghi, H., and Maihami, R., 2012. Optimization of total cost of production and time in three-machine robotic cell. *International Journal of Industrial Engineering*, 23(3), pp.293-302.
- Karagiannis, P., Togiass, T., Michalos, G., and Makris, S., 2021. Operators training using simulation and VR technology. *Procedia CIRP*, 96, pp.290-294.
- Khebouche, A., and Boudhar, M., 2024. Two-machine reentrant circular robotic cells with swap ability. *International Journal of Computing Science and Mathematics*, 19(3), pp.221-231.
- Kolny, D., Kaczmar-Kolny, E., and Dulina, L., 2023. Modeling and simulation of the furniture manufacturing and assembly process in the arena simulation software. *Technologia i Automatyizacja Montażu*, 119(1), pp.13-22.
- Leung, C.S., and Lau, H.Y., 2019. A multi-objective simulation-based optimization approach applied to material handling system. In: *Innovative Computing Trends and Applications*. Springer, Cham, pp.1-12.
- Linnéusson, G., Ng, A.H., and Aslam, T., 2020. A hybrid simulation-based optimization framework supporting strategic maintenance development to improve production performance. *European Journal of Operational Research*, 281(2), pp.402-414.
- Liu, J.S., Lu, L.Y., Lu, W.M., and Lin, B.J., 2013. A survey of DEA applications. *Omega*, 41(5), pp.893-902.
- Mohammed, A.J., Abdulghafour, A.B., and AL-Enzi, A.M.J., 2024. Modeling of automobile assembly line performance using ARENA simulation software. *Salud, Ciencia y Tecnología-Serie de Conferencias*, 3, pp.828-828.
- Moradi, V., Yousefi Nejad Attari, M., and Farughi, H., 2018. Modeling for minimizing cycle time in a three-machine robotic cell with assumption of tool switching. *Journal of Industrial Engineering Research in Production Systems*, 6(12), pp.1-17.
- Mourtzis, D., Doukas, M., and Bernidakis, D., 2014. Simulation in manufacturing: Review and challenges. *Procedia CIRP*, 25, pp.213-229.
- Mourtzis, D., Tsoubou, S., and Angelopoulos, J., 2023. Robotic cell reliability optimization based on digital twin and predictive maintenance. *Electronics*, 12(9), p.1999.
- Negahban, A., and Smith, J.S., 2014. Simulation for manufacturing system design and operation: Literature review and analysis. *Journal of Manufacturing Systems*, 33(2), pp.241-261.
- Pidd, M., 1986. *Computer Simulation in Management Science*. Wiley, United States.
- Pjevcevic, D., Nikolic, M., Vidic, N., and Vukadinovic, K., 2017. Data envelopment analysis of AGV fleet sizing at a port container terminal. *International Journal of Production Research*, 55(14), pp.4021-4034.
- Sethi, S.P., Sriskandarajah, C., Sorger, G., Blazewicz, J., and Kubiak, W., 1992. Sequencing of parts and robot moves in a robotic cell. *International Journal of Flexible Manufacturing Systems*, 4, pp.331-358.
- Sinha, R., Vaisi, B., and Edalatpanah, S.A., 2024. Does managerial ability promote firm efficiency? *Journal of Applied Research on Industrial Engineering*, (Articles in Press). doi: 10.22105/jarie. 2024.448994.1600
- Shannon, R.E., 1998. Introduction to the Art and Science of Simulation. In: *1998 Winter Simulation Conference. Proceedings (Cat. No. 98ch36274)*. Vol. 1. IEEE, Washington, DC, pp.7-14.
- Solgi, O., Gheidar-Kheljani, J., Saidi-Mehrabad, M., and Dehghani, E., 2019. Implementing an efficient data envelopment analysis method for assessing suppliers of complex product systems. *Journal of Industrial and Systems Engineering*, 12(2), pp.113-137.
- Vaisi, B., and Raissi, S., 2014. Productivity improvement in the pride's spare parts manufacturing using computer simulation and data envelopment analysis. *International Journal of Computer Applications*, 95(7), pp.12-18.
- Vaisi, B., Raissi, S., and Vaisi, A., 2015. A simulation based strategy using data envelope analysis-goal programming for increasing customer satisfaction in a chain store. *International Journal of Innovative Science and Research Technology*, 2, pp.513-520.
- Vaisi, B., 2017. Productivity improvement in a manufacturing system using computer simulation: A comparison between DEA and DEAGP. *Recent Applications of Data Envelopment Analysis*, pp. 210-217.
- Vaisi, B., Farughi, H., and Raissi, S., 2018. Two-machine robotic cell sequencing under different uncertainties. *International Journal of Simulation Modelling*, 17(2), pp.284-294.
- Vaisi, B., Farughi, H., and Raissi, S., 2020. Schedule-allocate and robust sequencing in three-machine robotic cell under breakdowns. *Mathematical Problems in Engineering*, 2020, p.24.
- Vaisi, B., Farughi, H., and Raissi, S., 2021. Utilization of response surface methodology and goal programming based on simulation in a robotic cell to optimize sequencing. *Journal of Quality Engineering and Management*, 10(4), pp.327-338.
- Vaisi, B., 2022. A review of optimization models and applications in robotic manufacturing systems: Industry 4.0 and beyond. *Decision Analytics Journal*, 2, p.100031.
- Vaisi, B., Farughi, H., Raissi, S., and Sadeghi, H., 2023. A bi-objective optimal task scheduling model for two-machine robotic-cell subject to probable machine failures. *Journal of Applied Research on Industrial Engineering*, 10(1), pp.141-154.
- Vaisi, B., 2023. Simulation-based optimization of a transport robot via super-efficiency DEAGP approach. In: *Transport and Logistics Planning and Optimization*. IGI Global, United States, pp.256-273.
- Wen, Q., Hong, J., Liu, G., Xu, P., Tang, M., and Li, Z., 2020. Regional efficiency disparities in China's construction sector: A combination of multiregional input-output and data envelopment analyses. *Applied Energy*, 257, p.113964.
- Woerner, S., Laumanns, M., and Wagner, S.M., 2018. Simulation-based optimization of capacitated assembly systems under beta-service level constraints. *Decision Sciences*, 49(1), pp.180-217.
- Yang, B., Chen, W., and Lin, C., 2017. The algorithm and simulation of multi-objective sequence and balancing problem for mixed mode assembly line. *International Journal of Simulation Modelling*, 16(2), pp.357-367.
- Zhao, X.F., and Guo, X.P., 2018. An effective chemical reaction optimization for cyclic multi-type parts robotic cell scheduling problem with blocking. *Journal of Intelligent and Fuzzy Systems*, 35, pp.3567-3579.
- Zhu, N., Zhu, C., and Emrouznejad, A., 2020. A combined machine learning algorithms and DEA method for measuring and predicting the efficiency of Chinese manufacturing listed companies. *Journal of Management Science and Engineering*, 6, pp.435-448.

# Dual Electrochemical Methods for Determination of Anesthetic Procaine: Square Wave Voltammetry and Differential Pulse Polarography

Gulan S. Qadir<sup>†</sup>, Amer T. Al-Tae, and Nabeel S. Othman

Department of Chemistry Science, College of Science, University of Mosul,  
Mosul, F.R. Iraq

**Abstract**—Procaine belongs to a type of medicine in which excessive dosage form creates cardiac problems and many allergic reactions. Thus, continuous monitoring of this drug and its metabolite is crucial for sustainable health management during treatment. In this study, electrochemical techniques such as square wave voltammetry (SWV) and differential pulse polarography (DPP) are utilized for assaying procaine amounts in standard and pharmaceutical formulations. In SWV, the reduction of diazotized procaine gives a reduction peak at  $-0.05$  V which is directly proportional with procaine hydrochloride concentration, whereas in DPP, the interaction of the drug with lead cation at  $-0.4$  V is followed by the decrease in peak current of the lead cation reduction peak, which is directly proportional with the concentration of the drug. Both methods indicate high accuracy, sensitivity and precision. Linear concentration ranges of both methods are  $0.0999$ – $5.996 \times 10^{-7}$  M for SWV and  $0.1999$ – $5.996 \times 10^{-7}$  M for DPP. The limit of detection (LOD) and limit of quantification (LOQ) are calculated for both SWV and DPP techniques, and found that LOD equals  $1.984 \times 10^{-9}$  M and LOQ equal  $6.611 \times 10^{-9}$  M for SWV, while for (DPP) LOD and LOQ were found to be  $3.519 \times 10^{-9}$  M and  $1.173 \times 10^{-8}$  M, respectively.

**Index Terms**— Electrochemical techniques, Polarography, Procaine hydrochloride, Voltammetry.

## I. INTRODUCTION

Procaine hydrochloride or (2-diethylaminoethyl 4-aminobenzoate hydrochloride) was synthesized for the 1<sup>st</sup> time in 1905, and it was the first injectable synthetic local anesthetic drug Fig. 1.

Procaine hydrochloride is a group of compounds that, at an appropriate concentration in the nerves reduce pain sensation from particular areas of the body by the reversible block of the impulse conduction throughout nerve axons and other excitable membranes in which use sodium channels

as the primary mean of action potential generation (Dutu, et al., 2014). It can also prevent cardiac ectopic pacing point autoregulation and dilate blood vessels, hence being adopted to cure ischemic cerebrovascular disease, hemiplegia, and acute renal failure (Zhu, Xu and Liu, 2021). This anesthetic drug is also given in combination with penicillin to treat bacterial infections. It is used as a substitute for cocaine because of its ease of production, sterilization, and the fact that it is non-psychoactive. Its length of activity is shorter than cocaine and it is considerably less toxic (Qader, et al., 2023). In spite of that, Excessive dosage of procaine hydrochloride may lead to central nervous system and cardiovascular reactions such as nausea, respiratory distress, and in severe cases, even anaphylaxis and death. Hence, it is vital to establish a simple, efficient and sensitive analytical method for the determination of procaine hydrochloride (Haroon, et al., 2021). There are many techniques used for determination of procaine among such as; UV-vis spectrophotometric methods (Khayoon, 2021, Marin, et al., 2019), polarography (Plotycya, et al., 2018), chemiluminescence (Golshani, et al., 2023), chromatography (Tonooka, et al., 2016), high-performance liquid chromatography (He, et al., 2013), and electrochemical methods (Guan, et al., 2016; Haghghian, Ghoreishi and Attaran, 2023). Voltammetric methods have easily met the needs in this field because they have been providing safe, accurate, sensitive and reproducible results for years (Altunkaynak, Yavuz and Levent, 2021).

Square wave voltammetry (SWV) is a set of matched amplitude pulses implemented under a staircase potential, in each forward pulse the chemical species diffuse to the electrode surface, and it is abruptly reduced or oxidized. During the backward pulse, the chemical species that was just oxidized or reduced returns to the initial state in a reversible reaction, or if the system is irreversible, no reaction will occur. Therefore, the current values are estimated before and at the end of each pulse, and the resulting or net current equals to reversed current minus forwarded current (Megale and Souza, 2023). While, the differential pulse polarography (DPP) the current is determined as a function of time and as a function of the potential between the reference and working electrodes (Alghamdi and Messali, 2018).

ARO-The Scientific Journal of Koya University  
Vol. XII, No. 2 (2024), Article ID: ARO.11659. 9 pages  
Doi: 10.14500/aro.11659

Received: 18 June 2024; Accepted: 18 September 2024  
Regular research paper: Published: 26 September 2024

<sup>†</sup>Corresponding author's e-mail: gulan.23scp77@student.uomosul.edu.iq  
Copyright © 2024 Gulan S. Qadir, Amer T. Al-Tae and Nabeel S. Othman. This is an open-access article distributed under the Creative Commons Attribution License (CC BY-NC-SA 4.0).



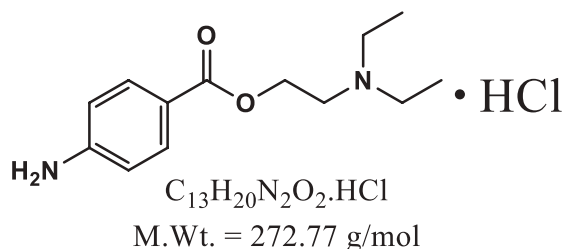


Fig. 1. Chemical structure of procaine hydrochloride.

Innovative electrochemical analysis instrumentation specifically techniques of voltammetry afford reliable and reproducible data for the assay of the analyte (Domergue, et al., 2023).

This study's intention is to evaluate procaine hydrochloride using electrochemical techniques such as SWV and DPP. The performance of the voltammetric techniques is strongly affected by the aspects of the working electrode material, such as the chemical and physical properties of electrode surfaces, applied potential, adsorption, and coatings applied to the electrode surface to enhance detection. Solid electrodes represent the most rapidly growing class of electrodes. In general, solid electrode materials have the advantage of being more mechanically stable, and they provide a larger anodic range than mercury-based electrodes. Furthermore, the handling of solid electrodes is much easier, such that they may readily be applied in flow streams due to their mechanical stability and hardness (Uslu and Ozkan, 2007). The method is simple, sensitive, and rapid.

## II. EXPERIMENTAL

### A. Apparatus

The measurements were carried out using a voltammetric analysis, model VA Computrace 797, equipped by the Swiss company Metrohm. In addition, the ultrasonic device was used which is of Chinese origin to dissolve solids and pharmaceutical preparations well and to clean the electrode surface using ultrasound waves. A sensitive balance of Japanese origin is also used and a device (Hanna) Model 211, Romanian origin is used to measure the pH.

### B. Chemicals and Materials

All chemicals used in this work were at a high degree of purity and were used without any further purification.  $1 \times 10^{-4}$  M of procaine hydrochloride (from Sigma-Aldrich), 1% w/v sodium nitrite solution (from BDH), hydrochloric acid (HCl), 0.2 M boric acid solution ( $H_3BO_3$ ), Phosphoric acid 0.2 M solution ( $H_3PO_4$ ), Acetic acid 0.2 M solution ( $CH_3COOH$ ), Britton-Robinson buffer (BRB) solution (pH 2.0), 250 ppm lead acetate [ $Pb(CH_3COO)_2 \cdot H_2O$ ].

### Preparation of pharmaceutical samples

For PenG (300,000 IU) injection powder

One ampoule of PenG is weighed totally (which contains 300,000 IU procaine hydrochloride). An aliquot quantity, that is equivalent to 0.1363 g of procaine hydrochloride, is dissolved in 50 mL of distilled water. An aliquot of the

diluted solution of the injection is analyzed employing the procedures outlined in methods SWV and DPP (Qader, et al., 2023).

For Deva (600,000 IU) injection powder

One ampoule of Deva is weighed totally (which contains 600,000 IU procaine hydrochloride). An aliquot quantity, equivalent to 0.1363 g of procaine hydrochloride, is dissolved in 50 mL of distilled water. An aliquot of the diluted solution of the injection is analyzed employing the procedures outlined in methods SWV and DPP (Qader, et al., 2023).

### C. Procedure and Working Steps in SWV

First, 8 mL of BRB is added to the electrochemical cell, and passing nitrogen gas for 5 min for deoxygenation, the applied voltage is  $-0.05$  to  $0.0$  volts. Then, 1.0 mL of 1% solution of sodium nitrite and 1.0 mL of 1 M hydrochloric acid under the same conditions are added, and nitrous acid is produced in the electrochemical cell instantaneously. To measure and determine the amount of procaine hydrochloride,  $5 \mu L$  of  $1 \times 10^{-3}$  M is added to the electrochemical cell, and all the data are collected under instrument conditions (Alallaf, Al-Tae and Othman, 2024).

### D. Procedure and Working Steps in DPP

10 mL of BRB was added to the electrochemical cell. Then, passing nitrogen gas for 5 min for deoxygenation, and a silver electrode was used as a WE. After that, 200  $\mu L$  of lead acetate was added, and optimization of the parameters was carried out. After completing the optimization, the procaine hydrochloride was added to the electrochemical cell, its interaction with lead acetate were observed and the decrease in reduction current of lead acetate was followed (Alhazmi et al., 2020).

## III. RESULTS AND DISCUSSION

### A. Principle of the Proposed Method SWV

SWV offers an attractive alternative in which the participation of non-faradaic current could be minimized in the voltammogram. As an alternative to linearly sweeping the potential with a defined sweep rate, the potentials are applied as a waveform of specific pulse amplitude ( $E_{amp}$ ) and width ( $t_p$ ) in a staircase fashion, in the first cycle a positive  $E_{amp}$  is followed by an oppositely directed negative  $E_{amp}$  of equal magnitude, immediately after that a next cycle starting at an increased potential according to Estep value (Pilz and Kielb, 2023).

SWV method includes an indirect determination of procaine hydrochloride in its pure form and pharmaceutical preparations by following the reduction of diazotized procaine hydrochloride prepared simultaneously inside the electrochemical cell. Indirect methods provide higher sensitivity and selectivity than direct methods, with the sharper peak shape of the voltammogram (Jones, et al., 2018).

Salts of Diazonium are a large group of organic compounds with the general formula  $R-N_2^+X^-$ , that R can be alkyl or

aryl and X is an organic or inorganic anion such as halogen (Tavakkoli, et al., 2021).

The aryl diazonium grafting mechanism involves a reductive electron transfer to the diazonium salt, occurring concurrently with the removal of dinitrogen and the subsequent formation of aryl radicals. These radicals subsequently attach to the surface of the electrode. It is generally accepted that aryl diazonium molecules form a covalent carbon-carbon or metal-carbon bond on carbon-based materials and silver substrates, respectively (Mezour, et al., 2018).

The reaction occurs between the amine group and the nitrite, Scheme 1, as a first step to form the corresponding diazonium salt. The azo group in diazonium salt is reduced to the -NHOH group and it will further reduce to  $\text{NH}_2$  and give rise to a reduction current as a result of the procaine hydrochloride concentration added.

#### Study of the electrochemical behavior of procaine hydrochloride using SWV

The electrochemical behavior of procaine hydrochloride was studied using SWV, BRB solution (pH 2.0) by scanning the potential between  $-0.5$  to  $0.0$  volt, no peak has appeared within the studied range of the buffer solution, Fig. 2. Nitrous acid was produced in the electrochemical cell. To measure and determine the amount of procaine hydrochloride,  $5 \mu\text{L}$  of  $1 \times 10^{-3} \text{ M}$  was added to the electrochemical cell. The diazotized procaine hydrochloride gives a reduction peak which is appeared at  $0.06$  volts, Fig. 2, with the current value of the peak  $25.4 \mu\text{A}$ .

#### B. Optimization of Parameters in SWV

##### Effect of $\text{NaNO}_2$

To determine the optimal amount of sodium nitrite and hydrochloric acid that have effect on the formation of diazonium salt and voltammogram, different volumes of  $0.5$ – $3.0$  mL with a concentration of  $1\%$  were taken to a fixed amount of hydrochloric acid  $1.0$  mL. The voltammogram was

recorded for each volume and the current was measured as shown in the results of Fig. 3 It is noted that the amount of  $2$  mL of sodium nitrite gave the highest current so the ratio of  $\text{HCl}:\text{NaNO}_2$  is  $1:2$  whereas more than this ratio cause noise in voltammogram shape and gave rise to bubble gas  $\text{NO}$  liberated (Binnewies, et al., 2010).

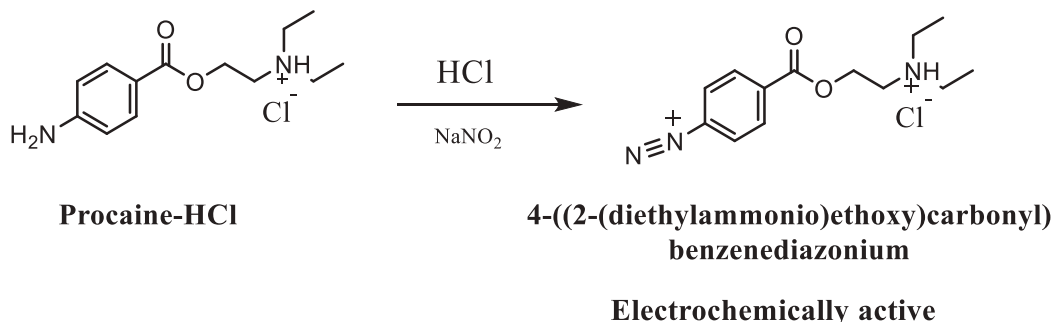
To enhance the shape and the reduction current of the peak that produced in Fig. 2, different parameters that affect the voltammogram shape and the reduction current value has been studied. The parameters under instrument condition and after optimized condition are listed in Table I. The square wave voltammogram of the blank solution and reduction of diazotized procaine hydrochloride measured after optimized condition Fig. 4.

#### Calibration curve of SWV

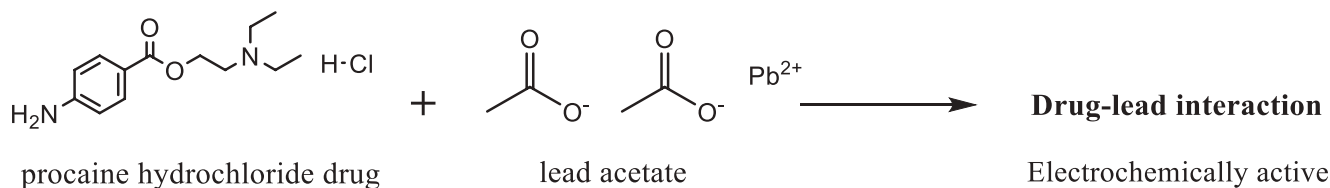
The SW-Voltammograms were recorded at  $E_p = -0.05\text{V}$  for sequence additions of procaine hydrochloride ( $1 \times 10^{-4} \text{ M}$ ) to the voltammetric cell containing  $1$  mL of  $1\text{M}$   $\text{HCl}$  and  $2$  mL of  $1\%$   $\text{NaNO}_2$ , under the fixed optimum conditions. A plot of  $I_p$  versus concentration of procaine hydrochloride added gives two straight lines, first at low concentration range ( $0.0999$ – $0.4997$ )  $\times 10^{-7} \text{ M}$  by a calibration equation  $Y = 48.125x + 3.0101$  and second, at high concentration range ( $0.9999$ – $5.996$ )  $\times 10^{-7} \text{ M}$ , (Fig. 5) by calibration equations  $Y = 4.3491x + 23.836$  with regression coefficient  $R^2 = 0.9842$  and  $0.9727$ , respectively.

#### C. Principle of the Proposed Method DPP

DPP is an effective and fast electroanalytical technique with many advantages, including low detection limits and good discrimination against background currents (Yilmaz, et al., 2015). The proposed method was based on the principle of drug–metal ion interaction, where the ionizable moieties of the drug molecules complexed with certain metal ions. As a result of their complexation, the reduction current was changed. Procaine hydrochloride interacts with  $\text{Pb}^{2+}$  ion to produce procaine-Pb complex (Alhazmi, et al., 2020). So, in this method



Scheme 1. Proposed reaction mechanism of reduction of diazonium ion (Alallaf, Al-Tae, and Othman, 2024).



Scheme 2. Proposed reaction of the interaction of procaine hydrochloride with  $\text{Pb}^{2+}$  in DPP.

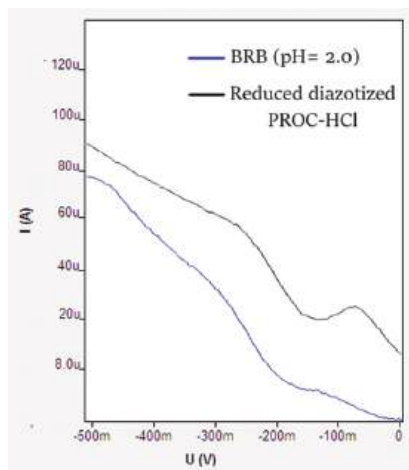


Fig. 2. Square wave voltammogram of reduced diazotized procaine HCl under instrument condition.

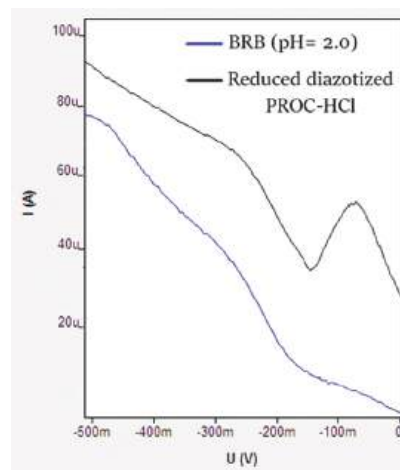


Fig. 4. Square wave voltammogram of reduced diazotized procaine HCl after optimum condition.

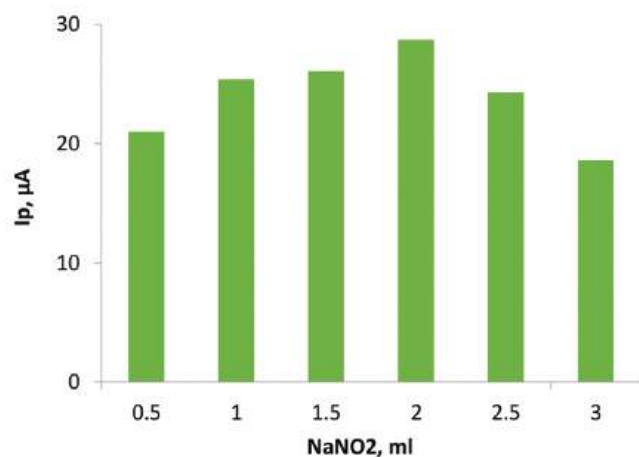


Fig. 3. Effect of amount of sodium nitrite.

procaine hydrochloride is determined indirectly. Scheme 2 shows the proposed interaction of the drug with  $Pb^{2+}$ .

*Study of the electrochemical behavior of lead acetate*

The applied voltage was  $-0.6$  to  $0.0$  V, no peak has appeared within the studied range of the buffer solution, see Fig. 6. Then,  $250 \mu\text{L}$  of  $250$  ppm lead acetate (electrochemical active) is added to the electrochemical cell, as a result, a peak appeared at a potential of  $-0.35$  V, with the current value of  $401 \mu\text{A}$ . The differential pulse voltammogram is recorded (Fig. 6) for the BRB solution ( $\text{pH} = 2$ ) and for the lead acetate under instrument condition.

*D. Optimization of Parameters in DPP*

The applied voltage was  $-0.6$  to  $0.0$  V, no peak has appeared within the studied range of the buffer solution, Fig. 7.  $250 \mu\text{L}$  of  $250$  ppm lead acetate (electrochemical active) is added to the electrochemical cell, as a result, a peak appeared at a potential of  $-0.35$  V, with the current value of  $401 \mu\text{A}$ . The differential pulse voltammogram is recorded (Fig. 7) for the BRB solution ( $\text{pH} = 2$ ) and for the lead acetate under instrument and optimized conditions listed in Table II.

TABLE I  
STUDY OF THE OPTIMUM CONDITION APPLIED FOR REDUCTION OF DIAZONIUM ION AT PH 2

Parameters	Studied range	Instrument condition	Optimized condition
Start potential (V)	----	$-0.05$	$-0.05$
End potential (V)	----	$0.0$	$0.0$
Voltage step (V)	$0.0005-0.007$	$0.003$	$0.005$
Frequency (Hz)	$40-70$	$50$	$50$
Pulse amplitude (V)	$0.01-0.07$	$0.03$	$0.05$
Deposition potential (V)	$(-0.2)-(-0.6)$	$-0.4$	$-0.5$
Deposition time (s)	$10-60$	$60$	$40$
Equilibration time (s)	$1-5$	$5$	$3$
No. of cycles	$1-6$	$5$	$5$
Cleaning potential (V)	$0.0-0.3$	$-0.3$	$-0.1$
Cleaning time (s)	$0-5$	$5$	$3$
Sweep rate (V/s)	$0.025-0.3500$	$0.1500$	$0.2500$

TABLE II  
INITIAL CONDITIONS OF THE INSTRUMENT APPLIED FOR LEAD ACETATE PEAK

Parameters	Studied range	Instrument condition	Optimum condition
Start potential (V)	----	$-0.6$	$-0.6$
End potential (V)	----	$0.0$	$0.0$
Pulse amplitude (V)	$0.09-0.35$	$0.1$	$0.3$
Pulse time (s)	$0.003-0.04$	$0.01$	$0.005$
Voltage step (V)	$0.001-0.025$	$0.015$	$0.025$
Voltage time (s)	$0.2-0.4$	$0.4$	$0.4$
Deposition potential (V)	$(-0.3)-(-0.7)$	$-0.5$	$-0.4$
Deposition time (s)	$10-50$	$50$	$40$
Equilibration time (s)		$5$	$3$
No. of cycles	$1-7$	$5$	$5$
Cleaning potential (V)	$1-5$	$-0.1$	$-0.5$
Cleaning time (s)	$0-4$	$4$	$3$
Sweep rate (V/s)	$0.0250-0.0417$	$0.0375$	$0.0625$

During the optimization process, the complexation behavior of certain metal ions including  $Cd^{2+}$ ,  $Zn^{2+}$ ,  $Cu^{2+}$ , and  $Pb^{2+}$  with procaine hydrochloride was investigated. After remarkable efforts,  $Pb^{2+}$  was selected for the current analysis because  $Pb^{2+}$  exhibited superior binding interaction with procaine drug molecule, and intense sharp peak was

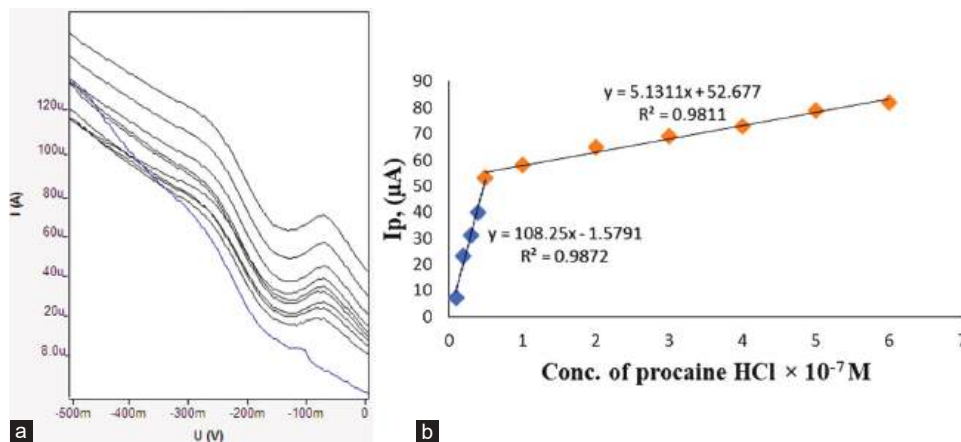


Fig. 5. (a) Voltammogram of serial addition of procaine hydrochloride, (b) Plot of calibration curve for evaluation of procaine HCl, in SWV technique.

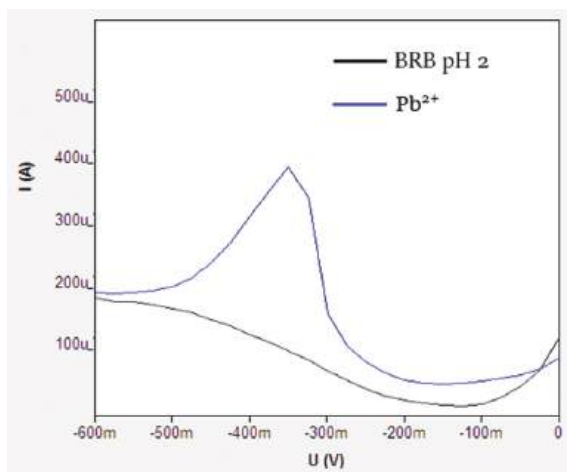


Fig. 6. Differential pulse voltammogram of the buffer and lead acetate ( $\text{Pb}^{2+}$ ) under instrument condition.

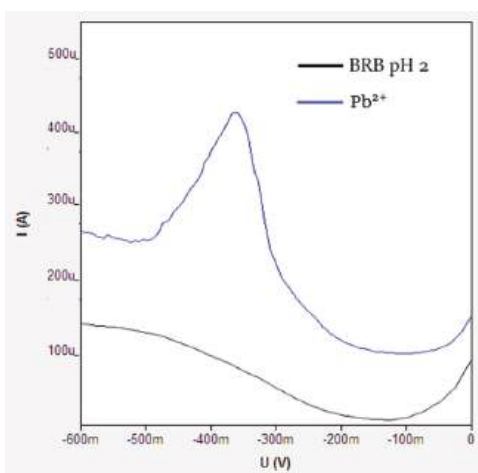


Fig. 7. Differential pulse voltammogram of the lead acetate ( $\text{Pb}^{2+}$ ) under optimum condition.

observed, while for other metal ions, no peak has observed that belong to the procaine-metal interaction. Lead ion has the least negative peak potential does not require greater range of deposition potential. The lead signal increased as the deposition potential became less negative, and vice versa (Van Staden and Matoetoe, 2000).

After completion of the studying optimization of the parameters, 10 mL of BRB (pH = 2) is added to the electrochemical cell. After ensuring no peak of the blank is observed 250  $\mu\text{L}$  of 250 ppm lead acetate is added. The enhanced shape of the lead acetate peak can be noticed in Fig. 7.

#### *Electrochemical behavior of procaine hydrochloride and procaine-Pb complex*

The electrochemical behavior of procaine hydrochloride was studied by adding 10 mL of BRB (pH = 2) in a glass cell as a supporting electrolyte. The voltammograms were recorded under the optimum conditions (Table II) for BRB and procaine hydrochloride as depicted in (Fig. 8a) one broad peak was observed ( $E_p = 1.21 \text{ V}$ ) for procaine hydrochloride. While, under the similar condition the voltammogram of procaine-Pb complex was recorded, in which a sharp and intense peak was observed at  $-0.4 \text{ V}$  for the complex (Fig. 8b).

The most interesting behavior was revealed for the procaine-Pb complex. DP-voltammograms showed higher current intensity and modified shapes for the reduction peak found approximately at  $-0.4 \text{ V}$ . In spite of the fact that the oxidation potential registered with free procaine shifted to lower values, the current intensity diminished, being comparable with that obtained with the complex. It was observed that the potentials of the peaks not only shifted, but that the shapes of peaks also changed, this may due to the high sensitivity of indirect methods over the direct methods.

#### *Calibration curve of DPP*

The DP-Voltammograms were recorded at  $E_p = -0.4 \text{ V}$  for sequence additions of procaine hydrochloride ( $1 \times 10^{-4} \text{ M}$ ) to the voltammetric cell containing 250  $\mu\text{L}$  of 250 ppm lead acetate, under the fixed optimum conditions. A plot of  $\Delta I_p$  versus concentration of procaine hydrochloride added gives two straight lines, first at low concentration range  $(0.0999-0.4997) \times 10^{-7} \text{ M}$  by a calibration equation  $Y = 205.14x + 3.5133$  and second, at high concentration range  $(0.9999-5.996) \times 10^{-7} \text{ M}$ , (Fig. 9) by calibration equations  $Y = 15.124x + 99.597$  with regression coefficient  $R^2 = 0.9964$  and  $0.9906$ , respectively.

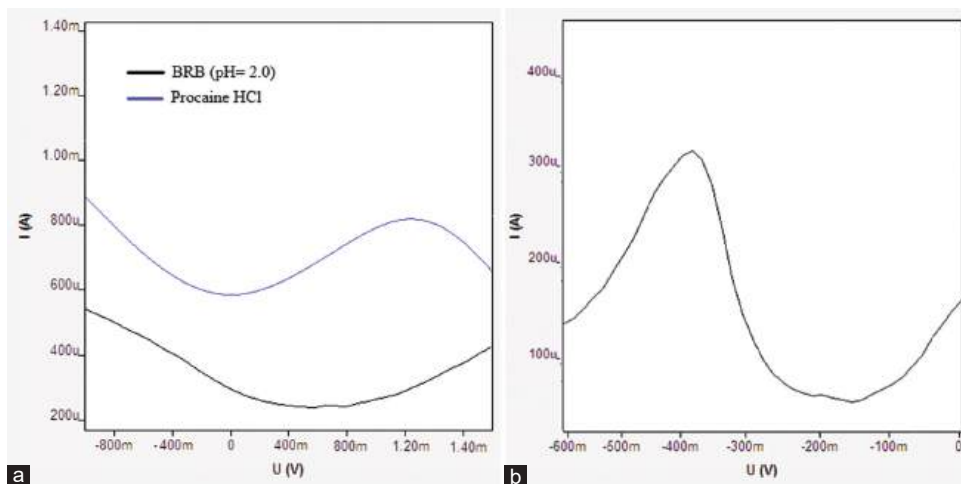


Fig. 8. Differential pulse voltammogram of (a) procaine HCl, (b) procaine-Pb complex.

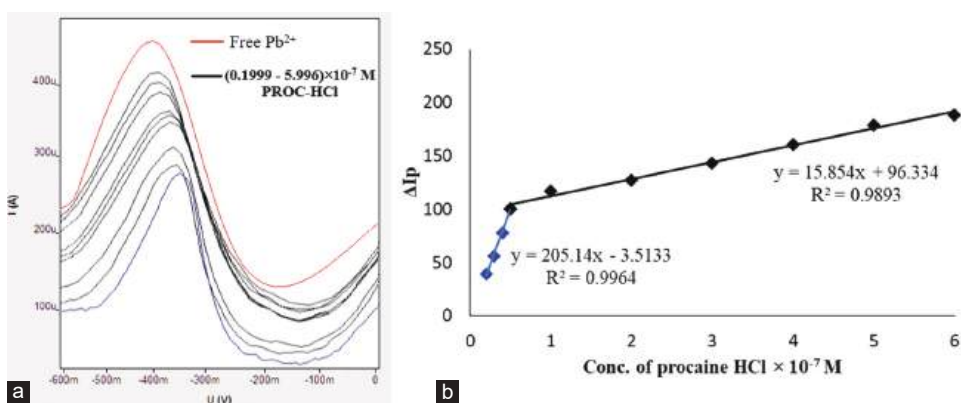


Fig. 9. (a) Voltammogram of serial addition of procaine hydrochloride, (b) Plot of calibration curve for evaluation of procaine HCl, in DPP technique.

*E. Analytical Figures of Merit*

The accuracy (recovery %), precisions (RSD), and the limits of detection (LOD), and quantitation (LOQ) of the two proposed methods in SWV and DPP techniques are assayed. The accuracy and precision of the proposed procedure in SWV were provided by measuring  $I_p$  of procaine HCl after formation of corresponding diazotized procaine of three different concentrations of standard procaine HCl  $(0.1999, 0.9999, 4.997) \times 10^{-7}$  M, while in DPP, measuring  $\Delta I_p$  of procaine-Pb complex after the interaction of procaine with lead acetate of three different concentrations of standard procaine HCl  $(0.1999, 1.999, 4.997) \times 10^{-7}$  M, individually in three replicate measurements. The values of recovery% and RSD% were between 97.49% and 99.74%, and 0.413–0.913%, respectively for SWV, while for DPP were 98.85–99.84%, and 0.523–0.951%, respectively. The results are shown in Tables III and IV, indicating that the proposed procedure is valid and applicative. The LOD and LOQ were  $(1.98433 \times 10^{-9})$  M,  $(6.61144 \times 10^{-9})$  M, respectively for SWV, while for DPP were  $(3.51923 \times 10^{-9})$  M, and  $(1.17307 \times 10^{-8})$  M, respectively. Remarkably lower LODs and LOQs for procaine HCl indicated that the proposed method was highly sensitive.

*F. Applications*

Both methods SWV and DPP were successfully applied to evaluate procaine hydrochloride in its pharmaceutical

TABLE III  
ANALYTICAL DATA AND OPTICAL CHARACTERISTICS OF THE PROPOSED METHODS SWV AND DPP

Parameters	Value	
	SWV	DPP
linear range (M)	$(0.0999-5.996) \times 10^{-7}$	$(0.1999-5.996) \times 10^{-7}$
LOD (M)	$1.98433 \times 10^{-9}$	$3.51923 \times 10^{-9}$
LOQ (M)	$6.61144 \times 10^{-9}$	$1.17307 \times 10^{-8}$
Recovery (%) range*	97.49–99.74	98.85–99.84
RSD%* range	0.413–0.913	0.523–0.951
$t_{exp}$ range	0.219–1.972	0.314–2.945
Determination coefficient ( $R^2$ )	0.9842, 0.9727	0.9964, 0.9894
Slope (a) <sup>#</sup>	48.125, 4.3491	205.14, 15.813
Intercept (b) <sup>#</sup>	3.0101, 23.836	3.5133, 96.384

\*Average of three determinations, <sup>#</sup>Regression equation ( $X=b+ac$ ), where c is procaine in M at low and high concentrations. LOQ: Limit of quantification

formulation (injection). The applicability of the proposed procedure for the analysis of procaine HCl in pharmaceutical formulations was examined by investigating two pharmaceutical injections (PenG, 300000 IU, 295 mg) and (Deva, 600000 IU, 590 mg) at three different concentrations  $(0.1999, 0.9999, 4.997) \times 10^{-7}$  M (SWV) and  $(0.1999, 1.999, 4.997) \times 10^{-7}$  M (DPP) of procaine hydrochloride. The results are shown in Table IV.

The performance of the proposed procedure was referred by calculating the experimental t-values. At a95% confidence

level, the calculated t-values did not overstep the theoretical values as noticeable from Table IV. Consequently, it was concluded that there is no significant difference between the proposed methods and the standard method. Moreover, the electrochemical methods for the determination of procaine HCl in pharmaceutical injection addressed in this work are simple, fast, inexpensive, precise, and accurate and they may be suitable for routine analysis and quality control laboratories.

#### Evolution of the proposed methods

The standard addition method was applied for the estimation of procaine hydrochloride in pharmaceutical products. In SWV two different concentrations  $0.999 \times 10^{-7}$  and  $1.999 \times 10^{-7}$  M of the pharmaceutical form (injection) of procaine hydrochloride were added to the voltammetric cell that contained BRB, 1 mL HCl, 2 mL  $\text{NaNO}_2$ , while for DPP  $0.1999 \times 10^{-7}$  and  $0.2999 \times 10^{-7}$  M of the pharmaceutical form (injection) of procaine hydrochloride were added to the voltammetric cell that contained BRB and lead acetate. In each case, a varying amount of standard procaine hydrochloride with a range of 0–5  $\mu\text{L}$  of  $1 \times 10^{-4}$  M was added and measured under the optimum instrument conditions that mentioned before. The results listed in Table V and shown in Fig. 10.

At present, unstable power grid accidents happen frequently; out of these, accidents caused by voltage

instability take up a great part, so research on voltage stability is imperative. Voltage instability may occur when the system voltage is either normal or abnormal, and it is more likely to occur after suffering disturbances in the system (Meng and Pian, 2016). The exact preparation of the pharmaceutical sample might have effect on recovery, these involved minor difference between the amount taken and found from the proposed methods. During the experimental procedure, the slight difference had no impact on the peak current strength, signifying the reliability of the applied method during the regular procedure. The good recovery implied the high selectivity, and efficiency of the method. Indicate that there is a high agreement between the standard addition method and the proposed methods (SWV and DPP) for the determination of procaine hydrochloride in its pharmaceutical preparations (injection).

#### G. Comparison of the Proposed Methods with other Electrochemical Methods

In the literature, procaine hydrochloride was quantified using different electrochemical techniques and working electrodes whether modified or unmodified. A number of analytical variables of the proposed methods were compared with the same variables of two other electrochemical methods and shown in Table VI.

TABLE IV  
ANALYSIS OF PROCAINE HCL IN PHARMACEUTICALS PREPARATIONS FOR METHODS SWV AND DPP

Drug	Certified Value (mg)	Method (A) SWV			Method (B) DPP		
		Found ( $\times 10^{-7}$ M)	Rec. (%) $\pm$ RSD* $t_{\text{exp}}$	Measured value (mg)	Found $\times 10^{-7}$ (M)	Rec. (%) $\pm$ RSD* $t_{\text{exp}}$	Measured value (mg)
PenG injection (Iran)	295	0.1949	97.49 $\pm$ 0.526 $t_{\text{exp}} = 1.972$	287.59	0.1991	99.59 $\pm$ 0.708 $t_{\text{exp}} = 1.995$	293.79
	295	0.9974	99.74 $\pm$ 0.760 $t_{\text{exp}} = 0.219$	294.23	1.979	98.99 $\pm$ 0.523 $t_{\text{exp}} = 2.171$	292.02
	295	4.979	99.63 $\pm$ 0.865 $t_{\text{exp}} = 0.426$	293.91	4.989	99.84 $\pm$ 0.764 $t_{\text{exp}} = 0.314$	294.52
Deva injection (Turkey)	590	0.1988	99.44 $\pm$ 0.913 $t_{\text{exp}} = 0.329$	586.69	0.1976	98.85 $\pm$ 0.872 $t_{\text{exp}} = 1.182$	583.21
	590	0.9866	98.66 $\pm$ 0.413 $t_{\text{exp}} = 1.923$	582588.09	1.992	99.65 $\pm$ 0.951 $t_{\text{exp}} = 0.438$	587.93
	590	4.984	99.74 $\pm$ 0.612 $t_{\text{exp}} = 1.224$	46	4.960	99.26 $\pm$ 0.743 $t_{\text{exp}} = 2.645$	585.63

\*Average of three determinations, \*\*Theoretical calculation of t at 95% confidence level (n=5) was 3.18, \*\*\*The values after the sign  $\pm$  are the relative standard deviation of the three replications of each sample

TABLE V  
THE RESULTS OF STANDARD ADDITION METHODS FOR ANALYSIS OF PROCAINE HYDROCHLORIDE IN ITS DRUGS

Drug	Certified value (mg)	Amount taken ( $\times 10^{-7}$ M)	Amount measured ( $\times 10^{-7}$ M)	Average of recovery (%)	Average of measured value (mg)
SWV					
PenG injection (Iran)	295	0.999	1.030	101.79	300.28
		1.999	2.004		
Deva injection (Turkey)	590	0.999	1.020	99.99	589.94
		1.999	1.957		
DPP					
PenG injection (Iran)	295	0.1999	0.2007	98.24	289.81
		0.2999	0.2882		
Deva injection (Turkey)	590	0.1999	0.1982	99.67	588.05
		0.2999	0.3005		



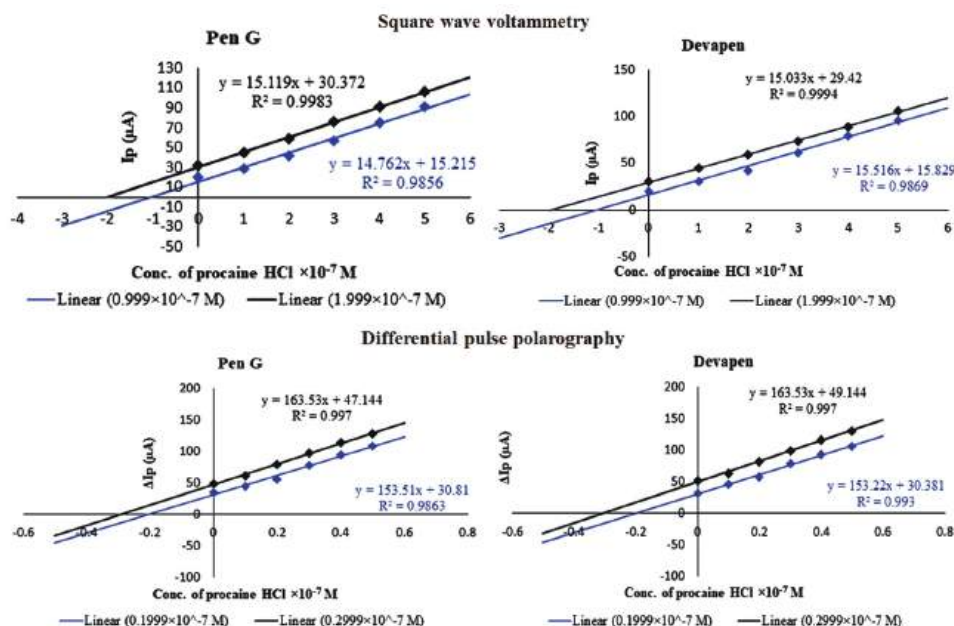


Fig. 10. Plot of standard addition method for determination of procaine HCl in pharmaceutical preparations using proposed methods SWV and DPP.

TABLE VI  
COMPARING A NUMBER OF VARIABLES OF THE PROPOSED METHOD WITH OTHER ELECTROCHEMICAL METHODS

Literature method	Literature method	Proposed method 2	Proposed method 1	Parameter
(Zhu, Xu and Liu, 2021)	(Silva, Salles and Paixão, 2015)			
Differential pulse voltammetry	Square wave voltammetry	Differential pulse polarography	Square wave voltammetry	Used technique
Molecular imprinting membrane/ diamond graphite surface	GCE/RuOHCF	Silver	Silver	Electrode
Phosphate Buffer/pH 7	NaNO <sub>3</sub> and HCl in deionized water	BRB/pH 2	BRB/pH 2	Supporting media
0.9	0	-0.4	-0.05	Ep (V)
4 × 10 <sup>-8</sup> –2.5 × 10 <sup>-5</sup>	(5–100) × 10 <sup>-6</sup>	(0.1999–5.996) × 10 <sup>-7</sup>	(0.0999–5.996) × 10 <sup>-7</sup>	Linearity (M)
1.5 × 10 <sup>-8</sup>	11 × 10 <sup>-9</sup>	3.5192 × 10 <sup>-9</sup>	1.9843 × 10 <sup>-9</sup>	LOD (M)
2.22–3.12	2.2–3.0	0.413–0.913	0.523–0.951	RSD %

LOD: Limit of detection

Based on the data shown in the Table above, the proposed methods are more sensitive than the other literature methods, have a better RSD% range compared to other methods, and can be applied for the determination of PROC-HCl at low concentrations. Despite that, some analytical methods have lower LOD values and wider linear range, but the proposed methods do not need pre-treatment of the sample besides the easy and short time of the analysis.

#### IV. CONCLUSION

The electrochemical estimation of procaine hydrochloride by SWV and DPP on the basis of reduction of diazotized procaine hydrochloride and interaction of procaine with lead ion, respectively, signifies a substantial and reliable analytical process. The proposed method has the expediency of simplicity and rapidity for the determination of procaine in both bulk and dosage forms (injection). The proposed methods offer high sensitivity, precision and accuracy for the quantification of procaine hydrochloride in pharmaceutical samples (injection). The sensitivity of method 1 (SWV) was

found to be greater than method 2 (DPP) with LOD value 1.9843 × 10<sup>-9</sup> M, and RSD% of method 1 was in a good range of 0.413–0.913%. The simplicity of the approach, linked with its cost-effectiveness and potential for automation, positions it as a critical tool for routine quality control analysis in the pharmaceutical sector.

#### ACKNOWLEDGMENTS

The authors intend to thank the University of Mosul, College of Science, Chemistry Department for offering up the necessary resources and facilities.

#### REFERENCES

- Alalaf, I.T., Al-Tae, A.T., and Othman, N.S., 2024. Indirect electrochemical determination of carvedilol through its interaction with nitrous acid. *Rafidain Journal of Science*, 33(2), pp.48-56.
- Alghamdi, A.F., and Messali, M., 2018. Green synthesis of new ionic liquid and its electrochemical determination at some detergents and cosmetics samples using differential pulse polarography. *Journal of Molecular Liquids*, 266, pp.112-117.

- Alhazmi, H.A., Nasib, A.A.B., Musleh, Y.A., Hijri, K.Q., Rehman, Z., Khuwaja, G., Al-Bratty, M., Javed, S.A., and Arbab, I.A., 2020. Application of drug–metal ion interaction principle in conductometric determination of imatinib, sorafenib, gefitinib and bosutinib. *Open Chemistry*, 18, pp.798-807.
- Altunkaynak, Y., Yavuz, Ö., and Levent, A., 2021. Firstly electrochemical examination of vildagliptin at disposable graphite sensor: Sensitive determination in drugs and human urine by square-wave voltammetry. *Microchemical Journal*, 170, p.106653.
- Binnewies, M., Finze, M., Schmidt, P., Willner, H., and Canham, G., 2010. *Allgemeine und Anorganische Chemie*. 3<sup>rd</sup> ed. Springer Spectrum, Heidelberg, pp.491.
- Domergue, L., Cimetière, N., Giraudet, S., and Hauchard, D., 2023. Determination of hydrogen peroxide by differential pulse polarography in advanced oxidation processes for water treatment. *Journal of Water Process Engineering*, 53, p.103707.
- Dutu, G., Tertis, M., Sandulescu, R., and Cristea, C., 2014. Differential pulse and square wave voltammetric methods for procaine hydrochloride determination using graphite based SPEs modified with p-tertbutyl-diester-calix[4]arene. *Revista de Chimie (Bucharest)*, 65(2), pp.142-147.
- Golshani, P., Iranifam, M., Al-Lawati, H.A.J., and Hassanpour-Khaneghah, M., 2023. FeS<sub>2</sub> nanosheets-H<sub>2</sub>O<sub>2</sub>-NaHCO<sub>3</sub> chemiluminescence method for procaine hydrochloride determination. *Luminescence*, 38, pp.421-427.
- Guan, X., Xinyi, L., Chai, Sh., Zhang, X., Zou, Q., and Zhang, J., 2016. A sensitive electrochemical sensor based on solution polymerized molecularly imprinted polymers for procaine detection. *Electroanalysis*, 28, pp.2007-2015.
- Haghighian, F., Ghoreishi, S.M., and Attaran, A., 2023. Electrochemical study for simultaneous detection of procaine hydrochloride and its metabolite in biological samples using a nanostructured strong sensor. *Korean Journal of Chemical Engineering*, 40, pp.650-656.
- Haroon, M., Abdulazeez, I., Saleh, T.A., and Al-Saadi, A.A., 2021. Electrochemically modulated SERS detection of procaine using FTO electrodes modified with silver-decorated carbon nanosphere. *Electrochimica Acta*, 387, p.138463.
- He, Y.T., Peng, J.D., Tang, J.X., and Zhang, C., 2013. Incorporation of high-performance liquid chromatography with resonance Rayleigh scattering detection for determination of procaine and lidocaine in human plasma. *Analytical Methods*, 5(24), pp.7110-7116.
- Jones, G.R.D., Haeckel, R., Loh, T.P., Sikaris, K., Streichert, T., Katayev, A., Barth, J.H., and Ozarda, Y., 2018. Indirect methods for reference interval determination-review and recommendations. *Clinical Chemistry and Laboratory Medicine*, 57(1), pp.20-29.
- Khayoon, W.S., 2021. Dispersive liquid-liquid microextraction (DLLME)-spectrophotometric determination of procaine hydrochloride in pharmaceutical preparations. *International Journal of Drug Delivery Technology*, 11, pp.722-727.
- Marin, N.M., Batrinescu, G., Nita-Lazar, M., Pascu, L.F., and Lehr, C.B., 2019. Simultaneous determination of procaine hydrochloride, procainamide hydrochloride and lidocaine by molecular absorption spectrometry. In: *International Symposium the Environmental and The Industry*, pp.318-324.
- Megale, J.D., and Souza, D.D., 2023. New approaches in antibiotics detection: The use of square wave voltammetry. *Journal of Pharmaceutical and Biomedical Analysis*, 234, p.115526.
- Meng, X., and Pian, Z., Eds., 2015. *Intelligent Coordinated Control of Complex Uncertain Systems for Power Distribution Network Reliability*. [e-book] Elsevier. Available from: <https://shop.elsevier.com/books> [Last accessed on 2015 Nov 12].
- Mezour, M.A., Oweis, Y., El-Hadad, A.A., Algizani, S., Tamimi, F., and Cerruti, M., 2018. Surface modification of CoCr alloys by electrochemical reduction of diazonium salts. *RSC Advances*, 8(41), pp.23191-23198.
- Pilz, F.H., and Kielb, P., 2023. Cyclic voltammetry, square wave voltammetry or electrochemical impedance spectroscopy? Interrogating electrochemical approaches for the determination of electron transfer rates of immobilized redox proteins. *BBA Advances*, 4, pp.1-10.
- Plotyca, S., Strontsitska, O., Pysarevska, S., Blazheyevskiy, M., and Dubenska, L., 2018. A new approach for the determination of benzocaine and procaine in pharmaceuticals by single-sweep polarography. *International Journal of Electrochemistry*, 2018, pp.3529-3537.
- Qader, I.B., Ismail, H.K., Alesary H.F., Kareem, J.H., Maarroof, Y.T., and Barton, S., 2023. Electrochemical sensor based on polypyrrole/triiron tetraoxide (PPY/Fe<sub>3</sub>O<sub>4</sub>) nanocomposite deposited from a deep eutectic solvent for voltammetric determination of procaine hydrochloride in pharmaceutical formulations. *Journal of Electroanalytical Chemistry*, 951, p.117943.
- Silva, T.G., Salles, M.O., and Paixão, T.R.L.C., 2015. Investigation of the use of glassy carbon electrode modified with ruthenium hexacyanoferrate for detection of procaine. *Química Nova*, 38(1), pp.85-90.
- Tavakkoli, Z., Goljani, H., Sepehrmansourie, H., Nematollahi, D., and Zolfigol, M.A., 2021. New insight into the electrochemical reduction of different aryldiazonium salts in aqueous solutions. *RSC Advances*, 11, pp.25811-25815.
- Tonooka, K., Naruki, N., Honma, K., Agei, K., Okutsu, M., Hosono, T., Kunisue, Y., Terada, M., Tomobe, K., and Shinozuka, T., 2016. Sensitive liquid chromatography/tandem mass spectrometry method for the simultaneous determination of nine local anesthetic drugs. *Forensic Science International*, 1(265), pp.182-185.
- Uslu, B., and Ozkan, S.A., 2007. Solid electrodes in electroanalytical chemistry: Present applications and prospects for high throughput screening of drug compounds. *Combinatorial Chemistry and High Throughput Screening*, 10(7), pp.495-513.
- Van Staden, J.F., and Matoetoe, M.C., 2000. Simultaneous determination of copper, lead, cadmium and zinc using differential pulse anodic stripping voltammetry in a flow system. *Analytica Chimica Acta*, 411, pp.201-207.
- Yilmaz, B., Kaban, S., Akcay, B.K., and Ciltas, U., 2015. Differential pulse voltammetric determination of diclofenac in pharmaceutical preparations and human serum. *Brazilian Journal of Pharmaceutical Sciences*, 51(2), pp.285-294.
- Zhu, Y., Xu, Y., and Liu, G., 2021. Electrochemical detection of the anesthetic drug procaine hydrochloride based on molecularly imprinted polymer/diamond-graphite composite electrode. *International Journal of Electrochemical Science*, 16, pp.1-12.

# Distributed Software-Defined Networking Management: An Overview and Open Challenges

Rawan S. Alsheikh<sup>1†</sup>, Etimad A. Fadel<sup>1</sup> and Nadine T. Akkari<sup>2</sup>

<sup>1</sup>Department of Computer Science, Faculty of Computing and Information Technology, King Abdulaziz University, Abdullah Sulayman, Jeddah 21589, Saudi Arabia.

<sup>2</sup>Department of Computer Science and Information Technology, Jeddah International College, Ibn Rasheed Elfehri, Jeddah 23831, Saudi Arabia.

**Abstract**—Distributed software-defined networking (SDN) architecture satisfies the minimum requirements for wide-area networks. The distributed controllers are connected in various topologies, including hierarchical and flat, which include logically centralized physically distributed, and fully distributed controllers. The distributed SDN architectures are qualitatively explored as a more suitable solution for managing fluctuating networks in large-scale deployments, with the goal of optimizing overall network performance, particularly for applications that can tolerate some level of inconsistency, such as load balancing or routing. The logically centralized physically distributed SDN controller architecture allows SDN controllers, in conjunction with the deployed SDN applications, to centrally coordinate the network due to the conciliated global network view. That is created through the synchronization process between controllers. However, inter-controller synchronization creates an overhead that affects the system's performance. In addition, the amount of inter-controller synchronization is vulnerable to the chosen consistency approach the application can tolerate. Although static eventual consistency is frequently employed in modern SDN systems to provide effective scalability, it is argued that it does not place limits on the state inconsistencies that SDN applications will tolerate. Hence, the adaptive consistency models need to be investigated. The study showed that a flat, logically centralized physically distributed architecture with an adaptive consistency approach would be more suitable for solving large-scale fluctuating network management considering scalability, reliability, and maximizing performance.

**Index Terms** –Adaptive consistency, Distributed SDN architecture, Large-scale networks, Logically centralized physically distributed controllers, Network performance optimization

## I. INTRODUCTION

Software-defined networking (SDN) is an evolving strategy that separates the network control plane from the data plane. SDN

operates across three layers: Application Layer (Management Plane), Control Layer (Control Plane), and Infrastructure Layer (Data Plane). Fig. 1 shows these interactions (Akyildiz, 2014), (Keshari, Kansal and Kumar, 2021).

SDN control plane architecture can be centralized (Fig. 1) or distributed (Fig. 2). This paper focuses on large-scale wide-area networks (WANs) with key scalability, reliability, and performance requirements.

The single SDN controller, as in Fig. 1, has a single point of failure (SPOF) problem. Moreover, it is challenging for one controller to handle the whole network due to the diversity of network application needs and the growth of network size. Getting the network view was difficult after that. These encourage network designers to consider including multi-controller architectures (Yu, Qi and Li, 2020), (Almadani, Beg and Mahmoud, 2021), (Aslan and Matrawy, 2016), (Blial, Ben Mamoun and Benaini, 2016), (Ahmad and Mir, 2021), (Oktian, et al., 2017), (Tadros, Mokhtar and Rizk, 2019).

In distributed SDN architectures, the data layer is divided into multiple domains, each managed by a controller. These controllers communicate through East/West-bound interfaces to exchange inter-domain information, allowing the deployment and configuration of SDN applications on large-scale networks (Ahmad and Mir, 2021), (Chen, et al., 2017), (Hoang, et al., 2022).

Distributed controllers are connected in various topologies, including hierarchical and flat, which include logically centralized physically distributed, and fully distributed controllers (Blial, Ben Mamoun and Benaini, 2016) (Espinell Sarmiento, et al., 2021). Each architecture has strengths and weaknesses. This paper qualitatively compares distributed SDN architectures and seeks to identify the most efficient SDN architecture for managing large-scale networks, balancing consistency, scalability, and performance.

Hierarchical architectures (e.g., Kandoo [Hassas Yeganeh and Ganjali, 2012] and B4 [Jain, et al., 2013]) feature a root controller with a global network view, whereas local controllers manage only their domains. Although easier to manage, this approach introduces latency due to cross-domain communication through the root controller, leading to performance degradation (Blial, Ben Mamoun and

ARO-The Scientific Journal of Koya University  
Vol. XII, No. 2 (2024), Article ID: ARO.11468. 166 pages  
Doi: 10.14500/aro.11468

Received: 09 November 2023; Accepted: 19 September 2024  
Regular review paper; Published: 30 September 2024

<sup>†</sup>Corresponding author's e-mail: rsalshaikh@kau.edu.sa  
Copyright © 2024 Rawan S. Alsheikh, Etimad A. Fadel and Nadine T. Akkari. This is an open-access article distributed under the Creative Commons Attribution License (CC BY-NC-SA 4.0).



Benaini, 2016), (Ahmad and Mir, 2021), (Oktian, et al., 2017), (Espinel Sarmiento, et al., 2021).

Flat architectures with logically centralized but physically distributed controllers (e.g., HyperFlow [Tootoonchian and Ganjali, 2010], Onix [Koponen, et al., 2010], ONOS [Open Network Operating System (ONOS) SDN Controller for SDN/NFV Solutions, no date], ElstiCon [Dixi, et al., 2014], and Orion [Ferguson, et al., 2021]). Allow each controller to manage intra- and inter-site operations, forming a global network view through synchronization (Blial, Ben Mamoun and Benaini, 2016), (Espinel Sarmiento, et al., 2021). However, synchronization can create overhead, affecting performance (Ahmad and Mir, 2021). Balancing consistency and performance remains a challenge.

Flat architectures with fully distributed controllers (such as DISCO [Phemius, Bouet and Leguay, 2014] or ODL [Home - OpenDaylight, no date]) operate with reduced inter-

controller communication, prioritizing local optimization over global interests (Blial, Ben Mamoun and Benaini, 2016), (Espinel Sarmiento, et al., 2021), (Bannour, Souihi and Mellouk, 2018b), (Informatique and Informatique, 2021).

A logically centralized, physically distributed approach is preferable for administering large-scale solutions. This enables any application within the cluster to access and manage the global network view (Tadros, Mokhtar and Rizk, 2019), (Espinel Sarmiento, et al., 2021). However, inter-controller communication costs remain a significant challenge, which does not receive as much concern in the research community (Blial, Ben Mamoun and Benaini, 2016), (Alowa and Fevens, 2020), (Espinel Sarmiento, et al., 2021).

Tradeoffs between strong and eventual consistency models impact network performance: strong consistency ensures accurate data but introduces synchronization overhead, whereas eventual consistency offers reduced overhead with temporary data inconsistencies. This paper explores adaptive consistency, which dynamically balances these tradeoffs to optimize performance in large-scale SDN networks (Aslan and Matrawy, 2016), (Ahmad and Mir, 2021), (Levin, et al., 2012), (Foerster, Schmid and Vissicchio, 2019), (Bannour, Souihi and Mellouk, 2018a).

This work's contributions are as follows:

- We analyze the key challenges distributed SDN architectures face, particularly focusing on scalability, reliability, consistency, and synchronization overhead in large-scale networks to determine the most effective architecture for network administration
- We provide a qualitative comparison of hierarchical, flat, and logically centralized physically distributed SDN architectures, highlighting their strengths and weaknesses in managing large-scale fluctuating networks. Based on this analysis, we suggest that a logically centralized, physically distributed architecture is most suitable for network administration

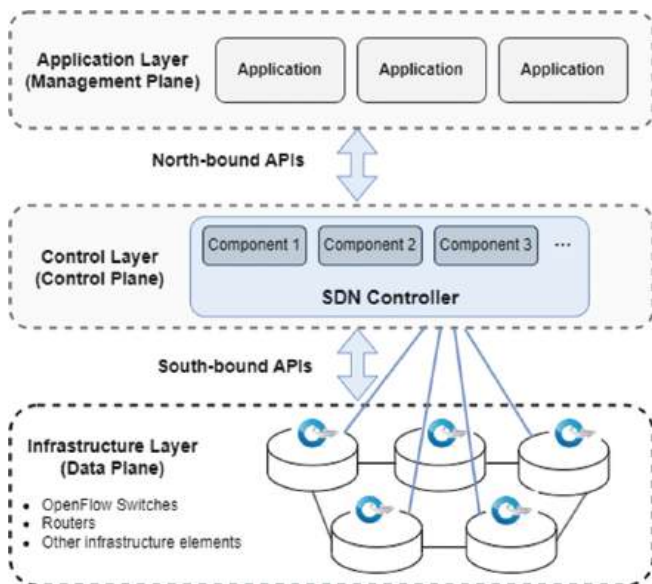


Fig. 1. Overview of software-defined networking architecture.

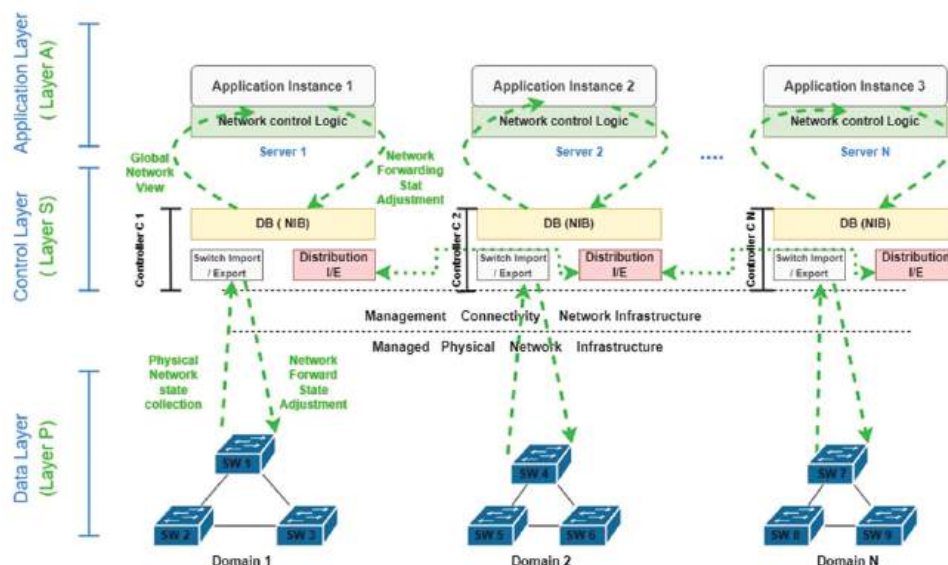


Fig. 2. Distributed software-defined networking architecture with network state distribution.

- We evaluate strong, eventual, and adaptive consistency models in the context of SDN, emphasizing their impact on network performance, scalability, and application requirements
- We propose using an adaptive consistency model for logically centralized, physically distributed SDN architectures. This approach aims to solve the synchronization overhead problem, which introduces latency and degrades performance. By employing dynamic consistency, the synchronization process can adapt to network conditions, reducing overhead whereas maintaining system performance, particularly for applications that can tolerate some inconsistency.

The rest of this paper is structured as follows: Section 2 discusses the Architecture and Components of Distributed SDN. Distributed SDN architecture challenges are discussed in section 3. Section 4 presents Distributed SDN Topologies and Qualitative Evaluation. Section 5 focuses on Network State Consistency. Section 6 discusses Distributed SDN: Future Directions. The study is concluded in section 7.

## II. THE ARCHITECTURE AND COMPONENTS OF DISTRIBUTED SDN

Understanding how distributed SDN architecture is designed and operates is crucial. Fig. 2 presents a distributed SDN system consisting of three main layers: the Application Layer (Layer A), the Control Layer (Layer S), and the Data Layer (Layer P). This layered structure resembles the Onix SDN control systems (Koponen, et al., 2010) and the work on (Levin, et al., 2012). The architecture consists of five essential components: Data layer, connectivity infrastructure, instances of the distributed control plane, control logic, and database. The green dashed and dotted arrows in Fig. 2 illustrate the points where network states are exchanged across the system.

### A. Data Layer

Network switches and routers are illustrated as blue boxes at the lowest layer in Fig. 2. These forwarding devices retain the network data plane state in the Forwarding Information Base and associated metadata such as flow ports and packet counters. These devices run the software necessary to support interfaces, such as OpenFlow, enabling controllers to read and modify the network state by updating forwarding table entries. A controller's domain includes all switches and hosts directly connected to it (Oktian, et al., 2017), (Koponen, et al., 2010), (Levin, et al., 2012).

### B. Connectivity

The connectivity framework supports bidirectional communication, depicted by the green dotted arrows in Fig. 2 for interactions between control plane instances, and by the green dashed arrows for communication between switches and control plane instances. It facilitates convergence during link failures and employs standard protocols, such as OSPF or IS-IS, to preserve the forwarding state (Koponen, et al., 2010).

The East-bound interface (red box in Fig. 2) allows SDN controllers to exchange information, whereas a West-bound interface can connect SDN controllers with legacy systems (Ahmad and Mir, 2021), (Hoang, et al., 2022).

Controllers can interconnect vertically (hierarchical) or horizontally (flat). However, intercontroller communication costs remain a significant challenge in distributed SDN environments (Blial, Ben Mamoun and Benaini, 2016), (Espinel Sarmiento, et al., 2021), (Alowa and Fevens, 2020).

### C. Distributed Control Plane Instances

The control plane operates as a distributed system, with each instance functioning as a network operating system (NOS) (Koponen, et al., 2010), (Levin, et al., 2012). Controllers oversee the management of the network state (Layer S) and provide programmatic interfaces for accessing and modifying control logic. Control plane instances collaborate within the cluster through distribution I/E, enabling SDN applications (Layer A) to interact with a simplified, abstract representation of the physical network (Koponen, et al., 2010), (Levin, et al., 2012). Each controller maintains a Network Information Base (NIB) housed in a database (yellow box in Fig. 2) (Levin, et al., 2012).

### D. Control Logic

The control logic, represented by the green box in Fig. 2, operates on the controller's API. It uses network state information to determine the intended network behavior (Koponen, et al., 2010), (Levin, et al., 2012).

### E. Database

The database management system (yellow box in Fig. 2) is crucial for the distributed control plane, storing intra- and inter-domain information for each controller. It could be utilized as a method of information sharing between controllers, obviating the necessity for a specific communication protocol. SDN solutions use either SQL or NoSQL databases (Espinel Sarmiento, et al., 2021).

A distributed database architecture facilitates the scalability of the control plane and enhances its ability to manage system failures efficiently (Koponen, et al., 2010).

## III. DISTRIBUTED SDN ARCHITECTURE CHALLENGES

While the SDN project has the potential to revolutionize and improve networks, it is still in its early phases of tackling a wide range of difficulties (Fig. 3), including scalability, reliability, consistency and synchronization overhead, interoperability, East–West interface implementations, and security (Informatique and Informatique, 2021), (Hussein, et al., 2018).

Although reliability and scalability are thought to be the two key drawbacks of centralized SDN control architectures, they are equally significant considerations when creating a physically distributed SDN architecture (Informatique and Informatique, 2021), (Hussein, et al., 2018), and (TS, 2019). This paper will address key issues such as interoperability



Fig. 3. The main challenges of physically distributed software-defined networking control.

and security; however, the primary focus will be on the challenges related to the consistency and synchronization overhead.

#### A. Consistency and Synchronization Overhead

In a physically distributed architecture, consistency necessitates preserving an up-to-date network-wide perspective (Ahmad and Mir, 2021). Consistency management is achieved through an inter-controller synchronization process, which ensures that the network view is aligned across all controllers (Oktian, et al., 2017).

Addressing consistency challenges whereas considering trade-offs in SDN controller platforms is vital. Achieving consistency necessitates a synchronization process, which can impose significant overhead on the system. While lower consistency levels reduce synchronization overhead, they increase the risk of state conflicts. On the other hand, strict consistency enforces more frequent synchronization, leading to higher overhead in the control plane (Sakic, et al., 2017). This overhead increases latency and impacts the system's scalability. Latency, often referred to as responsiveness, is the time the system requires to respond to flow requests (Tadros, Mokhtar and Rizk, 2019), (Hoang, et al., 2022), (Espinel Sarmiento, et al., 2021), (Informatique and Informatique, 2021), (Levin, et al., 2012), (Akyildiz, 2014).

#### B. Interoperability

Interoperability among SDN controllers is essential for the effective operation of distributed controller systems. Another significant operational problem related to SDN's maturity, growth, and commercial usage is the compatibility across various SDN controller systems from various suppliers (Yu, Qi and Li, 2020), (Informatique and Informatique, 2021).

The fact that each SDN controller has its own communication method makes it extremely challenging for SDN networks to communicate information between various domains (Yu, Qi and Li, 2020).

However, contrary to the wide acceptance of the standardization of OpenFlow's southbound interface, the

research community has not given the East–Westbound interface the required attention to provide interoperability and synchronization among SDN controllers. This is driven by the fact that there is no need for SDN network compatibility because the transition from the traditional network to SDN is still just a minor one. However, as SDN continues to demonstrate its benefits, The need for standard East-West protocol is essential to the internet's existence in the near future (Hoang, et al., 2022).

#### C. Security

Another significant issue that needs to be researched is SDN security. The integrity of data flows between SDN controllers and switches is still not guaranteed (Informatique and Informatique, 2021). In addition, authentication procedures are urgently needed in distributed control architecture to validate and verify controller instances (Ahmad and Mir, 2021). This paper does not consider security issues, as the focus is primarily on applications that can tolerate a certain level of inconsistency, such as load-balancing or routing applications.

### IV. DISTRIBUTED SDN TOPOLOGIES AND QUALITATIVE EVALUATION

Several research studies, such as Yu, Qi and Li, 2020, Hoang, et al., 2022, Espinel Sarmiento, et al., 2021), and Informatique and Informatique, 2021, have introduced a thorough evaluation of cutting-edge distributed SDN controller platforms.

Several topologies, such as hierarchical or flat, are used for distributed controller interconnection. The flat architecture can be logically centralized physically distributed, or fully distributed (Ahmad and Mir, 2021), (Espinel Sarmiento, et al., 2021). Logical classification in our research was adopted by (Espinel Sarmiento, et al., 2021), (Bannour, Souihi and Mellouk, 2018b), (Informatique and Informatique, 2021).

Fig. 4 illustrates some differences between these SDN distributed architectures and how each architecture preserves the network state. It distinguishes between local (domain-specific) and global (network-wide) states. The local state reflects the current network status within a controller's domain, tracking events such as host connections and link changes. In contrast, the global state represents the overall network status across all domains (Oktian, et al., 2017).

Each topology affects key issues in distributed SDN controllers, such as scalability, reliability, latency, consistency, and synchronization overhead (Keshari, Kansal and Kumar, 2021), (Ahmad and Mir, 2021), (Oktian, et al., 2017), (Bannour, Souihi and Mellouk, 2018b), (Hu, Li and Huang, 2014). Table I summarizes the characteristics of hierarchical, flat logically centralized, and flat fully distributed topologies based on these factors.

#### A. Hierarchical

The hierarchical architecture, such as Kandoo (Hassas Yeganeh and Ganjali, 2012) and B4 (Jain, et al., 2013),

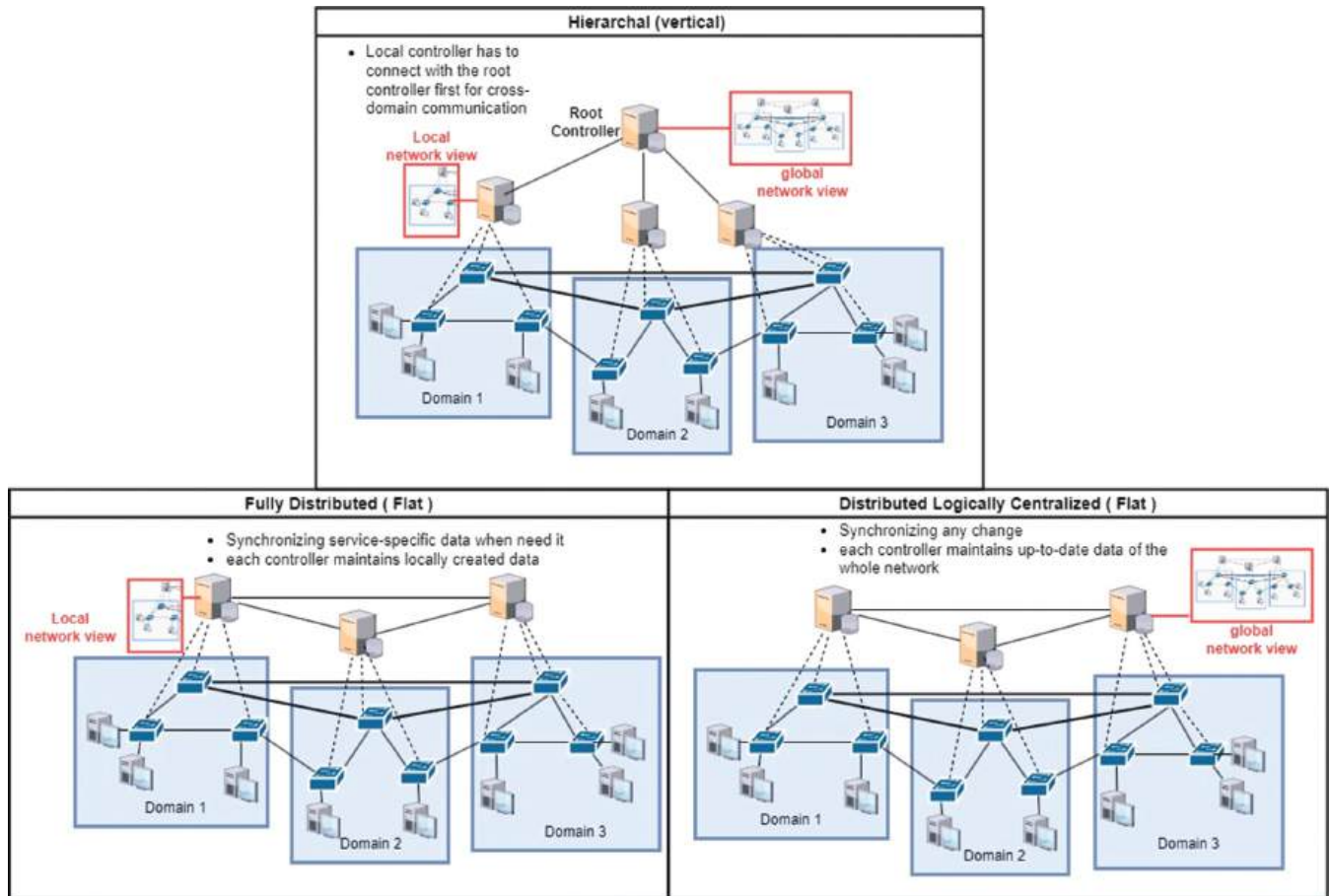


Fig. 4. Distributed software-defined networking topologies.

TABLE I  
DISTRIBUTED SDN TOPOLOGY CHARACTERISTICS

Distributed Controller Topology	Controller-to-Controller connectivity model	Scalability	Robustness (reliability)	Latency	Managing consistency	Synchronization Overhead	Real case scenarios
Hierarchical	Vertical	High	Low (root controller SPOF)	High	Centralized in the root controller	Medium	Kandoo (Hassas Yeganeh and Ganjali, 2012) and B4 (Jain, <i>et al.</i> , 2013)
Logically Centralized Physically Distributed	Horizontal (Flat)	Medium	High	Medium (depends on the technical execution of the solution)	By synchronization and creating a global view	High/Medium (depending on the chosen consistency model)	Elasticon (Dixi, <i>et al.</i> , 2014), HyperFlow (Tootoonchian and Ganjali, 2010), Orion (Ferguson, <i>et al.</i> , 2021), DragonFlow (OpenStack Docs: Distributed Dragonflow, no date), Onix (Koponen, <i>et al.</i> , 2010), and ONOS (Open Network Operating System (ONOS) SDN Controller for SDN/NFV Solutions, no date)
Fully Distributed	Horizontal (Flat)	Very High	Very High	Low	Manage consistency at the application level	Low (shares with other instances when necessary).	DISCO (Phemius, Bouet and Leguay, 2014) and ODL (Home - OpenDaylight, no date)

organizes controllers in a vertical arrangement, with the root controller positioned at the top. This root controller manages the global network state, whereas local controllers are responsible for handling their specific domains. The root controller ensures network-wide connectivity by overseeing

subordinate controllers (Blial, Ben Mamoun and Benaini, 2016), (Ahmad and Mir, 2021), (Oktian, et al., 2017), (Espinel Sarmiento, et al., 2021).

While this method improves scalability over centralized systems, robustness remains limited due to the root controller

being a SPOF (Blial, Ben Mamoun and Benaini, 2016), (Ahmad and Mir, 2021), (Espinel Sarmiento, et al., 2021), (Informatique and Informatique, 2021).

Replicating the root controller across multiple controllers can reduce SPOF risk, but having too many root controllers can complicate coordination and reduce network efficiency (Oktian, et al., 2017), (Espinel Sarmiento, et al., 2021).

There are no East/West-bound API connections between the local SDN controllers in the cluster. Instead, they communicate solely with the root controller. This dependency for cross-domain communication introduces latency and performance degradation (Ahmad and Mir, 2021), (Oktian, et al., 2017), (Espinel Sarmiento, et al., 2021).

### *B. Flat*

In flat architectures, controllers are arranged horizontally, each managing part of the network, whereas simultaneously carrying out the same responsibilities (Blial, Ben Mamoun and Benaini, 2016), (Ahmad and Mir, 2021).

To tackle consistency, flat systems can use either leader-based or leaderless coordination. In leader-based systems (e.g., Onix [Koponen, et al., 2010], ONOS [Open Network Operating System (ONOS) SDN Controller for SDN/NFV Solutions, no date], and ElstiCon [Dixi, et al., 2014]), a cluster elects a leader to manage communication (Oktian, et al., 2017). Leaderless systems (e.g., HyperFlow [Tootoonchian and Ganjali, 2010] or DISCO [Phemius, Bouet and Leguay, 2014]), allow controllers to communicate directly, sharing equal roles (Oktian, et al., 2017).

Flat architectures enhance failure resilience and performance but complicate consistency management (Blial, Ben Mamoun and Benaini, 2016), (Informatique and Informatique, 2021).

When a horizontal interface is used, it means that in addition to the time needed for the system to reply to a user request locally (such as CPU, memory, and thread utilization), the time required to synchronize with remote sites and provide a final response must also be taken into account. The synchronization process will create a synchronization overhead affecting the system's performance. The technical execution of the solution may cause this latency and will affect the total time required to provide an inter-site service, which affects the system responsiveness (Ahmad and Mir, 2021), (Oktian, et al., 2017), (Espinel Sarmiento, et al., 2021).

The Flat architecture can be logically centralized physically distributed, or fully distributed (Blial, Ben Mamoun and Benaini, 2016), (Espinel Sarmiento, et al., 2021), (as per Fig. 3). Both topologies will be explained in the following subtitles.

#### *Logically centralized physically distributed*

In this architecture, each site has one controller responsible for intra- and inter-site operations, as seen in systems such as, HyperFlow (Tootoonchian and Ganjali, 2010), Onix (Koponen, et al., 2010), ONOS (Open Network Operating System (ONOS) SDN Controller for SDN/NFV Solutions, no date), ElstiCon (Dixi, et al., 2014), and Orion (Ferguson, et al., 2021). Whenever a controller creates or modifies a

network resource, it broadcasts any changes (e.g., device or link failure) to other controllers through synchronizations. In synchronization, each controller in many domains must share a portion of their local network state with other controllers to build a global network state. However, no standards dictate what information must be shared (Blial, Ben Mamoun and Benaini, 2016), (Oktian, et al., 2017), (Tadros, Mokhtar and Rizk, 2019), (Hoang, et al., 2022), (Alowa and Fevens, 2020), (Levin, et al., 2012).

Distributed hash tables, transactional databases, and partial quorum techniques (Saito and Shapiro, 2010) are a few examples of distributed, replicated storage formats that can be utilized to implement the NOS state distribution and management (Levin, et al., 2012), (Saito and Shapiro, 2010).

As shown in Fig. 3, a logically centralized physically distributed structure allows multiple controllers to share network information, functioning as a single controller. This design mirrors the original SDN proposal, enabling centralized network control logic whereas distributing responsibility across controllers. It allows management from a global network perspective, improving control in SDN environments (Blial, Ben Mamoun and Benaini, 2016), (Tadros, Mokhtar and Rizk, 2019), (Espinel Sarmiento, et al., 2021), (Bannour, Souihi and Mellouk, 2018b).

There are several ways to obtain network information from SDN controllers. First, is polling, where controllers periodically request updates, even if no changes have occurred. Second, the more efficient publish/subscribe method, where controllers only receive updates when changes happen (Oktian, et al., 2017). In addition, a shared distributed data store allows controllers to exchange states (Espinel Sarmiento, et al., 2021).

The shift toward logical centralization of control within the distributed SDN paradigm helps mitigate the complexity of distributed systems. In this context, incorporating a Knowledge Plane into the architecture can leverage various machine learning (ML) techniques, such as Deep Learning. Collecting network knowledge and then utilizing that knowledge to control and manage the network, exploiting the capabilities of SDN logically centralized control (Mestres, et al., 2017).

However, these systems' effectiveness depends on the capabilities provided by the database system. Even that some of them have specific database systems built for them such as ONOS (Open Network Operating System (ONOS) SDN Controller for SDN/NFV Solutions, no date) distributed controllers linked through Atomix system (Atomix, no date), they fall short of issues such as network partitioning (depending on the database system) or data locality awareness (Espinel Sarmiento, et al., 2021).

#### *Fully distributed*

In fully distributed architectures such as DISCO (Phemius, Bouet and Leguay, 2014), controllers are both physically and logically distributed. Each controller maintains a local network view and communicates with other controllers only when necessary to exchange service-specific data. This approach reduces communication overhead and alleviates



scalability limitations encountered in centralized designs (Blial, Ben Mamoun and Benaini, 2016), (Espinel Sarmiento, et al., 2021), (Informatique and Informatique, 2021), (Bannour, Souihi and Mellouk, 2018b).

Fully distributed architecture avoids the initial tendency of SDN by giving many controllers different roles throughout the network (Blial, Ben Mamoun and Benaini, 2016). This architecture suits multi-domain heterogeneous environments, especially WANs and overlay networks. It has the ability to function under multiple Autonomous Systems (ASes) operating under various administrative domains in large-scale networks such as the Internet (Bannour, Souihi and Mellouk, 2018b), (Informatique and Informatique, 2021).

In this architecture, intra-domain modules handle core functions such as network monitoring, whereas inter-domain modules manage communication between domain controllers using protocols such as Advanced Message Queuing Protocol or Representational State Transfer APIs for the East-West interface (Almadani, Beg and Mahmoud, 2021), (Ahmad and Mir, 2021), (Espinel Sarmiento, et al., 2021), (Bannour, Souihi and Mellouk, 2018b).

Fully distributed systems provide robustness against network disconnections, as failures affect only part of the infrastructure (Espinel Sarmiento, et al., 2021). Fully distributed solutions face drawbacks such as static division into independent entities, contrasting with David D. Clark's Knowledge Plane theory (Clark, et al., 2003), which advocates centralized management. In addition, network optimization is local, with entities following their own policies rather than serving the overall network's interests (Bannour, Souihi and Mellouk, 2018b), (Informatique and Informatique, 2021).

Fully distributed systems face challenges in dynamic environments, where conflict resolution and tasks such as dynamic IP assignment are more complex. Moreover, in fully distributed architectures, consistency is managed at the application level due to independent local databases. The East-West interface lacks built-in conflict resolution, requiring additional calls to handle conflicts. These solutions focus on read/write operations and database concurrency, which is beyond our scope (Espinel Sarmiento, et al., 2021).

The researchers (Hu, Li and Huang, 2014) evaluate the SDN controller's scalability in handling flow initiation requests. According to their findings, the best scalability points are found in the flat fully distributed SDN controller with a slight gap. The hierarchical model competes for second place. Interestingly, in their experiment, the logically centralized physically distributed SDN controller suffers significantly (Oktian, et al., 2017).

From Table I and the discussion, logically centralized physically distributed architectures are better for management solutions due to the global network view. Applications can access and control the environment from any part of the cluster (Espinel Sarmiento, et al., 2021). However, the synchronization required for consistency introduces overhead, reducing scalability and increasing latency. The degree of synchronization depends on the consistency model used. In the next section, we explore different consistency approaches.

## V. NETWORK STATE CONSISTENCY

In distributed SDN architectures, controllers must maintain consistent network information across their data structures (Ahmad and Mir, 2021), (Informatique and Informatique, 2021), (Zhang, Wang and Huang, 2018).

According to the (CAP) theorem, (C) Consistency, (A) Availability, and (P) Partition Tolerance, only two of the three qualities can be met in case of failure (Brewer, 2000), (Seth Gilbert and Nancy Lynch, 2002), (Panda, et al., 2013). A network with several highly available partitions (A and P) specifically results in a lower level of consistency. As a result, this outdated state impacts how applications work correctly. A system with significant consistency (C and P), on the other hand, leads to reduced network availability (Hoang, et al., 2022).

In addition, on a regular working system without considering failure, the choice between consistency and latency has also impacted distributed SDN architecture. This tradeoff with CAP is combined in the novel formulation PACELC (Abadi, 2012)—the PACELC theorem, which stands for Partitioned, Availability, Consistency Else Latency, Consistency. In light of this new formulation, in the case of network partitioning (P), one must choose between availability (A) and consistency (C) in a distributed computer system. Else (E), if the system is functioning normally in the absence of partitions, one must choose between latency (L) and consistency (C) (Abadi, 2012).

These theorems are essential as the distributed SDN controller, specifically, the logically centralized physically distributed architecture, uses the datastore to store the state of the entire network, which needs to be consistent.

The distributed SDN controller will probably inherit the characteristic of the implemented datastore (i.e., whether it is CP or AP) (Oktian, et al., 2017).

The consistency issue arises from the hardness of resolving the update problems in the network. In other words, maintaining consistency depends on the order of operations computed sequence in the execution network devices (Foerster, Schmid and Vissicchio, 2019).

Besides the degradation of application performance, inconsistency can cause other severe problems in the networks, such as isolation and reachability violation, black holes, and forwarding loops (Aslan and Matrawy, 2016), (Poularakis, et al., 2019).

Three consistency approaches can be applied: strong, eventual, and adaptive. Table II compares the consistency models according to Consistency level, Scalability, Availability, State synchronization Overhead, and Latency.

### A. Strong Consistency Model

Strong consistency ensures that controllers operate with a consistent global view (Levin, et al., 2012). Strong consistency is based on a blocking synchronization procedure that prevents switches from reading data till the controllers are fully updated. It reduces the scalability and availability of the network and limits the system's responsiveness (Levin, et al., 2012), (Informatique and Informatique, 2021).

TABLE II  
CONSISTENCY MODELS FOR LOGICALLY CENTRALIZED PHYSICALLY DISTRIBUTED SDN ARCHITECTURE COMPARISONS

Consistency model	Consistency Level	Scalability	Availability	State Synchronization overhead	Latency
Strong consistency	Very high	Low	Low	Very High	High
Eventual consistency	Low	High	High	Medium	Medium
Adaptive consistency	Medium	High	High	Low	Low

Applications requiring high reliability, such as security-sensitive systems (e.g., firewalls), rely on strong consistency to prevent unauthorized traffic and ensure data accuracy (Aslan and Matrawy, 2016), (Espinel Sarmiento, et al., 2021), (Foerster, Schmid and Vissicchio, 2019).

However, most studies on distributed SDN networks focus on strong consistency (Hoang, et al., 2022). Network application developers may decide not to design their programs to be strongly consistent for various reasons. Strong consistency increases latency and reduces availability, which is problematic in dynamic networks with frequent node failures. Applications that require low latency or high availability often favor more flexible consistency models to maintain performance and responsiveness (Aslan and Matrawy, 2016).

### B. Eventual Consistency Model

Eventually, consistent designs incorporate information as it becomes available and eventually reconcile modifications as each domain has knowledge of them. In other words, all controller copies will “eventually” converge over time and achieve global network view consistency. This resolves the problem of blocking during the synchronization period, which is encountered in strong consistency (Levin, et al., 2012), (Informatique and Informatique, 2021), (Sakic, et al., 2017).

Accordingly, controllers can handle higher update rates and react quicker, but they can temporarily have inconsistent network views, which could lead to inappropriate application behavior (Levin, et al., 2012), (Informatique and Informatique, 2021), (Saito and Shapiro, 2010). Many emerging applications for SDN controller platforms with high availability and scalability on a large scale choose eventual consistency (Informatique and Informatique, 2021).

### C. Adaptive Consistency Models

Adaptively consistent architecture for distributed SDN controllers transforms the inconsistency issue into an automatic control in which the adaptivity module will automatically adjust the value of the synchronization period according to the performance of the target application. The adaptivity module utilizes a feedback loop from measurement or/and prediction extracted data from the fluctuating network environment (Aslan and Matrawy, 2016). In other words, the state synchronization takes place in accordance with performance and consistency restrictions established by the application at runtime by employing triggers according to specified thresholds to enable dynamic change of a consistency level (Bannour, Souihi and Mellouk, 2018a), (Sakic, et al., 2017). A system can use adaptive consistency to deploy applications that tolerate some inconsistency.

From Table II, whereas a strongly consistent network state leads to increased overhead, a weakly consistent network state will produce good performance but less accurate network functioning. Adaptive consistency is an effort to create a solution between the two consistency extremes.

## VI. DISTRIBUTED SDN: FUTURE DIRECTION

Standard static eventual consistency is commonly used for logically centralized physically distributed SDN Control. It suggests a method of synchronization process at fixed intervals, such as the one used by Orion (Ferguson, et al., 2021), in modern SDN systems to achieve effective scalability. It is argued that it provides no bounds on the tolerated state inconsistencies by SDN applications (Bannour, Souihi and Mellouk, 2018a). The fixed synchronization periods may result in utilizing outdated data, disrupt the network, and cause the application to perform less well by sending unnecessary synchronization messages.

Adopting the idea of adaptive consistency in SDN controllers is necessary to leverage administering solutions with a logically centralized physically distributed approach. Adaptive consistency addresses the limitations of static eventual consistency and strong consistency approaches (Aslan and Matrawy, 2016), (Bannour, Souihi and Mellouk, 2018a). This model combines the idea of eventual consistency with a cost-based approach to adjust the consistency level based on observed state convergence and the inefficiencies caused using stale state as inputs (Sakic, et al., 2017).

An adaptive controller can be defined as a controller that has the ability to dynamically and autonomously adjust its configuration to reach a predetermined level of performance based on its requirements and measured in developed metrics (Aslan and Matrawy, 2016), (Bannour, Souihi and Mellouk, 2018a). Several works in the literature recently introduced adaptive consistency, such as Aslan and Matrawy, 2016, Bannour, Souihi and Mellouk, 2018a, and Sakic, et al., 2017.

From Table II and the discussion, the key advantages and motivations behind adopting an adaptive consistency model for the logically centralized physically distributed SDN architecture are as follows:

*Reduced Complexity:* By dynamically adjusting the consistency level, the adaptive model reduces the complexity of application development. Developers do not need to explicitly handle synchronization or worry about inconsistencies in real time. The model abstracts away the complexity of consistency management, making it easier to build and maintain applications.

*Minimized Controller State Distribution Overhead:* In traditional synchronization approaches, controllers often

exchange unnecessary synchronization messages, leading to increased overhead. The adaptive consistency model removes the distribution of unused messages, reducing the synchronization overhead while still maintaining the required level of consistency. This optimization improves the scalability and performance of the system.

*Responding to Changing Network Conditions:* SDN environments are dynamic, and network conditions can change rapidly. The adaptive consistency model allows controllers to respond quickly to these changes. It ensures that the system adapts its consistency level based on observed convergence rates, enabling controllers to make decisions based on the up-to-date information available.

*Reduced Controller-to-Controller Contacts:* By adjusting the consistency level based on observed state convergence, the adaptive model can minimize the frequency of controller-to-controller contacts. This reduction in inter-controller communication leads to improved system response time and efficiency.

## VII. CONCLUSION

Distributed SDN architectures offer significant advantages over centralized designs, particularly in managing large-scale networks and addressing challenges such as SPOF, scalability, reliability, and performance bottlenecks. This study has shown that distributed architectures—whether hierarchical, flat, or logically centralized but physically distributed—each have their strengths and tradeoffs based on network needs. Hierarchical architectures improve scalability but introduce higher latency due to reliance on a root controller. Flat architectures enhance reliability and performance but complicate consistency management.

The logically centralized physically distributed architecture offers a balanced approach by combining centralized control logic with a global network perspective. This architecture is more efficient in resolving conflicts at the East-West interface and is better suited for global optimization than fully distributed architectures, which focus on local optimizations in multi-domain environments. However, synchronization overhead between controllers remains a key challenge, impacting scalability and latency.

Our analysis of consistency models—strong, eventual, and adaptive—reveals that strong consistency ensures data accuracy but adds overhead, whereas eventual consistency improves scalability at the cost of temporary inconsistencies. The adaptive consistency model, which dynamically adjusts synchronization levels based on real-time conditions, strikes a balance by reducing overhead and maintaining adequate performance, particularly for applications such as load balancing and routing.

In conclusion, our findings suggest that the logically centralized physically distributed architecture, combined with adaptive consistency, offers the best solution for managing large-scale fluctuating networks by minimizing synchronization overhead and improving scalability and reliability. Future work should further explore dynamic

consistency models to better optimize the balance between consistency, scalability, and performance in SDN systems.

## DECLARATIONS

All authors certify that they have no affiliations with or involvement in any organization or entity with any financial interest or non-financial interest in the subject matter or materials discussed in this manuscript. This study was not funded by any external sources or financially supporting bodies.

## DATA AVAILABILITY

No datasets were generated or analyzed during the current study.

## REFERENCES

- Abadi, D., 2012. Consistency tradeoffs in modern distributed database system design: CAP is Only part of the story. *Computer*, 45(2), pp.37-42.
- Ahmad, S., and Mir, A.H., 2021. Scalability, consistency, reliability, and security in SDN controllers: A survey of diverse SDN controllers. *Journal of Network and Systems Management*, 29(1), pp.1-59.
- Akyildiz, I.F., 2014. A roadmap for traffic engineering SDN-OpenFlow networks. *Computer Networks*, 71, pp.1-30.
- Almadani, B., Beg, A., and Mahmoud, A., 2021. DSF: A distributed SDN control plane framework for the East/West interface. *IEEE Access*, 9, pp.26735-26754.
- Alowa, A., and Fevens, T., 2020. Towards minimum inter-controller delay time in software defined networking. *Procedia Computer Science*, 175, pp.395-402.
- Aslan, M., and Matrawy, A., 2016. Adaptive Consistency for Distributed SDN Controllers. In: *2016 17th International Telecommunications Network Strategy and Planning Symposium, Networks 2016-Conference Proceedings*. Vo. 1, pp.150-157.
- Atomix. Available from: <https://atomix.io> [Last accessed on 2023 Jun 07].
- Bannour, F., Souihi, S., and Mellouk, A., 2018a. Adaptive State Consistency for Distributed ONOS Controllers. In: *2018 IEEE Global Communications Conference, GLOBECOM 2018-Proceedings*.
- Bannour, F., Souihi, S., and Mellouk, A., 2018b. Distributed SDN control: Survey, taxonomy and challenges. *IEEE Communications Surveys and Tutorials*, 20(1), pp.333-354.
- Blial, O., Ben Mamoun, M., and Benaini, R., 2016. An overview on SDN architectures with multiple controllers. *Journal of Computer Networks and Communications*, 2016, p.9396525.
- Brewer, E.A., 2000. Towards Robust Distributed Systems. In: *Proceedings of the Nineteenth Annual ACM Symposium on Principles of Distributed Computing*, p.7.
- Chen, M., Ding, K., Hao, J., Hu, C., Xie, G., Xing, C., and Chen, B., 2017. LCMSC: A lightweight collaborative mechanism for SDN controllers. *Computer Networks*, 121, pp.65-75.
- Clark, D.D., Partridge, C., Ramming, J.C., and Wroclawski, J.T., 2003. A knowledge plane for the internet. *Computer Communication Review*, 33(4), pp.3-10.
- Dixi, A., Hao, F., Mukherjee, S., Lakshman, T.V., and Kompella, R.R., 2014. ElastiCon: An elastic distributed SDN controller. In: *ANCS 2014-10th 2014 ACM/IEEE Symposium on Architectures for Networking and Communications Systems*, pp.17-27.

- Espinel Sarmiento, D., Lèbre, A., Nussbaum, L., and Chari, A., 2021. Decentralized SDN control plane for a distributed cloud-edge infrastructure: A survey. *IEEE Communications Surveys and Tutorials*, 23(1), pp.256-281.
- Ferguson, A.D., Gribble, S., Hong, C.Y., Killian, C., Mohsin, W., Muehe, H., Ong, J., Poutievski, L., Singh, A., Vicisano, L., Alimi, R., Chen, S.S., Conley, M., Mandal, S., Nagaraj, K., Bollineni, K.N., Sabaa, A., Zhang, S., Zhu, M., and Vahdat, A., 2021. Orion : Google's Software-Defined Networking Control Plane Proceedings of the 18<sup>th</sup> USENIX Symposium on Orion : Google's Software-Defined Networking Control Plane. *Proceedings of NSDI 2021: 18<sup>th</sup> USENIX Symposium on Networked Systems Design and Implementation*, pp.83-98.
- Foerster, K.T., Schmid, S., and Vissicchio, S., 2019. Survey of consistent software-defined network updates. *IEEE Communications Surveys and Tutorials*, 21(2), pp.1435-1461.
- Hassas Yeganeh, S., and Ganjali, Y., 2012. Kandoo: A Framework for Efficient and Scalable Offloading of Control Applications. In: *Proceedings of the First Workshop on Hot Topics in Software Defined Networks, HotSDN '12*. p.19.
- Hoang, N.T., Nguyen, H.N., Tran, H.N., and Souihi, S., 2022. A novel adaptive East-West interface for a heterogeneous and distributed SDN network. *Electronics (Switzerland)*, 11(7), pp.1-20.
- Home-OpenDaylight. Available from: <https://www.opendaylight.org> [Last accessed on 2023 Mar 14].
- Hu, J., Li, X., and Huang, J., 2014. Scalability of Control Planes for Software Defined Networks: Modeling and Evaluation. In: *IEEE International Workshop on Quality of Service, IWQoS*, pp.147-152.
- Hussein, A., Chehab, A., Kayssi, A.I., and Elhajj, I.H., 2018. Machine Learning for Network Resilience: The Start of a Journey. *2018 5<sup>th</sup> International Conference on Software Defined Systems, SDS 2018*, pp. 59-66.
- Informatique, S., and Informatique, G., 2021. Extending SDN Control to Large-scale Networks : Taxonomy, Challenges and Solutions To Cite this Version : HAL Id : Tel-03456621 Université Paris-Est Créteil THÈSE Docteur de l' Université Paris-Est Contributions Pour le Contrôle Distribué Dans les Résea.
- Jain, S., Kumar, A., Mandal, S., Ong, J., Poutievski, L., Singh, A., Venkata, S., Wanderer, J., Zhou, J., Zhu, M., Zolla, J., Hölzle, U., Stuart, S., and Vahdat, A., 2013. B4: Experience with a Globally-deployed Software-defined WAN. In: *Proceedings of the ACM SIGCOMM 2013 Conference on SIGCOMM*, pp.3-14.
- Keshari, S.K., Kansal, V., and Kumar, S., 2021. A systematic review of quality of services (QoS) in software defined networking (SDN). *Wireless Personal Communications*, 116(3), pp.2593-2614.
- Koponen, T., Casado, M., Gude, N., Stribling, J., Poutievski, L., Zhu, M., Ramanathan, R., Iwata, Y., Inoue, H., Hama, T., and Shenker, S., 2010. Onix: A Distributed Control Platform for Large-scale Production Networks. *USENIX Conference on Operating Systems Design and Implement*, 10, pp.1-14.
- Levin, D., Wundsam, A., Heller, B., Handigol, N., and Feldmann, A., 2012. Logically Centralized? State Distribution Trade-offs in Software Defined networks. *HotSDN'12-Proceedings of the 1st ACM International Workshop on Hot Topics in Software Defined Networks*, pp.1-6.
- Mestres, S.A., Rodríguez Natal, A., Carner Marsal, J., Barlet R., Alarcón C., Sole, M., Muntés, M., Meyer, D., Barkai, S., Hibbett, M.J., Estrada, G., Coras, F.T., Ermagan, V., Latapie, H., Cassar, C., Evans, J., Walrand, J., and Cabellos Aparicio, A., 2017. Knowledge-defined networking. *Computer Communication Review*, 47(3), pp.1-10.
- Oktian, Y.E., Lee S.G., Lee H.J., and Lam, J.H., 2017. Distributed SDN controller system: A survey on design choice. *Computer Networks*, 121, pp.100-111.
- Open Network Operating System (ONOS) SDN Controller for SDN/NFV Solutions. Available from: <https://opennetworking.org/onos> [Last accessed on 2022 Jun 26].
- OpenStack Docs: Distributed Dragonflow. Available from: [https://docs.openstack.org/developer/dragonflow/distributed\\_dragonflow.html](https://docs.openstack.org/developer/dragonflow/distributed_dragonflow.html) [Last accessed on 2021 Nov 21].
- Panda, A., Scott, C., Ghodsi, A., Koponen, T., and Shenker, S., 2013. CAP for Networks. *HotSDN 2013-Proceedings of the 2013 ACM SIGCOMM Workshop on Hot Topics in Software Defined Networking*, pp.91-96.
- Phemius, K., Bouet, M., and Leguay, J., 2014. DISCO: Distributed Multi-domain SDN Controllers. *IEEE/IFIP NOMS 2014 - IEEE/IFIP Network Operations and Management Symposium: Management in a Software Defined World*.
- Poularakis, K., Qin, Q., Ma, L., Kompella, S., Leung, K.K., and Tassiulas, L., 2019. Learning the Optimal Synchronization Rates in Distributed SDN Control Architectures. In: *Proceedings-IEEE INFOCOM, 2019-April*, pp.1099-1107.
- Saito, Y., and Shapiro, M., 2010. Optimistic replication. *ACM Computing Surveys*, 37(1), pp.42-81.
- Sakic, E., Sardis, F., Guck, J.W., and Kellerer, W., 2017. Towards Adaptive State Consistency in Distributed SDN Control Plane. In: *IEEE International Conference on Communications*.
- Seth Gilbert and Nancy Lynch, 2002. Brewer's conjecture and the feasibility of consistent, available, partition-tolerant web services. *ACM SIGACT News*, 33(2), pp.51-59.
- Tadros, C.N., Mokhtar, B., and Rizk, M.R.M., 2019. Logically Centralized-Physically Distributed Software Defined Network Controller Architecture. In: *2018 IEEE Global Conference on Internet of Things, GCIoT 2018*.
- Tootoonchian, A., and Ganjali, Y., 2010. HyperFlow: A Distributed Control Plane for OpenFlow. In: *2010 Internet Network Management Workshop/Workshop on Research on Enterprise Networking, INM/WREN 2010*.
- The Open Networking Foundation (ONF), 2019. *Reference Design SDN Enabled Broadband Access*. The Open Networking Foundation, United States.
- Yu, H., Qi, H., and Li, K., 2020. WECAN: An efficient West-East control associated network for large-scale SDN systems. *Mobile Networks and Applications*, 25(1), pp.114-124.
- Zhang, B., Wang, X., and Huang, M., 2018. Adaptive consistency strategy of multiple controllers in SDN. *IEEE Access*, 6, pp.78640-78649.

# AI-Based Evaluation of Homogeneous Flow Volume Fractions Independent of Scale Using Capacitance and Photon Sensors

Abdulilah M. Mayet<sup>1†</sup>, Salman A. Mohammed<sup>1</sup>, Shamimul Qamar<sup>2</sup>, Hassen Loukil<sup>1</sup>, Neeraj K. Shukla<sup>1</sup>

<sup>1</sup>Department of Electrical Engineering, King Khalid University, Abha 61411, Saudi Arabia

<sup>2</sup>Department of Computer Science and Engineering, Applied College, Dhahran Al Janoub Campus, King Khalid University, Abha, Saudi Arabia

**Abstract**—Metering fluids is critical in various industries, and researchers have extensively explored factors affecting measurement accuracy. As a result, numerous sensors and methods are developed to precisely measure volume fractions in multi-phase fluids. A significant challenge in multi-phase fluid pipelines is the formation of scale within the pipes. This issue is particularly problematic in the petroleum industry, leading to narrowed internal diameters, corrosion, increased energy consumption, reduced equipment lifespan, and, most crucially, compromised flow measurement accuracy. This paper proposes a non-destructive metering system incorporating an artificial neural network with capacitive and photon attenuation sensors to address this challenge. The system simulates scale thicknesses from 0 mm to 10 mm using COMSOL multiphysics software and calculates counted rays through Beer-Lambert equations. The simulation considers a 10% interval of volume variation in each phase, generating 726 data points. The proposed network, with two inputs—measured capacity and counted rays—and three outputs—volume fractions of gas, water, and oil—achieves mean absolute errors of 0.318, 1.531, and 1.614, respectively. These results demonstrate the system's ability to accurately gauge volume proportions of a three-phase gas-water-oil fluid, regardless of pipeline scale thickness.

**Index Terms**—Non-destructive metering, Scale thickness in pipelines, Multi-phase fluids, Artificial neural network, Capacitive sensors, Gamma-ray attenuation sensor.

## I. INTRODUCTION

Measuring the volume fraction (VF) of multiphase flows is a critical task and so important in a number of fields such as gas, oil, and water. This is because of many subjects, such as financial matters and environmental-oriented concepts.

Hence, researchers have been strived a lot to present new and optimized methods to avoid making delay and separation in the process being the worst part of conventional methods. Among introduced techniques, gamma-ray attenuation and capacitance-based sensors are so intriguing and this is because of their natures, which are non-destructive, non-invasive, and applicable to be utilized in harsh conditions unlike mechanical solutions, such as turbo meters, sampling tubes, and vibrating densitometers, which are intrusive in measurement and complex in their structures (Mayet, et al., 2024a). Regarding the gamma attenuation sensor, many works can be found that authors have utilized this type of sensor to measure volume fractions of fluids. In 1999, Abro and his coworkers developed a technique that used multiple radiation beams to detect flow patterns in two-phase flow within a narrow pipe (Ábro, et al., 1999). In a sophisticated system, Salgado et al. employed dual-energy gamma emitter radioisotopes. They had an emphasis on investigations into the complex nature of gas-oil-water multiphase flow in mostly understanding and identification of different flow patterns (Salgado, et al., 2010). Roshani and his colleagues conducted an analysis of the performance of a radial basis function (RBF) neural network alongside a photon attenuation sensor to predict various phases' proportions in water, oil, and gas annular mixtures. They evaluated 3 different structures of the mentioned model. The first one aimed at predicting the proportions of water and oil, the second focused on gas and water, and the third on gas and oil. They reported that the first RBF model was the most accurate in forecasting proportions in the three-phase annular mixture (Roshani, et al., 2017a). In the aspect of capacitive sensors, many works have been published so far. Researchers have used capacitive plates to measure both the resistance and capacitance of a three-phase blended liquid without physical intrusion. The examined Plexiglas pipeline was equipped with two semi-cylindrical electrodes each one of them covered about half of the pipeline's circular perimeter (Sheikh, Hassan and Iqbal, 2019). Fouladinia et al. have employed a capacitive sensor in a three-phase homogeneous regime to measure volumes of all phases. They have concluded that just one capacitive sensor is unable to do this action and there is a need for other

ARO-The Scientific Journal of Koya University  
Vol. XII, No. 2 (2024), Article ID: ARO.11791. 12 pages  
DOI: 10.14500/aro.11791

Received: 27 August 2024; Accepted: 26 October 2024

Regular research paper: Published: 09 November 2024

†Corresponding author's e-mail: amayet@kku.edu.sa

Copyright © 2024 Abdulilah M. Mayet, Salman A. Mohammed, Shamimu Qamar, Hassen Loukil, Neeraj K. Shukla. This is an open-access article distributed under the Creative Commons Attribution License (CC BY-NC-SA 4.0).



methodologies or using other types of sensors along with the utilized sensor. Hence, they measured the proportion of water, precisely (Mayet, et al., 2024b). Proposing new and optimized capacitance-oriented sensor is a hot topic and many papers can be found in this regard. For example, in (Syah, et al., 2023), a new sensor called arrow-shaped has been presented which has a good level of sensitivity for two-phase annular fluids. Similarly, a capacitive sensor called skewed has been proposed by authors which is able to measure volume fractions of oil and gas two-phase flows in stratified, annular, and homogeneous regimes (Ilyasu, et al., 2024). Scale layers that are formed within pipelines face oil and water industries with a number of challenges such as drilling tools, increasing the consumed energy, decreasing the efficiency, and the most important one, reducing the accuracy of flow measurement. Flowing water in pipes introducing some materials, such as calcium, barium, and strontium sulfate, leads to the forming of these challengeable layers. Therefore, many papers have been published to measure scale-oriented matters in pipelines. For instance, in (Oliveira, et al., 2015), authors have used a detector paired with a source to investigate the accumulation of scale within transmission channels. The authors collected gamma spectra at intervals of 0.5 cm. Their findings indicated that while gamma transmission scanning is capable of identifying the existence of scale in a pipe carrying a single-phase flow, it cannot accurately map the exact distribution of the scale. Salgado and his coworkers have employed a method for measuring the thickness of scale inside pipelines. Their introduced method included a source, a steel pipe, and a detector. The collected gamma spectra were given to an artificial neural network (ANN) resulting in the estimating of the scale thickness. The weakness of this approach is that it was able to measure the scale's thickness in pipelines with a one-phase flow, while in real conditions more phases inflows exist (Teixeira, et al., 2018). Authors in (Roshani, et al., 2021) tried to measure void fraction in two-phase gas and oil regardless of the effect of the scale layer in the measurement. This study was done by combining photon attenuation with artificial intelligence methods. They employed an ANN to classify the flow regimes and predict the void fraction. However, their outputs declared that the proposed method was unable to accurately identify all three flow regimes. Utilizing ANN in flow measurement is a popular tool that can be found in many studies such as (Mayet, et al., 2023), which has used a multilayer perceptron (MLP) ANN along with two capacitive sensors, ring, and concave, to measure void fraction of a two-phase water and gas fluid independent of temperature and pressure. Authors have utilized a combination of capacitive and gamma-ray attenuation sensors to measure volumes of oil, gas, and water by an ANN. They did this mission without any attention to the effect of scale in measurement accuracy (Fouladinia, et al., 2024). A gamma-based system including two sources and two detectors along with a couple of machine learning tools were used to analyze the water-airflow in a horizontal pipe. To do this mission, the cross-spectral density and 8 extracted parameters from the signal spectrum for one detector acted as input features for used machine learning (Hanus, et al., 2024). Authors have utilized a particle swarm optimization based feature selection system, and an ANN to detect a void fraction of a two-phase liquid-gas

fluid. The used sensor was a gamma-based sensor with one source and two detectors (Ilyasu, et al., 2023). In the aspect of homogeneous two-phase fluids, a study was conducted being measuring void fraction independent of the liquid phase density changes by an MLP model (Ilyasu, et al., 2023). Authors have done this for an annular two-phase fluid (Veisi, et al., 2023). The same can be found for an annular regime while authors have utilized concave and TRFLC sensors to measure void fraction regardless of liquid type (Al-Fayoumi, et al., 2023). In another study, capacitive and photon attenuation sensors were used to collect data for an MLP ANN. The model was able to measure a void fraction of an oil-gas annular regime, precisely (Mohammed, et al., 2022). By employing two different capacitance-oriented sensors (concave and ring), the void fraction of a two-phase homogeneous regime was measured independent of temperature and pressure changes (Chen, et al., 2023). Moreover, a temperature-independent measurement was done for a two-phase fluid by employing an ANN and an 8-electrode sensor (Qaisi, et al., 2023). While these papers have reported good accuracies, they have not considered the impact of scale thickness.

In this paper, the main idea is to eliminate the impact of the scale layer in volume fractions measuring. Scale is a common phenomenon in pipelines and highly effects the accuracy of measurement. While in many previous published papers, the impact of this material is not applied, the proposed metering system's objective is to solve this challenge by measuring all phases' volume fractions independent of scale thickness, precisely. This mission is done by combining an MLP ANN, capacitive and gamma-ray attenuation sensors. Investigated fluid is a homogeneous regime containing gas, water, and oil. To generate data for the proposed network, the concave sensor is simulated in the COMSOL software and acts as the first input of the network. The second input is then produced by calculating Beer-Lambert equations to count gamma rays in each ratio of the materials mixture. Moreover, the scale's thickness is considered from 0 mm to 10 mm of BaSO<sub>4</sub> being one of the most common materials in pipelines. After investigating a number of networks with various hyperparameters, the best one is proposed which has a mean absolute error (MAE) of 0.318, 1.531, and 1.614, for the gas, water, and oil phases, respectively. These errors illustrate the novelty of the approach being able to measure the volume proportions of a three-phase gas-water-oil homogeneous fluid independent of the scale thickness. This study includes 4 more main sections. While in section 2 the details of simulations and calculations are presented, the proposed network's details are reported in section 3. In section 4, the obtained results are illustrated and discussed. Finally, the conclusion of the whole paper is done in section 5.

## II. DESCRIBING SENSORS UTILIZED IN THE PROPOSED APPROACH

As it was mentioned, the main aim of this paper is to present an approach being able to measure the VFs of all three phases, precisely. To do this mission, the first step is selecting an appropriate sensor. Capacitive and gamma-based

sensors are highly popular among researchers to measure VFs of various fluids. One of the key reasons in this regard is their non-invasive nature. Another reason is their accuracy along with their installation being easy. The principle behind capacitive sensors is based on the variation in measured capacitance, which occurs due to changes in the material between the sensor's electrodes, referred to as the dielectric. In the case of a capacitance-based sensor, the material inside the pipe serves as the dielectric. Therefore, any alteration in the composition or ratio of the materials results in a change in the sensor's measured capacitance. This variation is attributed to the dielectric properties of the materials, with the most significant being their relative permittivity. Capacitive sensors are influenced by relative permittivity, and due to the similarity in the relative permittivity values of gas and oil, these sensors are unable to accurately measure the volume fractions of all three phases. As a result, an additional sensor based on a different physical property is required. A gamma-ray attenuation sensor, which operates based on density, is a suitable option. However, due to the similar densities of water and oil, it cannot effectively measure all three phases. While the gas phase has the lowest linear absorption coefficient, the challenge arises from the similarity between the liquid phases, making it difficult for the gamma sensor to differentiate between them. Therefore, both capacitive and gamma-ray sensors are used in conjunction to achieve the accurate measurement of all three phases. As it was mentioned before, the selected sensors must be non-destructive and non-invasive because the proposed approach is expected to do measurements without doing any separation or delay in the process. One critical point that must be considered is the parameters that impact the results produced by sensors. Since water and oil have close densities and oil and gas have close relative permittivity, the chosen sensors must be dependent on different parameters to generate various inputs to train and test the network much better and make it able to predict volumes. Density and relative permittivity are so important across various scientific and engineering disciplines. While density refers to the amount of mass contained within a specific volume, indicating how tightly matter is packed in a substance, relative permittivity indicates how effectively a material can save electrical-oriented energy within an electric-style field compared to empty space. Since capacitive and gamma-ray attenuation sensors are related to relative permittivity and density,

respectively, they can be good choices for this research's purpose. Therefore, these sensors along with an MLP ANN are utilized to measure the volumes of the phases. It is to be noted that, fluids could be divided into three main regimes, annular, stratified, and homogeneous shown in Fig. 1. Due to the main aim of this investigation being independent of scale thickness measurement of a homogeneous flow, the scale can be seen in Fig. 1 with brown color.

Capacitance-based sensors have two electrodes with an insulating material in between. The mix of three phases in the fluid affects its overall dielectric properties, which in turn, alters the capacitive sensor's capacitance. This shows how much capacitive sensors depend on relative permittivity. These sensors have several perks, including a straightforward design, low-cost implementation, the use of non-ionizing radiation, fast response times, and easy, non-intrusive installation (Heindel, Gray and Jensen, 2008 and Hammer, et al., 2006).

As it is clear from equation (1), the capacity of the capacitance-based sensor (C) and relative permittivity or  $\epsilon_r$  of material flowing inside the pipe are highly connected together. This parameter illustrates the amount of electrostatic energy that can be stored per unit of applied voltage. While A takes place as the area of electrodes, D is the gap between them. Finally, the permittivity of free space or  $\epsilon_0$  appears being about  $8.854 \times 10^{-12} \frac{F}{m}$  (Cui, et al., 2021).

$$C = \frac{\epsilon_r \times \epsilon_0 \times A}{D} \tag{1}$$

Since both of the used sensors, capacitive and gamma-based sensors, have been utilized in a number of previously published papers to measure VFs of various fluids, their application is proved. Hence, in the current study, a combination of them along with an ANN is applied to reach the main goal of this study being measuring volumes of all three phases regardless of scale thickness. According to previous studies by authors. A static experimental study was conducted to validate the generated data by COMSOL software. After measuring sensor capacity in various VFs by an LCR meter, collected data were compared with that of simulated data. After comparing both data, it was observed that they have similar trends and generated data by the software are valid. This approach can be found in a number of previous published studies (Veisi, et al., 2023 and Al-Fayoumi, et al., 2023 and Qaisi, et al., 2023).. Due

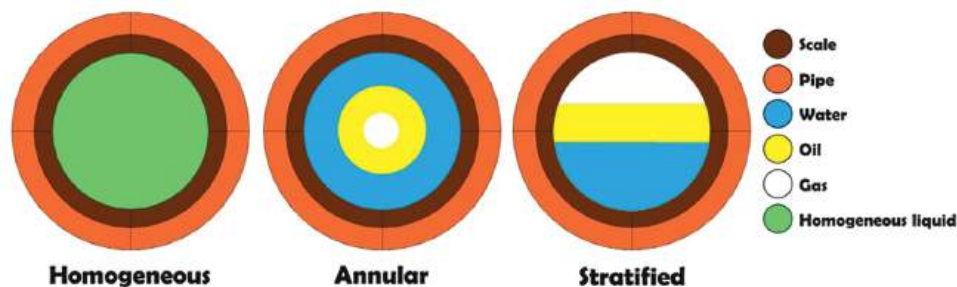


Fig. 1. Three main regimes of fluids.

to its good level of sensitivity and being easy to install on pipelines, the chosen sensor is concave being one of the most popular ones in this regard. To design and simulate this sensor the COMSOL software is utilized which is completely valid and has been benchmarked in a number of previous studies (Syah, et al., 2023 and Iliyasa, et al., 2024). The first stage of simulating this sensor in the mentioned software is creating an area to make an isolated condition for the study. Next, is the time for adding pipe followed by adding electrodes, both GND and VCC, to the surface of it. The liquid being a mixture of oil, water, and gas is then added inside the pipe. While (Fig. 2a) shows the 3D view of the simulated sensor, (Fig. 2b) do that of Mesh which was set on a Fine level before running the sensor for measuring capacities as much as accurate. In this figure, GND is gray and VCC is red. In Fig. 3, different lengths, radiuses, and the gap between electrodes are presented. While  $L_p$  is the length of the pipe and is equal to 180 mm, the length of the electrodes is depicted by  $L_e$  and is equal to 120 mm. Last but not least, the distance between electrodes is shown as  $G_e$  and is equal to 3 mm. Since the thickness of scale ( $R_s$ ) made of  $BaSO_4$  is alternative,  $R_l$  being the radius of the mixture is alternative, too. This happens while the radius of the pipe shown as  $R_p$  is equal to 32 mm. According to Fig. 4, various thicknesses of scale are considered for simulation ranging from 0 mm to 10 mm. The formula of  $R_l$  is  $26 - R_s$  and is alternative from 26 mm to 16 mm based on each amount of scale. In this figure, pipe, scale, and liquid are shown with orange, brown, and green colors, respectively. There are 11 states of scale and by considering 10% of interval for changing in materials'

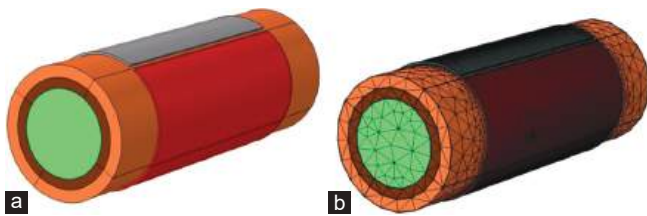


Fig. 2. (a) Simulated concave sensor and (b) Mesh view.

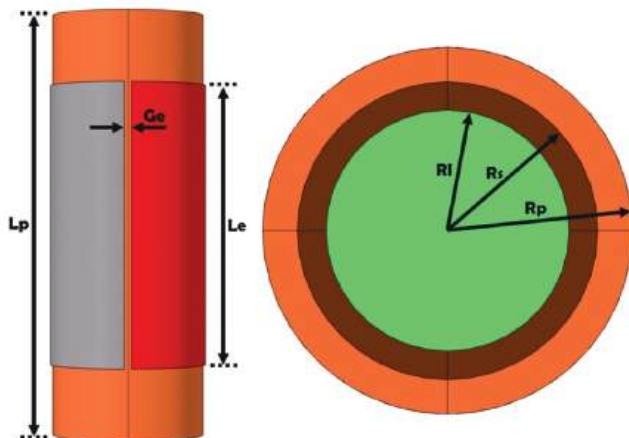


Fig. 3. Various dimensions of the simulated sensor.

volumes, 66 simulations are needed for each thickness of scale. Hence, by consuming a great amount of time, the simulations are done 726 times to generate the first input of the network.

As it was mentioned in (Mayet, et al., 2024b), just one capacitive sensor is unable to predict all phases and due to the closeness of the oil and gas phases' relative permittivity, this happens. To solve this problem, the solution is employing another type of sensor being sensitive to another physical parameter. Hence, a gamma-ray sensor could be a good choice because it is highly dependent on density and is non-destructive, too.

Since 1950s, gamma attenuation sensor has been utilized to measure volume fractions. The one-beam version of this density-dependent sensor works with the attenuation of the rays when cross the liquid. In fact, the ray starts from the source side and traverses the pipe (its diameter) to reach the detector side and be counted. It is obvious that the counted rays or the output of the sensor depends on the flow regime inside the pipe and for this reason, in this investigation, a homogeneous fluid of oil, gas, and water was considered. When gamma rays (like a narrow beam) move from a source has an initial intensity ( $I_1$ ). After passing the first wall of the pipe (the wall near the source side) it penetrates to the fluid and after exiting from the second wall (the wall near the detector side) rays reach the detector with the final intensity ( $I_2$ ). By these two intensities, the output of the sensor is calculated. Fig. 5 shows the details related to a gamma ray crossing the pipe and reaches to the detector to be counted.

The Beer-Lambert law is presented in equation (2) proving the fact of high impact of density on the gamma-ray attenuation sensor. In this equation,  $I_1(E)$  and  $I_2(E)$  are the energy of the ray emitted and the energy of the ray collected, respectively. While  $\eta$  is the absorption coefficient,  $\rho$  is the density of the material within the pipe and  $L$  stands for its thickness (Dong-hui, et al., 2005). By putting equation (3) being about the linear attenuation coefficients ( $\mu(E)$ ) in equation (2), equation (4) is earned giving the amount of  $\frac{I_2}{I_1}$ , the second input for the network. Since the investigated fluid is a three-phase oil-water-gas flow, equation (5) is replaced in equation (4) to reach the final equation being equation (6).  $\alpha$ ,  $\beta$ , and  $\gamma$  in equation (6) are VF of oil, water, and gas, respectively. Finally,  $L$  is the thickness of materials inside the pipe and is equal to 52 mm.

$$I_2(E) = I_1(E) \exp(-\eta(ZE) \rho L) \quad (2)$$

$$\mu(E) = \eta(ZE) \rho \quad (3)$$

$$I_2(E) = I_1(E) \exp(-\mu(E)L) \quad (4)$$

$$\mu(E) = \alpha\mu(E)_o + \beta\mu(E)_w + \gamma\mu(E)_g \quad (5)$$

$$\ln\left(\frac{I_2}{I_1}\right) = -[\alpha\mu(E)_o + \beta\mu(E)_w + \gamma\mu(E)_g] \times L \quad (6)$$

In this study, Cesium-137, emitting radiation at 0.662 MeV, was chosen. According to the linear attenuation coefficient of all three phases in (National Institute of Standards and Technology, 2023), equation (6) is calculated for various



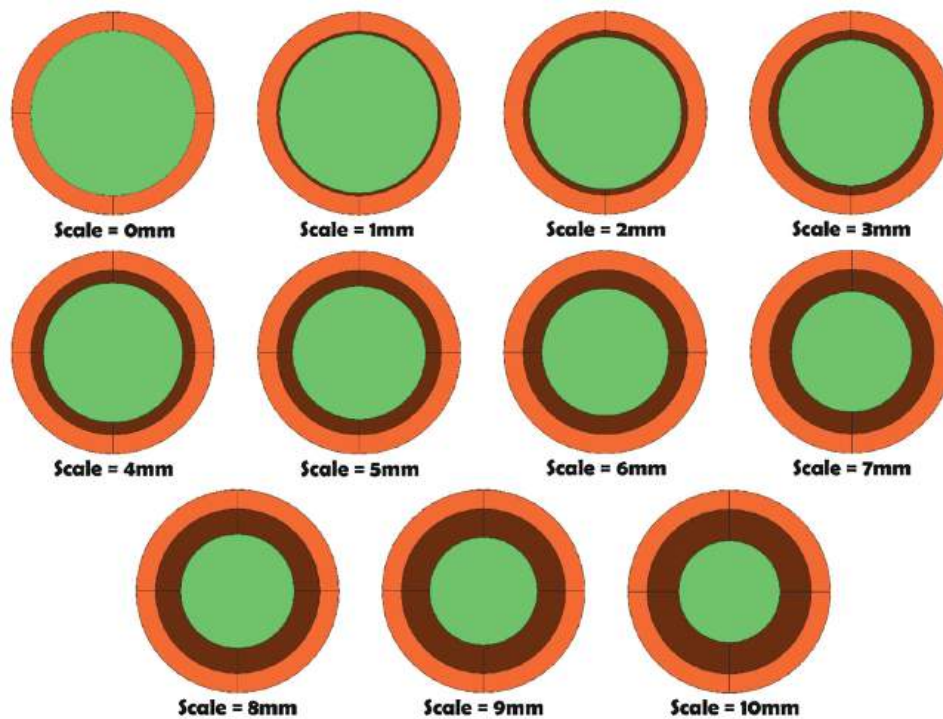


Fig. 4. Various thicknesses of the scale considered during simulations.

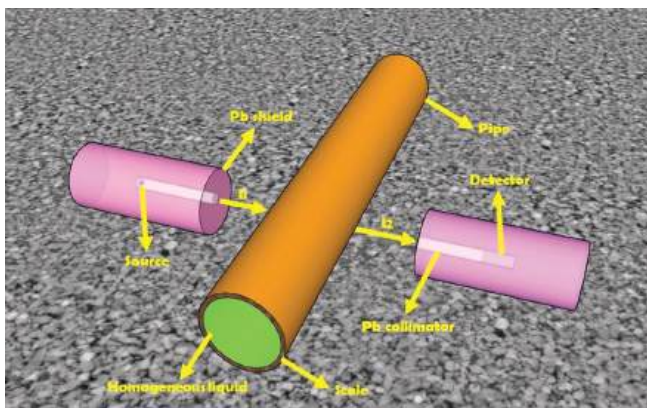


Fig. 5. The travel of gamma ray from source to detector to be counted.

ratios of materials and the second input of the network is generated. Table I presents all parameters and materials which are utilized in done simulations and calculations. Statistical analysis is a systematic process that involves selecting appropriate techniques, utilizing relevant software tools, and adhering to specific guidelines to facilitate the efficient collection and analysis of data. In this study, the statistical technique of data splitting was applied, where the dataset was randomly divided into training and testing subsets. Microsoft Excel, software offering basic statistical features useful for straightforward analyses, was employed. The criteria for data collection and analysis were based on data quality and sampling methods. Several steps were taken to process, clean, and prepare the data for analysis after extraction. First, the extracted data were examined to identify any missing values, outliers, duplicates, or inconsistencies, none of which were found. As the data were on the same scale, normalization and conversion were unnecessary.

TABLE I

CHARACTERISTICS OF THE SCALE AND PHASES OF THE INVESTIGATED FLUID

Characteristic	Value or Name
Utilized material for the scale	BaSO <sub>4</sub>
Relative permittivity of gas	1
Relative permittivity of water	81
Relative permittivity of oil	2.2
Relative permittivity of the used scale	11.4
Density of gas	0.001 g/cm <sup>3</sup>
Density of water	1 g/cm <sup>3</sup>
Density of oil	0.9 g/cm <sup>3</sup>
Density of the used scale	4.48 g/cm <sup>3</sup>
The range of volume fractions	0–100%
The step of volume fractions	10%
The number of simulations and calculations	11×66=726
Type of the investigated fluid	Homogeneous

Subsequently, the data were randomly split into training and testing sets. Finally, the verified data were saved using Excel software for further analysis. Last but not least, since the used data are simulated-based data, there is nothing about unreliability to do with this data because they are generated by software and ideal conditions are considered and noise is not considered a brining error to the results and decreases the reliability of outcomes.

It is to be noted that, before a sensor can be manufactured, it must undergo calibration using a reliable reference. This is essential because the sensor is designed to measure dynamic values for which no prior data exists. To achieve this, several studies are conducted using a static model across various phase ratios to produce calibration points. These points are then used to calibrate the sensor and can be generated using advanced software, such as the validated COMSOL Multiphysics software.

### III. UTILIZING ANN AS A POWERFUL TOOL TO PREDICT VOLUMES

ANN are utilized in many areas, such as signal processing and pattern recognition. The selection of ANNs was based on their demonstrated effectiveness in handling complex, non-linear relationships between input variables, such as those encountered in multiphase fluid measurement. Multiphase flow systems are highly dynamic, and the capacitance and gamma-ray sensor outputs often exhibit non-linearity and interdependence, which ANNs are well-suited to model due to their ability to learn complex mappings from data. As it was mentioned, due to the inherent complexity of multiphase fluids and the non-linear behavior between sensors' outcomes and volume proportions, ANNs are so intriguing for researchers in the aspect of flow measurement because they are so appropriate in non-linear-style systems. Among various types of ANN, such as Support Vector Machines (SVM) and XGBoost, Multi-Layer Perceptron (MLP) ANNs are widely used in measuring volumes. This is because of offering a more versatile framework, accommodating a wide range of configurations and activation functions being non-linear (Goodfellow, Bengio and Courville, 2016; Zhang and Suganthan, 2016). Another merit related to MLP ANNs is their flexibility in predicting continuous function providing enough data and appropriate architecture for modeling unpredictable systems, such as multi-phase fluids. Moreover, while some networks such as Gaussian process regression can become computationally challengeable in handling extensive data, MLP ANNs are compatible with advanced hardware such as GPUs resulting in enhancing training speeds (Hinton, et al., 2012; He, et al., 2016). Next, due to their learning and generalization capabilities of MLP ANNs, they exhibit robustness in dealing with noisy data. Hence, they are useful in the flow measurement industry (Bishop and Nasrabadi, 2006; Geman, Bienenstock and Doursat, 1992). According to all provided reasons, an MLP ANN is chosen and by using it, the metering of all phases of the investigated fluid is done. This kind of network has some layers, input, output, and hidden layers. Each one of these layers has neurons and activation functions, such as linear, sigmoid, *tansig*, and *purelin*. When the training process is in process, weights and biases are iteratively tuned to reach the lowest MAE. Convergence plays a crucial role in network performance, and its relationship with the learning rate is well-established. If the learning rate is set too high, it can cause instability or lead to oscillations in the algorithm, while a rate that is too low may result in extremely slow convergence. Therefore, determining the optimal learning rate often requires experimentation. In this study, the learning rate was set at 0.01 based on such considerations. Non-linear systems, such as multi-phase flow measurement, often prompt researchers to employ optimization algorithms to address complex challenges. One of the most commonly utilized algorithms is the Levenberg-Marquardt (LM) algorithm, which combines the features of both Gradient Descent and Gauss-Newton iteration, offering numerous advantages. For example, it reduces the demand for high-performance

computing resources while ensuring a fast convergence rate. As a result, the learning process for the network in this study was based on the LM algorithm, which has a broad spectrum of engineering applications, making it well-suited for this research (Levenberg, 1944; Marquardt, 1963). Data were generated by simulating a concave sensor in the COMSOL Multiphysics software under varying ratios of oil, water, and gas, along with solving the Beer-Lambert equations for a gamma-ray attenuation sensor using Cesium-137. The collected data were then normalized before being fed into the MLP ANN. In the next phase, multiple iterations were implemented in MATLAB to explore and evaluate different combinations of hyperparameters, including the number of hidden layers, neurons per hidden layer, activation functions for the input, output, and hidden layers, as well as the number of epochs, among other parameters. Ultimately, the model with the lowest MAE was selected and is presented in this paper. The proposed network has 2 inputs generated from simulations of a concave sensor in COMSOL software to measure capacitance of various ratios and calculations of the Beer-Lambert equations related to counted rays with Cesium-137 in its source side. Since the scale from 0mm to 10mm is investigated and the volume interval is 10%, totally, simulations and calculations are done for 726 times. After normalizing all data, 70% of them being 508 data are considered for training and the rest of them belong to testing the network. This data consideration is done, randomly. This network has 2 hidden layers, both of them have 10 neurons and their activation function is *tansig*. The activation function of both input and output layers is *purelin*. In Equation (7) and Equation (8), the function of *tansig* and *purelin* is presented, respectively. Last but not least, the best network with the lowest desired MAEs trained over 2100 epochs. The proposed network is illustrated in Fig. 6.

$$Tansig(n) = \frac{2}{1 + e^{-2n}} - 1 \quad (7)$$

$$Purelin(n) = n \quad (8)$$

In the measurement of volume fractions of a multiphase fluid using multiple sensors, such as a capacitance-based sensor and a gamma-ray attenuation sensor, the accurate and real-time transmission of sensor data are critical. The sensors generate continuous data regarding VFs of the fluid phases and this data can be transferred by various transferring protocols, one of the most popular ones is message queuing telemetry transport (MQTT). MQTT ensures that the sensor outputs are transmitted efficiently to the server in a way being lightweight, low-bandwidth, and reliable data transfer over networks with minimal latency. Once the data are received at the server, the modeled ANN starts to process and analyze the input, enabling the real-time estimation of the multiphase fluid's volume fractions. The combination of MQTT's protocol for data transmission and ANN's computational capabilities allows for robust and precise monitoring of the fluid composition, ensuring that the system is both scalable and adaptable to complex environments.

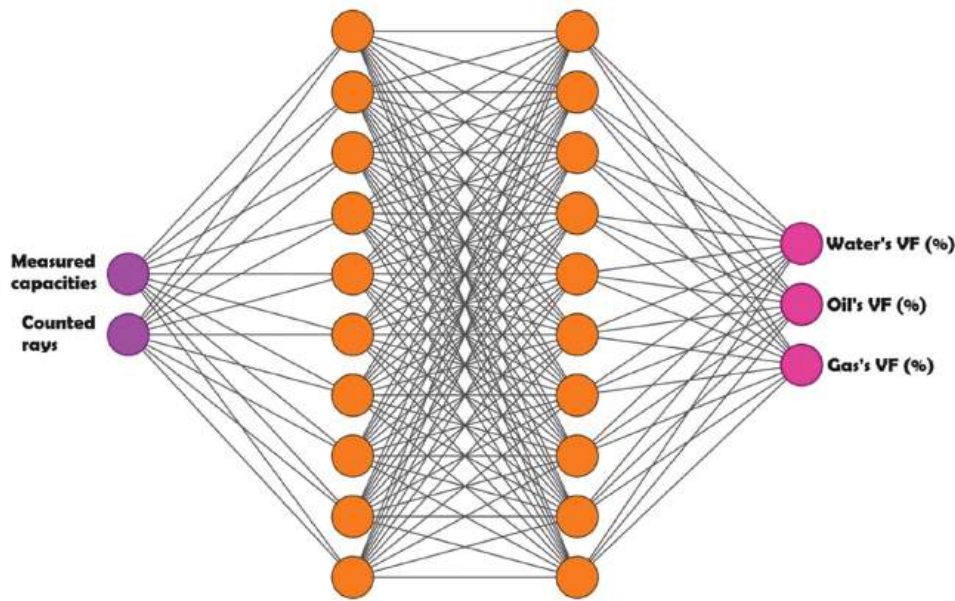


Fig. 6. Various layers of the proposed network.

IV. RESULTS AND DISCUSSION

After doing all required simulations and calculations, the obtained results are presented in this section. The main aim of this investigation was to measure the volume proportions of all three phases of a homogeneous fluid including gas, water, and oil independent of scale thickness presented in the wall of pipelines. To achieve this task, an MLP ANN along with capacitive and photon attenuation sensors were employed. As it was mentioned before, the proposed network had 2 distinct inputs generated from simulating the concave sensor in the COMSOL software and calculating Beer-Lambert equations for a gamma attenuation sensor with Cesium-137 in its source part. All 726 obtained data were randomly divided between the test and train sets of the network. The proposed metering system had 3 outputs, a void fraction of gas, and volumes of water and oil having MAE equal to 0.318, 1.527, and 1.608, respectively. These errors illustrate the novelty of the system being able to gauge volumes of a three-phase gas-water-oil homogeneous fluid regardless of the scale thickness. The flowchart of the way that the presented approach combined sensors and network is illustrated in Fig. 7. As it was said before, the main reason for choosing two types of sensors was dependent on the very close relative permittivity of oil and gas resulting in an inability of the capacitive sensor in VFs of all three phases. Hence, another kind of sensor being sensitive to another parameter was employed and it was a gamma-ray attenuation sensor being highly dependent to density. The combination of these two different sensors along with an MLP could measure all three phases' volumes, precisely.

When just one capacitance-oriented sensor is utilized for measuring VFs, due to the closeness of materials' relative permittivity, similar capacities for different ratios of combinations are generated and this confuses the network to predict volumes. In fact, some ratios of combinations exist that are different in the amount of materials but similar in the measured capacity. Therefore, to make the network able

to predict correct volumes, a gamma-ray attenuation sensor, being sensitive to density, can be used to generate another set of data being different with the first set, which were measured capacities. That is why; the combination of this sensor was used and made the proposed network able to measure all volume fractions regardless of the effect of scale thickness. The obtained results, test and train set from the proposed network for all phases are shown in Fig. 8. From the mentioned figure, it is clear that both overfitting and underfitting did not happen for the obtained outcomes.

After reaching the best network, the MAE of all three phases was calculated by Equation (9) (Chicco, Warrens and Jurman, 2021). The proposed metering system had 3 outputs, a void fraction of gas, and volumes of water and oil having MAE equal to 0.318, 1.527, and 1.608, respectively. These numbers were related to the test set, the train sets' MAE for gas, oil, and water was 0.304, 1.348, and 1.403, respectively. This very low error depicts the ability of the proposed metering system, a combination of two sensors and an MLP ANN, in gauging oil, gas, and water phases regardless on scale thickness in a homogeneous flow. In addition, other error metrics are also discussed in this paper. The formulas for root mean square error (RMSE), coefficient of determination (R-squared or R<sup>2</sup>), and symmetric mean absolute percentage error (SMAPE) are provided in equations (10), (11), and (12), respectively, as referenced in (Chicco, Warrens and Jurman, 2021).

$$MAE = \frac{1}{n} \sum_{i=1}^n |X_i - Y_i| \tag{9}$$

$$RMSE = \sqrt{\frac{1}{n} \sum_{i=1}^n (X_i - Y_i)^2} \tag{10}$$

$$R^2 = 1 - \frac{\sum_{i=1}^n (X_i - Y_i)^2}{\sum_{i=1}^n (X_i - Y)^2} \tag{11}$$

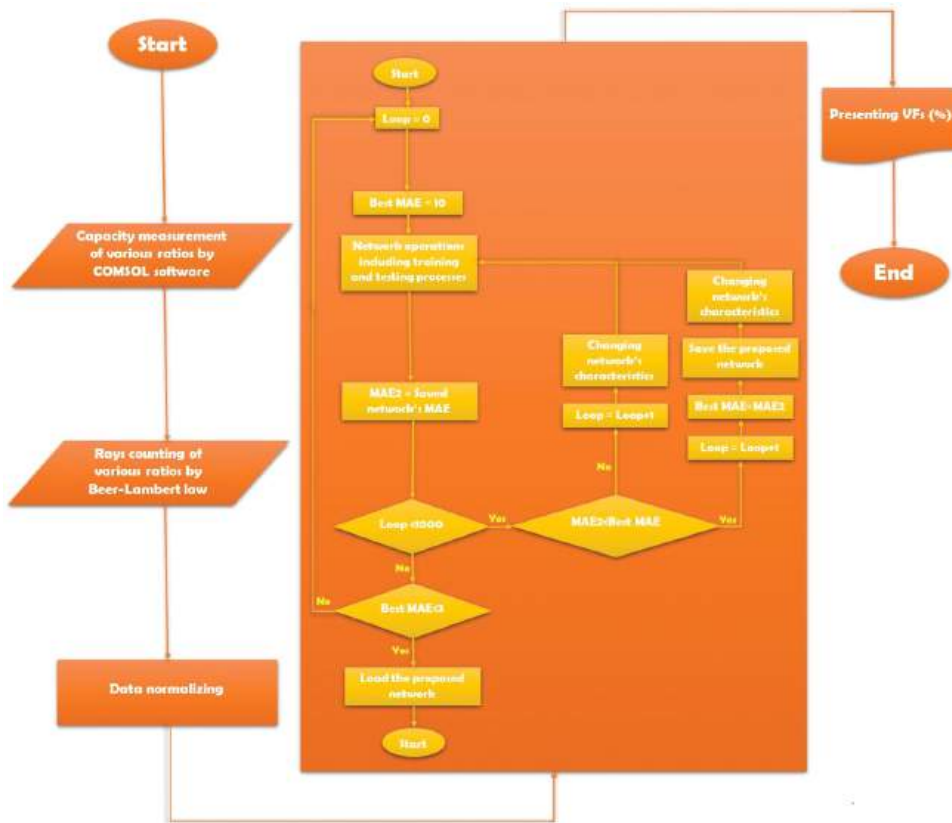


Fig. 7. The flowchart of the proposed approach contains an artificial neural network along with capacitive and photon attenuation sensors.

$$SMAPE = \frac{100\%}{n} \sum_{i=1}^n \frac{|X_i - Y_i|}{(|X_i| + |Y_i|) / 2} \quad (12)$$

In the aforementioned equations,  $n$  represents the total number of data points,  $X_i$  refers to the actual value for the  $i^{\text{th}}$  data point,  $Y_i$  is the predicted value for the  $i^{\text{th}}$  data point, and  $Y$  denotes the mean of all actual values. Similar to MAE, RMSE equals zero when the linear regression model perfectly matches the data, while a positive value indicates an imperfect fit. The  $R^2$  metric ranges from 0 to 1, with 1 indicating a perfect fit and 0 representing the worst fit. On the other hand, SMAPE ranges from 0% to 100%, where a perfect alignment between actual and predicted values results in a value of 0%, while the worst alignment leads to  $SMAPE = 100\%$ . For the proposed model,  $R^2$  values were found to be 0.9997 for gas, 0.9908 for water, and 0.9897 for oil phases. In terms of SMAPE, the gas, water, and oil phases showed values of 0.0012%, 0.0057%, and 0.0060%, respectively. In addition, the RMSE for the gas phase was 0.4105, whereas it was 2.5706 for the water phase, which was 0.1474 lower than that of the oil phase. In Fig. 9, various Error illustrations regarding the obtained results are shown. Error histograms for gas, water, and oil are presented in (a), (b), and (c) parts of this figure showing a great distribution of data around 0. While errors of all three phases are depicted in (d), (e), and (f), the figure for target versus predicted is illustrated in (g), (h), and (i) parts.

To highlight the novelty and performance of the metering system, its details are compared to that of some similar previous published works in Table II.

In the above table, 6 previously published papers were compared with the proposed metering system. Except for the presented approach, just authors in (Roshani, et al., 2021) have tried to eliminate the impact of scale thickness in their measurement being measuring the void fraction of a two-phase annular system including oil and gas. However, the proposed system is able to measure all three phases of a three-phase flow regardless of the scale's impact with a lower amount of MAE for all phases in comparison with reference (Roshani, et al., 2021). Moreover, authors in (Roshani, et al., 2021) have utilized 2 sources and 2 detectors for their investigations, 2 times higher than that of the presented method. It is obvious that when the number of sources and detectors increases, a much more accurate result is expected but the problem is rising in both complexity and cost of the system. This point is another merit of the presented metering system in comparison with references (Roshani, et al., 2021) and (Salgado, Dam and Salgado, 2021). While all phases including gas, water, and oil were presented in the proposed approach, references (Mayet, et al., 2024b) and (Pan, et al., 2019) have reported just one phase's volume. Last but not least, reference (Mayet, et al., 2024a) have reported all three phases' volumes with a good level of accuracy. Aside from having a lower amount of MAE in gas and oil phases, the presented method measures volumes independent of scale thickness, the point that the reference (Mayet, et al., 2024a) is unable to do it. Finally, reference (Peyvandi and Rad, 2017) can be seen that not only is not able to measure volumes regardless of scale but also have a higher amount

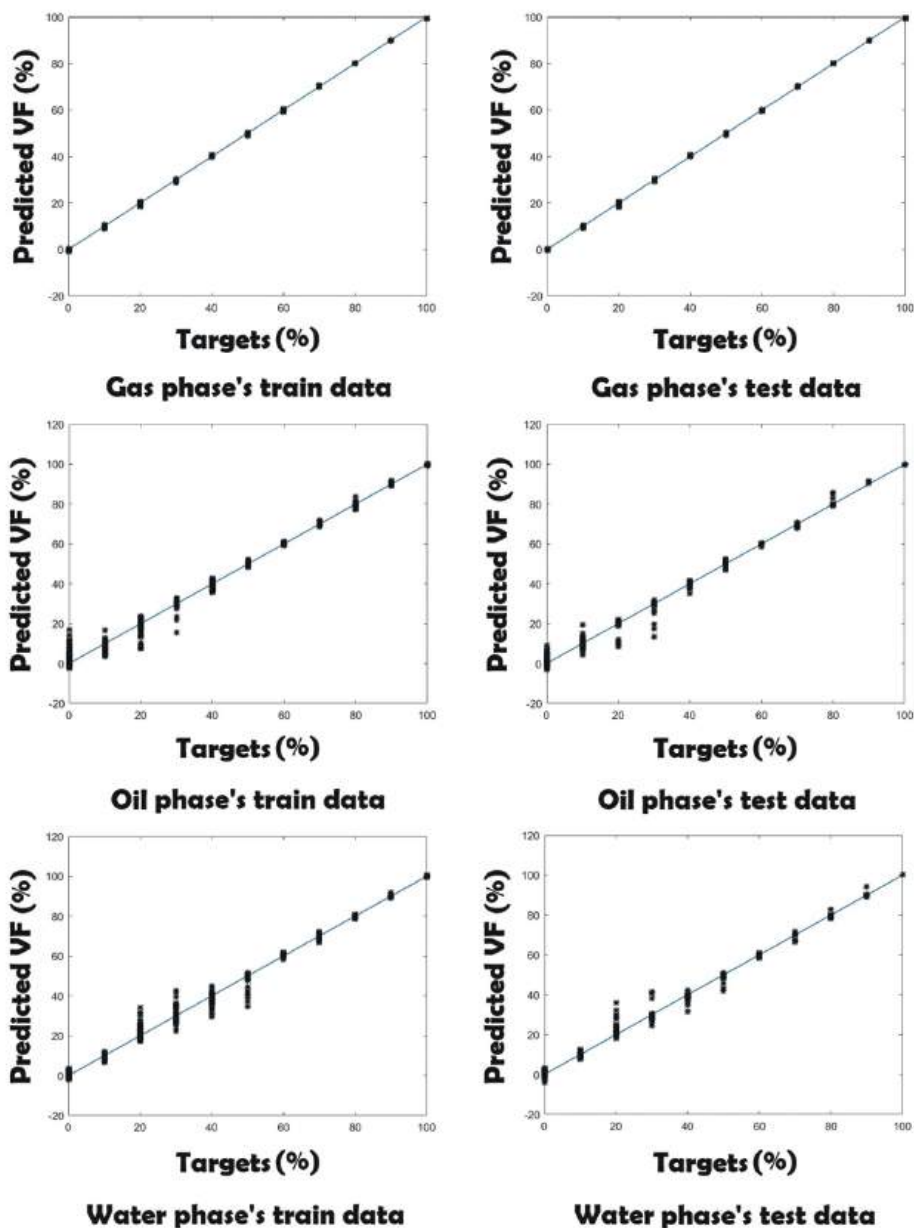


Fig. 8. The proposed network’s test and train performance for all three phases.

TABLE II  
COMPARING THE PROPOSED APPROACH WITH A COUPLE OF SIMILAR PREVIOUS WORKS

Study	Presented phases	Utilized sensors	Utilized sources	Utilized detectors	Mean Absolute Error	Independent of scale thickness
(Mayet, et al., 2024a)	Gas Water Oil	Capacitive+Gamma attenuation	1	1	1.6 0.29 1.67	No
(Mayet, et al., 2024b)	Water	Capacitive	---	---	1.66	No
(Roshani, et al., 2021)	Gas Oil	Gamma attenuation	2	2	2.81 ---	Yes
(Salgado, Dam, Salgado et al., 2021)	Water Gas	Gamma attenuation	2	2	1.79 0.4	No
(Pan, et al., 2019)	Gas	Gamma attenuation	1	1	7.72	No
(Peyvandi and Rad, 2017)	Gas Water Oil	Gamma attenuation	1	1	1.87 1.88 ---	No
Proposed approach	Gas	Capacitive+Gamma attenuation	1	1	0.318	Yes
	Water				1.531	
	Oil				1.614	

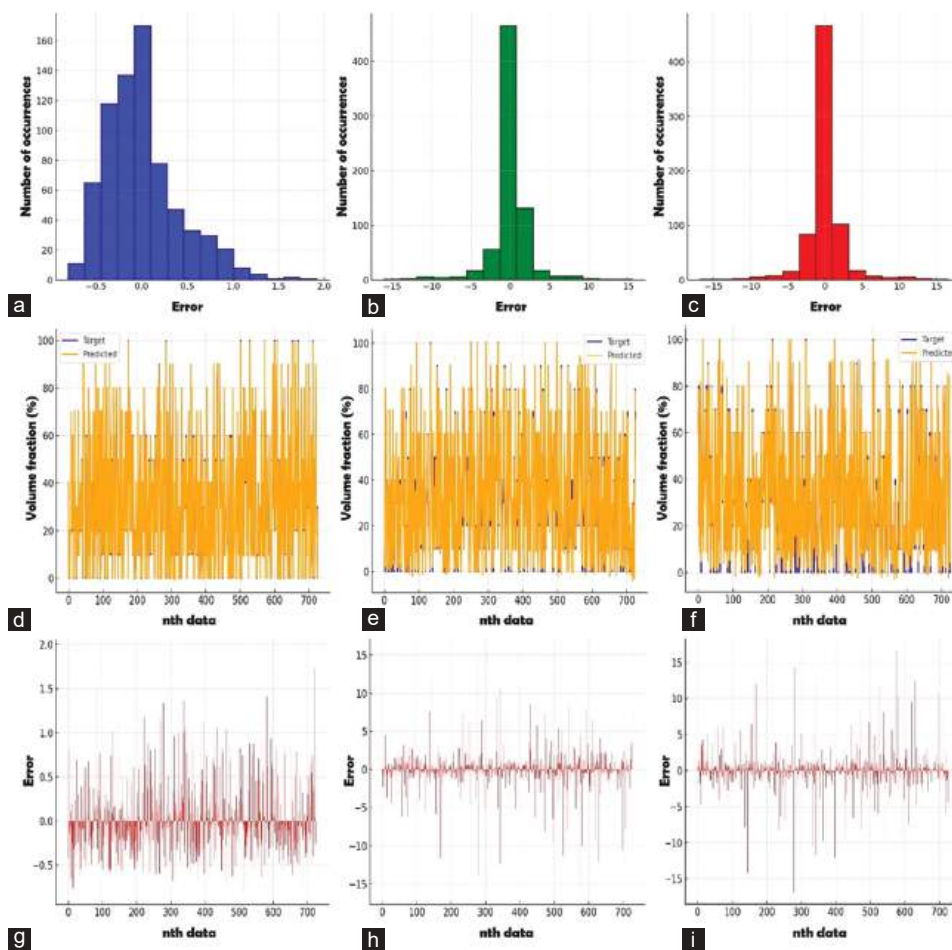


Fig. 9. Error illustration for the proposed metering approach, (a) Gas phase's Error histogram, (b) Water phase's Error histogram, (c) Oil phase's Error histogram, (d) target versus predicted values of gas phase, (e) target versus predicted values of water phase, (f) target versus predicted values of oil phase, (g) Gas phase's error, (h) Water phase's error, (i) Oil phase's error.

of MAE in comparison with this study. While the proposed metering system demonstrates accurate prediction of the volume fraction in all phases of a gas-oil-water homogeneous mixture, like any solution, it has certain limitations. One significant issue is the need to address radiation shielding, as it is critical to ensure the health and safety of personnel working with such systems. However, due to the flexibility in adjusting photon energy, the high intensity of photon emission, and the ability to switch X-ray tubes on and off, this method presents a viable alternative to the use of radioisotopes. In addition, the scope of this study is limited to homogeneous regimes and cannot measure VFs in other types of fluid mixtures. Finally, the effects of temperature and pressure variations, which significantly influence the liquid's relative permittivity and density inside the pipe, should also be considered.

## V. CONCLUSION

In this paper, a metering approach was proposed that was able to measure all three phases of a multi-phase fluid independent of scale thickness, accurately. The presented approach had 2 employed sensors and an MPL ANN. Capacitive and gamma

attenuation sensors were used to generate enough data for training and testing the network. After examining a numerous number of networks with various characteristics, the best one was presented in this study. This model had 2 inputs from sensors, and 3 outputs for phases' volume. The MAE of gas, water, and oil was 0.318, 1.531, and 1.614, respectively. It is to be noted that, just 1 source and 1 detector were employed to generate data by the gamma-ray attenuation sensor by calculating Beer-Lambert equations. Moreover, the simulated capacitive sensor was concave geometry. This metering system can be used in pipelines because they are faced with a scale during their processes and eliminating the effects of this material on measuring accuracy is a vital action. Variations in temperature and pressure significantly influence the capacitance-based method due to changes in liquids' relative permittivity and density. The experiments in this study were performed at room temperature (approximately 300 K), but future research should account for these variables and develop metering systems that are not dependent on them. To further reduce errors, enhancing feature extraction could lead to more accurate volume fraction predictions. In addition, experimenting with different learning algorithms or activation functions could offer further optimization for future studies. Although scale formation

can be non-uniform in real-world conditions, uniform scale formation (ideal condition) is assumed to simplify the analysis. Moreover, while uniform scale is a simplifying assumption, it serves as a baseline for further investigations to address non-uniform scale distributions.

#### ACKNOWLEDGMENT

The authors extend their appreciation to the Deanship of Research and Graduate Studies at King Khalid University for funding this work through Large Research Project under grant number RGP2/225/45.

#### REFERENCES

- Äbro, E., Khoryakov, V.A., Johansen, G.A., and Kocbach, L., 1999. Determination of void fraction and flow regime using a neural network trained on simulated data based on gamma-ray densitometry. *Measurement Science and Technology*, 10(7), pp.619.
- Al-Fayoumi, M.A., Almimi, H.M., Veisi, A., Al-Aqrabi, H., Daoud, M.S., and Eftekhari-Zadeh, E., 2023. Utilizing artificial neural networks and combined capacitance-based sensors to predict void fraction in two-phase annular fluids regardless of liquid phase type. *IEEE Access*, 11, pp.143745-143756.
- Bishop, C.M., and Nasrabadi, N.M., 2006. *Pattern Recognition and Machine Learning*. Springer, New York.
- Chen, T.C., Alizadeh, S.M., Alanazi, A.K., Grimaldo Guerrero, J.W., Abo-Dief, H.M., Eftekhari-Zadeh, E., and Fouladnia F., 2023. Using ANN and combined capacitive sensors to predict the void fraction for a two-phase homogeneous fluid independent of the liquid phase type. *Processes*, 11(3), p.940.
- Chicco, D., Warrens, M.J., and Jurman, G., 2021. The coefficient of determination R-squared is more informative than SMAPE, MAE, MAPE, MSE and RMSE in regression analysis evaluation. *PeerJ Computer Science*, 7, p.e623.
- Cui, Z., Zhang, Q., Gao, K., Xia, Z., and Wang, H., 2021. Electrical impedance sensors for multi-phase flow measurement: A review. *IEEE Sensors Journal*, 21(24), pp.27252-27267.
- Dong-Hui, L., Ying-Xiang, W., Zhi-Biao, L., and Xing-Fu, Z., 2005. Volumetric fraction measurement in oil-water-gas multiphase flow with dual energy gamma-ray system. *Journal of Zhejiang University-Science A*, 6, pp.1405-1411.
- Fouladnia, F., Alizadeh, S.M., Gorelkina, E.I., Hameed Shah, U., Nazemi, E., Guerrero, J.W., Roshani, G.H., and Imran, A., 2024. A novel metering system consists of capacitance-based sensor, gamma-ray sensor and ANN for measuring volume fractions of three-phase homogeneous flows. *Nondestructive Testing and Evaluation*, 8, pp.1-27.
- Geman, S., Bienenstock, E., and Doursat, R., 1992. Neural networks and the bias/variance dilemma. *Neural Computation*, 4(1), pp.1-58.
- Goodfellow, I., Bengio, Y., and Courville, A., 2016. *Deep Learning*. MIT Press, Cambridge, MA.
- Hammer, E.A., Johansen, G.A., Dyakowski, T., Roberts, E.P.L., Cullivan, J.C., Williams, R.A., Hassan, Y.A., and Claiborn, C.S., 2006. Advanced experimental techniques. In: Crowe, C.T., ed. *Multi-Phase Flow Handbook*. CRC Press, Boca Raton, FL.
- Hanus, R., Zych, M., Kusy, M., Roshani, G.H., and Nazemi, E., 2024. Application of selected methods of computational intelligence to recognition of the liquid-gas flow regime in pipeline by use gamma absorption and frequency domain feature extraction. *Measurement*, 238, p.115260.
- He, K., Zhang, X., Ren, S., and Sun, J., 2016. Deep Residual Learning for Image Recognition. In: *Proceedings of the IEEE Conference on Computer Vision and Pattern Recognition*, pp.770-778.
- Heindel, T.J., Gray, J.N., and Jensen, T.C., 2008. An X-ray system for visualizing fluid flows. *Flow Measurement and Instrumentation*, 19, pp.67-78.
- Hinton, G., Deng, L., Yu, D., Dahl, G.E., Mohamed, A.R., Jaitly, N., Senior, A., Vanhoucke, V., Nguyen, P., Sainath, T.N., and Kingsbury, B., 2012. Deep neural networks for acoustic modeling in speech recognition: The shared views of four research groups. *IEEE Signal Processing Magazine*, 29(6), pp.82-97.
- Ilyasu, A.M., Benselama, A.S., Bagaudinovna, D.K., Roshani, G.H., and Salama, A.S., 2023. Using particle swarm optimization and artificial intelligence to select the appropriate characteristics to determine volume fraction in two-phase flows. *Fractal and Fractional*, 7(4), p.283.
- Ilyasu, A.M., Fouladnia, F., Salama, A.S., Roshani, G.H., and Hirota, K., 2023. Intelligent measurement of void fractions in homogeneous regime of two phase flows independent of the liquid phase density changes. *Fractal and Fractional*, 7(2), p.179.
- Ilyasu, A.M., Shahsavari, M.H., Benselama, A.S., Nazemi, E., and Salama, A.S., 2024. An optimised and novel capacitance-based sensor design for measuring void fraction in gas-oil two-phase flow systems. *Nondestructive Testing and Evaluation*. 1-17.
- Levenberg, K., 1944. A method for the solution of certain non-linear problems in least squares. *Quarterly of Applied Mathematics*, 2, pp.164-168.
- Marquardt, D.W., 1963. An algorithm for least-squares estimation of nonlinear parameters. *Journal of the Society for Industrial and Applied Mathematics*, 11, pp.431-441.
- Mayet, A.M., Fouladnia, F., Alizadeh, S.M., Alhashim, H.H., Guerrero, J.W., Loukil, H., Parayangat, M., Nazemi, E., and Shukla, N.K., 2024. Measuring volume fractions of a three-phase flow without separation utilizing an approach based on artificial intelligence and capacitive sensors. *PLoS One*, 19(5), p.e0301437.
- Mayet, A.M., Ilyinichna, G.E., Fouladnia, F., Daoud, M.S., Ijyas, V.P.T., Shukla, N.K., and Habeeb, M.S., 2023. An artificial neural network and a combined capacitive sensor for measuring the void fraction independent of temperature and pressure changes for a two-phase homogeneous fluid. *Flow Measurement and Instrumentation*, 93, p.102406.
- Mohammed, S., Abdulkareem, L., Roshani, G.H., Eftekhari-Zadeh, E., and Haso, E., 2022. Enhanced multiphase flow measurement using dual non-intrusive techniques and ANN model for void fraction determination. *Processes*, 10(11), p.2371.
- Muhammad Ali, P.J., 2022. Investigating the impact of min-max data normalization on the regression performance of K-nearest neighbor with different similarity measurements. *Aro-the Scientific Journal of Koya University*, 10(1), pp.85-91.
- National Institute of Standards and Technology (NIST), 2023. *XCOM: Photon Cross Sections Database*. Available from: <https://physics.nist.gov/physrefdata/xcom/html/xcom1.html> [Last accessed on 2024 Sep 01].
- Oliveira, D.F., Nascimento, J.R., Marinho, C.A., and Lopes, R.T., 2015. Gamma transmission system for detection of scale in oil exploration pipelines. *Nuclear Instruments and Methods in Physics Research Section A: Accelerators, Spectrometers, Detectors and Associated Equipment*, 784, pp.616-620.
- Pan, Y., Li, C., Ma, Y., Huang, S., and Wang, D., 2019. Gas flow rate measurement in low-quality multiphase flows using Venturi and gamma ray. *Experimental Thermal and Fluid Science*, 100, pp.319-327.
- Peyvandi, R.G., and Rad, S.Z.I., 2017. Application of artificial neural networks for the prediction of volume fraction using spectra of gamma rays backscattered by three-phase flows. *European Physical Journal Plus*, 132, p.511.
- Qaisi, R.M., Fouladnia, F., Mayet, A.M., Guerrero, J.W., Loukil, H., Raja, M.R., Muqet, M.A., and Eftekhari-Zadeh, E., 2023. Intelligent measuring of

- the volume fraction considering temperature changes and independent pressure variations for a two-phase homogeneous fluid using an 8-electrode sensor and an ANN. *Sensors*, 23(15), p.6959.
- Roshani, G., Karami, A., Salehizadeh, A., and Nazemi, E., 2017. The capability of radial basis function to forecast the volume fractions of the annular three-phase flow of gas-oil-water. *Applied Radiation and Isotopes*, 129, pp.156-162.
- Roshani, M., Phan, G.T., Ali, P.J., Roshani, G.H., Hanus, R., Duong, T., Corniani, E., Nazemi, E., and Kalmoun, E.M., 2021. Evaluation of flow pattern recognition and void fraction measurement in two-phase flow independent of oil pipeline's scale layer thickness. *Alexandria Engineering Journal*, 60(1), pp.1955-1966.
- Salgado, C.M., Pereira, C.M., Schirru, R., and Brandão, L.E., 2010. Flow regime identification and volume fraction prediction in multiphase flows by means of gamma-ray attenuation and artificial neural networks. *Progress in Nuclear Energy*, 52(6), pp.555-562.
- Salgado, W.L., Dam, R.S., and Salgado, C.M., 2021. Optimization of a flow regime identification system and prediction of volume fractions in three-phase systems using gamma-rays and artificial neural network. *Applied Radiation and Isotopes*, 169, p.109552.
- Sheikh, S.I., Hassan, E.E., and Iqbal, S., 2019. Capacitance-based monitoring of a three-phase crude-oil flow. *IEEE Transactions on Instrumentation and Measurement*, 69(4), pp.1213-1218.
- Syah, R.B., Veisi, A., Hasibuan, Z.A., Al-Fayoumi, M.A., Daoud, M.S., and Eftekhari-Zadeh, E., 2023. A novel smart optimized capacitance-based sensor for annular two-phase flow metering with high sensitivity. *IEEE Access*, 11, pp.60709-60716.
- Teixeira, T.P., Salgado, C.M., Dam, R.S., and Salgado, W.L., 2018. Inorganic scale thickness prediction in oil pipelines by gamma-ray attenuation and artificial neural network. *Applied Radiation and Isotopes*, 141, pp.44-50.
- Veisi, A., Shahsavari, M.H., Roshani, G.H., Eftekhari-Zadeh, E., and Nazemi, E., 2023. Experimental study of void fraction measurement using a capacitance-based sensor and ANN in two-phase annular regimes for different fluids. *Axioms*, 12(1), p.66.
- Zhang, L., and Suganthan, P.N., 2016. A survey of randomized algorithms for training neural networks. *Information Sciences*, 364, pp.146-155.



# Surveillance of Antimicrobial Resistance in Iraq: A Comprehensive Data Collection Approach

Dhurgham K. Al-Fahad<sup>1</sup>, Jawad A. Alpofoad<sup>2</sup>, Mahmoud A. Chawsheen<sup>3,4†</sup>, Ahmed A. Al-Naqshbandi<sup>5</sup>, and Ali T. Abas<sup>1</sup>

<sup>1</sup>Department of Pharmaceutical Sciences, College of Pharmacy, University of Thi-Qar, Nasiriyah, 64001, F.R. Iraq.

<sup>2</sup>Department of Pharmaceutical Chemistry, College of Pharmacy, University of Thi-Qar, Nasiriyah, 64001, F.R. Iraq.

<sup>3</sup>Department of General Sciences, Faculty of Education, Soran University, Erbil, 44008, Kurdistan Region-F.R. Iraq.

<sup>4</sup>Medical Research Center, Hawler Medical University, Erbil, 44001, Kurdistan Region-F.R. Iraq.

<sup>5</sup>Department of Laboratory, Rizgary Teaching Hospital, Erbil, 44001, Kurdistan Region-F.R. Iraq.

**Abstract**—Antimicrobial resistance (AMR) generates serious negative impacts on health-care systems worldwide, and Iraq is not an exception. To uncover the prevalence of AMR and to visualize the magnitude of the multidrug-resistant (MDR) dilemma in Iraqi hospitals, this study is carried out. A total of 11592 clinical records from ten different health-care facilities in seven Iraqi provinces are collected and analyzed. Our data show that 4984 (43.0%) of all clinical samples are negative for bacterial growth. In adults, Gram-negative bacteria (GNB) represented 48.9% and Gram-positive bacteria (GPB) represented 51.1% of clinical isolates; in children, GNB represented 60.8% and GPB represented 39.2%. Furthermore, in adults, *Klebsiella pneumoniae* (30.1%) and *Staphylococcus aureus* (40.8%) are among the most common GNB and GPB isolates, respectively. In children, *K. pneumoniae* (37.9%) and *Staphylococcus haemolyticus* (41.8%) are the most common GNB and GPB, respectively. Adults' samples showed that *Escherichia coli* and *Proteus mirabilis* were the most resistant GNB; *S. aureus* and *Staphylococcus epidermidis* are among the most resistant GPB. In children, *K. pneumoniae* is found to be the most resistant GNB. This study confirms the persistence of antimicrobial resistance and multidrug-resistant gram negative and gram positive bacteria in adults and children alike. Ampicillin and oxacillin have been recognized as ineffective drugs in adults, and ampicillin, nafcillin, cefoxitin, and benzylpenicillin have been found to be highly resisted by pathogenic bacteria in children. The outcomes of this study confirm the necessity of conducting AMR

surveillance on a regular basis and establishing national antibiotic prescription guidelines to manage AMR development in Iraq.

**Index Terms**—Antimicrobial resistance, Multidrug resistant, *Klebsiella pneumoniae*, *Staphylococcus aureus*, *Escherichia coli*, Surveillance of AMR.

## I. INTRODUCTION

Antimicrobial resistance (AMR) is recognized as one of the global public health threats facing humanity (WHO, 2021). AMR is higher among populations of low- and middle-income countries in comparison with wealthy ones (Allel, et al., 2023). For decades now, AMR has been attracting more attention from researchers and policymakers worldwide for becoming an economic burden on the public health sector and for being linked to prolonged illnesses, extended hospitalization, and higher mortality rates (World Bank, 2017). Besides death, AMR may pose potential damage to humans, animals, plants, and food security alike (Murray, et al., 2022).

AMR could be defined as the failure of antibiotics to kill or inhibit microbial growth, and as a consequence, affected microorganisms become resistant to drugs that used to be effective in the past. Among the critical known factors involved in the emergence of AMR is the overuse of antibiotics and unnecessary clinical prescriptions (Coque, et al., 2023). At the molecular level, AMR is either intrinsic or acquired, and the latter is part of an evolutionary process taking place in microorganisms through mutations or horizontal gene transfer of mobile genetic elements from other microorganisms (Martínez, Coque and Baquero 2014).

The Middle East, like other regions of the world, suffers from AMR, but at different levels (Borgio, et al., 2021; Yıldız, et al., 2023; Torumkuney, et al., 2022a; Ruan,

ARO-The Scientific Journal of Koya University  
Vol. XII, No 2 (2024), Article ID: ARO.11689. 15 pages  
DOI: 10.14500/aro.11689

Received: 02 July 2024; Accepted: 27 October 2024

Regular research paper; Published: 19 November 2024

†Corresponding author's e-mail: mahmoud.hassan@soran.edu.iq

Copyright © 2024 Dhurgham K. Al-Fahad, Jawad A. Alpofoad, Mahmoud A. Chawsheen, Ahmed A. Al-Naqshbandi, and Ali T. Abas. This is an open access article distributed under the Creative Commons Attribution License (CC BY-NC-SA 4.0).



et al., 2023). The severity of AMR among the populations is reflected by the countermeasures that have been taken by local authorities to overcome or diminish this problem (Hassan, et al., 2023; Torumkuney, et al., 2022b). Iraq, like its neighboring countries, also suffers from AMR. AMR may have been growing worse in this country due to several factors, including political and economic instability, a lack of national antimicrobial guideline usage, and the challenging task of recovering the antibiotic prescription history of patients who visited hospitals for treatment. Meanwhile, troubling signs have been reported through several studies, suggesting the seriousness of this problem in Iraq (Häsler, et al., 2018; Raouf, et al., 2022; Abou Fayad, et al., 2023).

Studies on various regions and infection sites among Iraqi patients revealed differing rates of AMR and MDR pathogenic bacteria. Multidrug-resistant (MDR) *Enterococcus faecalis* and *Acinetobacter baumannii*, along with other Gram-positive bacteria (GPB) and Gram-negative bacteria (GNB), were isolated from patients with urinary tract infections (UTI) (Al-Jumaily and Zgaer, 2016; Al-Naqshbandi, et al., 2019). *Klebsiella pneumoniae* is linked to community-acquired pneumonia (Raouf, et al., 2022) and is the most common antibiotic-resistant pathogen identified in swabs from the nasal, oral, and groin regions of refugees recently immigrated to Germany (Häsler, et al., 2018). Methicillin-resistant *Staphylococcus aureus* and *Staphylococcus epidermidis* were isolated from patients with wound infections (Al-Naqshbandi, et al., 2021). MDR *Streptococcus parasanguinis* and *A. baumannii* were isolated from patients with lower respiratory tract infections (Chawsheen, Al-Naqshbandi and Abdulqader, 2020). MDR *Escherichia coli* has been isolated from various specimens, including urine, stool, blood, wound swabs, ear swabs, pus, abscess, sputum, and body fluids (Al-Hasani, Al-Rubaye, and Abdelhameed, 2023).

From what was mentioned earlier, there is clearly enough evidence suggesting the presence of AMR within Iraqi communities and, unfortunately, the existence of MDR pathogens as well. Most of the previous studies covered AMR-related pathogens only and in limited areas, such as a certain city or province. In this project, we aimed to investigate the prevalence and antimicrobial susceptibility, AMR rates, and MDR bacterial pathogens among local communities in seven different Iraqi provinces: Baghdad, Al-Anbar, Wasit, Babil, Maysan, Al-Najaf, and Dhi-Qar. This may help us to polymerize a comprehensive vision of the real scale of the AMR problem in Iraq. Moreover, a study like this one is a necessity to assist the health sector's policymakers in adopting legislation that culminates in issuing the National Antimicrobial Guidelines. Issuing such guidelines is, by itself, a crucial step toward overcoming or diminishing the AMR problem.

## II. MATERIALS AND METHODS

### A. Data Collection

A retrospective study was conducted on 11592 clinical records for samples collected during the period of July 2019–April 2021 from ten public hospitals and two private

laboratories in seven Iraqi provinces, as follows: Baghdad Hospital, Central Children Hospital, and Al-Buraq Lab (in Baghdad province); Al-Ramadi Hospital and Al-Ramadi Children Hospital (in Al-Anbar province); Al-Karama Hospital (in Wasit province); Babylon Hospital (in Babil province); Al-Sadr General Hospital (in Maysan province); Al-Hakeem Hospital, Al-Sadar Hospital, and Al-Amal Lab (in Al-Najaf province); and Al-Hussain Hospital (in Dhi-Qar) province (Fig. 1). Clinical specimens were collected from different sites, including urine, blood, stool, and swabs (wound, ear, nasal, oral, throat, and high vaginal swab), in addition to body fluids and discharges (ascites fluid, semen, pus, sputum, abscess, nipple discharges, and synovial fluid).

### B. Bacterial Culture and Identification

At all collection facilities, standard laboratory techniques were applied. After transferring clinical samples into the facilities' laboratories, samples were inoculated on Blood, MacConkey, Chocolate, Salmonella Shigella, Xylose Lysine Deoxycholate, and Thiosulfate–citrate–bile salts–sucrose agars, according to the type of specimens. During the inoculation process, striking methods (based on the type of specimen) were used to spread the specimens' inoculums on agar plates, and afterward, the plates were incubated overnight at 37°C. Aerobic bacterial growths were identified according to colony characteristics and Gram's staining by applying the Bhatia and Ichhpujani protocol (Bhatia and Ichhpujani, 2008). Identification of GPB, GNB, and antimicrobial sensitivity tests was performed following VITEK®2 compact system protocols using AST kits: VITEK®2 GN with reference numbers GN222, GN 69, 71, 76, and 82 and VITEK®2 GP Reference P580, P592, ST01, and ST03.

### C. Antibiotics

The above-mentioned health-care facilities have used VITEK®2 kits to investigate the following antibiotics: AM-Ampicillin, AMC-Amoxicillin/Clavulanic Acid, AN-Amikacin, ATM-Aztreonam, CAZ-Ceftazidime, C-Chloramphenicol, FOX-Cefoxitin, CRO-Ceftriaxone, CFM-Cefixime, CIP-Ciprofloxacin, CS-Colistin, CT-Ceftolozane/Tazobactam, CTX-Cefotaxime, CXMA-Cefuroxime axetil, CZA-Ceftazidime/Avibactam, CZ-Cefazolin, DO-Doxycycline, DOR-Doripenem, ETP-Ertapenem, FEP-Cefepime, FT-Nitrofurantoin, GM-Gentamicin, IPM-Imipenem, LEV-Levofloxacin, MEM-Meropenem, MNO-Minocycline, MUP-Mupirocin, MXF-Moxifloxacin, Nafcillin, OFL-Ofloxacin, P-Benzylpenicillin, PEF-Pefloxacin, TZP-Piperacillin/Tazobactam, PIP-Piperacillin, RA-Rifampicin, SAM-Ampicillin/Sulbactam, SPI-Piperacillin/Sulbactam, SXT-Trimethoprim/Sulfamethoxazole, TCC-Ticarcillin/Clavulanic Acid, TE-Tetracycline, TGC-Tigecycline, TIC-Ticarcillin, TMP-Trimethoprim, and TM-Tobramycin.

### D. Data Analysis

In regard to the recovered isolates' dominance and abundance, data were presented in percentages (%). When the resistance rate of recovered isolates toward a specific



Fig. 1. Map of Iraq and the administrative units (governorates). Numbers showing clinical cases in each of the seven governorates that data were collected from. The original “plain” map was sourced from www.burningcompass.com, and details were added by the authors.

antibiotic was  $\geq 70\%$ , they were considered to be resistant bacteria. For the collective antibiotic resistance in GPB and GNB, we also classified antibiotics that were resisted by 90% or more of the isolates as highly resisted drugs. The above-mentioned criteria were used in accordance with Al-Naqshbandi, et al. (2019).

### III. RESULTS AND DISCUSSION

#### A. Results

Our analysis of the collected data from the Iraqi hospitals revealed that out of 11592 tested clinical samples, 4984 (43.0%) were negative for bacterial growth, and the rest generated 3274 (49.5%) Gram-negative and 3334 (50.5%) Gram-positive pathogenic bacteria. Out of the total number of pathogenic isolates, 6248 (94.6%) were recovered from adults, and 360 (5.4%) were from children patients. From all recovered pathogenic GNB, 3055 (93.3%) of them were from adults and 219 (6.7%) of them were from children patients. Out of all pathogenic GPB isolates, 3193 (95.8%) were recovered from adults and 141 (4.2%) from children. In adults alone, GNB presented 48.9% and GPB 51.1% of the 6248 clinical isolates. In children only, GNB presented 60.8% and GPB 39.2% of 360 clinical isolates (Table I).

TABLE I  
THE DISTRIBUTION OF PATHOLOGIC BACTERIAL GROWTH IN CLINICAL SAMPLES FROM PATIENTS TREATED AT IRAQI HEALTH-CARE FACILITIES

All clinical cases	No. of pathogenic bacteria (%)	No. of negative growth (%)	Total (%)
	6608 (57.0)	4984 (43.0)	11592 (100)
Pathogenic isolates	No. (%)	Adults out of total	Children out of total
GNB	3274 (49.5)	3055 (93.3)	219 (6.7)
GPB	3334 (50.5)	3193 (95.8)	141 (4.2)
Total	6608	6248 (94.6)	360 (5.4)
	Adults only	Type of bacteria	No. of isolates
	6248 (94.6)	GNB	3055 (48.9)
		GPB	3193 (51.1)
	Children only	Type of bacteria	No. of isolates
	360 (5.4)	GNB	219 (60.8)
		GPB	141 (39.2)

GNB: Gram-negative bacteria; GPB: Gram-positive bacteria

The data also show that *K. pneumoniae* and *S. aureus* are among the most common GNB and GPB isolates, respectively, among the adult patients who attended Iraqi hospitals. In adult patients, it was also observed that the least detected GNB was *Acinetobacter haemolyticus*, and the least detected GPB was *Streptococcus alactolyticus*

TABLE II  
PREVALENCE OF GNB AND GPB IN ISOLATED SAMPLES OBTAINED FROM ADULTS AND CHILDREN PATIENTS IN IRAQI HEALTH-CARE FACILITIES

Adults			Children patients								
GNB	No.	%	GPB	No.	%	GNB	No.	%	GPB	No.	%
<i>Klebsiella pneumoniae</i>	921	30.1	<i>Staphylococcus aureus</i>	1304	40.8	<i>Klebsiella pneumoniae</i>	83	37.9	<i>Staphylococcus haemolyticus</i>	59	41.8
<i>Pseudomonas aeruginosa</i>	862	28.2	<i>Enterococcus faecalis</i>	443	13.9	<i>Pseudomonas aeruginosa</i>	51	23.3	<i>Staphylococcus aureus</i>	52	36.9
<i>Acinetobacter baumannii</i>	307	10	<i>Staphylococcus epidermidis</i>	417	13.1	<i>Acinetobacter baumannii</i>	37	16.9	<i>Staphylococcus epidermidis</i>	30	21.3
<i>Proteus mirabilis</i>	270	8.8	<i>Staphylococcus haemolyticus</i>	411	12.9	<i>Proteus mirabilis</i>	25	11.4	Total	141	100
<i>Enterobacter cloacae</i>	166	5.4	<i>Streptococcus agalactiae</i>	213	6.7	<i>Enterobacter cloacae</i>	23	10.5			
<i>Salmonella typhi</i>	88	2.9	<i>Staphylococcus hominis</i>	191	6	Total	219	100			
<i>Serratia marcescens</i>	82	2.7	<i>Streptococcus pneumoniae</i>	99	3.1						
<i>Klebsiella oxytoca</i>	65	2.1	<i>Enterococcus faecium</i>	78	2.4						
<i>Sphingomonas paucimobilis</i>	58	1.9	<i>Streptococcus alactolyticus</i>	19	0.6						
<i>Morganella morganii</i>	37	1.2	<i>Staphylococcus saprophyticus</i>	18	0.6						
<i>Enterobacter aerogenes</i>	34	1.1	Total	3193	100						
<i>Acinetobacter lwoffii</i>	26	0.9									
<i>Citrobacter freundii</i>	24	0.8									
<i>Serratia fonticola</i>	21	0.7									
<i>Pseudomonas fluorescens</i>	19	0.6									
<i>Pseudomonas luteola</i>	19	0.6									
<i>Shigella dysenteriae</i>	16	0.5									
<i>Achromobacter denitrificans</i>	14	0.5									
<i>Escherichia coli</i>	14	0.5									
<i>Acinetobacter haemolyticus</i>	12	0.4									
Total	3055	100									

GNB: Gram-negative bacteria; GPB: Gram-positive bacteria

and *Staphylococcus saprophyticus* (Tables II, S1-S3). *K. pneumoniae* was the predominant Gram-negative bacillus identified in pediatric patients, similar to adults. In regard to GPB, unlike adult patients, children showed *Staphylococcus haemolyticus* as the most common pathogenic bacteria. For children, the GNB, *Enterobacter cloacae*, and the GPB, *S. epidermidis*, were among the least detected pathogens (Tables II and S3).

The most resistant GNBs toward antibiotics in adults were *E. coli* and *Proteus mirabilis*. Whereas the first one was resistant to ampicillin, ceftriaxone, cefazolin, cefepime, and ceftiofex, the second one was resistant to ampicillin, trimethoprim/sulfamethoxazole, tetracycline, trimethoprim, and colistin. Furthermore, the GNBs that were resistant only to one type of antibiotic were *A. baumannii* (resistant to cefazolin), *Klebsiella oxytoca* (resistant to ampicillin), *Morganella morganii* (resistant to trimethoprim/sulfamethoxazole), and *Serratia marcescens* (resistant to cefazolin). Meanwhile, the most resistant GPB toward antibiotics in adults were *S. aureus*, *S. epidermidis*, *S. haemolyticus*, and *Staphylococcus hominis*, as they were all resistant to erythromycin, oxacillin, and benzylpenicillin. The least resistant GPBs were *Enterococcus faecium* and *Streptococcus agalactiae*, as they were both resistant only to tetracycline (Tables III and S1-S3).

In children, the situation was different, as the most resistant GNB was *K. pneumoniae* for resisting ampicillin, chloramphenicol, and ceftiofex, and the least resistant one was *Pseudomonas aeruginosa* for resisting nafcillin antibiotic only. Furthermore, for children, *S. epidermidis* and *S. haemolyticus* were the only spotted resistant pathogenic GPBs that were resistant to benzylpenicillin (Tables III and S3).

Collectively, while the most resisted antibiotic in GNB of the pathogenic isolates recovered from adults and children patients was ampicillin, the most resisted antibiotic in GPB was oxacillin in adults and benzylpenicillin in children (Table IV).

Nitrofurantoin was the least resisted antibiotic by GNB in adult and children isolates, being tolerated only by 5.8% and 10% of the isolates, respectively. For GPB isolates recovered from adults and children, linezolid and doripenem were the least resisted by 6.8% and 21.3%, respectively (Table IV).

### B. Discussion

The prevalence and rates of AMR among human populations vary, and this is due to socioeconomic factors, the rate of antibiotic consumption, access to clean water, sanitation, the rate of vaccination, and an efficient health-care system (Sriram, et al., 2021; Allel, et al., 2023). Lately, alarming signals of AMR have arisen in Iraq, necessitating thorough investigations to understand the scale of this dilemma. To better understand this issue and to cover as many clinical cases as possible, we have collected data from different public hospitals and private laboratories in Iraq. At the end of the collection process, a total of 11592 clinical records were retrieved and analyzed.

Our investigations showed that out of all recorded cases (from adults and children), 4984 were negative for bacterial growth (Table I). This may indicate that 43.0% of all clinical cases who suffered from certain health conditions were not caused by pathogenic bacteria, but still, their samples went through microbiology laboratories for suspected bacterial infections. In spite of the fact that this rate may be somehow

TABLE III  
THE MOST RESILIENT GNB AND GPB WERE RECOVERED FROM BOTH ADULT AND CHILDREN PATIENTS IN IRAQI HEALTH-CARE FACILITIES\*

GNB isolated from adults	Resisted antibiotics				
<i>Escherichia coli</i>	AM-Ampicillin	CRO-Ceftriaxone	CZ-Cefazolin	FEP-Cefepime	FOX-Cefoxitin
<i>Proteus mirabilis</i>	AM-Ampicillin	SXT-Trimethoprim/ Sulfamethoxazole	TE-Tetracycline	TMP-Trimethoprim	CS-Colistin
<i>Klebsiella pneumoniae</i>	AM-Ampicillin	CZ-Cefazolin	PIP-Piperacillin	TIC-Ticarcillin	
<i>Serratia fonticola</i>	CIP-Ciprofloxacin	CRO-Ceftriaxone	CZ-Cefazolin	LEV-Levofloxacin	
<i>Enterobacter cloacae</i>	CS-Colistin	CZ-Cefazolin	FOX-Cefoxitin		
<i>Pseudomonas aeruginosa</i>	AM-Ampicillin	CZ-Cefazolin	DOR-Doripenem		
<i>Enterobacter aerogenes</i>	CRO-Ceftriaxone	CZ-Cefazolin			
<i>Morganella morganii</i>	AM-Ampicillin	CZ-Cefazolin			
<i>Salmonella typhi</i>	AM-Ampicillin	CZ-Cefazolin			
<i>Acinetobacter baumannii</i>	CZ-Cefazolin				
<i>Klebsiella oxytoca</i>	AM-Ampicillin				
<i>Morganella morganii</i>	SXT-Trimethoprim/ Sulfamethoxazole				
<i>Serratia marcescens</i>	CZ-Cefazolin				
GNB isolated from adults	Resisted Antibiotics				
<i>Staphylococcus aureus</i>	E-Erythromycin	OX1-Oxacillin	P-Benzylpenicillin		
<i>Staphylococcus epidermidis</i>	E-Erythromycin	OX1-Oxacillin	P-Benzylpenicillin		
<i>Staphylococcus haemolyticus</i>	E-Erythromycin	OX1-Oxacillin	P-Benzylpenicillin		
<i>Staphylococcus hominis</i>	E-Erythromycin	OX1-Oxacillin	P-Benzylpenicillin		
<i>Enterococcus faecium</i>	E-Erythromycin	LEV-Levofloxacin			
<i>Staphylococcus saprophyticus</i>	E-Erythromycin	OX1-Oxacillin			
<i>Streptococcus pneumoniae</i>	E-Erythromycin	TE-Tetracycline			
<i>Enterococcus faecalis</i>	E-Erythromycin	TE-Tetracycline			
<i>Streptococcus alactolyticus</i>	E-Erythromycin	TE-Tetracycline			
<i>Enterococcus faecium</i>	TE-Tetracycline				
<i>Streptococcus agalactiae</i>	TE-Tetracycline				
GNB isolated from in Children patients	Resisted Antibiotics				
<i>Klebsiella pneumoniae</i>	AM-Ampicillin	C-Chloramphenicol	FOX-Cefoxitin		
<i>Acinetobacter baumannii</i>	FOX-Cefoxitin	Nafcillin			
<i>Enterobacter cloacae</i>	FOX-Cefoxitin	Nafcillin			
<i>Pseudomonas aeruginosa</i>	Nafcillin				
GPB isolated from Children patients	Resisted Antibiotics				
<i>Staphylococcus epidermidis</i>	P-Benzylpenicillin				
<i>Staphylococcus haemolyticus</i>	P-Benzylpenicillin				

\*This table displays only the isolates that have shown a resistance of 70% or higher to the specified antibiotic (s)

scary, similar and even higher ones have been reported in previous studies (Ibrahim, 2018; Al-Naqshbandi, et al., 2019; Allami, et al., 2021). The number of negative results may eventually cause tremendous pressure on hospitals with regard to time, effort, and resources. Thus, physicians may need to be more careful before deciding which cases should be sent to laboratories for analysis.

Our data also show that the distribution of the recovered isolates into GNB and GPB in adults was different than what has been seen in children, with 48.9% of GNB and 51.1% of GPB recovered from adults and 60.8% of GNB and 39.2% of GPB recovered from children (Table I). In this context, previous studies have shown that these values vary and fluctuate depending on age, sex, and site of infection (Lambers, et al., 2006; Allami, et al., 2021). Even within children, these fluctuations could be detected easily. For instance, Li, et al. (2021) reported that GPB represented more than 60% of all microorganisms isolated from cerebrospinal fluids; Dharmapalan, et al. (2017) explained in their study that 53.3% of bacteremia is promoted by GNB; Le Doare, et al. (2015) suggested that 66% of all isolates recovered from

children suffering from sepsis were of GNB; Ibrahim, (2018) uncovered that GNBs were isolated from more than 80% of all clinical cases attended intensive care units (ICU); and Salman, et al. (2022) concluded that GNB is more common in UTI.

Our analysis of children's patients' data also showed that the most common GNB and GPB were *K. pneumoniae* and *S. haemolyticus*, respectively. Moreover, the least detected GNB and GPB were *E. cloacae* and *S. epidermidis*, respectively. These findings were somehow consistent with previous studies, but the site of infection was found to be the most crucial factor in determining the prevalence of the recovered microorganism. GNBs such as *E. coli*, *Klebsiella* spp., *Shigella* spp., and *Pseudomonas* spp. are usually associated with digestive tract problems, and GPBs are rarely reported to be involved in such cases (Lambers, et al., 2006; Allami, et al., 2021). For the high rates of *Klebsiella* spp. detection (besides other multidrug-resistant [MDR] GNB) in children, Labib, et al. (2018) and Ibrahim, (2018) reported similar results for cases attending ICUs. Furthermore, Badry, Jameel and Mero (2014) reported that *Klebsiella* spp. placed second, after *E. coli*, for diarrheal children attending

TABLE IV

THE OVERALL RESISTANCE OF ISOLATED GNB AND GPB TO ANTIMICROBIALS IN SAMPLES COLLECTED FROM ADULT AND CHILDREN PATIENTS WHO WERE ADMITTED TO IRAQI HEALTH-CARE FACILITIES

Adults							
GNB				GPB			
Antimicrobial	R%	Antimicrobial	R%	Antimicrobial	R%	Antimicrobial	R%
AM-Ampicillin	91.1	GM-Gentamicin	36.5	OX1-Oxacillin	86	MXF-Moxifloxacin	4.9
TMP-Trimethoprim	80	CAZ-Ceftazidime	35.7	P-Benzylpenicillin	83.9	DAP-Daptomycin	4
CZ-Cefazolin	77.8	FOS-Fosfomycin	35	E-Erythromycin	74.9	TGC-Tigecycline	1.5
DOR-Doripenem	72	FOX-Cefoxitin	35	FOS-Fosfomycin	68.2	FT-Nitrofurantoin	0.4
SPI-Piperacillin/Sulbactam	68	LEV-Levofloxacin	33	TE-Tetracycline	60.5		
CZA-Ceftazidime/Avibactam	66	TZP-Piperacillin/Tazobactam	31.6	CTX-Cefotaxime	34		
CT-Ceftolozane/Tazobactam	64	ETP-Ertapenem	31.6	MUP-Mupirocin	31.5		
TIC-Ticarcillin	62.2	CS-Colistin	30.9	CIP-Ciprofloxacin	30.3		
CRO-Ceftriaxone	57.1	ATM-Aztreonam	30.5	CM-Clindamycin	28.3		
PIP-Piperacillin	54	FEP-Cefepime	29.8	CRO-Ceftriaxone	25.4		
SAM-Ampicillin/Sulbactam	52.1	MNO-Minocycline	29.6	LEV-Levofloxacin	24.5		
SXT-Trimethoprim/Sulfamethoxazole	51	MXF-Moxifloxacin	27.3	FA-Fusidic Acid	21.4		
C-Chloramphenicol	50	IPM-Imipenem	24.6	GM-Gentamicin	20.4		
TE-Tetracycline	50	PEF-Pefloxacin	24.3	RA-Rifampicin	18.9		
AMC-Amoxicillin/Clavulanic Acid	44.8	MEM-Meropenem	24.2	SXT-Trimethoprim/sulfamethoxazole	18.9		
TCC-Ticarcillin/Clavulanic Acid	41	AN-Amikacin	21.9	TM-Tobramycin	18.3		
CXMA-Cefuroxime Axetil	40.9	TGC-Tigecycline	13	AM-Ampicillin	14		
CXM-Cefuroxime	40.9	FT-Nitrofurantoin	5.8	C-Chloramphenicol	12.1		
TM-Tobramycin	38.5			VA-Vancomycin	10.6		
CFM-Cefixime	38.1			TEC-Teicoplanin	8.6		
CIP-Ciprofloxacin	37.2			LNZ-Linezolid	6.8		

Children patients					
GNB			GPB		
Antimicrobial	R%	Antimicrobial	R%	Antimicrobial	R%
AM-Ampicillin	96.9	DO-Doxycycline	30.2	P-Benzylpenicillin	81.6
Nafcillin	87.8	ATM-Aztreonam	20.5	SXT-Trimethoprim/Sulfamethoxazole	29.2
FOX-Cefoxitin	77.8	RA-Rifampicin	19.2	DO-Doxycycline	25.8
CRO-Ceftriaxone	46.7	FT-Nitrofurantoin	10	SAM-Ampicillin/Sulbactam	21.8
C-Chloramphenicol	39			DOR-Doripenem	21.3
SXT-Trimethoprim/Sulfamethoxazole	37.5				
TIC-Ticarcillin	34.6				

R, Resistance; Percentages of R = (number of tests with R response/total number of tests)\*100

hospitals in Duhok city. In a study that involved the isolation of bacteria from the blood stream of the pediatric population in India, *K. pneumoniae* and *S. aureus* placed first, GNB and GPB, respectively (Dharmapalan, et al., 2017).

This study also revealed that the most abundant GNB among adult patients was *K. pneumoniae*, and the least detected one was *A. haemolyticus*. For GPB in adults, the most common bacteria were *S. aureus*, and the least detected ones were *S. alactolyticus* and *S. saprophyticus*. As we explained with children's data, the site of infection in adults also plays an important role in explaining and comparing the prevalence of the above-mentioned GNB and GPB. Accordingly, in UTI patients, *E. coli* and *S. haemolyticus* were found to be the most prevalent GNB and GPB, respectively (Al-Naqshbandi, et al., 2019). While Raoofi, et al. (2023) reported that *E. coli* is the most dominant GNB in patients attending southern Iran hospitals, the majority of their data were extracted from UTI patients' records (Raoofi, et al., 2023). In a previous study of ours that covered isolates recovered from wound infections, GNB such as *E. coli* and *P. aeruginosa* and GPB such as *S. aureus* and *S. epidermidis* were found to

be the dominant pathogenic bacteria (Al-Naqshbandi, et al., 2021). In patients with lower respiratory tract infections, GNBs such as *A. baumannii* and *S. marcescens* and GPBs such as *S. parasanguinis* were among the most dominant pathogen isolates recovered in Erbil (Chawsheen, et al., 2020). Al-Jebouri and Mdish (2019) showed that GPBs were isolated from more than half of patients diagnosed with bacteriospermia, and the most dominant one was *S. aureus*. GNBs such as *E. coli*, *E. faecalis*, *K. pneumoniae*, *S. saprophyticus*, *P. mirabilis*, and *Neisseria gonorrhoeae* were also recovered from the semen of patients suffering from infertility problems (Al-Jebouri and Mdish, 2019).

We also evaluated the response of the detected pathogenic bacteria to a variety of antibiotics. Our data show that the most resilient GNB recovered from adults were *E. coli* and *P. mirabilis*, as the first one was resistant to ampicillin, ceftriaxone, cefazolin, cefepime, and cefoxitin, and the second one was resistant to ampicillin, trimethoprim/sulfamethoxazole, tetracycline, trimethoprim, and colistin. On the other hand, the most resilient GPBs were *S. aureus*, *S. epidermidis*, *S. haemolyticus*, and *S. hominis*, as all

of them were resistant to erythromycin, oxacillin, and benzylpenicillin. In regard to GNB recovered from children, *K. pneumoniae* was the most resilient, being resistant to ampicillin, chloramphenicol, and cefoxitin. *S. epidermidis* and *S. haemolyticus* were GPB recovered from children, and both were resistant to benzylpenicillin (Table S3). For the way that GNBs responded to ampicillin, previous studies reported similar results to ours. However, for the other antibiotics and bacteria, different results were reported. These studies indicated that antibiotics that were found to be ineffective in the Iraqi environment do not necessarily have the same outcomes in other countries (that is, the pathogenic isolates of the Iraqi environments are not identical to the same type of bacteria in other places in the world, and they do not respond to antibiotics in a similar way). This is mainly a reflection of the quality of health-care systems and the antibiotic prescribing guidelines that have been applied in these counties, which have definitely played a crucial role in diminishing AMR (Dharmapalan, et al., 2017; Li, et al., 2021; Alhumaid, et al., 2021). Furthermore, our findings clearly indicate the presence of MDR pathogenic bacteria among children and adult patients alike in Iraqi communities, and this is in agreement with previous studies reporting the same problem in the same or other locations within Iraq (Chawsheen, et al., 2020; Al-Naqshbandi, et al., 2021; Allami, et al., 2021; Hamza and Omran, 2022; Al-Hasani Al-Rubaye and Abdelhameed, 2023).

*E. coli*, for instance, is well known for being resistant to a wide range of antibiotics and at higher rates to ampicillin (Nji, et al., 2021). The mechanisms by which this bacterium acquires resistance toward different antibiotics include extended-spectrum  $\beta$ -lactamases, carbapenemases, 16S rRNA methylases, plasmid-mediated quinolone resistance genes, and *mcr* genes (Poirel, et al., 2018). Another study reported that in several clinical cases, *E. coli*, *P. mirabilis*, and *K. pneumoniae* showed the existence of plasmid ampC (pAmpC) in their genetic makeup (Santiago, et al., 2020).

For GPB, Xu, et al. (2020) reported in their study that many of their isolates of *S. epidermidis* and *S. aureus*, bearing MRSE, were associated with high resistance to penicillin and cefoxitin. The underlying mechanisms by which *S. aureus* and *S. epidermidis* show resistance toward antibiotics involve the following virulence genes: Staphyloxanthin crtN, hemolysin genes, capsular cap8H, toxic shock toxin *tst*, enterotoxin *sea*, *mecA*, *dfrG*, *tet*, *ermA*, *ermB*, and *ermC* (Ogundipe, et al., 2020; Derakhshan, Navidinia and Haghi, 2021; Mazloumi, Akbari and Yousefi, 2021).

Our evaluation of antibacterial resistance for all tested antibiotics “collectively” revealed that ampicillin, trimethoprim, cefazolin, and doripenem were resisted by 91.1, 80, 77.8, and 72%, respectively, of all GNB in adults. Our data also show that oxacillin, benzylpenicillin, and erythromycin were resisted by 86, 83.9, and 74.9%, respectively, by all GPB isolates. Among the children, these rates were different, as ampicillin, nafcillin, and cefoxitin were resisted by 96.9, 87.8, and 77.8%, respectively, by all GNBs, and benzylpenicillin was resisted by 81.6% of GPB (Table IV). These data suggest that the above-mentioned

antibiotics are becoming inefficient in treating infections caused by related pathogenic bacteria, and their prescriptions should be avoided through establishing a national guideline to overcome the AMR problem in Iraq.

The ineffectiveness of benzylpenicillin in fighting microorganisms isolated from children is a worldwide phenomenon that may require a profound measure to overcome it (Sivasankar, Goldman and Hoffman, 2023). Moreover, nitrofurantoin was found to be the least resisted antibiotic by GNB and GPB in adult and children patients. Accordingly, this drug could be recognized as the most effective drug against both GNB and GPB and may play an important role in eradicating the most resilient pathogenic bacteria in Iraqi hospitals. Nevertheless, this performance could be due to the low consumption and prescription rates of this antibiotic in Iraqi communities in comparison with other drugs, as a recent study indicates the emergence of AMR among UTI patients in association with this nitrofurantoin (Vallée, et al., 2023).

There is another threat that participates in accelerating AMR development, which is the spread of pandemics. The empirical approach to treating patients during the COVID-19 outbreak through unnecessary antibiotic prescriptions or usage, either by ordinary people or professionals, was found to contribute effectively to AMR progression (Raofi, et al., 2023; Rehman, 2023).

To promote health-care system efficiency in evaluating AMR in Iraq, the above-mentioned points should be taken seriously by the Ministry of Health. Moreover, by all means, the establishment of a uniform national antibiotic prescription guideline is a necessity to overcome the AMR challenge in this country; otherwise, it may get out of control and become a live-threat problem in the near future.

#### Limitation of the study

The authors of this study encountered the challenge of non-uniform records when collecting data from hospitals and laboratories in different governorates. Accordingly, they were unable to compare rates of prevalence of bacteria that are normally associated with certain sites of infection to their rates in previous studies “easily.” In addition, the targeted hospitals and laboratories have been using different AST kits of VITEK®2 compact systems, which has further complicated the interpretation of the extracted data.

#### IV. CONCLUSION

The outcome of this study indicates that more than 40% of clinical cases were not caused by bacterial infection, and it also confirms the persistence of AMR among Iraqi communities. This study uncovered the existence of GNB- and GPB-MDR pathogens in adults and children patients, respectively. Whereas in adults, *E. coli*, *P. mirabilis*, *K. pneumoniae*, *Serratia fonticola*, *E. cloacae*, *P. aeruginosa*, *S. aureus*, *S. epidermidis*, *S. haemolyticus*, and *S. hominis* were all identified as MDR pathogens, in children, *K. pneumoniae* was the only detected MDR pathogen.

Moreover, in adults, ampicillin and oxacillin have been recognized as ineffective drugs and trimethoprim, cefazolin, doripenem, oxacillin, benzylpenicillin, and erythromycin as highly resisted ones. In children, the detected bacteria were found to be highly resistant to ampicillin, nafcillin, cefoxitin, and benzylpenicillin. Moreover, nitrofurantoin was recognized as the most effective antibacterial drug against GNB and GPB in children and adults alike. Finally, this study supports the idea of running AMR surveillance at regular time intervals and establishing national antibiotic prescription guidelines to manage and overcome this problem in Iraq.

#### Supplementary Data

The supplementary data can be found at the end of this document.

#### ACKNOWLEDGMENT

We would like to express our gratitude to the directors and heads of laboratories at Baghdad Hospital, Central Children Hospital, and Al-Buraq Lab (Baghdad); Al-Ramadi Hospital and Al-Ramadi Children Hospital (Al-Anbar); Al-Karama Hospital (Wasit); Babylon Hospital (Babil); Al-Sadr General Hospital (Maysan); Al-Hakeem Hospital, Al-Sadar Hospital, and Al-Amal Lab (Al-Najaf); and Al-Hussain Hospital (Dhi-Qar) for their assistance during the data collection process.

#### REFERENCES

- Abou Fayad, A., Rizk, A., El Sayed, S., Kaddoura, M., Jawad, N.K., Al-Attar, A., Dewachi, O., Nguyen, V.K., and Sater, Z.A., 2023. Antimicrobial resistance and the Iraq wars: Armed conflict as an underinvestigated pathway with growing significance. *BMJ Global Health*, 7, p.e010863.
- Al-Hasani, H., Al-Rubaye, D., and Abdelhameed, A., 2023. The emergence of multidrug-resistant (MDR), extensively drug-resistant (XDR), and Pandrug-resistant (PDR) In Iraqi clinical isolates of *Escherichia coli*. *Journal of Population Therapeutics and Clinical Pharmacology*, 30, pp.469-482.
- Alhumaid, S., Al Mutair, A., Al Alawi, Z., Alzahrani, A.J., Tobaiqy, M., Alresasi, A.M., Bu-Shehab, I., Al-Hadary, I., Alhmeed, N., Alismail, M., Aldera, A.H., Alhbabi, F., Al-Shammari, H., Rabaan, A.A., and Al-Omari, A., 2021. Antimicrobial susceptibility of gram-positive and gram-negative bacteria: A 5-year retrospective analysis at a multi-hospital healthcare system in Saudi Arabia. *Annals of Clinical Microbiology and Antimicrobials*, 20, p.43.
- Al-Jebouri, M.M., and Mdish, S.A., 2019. Tracing of antibiotic-resistant bacteria isolated from semen of Iraqi males with primary infertility. *Open Journal of Urology*, 9, pp.19-29.
- Al-Jumaily, E.F.A., and Zgaer, S.H., 2016. Multidrug resistant *Proteus mirabilis* isolated from urinary tract infection from different hospitals in Baghdad City. *International Journal of Current Microbiology and Applied Sciences*, 5, pp.390-399.
- Allami, M., Mohammed, E.J., Alazzawi, F., and Bahreini, M., 2021. Prevalence and antibiotic resistance pattern of pathogenic bacteria isolated from urinary tract infections in Qal'at Saleh Hospital, Iraq. *Avicenna Journal of Clinical Microbiology and Infection*, 8, pp.117-122.
- Allel, K., Day, L., Hamilton, A., Lin, L., Furuya-Kanamori, L., Moore, C.E., Van Boeckel, T., Laxminarayan, R., and Yakob, L., 2023. Global antimicrobial-resistance drivers: An ecological country-level study at the human-animal interface. *The Lancet Planetary Health*, 7, pp.e291-e303.
- Al-Naqshbandi, A.A., Chawsheen, M.A., and Abdulqader, H.H., 2019. Prevalence and antimicrobial susceptibility of bacterial pathogens isolated from urine specimens received in Rizgary hospital-Erbil. *Journal of Infection and Public Health*, 12, pp.330-336.
- Al-Naqshbandi, A.A., Hassan, H.A., Chawsheen, M.A., and Abdul Qader, H.H., 2021. Categorization of Bacterial Pathogens Present in Infected Wounds and their Antibiotic Resistance Profile Recovered from Patients Attending Rizgary Hospital-Erbil. *Aro-the Scientific Journal of Koya University*, 9, pp.64-70.
- Badry, A., Jameel, A., and Mero, W., 2014. Pathogenic microorganisms associated with diarrhea in infants and children in Duhok Province, Kurdistan Region/Iraq. *Science Journal of University of Zakho*, 2, pp.266-275.
- Bhatia, R., and Ichhpujani, R.L., 2008. *Essentials of Medical Microbiology*. Jaypee Brothers Medical Publishers, New Delhi, p.47.
- Borgio, J.F., Rasdan, A.S., Sonbol, B., Alhamid, G., Almandil, N.B., and Abdulazeez, S., 2021. Emerging status of multidrug-resistant bacteria and fungi in the Arabian Peninsula. *Biology (Basel)*, 10, p.1144.
- Chawsheen, M.A., Al-Naqshbandi, A.A., and Abdulqader, H.H., 2020. Bacterial profile and antimicrobial susceptibility of isolates recovered from lower respiratory tract infection for patients in Rizgary Hospital, Erbil. *Aro-the Scientific Journal of Koya University*, 8, pp.64-70.
- Coque, T., Graham, D., Pruden, A., So, A., Topp, E., Echeverria, A., Vaughn Grooters, S., Halpaap, A., Hanna, N., and Salazar, M., 2023. *Bracing for Superbugs: Strengthening Environmental Action in the One Health Response to Antimicrobial Resistance*. UNEP-UN Environment Programme. Available from: <https://www.unep.org/resources/superbugs/environmental-action> [Last accessed on 2023 Sep 30].
- Derakhshan, S., Navidinia, M., and Haghi, F., 2021. Antibiotic susceptibility of human-associated *Staphylococcus aureus* and its relation to agr typing, virulence genes, and biofilm formation. *BMC Infectious Diseases*, 21, p.627.
- Dharmapalan, D., Shet, A., Yewale, V., and Sharland, M., 2017. High reported rates of antimicrobial resistance in Indian neonatal and pediatric blood stream infections. *Journal of the Pediatric Infectious Diseases Society*, 6, pp.e62-e68.
- Hamza, O.A., and Omran, R., 2022. Prevalence of multi-antibiotic resistant bacteria isolated from children with urinary tract infection from Baghdad, Iraq. *Journal of Biosciences and Medicines*, 10, pp.240-252.
- Häsler, R., Kautz, C., Rehman, A., Podschun, R., Gassling, V., Brzoska, P., Sherlock, J., Gräsner, J.T., Hoppenstedt, G., Schubert, S., Ferlinz, A., Lieb, W., Laudes, M., Heinsen, F.-A., Scholz, J., Harmsen, D., Franke, A., Eisend, S., Kunze, T., Fickenscher, H., Ott, S., Rosenstiel, P., and Schreiber, S., 2018. The antibiotic resistome and microbiota landscape of refugees from Syria, Iraq and Afghanistan in Germany. *Microbiome*, 6, p.37.
- Hassan, S.K., Dahmash, E.Z., Madi, T., Tarawneh, O., Jomhawi, T., Alkhob, W., Ghanem, R., and Halasa, Z., 2023. Four years after the implementation of antimicrobial stewardship program in Jordan: Evaluation of program's core elements. *Frontiers in Public Health*, 11, p.1078596.
- Ibrahim, M.E., 2018. High antimicrobial resistant rates among Gram-negative pathogens in intensive care units. *Saudi Medical Journal*, 39, pp.1035-1043.
- Labib, J.R., Ibrahim, S.K., Salem, M.R., Youssef, M.R.L., and Meligy, B., 2018. Infection with gram-negative bacteria among children in a tertiary pediatric hospital in Egypt. *American Journal of Infection Control*, 46, pp.798-801.
- Lambers, H., Piessens, S., Bloem, A., Pronk, H., and Finkel, P., 2006. Natural skin surface pH is on average below 5, which is beneficial for its resident flora. *International Journal of Cosmetic Science*, 28, pp.359-370.
- Le Doare, K., Bielicki, J., Heath, P.T., and Sharland, M., 2015. Systematic review of antibiotic resistance rates among gram-negative bacteria in children with sepsis in resource-limited countries. *Journal of the Pediatric Infectious Diseases Society*, 4, pp.11-20.
- Li, D., Zhang, X., Wang, Y., Xue, J., Ji, X., Shao, X., and Li, Y., 2021. Epidemiology and drug resistance of pathogens isolated from cerebrospinal fluids



- at a children's medical center in Eastern China during 2006-2020. *Infection and Drug Resistance*, 14, pp.5417-5428.
- Martínez, J.L., Coque, T.M., and Baquero, F., 2014. What is a resistance gene? Ranking risk in resistomes. *Nature Reviews Microbiology*, 13, pp.116-123.
- Mazloumi, M.J., Akbari, R., and Yousefi, S., 2021. Detection of inducible clindamycin resistance genes (ermA, ermB, and ermC) in *Staphylococcus aureus* and *Staphylococcus epidermidis*. *Microbiology and Biotechnology Letters*, 49, pp.449-457.
- Murray, C.J.L., Ikuta, K.S., Sharara, F., Swetschinski, L., Robles Aguilar, G., Gray, A., Han, C., Bisignano, C., Rao, P., Wool, E., Johnson, S.C., Browne, A.J., Chipeta, M.G., Fell, F.,... and, Naghavi, M., 2022. Global burden of bacterial antimicrobial resistance in 2019: A systematic analysis. *The Lancet*, 399, pp.629-655.
- Nji, E., Kazibwe, J., Hambridge, T., Joko, C.A., Larbi, A.A., Dampfey, L.A.O., Nkansa-Gyamfi, N.A., Stålsby Lundborg, C., and Lien, L.T.Q., 2021. High prevalence of antibiotic resistance in commensal *Escherichia coli* from healthy human sources in community settings. *Scientific Reports*, 11, p.3372.
- Ogundipe, F.O., Ojo, O.E., Feßler, A.T., Hanke, D., Awoyomi, O.J., Ojo, D.A., Akintokun, A.K., Schwarz, S., and Maurischat, S., 2020. Antimicrobial resistance and virulence of methicillin-resistant *Staphylococcus aureus* from human, chicken and environmental samples within live bird markets in three Nigerian Cities. *Antibiotics*, 9, p.588.
- Poirel, L., Madec, J.Y., Lupo, A., Schink, A.K., Kieffer, N., Nordmann, P., Schwarz, S., Aarestrup, F.M., Schwarz, S., Shen, J., and Cavaco, L., 2018. Antimicrobial resistance in *Escherichia coli*. *Microbiology Spectrum*, 6.
- Raoufi, R., Namavari, N., Rahmani, V., and Doustaghghi, M.H., 2023. Evaluation of antibiotics resistance in Southern Iran in light of COVID-19 pandemic: A retrospective observational study. *Health Science Reports*, 6, p.e1153.
- Raouf, F.E.A., Benyagoub, E., Alkudhairy, M.K., Akrami, S., and Saki, M., 2022. Extended-spectrum beta-lactamases among *Klebsiella pneumoniae* from Iraqi patients with community-acquired pneumonia. *Revista da Associação Médica Brasileira*, 68, pp.833-837.
- Rehman, S., 2023. A parallel and silent emerging pandemic: Antimicrobial resistance (AMR) amid COVID-19 pandemic. *Journal of Infection and Public Health*, 16, pp.611-617.
- Ruan, Z., Bizri, A.R., El-Fattah, A.A., Bazaraa, H.M., Al Ramahi, J.W., Matar, M., Ali, R.A.N., El Masry, R., Moussa, J., Abbas, A.J.A., and Aziz, M.A., 2023. Antimicrobial resistance landscape and COVID-19 impact in Egypt, Iraq, Jordan, and Lebanon: A survey-based study and expert opinion. *PLoS One*, 18, p.e0288550.
- Salman, H.A., Alhameedawi, A.K., Muhamad, S.M.S.G., and Taha, Z., 2022. Prevalence of multi-antibiotic resistant bacteria isolated from children with urinary tract infection from Baghdad, Iraq. *Microbiology and Biotechnology Letters*, 50, pp.147-156.
- Santiago, G.S., Gonçalves, D., Da Silva Coelho, I., De Mattos De Oliveira Coelho, S., and Neto Ferreira, H., 2020. Conjugative plasmidic AmpC detected in *Escherichia coli*, *Proteus mirabilis* and *Klebsiella pneumoniae* human clinical isolates from Portugal. *Brazilian Journal of Microbiology*, 51, pp.1807-1812.
- Sivasankar, S., Goldman, J.L., and Hoffman, M.A., 2023. Variation in antibiotic resistance patterns for children and adults treated at 166 non-affiliated US facilities using EHR data. *JAC-Antimicrobial Resistance*, 5, p.dlac128.
- Sriram, A., Kalanxhi, E., Kapoor, G., Craig, J., Balasubramanian, R., Brar, S., Criscuolo, N., Hamilton, A., Klein, E., and Tseng, K., 2021. State of the world's antibiotics 2021: A global analysis of antimicrobial resistance and its drivers. Center for Disease Dynamics, Economics and Policy, Washington, DC, USA, pp.1-115.
- Torumkuney, D., Behbehani, N., Van Hasselt, J., Hamouda, M., and Keles, N., 2022a. Country data on AMR in Kuwait in the context of community-acquired respiratory tract infections: Links between antibiotic susceptibility, local and international antibiotic prescribing guidelines, access to medicine and clinical outcome. *Journal of Antimicrobial Chemotherapy*, 77, pp.i77-i83.
- Torumkuney, D., Dolgum, S., Van Hasselt, J., Abdullah, W., and Keles, N., 2022b. Country data on AMR in Saudi Arabia in the context of community-acquired respiratory tract infections: Links between antibiotic susceptibility, local and international antibiotic prescribing guidelines, access to medicine and clinical outcome. *Journal of Antimicrobial Chemotherapy*, 77, pp.i70-i76.
- Vallée, M., Harding, C., Hall, J., Aldridge, P.D., and Tan, A., 2023. Exploring the *in situ* evolution of nitrofurantoin resistance in clinically derived uropathogenic *Escherichia coli* isolates. *Journal of Antimicrobial Chemotherapy*, 78, pp.373-379.
- World Bank (WB), 2017. *Drug-Resistant Infections: A Threat to Our Economic Future*. International Bank for Reconstruction and Development. The World Bank, United States.
- World Health Organization (WHO), 2021. *Antimicrobial Resistance*. World Health Organization. Available from: <https://www.who.int/news-room/fact-sheets/detail/antimicrobial-resistance> [Last accessed on 2023 Jan 01].
- Xu, Z., Cave, R., Chen, L., Yangkyi, T., Liu, Y., Li, K., Meng, G., Niu, K., Zhang, W., Tang, N., Shen, J., and Mkrtychyan, H.V., 2020. Antibiotic resistance and molecular characteristics of methicillin-resistant *Staphylococcus epidermidis* recovered from hospital personnel in China. *Journal of Global Antimicrobial Resistance*, 22, pp.195-201.
- Yıldız, S.S., Hekimoğlu, C.H., Sucaklı, M.B., Bakkaloğlu, Z., Çevik, Y.N., Ünalı, Ö., Arslantürk, H., Zikusooka, M., Keçik, M., Nellums, L., and Elci, O.C., 2023. Community-acquired antimicrobial resistance among Syrian refugees and the local population in Türkiye. *European Journal of Public Health*, 33, pp.809-814.

## SUPPLEMENTARY DATA

TABLE S1  
RESPONSES OF ISOLATED GNB TO DIFFERENT ANTIMICROBIAL DRUGS IN IRAQI HEALTH-CARE FACILITIES

Antibiotics VS GNB	<i>Achromobacter denitrificans</i> No. (14) (%)	<i>Acinetobacter baumannii</i> No. (307) (%)	<i>Acinetobacter haemolyticus</i> No. (12) (%)	<i>Acinetobacter hwoffii</i> No. (26) (%)	<i>Citrobacter freundii</i> No. (24) (%)	<i>Enterobacter aerogenes</i> No. (34) (%)	<i>Enterobacter cloacae</i> No. (166) (%)	<i>Escherichia coli</i> No. (14) (%)	<i>Klebsiella oxytoca</i> No. (65) (%)	<i>Klebsiella pneumoniae</i> No. (921) (%)
AM-Ampicillin	NT	NT	NT	NT	NT	NT	NT	R9 (90), S1 (10)	R30 (76.92), S9 (23.08)	R454 (95.18), S23 (4.82)
AMC-Amoxicillin/Clavulanic Acid	NT	NT	NT	NT	NT	NT	R7 (63.64), S4 (36.36)	NT	NT	R22 (36.07S39) (63.93)
AN-Amikacin	R5 (45.45S6) (54.55)	NT	R1 (10), S9 (90)	R1 (4.35), S22 (95.65)	R0 (0), S17 (100)	R2 (8.33), S22 (91.67)	R20 (15.38), S110 (84.62)	R4 (28.57), S10 (71.43)	R4 (7.14), S52 (92.86)	R138 (23.83), S441 (76.17)
ATM-Aztreonam	NT	NT	NT	NT	NT	R3 (25), S9 (75)	R14 (21.21), S52 (78.79)	NT	R0 (0), S17 (100)	R126 (38.77), S199 (61.23)
CAZ-Ceftazidime	R1 (9.09), S10 (90.91)	R145 (60.42), S95 (39.58)	R2 (20), S8 (80)	R6 (27.27), S16 (72.73)	R5 (29.41), S12 (70.59)	R10 (40), S15 (60)	R34 (25), S102 (75)	NT	R7 (12.5), S49 (87.5)	R295 (37.53), S491 (62.47)
CIP-Ciprofloxacin	R4 (36.36), S7 (63.64)	R153 (63.49), S88 (36.51)	R3 (30), S7 (70)	R1 (4.55), S21 (95.45)	R3 (17.65), S14 (82.35)	R11 (42.31), S15 (57.69)	R18 (12.95), S121 (87.05)	R7 (50), S7 (50)	R7 (12.5), S49 (87.5)	R269 (33.75), S528 (66.25)
CRO-Ceftriaxone	NT	R75 (66.37), S38 (33.63)	NT	NT	NT	R15 (83.33), S3 (16.67)	R44 (51.76), S41 (48.24)	R9 (90), S1 (10)	R12 (25), S36 (75)	R340 (61.15), S216 (38.85)
CS-Colistin	NT	R6 (4.69), S122 (95.31)	NT	R0 (0), S13 (100)	NT	NT	R78 (89.66), S9 (10.34)	NT	NT	R7 (14.58), S41 (85.42)
CZ-Cefazolin	NT	R101 (90.18), S11 (9.82)	NT	NT	NT	R17 (94.44), S1 (5.56)	R78 (89.66), S9 (10.34)	R9 (90), S1 (10)	R25 (52.08), S23 (47.92)	R411 (73.79), S146 (26.21)
ETP-Ertapenem	NT	NT	NT	NT	NT	R2 (11.11), S16 (88.89)	R21 (22.83), S71 (77.17)	NT	R3 (6.25), S45 (93.75)	R129 (23.04), S431 (76.96)
FEP-Cefepime	R5 (45.45), S6 (54.55)	R123 (52.56), S111 (47.44)	R0 (0), S10 (100)	R1 (4.35), S22 (95.65)	R3 (17.65), S14 (82.35)	R8 (32), S17 (68)	R30 (22.22), S105 (77.78)	R12 (85.71), S2 (14.29)	R3 (5.36), S53 (94.64)	R259 (32.74), S532 (67.26)
FOX-Cefoxitin	NT	NT	NT	NT	NT	R8 (57.14), S6 (42.86)	R48 (80), S12 (20)	R8 (80), S2 (20)	R9 (23.08), S30 (76.92)	R152 (36.28), S267 (63.72)
FT-Nitrofurantoin	NT	NT	NT	NT	NT	R0 (0), S15 (100)	R2 (2.9), S67 (97.1)	R3 (30), S7 (70)	R0 (0), S39 (100)	R17 (3.7), S443 (96.3)
GM-Gentamicin	R4 (36.36), S7 (63.64)	R129 (52.87), S115 (47.13)	R2 (20), S8 (80)	R0 (0), S21 (100)	R3 (17.65), S14 (82.35)	R10 (38.46), S16 (61.54)	R40 (28.78), S99 (71.22)	R7 (50), S7 (50)	R7 (12.5), S49 (87.5)	R293 (36.67), S506 (63.33)
Antibiotics VS GNB	<i>Achromobacter denitrificans</i> No. (14) (%)	<i>Acinetobacter baumannii</i> No. (307) (%)	<i>Acinetobacter haemolyticus</i> No. (12) (%)	<i>Acinetobacter hwoffii</i> No. (26) (%)	<i>Citrobacter freundii</i> No. (24) (%)	<i>Enterobacter aerogenes</i> No. (34) (%)	<i>Enterobacter cloacae</i> No. (166) (%)	<i>Escherichia coli</i> No. (14) (%)	<i>Klebsiella oxytoca</i> No. (65) (%)	<i>Klebsiella pneumoniae</i> No. (921) (%)
IPM-Imipenem	R0 (0), S11 (100)	R130 (54.39), S109 (45.61)	R0 (0), S10 (100)	R0 (0), S19 (100)	R0 (0), S17 (100)	R2 (8), S23 (92)	R26 (18.98), S111 (81.02)	R6 (42.86), S8 (57.14)	R3 (5.36), S53 (94.64)	R152 (19.24), S638 (80.76)
LEV-Levofloxacin	NT	R63 (52.94), S56 (47.06)	NT	NT	NT	R11 (57.89), S8 (42.11)	R10 (11.11), S80 (88.89)	R5 (50), S5 (50)	R6 (12.5), S42 (87.5)	R182 (32.21), S383 (67.79)
MEM-Meropenem	NT	R88 (55.7), S70 (44.3)	NT	R0 (0), S15 (100)	R0 (0), S11 (100)	R1 (9.09), S10 (90.91)	R10 (13.89), S62 (86.11)	NT	R0 (0), S17 (100)	R66 (20.31), S259 (79.69)
MNO-Minocycline	NT	R29 (22.31), S101 (77.69)	NT	R0 (0), S15 (100)	NT	NT	R5 (11.63), S38 (88.37)	NT	NT	R62 (27.56), S163 (72.44)
PEF-Pefloxacin	NT	NT	NT	NT	NT	NT	NT	NT	NT	R9 (18.75), S39 (81.25)
PIP-Piperacillin	NT	R87 (66.92), S43 (33.08)	NT	R5 (38.46), S8 (61.54)	NT	NT	R16 (34.04), S31 (65.96)	NT	NT	R188 (79.32), S49 (20.68)

(Contd...)

TABLE S1  
(CONTINUED)

Antibiotics VS GNB	Antibiotics VS GNB									
	<i>Achromobacter denitrificans</i> No. (14) (%)	<i>Acinetobacter baumannii</i> No. (307) (%)	<i>Acinetobacter haemolyticus</i> No. (12) (%)	<i>Acinetobacter hwoffii</i> No. (26) (%)	<i>Citrobacter freundii</i> No. (24) (%)	<i>Enterobacter aerogenes</i> No. (34) (%)	<i>Enterobacter cloacae</i> No. (166) (%)	<i>Escherichia coli</i> No. (14) (%)	<i>Klebsiella oxytoca</i> No. (65) (%)	<i>Klebsiella pneumoniae</i> No. (921) (%)
SAM-Ampicillin/Sulfactam	NT	R22 (53.66), S19 (46.34)	NT	NT	NT	NT	NT	NT	NT	R84 (59.15), S58 (40.85)
SXT-Trimethoprim/Sulfamethoxazole	R2 (18.18), S9 (81.82)	R119 (51.97), S110 (48.03)	NT	R1 (6.25), S15 (93.75)	R7 (43.75), S9 (56.25)	R16 (61.54), S10 (38.46)	R42 (30.88), S94 (69.12)	R9 (69.23), S4 (30.77)	R15 (26.79), S41 (73.21)	R436 (55.4), S351 (44.6)
TCC-Ticarcillin/Clavulanic Acid	NT	R79 (66.39), S40 (33.61)	NT	R1 (7.69), S12 (92.31)	NT	NT	R4 (11.76), S30 (88.24)	NT	NT	R60 (46.15), S70 (53.85)
TGC-Tigecycline	NT	R4 (3.7), S104 (96.3)	NT	NT	NT	R0 (0), S18 (100)	R2 (2.38), S82 (97.62)	R0 (0), S10 (100)	R0 (0), S48 (100)	R32 (6.26), S479 (93.74)
TIC-Ticarcillin	NT	R85 (69.11), S38 (30.89)	NT	R3 (25), S9 (75)	NT	NT	R14 (32.56), S29 (67.44)	NT	NT	R206 (93.21), S15 (6.79)
TM-Tobramycin	NT	R83 (48.54), S88 (51.46)	NT	R0 (0), S18 (100)	NT	R3 (23.08), S10 (76.92)	R14 (19.18), S59 (80.82)	NT	R3 (17.65), S14 (82.35)	R149 (39.01), S233 (60.99)
TZP-Piperacillin/Tazobactam	R2 (18.18), S9 (81.82)	R154 (63.37), S89 (36.63)	R2 (20), S8 (80)	R3 (23.08), S10 (76.92)	R3 (18.75), S13 (81.25)	R9 (34.62), S17 (65.38)	R30 (22.56), S103 (77.44)	R9 (64.29), S5 (35.71)	R5 (8.93), S51 (91.07)	R245 (31.33), S537 (68.67)
Antibiotics VS GNB	<i>Morganella morganii</i> Proteus mirabilis									
	No. (37) (%)	No. (270) (%)	<i>Pseudomonas aeruginosa</i> No. (862) (%)	<i>Pseudomonas fluorescens</i> No. (19) (%)	<i>Pseudomonas luteola</i> No. (19) (%)	<i>Salmonella typhi</i> No. (88) (%)	<i>Serratia fonticola</i> No. (21) (%)	<i>Serratia marcescens</i> No. (82) (%)	<i>Shigella dysenteriae</i> No. (16) (%)	<i>Shingomonas paucimobilis</i> No. (58) (%)
AM-Ampicillin	R12 (100), S0 (0)	R58 (82.86), S12 (17.14)	R35 (79.55), S9 (20.45)	NT	NT	R30 (81.08), S7 (18.92)	NT	NT	NT	NT
AMC-Amoxicillin/Clavulanic Acid	NT	R4 (25), S12 (75)	R23 (62.16), S14 (37.84)	NT	NT	NT	NT	NT	NT	NT
AN-Amikacin	R2 (6.06), S31 (93.94)	R7 (5.07), S131 (94.93)	R195 (33.39), S389 (66.61)	R4 (30.77), S9 (69.23)	R2 (20), S8 (80)	R1 (1.82), S54 (98.18)	R1 (7.14), S13 (92.86)	R3 (6.12), S46 (93.88)	NT	R2 (5.88), S32 (94.12)
ATM-Aztreonam	R5 (21.74), S18 (78.26)	R15 (11.63), S114 (88.37)	NT	NT	NT	R22 (50), S22 (50)	NT	R6 (23.08), S20 (76.92)	NT	R10 (55.56), S8 (44.44)
C-Chloramphenicol	NT	R5 (50), S5 (50)	NT	NT	NT	NT	NT	NT	NT	NT
CAZ-Ceftazidime	R6 (17.14), S29 (82.86)	R69 (37.3), S116 (62.7)	R213 (32.08), S451 (67.92)	R0 (0), S13 (100)	R0 (0), S10 (100)	R49 (68.06), S23 (31.94)	R4 (30.77), S9 (69.23)	R6 (10.91), S49 (89.09)	R0 (0), S15 (100)	R5 (13.16), S33 (86.84)
CFM-Cefixime	NT	R6 (54.55), S5 (45.45)	NT	NT	NT	R2 (20), S8 (80)	NT	NT	NT	NT
CIP-Ciprofloxacin	R15 (42.86), S20 (57.14)	R78 (41.27), S111 (58.73)	R309 (46.05), S362 (53.95)	R3 (25), S9 (75)	R2 (20), S8 (80)	R1 (1.37), S72 (98.63)	R10 (71.43), S4 (28.57)	R7 (12.73), S48 (87.27)	R0 (0), S13 (100)	R9 (23.68), S29 (76.32)
CRO-Ceftriaxone	R2 (11.11), S16 (88.89)	R55 (55.56), S44 (44.44)	R26 (55.32), S21 (44.68)	NT	NT	R32 (65.31), S17 (34.69)	R8 (80), S2 (20)	R14 (41.18), S20 (58.82)	NT	R3 (11.54), S23 (88.46)
CS-Colistin	NT	R22 (100), S0 (0)	R138 (27.06), S372 (72.94)	NT	NT	R0 (0), S14 (100)	NT	NT	NT	R6 (54.55), S5 (45.45)
CT-Ceftolozane/Tazobactam	NT	NT	R32 (64), S18 (36)	NT	NT	NT	NT	NT	NT	NT
CXM-Cefuroxime	NT	R7 (63.64), S4 (36.36)	NT	NT	NT	R2 (18.18), S9 (81.82)	NT	NT	NT	NT
CXMA-Cefuroxime axetil	NT	R7 (63.64), S4 (36.36)	NT	NT	NT	R2 (18.18), S9 (81.82)	NT	NT	NT	NT

(Contd...)

TABLE S1  
(CONTINUED)

Antibiotics VS GNB	<i>Achromobacter denitrificans</i> No. (14) (%)	<i>Acinetobacter baumannii</i> No. (307) (%)	<i>Acinetobacter haemolyticus</i> No. (12) (%)	<i>Acinetobacter lwoffi</i> No. (26) (%)	<i>Citrobacter freundii</i> No. (24) (%)	<i>Enterobacter aerogenes</i> No. (34) (%)	<i>Enterobacter cloacae</i> No. (166) (%)	<i>Escherichia coli</i> No. (14) (%)	<i>Klebsiella oxytoca</i> No. (65) (%)	<i>Klebsiella pneumoniae</i> No. (921) (%)
CZ-Cefazolin	R17 (94.44), S1 (5.56)	R60 (68.18), S28 (31.82)	R156 (89.66), S18 (10.34)	NT	NT	R29 (72.5), S11 (27.5)	R9 (90), S1 (10)	R34 (100), S0 (0)	NT	R4 (16), S21 (84)
CZA-Ceftazidime/Avibactam	NT	NT	R33 (66), S17 (34)	NT	NT	NT	NT	NT	NT	NT
DOR-Doripenem	NT	NT	R36 (72), S14 (28)	NT	NT	NT	NT	NT	NT	NT
ETP-Ertapenem	R2 (11.11), S16 (88.89)	R6 (6.67), S84 (93.33)	NT	NT	NT	R0 (0), S43 (100)	R1 (9.09), S10 (90.91)	R3 (8.33), S33 (91.67)	NT	NT
FEP-Cefepime	R3 (8.33), S33 (91.67)	R39 (19.7), S159 (80.3)	R180 (26.99), S487 (73.01)	R2 (16.67), S10 (83.33)	R0 (0), S10 (100)	R43 (55.13), S35 (44.87)	R3 (21.43), S11 (78.57)	R7 (12.73), S48 (87.27)	R0 (0), S14 (100)	R2 (6.06), S31 (93.94)
FOX-Cefoxitin	R0 (0), S11 (100)	R5 (8.93), S51 (91.07)	NT	NT	NT	R0 (0), S35 (100)	NT	R3 (13.64), S19 (86.36)	NT	NT
Antibiotics VS GNB	<i>Morganella morganii</i> No. (37) (%)	<i>Proteus mirabilis</i> No. (270) (%)	<i>Pseudomonas aeruginosa</i> No. (862) (%)	<i>Pseudomonas fluorescens</i> No. (19) (%)	<i>Pseudomonas luteola</i> No. (19) (%)	<i>Salmonella typhi</i> No. (88) (%)	<i>Serratia fonticola</i> No. (21) (%)	<i>Serratia marcescens</i> No. (82) (%)	<i>Shigella dysenteriae</i> No. (16) (%)	<i>Sphingomonas paucimobilitis</i> No. (58) (%)
FT-Nitrofurantoin	R0 (0), S12 (100)	R0 (0), S69 (100)	R23 (52.27), S21 (47.73)	NT	NT	R0 (0), S36 (100)	NT	R0 (0), S27 (100)	NT	NT
GM-Gentamicin	R19 (54.29), S16 (45.71)	R55 (29.89), S129 (70.11)	R278 (41.55), S391 (58.45)	R2 (16.67), S10 (83.33)	R2 (20), S8 (80)	R2 (2.7), S72 (97.3)	R5 (33.33), S10 (66.67)	R14 (25.45), S41 (74.55)	R0 (0), S16 (100)	R7 (17.95), S32 (82.05)
IPM-Imipenem	R1 (2.86), S34 (97.14)	R18 (9.89), S164 (90.11)	R234 (35.45), S426 (64.55)	R4 (36.36), S7 (63.64)	R0 (0), S10 (100)	R0 (0), S69 (100)	R1 (7.69), S12 (92.31)	NT	R0 (0), S15 (100)	R2 (5.26), S36 (94.74)
LEV-Levofloxacin	R3 (15), S17 (85)	R31 (31), S69 (69)	R107 (46.93), S121 (53.07)	NT	NT	R2 (4), S48 (96)	R8 (80), S2 (20)	R2 (5.71), S33 (94.29)	NT	R5 (19.23), S21 (80.77)
MEM-Meropenem	R1 (4.35), S22 (95.65)	R3 (2.33), S126 (97.67)	R167 (31.45), S364 (68.55)	NT	NT	R0 (0), S46 (100)	R1 (20), S4 (80)	R1 (3.57), S27 (96.43)	R0 (0), S13 (100)	R2 (10.53), S17 (89.47)
MNO-Minocycline	R9 (56.25), S7 (43.75)	R66 (61.68), S41 (38.32)	R20 (45.45), S24 (54.55)	R1 (10), S9 (90)	NT	R0 (0), S36 (100)	NT	R4 (22.22), S14 (77.78)	R0 (0), S11 (100)	R2 (15.38), S11 (84.62)
MXF-Moxifloxacin	NT	R3 (27.27), S8 (72.73)	NT	NT	NT	NT	NT	NT	NT	NT
PEF-Pefloxacin	NT	R6 (50), S6 (50)	R3 (21.43), S11 (78.57)	NT	NT	NT	NT	NT	NT	NT
PIP-Piperacillin	R6 (35.29), S11 (64.71)	R48 (44.44), S60 (55.56)	R214 (43.76), S275 (56.24)	NT	NT	R24 (60), S16 (40)	NT	R10 (52.63), S9 (47.37)	NT	R2 (16.67), S10 (83.33)
SAM-Ampicillin/Sulbactam	NT	R13 (29.55), S31 (70.45)	R27 (65.85), S14 (34.15)	NT	NT	R2 (12.5), S14 (87.5)	NT	NT	NT	NT
SPI-Piperacillin/Sulbactam	NT	NT	R34 (68), S16 (32)	NT	NT	NT	NT	NT	NT	NT
SXT-Trimethoprim/Sulfamethoxazole	R29 (82.86), S6 (17.14)	R157 (83.96), S30 (16.04)	R2 (55.32), S42 (44.68)	R4 (36.36), S7 (63.64)	NT	R3 (4.17), S69 (95.83)	R6 (46.15), S7 (53.85)	R7 (13.21), S46 (86.79)	NT	R9 (25), S27 (75)
TCC-Ticarcillin/Clavulanic Acid	R0 (0), S14 (100)	R3 (4.17), S69 (95.83)	R217 (44.93), S266 (55.07)	NT	NT	R2 (10), S18 (90)	NT	R5 (41.67), S7 (58.33)	NT	R1 (9.09), S10 (90.91)
TE-Tetracycline	NT	R10 (83.33), S2 (16.67)	NT	NT	NT	R1 (10), S9 (90)	NT	NT	NT	NT

(Contd...)

TABLE S1  
(CONTINUED)

Antibiotics VS GNB	<i>Achromobacter denitrificans</i> No. (14) (%)	<i>Acinetobacter baumannii</i> No. (307) (%)	<i>Acinetobacter haemolyticus</i> No. (12) (%)	<i>Acinetobacter lwoffii</i> No. (26) (%)	<i>Citrobacter freundii</i> No. (24) (%)	<i>Enterobacter aerogenes</i> No. (34) (%)	<i>Enterobacter cloacae</i> No. (166) (%)	<i>Escherichia coli</i> No. (14) (%)	<i>Klebsiella oxytoca</i> No. (65) (%)	<i>Klebsiella pneumoniae</i> No. (921) (%)
TGC-Tigeicycline	R0 (0), S20 (100)	R9 (10.47), S77 (89.53)	R97 (68.31), S45 (31.69)	NT	NT	R0 (0), S49 (100)	R0 (0), S10 (100)	R3 (10), S27 (90)	NT	R1 (4.76), S20 (95.24)
TIC-Ticarcillin	R7 (46.67), S8 (53.33)	R47 (48.96), S49 (51.04)	R263 (54.91), S216 (45.09)	NT	NT	R18 (64.29), S10 (35.71)	NT	R6 (33.33), S12 (66.67)	NT	R2 (16.67), S10 (83.33)
TM-Tobramycin	R7 (30.43), S16 (69.57)	R55 (41.04), S79 (58.96)	R277 (45.04), S338 (54.96)	R1 (10), S9 (90)	NT	R0 (0), S39 (100)	NT	R7 (22.58), S24 (77.42)	R0 (0), S13 (100)	R3 (12.5), S21 (87.5)
TMP-Trimethoprim	NT	R8 (80), S2 (20)	NT	NT	NT	NT	NT	NT	NT	NT
TZP-Piperacillin/Tazobactam	R1 (2.86), S34 (97.14)	R7 (3.8), S177 (96.2)	R247 (38.65), S392 (61.35)	R3 (30), S7 (70)	NT	R1 (1.43), S69 (98.57)	R2 (14.29), S12 (85.71)	NT	R0 (0), S15 (100)	R6 (18.18), S27 (81.82)

NT, not tested; R, Resistance; S, Sensitive; No., number of samples; Percentages of R or S = (number of tests with R or S response/total number of tests)\*100

TABLE S2  
RESPONSES OF ISOLATED GPB TO DIFFERENT ANTIMICROBIAL DRUGS IN IRAQI HEALTH-CARE FACILITIES

Antibiotics VS GPB	<i>Enterococcus faecalis</i> No. (443) (%)	<i>Enterococcus faecium</i> No. (78) (%)	<i>Staphylococcus aureus</i> No. (1304) (%)	<i>Staphylococcus epidermidis</i> No. (417) (%)	<i>Staphylococcus haemolyticus</i> No. (411) (%)	<i>Staphylococcus hominis</i> No. (191) (%)	<i>Staphylococcus saprophyticus</i> No. (18) (%)	<i>Streptococcus agalactiae</i> No. (213) (%)	<i>Streptococcus alactolyticus</i> No. (19) (%)	<i>Streptococcus pneumoniae</i> No. (99) (%)
AM-Ampicillin	R3 (6.67), S42 (93.33)	NT	NT	NT	NT	NT	NT	R15 (15.79), S80 (84.21)	R3 (30), S7 (70)	NT
C-Chloramphenicol	NT	NT	NT	NT	NT	NT	NT	R8 (10.13), S71 (89.87)	NT	R5 (17.86), S23 (82.14)
CIP-Ciprofloxacin	R14 (28), S36 (72)	NT	R10 (9.26), S98 (90.74)	R10 (14.08), S61 (85.92)	R75 (59.52), S51 (40.48)	R8 (25.81), S23 (74.19)	NT	NT	NT	NT
CM-Clindamycin	NT	NT	R330 (29.86), S775 (70.14)	R50 (16.18), S259 (83.82)	R84 (27.36), S223 (72.64)	R33 (24.63), S101 (75.37)	R5 (35.71), S9 (64.29)	R48 (32.21), S101 (67.79)	NT	R36 (65.45), S19 (34.55)
CRO-Ceftriaxone	NT	NT	NT	NT	NT	NT	NT	R16 (18.39), S71 (81.61)	NT	R20 (36.36), S35 (63.64)
CTX-Cefotaxime	NT	NT	NT	NT	NT	NT	NT	R19 (22.09), S67 (77.91)	R5 (50), S5 (50)	R27 (50), S27 (50)
DAP-Daptomycin	R0 (0), S16 (100)	NT	R2 (4.08), S47 (95.92)	R0 (0), S30 (100)	R3 (4.62), S62 (95.38)	R2 (14.29), S12 (85.71)	NT	NT	NT	NT
E-Erythromycin	R185 (72.83), S69 (27.17)	R22 (88), S3 (12)	R763 (70.26), S323 (29.74)	R219 (73.49), S79 (26.51)	R250 (93.98), S16 (6.02)	R115 (87.79), S16 (12.21)	R12 (85.71), S2 (14.29)	R48 (57.14), S36 (42.86)	R7 (70), S3 (30)	R43 (79.63), S11 (20.37)
FA-Fusidic Acid	NT	NT	R171 (16.51), S865 (83.49)	R94 (29.19), S228 (70.81)	R79 (23.8), S253 (76.2)	R47 (32.87), S96 (67.13)	R4 (25), S12 (75)	NT	NT	NT

(Contd...)

TABLE S2  
(CONTINUED)

Antibiotics VS GPB	<i>Enterococcus faecalis</i> No. (443) (%)	<i>Enterococcus faecium</i> No. (78) (%)	<i>Staphylococcus aureus</i> No. (1304) (%)	<i>Staphylococcus epidermidis</i> No. (417) (%)	<i>Staphylococcus haemolyticus</i> No. (411) (%)	<i>Staphylococcus hominis</i> No. (191) (%)	<i>Staphylococcus saprophyticus</i> No. (18) (%)	<i>Streptococcus agalactiae</i> No. (213) (%)	<i>Streptococcus alactolyticus</i> No. (19) (%)	<i>Streptococcus pneumoniae</i> No. (99) (%)
FOS-Fosfomicin	NT	NT	R259 (69.44), S114 (30.56)	R17 (58.62), S12 (41.38)	R13 (59.09), S9 (40.91)	NT	NT	NT	NT	NT
FT-Nitrofurantoin	R1 (0.41), S240 (99.59)	R0 (0), S27 (100)	R3 (0.28), S1071 (99.72)	R0 (0), S271 (100)	R0 (0), S227 (100)	R0 (0), S125 (100)	R0 (0), S14 (100)	R0 (0), S70 (100)	NT	NT
GM-Gentamicin	NT	NT	R224 (19.68), S914 (80.32)	R41 (12.46), S288 (87.54)	R123 (37.16), S208 (62.84)	R9 (6.21), S136 (93.79)	R3 (20), S12 (80)	NT	NT	NT
LEV-Levofloxacin	R87 (39.91), S131 (60.09)	R17 (77.27), S5 (22.73)	R223 (21.78), S801 (78.22)	R31 (12.2), S223 (87.8)	R80 (40), S120 (60)	R18 (15.79), S96 (84.21)	R3 (23.08), S10 (76.92)	R32 (20.92), S121 (79.08)	R2 (20), S8 (80)	R13 (23.64), S42 (76.36)
LNZ-Linezolid	R40 (13.70), S252 (86.30)	R3 (8.11), S34 (91.89)	R69 (5.84), S1113 (94.16)	R16 (4.66), S327 (95.34)	R19 (5.35), S336 (94.65)	R23 (14.94), S131 (85.06)	R3 (18.75), S13 (81.25)	R3 (1.76), S167 (98.24)	R0 (0), S10 (100)	R2 (3.64), S53 (96.36)
MUP-Mupirocin	NT	NT	R119 (31.48), S259 (68.52)	NT	NT	NT	NT	NT	NT	NT
MXF-Moxifloxacin	NT	NT	R62 (5.47), S1072 (94.53)	R2 (0.64), S310 (99.36)	R4 (1.38), S285 (98.62)	R4 (2.82), S138 (97.18)	R0 (0), S15 (100)	R22 (14.29), S132 (85.71)	R2 (25), S6 (75)	R8 (27.59), S21 (72.41)
OX1-Oxacillin	NT	NT	R937 (83.96), S179 (16.04)	R294 (90.74), S30 (9.26)	R306 (93.58), S21 (6.42)	R107 (75.35), S35 (24.65)	R10 (71.43), S4 (28.57)	NT	NT	NT
P-Benzylpenicillin	R0 (0), S16 (100)	NT	R776 (90.87), S78 (9.13)	R107 (90.68), S11 (9.32)	R156 (95.71), S7 (4.29)	R49 (83.05), S10 (16.95)	NT	R20 (22.99), S67 (77.01)	NT	R25 (46.3), S29 (53.7)
Antibiotics VS GPB	<i>Enterococcus faecalis</i> No. (443) (%)	<i>Enterococcus faecium</i> No. (78) (%)	<i>Staphylococcus aureus</i> No. (1304) (%)	<i>Staphylococcus epidermidis</i> No. (417) (%)	<i>Staphylococcus haemolyticus</i> No. (411) (%)	<i>Staphylococcus hominis</i> No. (191) (%)	<i>Staphylococcus saprophyticus</i> No. (18) (%)	<i>Streptococcus agalactiae</i> No. (213) (%)	<i>Streptococcus alactolyticus</i> No. (19) (%)	<i>Streptococcus pneumoniae</i> No. (99) (%)
RA-Rifampicin	NT	NT	R212 (18.73), S920 (81.27)	R44 (14.1), S268 (85.9)	R78 (26.99), S211 (73.01)	R26 (18.44), S115 (81.56)	R2 (14.29), S12 (85.71)	NT	NT	R2 (6.9), S27 (93.1)
SXT-Trimethoprim/ Sulfamethoxazole	R11 (23.40), S36 (76.60)	NT	R169 (15.36), S931 (84.64)	R30 (12.1), S218 (87.9)	R134 (42.95), S178 (57.05)	R19 (17.76), S88 (82.24)	R4 (33.33), S8 (66.67)	R2 (2.17), S90 (97.83)	NT	R1 (2.63), S37 (97.37)
TE-Tetracycline	R217 (81.27), S50 (18.73)	R23 (85.19), S4 (14.81)	R667 (58.87), S466 (41.13)	R157 (48.16), S169 (51.84)	R165 (50.3), S163 (49.7)	R57 (39.86), S86 (60.14)	R8 (57.14), S6 (42.86)	R145 (87.88), S20 (12.12)	R7 (70), S3 (30)	R48 (87.27), S7 (12.73)
TEC-Teicoplanin	R33 (11.42), S256 (88.58)	R14 (37.84), S23 (62.16)	R72 (6.09), S1110 (93.91)	R26 (7.65), S314 (92.35)	R28 (7.91), S326 (92.09)	R28 (18.06), S127 (81.94)	R3 (18.75), S13 (81.25)	NT	NT	NT
TGC-Tigecycline	R10 (3.50), S276 (96.50)	R1 (2.7), S36 (97.3)	R13 (1.11), S1155 (98.89)	R3 (0.88), S339 (99.12)	R4 (1.13), S351 (98.87)	R4 (2.58), S151 (97.42)	R1 (6.25), S15 (93.75)	R1 (0.63), S158 (99.37)	NT	R0 (0), S29 (100)
TM-Tobramycin	NT	NT	R210 (20.47), S816 (79.53)	R28 (10.89), S229 (89.11)	R47 (22.93), S158 (77.07)	R8 (7.02), S106 (92.98)	R2 (15.38), S11 (84.62)	NT	NT	NT
VA-Vancomycin	R26 (10.61), S219 (89.39)	R8 (38.1), S13 (61.9)	R122 (11.47), S942 (88.53)	R22 (7.46), S273 (92.54)	R21 (7.02), S278 (92.98)	R20 (16), S105 (84)	R4 (26.67), S11 (73.33)	R12 (7.59), S146 (92.41)	R1 (10), S9 (90)	R6 (10.91), S49 (89.09)

NT, not tested; R, Resistance; S, Sensitive; No., number of samples; Percentages of R or S = (number of tests with R or S response/total number of tests)\*100

TABLE S3  
RESPONSES OF GNB AND GPB THAT WERE ISOLATED IN IRAQI CHILDREN PATIENTS TO VARIOUS ANTIMICROBIAL AGENTS

Antibiotics	GNB Isolates				
	<i>Acinetobacter baumannii</i> No. (37) (%)	<i>Enterobacter cloacae</i> No. (23) (%)	<i>Klebsiella pneumoniae</i> No. (83) (%)	<i>Proteus mirabilis</i> No. (25) (%)	<i>Pseudomonas aeruginosa</i> No. (51) (%)
AM-Ampicillin	NT	NT	R63 (96.92), S2 (3.08)	NT	NT
ATM-Aztreonam	NT	R3 (13.64), S19 (86.36)	R18 (21.95), S64 (78.05)	R0 (0), S25 (100)	R15 (31.91), S32 (68.09)
C-Chloramphenicol	NT	NT	R12 (70.59), S5 (29.41)	R4 (16.67), S20 (83.33)	NT
CRO-Ceftriaxone	R24 (68.57), S11 (31.43)	R8 (36.36), S14 (63.64)	R41 (50), S41 (50)	R11 (44), S14 (56)	R15 (31.25), S33 (68.75)
DO-Doxycycline	R19 (54.29), S16 (45.71)	R4 (18.18), S18 (81.82)	R12 (14.63), S70 (85.37)	R11 (44), S14 (56)	R18 (37.5), S30 (62.5)
FOX-Cefoxitin	R9 (75), S3 (25)	R10 (76.92), S3 (23.08)	R51 (78.46), S14 (21.54)	NT	NT
FT-Nitrofurantoin	R2 (8.7), S21 (91.3)	NT	NT	NT	R4 (10.81), S33 (89.19)
Nafcillin	R9 (75), S3 (25)	R12 (100), S0 (0)	R55 (85.94), S9 (14.06)	NT	R10 (100), S0 (0)
RA-Rifampicin	NT	R1 (7.69), S12 (92.31)	R14 (21.54), S51 (78.46)	NT	NT
SXT-Trimethoprim/ Sulfamethoxazole	R16 (45.71), S19 (54.29)	R7 (33.33), S14 (66.67)	R39 (48.15), S42 (51.85)	R5 (20.83), S19 (79.17)	R11 (23.4), S36 (76.6)
TIC-Ticarcillin	NT	R9 (69.23), S4 (30.77)	R18 (27.69), S47 (72.31)	NT	NT
TM-Tobramycin	NT	R0 (0), S13 (100)	R0 (0), S65 (100)	NT	NT
Antibiotics	GPB Isolates				
	<i>Staphylococcus aureus</i> No. (52)	<i>Staphylococcus epidermidis</i> No. (30)	<i>Staphylococcus haemolyticus</i> No. (59)		
DO-Doxycycline	R3 (6.25), S45 (93.75)	R2 (8.33), S22 (91.67)	R28 (50), S28 (50)		
DOR-Doripenem	R7 (14.58), S41 (85.42)	R7 (30.43), S16 (69.57)	R13 (23.21), S43 (76.79)		
OFL-Ofloxacin	R0 (0), S21 (100)	NT	R0 (0), S23 (100)		
P-Benzylpenicillin	R14 (51.85), S13 (48.15)	R15 (100), S0 (0)	R33 (97.06), S1 (2.94)		
SAM-Ampicillin/Sulbactam	R2 (4.17), S46 (95.83)	R13 (54.17), S11 (45.83)	R13 (23.21), S43 (76.79)		
SXT-Trimethoprim/ Sulfamethoxazole	R2 (4.08), S47 (95.92)	R10 (40), S15 (60)	R26 (46.43), S30 (53.57)		

NT, not tested; R, Resistance; S, Sensitive; No., number of samples; Percentages of R or S = (number of tests with R or S response/total number of tests)\*100

# Artificial Intelligence Integration in Academic Writing: Insights from the University of Duhok

Deldar M. Abdulah<sup>1</sup>, Burhan A. Zaman<sup>2†</sup>, Zuhair R. Mustafa<sup>3</sup> and Lokman H. Hassan<sup>4</sup>

<sup>1</sup>Community and Maternity Nursing Unit, College of Nursing, University of Duhok, Duhok, Kurdistan Region - F.R. Iraq

<sup>2</sup>Department of Basic Sciences, College of Pharmacy, University of Duhok, Duhok, Kurdistan Region - F.R. Iraq

<sup>3</sup>Department of Adult and Fundamentals of Nursing, College of Nursing, University of Duhok, Duhok, Kurdistan Region - F.R. Iraq

<sup>4</sup>Department of Electrical and Computer Engineering, College of Engineering, University of Duhok, Duhok, Kurdistan Region - F.R. Iraq

**Abstract**—This study investigates the use of artificial intelligence (AI) technologies among academics at the University of Duhok (UoD), focusing on their perspectives, preferences, and intentions toward integrating AI within academic and research environments. A survey was conducted through Google Forms, targeting post-graduate students, recent alumni (since 2020), and faculty members of UoD in the Kurdistan region of Iraq. A total of 674 participants, aged 22–70 years, responded. The findings indicate that only 36.94% had employed AI technologies. Among AI users (n = 249), primary sources of information were friends or colleagues (46.59%) and social media (35.74%). Younger individuals and those holding master's degrees exhibited a stronger tendency toward AI usage ( $p < 0.0001$ ), whereas gender and academic discipline had minimal influence. ChatGPT was the most widely used tool (70.68%), followed by Quill Bot (42.17%), Grammarly (34.94%), and Google Bard (29.32%). The main AI applications were text paraphrasing (33.73%) and information retrieval (15.26%). Notably, 47.58% of respondents recommended AI for various academic tasks, including scientific research and idea generation. In conclusion, the study shows that only one-third of UoD faculty members utilize AI, predominantly for text paraphrasing. Nearly half of the participants suggested the adoption of AI by post-graduate students and academic staff.

**Index Terms**— Academic writing, Artificial intelligence, Technology adoption, University of Duhok.

## I. INTRODUCTION

Time is an invaluable resource, and advancements in artificial intelligence (AI) present new opportunities to optimize its use.

ARO-The Scientific Journal of Koya University  
Vol. XII, No. 2 (2024), Article ID: ARO.11794. 7 pages  
DOI: 10.14500/aro.11794

Received: 28 August 2024; Accepted: 04 November 2024

Regular research paper; Published: 20 November 2024

†Corresponding author's e-mail: burhan.zaman@uod.ac

Copyright © 2024 Deldar M. Abdulah, Burhan A. Zaman, Zuhair R. Mustafa, Lokman H. Hassan. This is an open-access article distributed under the Creative Commons Attribution License (CC BY-NC-SA 4.0).



Although AI language models have been in development for several years, their potential and widespread adoption became significantly more recognized following the launch of these technologies in November 2022 that enhance human-computer communication (Kacena, Plotkin and Fehrenbacher, 2024). AI technologies have significantly impacted industries such as healthcare, finance, and education by improving operational efficiency, enhancing decision-making, and providing innovative solutions (Coenen, et al., 2021; Nazari, Shabbir and Setiawan, 2021; Zhao, 2023). AI is transforming key sectors such as medicine (e.g., diagnostic algorithms) (Cestonaro, et al., 2023), education (e.g., personalized learning platforms) (Zohuri and Mossavar-Rahmani, 2024), business (e.g., automation of processes) (Aldoseri, Al-Khalifa and Hamouda, 2023), and scientific writing (e.g., automated text generation) (Kumar, Manikandan and Kishore, 2024); for instance, in medicine, AI enhances healthcare by assisting providers in making accurate diagnoses, identifying health risks, and developing personalized treatment plans. It also supports medical professionals in analyzing large datasets, uncovering patterns that may be overlooked by humans, thereby improving diagnostic accuracy and enabling more individualized therapeutic interventions. In addition, AI facilitates continuous patient health monitoring, aiding in the early detection of chronic diseases and predicting potential health risks (King, 2023).

Recently, AI-driven writing aids have garnered increasing interest within English as Foreign Language (EFL) communities. For writers learning EFL, the process of English writing presents significant challenges due to language barriers (Zhao, 2023). Some argue that the primary difficulty faced by EFL post-graduate students in academic writing is linguistic complexity. Studies have shown that digital writing tools can positively impact English writing proficiency (Nobles and Paganucci, 2015). Hence, it is proposed that AI-powered writing tools could serve as effective aids in fostering learning behaviors and promoting technology acceptance among non-native post-graduate students in the realm of English academic writing, primarily



through formative feedback and assessment (Coenen, et al., 2021; Nazari, Shabbir and Setiawan, 2021; Barrot, 2022).

Conversely, the utilization of these tools raises numerous ethical concerns, including the potential for plagiarism and inaccuracies (Khalil and Er, 2023; Steponenaite and Barakat, 2023), as well as access inequality, where certain institutions may lack the resources to fully benefit from AI's advancements (Imran, 2023; Farahani and Ghasemi, 2024). Consequently, there is an imminent need for consensus on how to regulate these technologies in scientific writing (Salvagno, Taccone and Gerli, 2023). In addition, Zhao (2023) argued that relatively few technologies have been developed to support writers during the actual process of writing. Moreover, while many writing tools focus on the revision and editing stages, offering services such as grammar correction and similarity reports is essential (Winans, 2021). Although much research has been done on AI integration in academic settings, studies focusing on developing regions, such as the Kurdistan Region of Iraq, remain scarce. Therefore, this study aims to fill this gap by providing real-world data on AI adoption and its challenges in this context. As well, it aims to investigate the adoption of AI technologies among academicians at the University of Duhok (UoD) in the Kurdistan Region of Iraq, exploring their perspectives, preferences, and intentions regarding the utilization of AI technologies in academic and research settings.

## II. METHODS

### A. Study Design and Sampling

This survey-based study targeted post-graduate students, recent graduates (from 2020 onward), and academic staff at the UoD, a leading public university in the Kurdistan Region of Iraq. The purpose of the study was to assess the usage and application of AI technologies within academic settings. The survey was administered using Google Forms, ensuring wide accessibility to participants. The study link was disseminated through official university email channels coordinated by the Quality Assurance and Post-graduate Affairs departments, providing access to all academic staff. In addition, Post-graduate Affairs representatives distributed the survey link to post-graduate students and recent graduates through established social media groups. It is important to note that AI optimization processes were excluded from the scope of this study. A preliminary pilot test was conducted with a small subset of participants to validate the survey. The topics examined included types of AI usage, reasons for use, and recommendations for AI adoption, ensuring that potential over- or underestimation of results was carefully considered. Since the survey was anonymous, the risk of bias in the responses was minimized. The results of the pilot study confirmed the reliability of the survey, allowing us to proceed with the full study.

### B. Setting

Since 1992, the UoD has been the largest public university in the Duhok Governorate and one of the most distinguished

universities in the Kurdistan Region of Iraq. With an enrollment of nearly 22,000 undergraduate students, 1,272 post-graduate students, and a faculty of 2,000 academic staff across 20 colleges, the institution offers diverse academic programs in disciplines including medicine, humanities, science, engineering, and agriculture. The survey aimed to gather responses from as many participants as possible. To enhance participation, reminders were sent throughout the 20-day data collection period, which lasted from February 21, 2024, to March 12, 2024. A total of 674 participants completed the survey. Data curation and visualization were meticulously handled by the first author. It is worth mentioning that inclusion criteria were strictly enforced to ensure that only post-graduate students, recent graduates, and academic staff from the UoD participated.

### C. Statistical Analyses

Participant characteristics were summarized using descriptive statistics, with age presented as mean and standard deviation, and categorical variables as frequencies and percentages. The prevalence of AI usage and the participants' perceptions were also reported as percentages. To examine the differences in AI usage across various participant characteristics, we employed the Pearson chi-squared test. The p-value was used to determine whether there is a statistically significant difference in the prevalence of AI use in participants with different characteristics. In addition, the motivations for and suggestions regarding AI use were analyzed using descriptive statistics (percentages). All statistical analyses were performed using JMP Pro version 17.3.0.

### D. Ethical Views

Participation in this study was voluntary, and participants' confidentiality was strictly protected throughout the research process. Ethical approval was obtained from the Scientific Affairs Department at the UoD before the commencement of the study.

## III. RESULTS

The study included participants of various ages and educational backgrounds, encompassing both genders. The age range spanned from 22 to 70 years, with a mean age of 37.65 years. Participants consisted of post-graduate students, graduates, and academic staff, with 52.67% holding M.Sc. degrees and 47.33% holding Ph.D. degrees. They represented diverse fields of study, including humanities (44.81%), medical/veterinary (24.78%), and science, engineering, and agriculture (30.42%). Results indicated that younger individuals and those with M.Sc. degrees were more inclined to utilize AI tools ( $p < 0.0001$ ). However, no significant differences were observed based on gender ( $p = 0.6362$ ) or educational field ( $p = 0.1569$ ) (Table I).

The research revealed that 36.94% of the participants at UoD had utilized AI tools. However, a significant portion had not yet used AI (55.04%) or were unaware of what it entailed

TABLE I  
GENERAL CHARACTERISTICS AND AI USE AMONG POST-GRADUATE STUDENTS AND ACADEMIC STAFF OF THE UNIVERSITY OF DUHOK

General characteristics	All participants no (%) (n=674)	Using AI (n=620) no (%)		p-value
		Not AI users (371, 55.04%)	AI users (249, 36.94%)	
Age (22–70 years.) mean (SD)	37.65 (7.57)	39.39 (7.68)	35.28 (7.17)	<0.0001
Std Err Mean: 0.30 year				
Age group				
22–29	82 (12.17)	22 (29.33)	53 (70.67)	<0.0001
30–39	318 (47.18)	173 (57.86)	126 (42.14)	
40–49	189 (28.04)	117 (68.02)	55 (31.98)	
50–59	58 (8.61)	41 (78.85)	11 (21.15)	
60–70	27 (4.01)	18 (81.82)	4 (18.18)	
Gender				
Female	331 (49.11)	183 (60.80)	118 (39.20)	0.6362
Male	343 (50.89)	188 (58.93)	131 (41.07)	
Education				
MSc student/graduate	355 (52.67)	176 (54.15)	149 (45.85)	0.0024
PhD student/graduate	319 (47.33)	195 (66.10)	100 (33.90)	
Education field				
Humanities	302 (44.81)	179 (63.70)	102 (36.30)	0.1569
Medical/veterinary	167 (24.78)	84 (54.55)	70 (45.45)	
Science, engineering, and agriculture	205 (30.42)	108 (58.38)	77 (41.62)	

(8.01%). Among those who had utilized AI (n = 249), the majority learned about it from friends/colleagues (46.59%), followed by social media (35.74%) and other sources (17.67%). The most popular AI tools included ChatGPT (70.68%), Quill Bot (42.17%), Grammarly (34.94%), and Google Bard (29.32%). Other AI tools were less frequently employed by the participants. AI usage served various purposes, such as paraphrasing text (33.73%), searching factual information and scientific data (15.26%), posing controversial questions (15.26%), generating research titles (13.65%), essay or review writing (12.85%), proofreading (12.85%), reference finding (12.05%), and proposal writing (6.43%) (Table II). ChatGPT, Quill Bot, Grammarly, and Google Bard were the most used AI tools among academic staff and post-graduate students. In addition, the most common purposes of using AI tools were paraphrasing text, searching factual information and scientific data, posing controversial questions, and generating research titles (Fig. 1).

The research revealed that nearly half of the participants (47.58%) recommended AI usage for post-graduate students and academic staff, while 28.87% indicated that they might make such a suggestion. However, the remaining 23.55% of the participants did not suggest AI tools for academic research and post-graduate purposes. Participants suggested AI applications in various areas, including searching factual information and scientific data (40.97%), paraphrasing (37.1%), generating research ideas (33.71%), resource findings (31.61%), posing controversial questions (30.32%), proofreading (29.52%), proposal writing (19.19%), and review composition (15.97%) (Table III).

#### IV. DISCUSSION

The literature suggests that most university students and faculty possess basic digital skills. Moreover, it is recommended that higher education institutions focus on

TABLE II  
ARTIFICIAL INTELLIGENCE USES AMONG POST-GRADUATE STUDENTS AND ACADEMIC STAFF OF THE UNIVERSITY OF DUHOK IN 2024

AI using features	All participants (n=674)	
	Number	Percentage
Using AI		
I do not know what is AI?	54	8.01
No	371	55.04
Yes	249	36.94
AI source, tools, and reasons	AI users (n=249)	
	Number	Percentage
Source of AI?		
Friends/colleagues	116	46.59
Others	44	17.67
Social Media	89	35.74
AI tools used		
ChatGPT	176	70.68
QuillBot	105	42.17
Grammarly	87	34.94
Google Bard	73	29.32
Wordtune	8	3.21
Bing	4	1.61
Asper	2	0.80
Google Gemini	2	0.80
Perplexity	2	0.80
DeepAI	1	0.40
Reasons for using AI		
Paraphrasing the text	84	33.73
Finding the fact information and science	38	15.26
Asking the controversial questions	38	15.26
Creating the ideas for the title of the research	34	13.65
Writing an essay or review	32	12.85
Proof-reading	32	12.85
Finding the references	30	12.05
Writing a proposal	16	6.43

AI: Artificial intelligence

enhancing digital competencies among both students and faculty, develop effective learning strategies, and implement

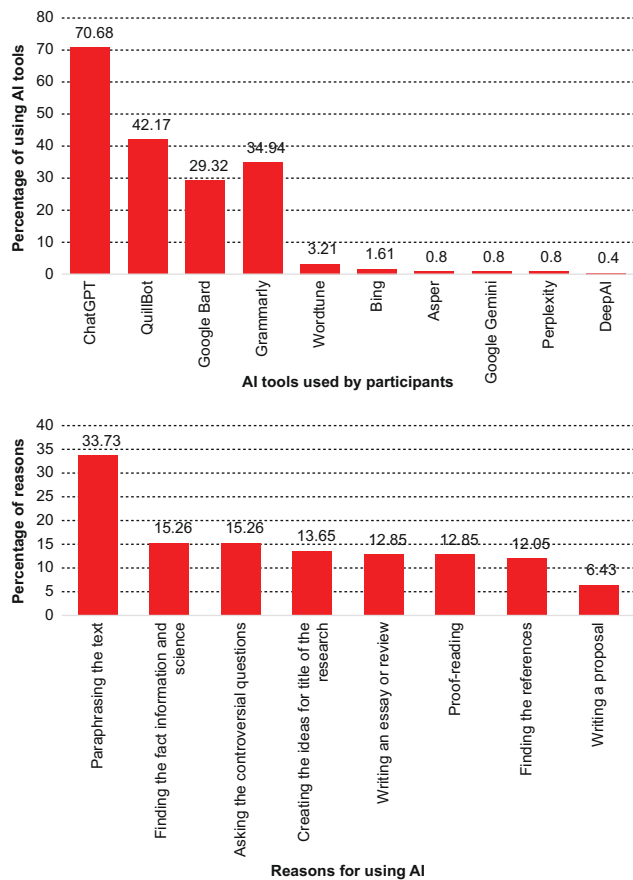


Fig. 1. AI tools used and their reasons for using the AI tools among academic staff and post-graduate students of the University of Duhok.

TABLE III  
SUGGESTING THE AI BY THE POST-GRADUATE STUDENTS AND ACADEMIC STAFF OF THE UNIVERSITY OF DUHOK

Suggestions (n=620)	Frequency distribution	
	Number	Percentage
Suggest AI		
Maybe	179	28.87
No	146	23.55
Yes	295	47.58
Areas of use of AI as suggested		
Searching for science and facts	254	40.97
Paraphrasing	230	37.1
Creating ideas for research	209	33.71
Finding the resources	196	31.61
Asking the controversial questions	188	30.32
Proof-reading	183	29.52
Writing a proposal	119	19.19
Writing a review	99	15.97

AI: Artificial intelligence

appropriate tools to improve the quality of education (Zhao, et al., 2021). Therefore, the results of this study underscore the uptake and utilization of AI platforms among members of the UoD academic community, including faculty, post-graduate students, and graduates. Indeed, our findings have broader implications for policymakers and educators in regions with developing technological infrastructure. By understanding the unique challenges faced in the Kurdistan

Region, educational strategies for AI integration can be more effectively tailored to similar contexts. Participants from diverse age groups and academic disciplines provided valuable insights into the current use of AI in academic and research settings. By examining the influences of age, gender, experience, and voluntarism on the predictive efficacy of the testing model (Venkatesh, et al., 2003), it was found that age attenuated all interactions between behavioral intentions and their determinants. Existing literature demonstrates a strong correlation between age and the use of AI tools (Roy, et al., 2022; Thai, et al., 2023), indicating that younger individuals with advanced academic qualifications are more likely to adopt innovative technologies. Similarly, the findings of this study revealed a significant correlation between age and AI adoption. Our analysis showed that younger academics, particularly those aged 22–49 with M.Sc. degrees, exhibited a higher propensity to use AI tools. This suggests potential differences in technology adoption across age groups and educational levels. While previous research has highlighted gender-based disparities in AI acceptance and use (Kucuk and Sisman, 2020; Alemi and Abdollahi, 2021; Roy, et al., 2022), our study found that both genders exhibited nearly identical rates of AI tool usage. However, a study by Gerlich (2023) also recognized the roles of income, educational attainment, and gender in AI adoption. It indicated that male participants with higher literacy, wealth, or technical expertise were more inclined to favor and promote AI usage.

Furthermore, our study found no significant variation in AI usage based on participants’ academic disciplines. This indicates that the integration of AI transcends both demographic and disciplinary boundaries at UoD, highlighting its diverse application across a wide range of academic fields, from the humanities to medical sciences. These findings challenge previous assumptions (Chanthiran, et al., 2022; Hajkowiec, et al., 2023) that AI adoption might be more prevalent in technical fields such as engineering or computer science. The uniformity across disciplines highlights the widespread applicability of AI tools, even in fields like the humanities, where digital tools have traditionally been slower to integrate. It is noteworthy to highlight that Williams, Rana and Dwivedi (2015) discovered that perceptions regarding ease of use, usefulness, attitude, perceived risk, gender, income, and experience exert a substantial influence on behavioral intention, whereas perceptions concerning age, anxiety, and training demonstrate comparatively lesser impact.

Conspicuously, AI technologies have significantly contributed to societal advancement, making their widespread adoption and acceptance inevitable (Zhao, 2023). However, factors such as cost, accessibility, and ethical concerns may influence the pace and extent of adoption (Cubic, 2020; Kabalisa and Altmann, 2021). Our study revealed that the vast majority of respondents from UoD had either not utilized AI services in their research or were unfamiliar with its capabilities. This lack of AI familiarity could be attributed to a combination of factors, including limited access to AI tools, inadequate training opportunities, or cultural hesitancy toward adopting new technologies in research contexts. These barriers may need to be addressed through

institutional strategies focused on enhancing AI literacy and access. This highlights the necessity for targeted educational programs and awareness campaigns to promote the benefits of AI in academic and research domains. In contemporary society, the importance of social media and digital platforms in disseminating information is undeniable (Hosen, et al., 2021; Yang, et al., 2023), making stakeholder engagement a central focus in this area. In our survey, individuals who utilized AI tools indicated that they primarily learned about these platforms from friends or colleagues and social media. This underscores the critical role of social media in providing information about AI tools and their academic advantages. This reliance on social media for information highlights a gap in formal institutional channels for AI training and knowledge dissemination. Given the increasing role that social media plays in shaping academic habits, institutions may need to adapt by integrating social media-based learning tools or campaigns to complement traditional AI training programs. Consequently, we strongly advise formalizing these internet-based platforms within universities and academic circles to enhance AI proficiency and encourage broader acceptance among scholars.

A derivative of GPT-3, ChatGPT is an advanced language model introduced by OpenAI in November 2022. It has emerged as a significant and unique AI platform with practical applications, garnering attention as a transformative, albeit controversial, tool for enhancing teaching and learning experiences (Lo, Hew and Jong, 2024). Remarkably, the AI chatbot ChatGPT has experienced unprecedented growth, potentially making it the fastest-growing internet application in history. As of January 2023, it boasts nearly 100 million users and approximately 1.8 billion website visitors per month (Bin-Nashwan, Sadallah and Bouteraa, 2023). Unsurprisingly, ChatGPT emerged as the predominant AI tool utilized by respondents in this study, followed by Quill Bot, Grammarly, and Google Bard. The findings of this investigation align with existing scholarly literature (Dergaa, et al., 2023; Livberber and Ayvaz, 2023; Lund and Wang, 2023), indicating that AI tools, particularly ChatGPT, can serve as effective aids in scientific research and educational endeavors, potentially acting as catalysts for the exploration of novel topics or research domains. However, the study also reveals ethical concerns among academics regarding ChatGPT, including issues related to plagiarism and the dissemination of misinformation. These risks have profound implications for academic integrity, as reliance on AI tools without appropriate checks can lead to the production of unoriginal or inaccurate content, compromising the quality of academic outputs. As AI becomes more integrated into scholarly workflows, we recommended addressing these ethical issues through clear guidelines which will be crucial to maintaining research standards. Our participants utilized these tools in research contexts for a variety of tasks, including paraphrasing text, answering questions, proofreading, finding references, and drafting proposals. This reflects the diverse needs and preferences of individuals engaged in scholarly writing and research activities. Notably, some universities worldwide have restricted access to ChatGPT or similar AI tools (Tlili,

et al., 2023), while others are hesitant to impose such bans (Huang, 2023), citing concerns about the submission of unoriginal or potentially plagiarized material. Conversely, technology experts advocate for universities to educate faculty, researchers, and students on the appropriate use of ChatGPT and AI platforms rather than implementing blanket prohibitions (Bin-Nashwan, Sadallah and Bouteraa, 2023). In this context, the UoD currently lacks definitive and uniform policies regarding the prohibition, use, or regulation of AI technologies. This could lead to inconsistent use of these technologies, raising concerns about the proper regulation of AI in academic work. Hence, establishing well-defined guidelines will be essential for ensuring that AI is used responsibly, particularly in safeguarding against academic dishonesty and maintaining the rigor of scholarly outputs.

Finally, while 52% of participants expressed reservations or ambivalence toward recommending AI usage, approximately 48% endorsed its use to their peers and colleagues. Empirically, individuals tend to place greater trust in human recommendations than in AI for practical or applied tasks (Jin and Zhang, 2023). Indeed, AI plays a growing role in modern scientific research, from automating data analysis to enhancing research reproducibility. As AI technologies evolve, their influence on knowledge production is likely to expand, though this will depend on continued advancements and regulatory frameworks (Harvey and Gowda, 2021; Adedokun, 2024). Consequently, participants in this study advocated for the adoption of AI platforms across various contexts, ranging from conducting scientific inquiries and generating empirical evidence to tasks such as paraphrasing text, proofreading, proposal writing, and content creation. This highlights the potential and significance of AI technologies in streamlining and enhancing academic processes, refining research workflows, and optimizing productivity. Following Cath et al. (2018), this survey effectively examines the diverse adoption and utilization of AI among academics at the UoD. Therefore, it is strongly recommended that universities, including our own, establish a comprehensive strategic vision and long-term plan to foster the development of a robust academic and higher education AI community. In addition, we suggest that universities create appropriate protocols for the use of AI among post-graduate students. While some prestigious journals have begun integrating AI tools, it is essential for other academic publications to allow researchers to leverage AI technologies to enhance both academic and linguistic aspects (Central Illustration).

#### *A. Strength and Limitations*

This study offers valuable insights into AI technology usage among academics at the UoD, highlighting trends across diverse age groups, disciplines, and education levels. Of importance, the large sample size enhances the reliability of the findings. However, limitations include potential biases from self-reported data, the cross-sectional nature of the survey, and the lack of qualitative insights. In addition, findings may not be generalizable to other institutions or



Central Illustration: AI Integration amid University of Duhok Academics and Alumni.

regions due to the study's focus on a specific academic environment in the Kurdistan region.

## V. CONCLUSION

The findings of this study indicated that only one-third of faculty members at the UoD utilize AI, specifically ChatGPT, primarily for text paraphrasing. Approximately half of the study's participants recommended the implementation of AI for use by post-graduate students and academic staff. In addition, this study provides a foundation for future research on the role of AI in education, particularly in emerging academic environments. Further studies could explore the long-term impact of AI on academic outcomes and the role of policy in facilitating technology adoption.

## ACKNOWLEDGMENT

The authors wish to extend their sincere gratitude to the UoD Presidency, particularly the Quality Assurance and Post-graduate Units, for their invaluable assistance in distributing the Google Forms. We sincerely thank the faculty and alumni of UoD for their invaluable cooperation and participation, which made this study possible.

## REFERENCES

- Adedokun, A., 2024. Global ai regulatory landscape challenges, trends, and future outlook. In: *Trends, and Future Outlook*. [SSRN Paper].
- Aldoseri, A., Al-Khalifa, K., and Hamouda, A., 2023. *A Roadmap for Integrating Automation with Process Optimization for Ai-powered Digital Transformation*. [Preprints].
- Alemi, M., and Abdollahi, A., 2021. A cross-cultural investigation on attitudes towards social robots: Iranian and chinese university students. *Journal of Higher Education Policy and Leadership Studies*, 2(3), pp.120-38.
- Barrot, J.S., 2022. Integrating technology into esl/efl writing through grammarly. *Relc Journal*, 53(3), pp.764-68.
- Bin-Nashwan, S.A., Sadallah, M., and Bouteraa M., 2023. Use of chatgpt in academia: Academic integrity hangs in the balance. *Technology in Society*, 75, pp.102370.
- Cath, C., Wachter, S., Mittelstadt, B., Taddeo, M., and Floridi L., 2018. Artificial intelligence and the 'good society': The us, eu, and uk approach. *Science and Engineering Ethics*, 24, pp.505-28.
- Cestonaro, C., Delicati, A., Marcante, B., Caenazzo, L., and Tozzo, P., 2023. Defining medical liability when artificial intelligence is applied on diagnostic algorithms: A systematic review. *Frontiers in Medicine (Lausanne)*, 10, pp.1305756.
- Chanthiran, M., Ibrahim, A.B., Rahman, M.H.A., Kumar, S., and Dandage, R.V., 2022. A systematic literature review with bibliometric meta-analysis of ai technology adoption in education. *Educatum Journal of Science, Mathematics and Technology*, 9, pp.61-71.
- Coenen, A., Davis, L., Ippolito, D., Reif, E., and Yuan, A., 2021. *Wordcraft: A Human-ai Collaborative Editor for Story Writing*. arXiv Preprint.
- Cubic, M., 2020. Drivers, barriers and social considerations for ai adoption in business and management: A tertiary study. *Technology in Society*, 62, pp.101257.
- Dergaa, I., Chamari, K., Zmijewski, P., and Saad, H.B., 2023. From human writing to artificial intelligence generated text: Examining the prospects and potential threats of chatgpt in academic writing. *Biology of Sport*, 40(2), pp.615-22.
- Farahani, M.S., and Ghasemi, G., 2024. Artificial intelligence and inequality: Challenges and opportunities. *Qeios*, 7, pp.1-14.
- Gerlich, M., 2023. Perceptions and acceptance of artificial intelligence: A multi-dimensional study. *Social Sciences*, 12(9), pp.502.
- Hajkowicz, S., Sanderson, C., Karimi, S., Bratanova, A., and Naughtin, C., 2023. Artificial intelligence adoption in the physical sciences, natural sciences, life sciences, social sciences and the arts and humanities: A bibliometric analysis of research publications from 1960-2021. *Technology in Society*, 74, pp.102260.
- Harvey, H.B., and Gowda, V., 2021. Regulatory issues and challenges to artificial intelligence adoption. *Radiologic Clinics*, 59(6), pp.1075-83.
- Hosen, M., Ogbeibu, S., Giridharan, B., Cham, T.H., Lim, W.M., and Paul, J., 2021. Individual motivation and social media influence on student knowledge sharing and learning performance: Evidence from an emerging economy. *Computers and Education*, 172, pp.104262.
- Huang, K., 2023. Alarmed by ai chatbots, universities start revamping how they teach. *The New York Times*, 16.
- Imran, A., 2023. Why addressing digital inequality should be a priority. *The*

- Electronic Journal of Information Systems in Developing Countries*, 89(3), pp.e12255.
- Jin, F., and Zhang X., 2023. Artificial intelligence or human: When and why consumers prefer AI recommendations. *Information Technology and People*, ahead-of-print.
- Kabalisa, R., and Altmann J., 2021. Ai Technologies and Motives for Ai Adoption by Countries and firms: A Systematic Literature Review. In: *Economics of Grids, Clouds, Systems, and Services: 18<sup>th</sup> International Conference, GECON 2021, Virtual Event, September 21-23, 2021, Proceedings*. Vol. 18. Springer, Berlin, pp.39-51.
- Kacena, M.A., Plotkin, L.I., and Fehrenbacher, J.C., 2024. The use of artificial intelligence in writing scientific review articles. *Current Osteoporosis Reports*, 22, pp.1-7.
- Khalil, M., and Er, E., 2023. Will Chatgpt Get you Caught? Rethinking of Plagiarism Detection. In: *International Conference on Human-Computer Interaction*. Springer, Berlin, pp.475-87.
- King, M.R., 2023. The future of ai in medicine: A perspective from a chatbot. *Annals of Biomedical Engineering*, 51(2), pp.291-95.
- Kucuk, S., and Sisman, B., 2020. Students' attitudes towards robotics and stem: Differences based on gender and robotics experience. *International Journal of Child-Computer Interaction*, 23, p.100167.
- Kumar, P., Manikandan, S., and Kishore, R., (2024). Ai-driven Text Generation: A Novel Gpt-based Approach for Automated Content Creation. In: *2<sup>nd</sup> International Conference on Networking and Communications (ICNWC)*. IEEE, New Jersey, pp.1-6.
- Livberber, T., and Ayvaz, S., 2023. The impact of artificial intelligence in academia: Views of turkish academics on chatgpt. *Heliyon*, 9(9), e19688.
- Lo, C.K., Hew, K.F., and Jong, M.S.Y., 2024. The influence of chatgpt on student engagement: A systematic review and future research agenda. *Computers and Education*, 219, pp.105100.
- Lund, B.D., and Wang, T., 2023. Chatting about chatgpt: How may ai and gpt impact academia and libraries? *Library Hi Tech News*, 40(3), pp.26-29.
- Nazari, N., Shabbir, M.S., and Setiawan, R., 2021. Application of artificial intelligence powered digital writing assistant in higher education: Randomized controlled trial. *Heliyon*, 7(5), e07014.
- Nobles, S., and Paganucci, L., 2015. Do digital writing tools deliver? Student perceptions of writing quality using digital tools and online writing environments. *Computers and Composition*, 38, pp.16-31.
- Roy, R., Babakerkhell, M.D., Mukherjee, S., Pal, D., and Funilkul, S., 2022. Evaluating the intention for the adoption of artificial intelligence-based robots in the university to educate the students. *IEEE Access*, 10, pp.125666-125678.
- Salvagno, M., Taccone, F.S., and Gerli, A.G., 2023. Can artificial intelligence help for scientific writing? *Critical Care*, 27(1), pp.99.
- Stepenenaite, A., and Barakat, B., (2023). *Plagiarism in ai empowered world. International Conference on Human-Computer Interaction*. Springer, Berlin, pp.434-442.
- Thai, K., Tsiandoulas, K.H., Stephenson, E.A., Menna-Dack, D., Shaul, R.Z., Anderson, J.A., Shinewald, A.R., Ampofo, A., and McCradden, M.D., 2023. Perspectives of youths on the ethical use of artificial intelligence in health care research and clinical care. *JAMA Network Open*, 6(5), p.e2310659.
- Tlili, A., Shehata, B., Adarkwah, M.A., Bozkurt, A., Hickey, D.T., Huang R., and Agyemang, B., 2023. What if the devil is my guardian angel: Chatgpt as a case study of using chatbots in education. *Smart Learning Environments*, 10(1), pp.15.
- Venkatesh, V., Morris, M.G., Davis, G.B., and Davis, F.D., 2003. User acceptance of information technology: Toward a unified view. *MIS Quarterly*, pp.425-78.
- Williams, M.D., Rana, N.P., and Dwivedi, Y.K., 2015. The unified theory of acceptance and use of technology (utaut): A literature review. *Journal of Enterprise Information Management*, 28(3), pp.443-488.
- Winans, M.D., 2021. Grammarly's tone detector: Helping students write pragmatically appropriate texts. *Relc Journal*, 52(2), pp.348-52.
- Yang, B., Zhang, R., Cheng, X., and Zhao, C., 2023. Exploring information dissemination effect on social media: An empirical investigation. *Personal and Ubiquitous Computing*, 27(4), pp.1469-82.
- Zhao, X., 2023. Leveraging artificial intelligence (ai) technology for english writing: Introducing wordtune as a digital writing assistant for efl writers. *RELC Journal*, 54(3), pp.890-94.
- Zhao, Y., Llorente, A.M.P., and Gómez, M.C.S., 2021. Digital competence in higher education research: A systematic literature review. *Computers and Education*, 168, p.104212.
- Zohuri, B., and Mossavar-Rahmani, F., 2024. Revolutionizing education: The dynamic synergy of personalized learning and artificial intelligence. *International Journal of Advanced Engineering and Management Research*, 9(1), pp.143-53.

# Design and Fabrication of a Microstrip Low-Pass Filter with a Wide Stopband Using a Windmill-Shaped Resonator

Sobhan Roshani<sup>1</sup>, Salah I. Yahya<sup>2,3</sup>, Shahram Khazaei<sup>4</sup>, Saeed Roshani<sup>1†</sup>, and Babak Karami<sup>5</sup>

<sup>1</sup>Department of Electrical Engineering, Kermanshah Branch, Islamic Azad University, Kermanshah, Iran

<sup>2</sup>Department of Communication and Computer Engineering, Cihan University-Erbil, Erbil, Iraq

<sup>3</sup>Department of Software Engineering, Faculty of Engineering, Koya University, Koya, Iraq

<sup>4</sup>Department of Electrical Engineering, Sanandaj Branch, Islamic Azad University, Sanandaj, Iran

<sup>5</sup>Department of Mechanical Engineering, Kermanshah Branch, Islamic Azad University, Kermanshah, Iran

**Abstract**—In this paper, a microstrip low-pass filter (LPF) with a wide stopband and a sharp transition band is presented using a windmill-shaped resonator. Traditional LPF designs often face challenges such as narrow stopbands, high insertion loss, and large physical sizes, which limit their performance in modern communication systems. To address these challenges, the proposed filter exhibits low insertion loss, a sharp response in the transition band, a wide stopband, and a compact size. The windmill-shaped resonator is applied to achieve a sharp response in the transition band, while two suppressor cells are added to extend the stopband. The filter has a 3 dB cutoff frequency ( $f_c$ ) of 1.61 GHz, with an  $S_{12}$  parameter value of  $-20$  dB at 1.7 GHz, resulting in a narrow transition band of 0.18 GHz, demonstrating its superior performance. In addition, the filter achieves a wide stopband that extends from 1.79 GHz to 11.26 GHz (a bandwidth of 9.47 GHz) with high attenuation. The physical size of the filter is  $13.34 \text{ mm} \times 12.78 \text{ mm}$  ( $0.097\lambda \times 0.093\lambda$ ). Overall, the proposed filter demonstrates excellent characteristics in both the passband and stopband regions, providing an effective solution for modern communication system requirements. The presented design effectively addresses key limitations in traditional LPF configurations, offering improved performance and compactness.

**Index Terms**—Low-pass filter, Microstrip, Resonator, Return loss, Stopband, Transition band.

ARO-The Scientific Journal of Koya University  
Vol. XII, No. 2 (2024), Article ID: ARO.11752. 8 pages  
DOI: 10.14500/aro.11752

Received: 06 August 2024; Accepted: 17 November 2024

Regular research paper; Published: 01 December 2024

†Corresponding author's e-mail: s\_roshani@iau.ir

Copyright © 2024 Sobhan Roshani, Salah I. Yahya, Shahram Khazaei, Saeed Roshani and Babak Karami. This is an open-access article distributed under the Creative Commons Attribution License (CC BY-NC-SA 4.0).



## I. INTRODUCTION

Microstrip low-pass filters (LPF) play a crucial role in modern microwave communication systems. To meet demands such as high performance and compact size, LPF with low power loss and wide stopbands are in high demand. Planar structures are highly advantageous in the design of LPF due to their simple geometry, which facilitates ease of fabrication and optimization. These structures offer a compact size, making them suitable for modern communication systems where space is a critical factor. In addition, planar designs are versatile and can be easily integrated with other components on a single substrate, enhancing overall system performance. Their ability to achieve sharp transition bands and wide stopbands while maintaining low insertion loss and good return loss further underscores their significance in LPF design. One of the most interesting techniques for microstrip filters is their structure, which employs a photonic bandgap (PBG) structure with a microstrip transmission line. The PBG structure exhibits slow-wave characteristics near the stopband in the passband region (Meade et al., 1991). In (Deng, Xue and Che, 2007), a LPF with a suitable wide stopband is presented, but the attenuation of unwanted signals in the stopband is insufficient. In (Li, Li and Wei, 2009), cone resonators are used to achieve a wide bandwidth, resulting in strong attenuation near the passband, which is an advantage, but the low sharpness of the filter's response is a drawback. In (Ting, Tam and Martins, 2006), a combination of DGS and dual U-shaped resonators are used to achieve high attenuation, but the return loss in the passband for this LPF is not acceptable. In (Luo, Zhu and Sun, 2008), another structure based on a coupled hairpin resonator is proposed, which has very small dimensions and performed well in the stopband and passband, but this structure also

suffered from gradual attenuation in the transition band. In (Mandal et al., 2006), a filter composed of complementary split-ring resonators is employed, which has a good return loss in the passband but not a very wide stopband. In (Park, Kim and Nam, 2007), a LPF with excellent performance is proposed, which utilizes parallel open stubs and a DGS structure simultaneously, achieving notable performance but having large dimensions. In (Yang et al., 2010), various types of DGS were also used for implementing LPF, including ring structures and stepped impedance, to achieve smaller dimensions while maintaining acceptable response performance. In (Ma and Yeo, 2010), a filter with a very wide stopband was achieved using modified radial resonators, but the structure is complex and has large physical dimensions. In (Roshani, Dehghani and Roshani, 2019), fountain-shaped resonators are used to create a compact LPF with a size of  $0.135\lambda_g \times 0.132\lambda_g$ . This LPF provides a wide stopband and sharp response but has complex structures. Resonators are also used to shape other types of microwave devices, such as dividers (Roshani et al., 2023b, Mohammadi et al., 2024), couplers (Hosseini and Rezaei, 2020), diplexers (Rezaei and Yahya, 2022), antenna arrays (Roshani et al., 2023a).

In (Wang et al., 2010), a LPF is reported with a cutoff frequency ( $f_c$ ) of 1.18 GHz. The relative stop bandwidth (RSB) of this filter is 1.32. Despite its reasonable performance in terms of cutoff frequency and sharpness, the size of this filter is large, and its frequency response is not as sharp as desired, making it less efficient for applications requiring compactness and high precision. In (Ma, Yeo and Lim, 2012), a microstrip LPF is reported with a 3.2 GHz cutoff frequency. This filter has a RSB of 1.66. The sharpness of this LPF is low and has a large size, making it less desirable for applications where space and precision are critical. In (Ge, Wang and Guo, 2010), a LPF is reported with a 1.3 GHz cutoff frequency and 37dB/GHz sharpness. This filter has a large size. The bulky design and lack of sharp frequency discrimination limit its suitability for compact and precise applications.

In (Challal et al., 2012), a LPF is reported with a 25 dB/GHz sharpness and 2.95 GHz cutoff frequency. This filter has a good response but occupies a large size. The large size and its gradual frequency response are significant drawbacks, which are not desirable.

In (Faraghi, Azarmanesh and Ojaroudi, 2013), a LPF is reported with a 3.4 GHz cutoff frequency. The filter features a RSB of 1.4 and a sharpness ( $\zeta$ ) of 37 dB/GHz. The overall size of the filter is large, and the frequency response is not sharp enough. These limitations make it less ideal for use in modern communication systems. Moreover, recently, the open stub technique has gained significant attention in the design of LPFs due to its effectiveness in enhancing filter performance. This method provides a simple approach for achieving an improved suppression of unwanted harmonics. Incorporating open stubs into microstrip filters has proven beneficial in minimizing insertion loss while extending the stopband, making it a suitable option for advanced filter designs (Lotfi, Roshani and Roshani, 2020, Bavandpour et al., 2021, Chakraborty and Verma, 2024).

The novelty of the proposed microstrip LPF lies in its innovative use of a windmill-shaped resonator combined with asymmetrical suppressor cells, which together address several challenges present in conventional LPF designs. Traditional filters often face limitations such as narrow stopbands, high insertion loss, and large physical size. By integrating a compact windmill-shaped resonator, the proposed LPF achieves a sharp transition band and a significantly wider stopband while maintaining low insertion loss. In addition, the design's simplicity enhances manufacturability and allows for easy integration into modern communication circuits. These unique design features distinguish the proposed LPF, offering a compact and efficient solution that overcomes key limitations of prior LPF configurations.

The proposed LPF has potential applications across various modern communication systems where high performance, compactness, and efficiency are crucial. Its compact size and wide stopband make it ideal for integration into wireless communication devices, including mobile phones, Wi-Fi systems, and satellite communication equipment. The filter's low insertion loss and sharp transition band are particularly beneficial in frequency-selective environments, where efficient signal transmission and interference suppression are essential. In addition, the filter's wide stopband enhances its utility in multi-band and ultra-wideband applications by effectively attenuating out-of-band signals and preventing harmonic distortions. Given these characteristics, the proposed LPF can play a vital role in improving signal quality and minimizing interference in advanced communication infrastructure, including 5G networks, radar systems, and Internet of Things devices.

In this paper, a windmill-shaped resonator and two microstrip suppressing cells are used to design a LPF. The proposed structure has been simulated, fabricated, and measured. The proposed LPF has a simple planar structure, compact size, low insertion loss in the passband, and provides a wide stop band.

## II. DESIGN OF THE PROPOSED RESONATOR

The design process of the proposed filter consists of two stages. The first stage involves designing a windmill-shaped resonator to achieve a sharp response in the passband. The second stage entails designing an attenuator and adding it to the proposed resonator to achieve a wide stopband bandwidth.

### A. Proposed Resonator

Fig. 1 shows the structure of the proposed resonator, which is formed by conical microstrip shapes arranged in the form of a windmill. The proposed structure has been simulated using the ADS simulator to provide the characteristics in both the passband and stopband.

The simulation results of the proposed resonator are shown in Fig. 2. The  $S_{12}$  curve is depicted with the blue line and the  $S_{11}$  curve is shown with red color. The results show that the cut-off frequency ( $f_c$ ) resonator is 1.4 GHz and



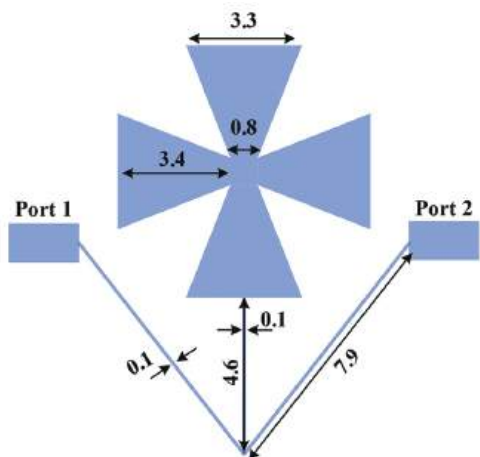


Fig. 1. Layout of the proposed resonator with conical microstrip shapes. All dimensions are written in millimeter.

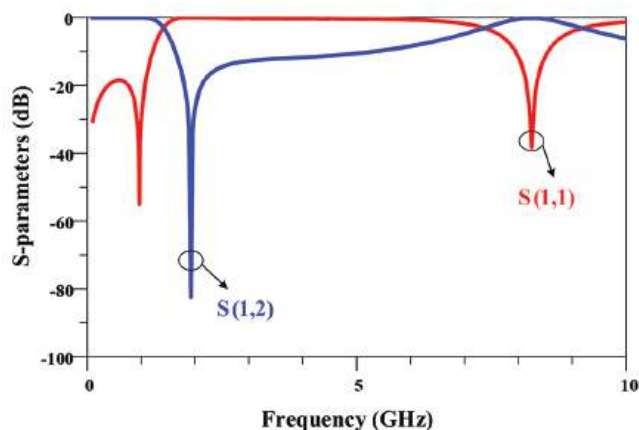


Fig. 2. Simulated Scattering parameter results of the proposed resonator.

provides transmission zero at 1.92 GHz with more than 80dB attenuation.

The equivalent LC circuit of the proposed resonator is shown in Fig. 3. In this equivalent circuit,  $L_2$  represents the inductance of the transmission lines between the input and output ports.  $L_1$  is the inductance of the transmission line connected to the resonator.  $C_1$  is an open stub, representing the capacitance related to the conical resonator. EM simulated Scattering parameters of the proposed resonator and the equivalent LC circuit Simulation are depicted in Fig. 4, which have good agreements.

### B. Proposed Suppressing Cells

The proposed resonator has suitable return loss, insertion loss, and sharpness of response. However, its stopband bandwidth is inadequate. Therefore, to improve the stopband bandwidth of the desired filter, as well as to enhance the sharpness of the response and the return loss, and considering the importance of simplicity in the filter structure, two asymmetrical stubs are used as suppressing cells. These open stubs create attenuation poles to suppress harmonics, resulting in significant attenuation at higher frequencies and providing a very wide stopband bandwidth. The structure of the suppressing cells is depicted in Fig. 5.

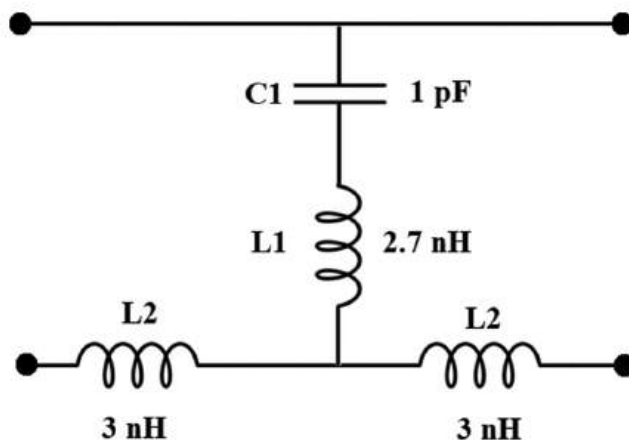


Fig. 3. Equivalent LC circuit of the proposed resonator.

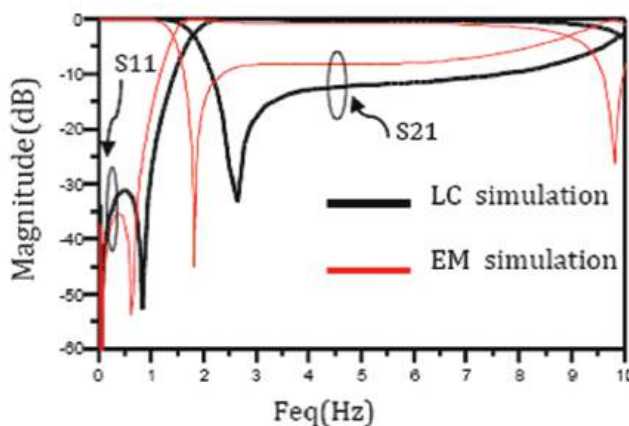


Fig. 4. EM simulated Scattering parameters the proposed resonator and the equivalent LC circuit Simulation.

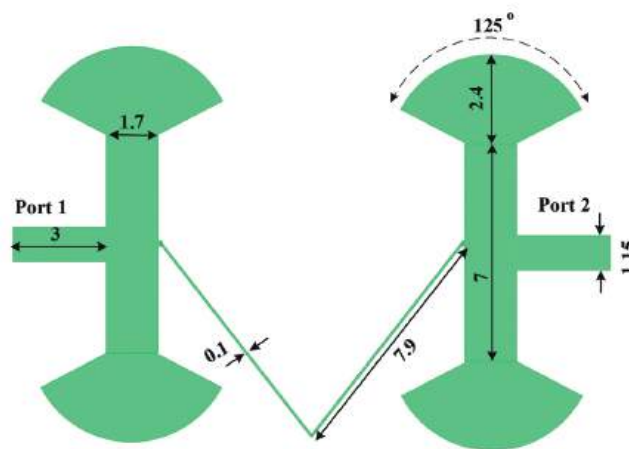


Fig. 5. Structure of the proposed suppressing cells. All dimensions are written in millimeter.

The simulated Scattering parameter results of the proposed suppressing cells are demonstrated in Fig. 6. The  $S_{12}$  curve is depicted with a blue line and the  $S_{11}$  curve is shown with red color. The results show that the cut-off frequency ( $f_c$ ) proposed suppressing cells is 1.42 GHz and provides two transmission zeros at 6.5 GHz and 7.5 GHz.

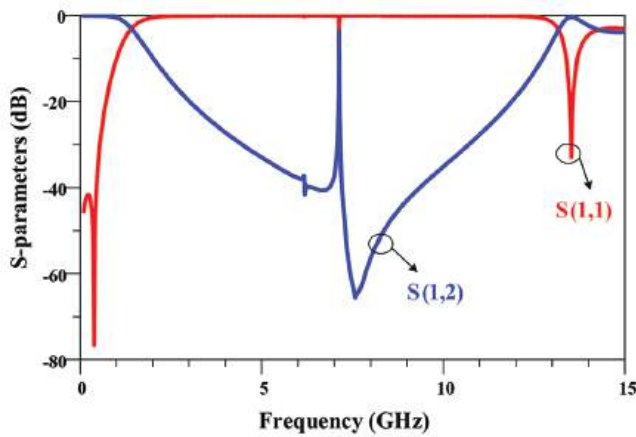


Fig. 6. Simulated Scattering parameter results of the proposed suppressing cells.

### III. DESIGN OF THE PROPOSED FILTER

The proposed structure is designed based on the RT/Duroid 5880 with a dielectric constant of 2.2, a height of 15 mils, and a loss tangent of 0.0009. The layout of the proposed LPF is depicted in Fig. 7. For impedance matching, at the input and output ports with 50-ohm connectors, two microstrip lines are used.

Fig. 8 shows the simulated results of the designed filter. This filter has a 3 dB cutoff frequency of 1.61 GHz. This filter has a 3 dB cutoff frequency ( $f_c$ ) of 1.61 GHz. The value of the  $S_{12}$  parameter at a frequency of 1.7 GHz is -20 dB, resulting in a narrow transition band of 0.18 GHz, which demonstrates the acceptable performance of the proposed filter. The filter provides a wide stopband and has high attenuation in the stopband. The stopband extends from 1.79 GHz to 11.26 GHz (bandwidth of 9.47 GHz). The return loss in the passband is -16.64 dB, indicating the filter's good ability to pass power from port 1 to port 2. The insertion loss in the passband from DC to 1.5 GHz, which is approximately 95% of the passband, is 0.1 dB. Two transmission zeros are located at 1.89 GHz and 11.2 GHz with -55.53 dB and -42.22 dB, values, respectively. The physical size of the filter is only 13.34 mm  $\times$  12.78 mm (0.097 $\lambda$   $\times$  0.093 $\lambda$ ). Overall, it can be claimed that the proposed filter has good characteristics in both the passband and stopband regions.

The proposed LPF incorporates a windmill-shaped resonator and symmetrical suppressor cells, each playing a distinct role in achieving the filter's overall performance. The windmill-shaped resonator serves as the core structure, designed to achieve a sharp cutoff and precise control over the passband and transition band frequencies. This unique resonator shape leverages conical microstrip geometries to create a compact and effective configuration, enabling high-frequency selectivity and a narrow transition band. The windmill shape not only optimizes space but also ensures that the resonator operates effectively within a compact footprint, which is essential for applications requiring minimal size.

To further enhance the stopband characteristics, suppressor cells are incorporated. These suppressor cells are strategically positioned to create transmission zeros at specific frequencies within the stopband, effectively broadening the stopband

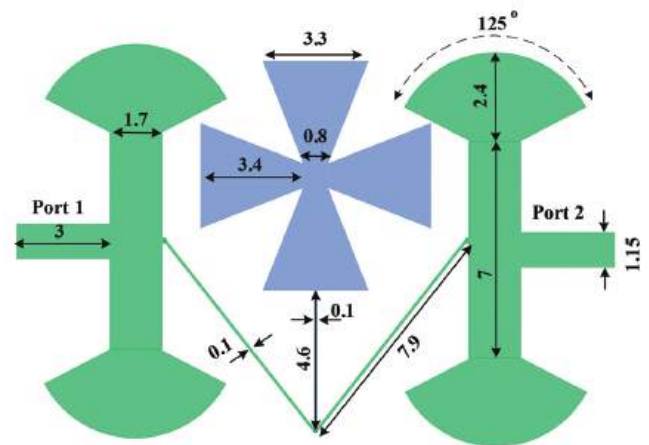


Fig. 7. Structure of the proposed low-pass filter. All dimensions are written in millimeter.

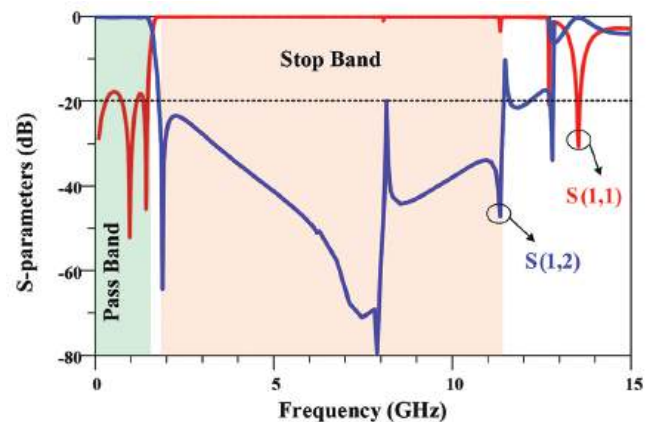


Fig. 8. Simulated and measured results of the designed Filter.

and ensuring strong attenuation of unwanted harmonics and interference. Suppressing cells introduces additional attenuation poles, which help maintain a high level of suppression across a wider frequency range, extending from 1.79 GHz to 11.26 GHz. This approach provides substantial interference reduction and minimizes signal leakage at frequencies above the passband. In addition, the LPF includes input and output matching networks formed by microstrip lines, which ensure impedance matching to 50 ohms, minimizing reflection losses at the interface with external circuitry. The filter is designed on an RT/Duroid 5880 substrate, chosen for its low dielectric loss and stable performance across high frequencies, further supporting low insertion loss and reliable performance.

Fig. 9 presents the surface current density distributions for the designed LPF at three different frequencies of 1.4 GHz, 7.7 GHz, and 12.2 GHz. At 1.4 GHz, which is located within the pass band, the surface current density is distributed such that the signal efficiently travels from the input to the output port. This indicates that the filter allows the desired frequency to pass through with minimal attenuation. Conversely, at 7.7 GHz and 12.2 GHz, both of which fall within the stop band, the surface current density plots demonstrate a significant reduction in current reaching port 2. This reduction signifies

the filter’s capability to attenuate higher frequencies, effectively preventing them from propagating through to the output. The comparison across these frequencies highlights the filter’s role in discriminating between the passband and stopband frequencies, ensuring that only frequencies below the cutoff of 1.61 GHz are transmitted, while higher frequencies are blocked.

#### IV. ANN MODEL FOR THE PROPOSED LPF

The ANN model used in this study is designed to predict the scattering parameters of the proposed LPF, providing a data-driven approach to understanding the filter’s behavior. The model architecture comprises three hidden layers with 20, 15, and 15 neurons, respectively, each optimized to capture the complex, non-linear relationships between input parameters and the LPF’s performance characteristics. The proposed neural network architecture is illustrated in Fig. 10. The multi-layer perceptron (MLP) network is used to model and predict the scattering parameters. The MLP architecture consists of an input layer, three hidden layers, and an output layer corresponding to the predicted S-parameters. The network was optimized using a backpropagation algorithm and mean squared error as the loss function to minimize prediction errors. In the applied neural network, the Levenberg-Marquardt algorithm is used for backpropagation.

Real and predicted values for  $S_{11}$  and  $S_{21}$  parameters in train and test procedures are depicted in Fig. 11. As seen the data is predicted perfectly in both train and test procedures.

The real and predicted S-parameters for the proposed device model are depicted in Fig. 12. The proposed model has achieved high accuracy results in test and train mode. The results of the proposed ANN model show the MRE of 0.5018 and 0.1410 for the train and test phases of the  $S_{21}$  parameter. Furthermore, the MRE of 0.1331 and 0.2071 for the train and test phases of the  $S_{11}$  parameter are achieved.

#### V. FABRICATED AND MEASURED RESULTS

The proposed structure is fabricated on RT/Duroid 5880 with a dielectric constant of 2.2, a height of 15 mils, and a loss tangent of 0.0009. The fabricated device is depicted in Fig. 13.

While the proposed LPF demonstrates excellent performance in terms of stopband bandwidth, insertion loss, and compact size, there are a few limitations in its design parameters. One notable constraint is the sensitivity of the filter’s performance to variations in substrate material and manufacturing tolerances. The filter was fabricated on an RT/Duroid 5880 substrate, which, while effective, is relatively costly and may not be feasible for all applications, especially those requiring large-scale production. In addition, the high precision required for the windmill-shaped resonator and symmetrical suppressor cells makes the device susceptible to fabrication-induced variations, which can slightly affect the cutoff frequency and stopband characteristics if manufacturing tolerances are not strictly maintained. Moreover, while the filter achieves a sharp transition band and wide stopband, it is optimized for frequencies up to 11.26 GHz, limiting its applicability in systems requiring even higher frequency performance. The design’s compactness also imposes some limitations on heat dissipation, which may impact performance in high-power applications. Despite these constraints, the proposed design remains highly effective within its intended operational range and offers a balanced solution for modern, compact communication systems. Further optimizations in materials and fabrication techniques could help mitigate these limitations and expand the filter’s applicability.

Fig. 14 presents the measured and simulated S-parameters ( $S_{11}$  and  $S_{21}$ ) of the designed LPF. The filter has a 3 dB cutoff frequency at 1.61 GHz, demonstrating its efficacy in passing frequencies below this threshold. Notably, the filter provides a wide stopband ranging from 1.79 GHz to 11.26 GHz, corresponding to a bandwidth of 9.47 GHz, and exhibits high

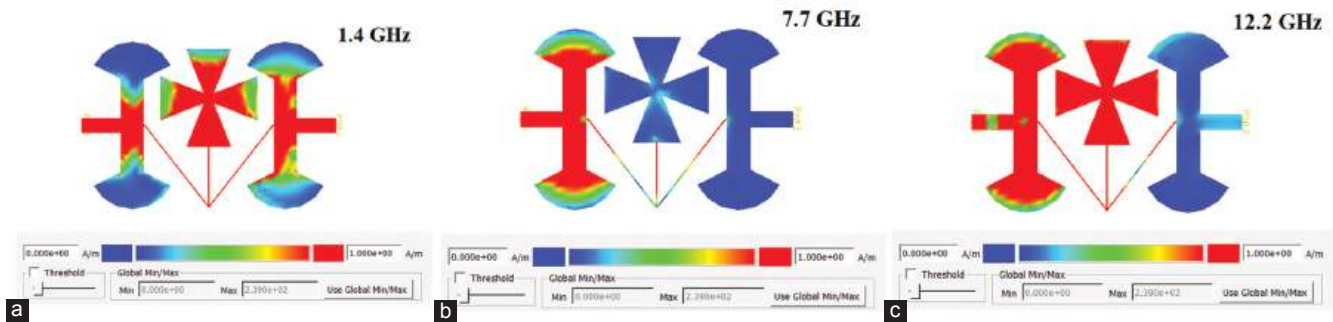


Fig. 9. Surface current density plots of the designed low-pass filter at three different frequencies: (a) 1.4 GHz (within the pass band), (b) 7.7 GHz (within the stop band), and (c) 12.2 GHz (within the stop band).



Fig. 10. Proposed neural network architecture of the designed low-pass filter with three hidden layers.

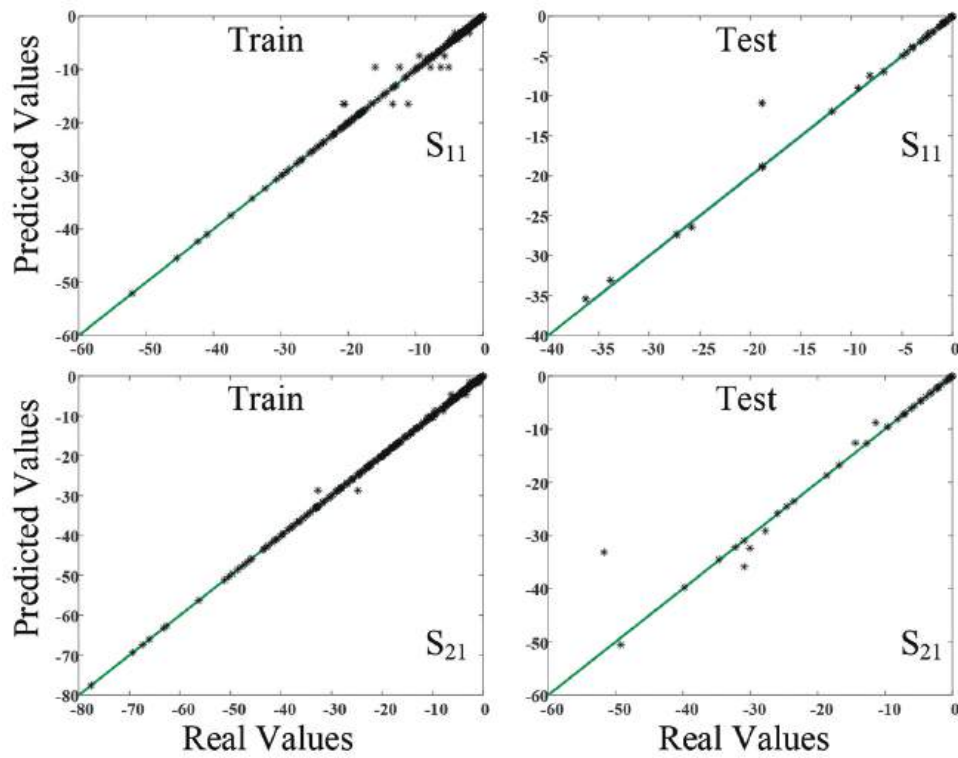


Fig. 11. Real and predicted values for  $S_{11}$  and  $S_{21}$  parameters in train and test procedures.

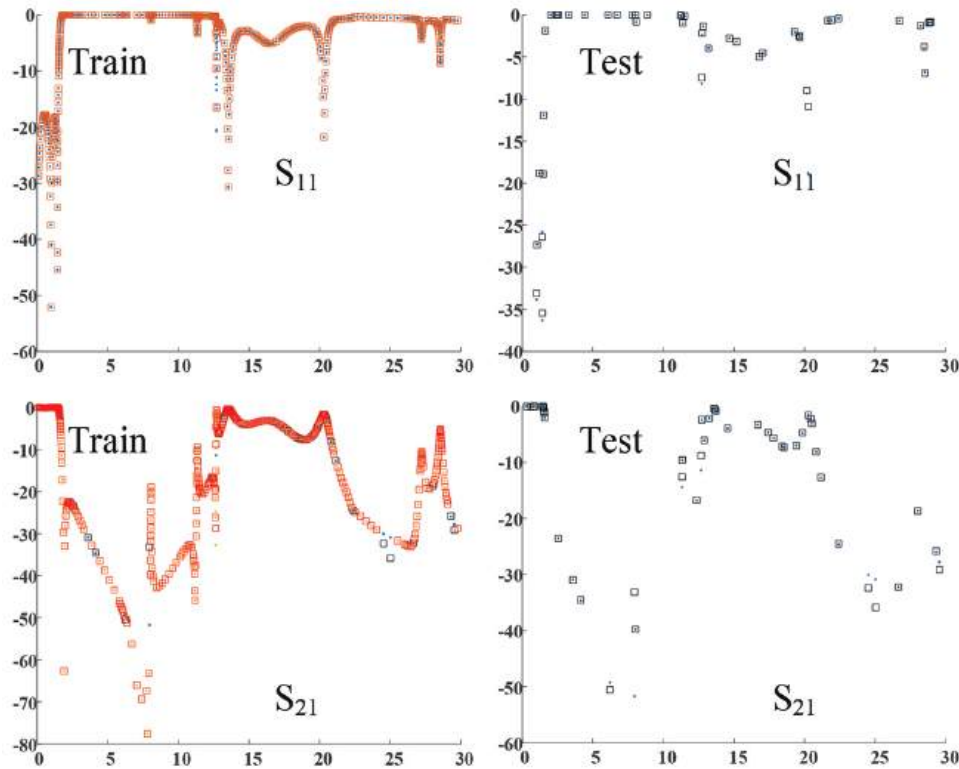


Fig. 12. Real and predicted S-parameters for the proposed device model.

attenuation in this range. The close agreement between the measured and simulated S-parameters highlights the accuracy of the design and the reliability of the fabrication process.

Table I presents a comparative analysis of the performance results of the proposed LPF with several previously filters.

The comparison parameters include cutoff frequency, relative stopband width, size, and sharpness of the filter response. The proposed filter exhibits a cutoff frequency of 1.61 GHz and demonstrates a wide RSB. Notably, the proposed design achieves the smallest size among the compared filters.

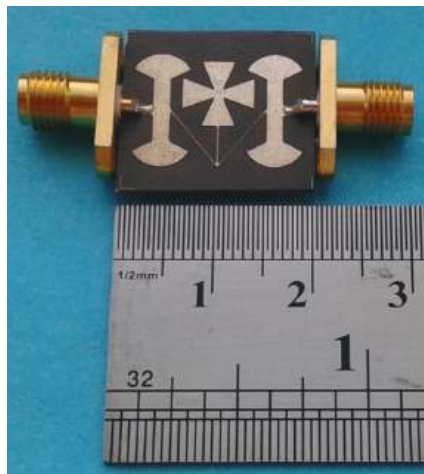


Fig. 13. Fabricated device of the proposed low-pass filter.

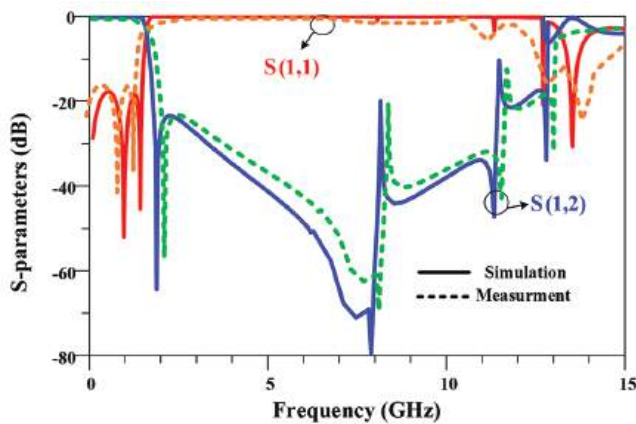


Fig. 14. Measured and simulated S-parameters ( $S_{11}$  and  $S_{21}$ ) of the fabricated low-pass filter with a 1.61 GHz cutoff frequency.

TABLE I  
COMPARISON BETWEEN THE PERFORMANCE RESULTS OF THE PROPOSED LPF AND PREVIOUS WORKS

FOM	NCS	RSB	$\zeta$	$f_c$ (GHz)	Ref.
11543	0.0062	1.32	36	1.18	(Wang et al., 2010)
4391	0.0076	1.66	10	3.2	(Ma et al., 2012)
11221	0.0085	1.52	37	1.3	(Ge, Wang and Guo, 2010)
315	0.116	1.46	25	2.95	(Challal et al., 2012)
350	0.009	1.4	37	3.4	(Faraghi, Azarmanesh and Ojaroudi, 2013)
7081	0.006	1.25	22.66	1.67	(Wei et al., 2011)
6009	0.01	1.65	24.28	1	(Wang, Cui and Zhang, 2012)
7815	0.007	1.55	23.53	0.85	(Cui, Wang and Zhang, 2012)
876	0.096	1.22	34.48	2.62	(Mohra, 2011)
4140	0.009	0.68	27.4	2.5	(Yang et al., 2010)
7095	0.02	1.65	43	1.5	(Mandal and Moyra, 2023)
235	0.046	1.32	7.17	2.85	(Ali and Boutejdar, 2017)
612	0.013	1.17	34	3	(Boutejdar, Challal and El Hani, 2018)
31270	0.009	1.49	94.44	1.61	This Work

NCS: Normalized circuit size

Furthermore, the Sharpness ( $\zeta$ ) of the filter response, is the highest in the proposed design. These results highlight the superior performance of the proposed LPF.

The sharpness ( $\zeta$ ) parameter is calculated according to equation (1).

$$\zeta = \frac{\alpha_{max} - \alpha_{min}}{f_s - f_c} \quad (1)$$

Where  $\alpha_{max}$  and  $\alpha_{min}$  are 60 dB and 3 dB attenuation levels and  $f_s$  and  $f_c$  are the frequency of the  $S_{12}$  parameter at 60 dB, which is equal to 2.21 GHz, and the frequency of the  $S_{12}$  parameter at 3 dB frequency which is equal to 1.61 GHz. The sharpness parameter for the proposed filter is 94.44 dB/GHz.

The suppression factor (SF) and related stopband bandwidth (RSB) parameters are calculated according to equations (2) and (3).

$$RSB = \frac{\text{stopband (20 dB attenuation level)}}{\text{stopband centre frequency}} \quad (2)$$

$$SF = \frac{\text{rejection level in stopband}}{10} \quad (3)$$

The designed filter provides a wide stopband from 1.79 GHz to 11.26 GHz, with more than 20dB attenuation level. According to (2) the SF parameter is equal to 2 and according to (3) the RSB parameter is equal to 1.49.

The normalized circuit size is calculated according to (4).

$$NCS = \frac{\text{physical size (length} \times \text{width)}}{\lambda g^2} \quad (4)$$

The figure of merit (FOM) parameter of the proposed filter, is calculated according (5).

$$FOM = \frac{\zeta \times RSB \times SF}{NCS \times AF} \quad (5)$$

## VI. CONCLUSION

A compact microstrip LPF has been designed using a novel windmill-shaped resonator and symmetrical suppressor cells, yielding a wide stopband bandwidth and a sharp transition in the frequency response. The proposed filter achieves a cutoff frequency of 1.61 GHz with a maximum insertion loss of just 0.1 dB within the passband, ensuring efficient signal transmission at desired frequencies. The stopband extends from 1.79 GHz to 11.26 GHz with a minimum attenuation level of 20 dB, significantly reducing out-of-band interference and harmonics over an impressive bandwidth of 9.47 GHz. This expansive stopband performance, combined with a compact size of 13.34 mm  $\times$  12.78 mm ( $0.097\lambda \times 0.093\lambda$ ), highlights the design's applicability in size-sensitive communication systems. The fabricated prototype was tested, and the experimental results showed excellent alignment with simulated data, confirming the reliability and effectiveness of the design approach. The filter's minimal insertion loss, sharp transition band, and wide stopband address limitations seen in traditional filters, offering a highly efficient, compact, and scalable solution for advanced communication technologies. These characteristics make the proposed filter particularly

suitable for use in modern wireless devices, multi-band communication systems, and ultra-wideband applications where precise frequency control and minimal signal distortion are critical. Overall, the proposed LPF represents a significant advancement in LPF design, providing a robust solution for high-performance communication circuits.

#### REFERENCES

- Ali, W.A.E., and Boutejdar, A., 2017. Design of low-pass filter using meander inductor and U-form Hi-Lo topology with high compactness factor for L-band applications. *Progress in Electromagnetics Research M*, 55, pp.95-107.
- Bavandpour, S.K., Roshani, S., Pirasteh, A., Roshani, S., and Seyedi, H., 2021. A compact low-pass-dual bandpass diplexer with high output ports isolation. *AEU-International Journal of Electronics and Communications*, 135, p.153748.
- Boutejdar, A., Challal, M., and El Hani, S., 2018. Design of a new Broad Stop Band (BSB) low-pass filter using compensated capacitor and II-H-II DGS resonator for radar applications. *Progress in Electromagnetics Research M*, 73, pp.91-100.
- Chakraborty, S., and Verma, A., 2024. Compact high attenuation wide rejection bandwidth 5-pole Butterworth LPF using transmission zeros in GaAs process. *Microelectronics Journal*, 150, p.106263.
- Challal, M., Boutejdar, A., Dehmas, M., Azrar, A., and Omar, A., 2012. Compact microstrip low-pass filter design with ultra-wide reject band using a novel quarter-circle DGS shape. *Applied Computational Electromagnetics Society Journal*, 27(10), pp.808-815.
- Cui, H., Wang, J., and Zhang, G., 2012. Design of microstrip low-pass filter with compact size and ultra-wide stopband. *Electronics Letters*, 48(14), pp.856-857.
- Deng, K., Xue, Q., and Che, W., 2007. Improved compact microstrip resonance cell low-pass filter with wide stopband characteristics. *Electronics Letters*, 43(8), pp.463-464.
- Faraghi, A., Azarmanesh, M.N., and Ojaroudi, M., 2013. Small microstrip low-pass filter by using novel defected ground structure for UWB applications. *The Applied Computational Electromagnetics Society Journal*, 28, pp.341-347.
- Ge, L., Wang, J., and Guo, Y.X., 2010. Compact microstrip low-pass filter with ultra-wide stopband. *Electronics Letters*, 46(10), pp.689-691.
- Hosseini, S.M., and Rezaei, A., 2020. Design of a branch-line microstrip coupler using spirals and step impedance cells for WiMAX applications. *ARO-The Scientific Journal of Koya University*, 8(1), pp.1-4.
- Li, L., Li, Z.F., and Wei, Q., 2009. Compact and selective low-pass filter with very wide stopband using tapered compact microstrip resonant cells. *Electronics Letters*, 45(5), pp.267-268.
- Lotfi, S., Roshani, S., and Roshani, S., 2020. Design of a miniaturized planar microstrip Wilkinson power divider with harmonic cancellation. *Turkish Journal of Electrical Engineering and Computer Sciences*, 28(6), pp.3126-3136.
- Luo, S., Zhu, L., and Sun, S., 2008. Stopband-expanded low-pass filters using microstrip coupled-line hairpin units. *IEEE Microwave and Wireless Components Letters*, 18(8), pp.506-508.
- Ma, K., and Yeo, K.S., 2010. New ultra-wide stopband low-pass filter using transformed radial stubs. *IEEE Transactions on Microwave Theory and Techniques*, 59(3), pp.604-611.
- Ma, K., Yeo, K.S., and Lim, W.M., 2012. Ultra-wide rejection band low-pass cell. *Electronics Letters*, 48(2), pp.99-100.
- Mandal, A., and Moyra, T., 2023. Compact low-pass filter (LPF) with wide harmonic suppression using interdigital capacitor. *Frequenz*, 77(1-2), pp.1-8.
- Mandal, M.K., Mondal, P., Sanyal, S., and Chakraborty, A., 2006. Low insertion-loss, sharp-rejection and compact microstrip low-pass filters. *IEEE Microwave and Wireless Components Letters*, 16(11), pp.600-602.
- Meade, R.D., Brommer, K.D., Rappe, A.M., and Joannopoulos, J., 1991. Photonic bound states in periodic dielectric materials. *Physical Review B*, 44(24), p.13772.
- Mohammadi, N., Moloudian, G., Roshani, S., Roshani, S., Parandin, F., and Lalbakhsh, A., 2024. A Wilkinson power divider with harmonic suppression through low-pass filter for GSM and LTE applications. *Scientific Reports*, 14(1), p.2429.
- Mohra, A.S., 2011. Microstrip low pass filter with wideband rejection using opened circuit stubs and Z-slots defected ground structures. *Microwave and Optical Technology Letters*, 53(4), pp.811-815.
- Park, J., Kim, J.P., and Nam, S., 2007. Design of a novel harmonic-suppressed microstrip low-pass filter. *IEEE Microwave and Wireless Components Letters*, 17(6), pp.424-426.
- Rezaei, A., and Yahya, S.I., 2022. A new design approach for a compact microstrip diplexer with good passband characteristics. *ARO-The Scientific Journal of Koya University*, 10(2), pp.1-6.
- Roshani, S., Dehghani, K., and Roshani, S., 2019. A low-pass filter design using curved and fountain shaped resonators. *Frequenz*, 73(7-8), pp.267-272.
- Roshani, S., Koziel, S., Yahya, S.I., Chaudhary, M.A., Ghadi, Y.Y., Roshani, S., and Golunski, L., 2023a. Mutual coupling reduction in antenna arrays using artificial intelligence approach and inverse neural network surrogates. *Sensors*, 23(16), pp.7089.
- Roshani, S., Yahya, S.I., Ghadi, Y.Y., Roshani, S., Parandin, F., and Yaghouti, B.D., 2023b. Size reduction and harmonics suppression in microwave power dividers. *ARO-The Scientific Journal of Koya University*, 11(2), pp.122-136.
- Ting, S.W., Tam, K.W., and Martins, R., 2006. Miniaturized microstrip low-pass filter with wide stopband using double equilateral U-shaped defected ground structure. *IEEE Microwave and Wireless Components Letters*, 16(5), pp.240-242.
- Wang, J., Cui, H., and Zhang, G., 2012. Design of compact microstrip low-pass filter with ultra-wide stopband. *Electronics Letters*, 48(14), pp.854-856.
- Wang, J., Xu, L.J., Zhao, S., Guo, Y.X., and Wu, W., 2010. Compact quasi-elliptic microstrip low-pass filter with wide stopband. *Electronics Letters*, 46(20), pp.1384-1385.
- Wei, X., Wang, P., Liu, M., and Shi, Y., 2011. Compact wide-stopband low-pass filter using stepped impedance hairpin resonator with radial stubs. *Electronics Letters*, 47(15), pp.862-863.
- Yang, M., Xu, J., Zhao, Q., Peng, L., and Li, G., 2010. Compact, broad-stopband low-pass filters using sirs-loaded circular hairpin resonators. *Progress in Electromagnetics Research*, 102, pp.95-106.

# Sonication Enhancement of Capsaicin Formation in Callus of Chili Pepper, *Capsicum annuum* L.

Hikmat M. Masyab<sup>†</sup>

Department of Biology, Faculty of Science and Health, Koya University,  
Koya KOY45, Kurdistan Region - F.R. Iraq

**Abstract**—The current study investigates the induction of callus from leaf explants of chili pepper *Capsicum annuum* L. coupled with the isolation of capsaicin from alcoholic extracts. To determine which isolated alkaloid has a positive reaction, the Dragen Droff test is used. Alkaloid is identified using conventional diagnostic techniques, such as measuring the absorbance values of the isolated alkaloid with an ultraviolet spectrophotometer; the alkaloid is identified. The results show a complete identity among them, and with control. Thin layer chromatography data shows a 0.8 cm distance between one location from each tested sample with the same rate, which is 0.8 cm from the control's rate flow value. The chemical structure of studied samples is subsequently determined using nuclear magnetic resonance, which reveals similarities between the isolated alkaloid's structure and standard capsaicin. A quantitative analysis of the isolated alkaloids reveals variations in the amounts of generated explants relative to other explants. This study shows that fruits are the most effective source of alkaloids. It's interesting to note that the composition of the explant and the sonicated callus are identical. Since capsaicin's discovery, it has been used as a homeopathic remedy to treat burning pain using the concept of "treating like with like" or counterirritant, relieve minor pain associated with rheumatoid arthritis or muscle sprains and strains, and due to large consumption of this fruit recently, the current study is achieved to find out the structure and quantity.

**Index Terms**—Callus, Capsaicin, *Capsicum annuum* L., Dragendroff, Nuclear magnetic resonance, Sonication.

## I. INTRODUCTION

The Solanaceae family includes the genus *Capsicum*, which includes pepper and is known for its global distribution. Five domesticated species *Capsicum baccatum*, *Capsicum annuum*, *Capsicum pubescens*, *Capsicum frutescens*, and *Capsicum chinense* along with more than 31 different species it is a diverse genus. Spices, such as capsaicin are widely used and prized for their distinct flavor and pungency.

Pepper contains good amounts of provitamin A, carotenoids, Vitamins E and C, and phenolic compounds such as luteolin, quercetin, and capsaicinoids. All of these substances have antioxidant properties and are linked to various biological functions. Remarkably, individuals have used capsicum fruits in their diet to cure wounds, rheumatism, toothaches, coughs, and parasite infections. In addition, it has antibacterial, antiseptic, immune-modulatory, anticancer, and counterirritating properties (Batiha, et al., 2022). *C. annuum* has many angular twigs and reaches heights of 0.75–1.8 m in cultivated areas. This shrub is an annual. The leaves are simple, elliptical to lanceolate, and alternating in shape. The entire smooth margins are usually wrinkled. The tiny flowers are arranged in groups of two or three and have a diameter of 1.0–1.5 cm. The berries are smooth, glossy, and have many seeds; when ripe, they turn crimson. They lack sutures and might be long, cylindrical, ovoid, obtuse, or oblong. They lack sutures and might be long, cylindrical, ovoid, obtuse, or oblong with numerous smooth, rounds, discoid, golden seeds with an outward spine-aroma. It is a maximum length of 25 cm and a maximum width of 7 mm (Kraft, et al., 2014).

The five main chemicals found in the majority of *Capsicum* species are capsaicin (69%), dihydrocapsaicin (22%), nordihydrocapsaicin (7%), homocapsaicin (1%), and homo dihydro capsaicin (1%) (Perry, et al., 2007).

Because of their pungency, pepper fruits are noted for their intense, spicy flavor, which is attributed to secondary metabolites called capsaicinoids. The placental tissue and interocular septum both generate a class of alkaloids. All peppers contain the two primary capsaicinoids, dihydrocapsaicin and capsaicin, in concentrations that can exceed 90% in the seeds, placenta, and pericarp of the fruit. Less than 20% of the total is made up of homodihydrocapsaicin, homocapsaicin, and nordihydrocapsaicin (Perucka and Oleszek, 2000; Giuffrida, et al., 2013). Even though capsaicin's pharmacological properties were first recognized in science in the middle of the 19<sup>th</sup> century, current research focuses on enhancing the compound's applications, isolation, and purification. Back then, capsaicin was said to be a substance with a variety of uses, such as a natural food addition and a host of health advantages (Papoiu and Yosipovitch, 2010).

In recent years, numerous techniques for obtaining capsaicinoids from spicy peppers have been devised,

ARO-The Scientific Journal of Koya University  
Vol. XII, No. 2 (2024), Article ID: ARO.11782. 7 pages  
DOI: 10.14500/aro.11782

Received: 20 August 2024; Accepted: 27 November 2024  
Regular research paper; Published: 15 December 2024

<sup>†</sup>Corresponding author's e-mail: hikmat.mustafa@koyauniversity.org  
Copyright © 2024 Hikmat M. Masyab. This is an open-access  
article distributed under the Creative Commons Attribution  
License (CC BY-NC-SA 4.0).



including organic solvent extraction, microwave-assisted extraction, supercritical fluid extraction, and ultrasound-assisted extraction (Marincas, et al., 2018; Teng, Zhang and Devahastin, 2019; Fabela, et al., 2019; Wang, et al., 2021). The first stage in designing an extraction process is selecting a good solvent producing a large amount of the targeted substance. The most abundance used solvents for removing capsaicinoids include water, acetonitrile, methanol, and ethanol (Barbero, et al., 2008). To achieve high extraction productivity, a number of additional relevant variables are also considered during the solvent selection process. These include sample quantity, temperature, extraction duration, solvent volume, and the operations' repeatability and reproducibility. This research investigated the induction of callus from leaf explant of *C. annuum* L. coupled with the isolation of capsaicin from alcoholic extracts of fruit and callus of the chili pepper plant.

## II. MATERIALS AND METHODS

### A. Plant Material and Processing of Explants

Healthy and uniform seeds of *C. annuum* were obtained from local markets, first washed then sterilized using 6% sodium hypochlorite solution (NaOCl) (Jadid, et al., 2023) for 5 times followed by rinsing them using sterilized distal water twice for 2.0 min then dried using sterilized filter paper. Sterile five seeds were transferred into flasks containing 25 mL of agar-solidified Murashige and Skoog Free of plant growth regulators (PGRs) MSO medium free of PGRs. Samples were kept in a tissue culture room at 23°C under 2000 lux light at (16/8) regime.

### B. Establishment of Callus

Two-month-old sterile seedlings were used to establish callus, 0.5 cm<sup>2</sup> leaf segments, 0.5 cm stem segments, 0.5 cm leaf petiole, and stem apex were cultured on 50 mL agar solidified MSO media enhanced with varying amounts

of PGRs (Table I). Induced calli were subcultured every 4 weeks.

### C. Exposure of Callus to Ultrasonic Wave

One gram of callus was exposed to the ultrasound wave, which was carried out at 47.6 kHz on the digital ultrasonic cleaner (Barasonic 221, Germany) for 30 min. Ultrasound treatments were performed in a water bath at a constant temperature of 25°C (El-Sattar and Tawfik, 2023).

### D. Callus, and Fruits Alcoholic Extraction Preparation

Fifty grams of fruit and callus samples were dried in an oven at 40°C for 24 h. The samples were then crushed in a mortar with 100 mL of 70% methanol added. After 45 min of centrifugation at 4°C and 13.000 g, the supernatant was removed. Next, 100 mL of methanol was added and allowed to sit for 24 h. Finally, it was heated at 50°C and allowed to cool before another 45-min centrifugation at 4°C and 13148× g was performed (Lucia, et al., 2020).

### E. Isolation of Capsaicin Alkaloid

The supernatant from the last step was transferred into rotary evaporator at 50°C to precipitate. To dissolve the precipitate 20 mL of 2 N HCL was added. This mixture undergoes filtration using filter paper and 20 mL of Ethyl acetate) (CH<sub>3</sub>-COO-CH<sub>2</sub>-CH<sub>3</sub>). The mixture was kept in a separating funnel and shaken manually. Then the ethyl acetate was neglected and ammonia solution was gradually added to reach pH 9. After passing the mixture through filter paper, 50 mL of chloroform were added to the filtrated product, which was then put in a separating funnel and manually Shacked 3 times. Then chloroform layer appeared in a bottle and discarded the remaining. The bottle was then placed in a 50°C water bath to evaporate the chloroform. The remaining product was weighed, and samples were kept at 5°C in a dark place (Berlink and Kossuga, 2007).

TABLE I  
MEDIA USED FOR CALLUS INDUCTION USING MS MEDIA THAT IS ENHANCED WITH DIFFERENT PGR (BENZYL ADENINE, NAPHTHALENE ACETIC ACID, AND 2,4-DICHLOROPHENOXY ACETIC ACID), FROM LEAF EXPLANT OF CHILI PEPPER, SEEDLINGS OF *CAPSICUM ANNUM* L.

Media	Plant growth regulator combinations		
MSO*		Control	
MS	BA 1 mg/0.1+0.2 mg/l NAA	BA 1 mg/0.3+0.2 mg/l NAA	BA 1 mg/0.5+0.2 mg/l NAA
	BA 1 mg/0.1+0.4 mg/l NAA	BA 1 mg/0.3+0.4 mg/l NAA	BA 1 mg/0.5+0.4 mg/l NAA
	BA 1 mg/0.1+0.8 mg/l NAA	BA 1 mg/0.3+0.8 mg/l NAA	BA 1 mg/0.5+0.8 mg/l NAA
MSO		Control	
MS	BA 1 mg/0.1+0.2 mg/l IAA	BA 1 mg/0.3+0.2 mg/l IAA	BA 1 mg/0.5+0.2 mg/l IAA
	BA 1 mg/0.1+0.4 mg/l IAA	BA 1 mg/0.3+0.4 mg/l IAA	BA 1 mg/0.5+0.4 mg/l IAA
	BA 1 mg/0.1+0.8 mg/l IAA	BA 1 mg/0.3+0.8 mg/l IAA	BA 1 mg/0.5+0.8 mg/l IAA
MSO		Control	
MS	BA 1 mg/0.1+0.2 mg/l IBA	BA 1 mg/0.3+0.2 mg/l IBA	BA 1 mg/0.5+0.2 mg/l IBA
	BA 1 mg/0.1+0.4 mg/l IBA	BA 1 mg/0.3+0.4 mg/l IBA	BA 1 mg/0.5+0.4 mg/l IBA
	BA 1 mg/0.1+0.8 mg/l IBA	BA 1 mg/0.3+0.8 mg/l IBA	BA 1 mg/0.5+0.8 mg/l IBA
MSO		Control	
MS	BA 1 mg/0.1+0.2 mg/l 2,4-D	BA 1 mg/0.3+0.2 mg/l 2,4-D	BA 1 mg/0.5+0.2 mg/l 2,4-D
	BA 1 mg/0.1+0.4 mg/l 2,4-D	BA 1 mg/0.3+0.4 mg/l 2,4-D	BA 1 mg/0.5+0.4 mg/l 2,4-D
	BA 1 mg/0.1+0.8 mg/l 2,4-D	BA 1 mg/0.3+0.8 mg/l 2,4-D	BA 1 mg/0.5+0.8 mg/l 2,4-D

MSO\*: Free from plant growth regulators.



*F. Characterization of Isolated Capsaicin Using DragenDroff*

Identification protocols were utilized to detect the presence of alkaloids in extracts to ensure that the isolated compound is alkaloid and its type.

To identify the type of alkaloids and make sure it was extracted in a good quality the DragenDroff method was followed:

The preparation of the DragenDroff solution was combining 2 g of bismuth nitrate Bi (NO<sub>3</sub>)<sub>3</sub>·5H<sub>2</sub>O with 25 mL of glacial acetic acid (solution 1), followed by 40 g of potassium iodide in 100 mL of distilled water (solution 2). Next, 10 mL of the first solution and 10 mL of the second, 20 mL of glacial acetic acid, and 100 mL of distilled water were combined to make the DragenDroff solution (Modified from Narasimhan and Shanta, 2003).

*G. Thin Layer Chromatography (TLC)*

Using a micropipette (0.5–10 µL), samples were manually loaded, 10 mm above the lower border of the plates, with up to 2 µL of the crude extract (corresponding to 4–8 mg of dry tissue). One consistent hit was used to deliver the entire sample volume, with adjacent samples placed 5 mm apart. In every instance, the application spot's diameter was <2 mm. After loading, warm air was used for 30 s to dry the application areas. A solvent mixture consisting of 95:5 ethanols to chloroform was used for the separation process (Wagner, Bladt and Zgainski, 1984). To ensure that the chamber environment was completely saturated, solvent mixes were made right before usage and introduced to the chromatography tank fifteen minutes before development.

*H. Ultraviolet (UV) Spectrophotometer*

For the UV technique analysis of capsaicin, a (AGILENT CARY 100/300 series Uv-Vis, Malaysia) twin beam UV/visible spectrophotometer with a 1.0 cm<sup>3</sup> matched quartz cell was used. Samples were dissolved in chloroform and applied to quartz cells. Standard capsaicin obtained from Chungwoo Food Republic of Korea. The analytical-grade, easily accessible chloroform was used to dilute the capsaicin (Baravkar, et al., 2023).

*I. Determination of Chemical Structure by nuclear magnetic resonance (NMR)*

The samples were dissolved in 500 µL of chloroform for the NMR analysis. Using an NMR spectrometry (Shimadzu 60MHz, Japan) coupled to a 5 mm probe at 295 K, NMR data gathering was carried out. To record 1 H NMR, a typical pulse program called zg30 was utilized. On customized graph paper that was improved by an NMR device, dates were recorded (Bora, et al., 2021).

*J. Statistical Analysis*

One-way analysis of variance was used to evaluate all the data using the GraphPad prism9 statistical package, version 9.3.1 software. The results were expressed as means ± Standard Division at 0.01(Gupta, et al., 2019).

III. RESULTS AND DISCUSSION

*A. Plant Material and Explant Preparation*

Leaf segments grown on MS medium with various amounts of PGRs added as supplements showed that the MS media supplemented with 0.4, 0.8 mg/L of NAA and its combinations with 0.3, 0.5 mg/L of BA had the greatest percentage (100%) of callus induction (Table II).

*B. Identification of Potential Capsaicin Derived FROM Alcoholic Extraction*

The orange color and sticky texture of capsaicin that was separated from fruit and callus adhered to the walls of the isolating vessels.

*C. Diagnosis of Capsaicin Derived from Leaf Callus and Fruit*

The results of detecting the alkaloids isolated from different plant parts of *C. annum* and the callus derived from them confirmed the effectiveness of this test, as it was turned orange when the solution was added (Fig. 1).

*D. Rate Flow*

Data showed that the flow distance rates for all spots separated from the alkaloids isolated from different

TABLE II  
INDUCTION OF CALLUS FROM *CAPSICUM ANNUM* LEAF SEGMENTS ON SOLIDIFIED MS MEDIUM SUPPLEMENTED WITH VARIOUS CONCENTRATIONS OF AUXINS (NAPHTHALENE ACETIC ACID, INDOLE ACETIC ACID, INDOLE BUTYRIC ACID, 2,4-DICHLOROPHENOXY ACETIC ACID) AND CYTOKININ (BENZYL ADENINE)

Auxins (mg/L)/ Cytokinin (mg/L)	Percentage of induction (%)								Number of callus-producing leaf segments							
	NAA				IAA				IBA				2,4-D			
	0.0	0.2	0.4	0.8	0.0	0.2	0.4	0.8	0.0	0.2	0.4	0.8	0.0	0.2	0.4	0.8
BA 0.0	0	2	3	6	0	4	5	5	0	3	4	6	0	4	6	6
	0	33	50	100	0	67	83	83	0	50	67	100	0	67	100	100
0.1	1	4	4	5	3	5	5	5	2	3	5	6	3	5	6	6
	17	67	67	83	50	83	83	83	33	50	83	100	50	83	100	100
0.3	3	5	6	6	6	6	6	6	6	6	6	6	6	6	6	6
	50	83	100	100	100	100	100	100	100	100	100	100	100	100	100	100
0.5	4	4	6	6	6	6	6	6	6	6	6	6	6	6	6	6
	67	67	100	100	100	100	100	100	100	100	100	100	100	100	100	100

explants of *C. annuum* (Chili pepper) and the callus derived from them were identical to each other and with the average flow distance of the standard capsaicin solution (Control) (Table III and Fig. 2), as the average flow distance for each of the spots that appeared was (0.8 cm). The spot flow rate is the same as the standard solution of capsaicin alkaloid.

#### E. UV Spectrophotometer

The results of estimating the absorption degree by photometric spectrometry confirmed that the alkaloid isolated from fruit and callus derived from different explants of *C. annuum* (Chili pepper) have the same degree of absorption at the highest wavelength  $\lambda_{max}$  (Fig. 3), as the degree of absorption reached 280 nm, which is similar to the degree of absorption at the highest wavelength of the capsaicin

alkaloid. These results confirm again that the alkaloid isolated is a capsaicin compound.

#### F. Quantitative Estimation of Capsaicin

The results related to the quantitative estimation of the capsaicin alkaloid isolated from fruit and callus derived from different explants of *C. annuum* (Chili pepper) showed a difference in the content of these tissues of callus (Table IV). Data showed that leaf callus was the type of callus that contained the most capsaicin, as its concentration reached 0.64 mg/10 g dry weight, superior to its concentration in fruit and other types of callus, more than that sonication treatment obviously rise the capsaicin quantity in the callus (Table V).

#### G. Determination of Chemical Structure by NMR

The results of determining the chemical structure of the alkaloid isolated from *C. annuum* (Chili pepper) fruits and callus derived from different plant parts confirmed that they have the same chemical structure of the standard capsaicin alkaloid (Fig. 4a-c). This confirms conclusively that the isolated alkaloid is the same as the capsaicin alkaloid.

Capsaicin is an alkaloid that is a member of the class Capsaicinoids. Its scientific name is [(E)-N-[(4-hydroxy-3-methoxyphenyl) methyl]-8-methylnon-6-enamide] and its

TABLE III  
AVERAGE VALUES OF FLOW DISTANCE OF THE SPOTS SEPARATED FROM FRUIT AND DIFFERENT CALLUS TYPES OF *CAPSICUM ANNUUM* (CHILI PEPPER), PLANTS

Isolated alkaloid source	Average flow distance (cm) $\pm$ SD
Standard capsaicin (control)	0.8 $\pm$ 0.002
Fruit	0.8 $\pm$ 0.003
Stem calli	0.8 $\pm$ 0.005
Leaf petiole calli	0.8 $\pm$ 0.008
Leaf calli	0.8 $\pm$ 0.009
Stem apex calli	0.8 $\pm$ 0.009

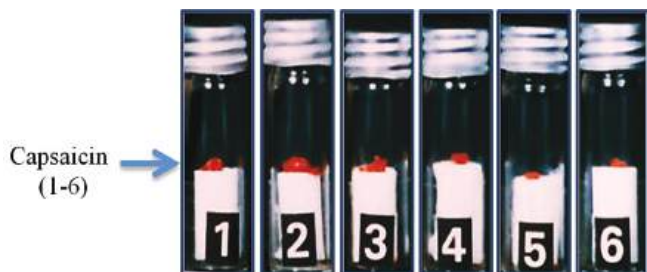


Fig. 1. Quantitative determination of capsaicin isolated from different explants of *Capsicum annuum* (Chili pepper) and the derived callus. (1) Standard capsaicin (Control) (arrowed). (2) Capsaicin isolated from fruit. (3) Capsaicin isolated from stem callus. (4) Capsaicin isolated from leaf petiole callus. (5) Capsaicin isolated from leaf callus. (6) Capsaicin isolated from stem apex callus.

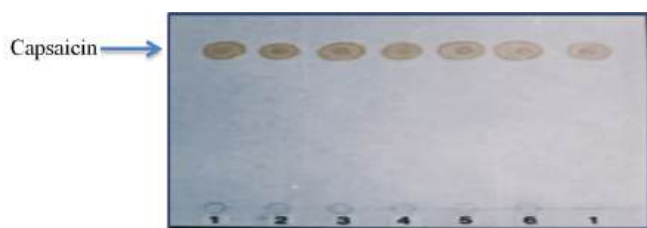


Fig. 2. Detection of capsaicin obtained from fruit and callus derived from different explants of *C. annuum* (Chili pepper) plants using thin layer chromatography technique. (1) Standard capsaicin (Control) (arrowed). (2) Capsaicin isolated from fruit. (3) Capsaicin isolated from stem callus. (4) Capsaicin isolated from leaf petiole callus. (5) Capsaicin isolated from leaf callus. (6) Capsaicin isolated from stem apex callus.

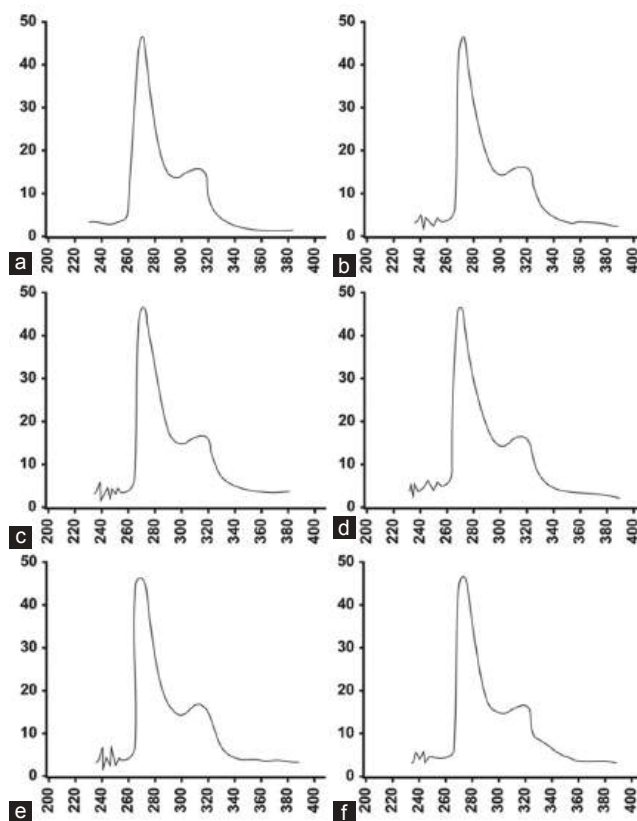


Fig. 3. Absorption Degree of alkaloid isolated from fruit and callus derived from different explants of *C. annuum* (Chili pepper) using UV spectrophotometer. (a) Standard capsaicin (Control). (b) Capsaicin isolated from the fruit. (c) Capsaicin isolated from stem callus. (d) Capsaicin isolated from leaf petiole callus. (e) Capsaicin isolated from leaf callus. (f) Capsaicin isolated from stem apex callus.

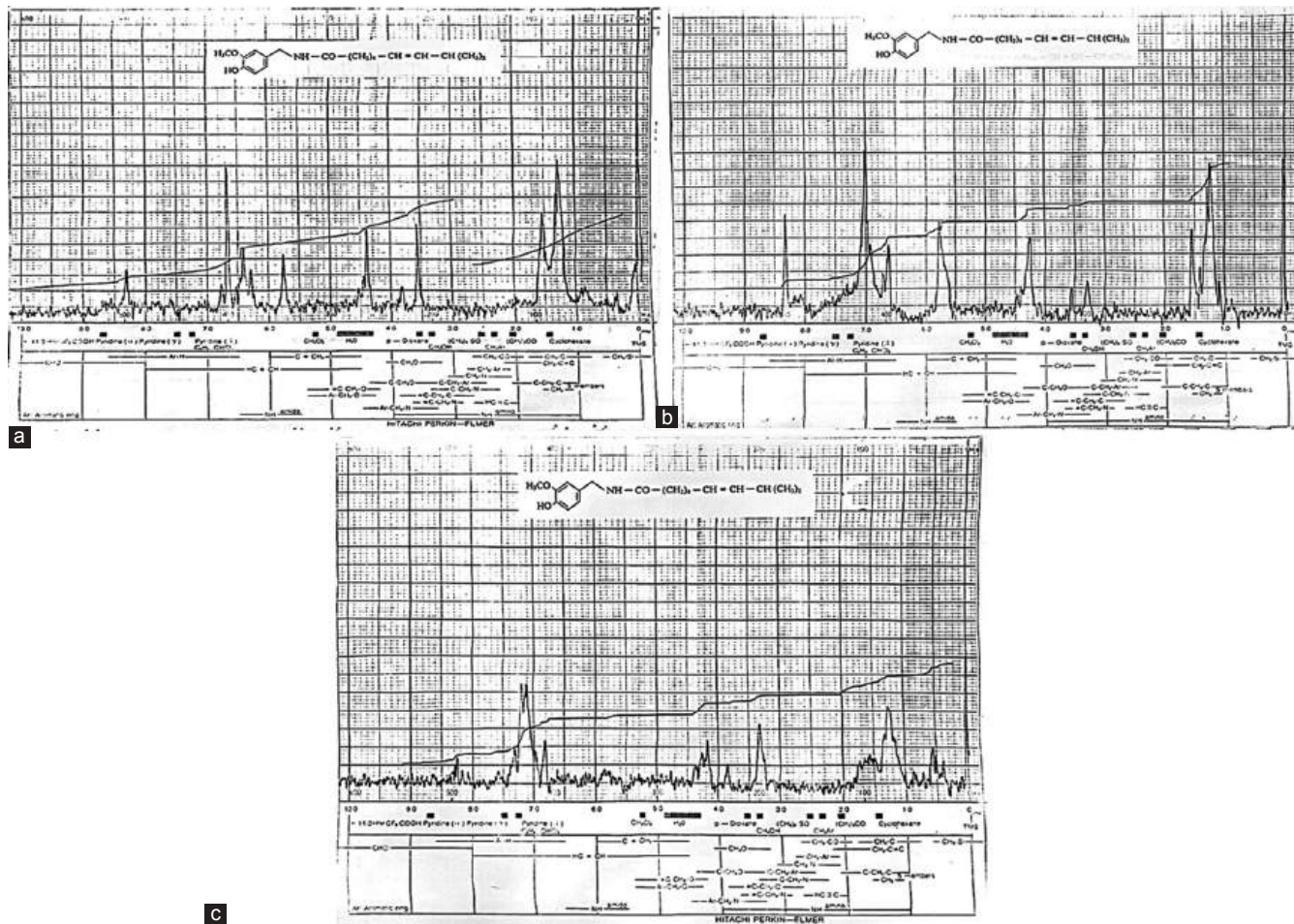


Fig. 4. Chemical composition of the capsaicin extracted from fruit and callus from several *C. annuum* (Chili pepper) explants through NMR technique. (a) Standard capsaicin (Control). (b) Capsaicin isolated from fruit. (c) Capsaicin isolated from different callus tissue.

TABLE IV

QUANTITATIVE ESTIMATION OF CAPSAICIN OBTAINED FROM FRUIT AND DIFFERENT CALLUS TYPES OF *C. ANNUM* (CHILI PEPPER)

Isolated capsaicin source	Weight mg/10 g dry weight
Fruit	5.0±0.002
Stem calli	0.48±0.004
Leaf petiole calli	0.36±0.005
Leaf calli	0.64±0.007
Stem apex calli	0.26±0.002

TABLE V

QUANTITATIVE ESTIMATION OF CAPSAICIN OBTAINED FROM SONICATED CALLUS OF *C. ANNUM* (CHILI PEPPER)

Source of capsaicin	Weight mg/10 g dry weight
Stem calli (cont.)	1.5±0.008
	0.48±0.004
Leaf petiole calli (cont.)	0.9±0.002
	0.36±0.005
Leaf calli (cont.)	1.9±0.011
	0.64±0.007
Stem apex calli (cont.)	0.7±0.001
	0.26±0.002

chemical formula is  $C_{18}H_{27}NO_3$ . Its weight in molecules is 305.4 g/mol (Mol, et al., 2024).

Tissue culturing is a useful method for producing natural phytochemicals on an industrial and laboratory scale (Gammoudi, et al., 2019). Fruits from the *C. annuum* plant, also known as chili pepper, have been utilized as natural colorants, flavorings, food veggies, and medicinal remedies since ancient times. These days, a huge range of sweet and spicy peppers are consumed in many different ways all over the world. It's interesting to note that *C. annuum*, which has a large variety, is the most significant chili pepper in terms of commerce worldwide (Hernández-Pérez, et al., 2020).

The low yields of target compounds have frequently hindered the use of plant cell cultures for biochemical synthesis. When it comes to *in vitro* chili pepper cultures, capsaicin levels have been artificially raised by the following methods nutritional limitation, adding pre-cursors and intermediate salts to the culturing medium (Nisha, 2024), or immobilization of cells (Yaacob, et al., 2022). All of these methods, nevertheless, have not been able to raise capsaicin quantities to levels seen in fruits bearing chili peppers.

Especially in the interlocular septum of fruits and the placenta's capsaicinoid-secreting structures, capsicum species produce and store capsaicin (Nisha, 2024). It's unclear if these structures are necessary for *in vitro* cultures to produce enough capsaicin. However, recent research has demonstrated

that immobilized placental tissues have a higher capability for producing capsaicin than immobilized cells, suggesting that competence in biosynthesis and capsaicin accumulation requires a particular state of organization and differentiation (Poornima, et al., 2024).

It is not unexpected to find competing effects on the accumulation of capsaicin in chili peppers because capsaicin is a consequence of a metabolic process that shares pre-cursors and intermediates with other biosynthetic routes (e.g., proteins, lignins, anthocyanins, coumarins, flavonoids, etc.) (Elshafie, et al., 2023).

Sonication serves as a substitute stressor for cells or tissues, and clinical medicine makes extensive use of ultrasound. The short wavelength and high frequency of sonication provide excellent directional properties. However, sonication can reflect off the surfaces of tissues and exhibit a limited variety of diffractive phenomena. The greater the number of living cells in the samples, the higher the total metabolic activity; Sonication is a form of alternate stress and an elastic mechanical wave in a medium. This type of energy-driven ultrasonic vibration can produce a variety of microscopic mechanical effects, including the mechanical transfer of materials, the heating effect, and the cavitation effect (Liu, et al., 2003).

Ultrasound may alter a cell's metabolism by causing an increase in enzyme activity. Furthermore, ultrasound has the potential to boost mass transfer, including the absorption of nutritional components, and to promote the selectivity and permeability of cell membranes and cell walls. It is well known that ultrasound makes it easier for molecules to flow through membranes. The function of Ca<sup>2+</sup>-ATPase, H<sup>+</sup>-ATPase, and other ion channels in the plasma membrane may be impacted by ultrasonic stimulation. These channels are critical for cell development. (Fontana, et al., 2021).

#### IV. CONCLUSION

The study focused on the induction of callus using the chili pepper explants, and 0.8 NAA mg/L of supplement added to MS medium only was suitable for the induction of callus from all explants. Isolation of capsaicin alkaloid was obtained from alcoholic extracts of fruit and leaf callus, The Dragendroff test showed a positive reaction and the UV spectrophotometer showed a complete identity of isolated capsaicin with control. TLC and NMR techniques also confirmed the similarity between isolated capsaicin and slandered capsaicin. The findings of this study showed that the production of capsaicin in chili pepper callus cultures and fruits differs, sonication leads to an increase in the quantity of capsaicin compared with un-sonicated tissues. Never forget that the variation in the rates of synthesis and breakdown affects the total amounts of a secondary byproduct in cell cultures. The pace at which capsaicin degrades within *in vitro* cultures has to be investigated further.

#### ACKNOWLEDGMENT

The author would like to thank the Research Center, Koya University's Faculty of Science and Health for the facilities that sustained this investigation.

#### REFERENCES

- Baravkar, A., Chopade, V., Dhonde, S., Mandhare, T., Kashid, P., Phadtare, G., Jawale, J., Jain, A., Kadam, D., and Zagade, A., 2023. Development of an UV spectroscopic method for Capsaicin quantification in dosage form and in a bulk formulation. *International Journal of Life Science and Pharma Research*, 13(3), pp.P62-P69.
- Barbero, G.F., Liazid, A., Palma, M., and Barroso, C.G., 2008. Ultrasound-assisted extraction of capsaicinoids from peppers. *Talanta*, 75(5), pp.1332-1337.
- Batiha, G.E.S., Alqahtani, A., Ojo, O.A., Shaheen, H.M., Wasef, L., Elzeiny, M., Ismail, M., Shalaby, M., Murata, T., Zaragoza-Bastida, A., and Rivero-Perez, N., 2020. Biological properties, bioactive constituents, and pharmacokinetics of some *Capsicum* spp. and capsaicinoids. *International Journal of Molecular Sciences*, 21(15), p.5179.
- Berlinck, R., and Kossuga, M., 2007. *Modern Alkaloids: Structure, Isolation, Synthesis and Biology*. Wiley, United States.
- Bora, P.K., Kemprai, P., Barman, R., Das, D., Nazir, A., Saikia, S.P., Banik, D., and Haldar, S., 2021. A sensitive 1H NMR spectroscopic method for the quantification of capsaicin and capsaicinoid: Morpho-chemical characterisation of chili land races from northeast India. *Phytochemical Analysis*, 32(1), pp.91-103.
- El-Sattar, A.M.A., and Tawfik, E., 2023. Effects of ultrasonic waves on seedling growth, biochemical constituents, genetic stability of fenugreek (*Trigonella foenum-graecum*) under salinity stress. *Vegetos*, 36, pp.1427-1436.
- Elshafie, H.S., Camele, I., and Mohamed, A.A., 2023. A comprehensive review on the biological, agricultural and pharmaceutical properties of secondary metabolites based-plant origin. *International Journal of Molecular Sciences*, 24(4), p.3266.
- Fabela, M., Miriam, F., Juan, C. Cuevas, B., Teresa Ayora, T., and Neith, P., 2019. Trends in capsaicinoids extraction from habanero chili pepper (*Capsicum Chinense* Jacq.): Recent advanced techniques. *Food Reviews International*, 36(2), pp.105-134.
- Fontana, F., Iberite, F., Cafarelli, A., Aliperta, A., Baldi, G., Gabusi, E., Dolzani, P., Cristino, S., Lisignoli, G., Pratellesi, T., Dumont, E., and Ricotti, L., 2021. Development and validation of low-intensity pulsed ultrasound systems for highly controlled *in vitro* cell stimulation. *Ultrasonics*, 116, p.106495.
- Gammoudi, N., Zerria, K., Nagaz, K., and Ali, F., 2019. Enhancement of capsaicinoids *in vitro* production by abiotic elicitors in placenta-derived callus of *Capsicum annum* L. Tunisian var. 'Baklouti Medenine'. *Biologia*, 74, pp.725-732.
- Giuffrida, D., Dugo, P., Torre, G., Bignardi, C., Cavazza, A., Corradini, C., and Dugo, G., 2013. Characterization of 12 *Capsicum* varieties by evaluation of their carotenoid profile and pungency determination. *Food Chemistry*, 140(4), pp.794-802.
- Gupta, V.K., Siddiqi, N.J., Ojha, A.K., and Sharma, B., 2019. Hepatoprotective effect of *Aloe vera* against cartap-and malathion-induced toxicity in Wistar rats. *Journal of Cellular Physiology*, 234(10), pp.18329-18343.
- Hernández-Pérez, T., Gómez-García, M.D.R., Valverde, M.E., and Paredes-López, O., 2020. *Capsicum annum* (hot pepper): An ancient Latin-American crop with outstanding bioactive compounds and nutraceutical potential. A review. *Comprehensive Reviews in Food Science and Food Safety*, 19(6), 2972-2993.
- Jadid, N., Widodo, A.F., Ermavitalini, D., Sa'adah, N.N., Gunawan, S., and Nisa, C., 2023. The medicinal umbelliferae plant fennel (*Foeniculum vulgare* Mill.): Cultivation, traditional uses, phytopharmacological properties, and application in animal husbandry. *Arabian Journal of Chemistry*, 16(3), p.104541.
- Kraft, K.H., Brown, C.H., Nabhan, G.P., Luedeling, E., Luna Ruiz, J.D.J., Coppens d'Eeckenbrugge, G., Hijmans, R.J., and Gepts, P., 2014. Multiple lines of evidence for the origin of domesticated chili pepper, *Capsicum annum*, in Mexico. *Proceedings of the National Academy of Sciences*, 111(17), pp.6165-6170.
- Liu, Y., Yoshikoshi, A., Wang, B., and Sakanishi, A. (2003), Influence of

ultrasonic stimulation on the growth and proliferation of *Oryza sativa* Nipponbare callus cells. *Colloids and Surfaces B: Biointerfaces*, 27(4), pp.287-293.

Lucia, P., Mattia, M., Vilberto, S., and Daniele, F. (2020), Biological potential of an ethanolic extract from “*Mela Rosa* Marchigiana” pulp callus culture, *Journal of Functional Foods*, 75, p.104269.

Marincas, O., Feher, I., Magdas, D.A., and Puscas, R., 2018. Optimized and validated method for simultaneous extraction, identification and quantification of flavonoids and capsaicin, along with isotopic composition, in hot peppers from different regions. *Food Chemistry*, 267, pp.255-262.

Mol, G.S., Aruldas, D., Joe, I.H., Selvaraj, S., and Nadh, A.G., 2024. Modeling the structural and reactivity properties of capsaicin [(E)-N-[(4-hydroxy-3-methoxyphenyl) methyl]-8-methylnon-6-enamide] wavefunction-dependent properties, pharmacokinetics, *in-silico* analysis, and molecular dynamics simulation. *Journal of Molecular Structure*, 1304, p.137591.

Narasimhan, S., and Shanta, M., 2003. Spectrophotometric method for estimation of alkaloids perceptible with dragendorff's reagent in plant materials, *Journal of AOAC International*, 86(6), pp.1124-1127.

Nisha, S., 2024. Biotechnological approaches for enhanced production of capsaicin. In: Swamy, M.K., and Kumar, A., Eds. *Capsaicinoids*. Springer, Singapore.

Papoiu, A.D.P., and Yosipovitch, G., 2010. Topical capsaicin. The fire of a 'hot' medicine is reignited. *Expert Opinion on Pharmacotherapy*, 11(8), pp.1359-1371.

Perry, L., Dickau, R., Zarrillo, S., Holst, I., Pearsall, D.M., Piperno, D.R., and Zeidler, J.A., 2007. Starch fossils and the domestication and dispersal of chili peppers (*Capsicum spp.* L.) in the Americas. *Science*, 315(5814), pp.986-988.

Perucka, I., and Oleszek, W., 2000. Extraction and determination of capsaicinoids in fruit of hot pepper *Capsicum annum* L. by spectrophotometry and high-performance liquid chromatography. *Food Chemistry*, 71(2), pp.287-291.

Poornima, K.N., Kavya, M.E., Arpita, S., and Mohan Rao, A., 2024. Biosynthesis of capsaicinoids in plants. In: Swamy, M.K., and Kumar, A., Eds. *Capsaicinoids*. Springer, Singapore.

Teng, X., Zhang, M., and Devahastin, S., 2019. New developments on ultrasound-assisted processing and flavor detection of spices: A review. *Ultrasonics Sonochemistry*, 55, pp.297-307.

Wagner, H., Bladt, S., and Zgainski, E.M., 1984. Plant drug analysis. In: *A Thin Layer Chromatography Atlas*. Springer Verlag, Berlin, Heidelberg, Germany.

Wang, F., Xue, Y., Fu, L., Wang, Y., He, M., Zhao, L., and Liao, X., 2021. Extraction, purification, bioactivity and pharmacological effects of capsaicin: A review. *Critical Reviews in Food Science and Nutrition*, 62(19), pp.5322-5348.

Yaacob, J.S., Ramli, M.A., Abd Rahim, M.H., and Marie, A., 2022. Comparative analysis on the role of 2, 4-dichlorophenoxyacetic acid in the expression of bioactive compounds in callus of *Capsicum frutescens*. *Sains Malaysiana*, 51(10), pp.3171-3182.

# Computational Insights into the Electronic, Optical, and Reactivity Behavior of Halogenated Phenanthrene Derivatives

Rebaz A. Omer<sup>1,2</sup>, Khdir A. Othman<sup>1</sup>, Yousif H. Azeez<sup>3</sup>, and Aryan F. Qader<sup>1†</sup>

<sup>1</sup>Department of Chemistry, Faculty of Science and Health, Koya University, Danielle Mitterrand Boulevard, Koya KOY45, Kurdistan Region – F.R. Iraq

<sup>2</sup>Department of Pharmacy, College of Pharmacy, Knowledge University, Erbil, 44001, Kurdistan Region – F.R. Iraq

<sup>3</sup>Department of Physics, University of Halabja, College of Science, Halabja, Kurdistan Region – F.R. Iraq

**Abstract**—This study explores the complex effects of halogenation on polycyclic aromatic hydrocarbons (PAHs), specifically focusing on phenanthrene. The research aims to understand how the substitution of halogens – namely fluorine (F), chlorine (Cl), and bromine (Br) – in the phenanthrene structure affects its electronic properties, reactivity, and potential applications. The results indicate that halogenation reduces the HOMO-LUMO gap by 0.0100 eV, 0.0064 eV, and 0.2438 eV for F, Cl, and Br, respectively. In addition, it increases the electronegativity (e.g., phenanthrene: 3.6371 eV; phenanthrene-Br: 3.8575 eV), enhancing electron attraction from the phenanthrene rings and lowering the chemical potential. Through detailed analyses of molecular orbitals and density of states, the study reveals significant shifts in energy levels and optical properties. It also employs NMR spectroscopy, potential energy maps, and charge distribution to provide a comprehensive understanding of the compounds. Reduced Density Gradient and Non-Covalent Interaction (NCI) analyses further elucidate the complexities of intermolecular forces in the halogenated derivatives. The research delves into drug-likeness, Natural Bond Orbital (NBO) analysis, and Non-linear Optical properties, highlighting potential applications in medicine, environmental science, and organic electronics. Notably, the halogenated molecules exhibit more intense coloration compared to undoped phenanthrene, with absorption peaks shifting to  $\lambda = 295.1$  nm for phenanthrene-Cl, 305.3 nm for phenanthrene-F, and 307.2 nm for phenanthrene-Br, compared to  $\lambda = 293.0$  nm for pure phenanthrene. These findings underscore the transformative impact of halogenation, positioning this study as a significant contribution to the understanding and potential utilization of halogenated PAHs.

**Index Terms**—Density functional theory, Doping, Electronic behavior, Energy gap, Halogen, Polycyclic aromatic hydrocarbons chemistry.

## I. INTRODUCTION

Polycyclic aromatic hydrocarbons (PAHs) are organic compounds characterized by multiple aromatic rings fused in unique and intricate arrangements. Among these, phenanthrene stands out, alongside other well-known PAHs such as naphthalene and anthracene, contributing significantly to the rich chemistry of this class of compounds (Roy, Karmakar and Dash, 2024, Omer, et al., 2024). These molecules exhibit distinct structural features and possess a wide range of versatile chemical and physical properties, making them valuable in various scientific and industrial applications. In recent years, considerable attention has been directed toward the process of halogenation, where the incorporation of halogen atoms such as fluorine, chlorine, or bromine into the PAH structure introduces new dimensions to their functionality. This modification not only alters the electronic and steric characteristics of PAHs but also enhances their potential for use in fields such as materials science, pharmaceuticals, and environmental studies (Tang, et al., 2018, Li, et al., 2024). Halogenation precisely modifies PAHs, altering their electronic structures and reactivity. The intentional introduction of halogens leads to changes in energy levels, absorption spectra, and fluorescence behaviors (Lawal and Fantke, 2017, Omer, Koparir and Ahmed, 2022b). This transformation influences the charge distribution within the phenanthrene framework, leading to noticeable yet nuanced electronic rearrangements. These subtle shifts in electron density highlight the redistribution of charges across specific molecular orbitals (MOs), altering the electronic environment of the system. Such modifications can significantly impact the molecule's overall reactivity, stability, and potential interactions, offering valuable insights into its chemical behavior under varying conditions (Ding, Tommasini and Maestri, 2019, Rebaz, et al., 2022, Arcadi, et al., 2023). Laying the groundwork for understanding the reactivity of halogenated PAHs is essential. Halogenated phenanthrene derivatives provide a versatile avenue for

ARO-The Scientific Journal of Koya University  
Vol. XII, No. 2 (2024), Article ID: ARO.11706. 13 pages  
DOI: 10.14500/aro.11706

Received: 08 July 2024; Accepted: 03 December 2024  
Regular research paper; Published: 15 December 2024

†Corresponding author's e-mail: [aryan.qader@koyauniversity.org](mailto:aryan.qader@koyauniversity.org)  
Copyright © 2024 Rebaz A. Omer, Khdir A. Othman, Yousif H. Azeez, Aryan F. Qader. This is an open-access article distributed under the Creative Commons Attribution License (CC BY-NC-SA 4.0).



exploration. In medicine, these derivatives exhibit potent antibacterial and antifungal properties, indicating their potential therapeutic applications (McCoull, et al., 1999, Omar, et al., 2023). Their adaptability in cancer treatment and infection control, along with the formation of intricate metal complexes, paves the way for advanced drug delivery (Sahoo, et al., 2020, Koparir, et al., 2022). In the environment, halogenated PAHs leave distinct footprints, altering their persistence and toxicity (Barbosa, et al., 2023, Palmer, et al., 2009). Halogenation enhances the optoelectronic properties of phenanthrene, highlighting its potential applications in organic photovoltaic cells, OLEDs, and field-effect transistors (Haritash and Kaushik, 2009, Ahmed and Rebaz, 2020, Abdel-Shafy and Mansour, 2016, Li and Wu, 2023, Li, et al., 2020). Despite the comprehensive findings, several gaps in this study warrant further investigation. Although the electronic, optical, and chemical properties of halogenated phenanthrene derivatives are extensively analyzed, the effects of halogenation on their thermal stability and mechanical properties remain unexplored. Furthermore, the long-term environmental effects and degradation pathways of halogenated PAHs have yet to be studied, which is critical for understanding their ecological impact. While potential applications in organic electronics and medicine are discussed, there is a lack of experimental validation of these properties in practical devices or biological systems. The goal of the research is to gain insight into how the substitution of halogens – fluorine (F), chlorine (Cl), and bromine (Br) – within the phenanthrene structure affects its electronic properties, reactivity, and potential applications. Fluorine, chlorine, and bromine are commonly chosen for the halogenation of phenanthrene because of their unique chemical and physical properties, which influence the molecule's reactivity, electronic structure, and interactions.

## II. COMPUTATIONAL DETAILS

In this research investigation, the method of Density Functional Theory (DFT) was harnessed to perform detailed calculations. These calculations were executed using the sophisticated Gaussian 09 computational software package, which is renowned for its capabilities in simulating and modeling molecular systems. Specifically, the B3LYP functional, a widely used functional in DFT, was chosen for molecular optimization. This involved intricately refining the arrangement of atoms within the molecules to achieve their most energetically stable configurations (Montgomery, et al., 1999, Koparir, et al., 2023, Omer, et al., 2022a). The 6-31G(d,p) basis sets represent the electron orbitals as a combination of Gaussian functions. These basis sets improve accuracy by including polarization functions (d,p) and diffuse functions (++, for anions or systems with long-range interactions). For DFT Calculations in Gaussian: Functional: B3LYP, Basis Set: 6-31G (d,p), Optimization: Opt=(tight), Frequency Analysis: Freq=NLO (to compute thermodynamic and NLO properties) and Charge and Multiplicity: Set according to the system (e.g., neutral or ionic), Fig. 1.

## III. RESULTS AND DISCUSSION

Phenanthrene and its derivatives doped with fluorine, chlorine, and bromine were meticulously designed through Gauss View. Subsequently, a DFT model was employed to optimize their structures using the suitable B3LYP/6-311G basis set known for its adeptness in capturing accurate configurations (Costa, et al., 2013; Tirado-Rives and Jorgensen, 2008; Nasidi, et al., 2022).

### A. MOs and Density of States (DOS) Analysis

The frontier MOs are the Highest Occupied MO (HOMO) and the Lowest Unoccupied MO (LUMO) of a molecule. They represent the ability of a molecule to donate and accept electrons, respectively. They also determine the chemical stability and reactivity of a molecule (Aihara, 1999, Sun and Wu, 2012). The energy gap between the HOMO and the LUMO is called the HOMO-LUMO gap, and it affects the optical properties of a molecule. The smaller the gap, the lower the energy and the higher wavelength of light that can excite the electrons from the HOMO to the LUMO (Clar, 1972, Becke, 1993, Aziz, et al., 2017). Fig. 2 shows that different halogens have different effects on the HOMO-LUMO gap, with fluorine having the smallest effect and bromine having the largest effect. This is because different halogens have different electronegativities, which affect how strongly they pull the electrons toward themselves. The HOMO-LUMO gap values of all molecules are reduced by substitution. The gap values of phenanthrene decrease by 0.0100, 0.0064, and 0.2438 eV upon substitution with -F, Cl, and Br atoms, respectively. Halogenated phenanthrene's negligible bandgap reduction suggests that halogenation causes minor electronic changes without substantially altering the molecule's basic characteristics. The stability and functioning of the original molecule are preserved, but these modifications are enough to affect applications that call for the fine-tuning of electronic properties.

Fig. 3 shows a DOS analysis of phenanthrene and its halogen-doped structures. A DOS analysis is a way of calculating the number of states per unit energy range that are available for electrons to occupy in a material (Wilbur, et al., 1982, Toriyama, et al., 2022, Sarmah and Hobza, 2020). A DOS analysis can reveal the electronic structure, band gap, and conductivity of a material. Phenanthrene has a large band gap of about 4.7186 eV, so it is an insulator or a poor conductor of electricity. The image also shows that doping phenanthrene with halogens reduces the band gap and increases the number of states near the Fermi level, which is the highest energy level occupied by electrons at zero temperature. This means that doping phenanthrene with halogens makes it more conductive or metallic.

The quantum chemical properties of phenanthrene and its halogen-substituted derivatives (Table I) exhibit a consistent trend with increasing halogen atom size. The total energy consistently decreases (Lazarou, et al., 2001), ranging from -14684.9890 eV for phenanthrene to -84714.3302 eV for phenanthrene-Br, due to the stabilizing effect of

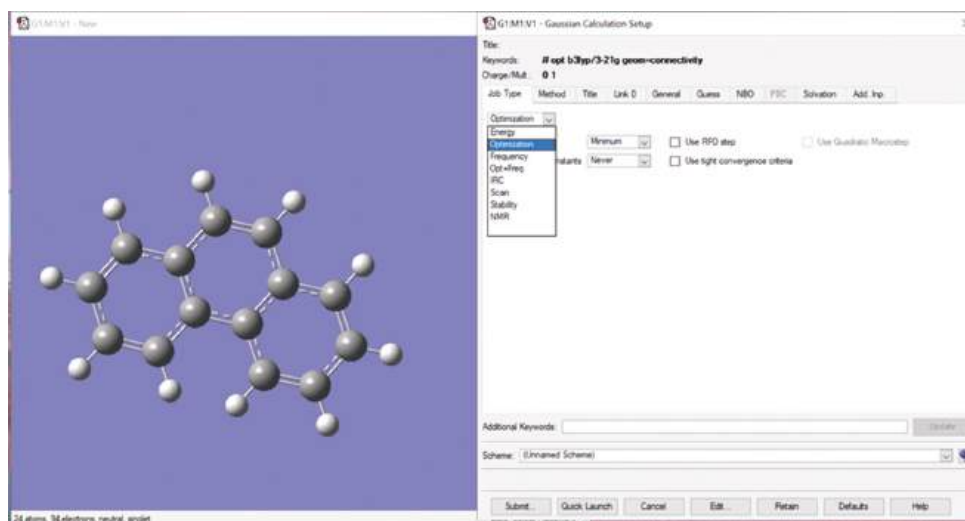


Fig. 1. The input molecule for the density functional theory calculation and the program setup.

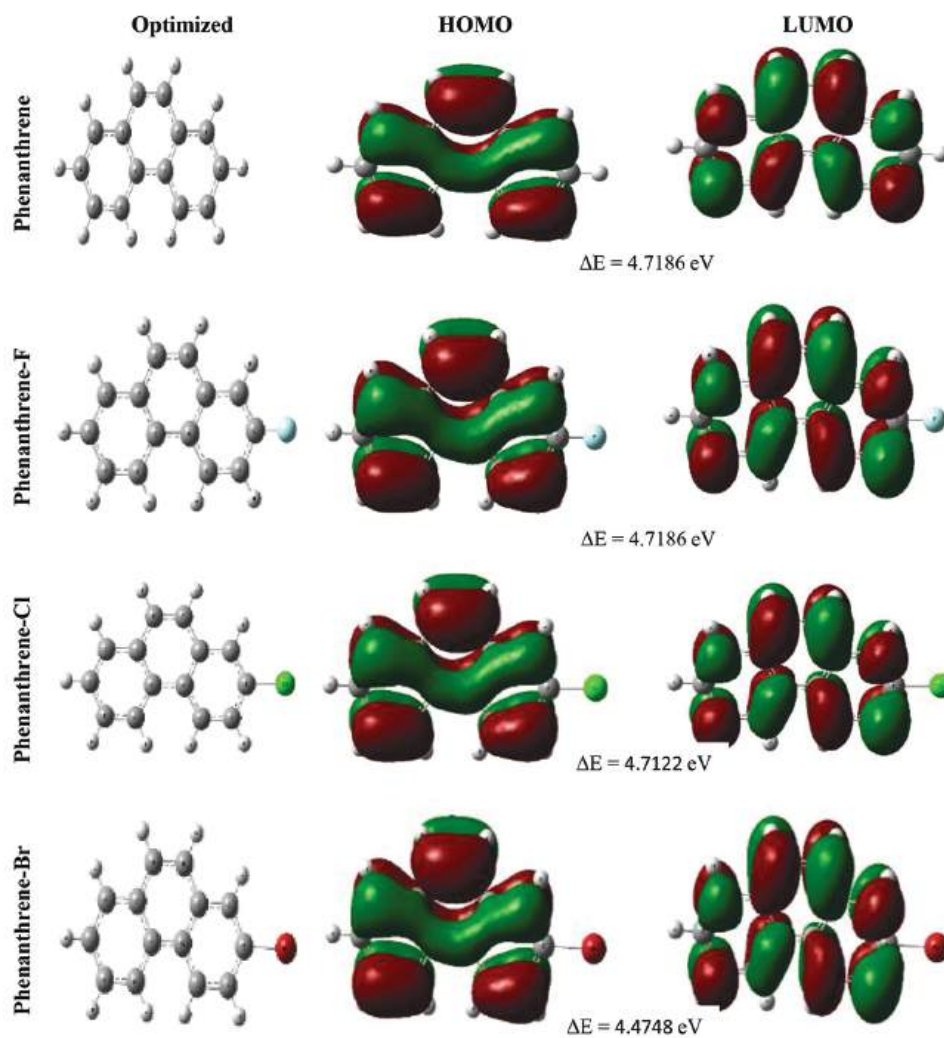


Fig. 2. Optimized structures and MOs of phenanthrene and its structures doped with halogens.

larger halogen atoms with extra electrons. Simultaneously, both HOMO and LUMO energies decrease because of the heightened electronegativity of larger halogen atoms,

resulting in enhanced electron repulsion. As a result, the energy gap between HOMO and LUMO energies contracts in the sequence phenanthrene > phenanthrene-F > phenanthrene-



Cl > phenanthrene-Br, reflecting augmented polarizability and heightened reactivity within the compounds (Tang and Bao, 2011, Akbas et al., 2023, Wang, et al., 2016, Kaka, et al., 2024).

Halogen doping increases the ionization energy ( $I = -E_{\text{HOMO}}$ ) and electron affinity ( $A = -E_{\text{LUMO}}$ ) of phenanthrene. The IP values range from 5.9964 eV for phenanthrene to 6.0949 eV for phenanthrene-Br, making electron removal harder. The EA values range from 1.2778 eV for phenanthrene to 1.6201 eV for phenanthrene-Br, making electron addition easier (Janietz, et al., 1998).

Larger halogens lower the chemical hardness ( $\eta$ ) and raise the softness ( $S$ ) of phenanthrene and its derivatives,

because of the reduced HOMO-LUMO gap and altered polarizability and reactivity (Pearson, 2005). The  $\eta$  values vary from 2.3593 eV for phenanthrene to 2.2374 eV for phenanthrene-Br, while the  $S$  values vary from 0.4239 eV<sup>-1</sup> for phenanthrene to 0.4469 eV<sup>-1</sup> for phenanthrene-Br.

Doping phenanthrene with halogens leads to an increase in the compounds' electronegativity (phenanthrene: 3.6371 eV, phenanthrene-Br: 3.8575 eV), intensifying electron attraction from the phenanthrene rings. This results in decreased chemical potential, making the compounds more prone to electron donation to other substances.

The electrophilic nature of the halogens modulates the electrophilicity ( $\omega$ ) and nucleophilicity ( $\text{Nu}$ ) of phenanthrene

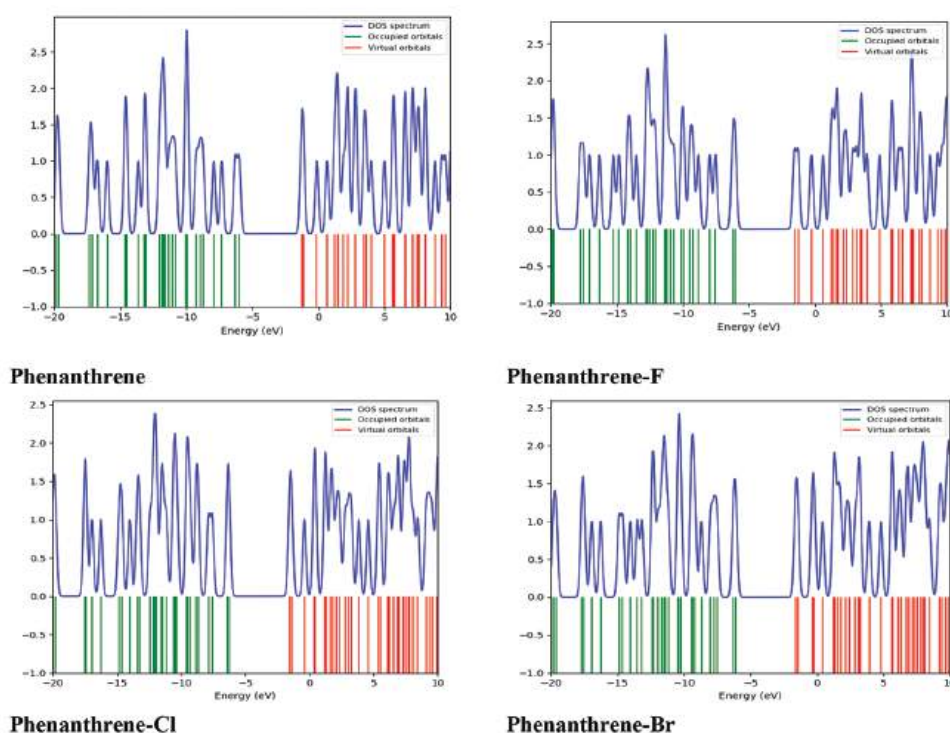


Fig. 3. DOS analysis for phenanthrene and its halogen-doped structures.

TABLE I  
QUANTUM CHEMICAL PARAMETER'S VALUES OF STUDY COMPOUNDS

Quantum chemical parameters	Phenanthrene	Phenanthrene-F	Phenanthrene-Cl	Phenanthrene-Br
Total Energy (eV)	-14684.9890	-17386.1068	-27191.9416	-84714.3302
$E_{\text{HOMO}}$ (eV)	-5.9964	-6.1925	-6.2557	-6.0949
$E_{\text{LUMO}}$ (eV)	-1.2778	-1.4839	-1.5435	-1.6201
$\Delta E$ (eV)	4.7186	4.7086	4.7122	4.4748
Ionization potential "I" (eV)	5.9964	6.1925	6.2557	6.0949
Electron affinity "A" (eV)	1.2778	1.4839	1.5435	1.6201
Chemical hardness " $\eta$ " (eV)	2.3593	2.3543	2.3561	2.2374
Chemical softness " $S$ " (eV <sup>-1</sup> )	0.4239	0.4248	0.4244	0.4469
Electronegativity " $\chi$ " (eV)	3.6371	3.8382	3.8996	3.8575
Chemical potential " $\mu$ " (eV)	-3.6371	-3.8382	-3.8996	-3.8575
Electrophilicity " $\omega$ " (eV)	2.8035	3.1286	3.2271	3.3254
Nucleophilicity "Nu" (eV-1)	0.3567	0.3196	0.3099	0.3007
$\Delta E$ back donation	-0.5898	-0.5886	-0.5890	-0.5593
transfer electron fraction $\Delta N$ (Fe)	3.9670	3.7220	3.6524	3.5155
Dipole- moment (Debye) " $\mu\text{D}$ "	0.0377	1.7148	2.3261	2.1622

and its derivatives. The  $\omega$  values exhibit an ascending trend from 2.8035 eV for phenanthrene to 3.3254 eV for phenanthrene-Br, while the  $\text{Nu}$  values display a descending trend accordingly (Chattaraj and Roy, 2007; Mayr and Patz, 1994).

The back-donation energy ( $\Delta E$ ) is a measure of the energy difference between the HOMO of the donor and the LUMO of the acceptor. The transfer electron fraction ( $\Delta N$ ) is a measure of the charge transfer from the donor to the acceptor. The halogen doping affects both parameters by lowering the HOMO energy and increasing the electronegativity of phenanthrene. Phenanthrene has a higher HOMO energy and a lower electronegativity, which makes it more favorable and efficient for electron donation to iron.

### B. Ultraviolet-Visible (UV-Vis) Analysis

Energy calculations used Gaussian software, optimizing the structure through the 6-311G (d,p) basis set. Employing the TD-SCF method, electronic transitions, and absorption spectrum were analyzed (Ceylan, et al., 2016; Esme, 2019; Jagdale, et al., 2020). Fig. 4 displays the absorption coefficient against incident light wavelength, revealing higher coefficients signify increased light absorption.

Phenanthrene possesses a series of conjugated double bonds, which impart them with various intriguing properties, notably their capability to absorb UV light (Li and Draine, 2002; Arfsten, et al., 1996; Wu, et al., 2010).

Doping phenanthrene with the first three halogens increases electron density in the HOMO and LUMO orbitals. This reduces the energy gap between the HOMO and LUMO orbitals and affects the optical properties of PAH molecules. The electrons at the HOMO of the doped molecules require

energy at a lower frequency and higher wavelength to transition from HOMO to LUMO (Makula, et al., 2018). This phenomenon enhances the likelihood of the doped molecules absorbing light in the visible spectrum (Fig. 4). As a result, the doped molecules exhibit more pronounced coloration compared to the undoped molecules (i.e.,  $\lambda = 293.0, 295.1, 305.3,$  and  $307.2$  nm for Phenanthrene, Phenanthrene-Cl, Phenanthrene-F, and Phenanthrene-Br, respectively).

### C. Infrared (IR) Analysis

Gaussian software was employed for energy calculations, yielding the optimized structure with the 6-311G (d,p) basis set (Li and Draine, 2002; Wodrich, et al., 2007).

The identification of conjugated rings within the phenanthrene structure is straightforward through aromatic C–H stretching patterns. Notably, the C–H stretching vibrations of PAHs are typically observed around  $3100\text{ cm}^{-1}$  (Swofford, Long and Albrecht, 1976; Ricks, Douberly and Duncan, 2009; McClellan and Pimentel, 1955; Srivastava and Singh, 2007). In this study, the theoretically calculated aromatic C–H stretching vibrational modes fall within the range of  $3155\text{--}3205\text{ cm}^{-1}$  (Fig. 5).

Exploring the repercussions of halogen doping on the IR spectra of the phenanthrene molecule reveals significant transformations. Primarily, introducing halogen atoms prompts shifts in absorption peak positions, signifying modifications in molecular vibrations and bond strengths (e.g., C=C-H in undoped phenanthrene at  $3155\text{--}3205\text{ cm}^{-1}$ , shifting to  $3292\text{--}3332\text{ cm}^{-1}$  for fluorine-doped phenanthrene). Novel absorption bands also emerge, showing the inception of fresh vibrational modes and functional groups. Alterations in intensity and bandwidth for

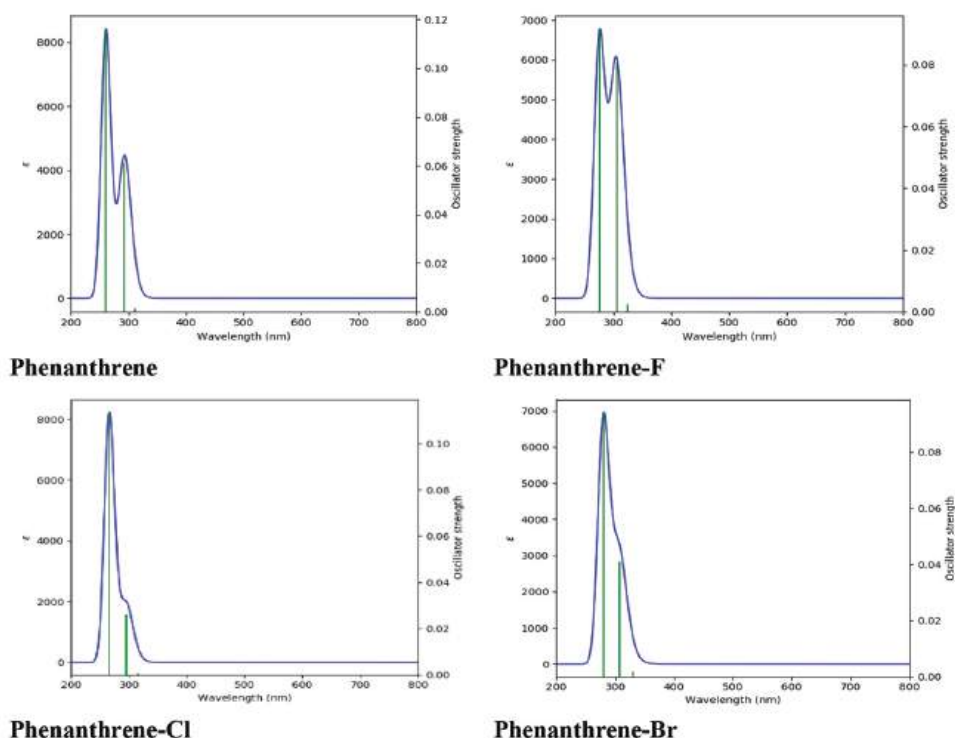


Fig. 4. UV-Vis. absorption spectra of phenanthrene and its halogen-doped derivatives ( $\epsilon$  is represented for absorption).

specific absorption peaks point to fluctuations in molecular flexibility and rigidity.

#### D. Nuclear Magnetic Resonance (NMR)

Fig. 6 shows the theoretically computed H-NMR and C-NMR structures of normal phenanthrene that doped with the first three members of the halogen group. The NMR calculations were performed using the Gaussian 09 software package. The shielding range for normal phenanthrene is from  $-50$  to  $100$  ppm (Arumugam, et al., 2013). When fluorine was introduced into the compound, there was a shift in ppm from  $-100$  to  $350$  ppm. The changes in ppm continued when fluorine was replaced with chlorine from  $-200$  to  $600$  ppm. The changes in ppm were intense when

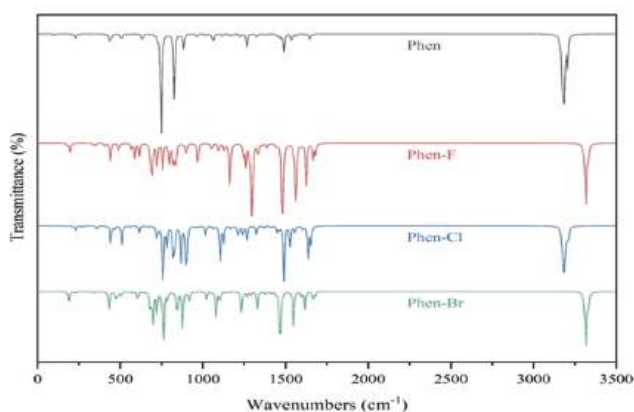


Fig. 5. IR spectrum for phenanthrene and its halogenated derivative.

bromine was introduced from  $-500$  to  $2000$  ppm. This shows that the shielding range increased with an increase in the halogen's electronegativity family.

The normal NMR peaks of undoped phenanthrene show more carbon at the upfield and less carbon at the downfield. However, when fluorine was introduced, the entire orientation of the molecules changed. A sharp medium peak of fluorine appears at  $289.317$  ppm, and both carbon atoms and hydrogen atoms change their chemical environment because of inductive and neighboring effects. The same trend occurred when fluorine was replaced with chlorine and, later, bromine; they have peaks at  $703.184$  and  $1975.342$  ppm, respectively. This proves that NMR peaks generated by members of the halogen family in phenanthrene have a close linear relationship with their electronegativity.

#### E. Potential Energy Map (PES) and Charge Distribution

The PES and charge distribution are important factors that affect the molecular orientation and the optical and electrical properties of the molecules (Haenen, 1977; Solano and Mayer, 2015; Ahmed and Rebaz, 2020; Pi, et al., 2019; Ryno, 2015). Fig. 6 shows the PESs of phenanthrene and its halogen-doped derivatives. These maps illustrate how the electron density of a molecule varies in three dimensions, using different colors to show high and low charge density regions. In phenanthrene, which comprises hydrogen and carbon, the electrons are mainly localized around the rings because of the resonance effect of the double bonds, which is stronger than the electronegativity difference between carbon and hydrogen atoms. However, when fluorine is introduced as a dopant, it

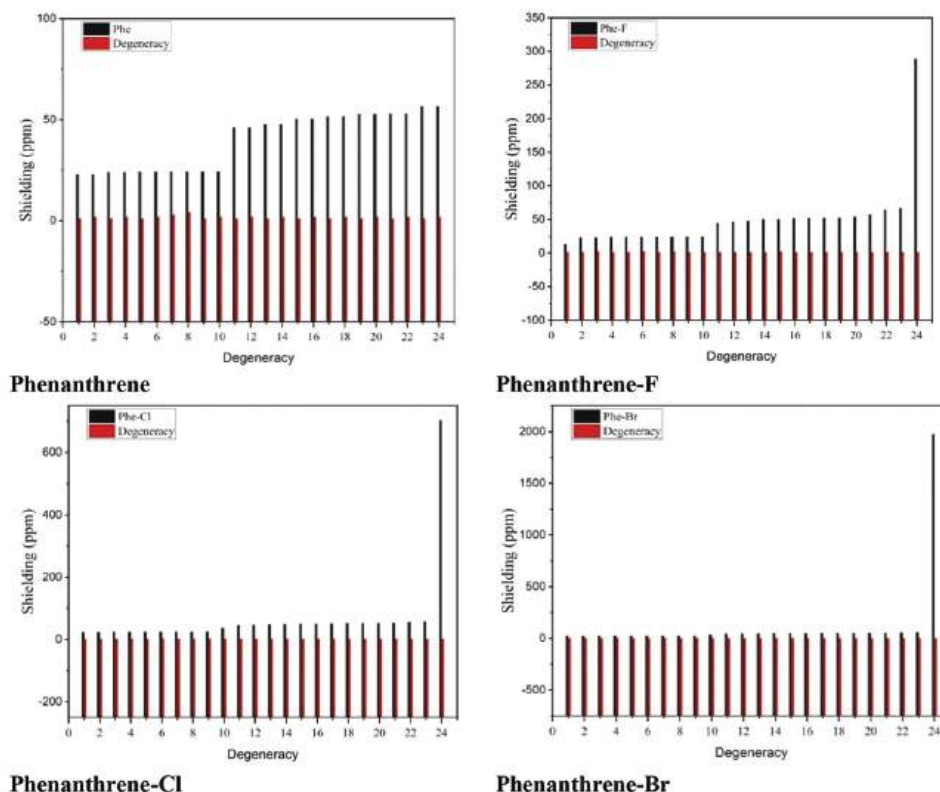


Fig. 6. NMR of phenanthrene and its halogen-doped derivatives.

alters the molecular orientation of phenanthrene. Fluorine has a higher electron affinity than carbon and hydrogen (Modelli, Mussoni and Fabbri, 2006) and thus attracts electrons toward it, resulting in a significant shift of electron density. Similar effects are observed when chlorine and bromine replace hydrogen atoms, making these atoms the most reactive sites of the doped molecule. The charge distribution in a molecule determines its physical and chemical properties. Halogen doping induces changes in charge separation and dipole moment. Halogens have higher electronegativity than carbon and thus draw more electrons, leading to an increased dipole moment and enhanced charge separation. The arrows in Fig. 7 represent the direction and magnitude of the dipole moments of each molecule. The dipole moment ( $\mu$ ) is a measure of molecular polarity, with larger values showing higher polarity. Fig. 7 shows that the net dipole moment follows the order of  $\text{Cl} > \text{Br} > \text{F} > \text{undoped phenanthrene molecule}$ . This trend suggests that chlorine-doped compounds exhibit the highest polarity, followed by bromine-doped compounds and then fluorine-doped ones.

#### F. Reduced Density Gradient (RDG) and Non-Covalent Interactions (NCI)

The utilization of RDG and NCIs in scientific inquiry has introduced innovative methodologies for comprehending and dissecting subtle intermolecular forces. The NCI index serves as a pivotal tool for delineating intermolecular interactions and scrutinizing the attributes inherent to feeble molecular affinities. Calculated through the RDG method, the NCI index furnishes empirical substantiation in favor of NCIs. The RDG, a dimensionless parameter, amalgamates density,

and its first derivative in its formulation, depicted by the following mathematical expression (Domingo, et al., 2002; Asath, et al., 2016; Boukabcha, et al., 2023).

$$RDG(r) = \frac{1 |\nabla \rho(r)|}{2 \left(3\pi r^2\right)^{\frac{1}{3}} \rho^{\frac{4}{3}}(r)}$$

Elaborating on this, the visually striking RDG scatter plots were generated through the utilization of the Multiwfn software (Lu and Chen, 2012), while the three-dimensional isosurfaces were visualized using the VMD software (Humphrey, Dalke and Schulten, 1996). The investigative NCI assessments were conducted employing an isosurface threshold of 0.5. It should be noted that the spectrum of the RDG isosurface ranges from  $-0.035$  to  $0.02$  atomic units. The graphical representation of these molecular attributes is aptly illustrated in Fig. 8, portraying both the bi-dimensional reaction-diffusion grid (RDG) plots and their corresponding three-dimensional isosurfaces.

Significantly enhancing the characterization and quantification of molecular interactions is the graphical portrayal of the function  $\rho(r)$  with the sign of  $\lambda_2$ . This determination of sign ( $\lambda_2$ ) bears substantial implications in predictive analyses. The negative sign of the second eigenvalue, signifying sign ( $\lambda_2$ )  $\rho < 0$ , denotes an attractive interaction, often denominated as a bound interaction. In contrast, a positive sign of sign ( $\lambda_2$ )  $\rho > 0$  points to the existence of a repulsive interaction, specifically typifying a non-bonded interaction. Within the scatter graphs depicted in Fig. 8, the conspicuous spikes manifest distinct categorization

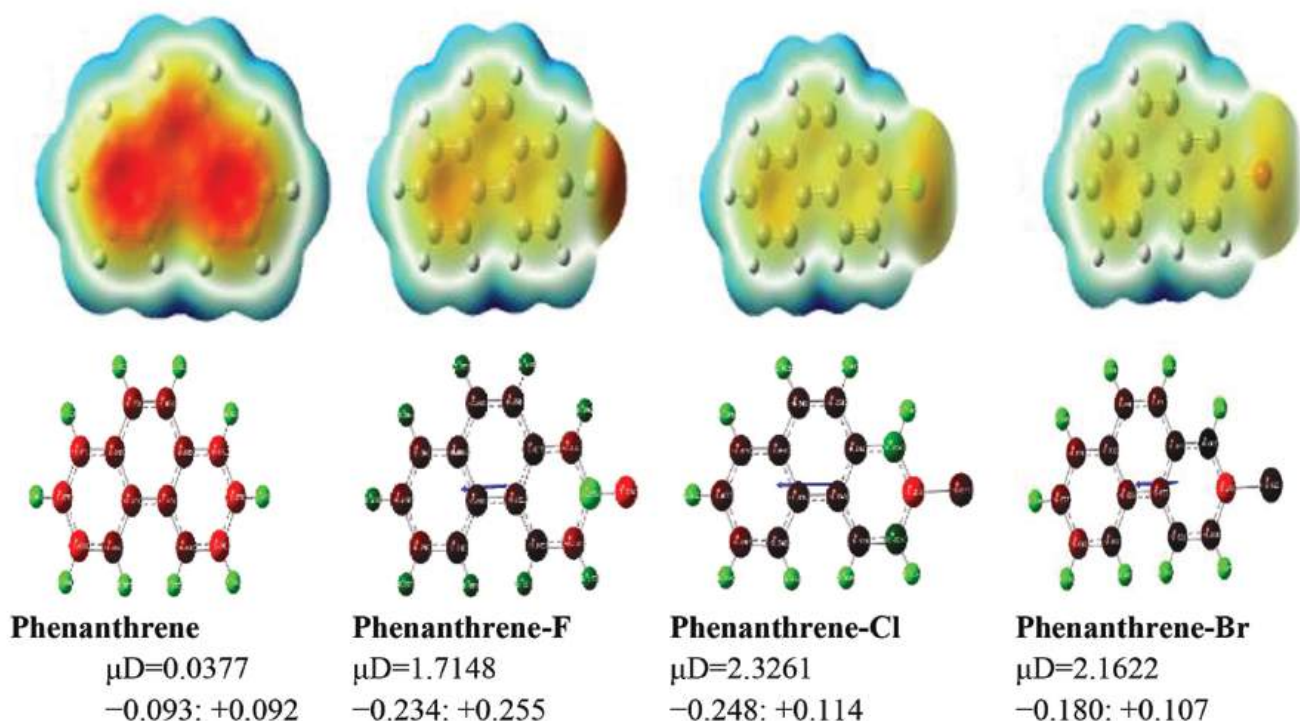


Fig. 7. PEM and charge distributions for phenanthrene and its halogen-doped structures.

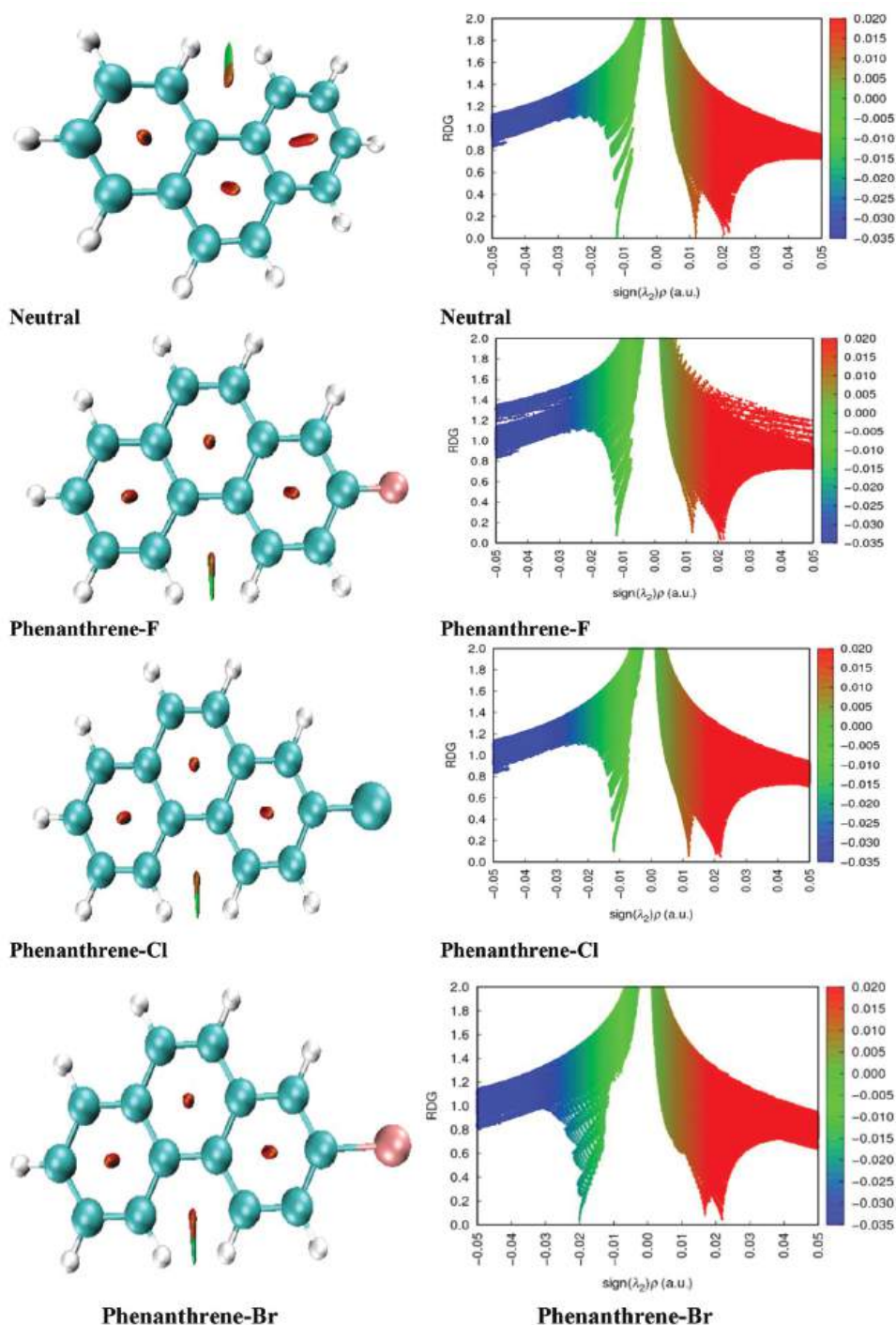


Fig. 8. RDG analysis of studied compounds – weak and strong interactions.

contingent upon the values of  $\text{sign}(\lambda_2)\rho$ . These spikes correspond to three distinct regions, each characterized by its distinctive hue: red, green, and blue. The red region denotes intense repulsive interactions, attributed to steric hindrances. In contrast, the green region signifies feeble attractive forces akin to van der Waals interactions. Notably, the blue zone is emblematic of substantial intermolecular associations, particularly robust hydrogen bonding (Saidj, et al., 2023).

Compared to other compounds, it is noteworthy that compounds containing fluorine exhibit a notably higher

density of points on the graph. This observation suggests that the weak hydrogen bonds and van Der Waals interactions within these fluorine-containing compounds possess enhanced strength. This is visually clear when examining Fig. 8, where regions colored in red are prominently concentrated within the aromatic rings. This observation serves to show a steric effect, indicative of substantial repulsive interactions within these regions. In the same Fig. 8, the appearance of a green-colored isosurface associated with the phenanthrene compound offers intriguing insights. This distinct green

isosurface shows van Der Waals (vdW) interactions. This isosurface's spatial arrangement within the phenanthrene compound points towards the existence of vdW interactions. In combination, these findings suggest a weak hydrogen bond interaction and supplementary contacts involving the two hydrogen atoms (H–H).

### G. Drug Likeness

Assessing a compound's drug-likeness stands as a pivotal pursuit, frequently accomplished using Molinspiration property values, harmonizing with Lipinski's rule of five. This rule outlines that effective drugs generally meet designated thresholds: fewer than five hydrogen bond donors, less than ten hydrogen bond acceptors, molar refractivity between 40 and 160, polar surface area under 140 Å<sup>2</sup>, molecular weight below 500, and fewer than ten rotatable bonds (Walters and Murcko, 2002; Moore, et al., 2007; Arumugam, et al., 2013).

Table II showcases Molinspiration property values for diverse compounds, centered on phenanthrene and its halogen derivatives (+Cl, +Br, +F). These descriptors illuminate their hydrogen bonding potential, polarizability, and structural attributes. The compounds generally lack hydrogen bond donors, except for phenanthrene-fluorine, which exhibits hydrogen bond acceptor capability. Molar refractivity values subtly differ, implying variations in solubility and intermolecular interactions. Low polar surface area values align with expected low polarity and membrane permeability. Elevated molecular weights in halogenated compounds stem from halogen additions, and all compounds exhibit limited rotatable bonds, showing structural rigidity. These findings offer insights into these compounds' structural traits, interaction capacities, and potential applications.

### H. Natural Bond Orbital (NBO) Analysis

The chemical under study underwent an in-depth exploration of its NBO configuration. The primary goal was to understand the interplay between its Lewis and non-Lewis orbitals, utilizing the B3LYP/6–31G(d, p) theoretical methodology. In addition, NBO analysis was executed using the same theoretical framework to uncover intramolecular and intermolecular hydrogen bonding and the dispersion of  $\pi$  electrons across the molecule. Stabilization energy, a measure of delocalization interactions, was determined using second-order energy for individual donor and acceptor NBOs, along with associated E(2) values depicting electron delocalization between donors and acceptors (Ranjith, et al., 2022; Sumathi, et al.; Abbaz, Bendjeddou and Villemin, 2017; Villemin, Abbaz and Bendjeddou, 2018; Abbaz, Bendjeddou and Villemin, 2018).

$$E^{(2)}q = \Delta E_{ij} = q_i \frac{F(i, j)^2}{\epsilon_j - \epsilon_i}$$

The symbol “ $q_i$ ” represents the occupancy of the donor orbital, while “ $\epsilon_j$ ” and “ $\epsilon_i$ ” denote diagonal elements, and “ $F(i, j)$ ” signifies the diagonal NBO Fock matrix elements.

Table III presents a comprehensive Second Order Perturbation Theory Analysis of the Fock Matrix in NBO for Phenanthrene and its derivatives (+Cl, +Br, +F). The table elucidates the intricate interactions between donor and acceptor

TABLE II  
MOLINSPIRATION PROPERTY VALUES FOR THE STUDIED COMPOUNDS

Descriptors	Phenanthrene				Expected range
	Neutral	+Cl	+Br	+F	
Hydrogen bond donor (HBD)	0	0	0	0	<5
Hydrogen bond acceptors (HBA)	0	0	0	1	<10
Molar Refractivity	60.70	66.46	69.15	61.41	40–160
Polar surface area (PSA)	0	0	0	0	<140
Molecular weight	182.26	212.67	257.13	196.22	<500
Number of rotatable bonds	0	0	0	0	<10

TABLE III  
SECOND-ORDER PERTURBATION THEORY ANALYSIS OF FOCK MATRIX IN NBO FOR STUDIED COMPOUNDS

Phenanthrene (neutral)				
Donor NBO (i)	Acceptor NBO (j)	E(2) kcal/mol	E(j)-E(i) a.u.	F(i,j) a.u.
$\pi$ C1-C6	$\pi^*$ C2-C3	17.5	0.29	0.067
$\sigma^*$ C1-H7	$\sigma$ C2-C3	4.48	1.07	0.062
$\pi$ C2-C3	$\pi^*$ C1-C6	18.26	0.28	0.066
$\pi$ C4-C5	$\pi^*$ C2-C3	17.64	0.29	0.067
$\pi$ C11-C12	$\pi^*$ C2-C3	16.68	0.28	0.061
$\pi$ C11-C12	$\pi^*$ C13-C14	14.49	0.28	0.061
$\pi$ C11-C12	$\pi^*$ C17-C20	18.26	0.28	0.066
$\pi$ C11-C12	$\pi^*$ C18-C19	17.85	0.28	0.065
$\pi$ C17-C20	$\pi^*$ C11-C12	17.5	0.29	0.067
$\pi$ C17-C20	$\pi^*$ C18-C19	18.4	0.29	0.066
Phenanthrene (+Cl)				
$\pi$ C1-C6	$\pi^*$ C4-C5	18.27	0.29	0.066
$\pi$ C2-C3	$\pi^*$ C1-C6	18.04	0.28	0.066
$\sigma$ C3-C4	$\sigma^*$ C2-C3	4.16	1.23	0.064
$\pi$ C4-C5	$\pi^*$ C1-C6	18.74	0.29	0.066
$\sigma$ C4-H8	$\sigma^*$ C2-C3	4.94	1.06	0.065
$\pi$ C11-C12	$\pi^*$ C17-C20	18.86	0.27	0.067
$\pi$ C11-C12	$\pi^*$ C18-C19	19.83	0.26	0.066
$\sigma$ C12-C19	$\sigma^*$ C18 -C124	5.58	0.82	0.061
LP (3) Cl 24	$\pi^*$ C18-C19	12.56	0.34	0.062
$\pi^*$ C18-C19	$\pi^*$ C11-C12	253.27	0.01	0.082
Phenanthrene (+Br)				
$\pi$ C1-C6	$\pi^*$ C4-C5	19.4	0.28	0.066
$\sigma$ C2-C3	$\sigma^*$ C2-C11	4.9	1.26	0.07
$\pi$ C2-C3	$\pi^*$ C4-C5	18.13	0.27	0.066
$\pi$ C2-C3	$\pi^*$ C11-C12	19.68	0.29	0.067
$\pi$ C4-C5	$\pi^*$ C1-C6	19.82	0.28	0.067
$\pi$ C4-C5	$\pi^*$ C2-C3	18.21	0.3	0.068
$\sigma$ C11-C12	$\sigma^*$ C2-C11	4.97	1.27	0.071
$\sigma$ C17-C20	$\sigma^*$ C18 -Br 24	5.26	0.79	0.058
LP (3) Br 24	$\pi^*$ C18-C19	10.27	0.31	0.054
$\pi^*$ C13-C14	$\pi^*$ C11-C12	230.06	0.01	0.08
Phenanthrene (+F)				
$\pi$ C1-C6	$\pi^*$ C4-C5	18.21	0.29	0.065
$\pi$ C2-C3	$\pi^*$ C1-C6	18.02	0.28	0.066
$\pi$ C2-C3	$\pi^*$ C4-C5	17.89	0.28	0.066
$\pi$ C4-C5	$\pi^*$ C1-C6	18.86	0.29	0.066
$\pi$ C4-C5	$\pi^*$ C2-C3	17.62	0.29	0.067
$\sigma$ C4-H8	$\sigma^*$ C2-C3	4.94	1.07	0.065
$\pi$ C11-C12	$\pi^*$ C17-C20	19.95	0.27	0.068
$\pi$ C11-C12	$\pi^*$ C18-C19	17.44	0.27	0.063
$\pi$ C17-C20	$\pi^*$ C18-C19	20.83	0.29	0.07
LP (3) F24	$\pi^*$ C18-C19	19.24	0.43	0.087

NBOs, showcasing E(2) values that represent significant stabilization energies, differences in energy (E(j)-E(i)) in atomic

units, and  $F(i,j)$  values in atomic units. Notably, Phenanthrene (+Br) demonstrates a remarkable stabilization energy of 230.06 kcal/mol through the transition from  $\pi$  C11 - C12 to  $\pi^*$  C13 - C14. The findings underscore that, while  $\sigma \rightarrow \sigma^*$  interactions generally possess lower delocalization energy,  $\pi \rightarrow \pi^*$  interactions dominate in this context. Resonance-induced interaction energies ( $n-\pi^*$ ) contribute substantively to the overall molecular stability, providing valuable insights into the intricate nature of these interactions.

### I. Non-linear Optical (NLO) Properties

NLO materials hold significance in non-linear optics, affecting IT and industries. Optimized geometry through B3LYP/6-31G+(d,p) was statically analyzed. Initial static hyper-polarizability ( $\beta_0$ ), a 3D tensor, influences total dipole moment ( $\mu_t$ ), mean polarizability ( $\alpha_0$ ), and starting hyper-polarizability (Obot, et al., 2015, Ranjith, et al., 2022).

$$\mu_t = \left[ \mu_x^2 + \mu_y^2 + \mu_z^2 \right]^{1/2}$$

$$\alpha_t = (\alpha_{xx} + \alpha_{yy} + \alpha_{zz}) / 3$$

$$\beta_t = (\beta_x^2 + \beta_y^2 + \beta_z^2)^{1/2}$$

$$\beta_x = \beta_{xxx} + \beta_{xyx} + \beta_{xzx}$$

$$\beta_y = \beta_{yyx} + \beta_{xyy} + \beta_{yzz}$$

$$\beta_z = \beta_{zzx} + \beta_{xzz} + \beta_{yzz}$$

The substantial magnitude of a specific component of polarizability and hyper-polarizability signifies a notable dispersion of charge in specific orientations (Khan, et al., 2021, Al-Shamiri, et al., 2022). The analysis of the NLO properties presented in Table IV provides insightful observations regarding various compounds (+Cl, +Br, +F) about the standard Urea benchmark. Notably, the dipole moment values for the investigated compounds consistently surpass that of Urea ( $\mu = 1.3732$  D), with the +Br derivative notably exhibiting a dipole moment of  $-2.16$  D. In terms of polarizability, the results showcase phenanthrene's heightened responsiveness to a positive inductive effect (+F), demonstrating a polarizability value of  $-95.53$  a.u., while phenanthrene displays the lowest polarizability under a positive inductive effect (+Br) at  $-87.00$  a.u. However, the calculated hyper-polarizability ( $\beta_0$ ) values for all compounds consistently fall short of the established Urea benchmark of  $343.272 \times 10^{-33}$  esu. This collective finding suggests that the compounds may possess a limited potential for practical applications within NLO systems, causing further exploration. Importantly, the values provided in Table IV, initially reported in atomic units (a.u.), have been effectively converted to electrostatic units (e.s.u.) for improved clarity and comparison.

TABLE IV  
NON-LINEAR OPTICAL PROPERTIES OF THE TITLE COMPOUNDS

Parameters	Phenanthrene			
	Neutral	+Cl	+Br	+F
$\mu_x$	0.00	2.33	-2.16	-1.71
$\mu_y$	0.00	-0.08	-0.08	-0.10
$\mu_z$	-0.04	0.00	0.00	0.00
$\mu_t$	0.04	2.33	2.16	1.71
$\alpha_{xx}$	-87.94	-93.21	-94.36	-85.49
$\alpha_{yy}$	-70.79	-81.24	-87.00	-73.47
$\alpha_{zz}$	-71.07	-99.80	-105.25	-91.32
$\alpha_0$	-76.60	-91.42	-95.53	-83.43
$\alpha$ (esu) $\times 10^{-24}$	-11.35	-13.55	-14.16	-12.36
$\beta_{xxx}$	0.00	-60.39	68.17	-40.49
$\beta_{xyx}$	0.00	0.49	29.70	11.82
$\beta_{xzx}$	0.00	12.19	54.36	17.64
$\beta_x$	0.00	-47.70	152.23	-11.03
$\beta_{yyy}$	0.00	-1.05	2.56	-2.21
$\beta_{xyy}$	0.00	0.20	0.58	-0.10
$\beta_{yzz}$	0.00	-0.28	-0.98	-0.67
$\beta_y$	0.00	-1.13	2.16	-2.98
$\beta_{zzz}$	-0.72	0.00	0.00	0.00
$\beta_{xxx}$	0.05	0.00	0.00	0.00
$\beta_{yyz}$	-0.55	0.00	0.00	0.00
$\beta_z$	-1.22	0.00	0.00	0.00
$\beta_0$ (esu) $\times 10^{-33}$	1.22	47.72	152.24	11.43

### IV. CONCLUSIONS

This comprehensive computational investigation provides an in-depth exploration of halogenated derivatives of phenanthrene, revealing their varied effects on molecular properties. Utilizing computational methods, the study examined electronic structure, reactivity, and complex behaviors. The interactions of halogens were highlighted through UV-Vis absorption spectra, NMR spectroscopy, PESs, and intermolecular interactions. In addition, the analysis of drug-likeness and NBO offered insights into the potential applications and intricate bonding patterns of these compounds. The investigation into NLO properties suggested practical applications as well. This journey culminated not only in theoretical insights but also in implications for fields such as medicine, environmental science, and organic electronics. The findings presented here enhance our understanding of halogenated phenanthrene derivatives and provide a foundation for further interdisciplinary research and applications.

### REFERENCES

- Abbaz, T., Bendjeddou, A., and Villemin, D., 2017. Structure, electronic properties, NBO, NLO and chemi-cal reactivity of bis (1, 4-dithiafulvalene) derivatives: Functional density theory study. *International Journal of Advanced Chemistry*, 6, pp.18-25.
- Abbaz, T., Bendjeddou, A., and Villemin, D., 2018. Molecular structure, NBO analysis, first hyper polarizability, and homo-lumo studies of  $\pi$ -extended tetrathiafulvalene (EXTTF) derivatives connected to  $\pi$ -nitro phenyl by density functional method. *International Journal of Advanced Chemistry*, 6, p.114.
- Abdel-Shafy, H.I., and Mansour, M.S.M., 2016. A review on polycyclic aromatic hydrocarbons: Source, environmental impact, effect on human health and remediation. *Egyptian Journal of Petroleum*, 25, pp.107-123.

- Ahmed, L., and Rebaz, O., 2020. Computational study on paracetamol drug. *Journal of Physical Chemistry and Functional Materials*, 3, pp.9-13.
- Aihara, J.I., 1999. Reduced HOMO-LUMO gap as an index of kinetic stability for polycyclic aromatic hydrocarbons. *The Journal of Physical Chemistry A*, 103, pp.7487-7495.
- Akbas, E., Othman, K.A., Çelikezen, F.Ç., Aydoğan Ejder, N., Turkez, H., Yapca, O.E., and Mardinoglu, A., 2023. Synthesis and biological evaluation of novel benzylidene thiazolo pyrimidin-3(5H)-one derivatives. *Polycyclic Aromatic Compounds*, 44, pp.1-18.
- Al-Shamiri, H.A., Sakr, M.E., Abdel-Latif, S.A., Negm, N.A., Abou Kana, M.T., EL-Daly, S.A., and Elwahy, A.H., 2022. Experimental and theoretical studies of linear and non-linear optical properties of novel fused-triazine derivatives for advanced technological applications. *Scientific Reports*, 12, p.19937.
- Arcadi, A., Fabrizi, G., Goggiamani, A., Iazzetti, A., Iavarone, F., Marrone, F., Mazzocanti, G., and Sferrazza, A., 2023. Synthesis of 9,10-dibenzoyl-phenanthrene derivatives through a palladium-catalyzed domino approach. *Advanced Synthesis and Catalysis*, 365, pp.3277-3283.
- Arfsten, D.P., Schaeffer, D.J., and Mulveny, D.C. 1996. The effects of near ultraviolet radiation on the toxic effects of polycyclic aromatic hydrocarbons in animals and plants: A review. *Ecotoxicology and Environmental Safety*, 33, pp.1-24.
- Arumugam, M., Lulu, S., Kumari, S., and Veena, N., 2013. Computational screening and evaluation of bioactive compounds against NS3 helicase of HCV. *International Journal of Pharmacy and Pharmaceutical Sciences*, 5, pp.370-376.
- Asath, R.M., Rekha, T., Premkumar, S., Mathavan, T., and Benial, A.M.F., 2016. Vibrational, spectroscopic, molecular docking and density functional theory studies on N-(5-aminopyridin-2-yl) acetamide. *Journal of Molecular Structure*, 1125, pp.633-642.
- Aziz, S.B., Abdullah, O.G., Hussein, A.M., Abdulwahid, R.T., Rasheed, M.A., Ahmed, H.M., Abdalqadir, S.W., and Mohammed, A.R., 2017. Optical properties of pure and doped PVA: PEO based solid polymer blend electrolytes: Two methods for band gap study. *Journal of Materials Science: Materials in Electronics*, 28, pp.7473-7479.
- Barbosa, F. Jr., Rocha, B.A., Souza, M.C.O., Bocato, M.Z., Azevedo, L.F., Adeyemi, J.A., Santana, A., and Campiglia, A.D., 2023. Polycyclic aromatic hydrocarbons (PAHs): Updated aspects of their determination, kinetics in the human body, and toxicity. *Journal of Toxicology and Environmental Health, Part B: Critical Reviews*, 26, pp.28-65.
- Becke, A.D., 1993. Density-functional thermochemistry. III. The role of exact exchange. *The Journal of Chemical Physics*, 98, pp.5648-5652.
- Boukabcha, N., Benmohammed, A., Belhachemi, M.H.M., Goudjil, M., Yahiaoui, S., Megrouss, Y., Djafri, A., Khelloul, N., Benyehlou, Z.D., and Djafri, A., 2023. Spectral investigation, TD-DFT study, Hirshfeld surface analysis, NCI-RDG, HOMO-LUMO, chemical reactivity and NLO properties of 1-(4-fluorobenzyl)-5-bromolindolin-2, 3dione. *Journal of Molecular Structure*, 1285, p.135492.
- Ceylan, Ü., Tari, G.Ö., Gökce, H., and Açar, E., 2016. Spectroscopic (FT-IR and UV-Vis) and theoretical (HF and DFT) investigation of 2-Ethyl-N-[(5-nitrothiophene-2-yl) methylidene] aniline. *Journal of Molecular Structure*, 1110, pp.1-10.
- Chattaraj, P.K., and Roy, D.R., 2007. Update 1 of: electrophilicity index. *Chemical Reviews*, 107, pp.PR46-PR74.
- Clar, E., 1972. Aromaticity of polyhedral boranes, carboranes, and metallocarboranes. *Angewandte Chemie International Edition in English*, 11, pp.1111-1115.
- Costa, A.C. Jr., Ondar, G.F., Versiane, O., Ramos, J.M., Santos, T.G., Martin, A.A., Raniero, L., Bussi, G.G., and Tellez Soto, C.A., 2013. DFT: B3LYP/6-311G (d, p) vibrational analysis of bis-(diethylthiocarbamate) zinc(II) and natural bond orbitals. *Spectrochimica Acta Part A: Molecular and Biomolecular Spectroscopy*, 105, pp.251-258.
- Ding, Z.B., Tommasini, M., and Maestri, M., 2019. A topological model for predicting adsorption energies of polycyclic aromatic hydrocarbons on late-transition metal surfaces. *Reaction Chemistry and Engineering Journal*, 4, pp.410-417.
- Domingo, L.R., Aurell, M.J., Pérez, P., and Contreras, R., 2002. Quantitative characterization of the global electrophilicity power of common diene/dienophile pairs in Diels-Alder reactions. *Tetrahedron*, 58, pp.4417-4423.
- Esme, A., 2019. Experimental (FT-IR, FT-Raman, and UV-Vis) and quantum chemical calculations on monomer and dimer structures of 1-hydroxy-2-naphthoic acid using the DFT and TD-DFT methods. *Indian Journal of Pure and Applied Physics*, 57, pp.822-835.
- Haenen, H.T.M., 1977. Potential probe measurement analysis and charge distribution determination. *Journal of Electrostatics*, 2, pp.203-222.
- Haritash, A.K., and Kaushik, C.P., 2009. Biodegradation aspects of polycyclic aromatic hydrocarbons (PAHs): A review. *Journal of Hazardous Materials*, 169, pp.1-15.
- Humphrey, W., Dalke, A., and Schulten, K., 1996. VMD: Visual molecular dynamics. *Journal of Molecular Graphics*, 14, pp.33-38.
- Jagdale, B.S., Ashok Adole, V., Bhavsing Pawar, T., and Desale, B.S., 2020. Molecular structure, frontier molecular orbitals, MESP and UV-visible spectroscopy studies of ethyl 4-(3,4-dimethoxyphenyl)-6-methyl-2-oxo-1,2,3,4-tetrahydropyrimidine-5-carboxylate: A theoretical and experimental appraisal. *Material Science Research India*, 17, pp.13-26.
- Janietz, S., Bradley, D., Grell, M., Giebeler, C., Inbasekaran, M., and Woo, E., 1998. Electrochemical determination of the ionization potential and electron affinity of poly (9, 9-dioctylfluorene). *Applied Physics Letters*, 73, pp.2453-2455.
- Kaka, K.N., Omer, R.A., Mamand, D.M., and Qader, A.F., 2024. Bromination of chalcone. *Aro-The Scientific Journal of Koya University*, 12, pp.48-53.
- Khan, M.U., Khalid, M., Asim, S., Momina, Hussain, R., Mahmood, K., Iqbal, J., Akhtar, M.N., Hussain, A., and Imran, M., 2021. Exploration of nonlinear optical properties of triphenylamine-dicyanovinylene coexisting donor- $\pi$ -acceptor architecture by the modification of  $\pi$ -conjugated linker. *Frontiers in Materials*, 8, p.719971.
- Koparir, P., Omar, R.A., Sarac, K., Ahmed, L.O., Karatepe, A., Taskin-Tok, T., and Safin, D.A., 2023. Synthesis, characterization and computational analysis of thiophene-2, 5-diylbis ((3-mesityl-3-methylcyclobutyl) methanone). *Polycyclic Aromatic Compounds*, 43, pp.6107-6125.
- Koparir, P., Parlak, A.E., Karatepe, A., and Omar, R.A., 2022. Elucidation of potential anticancer, antioxidant and antimicrobial properties of some new triazole compounds bearing pyridine-4-yl moiety and cyclobutane ring. *Arabian Journal of Chemistry*, 15, p.103957.
- Lawal, A.T., and Fantke, P., 2017. Polycyclic aromatic hydrocarbons. A review. *Cogent Environmental Science*, 3, p.1339841.
- Lazarou, Y.G., Prosmittis, A.V., Papadimitriou, V.C., and Papagiannakopoulos, P., 2001. Theoretical calculation of bond dissociation energies and enthalpies of formation for halogenated molecules. *The Journal of Physical Chemistry A*, 105, pp.6729-6742.
- Li, A., and Draine, B., 2002. Do the infrared emission features need ultraviolet excitation? The polycyclic aromatic hydrocarbon model in UV-poor reflection nebulae. *The Astrophysical Journal*, 572, p.232.
- Li, S., Zhang, Q., Gao, M., Li, H., Yang, Z., Wang, Y., and Sun, H., 2024. Polycyclic aromatic hydrocarbons and their halogenated derivatives in soil from Yellow River Delta: Distribution, source apportionment, and risk assessment. *Marine Pollution Bulletin*, 202, p.116308.
- Li, W., and Wu, S., 2023. Challenges of halogenated polycyclic aromatic hydrocarbons in foods: Occurrence, risk, and formation. *Trends in Food Science and Technology*, 131, pp.1-13.
- Li, Z., Hu, W., Li, Z., and Wang, Z., 2020. High performance n-type organic field-effect transistors based on halogenated derivatives of naphthalene tetracarboxylic



- diimides. *Materials Science in Semiconductor Processing*, 120, p.105273.
- Lu, T., and Chen, F., 2012. Multiwfn: A multifunctional wavefunction analyzer. *Journal of Computational Chemistry*, 33, pp.580-592.
- Makula, P., Pacia, M., and Macyk, W., 2018. How to correctly determine the band gap energy of modified semiconductor photocatalysts based on UV-Vis spectra. *The Journal of Physical Chemistry Letters*, 9, pp.6814-6817.
- Mayr, H., and Patz, M., 1994. Scales of nucleophilicity and electrophilicity: A system for ordering polar organic and organometallic reactions. *Angewandte Chemie International Edition in English*, 33, pp.938-957.
- McClellan, A.L., and Pimentel, G.C., 1955. Vibrational assignment and thermodynamic properties of naphthalene. *The Journal of Chemical Physics*, 23, pp.245-248.
- McCoull, K.D., Rindgen, D., Blair, I.A., and Penning, T.M., 1999. Synthesis and characterization of polycyclic aromatic hydrocarbon o-quinone depurinating N7-guanine adducts. *Chemical Research in Toxicology Journal*, 12, pp.237-46.
- Modelli, A., Mussoni, L., and Fabbri, D., 2006. Electron affinities of polycyclic aromatic hydrocarbons by means of B3LYP/6-31+G\* calculations. *The Journal of Physical Chemistry A*, 110, pp.6482-6486.
- Montgomery, J.A., Frisch, M.J., Ochterski, J.W., and Petersson, G.A., 1999. A complete basis set model chemistry. VI. Use of density functional geometries and frequencies. *The Journal of Chemical Physics*, 110, pp.2822-2827.
- Moore, T.J., Cohen, M.R.A., and Furberg, C.D., 2007. A decade of drug-likeness. *Nature Reviews Drug Discovery*, 6, pp.853-853.
- Nasidi, I.I., Kaygili, O., Majid, A., Bulut, N., Alkhedher, M., and Eldin, S.M., 2022. Halogen doping to control the band gap of ascorbic acid: A theoretical study. *ACS Omega*, 7, pp.44390-44397.
- Obot, I., Macdonald, D., and Gasem, Z., 2015. Density functional theory (DFT) as a powerful tool for designing new organic corrosion inhibitors. Part 1: An overview. *Corrosion Science*, 99, pp.1-30.
- Omar, R.A., Koparir, P., Sarac, K., Koparir, M., and Safin, D.A., 2023. A novel coumarin-triazole-thiophene hybrid: Synthesis, characterization, ADMET prediction, molecular docking and molecular dynamics studies with a series of SARS-CoV-2 proteins. *Journal of Chemical Sciences*, 135, p.6.
- Omer, R., Koparir, P., Koparir, M., Rashid, R., Ahmed, L., and Hama, J., 2022a. Synthesis, characterization and DFT study of 1-(3-Mesityl-3-methylcyclobutyl)-2-((4-phenyl-5-(thiophen-2-yl)-4H-1, 2, 4-triazol-3-yl) thio) ethan-1-one. *Protection of Metals and Physical Chemistry of Surfaces*, 58, pp.1077-1089.
- Omer, R.A., Ahmed, K.M., Othman, K.A., Hamad, W.M., Faraj, R.K., Muhiyaldin, A.J., and Salih, S.K., 2024. New thiazole derivatives. *Aro-The Scientific Journal of Koya University*, 12, pp.10-22.
- Omer, R.A., Koparir, P., and Ahmed, L., 2022b. Theoretical determination of corrosion inhibitor activities of 4-allyl-5-(pyridin-4-yl)-4H-1, 2, 4-triazole-3-thiol-thione tautomerism. *Indian Journal of Chemical Technology*, 29, pp.75-81.
- Palmer, A.J., Ghani, R.A., Kaur, N., Phanstiel, O., and Wallace, H.M., 2009. A putrescine-anthracene conjugate: A paradigm for selective drug delivery. *Biochemical Journal*, 424, pp.431-438.
- Pearson, R.G., 2005. Chemical hardness and density functional theory. *Journal of Chemical Sciences*, 117, pp.369-377.
- Pi, X., Sun, F., Gao, J., Qu, Z., Wang, A., Qie, Z., Wang, L., and Liu, H., 2019. A new insight into the SO(2) adsorption behavior of oxidized carbon materials using model adsorbents and DFT calculations. *Physical Chemistry Chemical Physics*, 21, pp.9181-9188.
- Ranjith, P., Ignatious, A., Panicker, C.Y., Sureshkumar, B., Armakovic, S., Armakovic, S.J., Van Alsenoy, C., and Anto, P., 2022. Spectroscopic investigations, DFT calculations, molecular docking and MD simulations of 3-[(4-Carboxyphenyl) carbamoyl]-4-hydroxy-2-oxo-1, 2-dihydroxy quinoline-6-carboxylic acid. *Journal of Molecular Structure*, 1264, p.133315.
- Rebaz, O., Ahmed, L., Koparir, P., and Jwameer, H., 2022. Impact of solvent polarity on the molecular properties of dimetridazole. *El-Cezeri*, 9, pp.740-747.
- Ricks, A.M., Doublerly, G.E., and Duncan, M.A., 2009. The infrared spectrum of protonated naphthalene and its relevance for the unidentified infrared bands. *The Astrophysical Journal*, 702, p.301.
- Roy, C.P., Karmakar, S., and Dash, J., 2024. Synthesis of phenanthrenes and 1-hydroxyphenanthrenes via aromatization-assisted ring-closing metathesis: Toward polynuclear aromatic hydrocarbons. *The Journal of Organic Chemistry*, 89, pp.10511-10523.
- Ryno, S., 2015. Molecular-Scale Understanding of Electronic Polarization in Organic Molecular Crystals. *Georgia Institute of Technology*, p.1-12.
- Sahoo, B.M., Ravi Kumar, B.V.V., Banik, B.K., and Borah, P., 2020. Polyaromatic hydrocarbons (PAHs): Structures, synthesis and their biological profile. *Current Organic Synthesis*, 17, pp.625-640.
- Saidj, M., Djafri, A., Rahmani, R., Belkafouf, N.E.H., Boukabcha, N., Djafri, A., and Chouaih, A., 2023. Molecular structure, experimental and theoretical vibrational spectroscopy, (HOMO-LUMO, NBO) investigation, (RDG, AIM) analysis, (MEP, NLO) study and molecular docking of Ethyl-2-[[4-Ethyl-5-(Quinolin-8-yloxyMethyl)-4H-1, 2, 4-Triazol-3-yl] Sulfanyl] acetate. *Polycyclic Aromatic Compounds*, 43, pp.2152-2176.
- Sarmah, A., and Hobza, P., 2020. Directly linked metalloporphyrins: A quest for bio-inspired materials. *Materials Advances*, 1, pp.1895-1908.
- Solano, E.A., and Mayer, P.M., 2015. A complete map of the ion chemistry of the naphthalene radical cation? DFT and RRKM modeling of a complex potential energy surface. *The Journal of Chemical Physics*, 143, 104305.
- Srivastava, A., and Singh, V.B., 2007. Theoretical and experimental studies of vibrational spectra of naphthalene and its cation. *Indian Journal of Pure and Applied Physics*, 45, pp.714-720.
- Sumathi, D., Thanikachalam, V., Bharanidharan, S., Saleem, H., and Babu, N.R. Vibrational spectroscopy (FT-IR, FT-Raman and UV) studies of E-[1-Methyl-2, 6-diphenyl-3-(propan-2-yl) piperidin-4-ylidene] amino 3-methylbenzoate] using DFT method. *International Journal of Scientific Research*, 5, pp. 2277-8179.
- Sun, Z., and Wu, J., 2012. Open-shell polycyclic aromatic hydrocarbons. *Journal of Materials Chemistry*, 22, pp.4151-4160.
- Swofford, R.L., Long, M.E., and Albrecht, A.C., 1976. C-H vibrational states of benzene, naphthalene, and anthracene in the visible region by thermal lensing spectroscopy and the local mode model. *The Journal of Chemical Physics*, 65, pp.179-190.
- Tang, M., Yu, Q., Wang, Z., Zhang, C., Sun, B., Yi, Y., and Zhang, F.L., 2018. Synthesis of polycyclic aromatic hydrocarbons (PAHs) via a transient directing group. *Organic Letters*, 20, pp.7620-7623.
- Tang, M.L., and Bao, Z., 2011. Halogenated materials as organic semiconductors. *Chemistry of Materials*, 23, pp.446-455.
- Tirado-Rives, J., and Jorgensen, W.L., 2008. Performance of B3LYP density functional methods for a large set of organic molecules. *Journal of Chemical Theory and Computation*, 4, pp.297-306.
- Toriyama, M.Y., Ganose, A.M., Dylla, M., Anand, S., Park, J., Brod, M.K., Munro, J.M., Persson, K.A., Jain, A., and Snyder, G.J., 2022. How to analyse a density of states. *Materials Today Electronics*, 1, p.100002.
- Villemin, D., Abbaz, T., and Bendjedou, A., 2018. Molecular structure, HOMO, LUMO, MEP, natural bond orbital analysis of benzo and anthraquinodimethane derivatives. *Pharmaceutical and Biological Evaluations*, 5, p.27.
- Walters, W.P., and Murcko, M.A., 2002. Prediction of "drug-likeness". *Advanced Drug Delivery Reviews*, 54, pp.255-271.
- Wang, D., Chen, L., Shi, C., Wang, X., Cui, G., Zhang, P., and Chen, Y., 2016. Quantum spin Hall insulator in halogenated arsenene films with sizable energy

gaps. *Scientific reports*, 6, p.28487.

Wilbur, D., Manning, W.B., Hilton, B.D., and Muschik, G.M., 1982. Carbon-13 NMR of polycyclic aromatic compounds. 1-Methoxybenz[a]anthracene-7, 12-diones. *Organic Magnetic Resonance*, 18, pp.63-67.

Wodrich, M.D., Corminboeuf, C., Schreiner, P.R., Fokin, A.A., and

Schleyer, P.V.R., 2007. How accurate are DFT treatments of organic energies? *Organic Letters*, 9, pp.1851-1854.

Wu, M., Nie, M., Wang, X., Su, J., and Cao, W., 2010. Analysis of phenanthrene biodegradation by using FTIR, UV and GC-MS. *Spectrochimica Acta Part A: Molecular and Biomolecular Spectroscopy*, 75, pp.1047-1050.

# *Helicobacter pylori* Infection Associated with Type 2 Diabetes: A Case–Control Study

Aza B. Taha<sup>†</sup>

Medical Research Center, Hawler Medical University,  
Erbil, Kurdistan Region – F.R. Iraq

**Abstract**—*Helicobacter pylori* (Hp) is a spiral Gram-negative bacterium that causes gastritis and peptic ulcers. It has been identified as a risk factor for gastric cancer and has become a significant global health burden. This is further complicated by being associated with increasing the prevalence of Type 2 diabetes (T2D). The study aimed to evaluate the possible associations between Hp infection and T2D, as well as its impact on glycated hemoglobin. A 1:1 matching case–control study is conducted on 548 individuals with T2D as cases and 548 controls, and a <sup>14</sup>C-urea breath test is used to determine the presence of Hp infection. All diabetic subjects are tested for glycated hemoglobin, and binary logistic regression analysis is used to evaluate the associations between Hp infection and T2D. The prevalence of Hp infection is higher among cases (58.94%) than control subjects (38.69%) ( $p < 0.001$ ). A significant association is observed between Hp infection and T2D according to logistic regression analysis (OR = 2.275; 95% CI: 1.786–2.898;  $p < 0.001$ ), and there is a significant association ( $p = 0.022$ ) between glycated hemoglobin levels and Hp infection. Individuals infected with Hp had a higher-level glycated hemoglobin ( $7.84 \pm 1.797$ ) than Hp-negative individuals ( $p < 0.001$ ). Hp infection is associated with elevated glycated hemoglobin levels. Type 2 diabetes is considered a risk factor for developing Hp infection.

**Index Terms**—<sup>14</sup>C-urea breath test, Case–control study, Diabetes mellitus, HbA1C, *Helicobacter pylori*

## I. INTRODUCTION

*Helicobacter pylori* (Hp) is a gram-negative microaerophilic pathogen that causes gastrointestinal disorders such as chronic inflammation, gastric ulcers, and gastric cancer (Malfertheiner, et al., 2023). It was noted that chronic Hp infection is a significant contributor to cancer-related mortality on a global scale (Thrift and El-Serag, 2020). Up to 3% of individuals with Hp-infection develop gastric cancer (Uemura, et al., 2001). However, early detection of Hp-infection with accurate testing can help prevent this progression (Dore and Graham, 2022). In which the <sup>14</sup>C-urea

breath test was a reliable diagnostic tool for identifying active Hp-infections (Sabbagh, et al., 2019).

The Hp-infections affect more than half of the population worldwide, and their prevalence varies depending on geographical location, which recorded a higher rate of infections in developing regions than in developed countries (Li, et al., 2023; Shah, et al., 2024). However, the chronic metabolic disorder Type 2 diabetes (T2D) has been increasing and linked to various complications (Andrew and Adrian, 2022), and the incidence has rapidly increased globally in the past three decades, particularly in developing countries (Lovic, et al., 2020; Liu, et al., 2022). In which individuals with T2D have increasing susceptibility to infections (Cooke, 2022) and become a significant risk factor for all types of infections when blood glucose levels are uncontrolled (Chávez-Reyes, et al., 2021). Moreover, individuals with T2D are more likely to have Hp infections compared to those without T2D (Kouitcheu Mabeku, Noundjeu Ngamga, and Leundji, 2020).

The exact mechanism by which Hp-infection might contribute to the development of diabetes is incompletely understood. One hypothesis states that Hp-induced chronic inflammation and release of inflammatory cytokines may increase insulin resistance and affect the pancreatic B cells, then reduce insulin secretion (Hosseininasab Nodoushan and Nabavi, 2019). Besides, Hp-infection can disrupt the composition and diversity of the gut microbiota, possibly affecting the host's serum metabolism (Zang, et al., 2023). However, the findings on the association between Hp-infection and T2D have yielded conflicting results. Several studies have revealed no significant link between Hp-infection and T2D (Xia, et al., 2001; Tamura, et al., 2015; Man, et al., 2020). Others found a significant positive correlation between Hp-infection and T2D (Bajaj, et al., 2014; Mansori, et al., 2020).

The correlation between T2D and Hp infection is still unclear and poorly understood. Thus, the relationship remains unclear and warrants further exploration. The impact of this research may result in the development of new prevention and intervention strategies for T2D and Hp infections. These strategies will improve patient outcomes, particularly in populations where these conditions are common. Therefore, the present study has been conducted to evaluate the link between T2D and Hp infection and the impact of glycemic control on this relationship.

ARO-The Scientific Journal of Koya University  
Vol. XII, No. 2 (2024), Article ID: ARO.11824. 5 pages  
DOI: 10.14500/aro.11824

Received: 18 August 2024; Accepted: 27 November 2024  
Regular research paper; Published: 18 December 2024

<sup>†</sup>Corresponding author's e-mail: aza.taha@hmu.edu.krd

Copyright © 2024 Aza B. Taha. This is an open-access article distributed under the Creative Commons Attribution License (CC BY-NC-SA 4.0).



## II. MATERIALS AND METHODS

### A. Study design and participants

A 1:1 matching case-control study in Erbil, Iraq, was undertaken from January 2020 to July 2022. The study was conducted on 548 cases and an equal number of controls attending private clinics in the same residential area by a convenience sampling technique. The case group was defined as individuals with T2D who were diagnosed by official documents indicating they have been having T2D for two years and excluded individuals who had Type 1 diabetes. The control group was composed of 548 healthy non-diabetic individuals matching cases based on gender, age, and body mass index (BMI). Furthermore, the study excluded individuals who had a history of gastric surgery, used antibiotics or proton pump inhibitors in the past two months, smoked, were pregnant or lactating, or had any other chronic diseases that could potentially impact the results. As well, case-control pairs that were not matched were excluded from the data analysis.

Data were collected from both groups using a questionnaire that collected information on demographics. Height and weight measurements were taken for each participant, and their BMI was calculated by dividing their weight in kilograms by the square of their height in meters. To estimate glycated hemoglobin (HbA1c) levels, blood venous samples were withdrawn from participants with T2D into EDTA tubes and subsequently analyzed using the Roche Diagnostics Cobas analyzer.

### B. Detection of Hp infection status

The <sup>14</sup>C-urea breath test was used to detect Hp-infection status under the instructions provided by the manufacturer (Headway, China). Briefly, each participant swallowed a capsule containing <sup>14</sup>C-labeled urea with 200 mL of water. After 15 min, a breath sample was obtained by blowing it into a collection card for 3-5 min. The presence of Hp was then determined by measuring the quantity of <sup>14</sup>C-labeled urea within the breath sample using the Hp-detector (Headway, China).

### C. Ethical approval

The study strictly adheres to ethical guidelines and obtains ethical approval from the Ethical Committee at Hawler Medical University. Before inclusion in the study, the participants provided their informed consent. Throughout the study process, data were consistently maintained, and participants were informed of their right to withdraw without facing any negative consequences. The use of a <sup>14</sup>C-urea breath test is safe and involves minimal radiation exposure.

### D. Statistical analysis

The statistical data analysis was conducted using SPSS software version 25.0 for Microsoft Windows. Descriptive statistics were used to summarize the characteristics of both case and control subjects. Logistic regression was applied to determine the odds ratio (OR) and 95% confidence interval (CI) to express the association between Hp-infection and T2D.

Categorical data are provided as frequencies (percentages), while continuous variables are reported as means  $\pm$  standard deviation (SD). The Pearson chi-square test was applied to analyze associations between categorical variables, and the t-test was applied to compare the mean values of continuous variables between groups. The p-value  $< 0.05$  was considered statistically significant.

## III. RESULTS AND DISCUSSION

### A. Results

Table I presents the baseline characteristics of the 1096 subjects, comprising 548 individuals with T2D as the case group and 548 non-diabetic individuals as the control group. Of all participants, 509 (46.44%) were male, and 587 (53.56%) were female. The participants had an average age of 60.48 years, with 39.60% between 55 and 64 years old, and 35.13% aged 65 or older. Approximately 69% of participants were obese, with a mean BMI of  $32.77 \pm 4.01$  for cases and  $31.55 \pm 3.63$  for controls.

Among all participants, 48.81% (535 out of 1,096) were identified as having Hp-infection based on the urea breath test. This prevalence was significantly higher ( $p < 0.001$ ) in participants with T2D (58.94%, 323 out of 548) compared to non-diabetic control subjects (38.69%, 212 out of 548). A logistic regression analysis further confirmed the association between Hp infection and T2D (OR = 2.275; 95% CI: 1.786–2.898;  $p < 0.001$ ) (Table II).

A total of 535 individuals were infected with Hp, with 323 in the case group (T2D individuals) and 212 in the control group. The prevalence of males was 45.82% (148 out of 323) in the case group and 47.64% (101 out of 212) in the control group. Among the cases, 40.87% were aged 65 years or older, and 40.56% were aged 55 to 64 years, with a mean age of  $61.76 \pm 7.816$  years. In the control group, the mean age was  $60.60 \pm 8.333$  years. The majority (70.84%) of all Hp-infected individuals were classified as obese, with a mean BMI of  $33.08 \pm 3.936$  in the cases and  $31.40 \pm 3.30$  in the

TABLE I  
BASELINE CHARACTERISTICS OF INDIVIDUALS WITH T2D AS THE CASE GROUP AND NON-DIABETIC CONTROL GROUPS

Characteristics	Case group (n=548)	Control group (n=548)	All subjects (n=1,096)
Gender			
Male	255 (46.53%)	254 (46.35%)	509 (46.44%)
Female	293 (53.47%)	294 (53.65%)	587 (53.56%)
Age groups (years)			
35-44	9 (1.64%)	10 (1.82%)	19 (1.73%)
45-54	130 (23.72%)	128 (23.36%)	258 (23.54%)
55-64	214 (39.05%)	220 (40.15%)	434 (39.6%)
$\geq 65$	195 (35.58%)	190 (34.67%)	385 (35.13%)
Age (mean $\pm$ SD)	60.57 $\pm$ 8.313	60.39 $\pm$ 8.471	60.48 $\pm$ 8.389
BMI (kg/m <sup>2</sup> )			
Normal (18.5–<25)	20 (3.65%)	19 (3.47%)	39 (3.56%)
Overweight (25.0–<30)	148 (27.01%)	154 (28.1%)	302 (27.55%)
Obese (30.0 or higher)	380 (69.34%)	375 (68.43%)	755 (68.89%)
BMI (Mean $\pm$ SD)	32.77 $\pm$ 4.012	31.55 $\pm$ 3.629	32.16 $\pm$ 3.872

BMI: Body mass index, HbA1c: Glycosylated hemoglobin

controls. There were no statistically significant differences in the prevalence of Hp-infection based on gender, age, or BMI between the case and control groups (Table III).

Among the individuals with T2D who were positive for Hp, 55.72% (180 out of 323) had an HbA1c level of 7% or higher. In contrast, the rate was 45.33% (102 out of 225) in individuals with Hp-negative (Table IV). Statistical analysis using the Pearson Chi-Square test revealed a significant association between Hp-infection and HbA1c levels ( $p = 0.022$ ). Moreover, the individuals with Hp-infection had slightly higher mean HbA1c levels ( $7.84 \pm 1.797$ ) compared to those without Hp-infection, and this difference is statistically significant ( $p < 0.001$ ).

*B. Discussion*

An important issue is the growing coexistence of Hp infection and T2D, which poses a significant public health burden, particularly in developing countries (Hooi, et al., 2017; Ren, et al., 2022; Ye, et al., 2023). The present study demonstrated an association between Hp-infection and T2D. The individuals with T2D and simultaneous Hp-infection

showed a high value of HbA1c in comparison to those without Hp infection. The logistic regression analysis further confirmed this relationship and demonstrated that the individuals with T2D were 2.275 times more likely to be infected with Hp. Hence, this suggests a potential role of T2D in Hp acquisition, and this was in line with previous studies (Shi, et al., 2018; Chen, et al., 2019a; Bener, et al., 2020).

It has been reported that Hp infection can increase the risk of T2D in the Chinese elderly and middle-aged population (Zhou, et al., 2022). On the contrary, three previous studies reported no association between T2D and Hp-infection (Alzahrani, et al., 2017; Pyo, et al., 2019; Alias and Elkarsany, 2022). In my opinion, there are several reasons why different studies have reported varied results. Some of the critical contributors to these differences are due to different study designs and the inclusion of studied different populations. In addition, the diverse methods applied for the diagnosis of Hp infection may be a potential source for different results. In the current study, Hp infection was confirmed by a <sup>14</sup>C-urea breath test that gave high sensitivity

TABLE II  
BINARY LOGISTIC REGRESSION ANALYSIS OF THE ASSOCIATION BETWEEN HP INFECTION AND TYPE 2 DIABETES (T2D)

Hp status	Case group (n=548) (%)	Control group (n=548) (%)	All subjects (n=1,096) (%)	p-value*	Logistic regression	
					OR (95 CI)	p-value
Hp-positive	323 (58.94)	212 (38.69)	535 (48.81)	<0.001	2.275 (1.786–2.898)	<0.001
Hp-negative	225 (41.06)	336 (61.31)	561 (51.19)			

\*Pearson Chi-square. Hp: *Helicobacter pylori*, OR: Odds ratio, CI: Confidence interval

TABLE III  
CHARACTERISTICS OF INDIVIDUALS WITH *HELICOBACTER PYLORI* INFECTIONS IN THE CASE (TYPE 2 DIABETES) AND CONTROL GROUPS

Characteristics	Case group (n=323)	Control group (n=212)	All subjects (n=535)	p-value*
Gender				0.68
Male	148 (45.82%)	101 (47.64%)	249 (46.54%)	
Female	175 (54.18%)	111 (52.36%)	286 (53.46%)	
Age groups (years)				0.272
35–44	2 (0.62%)	3 (1.42%)	5 (0.93%)	
45–54	58 (17.96%)	50 (23.58%)	108 (20.19%)	
55–64	131 (40.56%)	84 (39.62%)	215 (40.19%)	
≥65	132 (40.87%)	75 (35.38%)	207 (38.69%)	
Age (mean±SD)	61.76±7.816	60.60±8.333	61.30±8.038	
BMI (kg/m <sup>2</sup> )				0.508
Normal (18.5–<25)	9 (2.79%)	5 (2.36%)	14 (2.62%)	
Overweight (25.0–<30)	80 (24.77%)	62 (29.25%)	142 (26.54%)	
Obese (30.0 or higher)	234 (72.45%)	145 (68.4%)	379 (70.84%)	
BMI (mean±SD)	33.08±3.936	31.40±3.301	32.42±3.784	

BMI: Body mass index, HbA1c: Glycosylated hemoglobin.

\*Pearson Chi-square

TABLE IV  
ASSOCIATION BETWEEN HP INFECTION AND GLYCATED HEMOGLOBIN (HbA1c) LEVELS IN THE CASE GROUP (TYPE 2 DIABETES)

HbA1c levels	Hp-positive		Hp-negative		Total	
	n (%)	Mean±SD	n (%)	Mean±SD	n (%)	Mean±SD
Below 7%	143 (44.27%)	6.30±0.455	123 (54.67%)	6.06±0.534	266 (48.54%)	6.19±0.506
7–10%	139 (43.03%)	8.38±0.879	86 (38.22%)	7.90±0.738	225 (41.06%)	8.19±0.859
Above 10%	41 (12.69%)	11.36±0.682	16 (7.11%)	10.20±1.396	57 (10.4%)	11.03±1.063
Total	323	7.84±1.797	225	7.06±1.418	548	7.52±1.694

Hp: *Helicobacter pylori*, SD: Standard deviation. The Chi-square test demonstrated a statistically significant association between Hp infection and HbA1c levels ( $p=0.022$ ). The t-test indicated significantly elevated mean HbA1c levels in Hp-positive individuals compared to those who were Hp-negative ( $p < 0.001$ )

and specificity results (Chey, 2000). This test is considered more accurate and reliable than serological or stool tests as it directly identifies active Hp infection by detecting  $^{14}\text{C}$ -labeled carbon dioxide produced when bacterial urease breaks down labeled urea. In contrast to stool tests, which may yield false positives due to residual antigens after infection resolution, or serological tests, which detect long-lasting antibodies even after the infection has been eradicated (Talebi Bezmin Abadi, 2018; Costa, et al., 2024).

The relationship between Hp infection and T2D cannot be confirmed due to the lack of enough evidence. Still, there are a few reasons that can be suggested to support this association. First, it has been shown that the immune system response in individuals with T2D is suppressed and they are more prone to Hp-infection (Daryabor, et al., 2020). Second, changes in glucose metabolism can result in alterations in the production of chemicals in the gastric mucosa and increase the colonization by bacteria (Martin-Nuñez, et al., 2021). Third, diabetic patients are more exposed to pathogens than healthy patients, possibly due to the great number of interactions with the healthcare environment (Toniolo, et al., 2019). Fourth, diabetes reduces gastrointestinal movements and gastric acid secretion and increases colonization, overgrowth, and subsequent infections (Singh, et al., 2021). Diabetes also causes damage to the stomach lining, making it more susceptible to Hp colonization (Sharndama and Mba, 2022).

The present study demonstrates a significant correlation between Hp-infection and elevated HbA1c levels. In addition, the T2D subjects with Hp infection had significantly higher median HbA1c levels compared to Hp-negative subjects. These results are consistent with the preceding studies (Wan, et al., 2020; Chen, et al., 2023). They support the hypothesis that Hp-infections are associated with T2D and raised HbA1c levels. Furthermore, a meta-analysis and systematic review that included 36 studies provided evidence that Hp-eradication could improve HbA1c control (Song, et al., 2021). On the other hand, HbA1c levels remained unchanged after Hp-eradication in T2D patients based on another study (Wada, et al., 2013). Moreover, a study observing high HbA1c levels could contribute to the susceptibility of Hp infection (Maluf, et al., 2020). A meta-analysis report indicated a potential relationship between Hp infection and HbA1c level in diabetic patients (Chen, et al., 2019b). Those with both T2D and an existing Hp infection may require improved glycemic control. A cross-sectional study in Taiwan showed that eradication of Hp can decrease HbA1c levels and improve glycemic control (Cheng, et al., 2019).

The author concludes that Hp status may represent an aggravating factor of glycemic control in individuals with T2D and argues that individuals with diabetes should undergo screening for a status of Hp infection. Gender, age, and BMI have not been a factor in the relationship between Hp infection and T2D in the present study. However, further investigations need to investigate the role of BMI on the association between Hp infection and T2D, and the research should consider a broader range of factors and employ more

robust study designs. In addition, more well-designed studies such as longitudinal and cohort studies need verification of the causal relations between Hp and T2D as well as to explore the biological pathways.

#### IV. CONCLUSION

The study revealed a definite association of T2D with Hp infection. Individuals diagnosed with T2D are at more risk for Hp infection than the control population, and the logistic regression analysis further proves this association. Furthermore, HbA1c was significantly increased in T2D individuals with positive Hp infection when compared with uninfected counterparts. This suggests that T2D and worse glycemic control might be important risk factors for Hp-infection.

#### REFERENCES

- Alias, N.M., and Elkarsany, M.S.M., 2022. Effect of *H. pylori* among Diabetic Patients Living in Khartoum State, Sudan. *International Blood Research and Reviews*, 13, pp.1-8.
- Alzahrani, S., Nelson, J., Moss, S.F., Paulus, J.K., Knowler, W.C., and Pittas, A.G., 2017. *H. pylori* seroprevalence and risk of diabetes: An ancillary case-control study nested in the diabetes prevention program. *Journal of Diabetes and Its Complications*, 31, pp.1515-1520.
- Andrew, W., and Adrian, V., 2022. What is type 2 diabetes? *Medicine*, 50, pp.625-631.
- Bajaj, S., Rekwal, L., Misra, S.P., Misra, V., Yadav, R.K., and Srivastava, A., 2014. Association of *Helicobacter pylori* infection with type 2 diabetes. *Indian Journal of Endocrinology and Metabolism*, 18, pp.694-699.
- Bener, A., Ağan, A.F., Al-Hamaq, A., Barisik, C.C., Öztürk, M., and Ömer, A., 2020. Prevalence of *Helicobacter pylori* infection among Type 2 diabetes mellitus. *Advanced Biomedical Research*, 9, p.27.
- Chávez-Reyes, J., Escárcega-González, C.E., Chavira-Suárez, E., León-Buitimea, A., Vázquez-León, P., Morones-Ramírez, J.R., Villalón, C.M., Quintanar-Stephano, A., and Marichal-Cancino, B.A., 2021. Susceptibility for some infectious diseases in patients with diabetes: The key role of glycemia. *Front Public Health*, 9, p.559595.
- Chen, J., Xing, Y., Zhao, L., and Ma, H., 2019b. The association between *Helicobacter pylori* infection and glycated hemoglobin A in diabetes: A meta-analysis. *Journal of Diabetes Research*, 2019, p.3705264.
- Chen, Y., Yang, C., You, N., and Zhang, J., 2023. Relationship between *Helicobacter pylori* and glycated hemoglobin: A cohort study. *Frontiers in Cellular and Infection Microbiology*, 13, p.1196338.
- Chen, Y.Y., Fang, W.H., Wang, C.C., Kao, T.W., Chang, Y.W., Wu, C.J., Zhou, Y.C., Sun, Y.S., and Chen, W.L., 2019a. *Helicobacter pylori* infection increases risk of incident metabolic syndrome and diabetes: A cohort study. *PLoS One*, 14, p.e0208913.
- Cheng, K.P., Yang, Y.J., Hung, H.C., Lin, C.H., Wu, C.T., Hung, M.H., Sheu, B.S., and Ou, H.Y., 2019. *Helicobacter pylori* eradication improves glycemic control in type 2 diabetes patients with asymptomatic active *Helicobacter pylori* infection. *Journal of Diabetes Investigation*, 10, pp.1092-1101.
- Chey, W.D., 2000. Accurate diagnosis of *Helicobacter pylori*:  $^{14}\text{C}$ -Urea Breath test. *Gastroenterology Clinics of North America*, 29, pp.895-902.
- Cooke, F.J., 2022. Infections in people with diabetes. *Medicine*, 50, pp.729-732.
- Costa, L.C.M.C., Das Graças Carvalho, M., La Guárdia Custódio Pereira, A.C.,

- Teixeira Neto, R.G., Andrade Figueiredo, L.C., and Barros-Pinheiro, M., 2024. Diagnostic methods for *Helicobacter pylori*. *Medical Principles and Practice*, 33, pp.173-184.
- Daryabor, G., Atashzar, M.R., Kabelitz, D., Meri, S., and Kalantar, K., 2020. The effects of type 2 diabetes mellitus on organ metabolism and the immune system. *Frontiers in Immunology*, 11, p.1582.
- Dore, M.P., and Graham, D.Y., 2022. Modern approach to the diagnosis of *Helicobacter pylori* infection. *Alimentary Pharmacology and Therapeutics*, 55, pp.S14-S21.
- Hooi, J.K., Lai, W.Y., Ng, W.K., Suen, M.M., Underwood, F.E., Tanyingoh, D., Malfertheiner, P., Graham, D.Y., Wong, V.W., and Wu, J.C., 2017. Global prevalence of *Helicobacter pylori* infection: Systematic review and meta-analysis. *Gastroenterology*, 153, pp.420-429.
- Hosseininasab Nodoushan, S.A., and Nabavi, A., 2019. The interaction of *Helicobacter pylori* infection and type 2 diabetes mellitus. *Advanced Biomedical Research*, 8, p.15.
- Kouitcheu Mabeku, L.B., Noundjeu Ngamga, M.L., and Leundji, H., 2020. *Helicobacter pylori* infection, a risk factor for Type 2 diabetes mellitus: A hospital-based cross-sectional study among dyspeptic patients in Douala-Cameroon. *Scientific Reports*, 10, p.12141.
- Li, Y., Choi, H., Leung, K., Jiang, F., Graham, D.Y., and Leung, W.K., 2023. Global prevalence of *Helicobacter pylori* infection between 1980 and 2022: A systematic review and meta-analysis. *Lancet Gastroenterol Hepatol*, 8, pp.553-564.
- Liu, J., Bai, R., Chai, Z., Cooper, M.E., Zimmet, P.Z., and Zhang, L., 2022. Low-and middle-income countries demonstrate rapid growth of type 2 diabetes: An analysis based on Global Burden of Disease 1990-2019 data. *Diabetologia*, 65, pp.1339-1352.
- Lovic, D., Piperidou, A., Zografou, I., Grassos, H., Pittaras, A., and Manolis, A., 2020. The growing epidemic of diabetes mellitus. *Current Vascular Pharmacology*, 18, pp.104-109.
- Malfertheiner, P., Camargo, M.C., El-Omar, E., Liou, J.M., Peek, R., Schulz, C., Smith, S.I., and Suerbaum, S., 2023. *Helicobacter pylori* infection. *Nature Reviews Disease Primers*, 9, p.19.
- Maluf, S., Salgado, J.V., Cysne, D.N., Camelo, D.M.F., Nascimento, J.R., Maluf, B.V.T., Silva, L.D.M., Belfort, M.R.C., Silva, L.A., and Guerra, R.N.M., 2020. Increased glycosylated hemoglobin levels in patients with *Helicobacter pylori* infection are associated with the grading of chronic gastritis. *Frontiers in Immunology*, 11, p.2121.
- Man, S., Ma, Y., Jin, C., Lv, J., Tong, M., Wang, B., Li, L., and Ning, Y., 2020. Association between *Helicobacter pylori* infection and diabetes: A cross-sectional study in China. *Journal of Diabetes Research*, 2020, p.7201379.
- Mansori, K., Moradi, Y., Naderpour, S., Rashti, R., Moghaddam, A.B., Saed, L., and Mohammadi, H., 2020. *Helicobacter pylori* infection as a risk factor for diabetes: A meta-analysis of case-control studies. *BMC Gastroenterology*, 20, p.77.
- Martin-Núñez, G.M., Cornejo-Pareja, I., Clemente-Postigo, M., and Tinahones, F.J., 2021. Gut microbiota: The missing link between *Helicobacter pylori* infection and metabolic disorders? *Frontiers in Endocrinology*, 12, p.639856.
- Pyo, J.H., Lee, H., Choi, S.C., Cho, S.J., Choi, Y.H., Min, Y.W., Min, B.H., Lee, J.H., Yoo, H., Kim, K., and Kim, J.J., 2019. Lack of association between past *Helicobacter pylori* infection and diabetes: A two-cohort study. *Nutrients*, 11, p.1874.
- Ren, S., Cai, P., Liu, Y., Wang, T., Zhang, Y., Li, Q., Gu, Y., Wei, L., Yan, C., and Jin, G., 2022. Prevalence of *Helicobacter pylori* infection in China: A systematic review and meta-analysis. *Journal of Gastroenterology and Hepatology*, 37, pp.464-470.
- Sabbagh, P., Mohammadnia-Afrouzi, M., Javanian, M., Babazadeh, A., Koppolu, V., Vasigala, V.R., Nouri, H.R., and Ebrahimpour, S., 2019. Diagnostic methods for *Helicobacter pylori* infection: Ideals, options, and limitations. *European Journal of Clinical Microbiology and Infectious Diseases*, 38, pp.55-66.
- Shah, S.C., Halvorson, A.E., Lee, D., Bustamante, R., McBay, B., Gupta, R., Denton, J., Dorn, C., Wilson, O., and Peek, R Jr., 2024. *Helicobacter pylori* burden in the United States according to individual demographics and geography: A nationwide analysis of the Veterans Healthcare System. *Clinical Gastroenterology and Hepatology*, 22, pp.42-50, e26.
- Sharmada, H.C., and Mba, I.E., 2022. *Helicobacter pylori*: An up-to-date overview on the virulence and pathogenesis mechanisms. *Brazilian Journal of Microbiology*, 53, pp.33-50.
- Shi, Y., Duan, J.Y., Liu, D.W., Qiao, Y.J., Han, Q.X., Pan, S.K., Tang, L., Cai, G.Y., Chen, X.M., Liu, Z.S., and Zhu, H.Y., 2018. *Helicobacter pylori* infection is associated with occurrence of proteinuria in type 2 diabetes patients: A systemic review and meta-analysis. *Chinese Medical Journal*, 131, pp.2734-2740.
- Singh, R., Zogg, H., Wei, L., Bartlett, A., Ghoshal, U.C., Rajender, S., and Ro, S., 2021. Gut microbial dysbiosis in the pathogenesis of gastrointestinal dysmotility and metabolic disorders. *Journal of Neurogastroenterology and Motility*, 27, p.19.
- Song, X., Cai, C., Jin, Q., Chen, X., and Yu, C., 2021. The efficacy of *Helicobacter pylori* eradication in diabetics and its effect on glycemic control: A systematic review and meta-analysis. *Helicobacter*, 26, p.e12781.
- Talebi Bezmin Abadi, A., 2018. Diagnosis of *Helicobacter pylori* using invasive and noninvasive approaches. *Journal of Pathogens*, 2018, p.9064952.
- Tamura, T., Morita, E., Kawai, S., Sasakabe, T., Sugimoto, Y., Fukuda, N., Suma, S., Nakagawa, H., Okada, R., and Hishida, A., 2015. No association between *Helicobacter pylori* infection and diabetes mellitus among a general Japanese population: A cross-sectional study. *Springerplus*, 4, pp.1-7.
- Thrift, A.P., and El-Serag, H.B., 2020. Burden of gastric cancer. *Clinical Gastroenterology and Hepatology*, 18, pp.534-542.
- Toniolo, A., Cassani, G., Puggioni, A., Rossi, A., Colombo, A., Onodera, T., and Ferrannini, E., 2019. The diabetes pandemic and associated infections: Suggestions for clinical microbiology. *Reviews in Medical Microbiology*, 30, p.1.
- Uemura, N., Okamoto, S., Yamamoto, S., Matsumura, N., Yamaguchi, S., Yamakido, M., Taniyama, K., Sasaki, N., and Schlemper, R.J., 2001. *Helicobacter pylori* infection and the development of gastric cancer. *New England Journal of Medicine*, 345, pp.784-789.
- Wada, Y., Hamamoto, Y., Kawasaki, Y., Honjo, S., Fujimoto, K., Tatsuoka, H., Matsuoka, A., Ikeda, H., Fujikawa, J., and Koshiyama, H., 2013. The eradication of *Helicobacter pylori* does not affect glycemic control in Japanese subjects with type 2 diabetes. *Japanese Clinical Medicine*, 4, p.41-43.
- Wan, Z., Song, L., Hu, L., Hu, M., Lei, X., Huang, Y., and Lv, Y., 2020. *Helicobacter pylori* infection is associated with diabetes among Chinese adults. *Journal of Diabetes Investigation*, 11, pp.199-205.
- Xia, H.H., Talley, N.J., Kam, E.P., Young, L.J., Hammer, J., and Horowitz, M., 2001. *Helicobacter pylori* infection is not associated with diabetes mellitus, nor with upper gastrointestinal symptoms in diabetes mellitus. *American Journal of Gastroenterology*, 96, pp.1039-1046.
- Ye, J., Wu, Y., Yang, S., Zhu, D., Chen, F., Chen, J., Ji, X., and Hou, K., 2023. The global, regional and national burden of type 2 diabetes mellitus in the past, present and future: A systematic analysis of the global burden of disease study 2019. *Frontiers in Endocrinology*, 14, p.1192629.
- Zang, H., Wang, J., Wang, H., Guo, J., Li, Y., Zhao, Y., Song, J., Liu, F., Liu, X., and Zhao, Y., 2023. Metabolic alterations in patients with *Helicobacter pylori*-related gastritis: The *H. pylori*-gut microbiota-metabolism axis in progression of the chronic inflammation in the gastric mucosa. *Helicobacter*, p.e12984.
- Zhou, J., Wang, X., Liu, K., and Chen, K., 2022. Association between *Helicobacter pylori* infection and the risk of type 2 diabetes mellitus based on a middle-aged and elderly Chinese population. *Endocrine Journal*, 69, pp.839-846.

# A Novel Digital Audio Encryption Algorithm Using Three Hyperchaotic Rabinovich System Generators

Ameer K. Jawad, Gholamreza Karimi<sup>†</sup>, and Mazdak Radmalekshahi

Department of Electrical Engineering, Faculty of Electrical and Computer Engineering,  
Razi University, Kermanshah, Iran

**Abstract**—Improved speech encryption is needed for digital voice communications. Data security requires advanced encryption against cyberattacks. Traditional encryption may not be able to handle advanced threats or large datasets. This study uses chaotic system features to create a secure and adaptive digital audio encryption algorithm and enhances public audio encryption. Three hyperchaotic systems allow digital audio signal randomized encryption. The first system generates chaotic random integer numbers as keys, the second selects non-sequential indices to increase unpredictability, and the third randomly samples the digital audio signal and encrypts it through XOR operations with selected key, making it harder for intruders to learn the encryption pattern. The proposed system uses Diffie-Hellman key exchange for key agreement. We have tested and proven the efficiency of the proposed algorithm. The encrypted audio signals, achieving a Peak Signal-to-Noise Ratio (PSNR) of around  $-20$  dB, exhibit high distortion, spectral complexity, very low correlation (round to zero), high entropy, and minimal time delay compared to other articles, making them resistant to decryption attempts by attackers. The system has a large key space of 1345 bits, and its randomized nature and extensive key space protect sensitive audio data in public communication channels, even with minor changes to hyper-chaos generators. The proposed algorithm represents a significant advancement in the field of digital audio encryption. The researchers have utilized chaotic systems to create a strong and flexible encryption system. This algorithm is suitable for military and medical communications that require a high level of audio data security.

**Index Terms**—Audio encryption, Chaotic sequences, Hyperchaotic systems, Key space, Randomized encryption.

## I. INTRODUCTION

Digital audio systems are popular for their technical and practical benefits. Effective recording, storage, signal processing, and quality are available (Nguyen, et al., 2005).

ARO-The Scientific Journal of Koya University  
Vol. XII, No. 2 (2024), Article ID: ARO.11869. 12 pages  
DOI: 10.14500/aro.11869

Received: 15 October 2024; Accepted: 11 December 2024  
Regular research paper; Published: 21 December 2024

<sup>†</sup>Corresponding author's e-mail: [ghkarimi@razi.ac.ir](mailto:ghkarimi@razi.ac.ir)  
Copyright © Ameer K. Jawad, Gholamreza Karimi, Mazdak Radmalekshahi. This is an open-access article distributed under the Creative Commons Attribution License (CC BY-NC-SA 4.0).



Digital audio works well with new technology, enabling interoperability. Its portability and storage enable high-quality, lossless data transfer over communication networks and efficient file storage on digital media. Due to these benefits, digital audio systems are preferable for communications, audio recording, and file storage. Digital speech encryption encrypts speech for privacy and security (Abdullah, et al., 2022; Hussein, Khashan and Jawad, 2020). Cryptographic methods render audio signals or speech data incomprehensible to unauthorized listeners. Only authorized recipients with decryption keys can decipher encrypted speech. Speech encryption uses digital signal processing, symmetric or asymmetric encryption, and secure key management (Dai, et al., 2022). Symmetric encryption uses a shared secret key for encryption and decryption (Ibrahim and Mohammed, 2022; Kumar Shrivasta, Bhatnagar and Pangaria, 2013), while asymmetric encryption involves a pair of public and private keys. The encrypted speech data are transmitted over secure channels or networks to prevent interception and eavesdropping. Encryption protects sensitive information exchanged during audio calls, conference calls, audio messages, or other verbal communication (Hassan, Al-Adhami and Mahdi, 2022).

### A. Chaos-Based Audio Encryption

Audio encryption based on chaos utilizes chaotic systems and their properties to encrypt speech signals. Chaos theory studies complex and unpredictable behavior arising from simple non-linear dynamical systems (Nien, et al., 2007). Chaotic systems exhibit sensitivity to initial conditions (Ene, Pop and Lapadat, 2022), non-periodic behavior (Hasan, Mosleh and Abdulhameed, 2021), and deterministic randomness. In speech encryption based on chaos, chaotic systems generate encryption keys or transform the speech signal itself. The chaotic properties of the system introduce randomness and complexity, making it difficult for unauthorized individuals to decipher the encrypted speech (Sathiyamurthi, et al., 2018; Tolba, et al., 2018). Chaotic maps or flows, such as the logistic map or Lorenz system, generate pseudo-random numbers that can be encrypted using a chaotic encryption algorithm. These systems are ideal for encryption due to their randomness and starting condition sensitivity, and can withstand cryptographic attacks and cryptanalysis (Abdullah, Hreshee and Jawad, 2015; Mahdi, Jawad and Hreshee, 2016).



### B. The Primary Objective of this Article

The main aim of this research is to develop a secure and efficient audio encryption algorithm capable of protecting sensitive audio data transmitted over public channels. We intend to propose a solution that provides enhanced security and performance by examining the shortcomings of current techniques and exploiting the advantages of hyperchaotic systems.

### C. The Specific Contributions of this Study Include

- A novel audio encryption algorithm based on three hyperchaotic Rabinovich systems
- A detailed analysis of the security and performance of the proposed algorithm
- A comparison of the proposed algorithm with existing techniques and future research directions.

By addressing these issues, this research contributes to the advancement of audio encryption techniques and enhances the security of digital audio communication systems.

### D. Limitations

While the proposed algorithm offers significant improvements in security and efficiency, it is important to acknowledge its limitations. The computational complexity of the algorithm may increase with larger audio files. In addition, the security of the system relies on the secrecy of the initial conditions and parameters of the hyperchaotic systems. Because cryptographic algorithms use symmetric encryption, key management remains challenging and has limitations.

### E. The Main Contributions

This study introduces a novel audio encryption system that utilizes three hyperchaotic systems based on the Rabinovich system to enhance the security of public communication channels. The proposed algorithm uses three hyperchaotic systems or one with different initial values and parameters. The first chaotic system generates chaotic random integer numbers (CRINs) between 0 and  $65535 (2^{16})$ , the second selects a random index from the sequence of the first system, and the third selects digital audio samples (DAS) from the digitized audio signal. XOR the third chaotic selector selects DAS and CRIN bit by bit. Unlike traditional systems, the proposed encryption system uses random DAS numbers instead of sequential ones.

### F. Paper Structures and Sections

The article is organized as follows: Starting with the abstract and section one for introduction, the literature review in the second section, and then defining chaotic systems and their types, especially the hyper-chaotic Rabinovich system in the third section, and then the encryption algorithm is explained in full steps in the fourth section. The fifth section describes the subjective and objective measurements used in the evaluation of cryptography are described. The sixth section contains the simulation results of encryption, decryption, and calculating the key space reached in this

paper. The seventh section of the paper deals with the final conclusions.

## II. LITERATURE REVIEW

There are many methods for audio signal encryption: Time domain scrambling (TDS), frequency domain scrambling, Two-Dimensional Scrambling Based on Time and Frequency (2DS), and Chaotic Masking (Abdullah, Hreshee and Jawad, 2016). In (Hreshee, Abdullah and Jawad, 2018; Jawad, Abdullah and Hreshee, 2018), a secure communication system that is based on two levels of encryption, namely chaotic scrambling and chaotic masking, was proposed. In (Ouannas, et al., 2021), a secure communication method combines chaotic modulation, recursive encryption, and chaotic masking using backstepping control rules, synchronizing two hyperchaotic Lorenz systems with encrypted states, and recursive encryption techniques. In (Yousif, 2023), a comparison of the performance of the RSA and El-Gamal algorithms for the encryption and decryption of speech data were presented. In (Ameen and Hreshee, 2023), the security of encrypted audio based on elliptic curves and hybrid chaotic maps was investigated in the context of 5G networks. In (Qasim, 2023), a new audio encryption algorithm that is based on a hyper-chaotic system was proposed. In (Tomita, Okumura and Okamoto, 2023), a chaos-based radio encryption modulation system using LabVIEW, program-defined radio, and Universal Software Radio Peripheral demonstrated effectiveness in binary phase-shift keying and information-theoretic and computational security. In (Ilyas, et al., 2022), the reconfigurable 4D Lorenz Hyperchaotic-based IoT device security core platform was proposed to secure real-time communication between embedded systems linked to networks using IoT standards. It is built using VHDL Hardware Description Language architecture. In (Samimi, Majidi and Khorashadizadeh, 2020), a safe communication system based on chaotic synchronization, an intelligent controller with a brain-based emotional learning architecture is presented. Emotional learning is applied to assess uncertainty and provide the correct information to the receiver. In (Gao, et al., 2022), the TDS can be hidden with the help of a suggested system that uses two optical dispersion components and an electro-optic self-feedback phase modulation loop. In (Giap, Nguyen and Huang, 2021), a linear synchronization control strategy was implemented by converting Lorenz chaotic system-based secure communication into Takagi-Sugeno fuzzy systems. (Zhang, et al., 2022) suggested that modified projective difference function synchronization (CMPDFS) of CVCSs might provide a safe communication method for wireless sensor networks while also addressing amplitude concerns. (Abdullah, et al., 2022; Abdullah, Hreshee and Jawad, 2015; Mahdi, Jawad and Hreshee, 2016) presented speech encryption based on chaotic masking by the Lorenz system and multiple methods to reduce the noise effect on the recovered speech signal at the receiver side. (Hussein, Khashan and Jawad, 2020) presented two stages of chaotic

masking based on Lorenz and Rossler systems and proposed a noise reduction scheme based on an analog-to-digital converter. In (Abdelfatah, 2020), self-adaptive scrambling, multi-chaotic maps, dynamic DNA encoding, and cipher feedback encryption are four independent audio encryption approaches used in the same framework to provide the described safe audio encryption. In (Pirdawood, Kareem and Zahir, 2023), the Laplace transformation is used in the framework that has been proposed for the purpose of audio encryption. In (Barua and Kabir, 2022), encryption and decryption of audio by changing properties and noise reduction was proposed. In (Sajaa and Al-Mothafar, 2024), it was proposed to perform an evaluation of the Rijndael algorithm for audio encryption using brute force attack is carried out.

### III. CHAOS AND HYPER CHAOS DEFINITION AND TYPES

Chaos signals are non-periodic, dynamic, and random signals originating from non-linear processes, controlled by ordinary differential equations (ODE) in an interactive system. These signals fluctuate in a limited, non-periodic, random-like manner, resulting in two-state variable motions or trajectories that are easily uncorrelated (Abdullah, et al., 2022; Abdullah, Hreshee and Jawad, 2015; Khalid, et al., 2019). Chaos can be classified into chaotic maps and chaotic flows, with chaotic maps being evolution functions that behave in some way. Discrete-time maps, such as Logistic, Duffing, and Henon maps, are typical representations of discrete maps. Chaotic-Flow systems, such as the Lorenz, Rössler, and Chua systems, are well-known chaotic flow systems with differential equations (Hussein, Khashan and Jawad, 2020; Mahdi, Jawad and Hreshee, 2016).

Hyper-Chaos is an autonomous continuous-time system (a part of chaotic flows) with at least four dimensions and two positive Lyapunov exponents (Alsaabri and Hreshee, 2021; Shakir, Mehdi and Hattab, 2023). The Les for the Rabinovich system is (9.712, 1.457, -4.445, and -15.724), which indicates that it is a hyper-chaotic system. As a result, it gains from increased randomness and unpredictability, which is crucial in communication security. Fig. 1 shows a time series for all vectors and non-uniform 3D attractors of the studied HCRS. The following equations comprise the HCRS (Alsaabri and Hreshee, 2021):

$$\left. \begin{aligned} \dot{x} &= ry - ax + yz \\ \dot{y} &= rx - by - xz \\ \dot{z} &= -dz + xy + w^2 \\ \dot{w} &= xy + cw \end{aligned} \right\} \quad (1)$$

Where (x, y, z, and w) are the state vectors, (r, a, b, c, and d) are the control parameters.

The HCRS is susceptible to slight changes in the control parameters or initial conditions, resulting in a significant difference in the system's behavior. Fig. 2 illustrates the concept by showing the waveform in the time domain of the x(t) state after changing  $X_0$  and parameter C by  $10^{-15}$ .

### IV. THE PROPOSED ENCRYPTION AND DECRYPTION SYSTEM

The proposed system (Fig. 3) uses three hyperchaotic systems to encrypt a digital audio signal. The system works as follows:

1. The first chaotic system generates a sequence of CRINs between 0 and  $(2^{16}-1)$ . These numbers are then used to encrypt the digital audio signal.

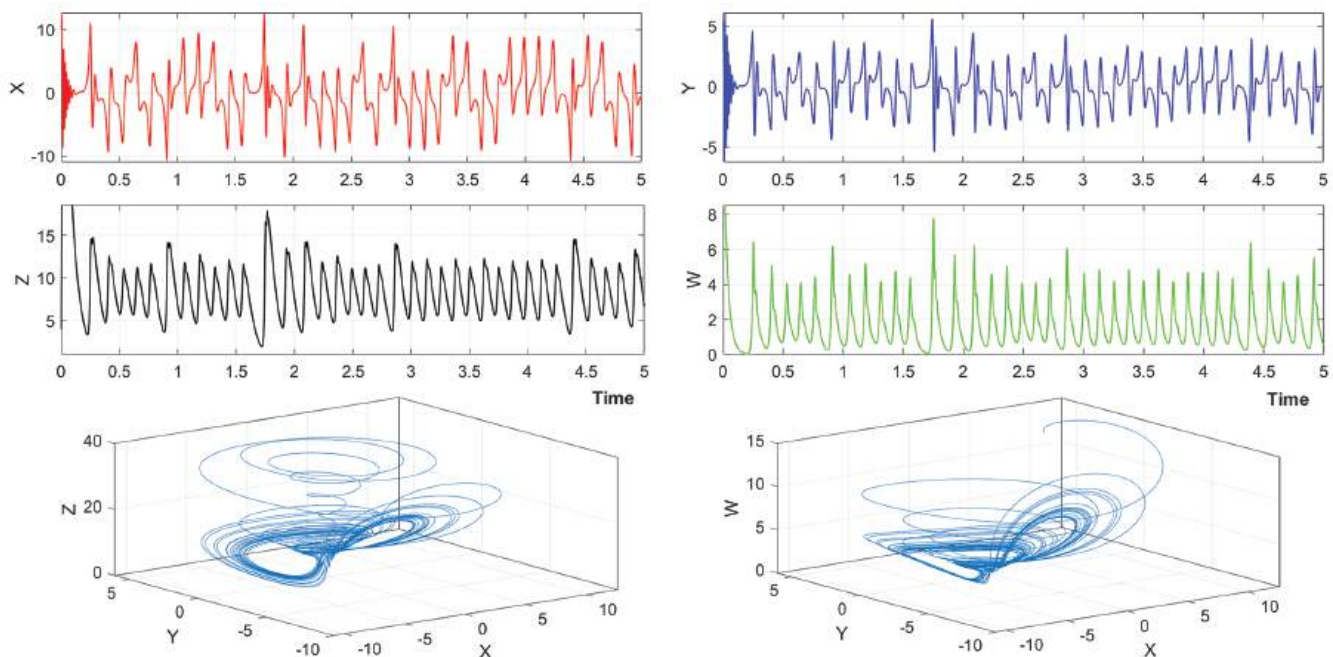


Fig. 1. Time series (X, Y, Z, and W) vectors and 3D attractors (X, Y, and Z), (X, Y, and W) for the HCRS.

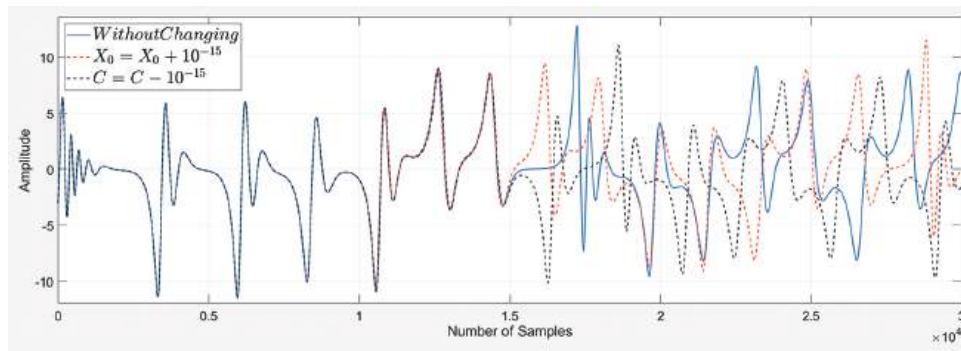


Fig. 2. Sensitivity to any slight change in initial values and control parameters.

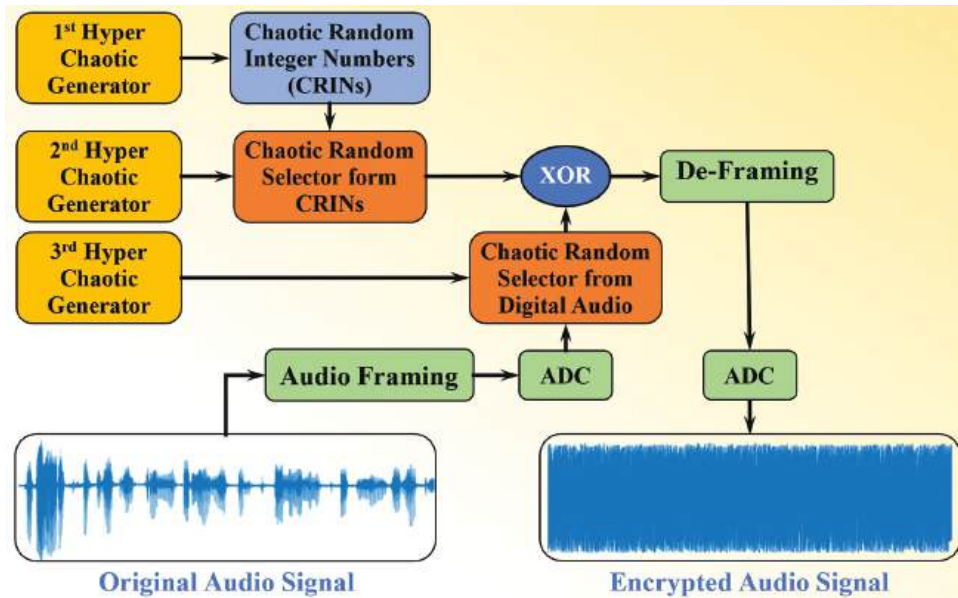


Fig. 3. Block diagram of the proposed audio encryption model.

2. The second chaotic system selects a random index from the sequence of CRINs generated by the first system to ensure that the CRINs used to mask the audio signal are not used in a predictable order.
3. The third chaotic system selects a random sample from the digital audio signal. This sample is then XORed with the CRIN chosen by the second system. This XOR operation encrypts the audio signal.

The proposed scrambling algorithm is described in the following steps:

**Step 1. Initialization**

This step establishes the three hyperchaotic systems' initial conditions and parameters. These initial conditions and parameters greatly affect chaotic dynamics and random numbers. Different initial conditions and parameters produce different chaotic sequences, improving system security.

**Step 2. Generating chaotic signals**

The simplest numerical method used to solve the ODE of the Rabinovitch system is the Euler method (Sathiyamurthi, et al., 2018; Xu and Cao, 2020), as shown in the following Equation:

$$y_{n+1} = y_n + hf(x) \tag{2}$$

Where h represents a step size, usually a small value such as 0.001. Generating (X, Y, Z, and W) by the Euler method solving the Rabinovitch system given in (1), as shown in the following equations:

$$\begin{aligned} x_{n+1} &= x_n + h(ry_n - ax_n + yz_n) \\ y_{n+1} &= y_n + h(rx_n - by_n - x_nz_n) \\ z_{n+1} &= z_n + h(-dz_n + x_ny_n + w_n^2) \\ w_{n+1} &= w_n + h(x_ny_n + cw_n) \end{aligned} \tag{3}$$

Where (n) and (n + 1) are the present and the next state. This Equation will generate a number with a high correlation between adjacent chaotic samples.

**Step 3. Addressing correlation and generating CRINs**

This step addresses the high correlation between adjacent chaotic samples (CS), which can weaken the randomness of the generated sequence. Multiplying by a large number and taking the remainder helps decorate the sequence but might limit the possible values obtained. This step converts the continuous chaotic signal into a sequence of "Chaotic Random Integer Numbers" (CRINs) (Fig. 4) suitable for masking the audio samples. Modulo operation ensures the CRINs remain within a specific range (0–65535 in this case), allowing for efficient

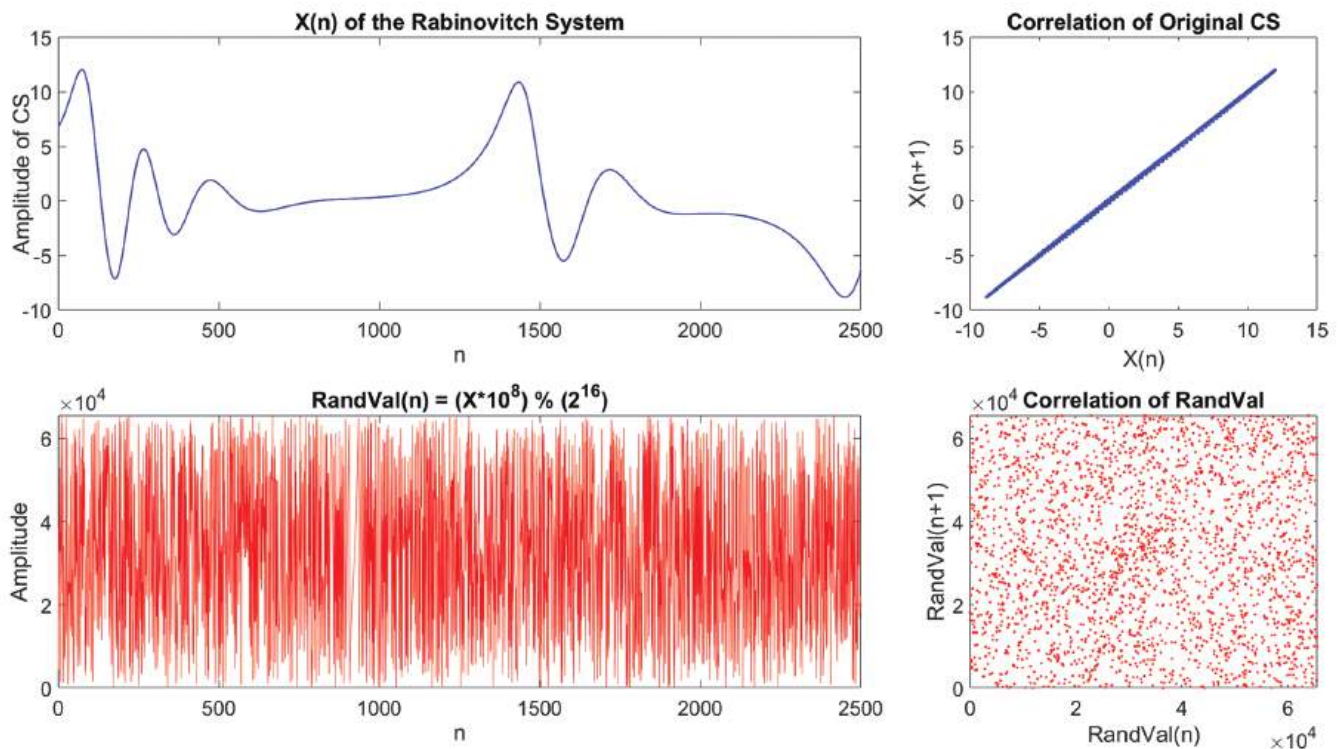


Fig. 4. The correlation between chaotic samples for original and random chaotic signals.

manipulation during encryption, as shown in the following equation:

$$\text{RandVal} = \text{mod}(x(n) \cdot 10^8, 2^{16}) \quad (4)$$

$$\text{CRIN} = \text{round}(\text{RandVal}) \quad (5)$$

Where: CS is Chaotic Sequences, and CRIN is a “Chaotic Random Integer Numbers” generated based on hyperchaotic signals.

#### Step 4. Sorting and indexing

Sorting the results from the second and third hyperchaotic systems introduces non-linearity and randomness into the selection process. Assigning new indices based on the sorted order further obfuscates the relationship between the original chaotic sequence and the selected indices (Fig. 5). In step 4, we have  $n = 12$  in our sequence. Thus, the new index representation is in Table I.

#### Step 5. Audio encryption

To encrypt audio, a DAS (Digital Audio Sample) based on a chaotic selection from the second and third systems XORs the CRINs from the first hyperchaotic system. The XOR operation encrypts audio data by masking it with random values, as shown in equation (6). After converting the digital encryption samples back to analog, we de-frame the encrypted frames to create an encrypted audio signal.

$$\text{Encrypted} = \text{CRIN}(\text{CRS}_1) \otimes \text{DAS}(\text{CRS}_2) \quad (6)$$

Where  $\text{CRS}_1$  &  $\text{CRS}_2$ : Chaotic Random Selectors from the second and third HCRSSs.

#### Step 6. Audio decryption

Finally, on the receiver side, employing identical keys as those used in the transmitter (the same initial values and parameters) and obtaining similar results ( $\text{CRIN}_s$ ,  $\text{CRS}_1$ , and  $\text{CRS}_2$ ) from three HCRSSs, the following equation governs the decryption process:

$$\text{Decrypted}(\text{CRS}_2) = \text{CRIN}(\text{CRS}_1) \otimes \text{Encrypted} \quad (7)$$

### V. THE ASSESSMENT OF AUDIO ENCRYPTION INVOLVES BOTH SUBJECTIVE AND OBJECTIVE TESTING

The proposed audio encryption scheme will undergo rigorous statistical tests and visual comparisons to assess its security and overall performance. Key metrics include mean squared error (MSE), PSNR, signal-to-noise ratio (SNR), correlation, entropy, number of pixels with a change in intensity, and unified average changed intensity. Visual comparisons include waveform, histogram, correlation, and FFT plots.

#### A. Correlation and Histogram Plots

The correlation figure represents the relationship between the Audio Sample ( $t$ ) and Audio Sample ( $t + 1$ ) by scattering plot. A high relationship and correlation between the adjacent audio samples is in the clear or original audio. While, for encrypted audio, the relationship and correlation are neglected. The proposed system will change the audio sample values, changing the histogram of the encrypted audio, increasing the encryption strength of the proposed method (Tan and Zhou, 2010; Vaseghi, et al., 2021).

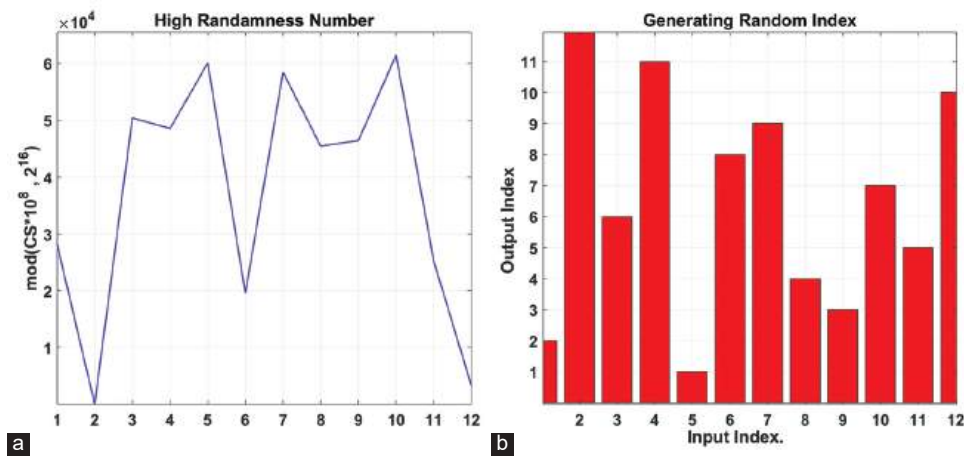


Fig. 5. (a) A high randomness numbers. (b) Generate random locations (steps 4 and 5).

TABLE I

THE OUTPUT RANDOM INDICES USED AS A CHAOTIC RANDOM SELECTOR

Output index	2	12	6	11	1	8	9	4	3	7	5	10
--------------	---	----	---	----	---	---	---	---	---	---	---	----

**B. PSNR and MSE**

The fundamental goal of every cryptographic method is to maximize the difference between ciphered and original data to withstand differential and statistical assaults. The MSE and the PSNR determine the difference between the original and recovered or ciphered audio signals. The mathematical description of MSE and PSNR can be found in equations (8) and (9). (Abood, et al., 2023; Belagali and Udipi, 2023; Hanif, et al., 2020; Majid Msallam and Fayeze Aldoghan, 2023):

$$MSE = \frac{\sum_i |x_i - y_i|}{N_{AS}} \tag{8}$$

$$PSNR_{dB} = 10 \log \left( \frac{65535^2}{MSE} \right) \tag{9}$$

Where  $x$  and  $y$  are the original and the encrypted or decrypted audio signal,  $N_{AS}$  the number of audio samples.

**C. Signal-to-Noise Ratio**

The reconstructed signal exhibits greater quality and less distortion than the original signal, indicating potentially skewed or inaccurate data, necessitating subjective metrics (Elkamchouchi, Salama and Abouelseoud, 2020; Hreshee, Abdullah and Jawad, 2018). The formula of SNR is:

$$SNR_{db} = 10 \log_{10} \left( \frac{\sum x^2}{\sum (x - y)^2} \right) \tag{10}$$

Where  $x$  is the original audio signal and  $y$  is the audio signal that was encrypted or decrypted.

**D. Correlation Coefficients**

The correlation coefficient is used to obtain the similarity between two audio signals.

$$Corr. = \frac{\sum_{i=1}^N (x_i - E(x))(y_i - E(y))}{\sqrt{\sum_{i=1}^N (x_i - E(x))^2} \sqrt{\sum_{i=1}^N (y_i - E(y))^2}} \tag{11}$$

Where  $E(x) = \frac{1}{N} \sum_{i=1}^N x(i)$ ,  $x$  and  $y$  are the audio sample values of the original and the encrypted audio signal, respectively. When it's 0, the audio signals are different (the original and the encrypted audio signals). If it's 1, the encryption fails to obscure the original audio signal's features (Min, Ting and Yu-jie, 2013).

**E. Entropy**

Information entropy analysis measures randomness and encryption quality by comparing the Entropy of original and cipher audio signals, calculated using a specific method.

$$E = \sum_{i=0}^{2^r-1} \left[ p(i) * \log_2 \left( \frac{1}{p(i)} \right) \right] \tag{12}$$

Where  $p(i)$  is the bit-valued I probability, for audio signals with 65536 audio levels (0–65535), the maximum Entropy equals 16, and it's considered optimum randomness. Practical audio signal entropy is lower than maximal Entropy (Ahmad and Ahmed, 2010).

**F. Root Mean Square (RMS) and Crest Factor (CF) Value**

Calculating the average audio source amplitude or input signal standard deviation with a mean of zero yields the RMS value (Abdelfatah, 2020; Rahman, et al., 2020). CF is a waveform parameter calculated by dividing peak values by effective value (Abdelfatah, 2020). A higher CF indicates signal peaks, while a 0 Db ratio indicates no peaks. Information is presented:

$$CF = 20 \log_{10} \left| \frac{V_{Peak}}{V_{RMS}} \right| \tag{13}$$

**G. The Audio Signals that are used to evaluate the Proposed System**

There are two types of audio signals that are used to evaluate the proposed system; the standard audio signal (audio signal (1) in Fig. 6) is used in these papers: (Abdullah, et al., 2022; Abdullah, Hreshee and Jawad, 2015; 2016; Hreshee, Abdullah and Jawad, 2018; Hussein, Khashan and Jawad, 2020; Mahdi, Jawad and Hreshee,

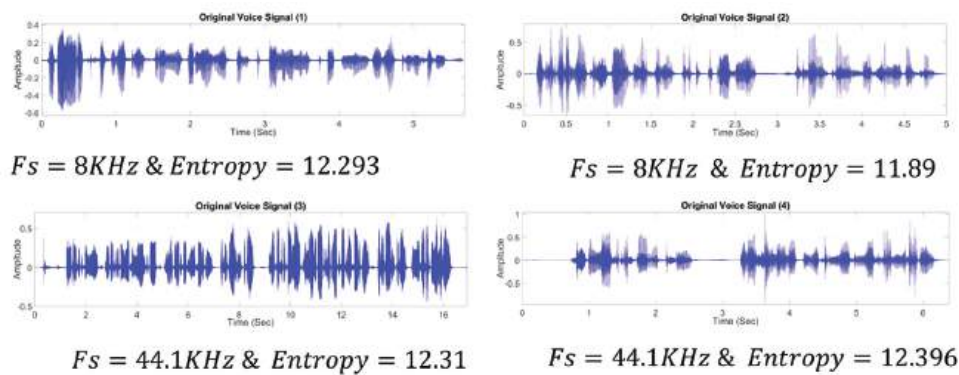


Fig. 6. Time series of the original audio signals.

2016), and recorded immediately with varying lengths (5, 16.6, and 6.5 s) and frequency sampling (8 kHz to 44.1 kHz), respectively, as audio signals (2, 3, and 4 in Fig. 6). The comparison table uses the results from the audio signal (1).

## VI. SIMULATION RESULTS AND DISCUSSIONS

### A. Encryption Results

The following Table II provides an illustration of the encryption results of the four audio signals based on the proposed algorithm.

According to Table II, The proposed encryption algorithm introduces high distortion to the signal, resulting in low-quality encrypted audio signals with PSNR values of  $-19.942$  Db or less and SNR values of  $-39.26$  Db, significantly different from the original audio signal. Furthermore, from Table II, The encrypted audio signal significantly differs from the original, making it difficult for eavesdroppers to recover without the encryption key. The Entropy values above  $14.74$ – $15.936$  indicate that the encrypted signal is unpredictable, making it difficult for eavesdroppers to analyze and decrypt without the encryption key. The proposed algorithm can scramble and encrypt the audio signal, making it unintelligible to eavesdroppers. Furthermore, from Table II, The encryption algorithm is practical for real-time audio communication, with a mean delay of  $5$  MS for  $1$  s of encryption at  $8,000$  Hz and  $18.5$  MS at  $44,100$  Hz. The encrypted audio signals have RMS and CF values of  $0.57$  and  $1.73$ , respectively, indicating no statistical correlation between the original and encrypted signals. The analysis visually compares the characteristics of original and encrypted audio signals, showing waveforms, correlation plots, histograms, frequency domain representation, and color-coded illustrations of energy across frequencies over time exclusively for an encrypted signal.

From Figs. 7 and 8 the encrypted audio signals display negligible correlation between adjacent samples, contributing significantly to the system's security. Histogram plots, revealing a flat distribution, underscore the randomness, and unpredictability introduced through encryption; this intentional obfuscation of signal patterns enhances resistance

TABLE II  
THE OBJECTIVE ENCRYPTION RESULTS OF THE FOUR AUDIO SIGNALS

Audio	PSNR <sub>Db</sub>	SNR <sub>Db</sub>	Corr.	Entropy	RMS	CF	Delay
Audio1	$-21.137$	$-40.105$	$-0.0014$	$14.737$	$0.5776$	$1.7312$	$0.021$ Sec
Audio2	$-19.942$	$-39.262$	$-0.0075$	$14.743$	$0.5780$	$1.7301$	$0.020$ Sec
Audio3	$-20.009$	$-39.654$	$0.0008$	$15.821$	$0.5767$	$1.7341$	$0.083$ Sec
Audio4	$-20.851$	$-40.105$	$-0.0020$	$15.936$	$0.5769$	$1.7335$	$0.323$ Sec

against cryptographic attacks. The FFT plots demonstrate a wide frequency range in the encrypted audio signals. This spectral complexity enhances the difficulty of signal analysis and attack, fortifying the encryption process against adversaries aiming to exploit specific frequency patterns or weaknesses.

### B. Decryption Results

The following Table III provides an illustration of the encryption results of the four audio signals based on the proposed algorithm.

From Table III, The proposed encryption algorithm effectively recovers the original audio signal from the encrypted signal without distortion or noise, with minimal decryption delay. The decrypted signal's quality is close to the original, with a MSE value of zero and a PSNR value of  $94.5$  Db, indicating accurate recovery and no significant alteration in the signal's statistical properties.

The graphical encryption (subjective) results from Figs. 9 and 10 showed that the time plots showed the audio signal's amplitude over time, and the decrypted audio signal was similar to the original. FFT plots revealed a similar spectrum to the original audio signal, with highly correlated correlation plots over time. The amplitude of the audio signal at time ( $t$ ) is similar to time ( $t + 1$ ), with points clustered around a line with a slope of  $1$ . Decrypted audio signal histogram plots were typically bell-shaped, with most samples clustered around the mean value.

### C. Key Sensitivity and Space

Key sensitivity refers to the difficulty in decrypting an encrypted signal if there is a change between encryption and decryption keys. Secure cryptosystems require large sensitivity; meaning only one key factor remains unchanged.

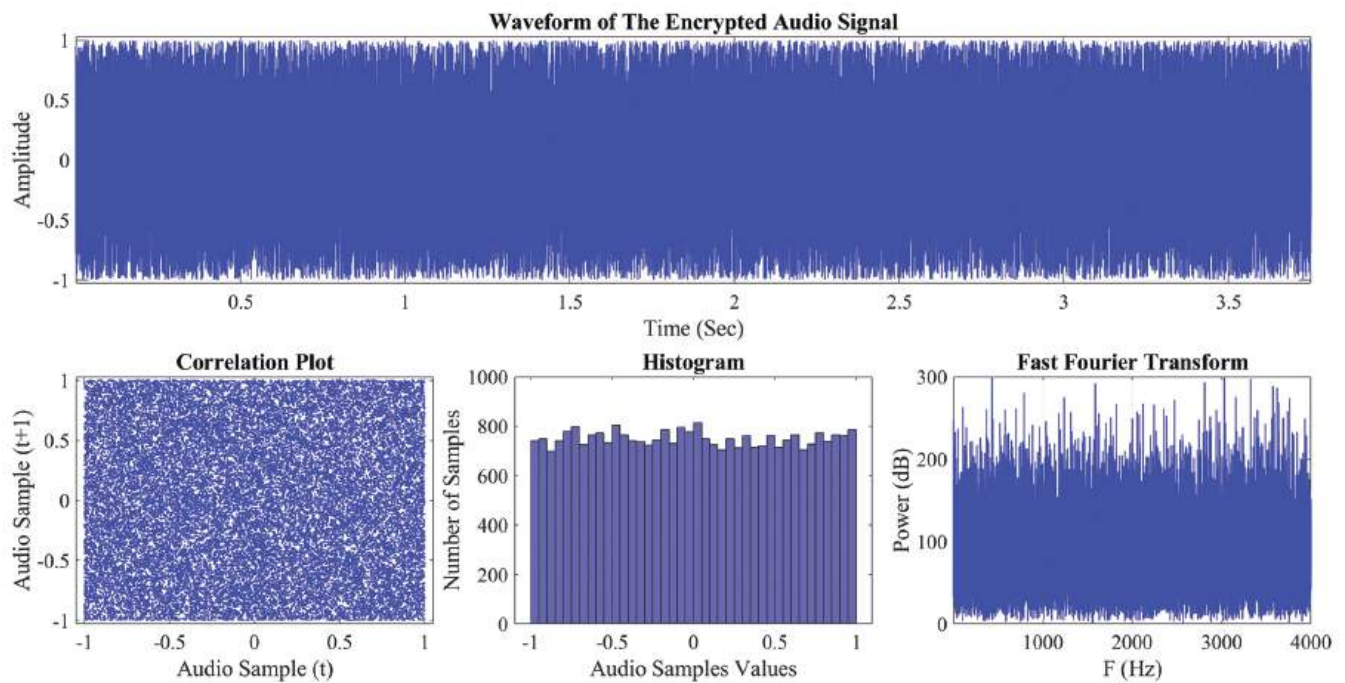


Fig. 7. Subjective encryption results for the 1<sup>st</sup> audio signal.

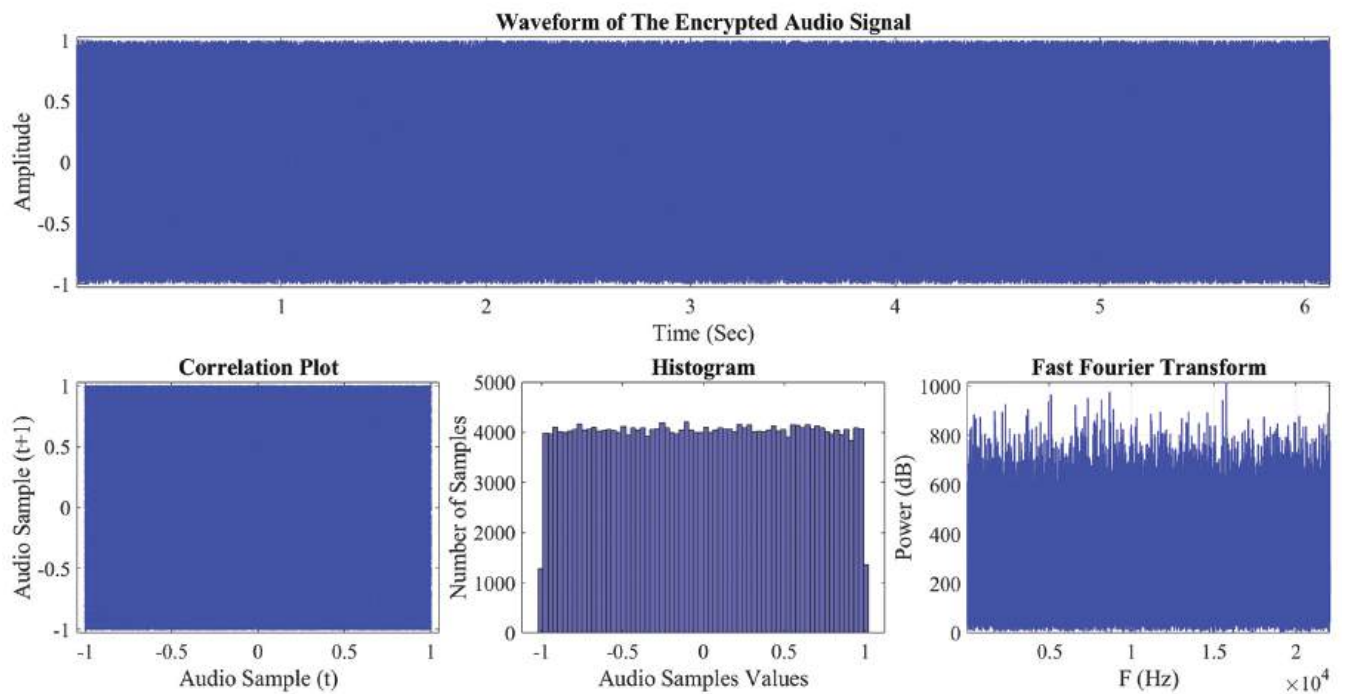


Fig. 8. Subjective encryption results for the 3<sup>rd</sup> audio signal.

TABLE III  
THE OBJECTIVE DECRYPTION RESULTS OF THE FOUR AUDIO SIGNALS

Audio	PSNR <sub>Db</sub>	SNR <sub>Db</sub>	Corr.	Entropy	RMS	CF	Delay
Audio1	93.717	79.541	1	12.293	0.0850	8.1785	0.018 Sec
Audio2	94.116	75.652	1	11.89	0.0882	8.3798	0.017 Sec
Audio3	96.684	74.472	1	12.31	0.0775	12.901	0.071 Sec
Audio4	93.001	73.748	1	12.396	0.0713	0.0713	0.323 Sec

Even a small change in the initial condition of a key, such as  $1 \times 10^{-15}$ , cannot retrieve information from an attacker.

From Table IV and Fig. 11 notice that when we make a minimal change in any parameter or initial value in the 1<sup>st</sup>, 2<sup>nd</sup>, or 3<sup>rd</sup> HCS generators, the attacker cannot retrieve the audio initially stored. The key space of the proposed scheme used in this paper mainly depends on the five parameters

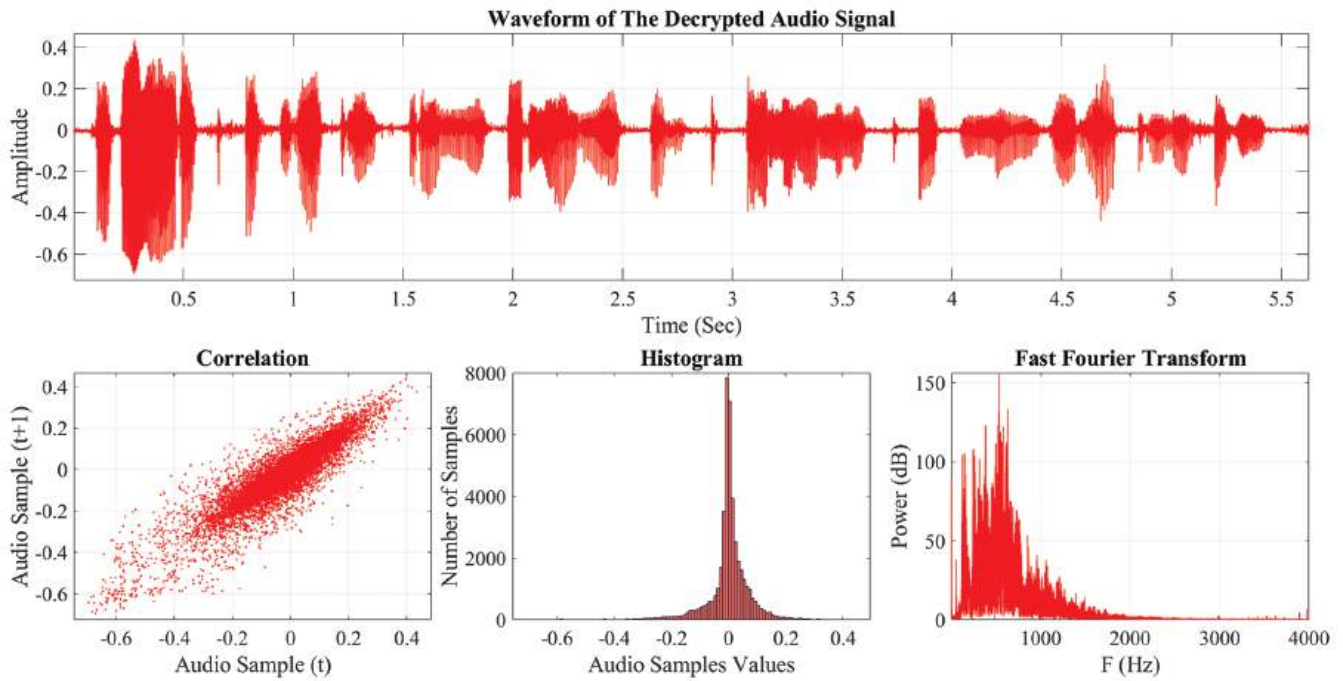


Fig. 9. Subjective decryption results for the 1<sup>st</sup> audio signal.

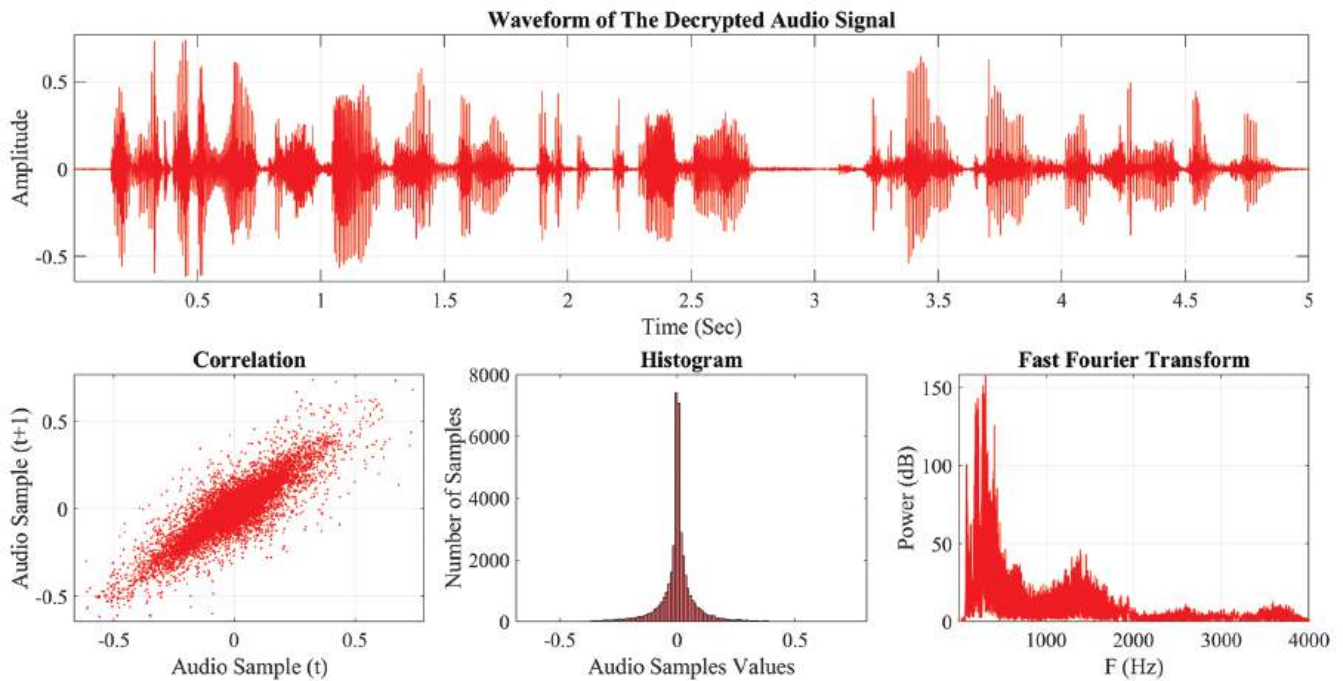


Fig. 10. Subjective encryption results for the 2<sup>nd</sup> audio signal.

TABLE IV  
THE DECRYPTION RESULTS WHEN CHANGING ONE PARAMETER OR INITIAL CONDITION

Change one key	PSNR <sub>Db</sub>	SNR <sub>Db</sub>	Corr.	Ent.	RMS	CF
$\Delta y_1 = +10^{-15}$	-20.851	-40.105	0.00043	15.935	0.5771	1.7329
$\Delta r_1 = -10^{-15}$	-20.854	-40.108	-0.00007	15.941	0.5776	1.7312
$\Delta c_2 = +10^{-15}$	-20.853	-40.107	0.0004	15.936	0.5769	1.7333
$\Delta x_2 = -10^{-15}$	-20.848	-40.102	0.00055	15.935	0.5774	1.7320
$\Delta w_2 = +10^{-15}$	-20.850	-40.105	0.00116	15.935	0.5775	1.7316
$\Delta a_3 = +10^{-15}$	16.246	-3.008	0.00051	12.396	0.0713	9.1777
$\Delta z_3 = +10^{-15}$	16.243	-3.011	-0.00031	12.399	0.0714	9.1778

[r, a, b, c, and d] and four initial conditions ( $x_0, y_0, z_0$  &  $w_0$ ). There are nine coefficients used in the system. The key space of this article is at least.

$$\text{Keys for one HCS} = \prod_1^{11} \frac{1}{10^{-15}} = \left(\frac{1}{10^{-15}}\right)^9 = 10^{135} \quad (14)$$

$$\text{All Keys for three HCS} = (10^{135})^3 = 10^{405} \quad (15)$$

$$\text{All Keys in Bits Representation} = 2^{1345} = 1345 \text{ bits} \quad (16)$$



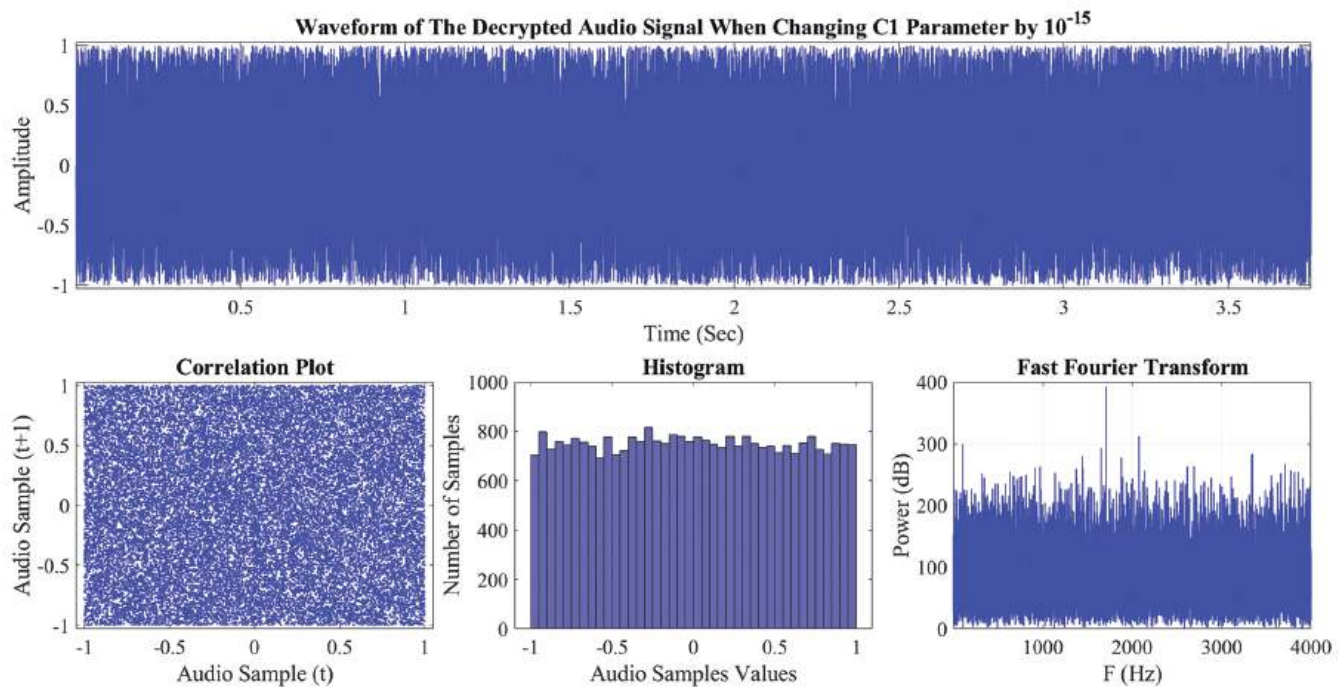


Fig. 11. Decrypted by changing the ©-parameter of the 1<sup>st</sup> HCS by  $10^{-15}$ .

TABLE V  
COMPARING THE PROPOSED STUDY WITH PREVIOUS ARTICLES

Scheme	Key space	PSNR <sub>Db</sub>	SNR <sub>Db</sub>	Corr.	Entropy	Delay (Sec)
(Ameen and Hreshee, 2023)	510 bits	0.914	-27.81	-	15.911	-
(Ameen and Hreshee, 2022)	500 bits	7.7596	-19.394	-0.0148	13.727	0.022
(Hassan, Al-Adhami and Mahdi, 2022)	512 bits	12.881	7.020	0.4703	-	0.050
El-Gamal (Yousif, 2023)	-	-	-35.56	0.0200	-	0.0175
RSA (Yousif, 2023)	-	-	-38.80	0.032	-	0.0814
(Qasim, 2023)	420 bits	-	-	0.0167	7.9918	0.0687
(Abdelfatah, 2020)	928 bits	4.25	-38.02	0.0005	-	0.0370
Our	1345 bits	-20.84	-40.097	-0.0009	15.936	0.0210

Compare the key space of this article with the algorithms, as illustrated in Table V.

Table V shows that the suggested strategy has the greatest key space (1345 bits) and the strongest brute-force resistance. The proposal has the lowest PSNR (-20.84 Db) and the greatest negative SNR (-40.097 Db).

### VII. CONCLUSIONS

Three hyperchaotic systems randomly encrypt digital audio signals, increasing security and reducing predictability. The system’s random selection and CRIN generation make it hard for intruders to guess next. Eavesdroppers cannot understand the audio signal because the algorithm scrambles and encrypts it. The proposed algorithm distorts encryption, highlighting the encryption strength-signal fidelity trade-off. The algorithm intentionally distorts audio for security. Correlation, histogram, and FFT plots show the algorithm’s effectiveness. Decryption yields the original audio signal with zero MSE, minimal distortion, and high PSNR values around 96 Db. Decrypted audio signal correlation plots show a high correlation with

themselves over time, ensuring accurate signal recovery. Success in decryption and signal restoration is shown by bell-shaped histogram plots. These visual verifications prove decryption works. This encryption system is suitable for real-time audio communication due to its low delay and consistent graphical encryption results. It is promising for secure communication environments that prioritize efficiency and security. The researcher’s recommendation for future work is to use artificial intelligence such as convolutional neural networks for chaotic behavior testing before the encryption process.

### REFERENCES

Abdelfatah, R.I., 2020. Audio encryption scheme using self-adaptive bit scrambling and two multi chaotic-based dynamic DNA computations. *IEEE Access*, 8, pp.69894-69907.

Abdullah, H.N., Hreshee, S.H., and Jawad, A.K., 2015. Design of efficient noise reduction scheme for secure speech masked by chaotic signals. *Journal of American Science*, 11(7), pp.49-55.

Abdullah, H.N., Hreshee, S.H., and Jawad, A.K., 2016. *Noise Reduction of Chaotic Masking System Using Repetition Method*. Available from: <https://www.researchgate.net/publication/291356303> [Last accessed on 2024 Oct 10].

- Abdullah, H.N., Hreshee, S.S., Karimi, G., and Jawad, A.K., 2022. Performance Improvement of Chaotic Masking System Using Power Control Method. In: *International Middle Eastern Simulation and Modelling Conference 2022, MESM 2022*, pp.19-23.
- Abood, E.W., Hussien, Z.A., Kawi, H.A., Abduljabbar, Z.A., Nyangaresi, V.O., Ma, J., Al Sibahee, M.A., and Ali Kalafy, S.A., 2023. Provably secure and efficient audio compression based on compressive sensing. *International Journal of Electrical and Computer Engineering*, 13(1), pp.335-346.
- Ahmad, J., and Ahmed, F., 2010. Efficiency analysis and security evaluation of image encryption schemes. *Computing*, 23(4), p.25.
- Alsaabri, H.H., and Hreshee, S.S., 2021. Robust Image Encryption Based on Double Hyper Chaotic Rabinovich System. In: *7<sup>th</sup> International Conference on Contemporary Information Technology and Mathematics, ICCITM 2021*, pp.146-152.
- Ameen, M.J.M., and Hreshee, S.S., 2022. Securing physical layer of 5G wireless network system over GFDM using linear precoding algorithm for massive MIMO and hyperchaotic QR-decomposition. *International Journal of Intelligent Engineering and Systems*, 15(5), pp.579-591.
- Ameen, M.J.M., and Hreshee, S.S., 2023. Security analysis of encrypted audio based on elliptic curve and hybrid chaotic maps within GFDM modulator in 5G networks. *Bulletin of Electrical Engineering and Informatics*, 12(6), pp.3467-3479.
- Barua, N., and Kabir, A., 2022. Encryption and decryption of audio by changing properties and noise reduction. *International Journal of Innovative Science and Research Technology* 7(9), pp.805-809.
- Belagali, P., and Udipi, V.R., 2023. Image steganography based on enhanced payload capacity using hybrid edge detection and least significant bit steganography. *Journal of Harbin Engineering University*, 44(8), pp.1952-1960.
- Dai, W., Xu, X., Song, X., and Li, G., 2022. Audio encryption algorithm based on chen memristor chaotic system. *Symmetry*, 14(1), p.17.
- Elkamchouchi, H., Salama, W.M., and Abouelseoud, Y., 2020. New video encryption schemes based on chaotic maps. *IET Image Processing*, 14(2), pp.397-406.
- Ene, R.D., Pop, N., and Lapadat, M., 2022. Approximate closed-form solutions for the rabinovich system via the optimal auxiliary functions method. *Symmetry*, 14(10), p.2185.
- Gao, Z., Su, B., Wu, S., Liao, L., Li, Z., Wang, Y., and Qin, Y., 2022. Security-enhanced chaotic optical communication based on external temporal self-feedback hardware encryption and decryption. *IEEE Photonics Journal*, 14(4), pp.1-8.
- Giap, V.N., Nguyen, Q.D., and Huang, S.C., 2021. Synthetic adaptive fuzzy disturbance observer and sliding-mode control for chaos-based secure communication systems. *IEEE Access*, 9, pp.23907-23928.
- Hanif, M., Ali Naqvi, R., Abbas, S., Khan, M.A., and Iqbal, N., 2020. A novel and efficient 3D multiple images encryption scheme based on chaotic systems and swapping operations. *IEEE Access*, 8, pp.123536-123555.
- Hasan, F.S., Mosleh, M.F., and Abdulhameed, A.H., 2021. FPGA implementation of LDPC soft-decision decoders based DCSK for spread spectrum applications. *International Journal of Electrical and Computer Engineering*, 11(6), pp.4794-4809.
- Hassan, N.F., Al-Adhami, A., and Mahdi, M.S., 2022. Digital speech files encryption based on hénon and gingerbread chaotic maps. *Iraqi Journal of Science*, 63(2), pp.830-842.
- Hreshee, S.S., Abdullah, H.N., and Jawad, A.K., 2018. A high security communication system based on chaotic scrambling and chaotic masking. *International Journal on Communications Antenna and Propagation*, 8(3), pp.257-264.
- Hussein, E.A.R., Khashan, M.K., and Jawad, A.K., 2020. A high security and noise immunity of speech based on double chaotic masking. *International Journal of Electrical and Computer Engineering*, 10(4), pp.4270-4278.
- Ibrahim, M.K., and Mohammed, F.T., 2022. Image cryptography based on image processing technique and classification algorithm. *Journal of Algebraic Statistics*, 13(2), pp.989-1001.
- Ilyas, B., Raouf, S.M., Abdelkader, S., Camel, T., Said, S., and Lei, H., 2022. An efficient and reliable chaos-based iot security core for UDP/IP wireless communication. *IEEE Access*, 10, pp.49625-49656.
- Jawad, A.K., Abdullah, H.N., and Hreshee, S.S., 2018. Secure Speech Communication System based on Scrambling and Masking by Chaotic Maps. In: *IEEE, International Conference on Advances in Sustainable Engineering and Applications, ICASEA 2018 - Proceedings*, pp.7-12.
- Khalid, M., Hussein, E.A., and Jawad, A.K., 2019. Digital image encryption based on random sequences and XOR operation. *Journal of Engineering and Applied Sciences*, 14(8), pp.10331-10334.
- Kumar Shrivasta, V., Bhatnagar, A., and Pangaria, M., 2013. Enhancement of security in international data encryption algorithm (Idea) by increasing its key length. *International Journal of Advanced Research in Computer and Communication Engineering*, 2, pp.3869-3871.
- Mahdi, A., Jawad, A.K., and Hreshee, S.S., 2016. Digital chaotic scrambling of voice based on duffing map. *Communications Engineering Journal*, 1(2), pp.16-21.
- Majid Msallam, M., and Aldoghan, F., 2023. Multistage encryption for text using steganography and cryptography. *Journal of Technique*, 5(1), pp.38-43.
- Min, L., Ting, L., and Yu-Jie, H., 2013. Arnold Transform Based Image Scrambling Method. In: *3<sup>rd</sup> International Conference on Multimedia Technology (ICMT-13)*, Atlantis Press, pp.1302-1309.
- Nguyen, K., Adams, R., Sweetland, K., and Chen, H., 2005. A 106-DB SNR hybrid oversampling analog-to-digital converter for digital audio. *IEEE Journal of Solid-State Circuits*, 40(12), pp.2408-2415.
- Nien, H.H., Huang, C.K., Changchien, S.K., Shieh, H.W., Chen, C.T., and Tuan, Y.Y., 2007. Digital color image encoding and decoding using a novel chaotic random generator. *Chaos, Solitons and Fractals*, 32(3), pp.1070-1080.
- Ouannas, A., Karouma, A., Grassi, G., Pham, V.T., and Luong, V.S., 2021. A novel secure communications scheme based on chaotic modulation, recursive encryption and chaotic masking. *Alexandria Engineering Journal*, 60(1), pp.1873-1884.
- Pirdawood, M.A., Kareem, S.R., and Zahir, D.C., 2023. Audio encryption framework using the laplace transformation. *Aro-the Scientific Journal of Koya University*, 11(2), pp.31-37.
- Qasim, H.A., 2023. A new audio encryption algorithm based on hyper-chaotic system. *Mustansiriyah Journal of Pure and Applied Sciences*, 1(3), pp.85-94.
- Rahman, S., Masood, F., Khan, W.U., Ullah, N., Khan, F.Q., Tsaramiris, G., Jan, S., and Ashraf, M., 2020. A novel approach of image steganography for secure communication based on LSB substitution technique. *Computers, Materials and Continua*, 64(1), pp.31-61.
- Sajaa, G.M., and Al-Mothafar, N.S., 2024. Evaluation of rijndael algorithm for audio encryption by brute force attack. *Journal of Engineering*, 30(1), pp.128-141.
- Samimi, M., Majidi, M.H., and Khorashadizadeh, S., 2020. Secure communication based on chaos synchronization using brain emotional learning. *AEU - International Journal of Electronics and Communications*, 127, p.153424.
- Sathiyamurthi, P., Ramakrishnan, S., Shobika, S., Subashri, N., and Prakavi, M., 2018. Speech and Audio Cryptography System Using Chaotic Mapping and Modified Euler's System. In: *IEEE, International Conference on Inventive Communication and Computational Technologies, ICICCT 2018 (Icict)*, pp.606-611.
- Shakir, H.R., Mehdi, S.A., and Hattab, A.A., 2023. A new four-dimensional hyper-chaotic system for image encryption. *International Journal of Electrical and Computer Engineering* 13(2), pp.1744-1756.

- Tan, Y., and Zhou, W., 2010. Image Scrambling Degree Evaluation Algorithm based on Grey Relation Analysis. In: *Proceedings - 2010 International Conference on Computational and Information Sciences, ICCIS 2010*, pp.511-514.
- Tolba, M.F., Sayed, W.S., Radwan, A.G., and Abd-El-Hafiz, S.K., 2018. Chaos-based Hardware Speech Encryption Scheme Using Modified Tent Map and Bit Permutation. In: *International Conference on Modern Circuits and Systems Technologies*, pp.1-4.
- Tomita, K., Okumura, M., and Okamoto, E., 2023. Demonstration of chaos-based radio encryption modulation scheme through wired transmission experiments. *IEICE Transactions on Communications*, E106, pp.686-695
- Vaseghi, B., Hashemi, S.S., Mobayen, S., and Fekih, A., 2021. Finite time chaos synchronization in time-delay channel and its application to satellite image encryption in OFDM communication systems. *IEEE Acces*, 9, pp.21332-21344.
- Xu, W., and Cao, N., 2020. Hardware design of a kind of grid multi-scroll chaotic system based on a MSP430F169 chip. *Journal of Circuits, Systems and Computers*, 29(12), p.20501893.
- Yousif, S.F., 2023. Performance comparison between RSA and El-gamal algorithms for speech data encryption and decryption. *Diyala Journal of Engineering Sciences*, 16, pp.123-137.
- Zhang, F., Gao, R., Huang, Z., Jiang, C., Chen, Y., and Zhang, H., 2022. Complex modified projective difference function synchronization of coupled complex chaotic systems for secure communication in WSNs. *Mathematics*, 10(7), p.1202.

# Fungal Population Analysis of Hydrocarbons Contaminated Soil: Samples from Taq-taq Oil Field in Koya City, Kurdistan Region, Iraq

Srwa A. Mohammed<sup>1†</sup>, Taha J. Omar<sup>1</sup> and Ayad H. Hasan<sup>1,2</sup>

<sup>1</sup>Department of Medical Microbiology, Faculty of Science and Health, Koya University, Danielle Mitterrand Boulevard, Koya KOY45, Kurdistan Region – F.R. Iraq

<sup>2</sup>Department of Biomedical Sciences, College of Health Technology, Cihan University – Erbil, Kurdistan Region – F.R. Iraq

**Abstract**—Petroleum is often regarded as one of the environmental hazards that pose the greatest threat to human health. After radiation, petroleum and all of its byproducts and wastes are considered to have the second-worst effect on the environment. Demonstrating fungal microbiomes that flourish on soil heavily polluted by petroleum and moderately contaminated soil samples, comparing them with uncontaminated soil samples from Taq-taq (TPOPCO) through metagenomic analysis through sequencing of the 18S-V4 region. Metagenomic analysis is conducted using high-throughput sequencing technology, targeting 18 subunit ribosomal ribonucleic acid amplicons through the Illumina-HiSeq platform. In general, an increase in fungal community richness and diversity is reported in soil contaminated with petroleum. This is determined by counting the number of operational taxonomic units, performing principal coordinate analysis, and calculating  $\alpha$  (Chao1 and Shannon indices) and  $\beta$  diversity. The composition of microbial communities is significantly altered by crude oil exposure. At the phylum level, there are considerable transitions between groups B and C for Ascomycota, Basidiomycota, Chytridiomycota, Olpidiomycota, Zoopagomycota, Cryptomycota, and Mucoromycota. In examining Group D relative to Group C, there are significant differences in Ascomycota, Basidiomycota, Chytridiomycota, Olpidiomycota, and Cryptomycota. This study is an important first step in determining and understanding the fungal population of soil extensively contaminated with crude oils of the Taq-taq/Kurdistan Region of Iraq.

**Index Terms**—Fungal community, Metagenomics, Operational taxonomic unit number, Statistical analysis, V4 18S rRNA gene.

## I. INTRODUCTION

Contaminated soil resulting from spilled oil is one of the most serious ecological disasters, adversely affecting both marine

and terrestrial ecosystems and incurring substantial economic losses. Moreover, oil spills are among the most prevalent natural catastrophes. Due to the toxicological properties of the oil's components, oil spills provide possible health risks to both cleanup personnel and coastal people (Laffon, et al., 2016). The Kurdistan Region of Iraq (KRI) is located north and north-east of the Arabian plate. The region is one of the oil-rich areas of Iraq (Shlimon, et al., 2020). One of the most significant fields in this region is the Taq-Taq oil field. As a result of factors such as an increasing worldwide demand, an expanding population, and widespread consumption of petroleum products, the petrochemical sector has been expanding at a steady rate and is continuing to contaminate both marine and terrestrial habitats (Ramadass, et al. 2018; Baoune, et al. 2019). Microorganisms use hydrocarbons as their only carbon source or modify them to reduce their toxicity. Most pathways in microbial hydrocarbon degradation transpire in aerobic circumstances; fungi possess the capability to break down polycyclic aromatic hydrocarbons. Bacteria metabolize hydrocarbons through specialized pathways, including alkane monooxygenase and dioxygenase, whereas fungi employ various hydrocarbons through non-specific enzyme complexes, such as cytochrome P450, lignin peroxidase, manganese peroxidase, and laccase that assist them to decompose lignin as well as cellulose (Asemoloye, et al., 2020). Molecular approaches to studying biodiversity may also be analyzed according to the kind of nucleic acid that was extracted (DNA or RNA) or using an analytical technique that is based on either partial or entire community analysis (Wydro, 2022). Microbial community analysis of contaminated soil with crude oils involves the study of the diverse array of microorganisms present in the soil and their response to oil contamination. Using advanced molecular techniques such as next-generation sequencing, researchers can identify and quantify the different microbial species present in the soil (Bonomo, et al. 2022). The field of metagenomics has revolutionized our understanding of microbial diversity by allowing researchers to investigate the vast array of non-cultivable bacteria and fungi that thrive in diverse environmental settings. Traditional cultivation

ARO-The Scientific Journal of Koya University  
Vol. XII, No. 2 (2024), Article ID: ARO.11745. 8 pages  
DOI: 10.14500/aro.11745

Received: 03 August 2024; Accepted: 03 December 2024  
Regular research paper; Published: 25 December 2024

<sup>†</sup>Corresponding author's e-mail: srwa.ali@koyauniversity.org  
Copyright © 2024 Srwa A. Mohammed, Taha J. Omar and Ayad H. Hasan. This is an open access article distributed under the Creative Commons Attribution License (CC BY-NC-SA 4.0).



methods often fail to capture the full microbial diversity present in the environment. Metagenomics overcomes this limitation by directly sequencing the DNA of uncultured microorganisms, revealing valuable genetic information that can be harnessed for novel biotechnological applications (Chandran, Meena and Sharma, 2020).

In this study, our objective was to characterize and introduce the original surface fungal microbiome aerobically that was associated with crude oils and compare it with clean or control samples of the Taq-Taq (TTOPCO) oil field soil of the Kurdistan Region/Iraq through metagenomic analysis through sequencing of the 18S-V4 region. This provides valuable contributions to environmental restoration.

## II. MATERIALS AND METHODS

### A. Sample Collection

Nineteen soil oil samples were collected from the asphalt seep at Koya City Taq Taq Operating Company (TTOPCO) in the KRI. Oil-contaminated soil samples were taken from three places in the seep on October 13, 2020, and a control soil sample was taken from the uncontaminated region. Table I lists the sample sites' coordinates and related attributes. The samples were taken at 5–10 cm deep to obtain representative soil profiles for examination. To ensure proper handling and preservation, all the collected samples were carefully placed into sterilized polyethylene bags.

### B. Fungal Detection and Identification from Soil Samples using Molecular Analysis

Nineteen soil samples were extracted for whole DNA using the DNeasy® Power Soil® Pro Kit (LOT 169043419/Qiagen-Germany). Add 250 mg of soil in each PowerBead Pro tube, and add 800 µL of solution CD1 (lysis buffer) in the PowerBead Pro tubes. Then, increasing the vortex time to 20 min and letting the mixture sit at room temperature for an hour, then following the kit protocol, after following all the steps, the eluted DNA was quantified using a Nanodrop spectrophotometer (Nano Drop Spectro 117 432-UK) for evaluating the concentration of DNA. For metagenomic analysis, total DNA that was extracted from all nineteen soil samples was sequenced at BGI Sequencing Centre Hong Kong/China. The outcomes of library construction were displayed. Eighteen samples were passed successfully with 50,000 tag numbers for 18S-V4 with SILVA\_18S. 30 ng of qualified DNA template and the 18S rRNA fusion primers are added for polymerase chain reaction (PCR). All PCR

products are purified by Agencourt AMPure XP beads. These beads were dissolved in the elution buffer, and the resulting mixture was used to complete the library construction process. Subsequently, the library size and concentration were determined using the Agilent 2100 Bioanalyzer. Only libraries that met the required criteria were selected for sequencing on the HiSeq 2500 platform (PE300), based on their insert size.

### C. Bioinformatics Analysis Workflow

Raw data were filtered to generate high-quality clean reads (Fadrosh, et al., 2014) with truncated reads whose average phred quality values are lower than 20. Then, those whose lengths are 75% of their original lengths after truncation, contaminated by adapter sequences (Martin, et al. 2011), ambiguous bases (N bases), and low-complexity reads should be removed. Paired-end reads were merged using Fast Length Adjustment of Short reads (v1.2.11), with a minimum overlapping length of 15 bp and a mismatching ratio of the overlapped region of  $\leq 0.1$  (Martin, et al., 2011). After which clean reads that can overlap with each other are merged to tags and further clustered to Operational Taxonomic Units (OTU) with USEARCH (v7.0.1090): OTU are a unified marker for analyzing a taxon unit (seven taxonomy levels) (kingdom, phylum, class, order, family, genus, and species). Software used for statistics: USEARCH (v7.0.1090) (Edgar 2013) and UCHIME (v4.2.40) (Edgar 2011).

## III. RESULTS AND DISCUSSIONS

The following fungus genera were discovered by molecular techniques using the same soil samples used for metagenomic analysis: Group A included *Aspergillus lentulus* 28S ribosomal RNA (accession number XR 004500616.1). Group B included *Aspergillus fellis* strain FM324 chromosome 3 (accession number CP066505.1), *Aspergillus luteonubrus* strain MST FP2246 (accession number MT196912.1), and *Aspergillus arizonicus* isolate CCF 5341 (accession number OK321187.1). Group C included *Rhizopus arrhizus* strain SC49B03 (accession number MW113537.1) (Srwa, Taha and Ayad, 2023).

### A. Taxonomic Profiling of Fungal Population

The whole DNA extraction was carried out on each sample on an individual basis. It was found through the creation and analysis of 18S rRNA sequencing libraries that the entire complete genome DNA was used for library

TABLE I  
SOIL SAMPLES AND SAMPLING LOCATIONS

Groups of soil samples	Given numbers	Location of the samples	Coordinate (°N, °E)
A	1,2,3,4	Oil and water mixed samples were collected from an area close to the drilled pool of oil at the Taq-taq oil field.	35° 40' 33" N 44° 31' 30" E (Sardar and Dler, 2017)
B	5,6,7,8,9	Underlying and flanking region of the Taq-taq asphalt seep flow.	
C	10,11,12,13,14	Control: Ten meters away from site Group B, it had not been contaminated by oil spills.	
D	15,16,17,18,19	Transportation area where the soil was contaminated with spilt oil was 20 m away from site number two.	

construction, and the findings showed that every single one of the 18 samples was able to pass profitably. Then, raw data are filtered, clean data are created, after which clean data are merged with tags and further clustered to OTU. The preprocessing of the 18S amplicon sequences produced a total of 1296 OTUs. Table II, which were comprised of 1163942 paired reads, respectively, and with the connect tag number ranging from 69129 to 64147 Table III, which included the control samples as well as the results, showed that for Group A soil samples, there were 110 OTU numbers with 137189 tag numbers out of three subsamples, 524 OTU numbers for Group B soil samples with 246320 tag numbers out of five subsamples, the soil samples from Group C have 188 OTU numbers and 249182 tag numbers out of five subsamples, whereas the soil samples from Group D have 447 OTU numbers and 248661 tag numbers out of five subsamples, as shown in Table II. The soil sample from Group B, which had been long-term contaminated with crude oil, had a higher number of OTUs when compared to both the clean soil samples used as a control and other crude oil-contaminated samples. While the soil sample from Group C, which was uncontaminated, had the most diverse tag number when compared to the other groups. And the results showed that out of 475 OTUs, 46 OTUs were related to the kingdom of fungi, while the remaining were other eukaryotes.

TABLE II  
OTU STATISTICS

Sample name	Tag number	OTU number
A1	49917	35
A2	39087	28
A3	48185	47
B5	49625	60
B6	49028	195
B7	49414	101
B8	48748	106
B9	49505	62
C10	49835	41
C11	49913	37
C12	49891	42
C13	49602	32
C14	49941	36
D15	49819	83
D16	49502	72
D17	49747	53
D18	49811	63
D19	49782	176

TABLE III  
ALPHA DIVERSITY RESULTS

# Alpha	Mean (A)	SD (A)	Mean (B)	SD (B)	Mean (C)	SD (C)	Mean (D)	SD (D)	p-value
sobs	36.66	9.609	104.8	54.75126	37.6	4.037	89.4	49.661	0.005
chao	43.8	15.661	127.71	69.81464	47.45	11.023	105.835	46.765	0.011
ace	51.40	24.355	128.15	66.59791	49.400	13.044	118.056	48.220	0.021
shannon	2.01	0.367	2.92	0.42379	1.817	0.770	2.634	1.134	0.052
simpson	0.19	0.065	0.119	0.06738	0.261	0.171	0.192	0.251	0.261
coverage	0.99	0.00009	0.999	0.0002	0.999	0.0001	0.999	0.0001	0.170

### B. OTU Abundance Table/OTU Analysis/OTU Venn Map

The results of the OTU analysis presented on the samples achieved from oil-contaminated soil and clean soil are shown in the following diagrams. Fig. 1 Venn diagram OTU shows specific number of OTU in each group, and samples (A, B, C, and D) were displayed (9, 178, 6, and 108), respectively, while overlapping OTUs for each group sample with other groups (A, B, C, and D) was shown to be 66, 157, 99, and 141, respectively. Thus, the results of the diagram and statistical analysis showed that the region with the largest concentration of OTU 18S fungal communities was the area corresponding to Group B's soil sample, which was a long-term oil-contaminated soil sample. Group D, which consisted of an area that had been contaminated by spilled crude oil, came next after Group B. The findings from the study conducted by Galitskaya, et al. (2021) align closely with the outcomes of the current study. Their investigation demonstrated the utility of Venn diagrams in comparing OTUs across samples or subgroups. These diagrams serve to illustrate the extent of similarity and overlap in OTU compositions among various environmental samples.

As a result, Galitskaya's work indicated that 25% (samples D and C) to 43% (sample S) of fungal OTUs were unique to each sample, with only approximately 45% being consistently present across all samples. This discrepancy could potentially stem from the stronger associations between soil fungi and plant communities compared to the relationships between plants and bacteria within the bulk soil (Mueller, et al. 2014; Sun, et al. 2017).

### C. Diversity Analysis across Distinct Locations

#### Alpha diversity assessment

The evaluation of species diversity within a sample, known as alpha diversity, can be evaluated through various indices, including the observed species index, Chao index, ACE index, Shannon index, Simpson index, and the Good-coverage index. The outcomes of this analysis demonstrated distinct p-values for the 18S fungal community, which were 0.261 for Groups A, B, C, and D combined. Furthermore, a higher value of the Good-coverage index signifies a lower count of undiscovered species in samples among Groups B, C, and D, with p-values of 0.171 as shown in (Fig. 2 and Table IV). In the realm of statistical analysis for alpha diversity, the 18S data indicated peak diversities within soil Group B (14.62) followed by Group D (13.16). The richness value for 18S, soil group B, exhibited greater richness (sobs =

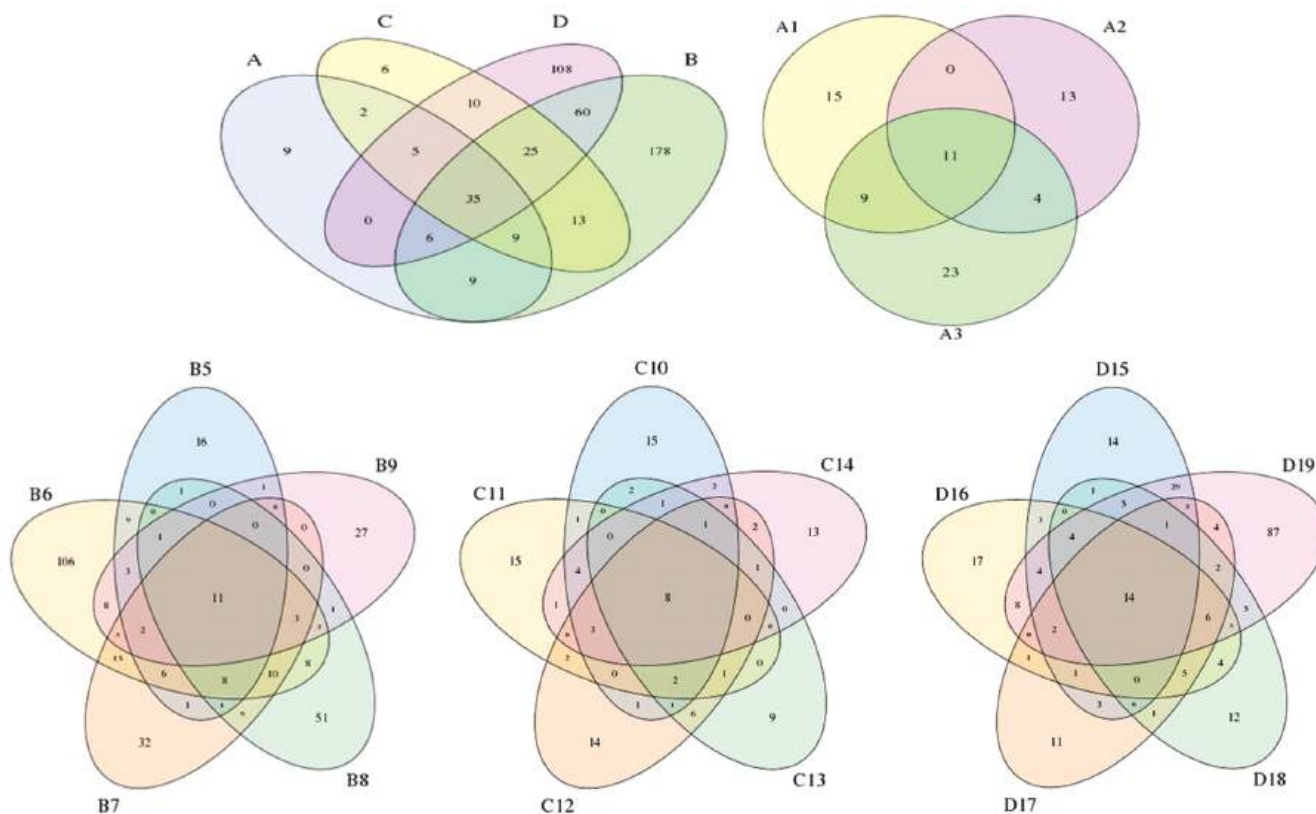


Fig. 1. OTU Venn diagrams.

The Venn diagrams illustrate the distribution of Operational Taxonomic Units (OTUs) among different groups/ samples. Each group/sample is visually distinguished by a unique color fill. The numerical values within the distinct, non-overlapping regions represent the count of OTUs exclusive to each specific group/sample. Conversely, the integers within the intersecting regions indicate the quantity of OTUs that are shared among multiple groups/samples.

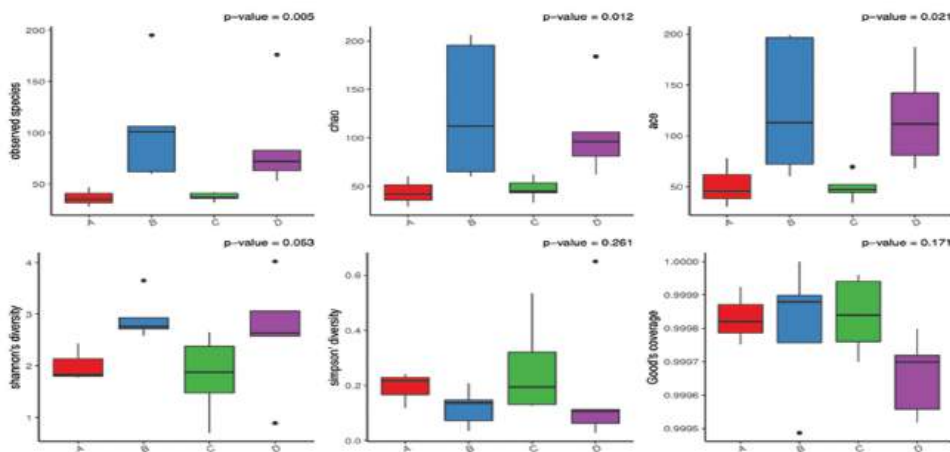


Fig. 2. Boxplot of alpha-diversity.

524.000000). In addition, the Simpson index of diversity showcased its lowest value. The Simpson index's nadir was evident in the subsamples of Group B (B8 = 0.035294) and the subsamples of Group D (D19 = 0.027964), as presented in Table V. The average and standard deviation of alpha diversity were computed for each group. A significance level of  $p < 0.05$  indicates noteworthy variations in alpha diversity between at least two groups, underscoring meaningful distinctions in species diversity across these groups. This

outcome potentially suggests that over an extended period of contamination, native microorganisms have acclimatized to thrive within this environment. These microorganisms have seemingly evolved to effectively harness total petroleum hydrocarbons (TPH) as their exclusive carbon and energy source.

*Beta diversity analysis*

a. Heatmap and Bray-Curtis distance: A heatmap depicting the beta diversity index was generated for 18S datasets.

TABLE IV  
TAGS CONNECTION FOR OVERLAPPED PAIRED-END

Sample name	Total pairs read number	Connect tag number	Connect ratio (%)	Average length and SD
A1	68156	67440	98.95	370/21
A2	39140	39097	99.89	383/12
A3	68278	67327	98.61	383/16
B5	50451	50393	99.89	377/13
B6	72504	72269	99.68	399/24
B7	68407	67491	98.66	380/11
B8	62954	62279	98.93	378/9
B9	54163	54101	99.89	385/7
C10	68233	67408	98.79	377/11
C11	68206	67309	98.68	384/6
C12	60593	60546	99.92	385/10
C13	74302	74226	99.9	381/8
C14	68545	67677	98.73	378/4
D15	67606	66706	98.67	385/12
D16	68171	67252	98.65	386/8
D17	68108	67193	98.66	389/4
D18	68520	67601	98.66	381/8
D19	67605	66503	98.37	391/17

TABLE V  
STATISTICAL TABLE OF ALPHA DIVERSITY

Sample name	Sobs	Chao	Ace	Shannon	Simpson	Coverage
A1	35	42.2	45.678	1.770	0.216	0.999
A2	28	29	30.417	1.831	0.241	0.999
A3	47	60.2	78.109	2.436	0.117	0.999
B5	60	60	60	2.757	0.147	1
B6	195	195.55	196.712	2.579	0.207	0.999
B7	101	112	112.900	2.710	0.136	0.999
B8	106	206	199.028	3.649	0.035	0.999
B9	62	65	72.117	2.930	0.071	0.999
C10	41	45	47.270	1.877	0.193	0.999
C11	37	53.5	51.937	1.475	0.321	0.999
C12	42	43.5	44.410	2.652	0.131	0.999
C13	32	33	33.885	2.377	0.126	0.999
C14	36	62.25	69.500	0.703	0.534	0.999
D15	83	106	111.681	2.631	0.113	0.999
D16	72	81	80.971	3.058	0.062	0.9997
D17	53	62.1	68.121	0.889	0.650	0.999
D18	63	96	142.061	2.575	0.106	0.999
D19	176	184.076	187.447	4.019	0.027	0.999

The Bray-Curtis distance, a widely employed index for evaluating dissimilarities between two communities, was employed. This index's range spans from zero to one, with zero indicating an exact similarity in community structure, as illustrated in the accompanying histograms. Among the 18 soil samples analyzed for the 18S dataset, each sample showcased dissimilarity with other subsamples, with values deviating from zero. Notably, soil subsample A1 demonstrated pronounced similarity only with subsamples A3, A2, and B5, while markedly differing from subsamples D16, D17, and D19, as depicted in Fig. 3a.

The research conducted by Galitskaya et al. (2021) employed NMDS analysis of fungal communities in three soil samples contaminated with crude oil, confirming that

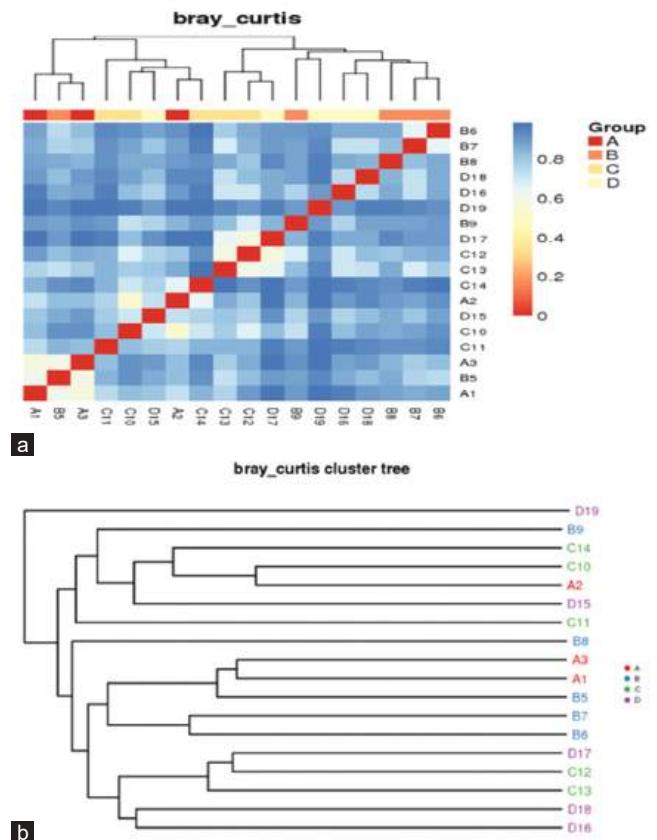


Fig. 3. (a) Heatmap beta-diversity. (b) Sample clustering tree for beta-diversity.

(a) This figure showcases a heatmap depicting the beta diversity indices. A larger index value corresponds to a more pronounced dissimilarity between samples. (b) This figure displays the results of sample clustering analysis. Samples belonging to the same group are depicted with identical colors, and shorter branch lengths or closer distances between samples indicate a higher degree of similarity.

the original fungal communities of the three soils exhibited more significant differences from one another than the bacterial communities and that the fungal communities of the unpolluted soils underwent substantial alterations over time. The primary explanation for the lack of a unified response of the fungal communities in the three distinct soils to petroleum contamination was likely these disparities. Non-metric multidimensional scaling indicated that the successions of fungal communities in contaminated soil varied based on the duration of crude oil contamination.

b. The samples clustering tree displayed the arrangement of the 18 soil samples into four primary clusters representing diverse soil fungal communities. The Bray-Curtis cluster tree indicated the grouping of branches was corresponding to B6, B7, B5, A1, A3, and B8, as well as the clustering of branches corresponding to D17, C12, and C13, and finally, the clustering of branches was corresponding to A2, C10, and C14. Similar fungal populations were observed within these groups, characterized by shorter branch lengths. Conversely, sample D19 stood apart from the fungal communities of the other D samples, as evidenced by its extended branch length, as depicted in Fig. 3b. The study conducted by Gałzka et al.



(2018) demonstrated that soil samples directly obtained from oil wells exhibited the highest levels of biological diversity, as quantified by the Shannon–Weaver index. This discovery aligns with the outcomes of a previous investigation. In a study by Zhang, Ju and Zuo (2018), the metagenomic-based phylogeny of isolated strains predominantly placed them within the Ascomycota phylum, with a few isolates belonging to Basidiomycota.

*D. Correlation Analysis/Species-Specific Spearman Coefficients*

We conducted a comprehensive investigation of correlations among fungal species (18S), separating connections of significance:

- (1) The *Saccharomyces cerevisiae* group (C) demonstrated the highest abundance of this species. It displayed correlations with *Chaetomium globosum* (1) and *Yarrowia lipolytica* (1), both of which were most abundant in groups C and A, respectively. However, *Saccharomyces cerevisiae* exhibited no correlation with *Pichia kudriavzevii* (0), which were most abundant in groups (C). *Pichia kudriavzevii*, this species showed a notable association with *Yarrowia lipolytica* (1) and *Albugo laibachii* (1), while lacking any connection with *Saccharomyces cerevisiae* (0).
- (2) *Chaetomium globosum*: Significant connections were observed with *Saccharomyces cerevisiae* (0.7) and *Albugo laibachii* (1). It also had a modest correlation with *Pichia kudriavzevii* (0.1) but a negative correlation with *Yarrowia lipolytica* (−0.2), as depicted in Fig. 4. These correlations clarify complicated interplays among species within various groups, providing valuable insights into the ecological dynamics of the studied communities.

*E. Species Abundance/Species Composition and Abundance*

To brilliantly illustrate the absolute diversity of fungal species within various soil samples, along with their respective composition and distribution, our study employed a multifaceted approach. This included the utilization of species abundance bar plots. This graphical representation provides an insightful visual of the relative abundance of different

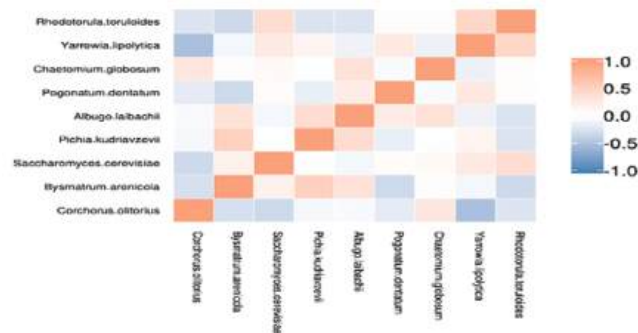


Fig. 4. Species spearman coefficients analysis.

The map shows the correlation between the species level (relative abundance >0.5%). The darker the color, the stronger the correlation between species.

species within the soil samples. Fig. 5 presents an attractive view, showcasing the top 15 most divergent eukaryotic phyla depicted in the annotated phylum barplot. This elucidates the fungal population profiles at the phylum level, highlighting remarkable variations. Our findings reveal noteworthy shifts in fungal phylum abundance between Group B and Group C; we observed significant abundance differences, with shifts in Other (48.47% vs. 38.89%), Ascomycota (2.76% vs. 21.26%), Basidiomycota (3.78% vs. 0.348%), Chytridiomycota (2.193% vs. 0.961%), Olpidiomycota (0% vs. 0.0081%), Zoopagomycota (0.084% vs. 0%), Cryptomycota (0.0154% vs. 0%), and Mucoromycota (0.018% vs. 0%). In exploring Group D in comparison to Group C, we noted substantial differences in Other (58.24% vs. 38.89%), Ascomycota (0.350% vs. 21.26%), Basidiomycota (0.175% vs. 0.348%), Chytridiomycota (0.033% vs. 0.961%), Olpidiomycota (0.357% vs. 0.0081%), and Cryptomycota (0.003% vs. 0%) Table VI.

In support of our fungal microbiome findings, Wang, et al. (2021) analyzed 18S rDNA sequencing data of fungal microbiomes in Ecopile soils. Their analysis revealed that approximately 55% (range 48–64%) of sequence reads could be attributed to the fungal kingdom, while the remaining sequences were assigned to various eukaryotic soil organisms. The majority of fungal reads (an average of 70%) were assigned to the Ascomycota phylum, while other fungal phyla were also identified. At the genus level, they identified 145 different fungal genera, with Ascomycota and Basidiomycota being prominent members of the fungal community.

*F. Methods for Differential Species Composition Analysis*

In this section, principal component analysis (PCA) was employed for assessing differences in species composition between two sites or two groups. The results revealed a robust correlation between two key variables, which are represented along the X and Y axes as PC1 and PC2, respectively. PC1 and PC2 account for 26.49% and 22.22% of the variance, respectively, Fig. 6. This analysis also delineates discrete taxonomic groups associated with each site, confirming the significant divergence in environmental conditions between Groups A and B, which are horizontally separated from each other. In addition, Group C is notably distant from the other groups, further emphasizing the distinct environmental conditions of Group D when compared to the rest.

These collective studies offer valuable insights into fungal community structures in various environmental contexts, contributing to our understanding of microbiome dynamics and adaptation to contaminants. Numerous studies have consistently reported higher fungal diversity in contaminated soils compared to control soils, as documented in studies by Deshmukh, Khardenavis and Purohit (2016) and Borowik, et al. (2019). These combined findings provide a comprehensive understanding of the fungal community in different soil environments, shedding light on their composition and diversity.

TABLE VI  
GROUPS BARPLOT STATISTICAL ANALYSIS

Taxon	A	A%	B	B%	C	C%	D	D%
Mucoromycota	0	0	0.000182	0.0182	0	0	0	0
Cryptomycota	0	0	0.000154	0.0154	0	0	0.00003	0.003
Zoopagomycota	0	0	0.00084	0.084	0	0	0	0
Olpidiomycota	0	0	0	0	0.000081	0.0081	0.00357	0.357
Chytridiomycota	0.000262	0.0262	0.021938	2.193	0.009619	0.961	0.000337	0.033
Basidiomycota	0.027334	2.733	0.037873	3.787	0.003487	0.348	0.001753	0.175
Ascomycota	0.204608	20.460	0.027663	2.766	0.212647	21.26	0.003502	0.3502
Other	0.633286	63.328	0.484723	48.47	0.388980	38.89	0.582459	58.24

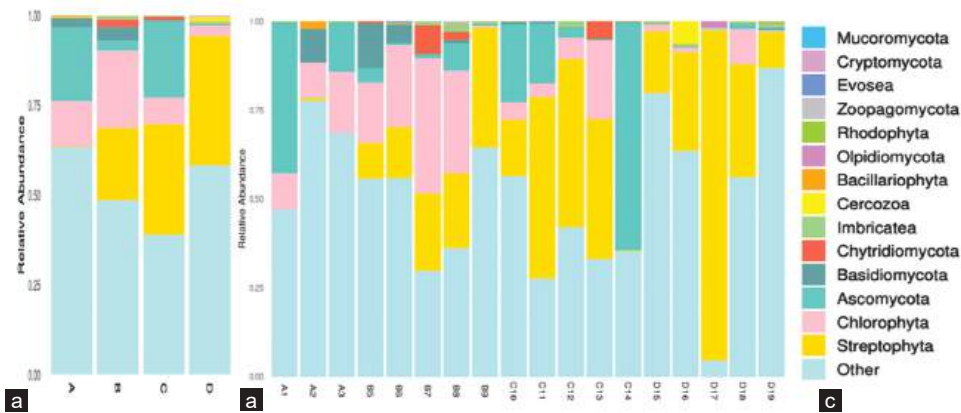


Fig. 5. Phylum abundance barplot (a) groups (b) samples (c) key of a and b.

The GraPhlan map allows us to spatially represent the taxonomic relationships among various species. It visualizes the intricate web of connections between microbial groups, aiding in the understanding of community structure.

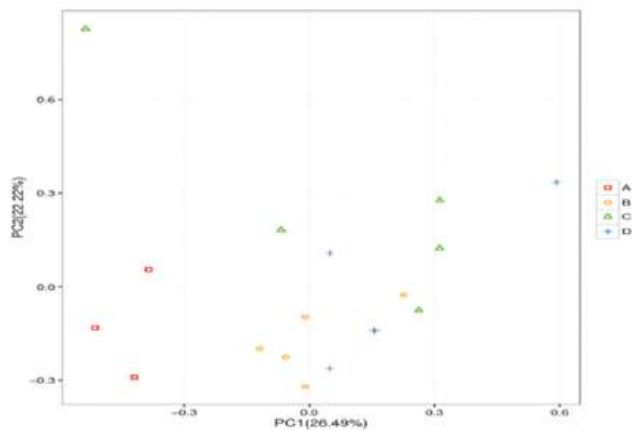


Fig. 6. Species principal component analysis.

Points depicted in various colors and shapes represent samples collected from distinct environments or conditions.

#### IV. CONCLUSION

Employing high-throughput sequencing technology, we investigated the soil microbial diversity through the analysis of 18S amplicons on the Illumina-HiSeq platform. The results illuminated significant shifts in fungal community structures within long-term crude oil-contaminated soil; this manifested in the emergence of distinct fungal groups. As well as underscores the resilience of soils, even in the face of extensive petroleum contamination. This vital insight holds the potential for exploitation in large-scale oil spill

clean-up initiatives, reaffirming the importance of harnessing the natural capacity of microbial communities to mitigate environmental hazards.

#### V. ACKNOWLEDGMENT

We would like to thank the staff of the Deanship of Research and Development Center at Koya University for their help and technical support.

#### REFERENCES

- Asemoloye, M.D., Tosi, S., Daccò, C., Wang, X., Xu, S., Marchisio, M.A., Gao, W., Jonathan, S.G., and Pecoraro, L., 2020. Hydrocarbon degradation and enzyme activities of *Aspergillus oryzae* and *Mucor irregularis* isolated from nigerian crude oil-polluted sites. *Microorganisms*, 8(12), p.1912.
- Baoune, H., Aparicio, J.D., Acuña, A., El Hadj-khelil, A.O., Sanchez, L., Polti, M.A., and Alvarez, A., 2019. Effectiveness of the *Zea mays*-*Streptomyces* association for the phytoremediation of petroleum hydrocarbons impacted soils. *Ecotoxicology and Environmental Safety*, 184, p.109591.
- Bonomo, M.G., Calabrone, L., Scrano, L., Bufo, S.A., Di Tomaso, K., Buongarzone, E., and Salzano, G., 2022. Metagenomic monitoring of soil bacterial community after the construction of a crude oil flowline. *Environmental Monitoring and Assessment*, 194(2), p.48.
- Borowik, A., Wyszowska, J., Kucharski, M., and Kucharski, J., 2019. Implications of soil pollution with diesel oil and bp petroleum with active technology for soil health. *Environmental Research and Public Health*, 16(14), p.2474.

- Chandran, H., Meena, M., and Sharma, K., 2020. Microbial biodiversity and bioremediation assessment through omics approaches, *Frontiers in Environmental Chemistry*, 1, p.570326.
- Deshmukh, R., Khardenavis, A.A., and Purohit, H.J., 2016. Diverse metabolic capacities of fungi for bioremediation. *Indian Journal of Microbiology*, 56(3), pp.247-264.
- Edgar, R.C., 2013. UPARSE: Highly accurate OTU sequences from microbial amplicon reads. *Nature Methods*, 10(10), pp.996-998.
- Fadrosh, D.W., Ma, B., Gajer, P., Sengamalay, N., Ott, S., Brotman, R.M., and Ravel, J., 2014. An improved dual-indexing approach for multiplexed 16S rRNA gene sequencing on the Illumina MiSeq platform. *Microbiome*, 2(1), p.6.
- Gałązka, A., Grządziel, J., Gałązka, R., Ukalska-Jaruga, A., Strzelecka, J., and Smreczak, B., 2018. Genetic and functional diversity of bacterial microbiome in soils with long term impacts of petroleum hydrocarbons. *Frontiers in Microbiology*, 9, p.1923.
- Galitskaya, P., Biktasheva, L., Blagodatsky, S., and Selivanovskaya, S., 2021. Response of bacterial and fungal communities to high petroleum pollution in different soils. *Scientific Reports*, 11(1), p.164.
- Martin, M., 2011. Cutadapt removes adapter sequences from high-throughput sequencing reads. *EMBnet Journal*, 17(1), pp.10-12.
- Mueller, R.C., Paula, F.S., Mirza, B.S., Rodrigues, J.L.M., Nüsslein, K., and Bohannan, B.J.M., 2014. Links between plant and fungal communities across a deforestation chronosequence in the Amazon rainforest. *International Society for Microbial Ecology*, 8(7), pp.1548-1550.
- Ramadass, K., Megharaj, M., Venkateswarlu, K., and Naidu, R., 2018. Bioavailability of weathered hydrocarbons in engine oil-contaminated soil: Impact of bioaugmentation mediated by *Pseudomonas spp.* on bioremediation. *Science of the Total Environment*, 636, pp.968-974.
- Shlimon, A.G., Mansurbeg, H., Othman, R.S., Gittel, A., Aitken, C.M., Head, I.M., Finster, K.W., and Kjeldsen, K.U., 2020. Microbial community composition in crude oils and asphalts from the Kurdistan Region of Iraq. *Geomicrobiology Journal*, 37(7), pp.635-652.
- Srwa, A.M., Taha, J.O., and Ayad, H.H., 2023 Degradation of crude oil and the pure hydrocarbon fractions by indigenous soil microorganisms. *Biologia*, 78(12), pp.3637-3651.
- Sun, S., Li, S., Avera, B.N., Strahm, B.D., and Badgley, B.D., 2017. Soil bacterial and fungal communities show distinct recovery patterns during forest ecosystem restoration. *Applied and Environmental Microbiology*, 83(14), p.e00966-17.
- Wang, M., Garrido-Sanz, D., Sansegundo-Lobato, P., Redondo-Nieto, M., Conlon, R., Martin, M., Mali, R., Liu, X., Dowling, D.N., Rivilla, R., and Germaine, K.J., 2021. Soil microbiome structure and function in ecopiles used to remediate petroleum-contaminated soil. *Frontiers in Environmental Science*, 9, p.624070.
- Wydro, U., 2022. Soil microbiome study based on DNA extraction: A review. *Water*, 14(24), p.3999.
- Zhang, N., Ju, Z., and Zuo, T., 2018. Time for food: The impact of diet on gut microbiota and human health. *Nutrition*, 51, pp.80-85.

# Extraction of Sulfur Compounds from Model Petroleum Products using $\text{Fe}_3\text{O}_4$ Nanoparticles and Acetic Acid-1-Butyl-3-Methylimidazolium Chloride based on Deep Eutectic Solvents

Yousif T. Maaroo<sup>1</sup>, Idrees B. Qader<sup>2,3</sup>, Hani K. Ismail<sup>4†</sup>,  
Hardi Q. Hamad<sup>5</sup> and Sardasht R. Taher<sup>5</sup>

<sup>1</sup>Department of Petroleum Technology, Erbil Technology College, Erbil Polytechnic University, Erbil, Kurdistan Region – F.R. Iraq

<sup>2</sup>Department of Pharmaceutical Chemistry, College of Pharmacy, Hawler Medical University, Erbil, Kurdistan Region, Iraq

<sup>3</sup>Department of Pharmacy, College of Medicine, University of Kurdistan-Hawler, Erbil, Kurdistan Region – F.R. Iraq

<sup>4</sup>Department of Chemistry, Faculty of Science and Health, Koya University, Koya, KOY45, Kurdistan Region – F.R., Iraq

<sup>5</sup>Department of Petroleum Technology, Chemical Analysis, Koya Technical Institute, Erbil Polytechnic University, Erbil, Kurdistan Region – F.R. Iraq

**Abstract**—This research demonstrates that deep eutectic solvents (DESs) can eliminate sulfur compounds, which are corrosive and carcinogenic species, from model petroleum products through liquid-liquid extraction. Several monoprotic acids, including formic acid and acetic acid, are used to make DESs, along with 1-butyl-3-methylimidazolium chloride (BmimCl) as a hydrogen bond acceptor. These DESs are used for the first time to remove sulfur compounds (thiophene and dibenzothiophene) from an alkane as a model hydrocarbon (n-octane), which is used instead of crude oil as the latter contains a variety of species, including nitrogen compounds, hydrocarbons, and oxygen. The optimal parameters for the removal of sulfur are discussed, including the extraction temperature, reaction time, and mass ratio of DES to the model hydrocarbon, whilst the regeneration of DESs is also considered.  $\text{H}_2\text{O}_2$  and iron oxide ( $\text{Fe}_3\text{O}_4$ ) are also used as nanoparticle (NP) catalysts to enhance the sulfur removal process. Several characterization methods, including scanning electron microscopy, Fourier transform infrared, energy dispersive X-ray, and transmission electron microscopy, are used to determine the structural characteristics of the  $\text{Fe}_3\text{O}_4$  NPs. The results show that acetic acid, as a monoprotic acid-based DES, is able to remove more than 86% of the sulfur molecules from model petroleum products

when the mass ratio of DES to model petroleum products is 2:1, at 30°C and within 60 min. This research provides an important opportunity to advance our understanding of the role of DESs in removing carcinogenic and corrosive particles in industrial processes.

**Index Terms**—Air pollution, Desulfurization, Deep eutectic solvents, Model petroleum, Solvent extraction

## I. INTRODUCTION

With the rapid increase in the worldwide population, the consumption of fuels is very likely to show a commensurate increase itself. Therefore, it is vital to utilize a fuel with minimal health and environmental hazards. Consequently, we must employ a technique to obtain a fuel of superior quality, such as through enhancing the octane number of petrol (Qader, et al., 2021). With the present rate of progress in today's world, petroleum refineries should be able to produce more environmentally friendly fuels because of the unwanted and dangerous emissions currently related to their usage (Kiran, et al., 2019; Zhang, et al., 2017). Desulfurization of fuel plays a crucial role in the refining of crude oil. Hydrodesulfurization (HDS), which is commonly used in industry, is ineffective with regard to extracting complex-structured sulfur and aromatic compounds; thus, researchers have been using different methods as alternatives to desulfurization via this method (Gao, et al., 2018). Recently, Adsorption, oxidation, bioprocesses and ionic liquids (ILs) have been used as extractants and catalysts to reduce sulfur in diesel fuel as alternative manners to HDS. In addition,

ARO-The Scientific Journal of Koya University  
Vol. XII, No. 2 (2024), Article ID: ARO.11776. 10 pages  
DOI: 10.14500/aro.11776

Received: 16 August 2024; Accepted: 07 December 2024

Regular research paper; Published: 29 December 2024

†Corresponding author's e-mail: hani.khalil@koyauniversity.org

Copyright © 2024 Yousif T. Maaroo, Idrees B. Qader, Hani K. Ismail, Hardi Q. Hamad and Sardasht R. Taher. This is an open access article distributed under the Creative Commons Attribution License (CC BY-NC-SA 4.0).



electrochemical photo-oxidation was used to minimize sulfur in diesel fuel, which represents an eco-friendly process. The authors converted sulfur compounds to more polar compounds like sulfones or sulfoxide using stainless steel and titanium to enhance desulfurization (Humadi, et al., 2024). Furthermore, the solid sorbent adsorption technique was applied to desulfurize diesel fuel via catalytic oxidization (Mohammed, et al., 2024).

ILs, which are compounds made up of anions and cations salts, have recently found use in various industrial applications (Abbott, et al., 2017a). They typically have melting points below 100°C and exhibit large potential ranges and significant levels of ionic conductivity that are effective in the desulfurization process. In the current study, a number of new deep eutectic solvents (DESs) (which behave in a similar manner to ionic ILs) are used to extract sulfur compounds. DESs are biodegradable solvents that include hydrogen bond donors like amides, carboxylic acids, and alcohols with quaternary ammonium moieties (Ismail, et al., 2022a). DESs are used in a variety of fields, such as conducting polymers (Alabdullah, et al., 2020), alloy and metal electrodeposition (Alesary, et al., 2023; Ismail, 2020), metal polishing (Abbott, et al., 2017b), natural product extraction (Qader, et al., 2023b), desulfurization (Qader, et al., 2021), medicines (Qu, Qader and Abbott, 2022; Qader, et al., 2024), and energy storage (Ismail, et al., 2022b). This is due to their affordability, ease of preparation, low volatility, biodegradability, insensitivity to water, and low toxicity, making them desirable for use in large-scale applications (Hillman, et al., 2017).

There are various methods that can be used in the extraction of the sulfur compounds present in kerosene, gasoline, diesel, or indeed any petroleum product, via ILs and/or DESs. These methods may involve varying temperatures and durations of extraction (Norouzi, et al., 2016). The existence of sulfur compounds is mainly responsible for affecting health, and in spite of that, the absorption of sulfur oxides in the effective place of catalysts during refining chemical processes can perform to deactivate it (Eßer, Wasserscheid and Jess, 2004). When sulfur compounds exceed the standard weight in crude oil, they must be treated in all areas during petroleum refinement because their presence as impurities can lead to major challenges during production, transportation, and refining, in addition to environmental pollution resulting from fuel combustion (Pauca, et al., 2021). Furthermore, nitrogen and sulfur compounds in fuels like  $\text{NO}_x$  and  $\text{SO}_x$  cause an imperfect change in air components, which can lead to the production of acid rain (Zolotareva, et al., 2019). Accordingly, the extraction of sulfur from fuel is one of the most studied and utilized technologies worldwide with regard to environmental considerations (Ahmad, et al., 2021).

Recently, nanoparticles (NPs) such as ZnO, iron oxide ( $\text{Fe}_3\text{O}_4$ ), NiO,  $\text{Ti}_2\text{O}_3$ ,  $\text{SiO}_2$ , and  $\text{MoO}_2$  have begun to see significant use in different fields, including biology, pharmacy, chemistry, etc. They exist in several forms, with sizes ranging from 1 to 100 nanometers. Furthermore, their nanoscale dimensions and extensive surface area contribute to their distinctive chemical and physical characteristics

(Khan, Saeed and Khan, 2019). In this study, a green synthesis method was employed to produce iron NPs using plant extracts from *Quercus infectoria*. *Q. infectoria* is known for having strong anticancer, antibacterial, and antioxidant properties. Because of this, it can be used as both a capping and reducing agent to synthesize these NPs without the need for costly, toxic, and abrasive substances.

In this study, the novel approach of a desulfurization-based DES and  $\text{Fe}_3\text{O}_4$  NPs was applied for the first time to remove sulfur compounds (such as thiophen and dibenzothiophene) from model petroleum products, using X-ray fluorescence to determine the extent of their removal. The novel DES was formed from 1-butyl-3-methylimidazolium chloride (BmimCl) and acetic acid/formic acid. Optimal parameters for this removal were studied, including extraction temperature, reaction time, NP used, and mass ratio of DES to alkane (n-octane), as well as the regeneration of the DES used in the desulfurization process.  $\text{Fe}_3\text{O}_4$  was utilized as a catalyst in this work to enhance the sulfur removal in a mixture of dibenzothiophene and thiophene prepared in n-octane. We will specifically evaluate the removal of sulfur compounds (thiophene and dibenzothiophene) from petroleum products in the presence and absence of the  $\text{Fe}_3\text{O}_4$  catalyst. In addition, The  $\text{Fe}_3\text{O}_4$  NPs were characterized using scanning electron microscopy (SEM), energy dispersive X-ray (EDX), Fourier-transform infrared spectroscopy (FTIR), and transmission electron microscopy (TEM) techniques.

## II. EXPERIMENTAL AND METHODS

### A. Materials and Instrumentation

All the chemicals reported in Table I were used in this study without further purification. In addition, a water bath with a single chamber controlled by a thermostatic system and a laboratory reactor system were utilized. SEM and EDX analyses were conducted using a Philips XL20SEM instrument with an accelerator voltage of 20 keV. TEM images were obtained using a ZEISS EM900 microscope operating at 80 kV. The  $\text{Fe}_3\text{O}_4$  sample was examined via FTIR using a Bruker Equinox55 spectrophotometer, covering a wavenumber range of 400–4000  $\text{cm}^{-1}$ .

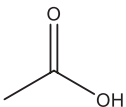
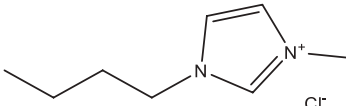
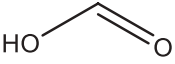
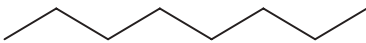
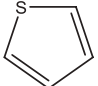
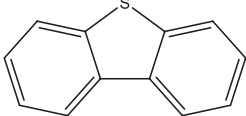
### B. Preparation of DESs

The preparation of DESs follows a previously reported method (Qader, et al., 2021). Typically, acetic acid and formic acid, as hydrogen bond donors, were separately mixed with 1-butyl-3-methylimidazolium chloride, as a quaternary ammonium salt, in molar ratios of 2:1, respectively. This is in agreement with the study conducted previously by Qader in terms of the formation of DESs from hydrogen bond donors and acceptors (Qader, 2021). We then placed the prepared mixtures on a hotplate, stirring them at 50°C until they formed clear, homogenous liquids, and then stored them in an oven at 40°C for later use.

### C. Synthesis of $\text{Fe}_3\text{O}_4$ NPs

The *Q. infectoria* solution was made by dissolving 5.0 g of *Q. infectoria* powder in 200 mL of distilled water and heating

TABLE I  
THE STRUCTURE, PURITY, AND SOURCES OF THE CHEMICALS EMPLOYED IN THIS WORK

Chemicals	Structure	Source	Purity %
Acetic acid		Thomas Baker	99
1-Butyl-3-methylimidazolium chloride		Sigma-Aldrich	≥99
Hydrogen peroxide	H <sub>2</sub> O <sub>2</sub>	Scharlau	50
Ferric chloride	FeCl <sub>3</sub>	Sigma-Aldrich	97
Formic acid		Sigma-Aldrich	98
n-octane		Carlo Erba	99
Thiophene		Merck	≥99
Dibenzothiophene		Merck	≥99

the solution to a temperature of 70°C for 2 h. Subsequently, the solution was filtered using a Whatman No. 1 filter paper to isolate the individual components. Further, a 0.10 M FeCl<sub>2</sub> solution was prepared by dissolving 1.99 g of solid FeCl<sub>2</sub>·4H<sub>2</sub>O in 100 mL of deionized water. Thereafter, the FeCl<sub>2</sub> solution was combined with the *Q. infectoria* solution. 1.0 M NaOH solution was subsequently added to the above mixture and agitated using a magnetic stirrer until the pH was 6.0. This led to the formation of Fe<sub>3</sub>O<sub>4</sub> NPs, which appeared as a black precipitate within the solution. After reducing the volume of the solution by half through evaporation using a hot plate at a temperature of 70°C, the Fe<sub>3</sub>O<sub>4</sub> NPs were then isolated using a magnetic field. The solid Fe<sub>3</sub>O<sub>4</sub> obtained was thoroughly washed with deionized water and then dried for 12 h in a fume hood. It was further dried for an additional 12 h in a vacuum oven at a temperature of 100°C (Qader, et al., 2023a).

#### D. Preparation of Petroleum Model

A model petroleum product (sulfur compounds) was prepared by dissolving 0.25 g of thiophene and 0.25 g of dibenzothiophene in 500 mL of n-octane. A number of groups have reported that DESs and ILs can effectively remove sulfur compounds such as thiophene and dibenzothiophene from model petroleum products (Kareem, 2017). In our case, we used two new DESs: acetic acid + BmimCl and formic acid + BmimCl. It is known that real diesel contains impurities in the form of a number of organic compounds, including oxygen and nitrogen species. In addition, real diesel contains aromatic compounds, which are problematic to the desulfurization processes (Zhu, et al., 2015); therefore, we used a model petroleum product to avoid this effect on sulfur extraction.

#### E. Extraction of Sulfur Compounds

In this study, sulfur was extracted using DESs mixed with the model petroleum products in different molar ratios (wt/wt%), see appropriate figure caption. After that, the mixture was stirred for specific reaction times at 30 ± 2°C. Furthermore, the quantity ( $X$ ) of sulfur compounds removed at 1 atm pressure was determined using equation (1):

$$X = \frac{Ci - Cr}{Ci} * 100\% \quad (1)$$

whereas  $Ci$  is the original sulfur amount in model diesel fuel, and  $Cr$  is the remaining amount of sulfur in the model diesel phase after the reaction had continued for a definite period of time. The same procedure was conducted after adding 1.0 mol H<sub>2</sub>O<sub>2</sub> and 0.01 g Fe<sub>3</sub>O<sub>4</sub> NPs as a catalyst into the DESs phase. The amount of sulfur in the treated model petroleum products phase before and after removal was measured via X-ray fluorescence spectroscopy.

$Ci$  represents the initial sulfur content in the model diesel fuel, whereas  $Cr$  represents the sulfur content that remains in the model diesel phase after a specific period has passed in the course of the reaction.

### III. RESULTS AND DISCUSSION

#### A. Effect of Different Hydrogen Bond Donors

The extraction processes are principally controlled by functional groups and intermolecular forces. For this investigation, three extraction agents, which are commonly associated with DESs, were utilized. The DESs used in this study consist of formic acid, acetic acid, and a combination of formic acid and acetic acid, with each individually combined

with 1-butyl-3-methylimidazolium chloride. It is important to note that the eutectic point varies for each solvent. Fig. 1 shows that the DES containing BmimCl: acetic acid had the highest sulfur removal percentage, approximately 36%, compared to the other DES mixtures. It is well known that formic acid is stronger than acetic acid in terms of acidity. This means that the species in the DES formed by formic acid and 1-butyl-3-methylimidazolium chloride physically interact more strongly than the species in the DES formed by acetic acid. As a result, the latter mixture interacted and removed sulfur more effectively than the former from the model petroleum products, as shown in Fig. 1. Therefore, we selected BmimCl: acetic acid for further research.

### B. Influence of Temperature

Temperature is a key factor that has a considerable impact on sulfur removal. Caero, et al. studied the elimination of aromatic sulfur-containing species from a petroleum phase, as accomplished at a reaction temperature of around 70°C (Caero, et al., 2005). Correspondingly, Shiraishi et al. noted that the removal of sulfur species from the petroleum into the extractants part increases with increasing reaction temperature (Shiraishi, et al., 2002). To investigate the optimal temperature for desulfurization processes, the sulfur extraction from the model petroleum products was performed over a range of temperatures. Fig. 2 illustrates the influence of temperature (20–70°C) on the desulfurization of the selected DES (2 acetic acid: 1 BmimCl) from model petroleum products. The model petroleum product and DES phases were mixed in a mass ratio of 2:1 for 30 min under constant stirring at 500 rpm.

According to Fig. 2, the removal effectiveness of sulfur species increases from 38% to 58.2% as the temperature rises from 20 to 30°C. However, the ability to extract sulfur from petroleum product into a DES containing acetic acid did not significantly change as the temperature increased from 30 to 70°C, with only a slight increase in the extraction percentage from 58.2% to 59.9%. A decline in extraction efficiency as extraction temperature increased could potentially indicate that elevated temperatures are detrimental to extraction-desulfurization employing DESs. The exothermic process related to acid-base complexation is believed to have impeded the reaction more at elevated temperatures (Chandran, et al., 2019). Concerning the exothermic phenomena, elevated temperatures accelerate electrophilic substitution onto the thiophene and dibenzothiophene aromatic rings (Tang, et al., 2015). This suggests that the process can be conducted at ambient temperature, in contrast to the conventional HDS approach which necessitates temperatures of up to 623 K. The viscosity of DESs varies linearly with temperature, as seen in Equation 2. Increased temperatures result in a decrease in the sulfur partitioning coefficient ( $K_N$ ). This further substantiates the hypothesis that reduced temperatures are adequate for this process (Wang, et al., 2016). Comparable results were also found in several other research efforts (Gano, et al., 2015; Jiang, et al., 2016; Li, et al., 2016).

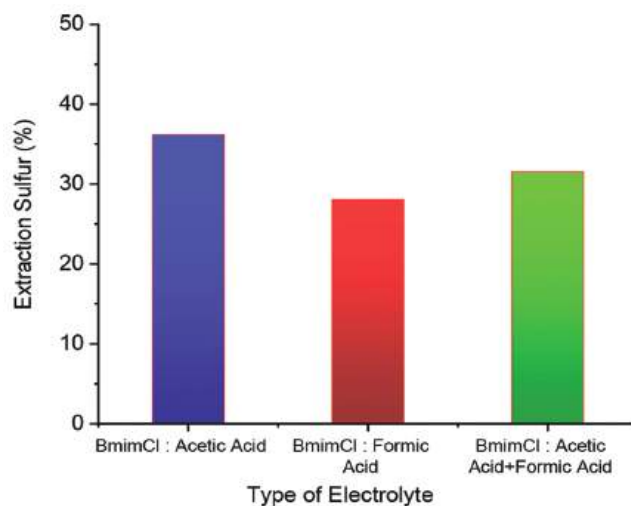


Fig. 1. Sulfur removal as a function of deep eutectic solvent (DES) at 20°C. The mass ratio was two parts model petroleum product (thiophene + dibenzothiophene in n-octane) to one part DES for 30 min while stirring at 500 rpm.

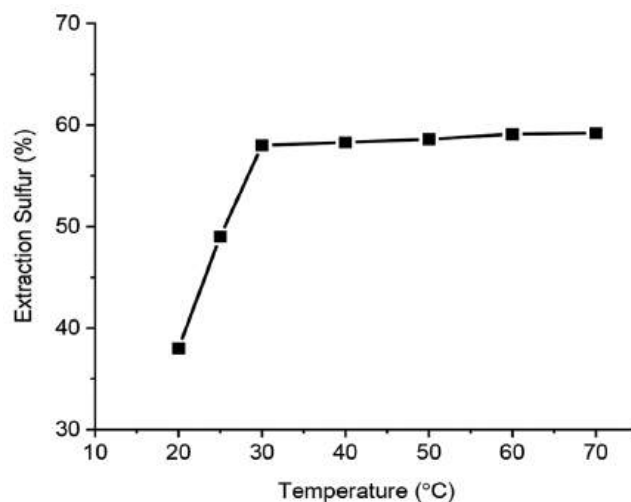


Fig. 2. Effect of temperature on the extraction efficiency of sulfur. The mass ratio was 2:1 for the model petroleum product (thiophene + dibenzothiophene in n-octane) to the deep eutectic solvent (1 BmimCl: 2 acetic acid). The stirring rate was 500 rpm at 30°C for 30 min.

For the current investigation, 30°C was chosen as the ideal temperature for the constructed system to avoid the consumption of large amounts of energy, as mentioned above.

$$\ln(\eta) = \ln \eta_0 + \frac{E_\eta}{RT} \quad (2)$$

### C. Influence of Reaction Time

This study investigated the impact of extraction time on sulfur species. The experiment was run using a mass ratio of 1:2 between the fuel and BmimCl + acetic acid at 30°C and a 500-rpm stirring speed. Fig. 3 illustrates the impact of reaction time on the sulfur compounds present in the modeled oil sample (n-octane). The elimination of

sulfur compounds improves significantly from 31% to 65% as the response time is extended from 5 min to 60 min; however, it plateaus after 60 min and then gradually drops from 65% to 58% as the reaction time is extended further. There are a number of possible reasons for this beyond the effect of reaction time itself in the extraction of sulfur molecules, as follows: first, according to Abbott et al., the extraction reaction most likely approaches equilibrium after about an hour, at which point the desulfurization process' effectiveness decreases (Abbott, et al., 2017b). Sulfur uptake was rapid during the early contact period, specifically between 10 and 60 min of extraction. This observation can be ascribed to the disparity in the concentration of polar sulfur between the model petroleum and the extracting agent, the DES, leading to the swift movement of sulfur compounds from the model petroleum to the DES, to which they can easily attach. With an increase in contact duration, a greater quantity of sulfur compounds adhered to the DES (extracting agent), resulting in a reduction of accessible sites. At this juncture, electrostatic repulsion transpired between sulfur compounds adhered to the DES (extracting agent) and those retained in the model petroleum. Similar behavior has also been documented in previous research (De Luna, et al., 2018; Almashjary, et al., 2018; Tahir, et al., 2021). Moreover, the extraction rate may exhibit a natural drop due to thermodynamic or kinetic constraints, contingent upon factors such as temperature, solvent, and the characteristics of the sulfur compounds. Subsequently, the reaction may attain an equilibrium state, resulting in a substantial reduction in the rate of sulfur extraction (Chandran, et al., 2019). In summary, the reduction in sulfur extraction after 60 min may be attributed to DES saturation, depletion of sulfur compounds, thermodynamic or kinetic constraints, or the generation of inhibitory by-products. In general, we observed the most positive results within a 60-min period after treatment. Therefore, we conclude that

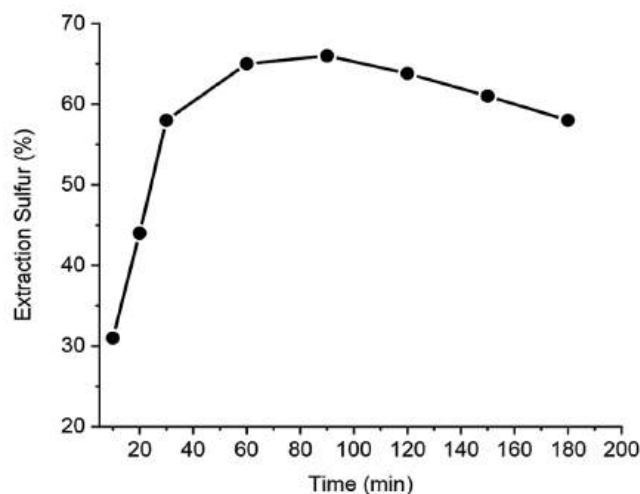


Fig. 3. Effect of reaction time on the extraction efficiency of sulfur. The stirring speed was 500 rpm at a constant temperature of 30°C. The mass ratio of model petroleum product (thiophene + dibenzothiophene in n-octane) to the deep eutectic solvent (1 BmimCl: 2 acetic acid) was 2:1

60 min is a suitable period for the oxidation system in this specific investigation.

#### D. Effect of DES/Model Petroleum Product Mass Ratio

In terms of environmental safety, the removal of sulfur compounds from petroleum products is vital. Hence, five different mass ratios for the DES (acetic acid + BmimCl)/petroleum products were used to investigate the efficiency of the removal of sulfur compounds from petroleum products, keeping other parameters constant (Fig. 4). Fig. 4 shows that changing the mass ratio of DES to petroleum products affects sulfur removal from petroleum products. The proportion of sulfur compounds extracted from the petroleum products into the DES (2 acetic acid: 1BmimCl) was 28.1% when the ratio of the mass of the petroleum products to the DES was 3:1, which may be due to a less active interaction between the DES and petroleum products, leading to lesser desulfurization efficiency. The results obtained are presented in Fig. 4, showing that a maximum removal of sulfur compounds of up to 75% could be achieved at a molar ratio of 2:1 for the DES (1 BmimCl: 2 acetic acid) to the model petroleum product. However, for other ratios, the percentage of desulfurization decreases. The study suggests that mass ratio affects extraction efficiency.

#### E. Influence of Stirring Speed

In this section, we studied the effect of the stirring speed on the extraction of sulfur by varying the stirrer speed from 100 to 2000 rpm, as shown in Fig. 5. It was observed that the percentage removal of sulfur compounds increased from 35% (100 rpm) to 74.8% with increasing the stirrer speed up to 500 rpm, beyond which there was a slight decrease with increasing stirring speed. Exceeding the optimal speed might hinder effective interaction between species in the system, resulting in reduced desulfurization efficiency due to the dispersion of species in the system. Therefore, all subsequent experiments were carried out at 500 rpm. This was in

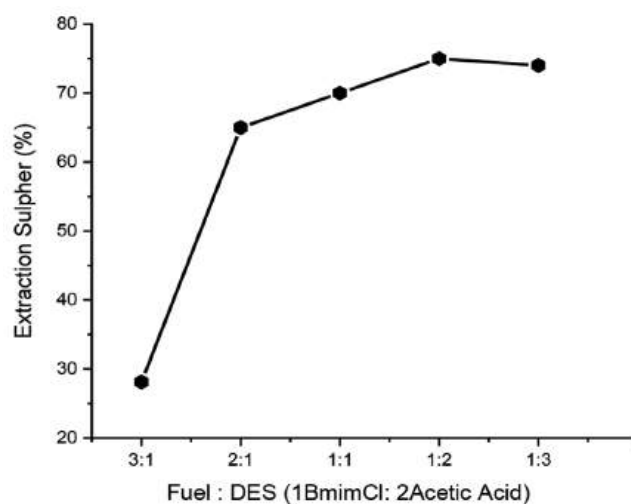


Fig. 4. Effect of mass ratio of deep eutectic solvent (1 BmimCl: 2 acetic acid) to model petroleum product on sulfur removal at 30°C for 60 min and a stirring rate of 500 rpm.



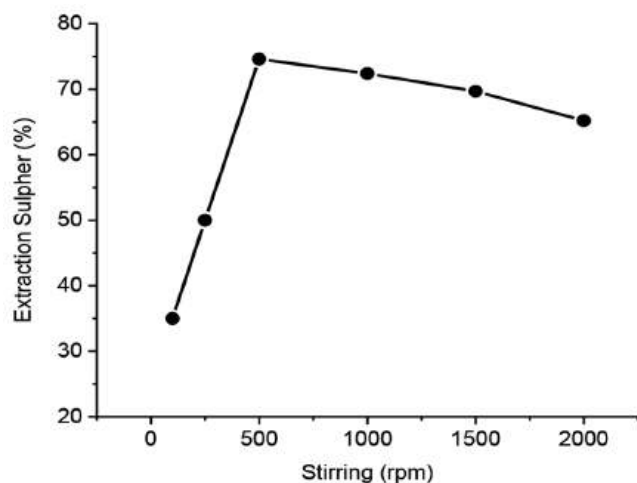


Fig. 5. Effect of stirring rate on the efficiency of sulfur removal from the petroleum model. The extraction time was 60 min with a 1:2 mass ratio of model petroleum product (thiophene + dibenzothiophene in n-octane) to deep eutectic solvent (1 BmimCl: 2 acetic acid) at a fixed temperature of 30°C.

agreement with the study conducted by Qader et al. (2021) in which they used phenol and ChCl as a DES to remove sulfur from diesel.

#### F. Effect of $H_2O_2$ and Fe NPs as Catalysts on the Sulfur Extraction Process

According to Yang, et al.'s investigation, the production of catalytic present species increases the desulfurization rate when  $H_2O_2$  is used as a catalyst in certain concentrations (Yang, et al., 2019). In a similar vein, Al-Shahrani et al. demonstrated that hydrogen peroxide ( $H_2O_2$ ) can effectively serve as a catalyst in the elimination of sulfur from fuel (Al-Shahrani, et al., 2007). In order to examine the impact of  $H_2O_2$  as an oxidizing agent on the desulfurization process of actual diesel fuel, experiments were conducted at a temperature of 30°C, keeping other parameters constant, as described in the caption to Fig. 6. The molar ratio between the petroleum model and the oxidant was 8:1, according to our previous study (Qader, et al., 2021). Depending on the particular monoprotic acid (DES) employed, the effectiveness of the sulfur removal from model petroleum products was improved by adding hydrogen peroxide ( $H_2O_2$ ). The findings show that when the  $H_2O_2$  catalyst was introduced, a maximum removal of 78% of the sulfur compounds could be achieved.

Previous research has demonstrated that the utilization of Fe NPs as a catalyst is significant in desulfurization when using  $H_2O_2$ . For example, the presence of Fe NPs in the organic phase resulted in a considerable reduction of sulfur compounds in diesel fuel, as shown when the concentration of  $Fe^{3+}$  was increased (Zhu, et al., 2012; Zhang, Zhang and Zhang, 2004). Consequently, this point was further examined in the current research. The catalytic role of  $Fe_3O_4$  in combination with  $H_2O_2$  enhances the extraction of sulfur by facilitating the oxidation of sulfur-containing compounds to more extractable forms. The generation of hydroxyl

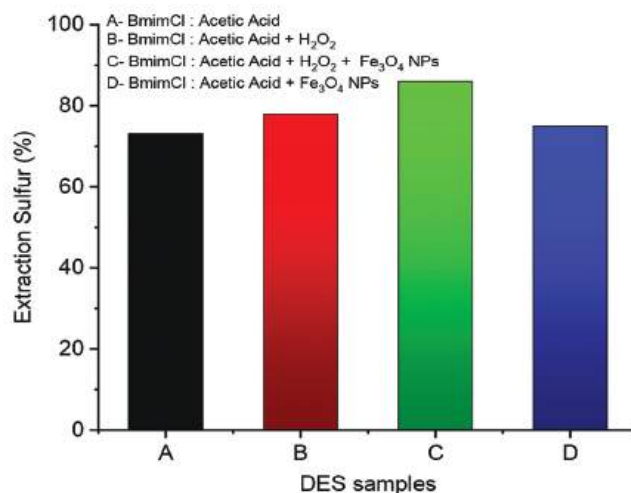


Fig. 6. Effect of  $H_2O_2$  and  $Fe_3O_4$  nanoparticles on sulfur removal. The extraction time was 60 min at 30°C whilst stirring at 500 rpm. The mass ratio of the model petroleum product (thiophene + dibenzothiophene in n-octane) to the deep eutectic solvent (1 BmimCl: 2 acetic acid) was 1:2.

radicals and other ROS accelerates the breakdown of the sulfur species, leading to improved extraction efficiency. This approach holds promise for more sustainable and efficient sulfur recovery processes (Liochev, 1996).

Fig. 6 illustrates the impact of adding  $Fe_3O_4$  on the effectiveness of sulfur removal. The addition of  $Fe_3O_4$  was found to significantly enhance the effectiveness of sulfur removal by up to 86%. This improvement could be attributed to the presence of Fe=O catalytic sites, which play a crucial role in activating iron superoxide for the oxidation reaction. Thus, the BmimCl: Acetic acid:  $H_2O_2$ :  $Fe_3O_4$  NP model yielded the most efficient desulfurization.

#### G. Regeneration of BmimCl: Acetic Acid

The recycling of the spent DES following extractive desulfurization is undeniably important (Jeong, et al., 2015). Fig. 7 shows the extractive desulfurization ability of sulfur species in model petroleum products into DES. The current experiment was conducted at 30°C and a stirring speed of 500 rpm for 60 min with a mass ratio for the DES (2 acetic acid + 1BmimCl) to the model petroleum product of 2:1.

After completing the extraction process for the sample, the DES (BmimCl: acetic acid) was regenerated and thereafter utilized for a maximum of three cycles. This shows that all such cycles allowed for the regeneration of the prepared DESs without any reduction in their sulfur-removal capability. We regenerated the BmimCl: acetic acid solvent employed through extraction using diethyl ether in a rotary evaporator. Each instance showed no alteration in the synthesized DES composition subsequent to recycling. Fig. 7 shows that using BmimCl: acetic acid as a DES for a minimum of three cycles does not reduce the extraction effectiveness. In addition, the synthesis of DESs is straightforward and does not require organic solvents, thereby mitigating the environmental repercussions associated with toxic organic solvents. These DESs are degradable and environmentally benign due to their

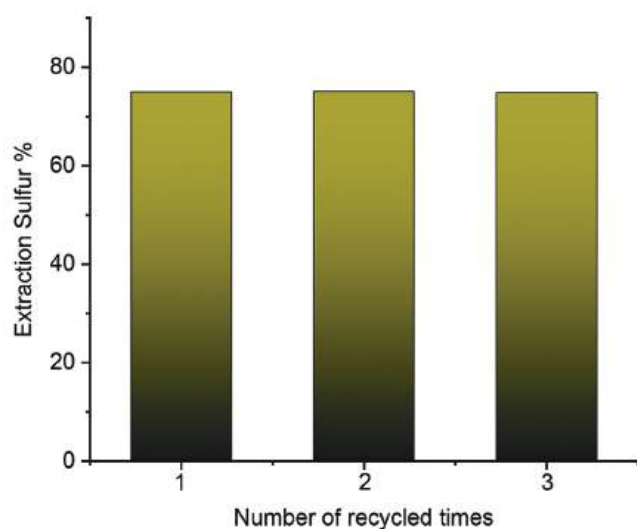


Fig. 7. Extraction performance with recycled BmimCl: Acetic acid. Reactions conditions: 2:1 mole ratio of deep eutectic solvent to model petroleum product (thiophene + dibenzothiophene in n-octane), 60 min reaction time. Stirring at 500 rpm, at a fixed temperature of 30°C.

components being interconnected through hydrogen bonding. The interacting components consist of environmentally friendly, readily accessible, and inexpensive raw materials. DESs benefit from this, as they can allow for extraction-desulfurization at ambient temperature and pressure, unlike the traditional HDS procedure, which requires elevated temperatures and pressures.

#### H. Characterization of $Fe_3O_4$ NPs

The synthesized  $Fe_3O_4$  NPs were characterized via the SEM, EDX, TEM, and FTIR techniques. In order to examine the various bonds and functional groups present in the  $Fe_3O_4$  NPs, an FTIR analysis was conducted, as depicted in Fig. 8. The features in the FTIR spectrum observed at about 3440 and 625  $cm^{-1}$  were indicative of the presence of  $Fe_3O_4$ , as illustrated in Fig. 8a. These peaks can be attributed to the bending vibrations of the O–H groups (due to solvent that has been adsorbed) and the stretching vibration of the Fe–O bonds, respectively. In addition, peaks were observed at about 1606 and 1388  $cm^{-1}$ , which could be attributed to out-of-plane and in-plane O–H vibrations (Babakir, et al., 2022; Qader, et al., 2023a).

When compared to Fig. 8b (after desulfurization), all the peaks associated with  $Fe_3O_4$  (described above) are observed at lower wavenumbers (3350, 1559, 1365, and 597  $cm^{-1}$ ) and exhibit reduced band intensities. In addition, numerous additional peaks were seen in the FTIR spectrum of  $Fe_3O_4$  during the process of desulfurization. The absorption peak located around 1511  $cm^{-1}$  corresponds to the vibration of a C=C bond in the thiophene and dibenzothiophene. The bands detected around 1175, 1042, and 783  $cm^{-1}$  represent a C–C vibration in an organic ring, an in-plane =C–H stretch, and an out-of-plane C–H bend, respectively, for thiophene and/or dibenzothiophene. The peaks observed at 1313 and 1365  $cm^{-1}$  correspond to the presence of an S=O bond in

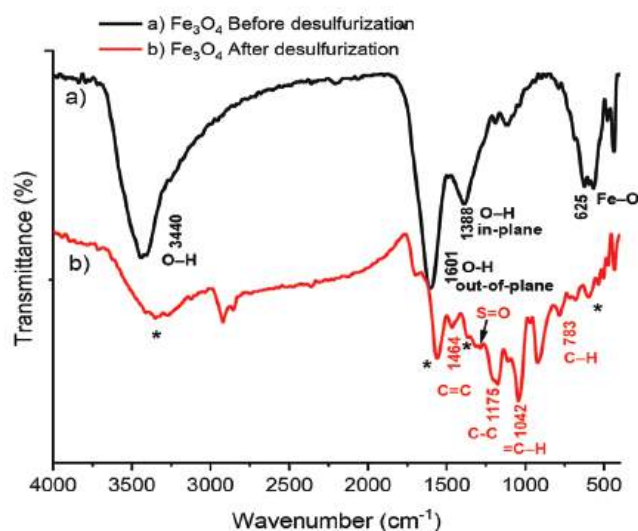


Fig. 8. Fourier-transform infrared spectroscopy spectra of  $Fe_3O_4$ , (a) before and (b) after the desulfurization process.

a sulfone and an organic sulfate compound, respectively, in thiophene and/or dibenzothiophene. Accordingly, the FTIR data confirmed that sulfur compounds (such as thiophene and dibenzothiophene) had been adsorbed onto the  $Fe_3O_4$  composite.

The surface morphologies and particle size of the  $Fe_3O_4$  composite were analyzed via SEM and TEM, as shown in Fig. 9, both before and after the desulfurization process. The surface of  $Fe_3O_4$  before desulfurization, shown in Fig. 9a has a uniform and porous structure made up of almost separate spherical formations. These spherical formations range in size from 5 nm to 50 nm, contributing to the nanostructure of the particles created. However, on desulfurization (Fig. 9b), the morphology of the  $Fe_3O_4$  surface changes (as compared to Fig. 9a) to show more irregular structures and smaller pores, indicating the presence of sulfur compounds on the surface of the  $Fe_3O_4$  nanocomposites.

Furthermore, the TEM image in Fig. 9c provides further proof of the porous nanostructure shape of  $Fe_3O_4$  particles smaller than 50 nm. The image reveals a semi-spherical, nearly hexagonal shape for  $Fe_3O_4$ . On the other hand, Fig. 9d shows a structure that is less porous, a result of the desulfurization process that occurred on the surface of  $Fe_3O_4$  and which is consistent with the SEM data.

In order to verify the successful formation of  $Fe_3O_4$  NPs and validate the adsorption of sulfur compounds onto the  $Fe_3O_4$  adsorbent surface, an EDX study was conducted, as shown in Fig. 9e and f. This research effectively demonstrates the presence of iron (Fe) and oxygen (O) atoms in the composition of the  $Fe_3O_4$  composite catalyst (Fig. 9e). The EDX spectra display the distinctive peaks of iron at 0.85 keV ( $L\alpha_1$ ) and 6.45 keV ( $K\alpha_1$ ), which is consistent with earlier findings (Kargar, et al., 2021; Luis, Behera and Sorokhaibam, 2023). The EDX spectrum (Fig. 9f) showed that after desulfurization, there was an extra peak associated with sulfur (S) at around 2.85 keV ( $K\alpha_1$ ), along with Fe, O, and N. This confirms the adsorption of sulfur compounds

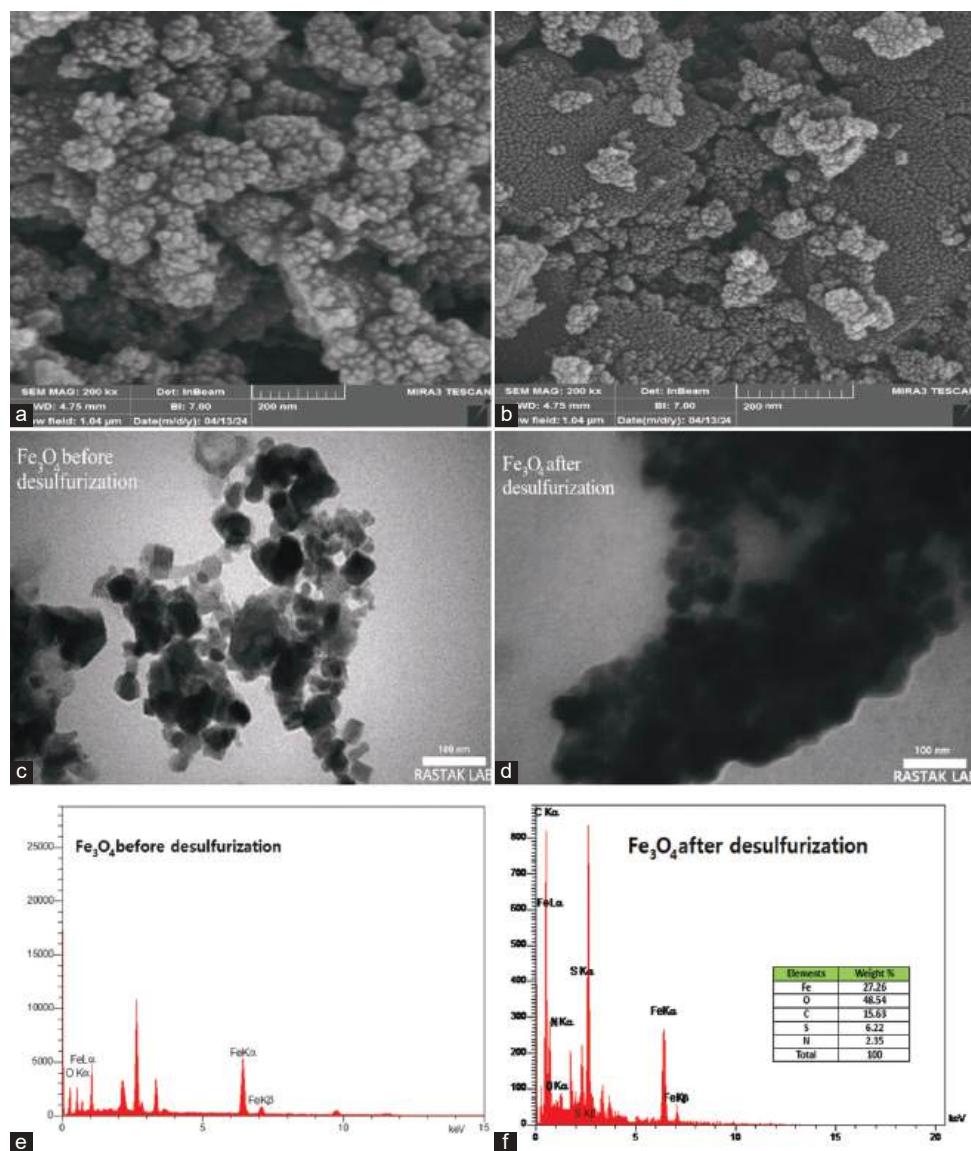


Fig. 9. (a and b) Scanning electron microscopy images of  $\text{Fe}_3\text{O}_4$  before and after the desulfurization process; (c and d) transmission electron microscopy images of  $\text{Fe}_3\text{O}_4$  before and after the desulfurization process; and (e and f) energy dispersive X-ray data of  $\text{Fe}_3\text{O}_4$  before and after the desulfurization process, respectively.

onto the adsorbent's surface, a process associated with the presence of thiophene and dibenzothiophene compounds in the petroleum model.

Following the desulfurization process, we can conclude that the FTIR, SEM, EDX, and TEM approaches provided clear evidence of the adsorption of sulfur compounds onto the  $\text{Fe}_3\text{O}_4$ 's spherical surface, thereby enhancing the removal of sulfur compounds from the petroleum models.

#### IV. CONCLUSION

This study involved the extraction of sulfur compounds from model petroleum products (thiophene and dibenzothiophene in n-octane) using liquid-liquid extraction in new types of DES. Two hydrogen bond donors, acetic acid and formic acid, were utilized to create DESs in various molar ratios with 1-butyl-3-methylimidazolium chloride (BmimCl), which served as

a quaternary ammonium salt. The hydrocarbon-based fuels (HBDs) used in this study play a crucial role in extraction procedures across various practical domains. Experiments were conducted to investigate the impact of monoprotic acids in HBDs, as well as the presence of oxidants ( $\text{H}_2\text{O}_2$ ) and  $\text{Fe}_3\text{O}_4$  in the petroleum model, on the process of desulfurization. Within the optimization parameters, we also examined the impact of temperature, reaction duration, and the mass ratio of DES to the petroleum model. The study's results indicate that increasing the temperature from  $20^\circ\text{C}$  to  $30^\circ\text{C}$  enhanced the removal of sulfur from the petroleum model into an acetic acid-containing DES. However, above  $30^\circ\text{C}$ , the removal of sulfur declined slightly.

Furthermore, the results show that the BmimCl:acetic acid:  $\text{H}_2\text{O}_2$ : $\text{Fe}_3\text{O}_4$  NP model successfully eliminated the largest proportion of sulfur, up to 86%, in 60 min at  $30^\circ\text{C}$  using 2:1 mass ratio of DES (1BmimCl: 2acetic) to model

petroleum product, owing to the synergistic impact of the materials and the absence of intramolecular hydrogen bonding in this composite. The synthesized  $\text{Fe}_3\text{O}_4$  was characterized using various techniques, including FTIR, SEM, EDX, and TEM. Following the desulfurization process, these approaches provided evidence of the presence of sulfur compounds on  $\text{Fe}_3\text{O}_4$ 's spherical surface, enhancing the removal of sulfur compounds from the petroleum models. Finally, the ability to regenerate the DES was tested over a series of repeated recovery cycles, which demonstrated that DESs may be regenerated without any decline in the sulfur removal potential after three desulfurization cycles. The results of this study have significant implications for potential future applications; specifically, they could be valuable in addressing environmental concerns by eliminating cancer-causing and corrosive substances in industrial operations.

#### ACKNOWLEDGMENT

The authors extend their appreciation to Hawler Medical University for funding this study. They also want to thank Erbil Polytechnic University's Scientific Research Centre for their help and for granting them access to their facilities.

#### REFERENCES

- Abbott, A.P., Ahmed, E.I., Prasad, K., Qader, I.B., and Ryder, K.S., 2017a. Liquid pharmaceuticals formulation by eutectic formation. *Fluid Phase Equilibria*, 448, pp.2-8.
- Abbott, A.P., Al-Murshedi, A.Y., Al-Shammari, O.A., Harris, R.C., Kareem, J.H., Qader, I.B., and Ryder, K., 2017b. Thermodynamics of phase transfer for polar molecules from alkanes to deep eutectic solvents. *Fluid Phase Equilibria*, 448, pp.99-104.
- Ahmad, W., UR Rahman, A., Ahmad, I., Yaseen, M., Mohamed Jan, B., Stylianakis, M.M., Kenankis, G., and Ikram, R., 2021. Oxidative desulfurization of petroleum distillate fractions using manganese dioxide supported on magnetic reduced graphene oxide as catalyst. *Nanomaterials (Basel)*, 11, p.203.
- Alabdullah, S.S., Ismail, H.K., Ryder, K.S., and Abbott, A.P., 2020. Evidence supporting an emulsion polymerisation mechanism for the formation of polyaniline. *Electrochimica Acta*, 354, p.136737.
- Alessary, H.F., Ismail, H.K., Kareem, J.H., Qader, I.B., Odda, A.H., Halbus, A.F., Athab, Z.H., Al-Yasari, A., Watkins, M.J., and Ryder, K.S., 2023. Characterization of the electrochemical deposition of aluminum from an  $\text{AlCl}_3$ : N-methylacetamide eutectic solvent modified with nicotinamide. *Surface and Coatings Technology*, 475, p.130160.
- Almashjary, K.H., Khalid, M., Dharaskar, S., Jagadish, P., Walvekar, R., and Gupta, T.C.S.M., 2018. Optimisation of extractive desulfurization using choline chloride-based deep eutectic solvents. *Fuel*, 234, pp.1388-1400.
- Al-Shahrani, F., Xiao, T., Llewellyn, S.A., Barri, S., Jiang, Z., Shi, H., Martinie, G., and Green, M.L.H., 2007. Desulfurization of diesel via the  $\text{H}_2\text{O}_2$  oxidation of aromatic sulfides to sulfones using a tungstate catalyst. *Applied Catalysis B: Environmental*, 73, pp.311-316.
- Babakir, B.A.M., Abd Ali, L.I., and Ismail, H.K., 2022. Rapid removal of anionic organic dye from contaminated water using a poly(3-aminobenzoic acid/graphene oxide/cobalt ferrite) nanocomposite low-cost adsorbent via adsorption techniques. *Arabian Journal of Chemistry*, 15, p.104318.
- Caero, L.C., Hernandez, E., Pedraza, F., and Murrieta, F., 2005. Oxidative desulfurization of synthetic diesel using supported catalysts: Part I. Study of the operation conditions with a vanadium oxide based catalyst. *Catalysis Today*, 107-108, pp.564-569.
- Chandran, D., Khalid, M., Walvekar, R., Mubarak, N.M., Dharaskar, S., Wong, W.Y., and Gupta, T.C.S.M., 2019. Deep eutectic solvents for extraction-desulfurization: A review. *Journal of Molecular Liquids*, 275, p.312-322.
- De Luna, M.D.G., Samaniego, M.L., Ong, D.C., Wan, M.W., and Lu, M.C., 2018. Kinetics of sulfur removal in high shear mixing-assisted oxidative-adsorptive desulfurization of diesel. *Journal of Cleaner Production*, 178, p.468-475.
- Eßer, J., Wasserscheid, P., and Jess, A., 2004. Deep desulfurization of oil refinery streams by extraction with ionic liquids. *Green Chemistry*, 6, p.316-322.
- Gano, Z.S., Mjalli, F.S., Al-Wahaibi, T., and Al-Wahaibi, Y., 2015. The novel application of hydrated metal halide ( $\text{SnCl}_4 \cdot 2\text{H}_2\text{O}$ )-based deep eutectic solvent for the extractive desulfurization of liquid fuels. *Journal of Chemical Engineering and Applications*, 6, pp.367-371.
- Gao, S., Li, J., Chen, X., Abdeltawab, A.A., Yakout, S.M., and Yu, G., 2018. A combination desulfurization method for diesel fuel: Oxidation by ionic liquid with extraction by solvent. *Fuel*, 224, pp.545-551.
- Hillman, A.R., Ryder, K.S., Ismail, H.K., Unal, A., and Voorhaar, A., 2017. Fundamental aspects of electrochemically controlled wetting of nanoscale composite materials. *Faraday Discussions*, 199, pp.75-99.
- Humadi, J.I., Aabid, A.A., Mohammed, A.E., Ahmed, G.S., and Abdulqader, M.A., 2024. New design of eco-friendly catalytic electro-photo desulfurization process for real diesel fuel. *Chemical Engineering Research and Design*, 206, pp.285-301.
- Ismail, H.K., Alesary, H.F., Juma, J.A., Hillman, A.R., and Ryder, K.S., 2022a. A comparative study of the formation, and ion and solvent transport of polyaniline in protic liquid-based deep eutectic solvents and aqueous solutions using EQCM. *Electrochimica Acta*, 418, p.140348.
- Ismail, H.K., 2020. Electrodeposition of a mirror zinc coating from a choline chloride-ethylene glycol-based deep eutectic solvent modified with methyl nicotinate. *Journal of Electroanalytical Chemistry*, 876, p.114737.
- Ismail, H.K., Qader, I.B., Alesary, H.F., Kareem, J.H., and Ballantyne, A.D., 2022b. Effect of graphene oxide and temperature on electrochemical polymerization of pyrrole and its stability performance in a novel eutectic solvent (choline chloride-phenol) for supercapacitor applications. *ACS Omega*, 7, pp.34326-34340.
- Jeong, K.M., Lee, M.S., Nam, M.W., Zhao, J., Jin, Y., Lee, D.K., Kwon, S.W., Jeong, J.H., and Lee, J., 2015. Tailoring and recycling of deep eutectic solvents as sustainable and efficient extraction media. *Journal of Chromatography A*, 1424, pp.10-17.
- Jiang, W., Li, H., Wang, C., Liu, W., Guo, T., Liu, H., Zhu, W., and Li, H., 2016. Synthesis of ionic-liquid-based deep eutectic solvents for extractive desulfurization of fuel. *Energy and Fuels*, 30, pp.8164-8170.
- Kareem, J.H., 2017. *Sulfur Extraction from Oil Using Ionic Liquids*. University of Leicester, England.
- Kargar, H., Ghahramaninezhad, M., Shahrak, M.N., and Balula, S.S., 2021. An effective magnetic catalyst for oxidative desulfurization of model and real fuels:  $\text{Fe}_3\text{O}_4/\text{ZIF-8}/\text{TiO}_2$ . *Microporous and Mesoporous Materials*, 317, p.110992.
- Khan, I., Saeed, K., and Khan, I., 2019. Nanoparticles: Properties, applications and toxicities. *Arabian Journal of Chemistry*, 12, pp.908-931.
- Kiran, N., Abro, R., Abro, M., Shah, A.A., Jatoti, A.S., Bhutto, A.W., Qureshi, K., Sabzoi, N., Gao, S., and Yu, G., 2019. Extractive desulfurization of gasoline using binary solvent of bronsted-based ionic liquids and non-volatile organic compound. *Chemical Papers*, 73, pp.2757-2765.
- Li, C., Zhang, J., Li, Z., Yin, J., Cui, Y., Liu, Y., and Yang, G., 2016. Extraction desulfurization of fuels with 'metal ions' based deep eutectic solvents (MDESs). *Green Chemistry*, 18, pp.3789-3795.

- Liochev, S.I., 1996. Commentary: The role of iron-sulfur clusters in *in vivo* hydroxyl radical production. *Free Radical Research*, 25, pp.369-384.
- Luis, M., Behera, P., and Sorokhaibam, L.G., 2023. Magnetic iron nanoparticles ( $\text{Fe}_3\text{O}_4$ ) supported on activated carbon as a hybrid adsorbent for desulphurisation of liquid fuels. *International Journal of Environmental Analytical Chemistry*, 103, pp.2659-2680.
- Mohammed, A.E., Mohammed, W.T., and Gheni, S.A., 2024. Environmental benefits of agricultural waste-derived catalysts in diesel desulfurization: A review. *Cleaner Materials*, 13, p.100262.
- Norouzi, O., Jafarian, S., Safari, F., Tavasoli, A., and Nejati, B., 2016. Promotion of hydrogen-rich gas and phenolic-rich bio-oil production from green macroalgae *Cladophora glomerata* via pyrolysis over its bio-char. *Bioresource Technology*, 219, pp.643-651.
- Paucar, N.E., Kiggins, P., Blad, B., De Jesus, K., Afrin, F., Pashikanti, S., and Sharma, K., 2021. Ionic liquids for the removal of sulfur and nitrogen compounds in fuels: A review. *Environmental Chemistry Letters*, 19, pp.1205-1228.
- Qader, I.B., 2021. Enhance dissolution rate and solubility of solid drugs through pharmaceutical deep eutectic solvents. *Zanco Journal of Pure and Applied Sciences*, 33, pp.98-106.
- Qader, I.B., Ganjo, A.R., Ahmad, H.O., Qader, H.A., and Hamadameen, H.A., 2024. Antibacterial and antioxidant study of new pharmaceutical formulation of didecyldimethylammonium bromide via pharmaceutical deep eutectic solvents (PDESs) principle. *AAPS PharmSciTech*, 25, p.25.
- Qader, I.B., Isamil, H.K., Alesary, H.F., Kareem, J.H., Maaroo, Y.T., and Barton, S., 2023a. Electrochemical sensor based on polypyrrole/triiron tetraoxide (PPY/ $\text{Fe}_3\text{O}_4$ ) nanocomposite deposited from a deep eutectic solvent for voltammetric determination of procaine hydrochloride in pharmaceutical formulations. *Journal of Electroanalytical Chemistry*, 951, p.117943.
- Qader, I.B., Kareem, J.H., Ismail, H.K., and Mahmood, H.K., 2021. Novel phenolic deep eutectic solvents for desulfurisation of petrodiesel. *Karbala International Journal of Modern Science*, 7, p.12.
- Qader, I.B., Laguerre, M., Lavaud, A., Tenon, M., Prasad, K., and Abbott, A.P., 2023b. Selective Extraction of antioxidants by formation of a deep eutectic mixture through mechanical mixing. *ACS Sustainable Chemistry and Engineering*, 11, pp.4168-4176.
- Qu, W., Qader, I.B., and Abbott, A.P., 2022. Controlled release of pharmaceutical agents using eutectic modified gelatin. *Drug Delivery and Translational Research*, 12, pp.1187-1194.
- Shiraishi, Y., Tachibana, K., Hiral, T., and Komasa, I., 2002. Desulfurization and denitrogenation process for light oils based on chemical oxidation followed by liquid-liquid extraction. *Industrial and Engineering Chemistry Research*, 41, pp.4362-4375.
- Tahir, S., Qazi, U.Y., Naseem, Z., Tahir, N., Zahid, M., Javaid, R., and Shahid, I., 2021. Deep eutectic solvents as alternative green solvents for the efficient desulfurization of liquid fuel: A comprehensive review. *Fuel*, 305, p.121502.
- Tang, X.D., Zhang, Y.F., Li, J.J., Zhu, Y.Q., Qing, D.Y., and Deng, Y.X., 2015. Deep extractive desulfurization with arenium ion deep eutectic solvents. *Industrial and Engineering Chemistry Research*, 54, pp.4625-4632.
- Wang, X., Jiang, W., Zhu, W., Li, H., Yin, S., Chang, Y., and Li, H., 2016. A simple and cost-effective extractive desulfurization process with novel deep eutectic solvents. *RSC Advances*, 6, pp.30345-30352.
- Yang, W., Guo, G., Mei, Z., and Yu, Y., 2019. Deep oxidative desulfurization of model fuels catalysed by immobilized ionic liquid on MIL-100(Fe). *RSC Advances*, 9, pp.21804-21809.
- Zhang, L., Wang, J., Sun, Y., Jiang, B., and Yang, H., 2017. Deep oxidative desulfurization of fuels by superbase-derived Lewis acidic ionic liquids. *Chemical Engineering Journal*, 328, pp.445-453.
- Zhang, S., Zhang, Q., and Zhang, Z.C., 2004. Extractive desulfurization and denitrogenation of fuels using ionic liquids. *Industrial and Engineering Chemistry Research*, 43, pp.614-622.
- Zhu, W., Wang, C., Li, H., Wu, P., Xun, S., Jiang, W., Chen, Z., Zhao, Z., and Li, H., 2015. One-pot extraction combined with metal-free photochemical aerobic oxidative desulfurization in deep eutectic solvent. *Green Chemistry*, 17, pp.2464-2472.
- Zhu, W., Zhang, J., Li, H., Chao, Y., Jiang, W., Yin, S., and Liu, H., 2012. Fenton-like ionic liquids/ $\text{H}_2\text{O}_2$  system: One-pot extraction combined with oxidation desulfurization of fuel. *RSC Advances*, 2, pp.658-664.
- Zolotareva, D., Zazybin, A., Rafikova, K., Dembitsky, V.M., Dauletbaev, A., and Yu, V., 2019. Ionic liquids assisted desulfurization and denitrogenation of fuels. *Vietnam Journal of Chemistry*, 57, pp.133-163.

## General Information

**ARO's Mission:** ARO seeks to publish those papers that are most influential in their fields or across fields and that will significantly advance scientific understanding. Selected papers should present novel and broadly important data, syntheses, or concepts. They should merit the recognition by the scientific community and general public provided by publication in ARO, beyond that provided by specialty journals.

We welcome submissions from all fields of natural science and technology, and from any source. We are committed to the prompt evaluation and publication of submitted papers. ARO is published biannually; selected papers are published online ahead of print.

### Submission

Manuscripts should be submitted by the correspondent authors of the manuscript via the on-line submission page. Regardless of the source of the word-processing tool, only electronic Word (.doc, .docx, .rtf) files can be submitted on-line. There is no page limit. Only online submissions are accepted to facilitate rapid publication and minimize administrative costs. Submissions by any other one but the authors will not be accepted. The submitting author takes responsibility for the paper during submission and peer review. If for some technical reason submission through the email is not possible, the author can contact [aro.journal@koyauniversity.org](mailto:aro.journal@koyauniversity.org) for support. Before submitting, please check ARO's guide to authors thoroughly to avoid any delay in the review and publication process.

Authors are explicitly responsible for the language of their texts. Paper should be submitted in a well written in understandable English. Authors should not expect the editor or editorial board to rewrite their paper. Prior to submission, authors should have their paper proofread by a possible academic native speaker of English.

- Submit the Article with contact Information
- File name should be your article title
- Don't submit your article in multiple journals, we are taking only minimum time for the review process. please don't waste our time
- Once the paper is accepted, it can't be withdrawn
- Please follow publication ethics and regulation
- Avoid plagiarism and copied material
- Strictly Follow ARO's template

### Terms of Submission

Papers must be submitted on the understanding that they have not been published elsewhere and are not currently under consideration by another journal or any other publisher. ARO accepts original articles with novel impacts only. Post conference papers are not accepted "as is", however, regular papers on the same topic but with a different title can be submitted. The new paper should contain significant improvements in terms of extended content, analysis, comparisons with popular methods, results, figures, comments, etc. Please do not forget that the publication of the same or similar material in ARO constitutes the grounds for filing an (auto) plagiarism case.

The submitting author is responsible for ensuring that the article's publication has been approved by all the other co-authors. It is also the authors' responsibility to ensure that the articles emanating from a particular institution are submitted with the approval of the necessary institution. Only an acknowledgement from the editorial office officially establishes the date of receipt. Further correspondence and proofs will be sent to the author(s) before publication unless otherwise indicated. It is a condition of submission of a paper that the authors permit editing of the paper for readability. All enquiries concerning the publication of accepted papers should be addressed to [aro.journal@koyauniversity.org](mailto:aro.journal@koyauniversity.org).

## **Peer Review**

All manuscripts are subject to peer review and are expected to meet standards of academic excellence. Submissions will be considered by an editor and “if not rejected right away” by peer-reviewers, whose identities will remain anonymous to the authors.

## **Guide to Author**

We welcome submissions from all fields of science and from any source. We are committed to the prompt evaluation and publication of submitted papers. Selected papers are published online ahead of print. Authors are encouraged to read the instructions below before submitting their manuscripts. This section is arranged into an overview of the of the speedy guidelines below and is more detailed in the bottom section of this page.

## **Manuscript Preparation**

Submitting your manuscript will be in two stages namely before final acceptance and after.

### ***Stage One:***

For the initial submission, the manuscript should be prepared electronically in Microsoft Word (.doc, .docx, .rtf) and PDF formats. Submit it through the online submission system after completing the registration. The Word file should be in a single-column format, double-spaced, with Times New Roman font, and 12-point font size. The authors' names and affiliations should be removed from the manuscript for the double-blind review process. Referencing and citation should follow the Harvard/ARO system. You can download the stage-one manuscript template by clicking [here](#).

### ***Stage Two:***

Once the manuscript is accepted, the production team of ARO Journal will prepare the camera-ready paper.

## **Units of Measurement**

Units of measurement should be presented simply and concisely using System International (SI) units.

## **Title and Authorship Information**

The following information should be included;

- Paper title.
- Full author names.
- Affiliation.
- Email addresses.

## **Abstract**

The manuscript should contain an abstract. The abstract should be self-contained and citation-free and should not exceed 250 words.

## **Introduction**

This section should be succinct, with no subheadings.

## **Materials and Methods**

This part should contain sufficient detail so that all procedures can be repeated. It can be divided into subsections if several methods are described.

## **Results and Discussion**

This section may each be divided by subheadings or may be combined.

## **Conclusions**

This should clearly explain the main conclusions of the work highlighting its importance and relevance.

## **Acknowledgements**

All acknowledgements (if any) should be included at the very end of the paper before the references and may include supporting grants, presentations, and so forth.

## **References**

References must be included in the manuscript and authors are responsible for the accuracy of references. Manuscripts without them will be returned. ARO is following Harvard System of Referencing. (Learn how to import and use Harvard Styling in your Microsoft Office by following this link:

<http://bibword.codeplex.com/releases/view/15852>)

## **Preparation of Figures**

Upon submission of an article, authors are supposed to include all figures and tables in the PDF file of the manuscript. Figures and tables should be embedded in the manuscript. Figures should be supplied in either vector art formats (Illustrator, EPS, WMF, FreeHand, CorelDraw, PowerPoint, Excel, etc.) or bitmap formats (Photoshop, TIFF, GIF, JPEG, etc.). Bitmap images should be of 300 dpi resolution at least unless the resolution is intentionally set to a lower level for scientific reasons. If a bitmap image has labels, the image and labels should be embedded in separate layers.

## **Preparation of Tables**

Tables should be cited consecutively in the text. Every table must have a descriptive title and if numerical measurements are given, the units should be included in the column heading. Vertical rules should not be used.

## **Copyright**

Open Access authors retain the copyrights of their papers, and all open access articles are distributed under the terms of the Creative Commons Attribution License, which permits unrestricted use, distribution and reproduction in any medium, provided that the original work is properly cited.

The use of general descriptive names, trade names, trademarks, and so forth in this publication, even if not specifically identified, does not imply that these names are not protected by the relevant laws and regulations.

While the advice and information in this journal are believed to be true and accurate on the date of its going to press, neither the authors, the editors, nor the publisher can accept any legal responsibility for any errors or omissions that may be made. The publisher makes no warranty, express or implied, with respect to the material contained herein.



## ARO Reviewer/Associate Editor Application Form

ARO is a scientific journal of Koya University (p-ISSN: 2410-9355, e-ISSN: 2307-549X) which aims to offer a novel contribution to the study of Science. The purpose of ARO is twofold: first, it will aim to become an ongoing forum for debate and discussion across the sciences and Engineering. We hope to advance our problem-solving capacity and deepen our knowledge regarding a comprehensive range of collective actions. Second, ARO accepts the challenges brought about by multidisciplinary scientific areas and aspires to expand the community of academics who are able to learn from and help to produce advances in a variety of different disciplines.

The Journal is seeking reviewers who can provide constructive analysis of papers thus enhancing the overall reputation of the Journal. If any expert is interested in participating in the review process, we highly encourage you to sign up as a reviewer for our Journal and help us improve our presence in the domain of your expertise. Appropriate selection of reviewers who have expertise and interest in the domain relevant to each manuscript are essential elements that ensure a timely, productive peer review process. We require proficiency in English.

### How to apply

To apply for becoming a reviewer of ARO, please submit the application form by following the link:

<https://aro.koyauniversity.org/user/register>

To apply for becoming a member of the Editorial Board of ARO, please submit the application form by completing the [application form](#).

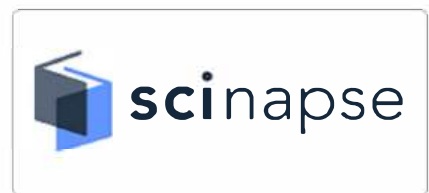
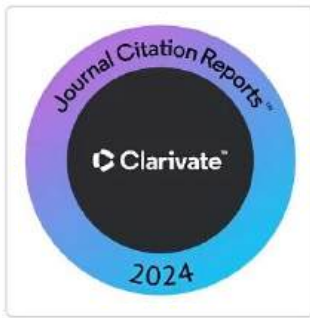
Both Associate Editor and Reviewers should specify their areas of research and expertise. Applicants must have a doctorate (or an equivalent degree), and if Master degree they need to have significant publishing experience. Please note that;

- You will need to write your full official name.
- Please provide an email which reflects your official name, such as nameOne.NameTwo@... , or your institute's official email.
- All data need to be written in English.

**Note:** For more information, kindly visit the following websites:

1. [aro.koyauniversity.org](http://aro.koyauniversity.org).
2. <http://libweb.anglia.ac.uk/referencing/harvard.htm>.
3. <http://bibword.codeplex.com/releases/view/15852>.







Koya University is a young University established in 2003 and it is located in the city of Koya (Koysinjaq), short distance to the East of regional capital city of Erbil (Arbil, Hewlêr) in Kurdistan Region of Iraq. It is on the foothills of beautiful High Mountain. Its campus has been carefully laid out to embrace the beautiful mountainous nature. The Koya University has a Faculty system which enhances the interactions between similar academic fields. Today, Koya University has four Faculties: Engineering, Science and Health, Humanities and Social Sciences and Education in addition to the School of Medicine, which all consist of twenty-five scientific departments in different fields, such as Petroleum Engineering, Geotechnical Engineering, Software Engineering, Physics, Chemistry, Clinical Psychology, Social Science, Medical Microbiology and Sport Education.

ARO-The Scientific Journal of Koya University is a biannual journal of original scientific research, global news, and commentary in the areas of Science and Technology. ARO is a Peer-reviewed Open Access journal with CC BY-NC-SA 4.0 license. It provides immediate, worldwide and barrier-free access to the full text of research articles without requiring a subscription to the journal, and has no article processing charge (APC). ARO Journal seeks to publish those papers that are most influential in their fields or across fields and that will significantly advance scientific understanding. ARO Journal is a member of ROAD and Crossref agencies and has got ESCI, DOAJ seal, SHERPA/RoMEO deposit policy, and LOCKSS archiving policy.

**ARO**

---

The Scientific Journal of Koya University

---

Koya University (KOU)  
University Park  
Danielle Mitterrand Boulevard  
Koya KOY45, Kurdistan Region - Iraq